

National Seminar

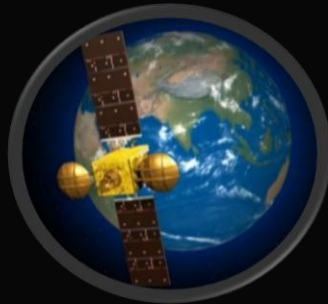
on

Recent Advances in Geospatial Technology & Applications

(for Post-graduate Students and Research Scholars)

March 2, 2020

Dehradun



Proceedings

iirs

Jointly organised by



**Indian Institute of Remote Sensing
&**

**Indian Society of Remote Sensing
(Dehradun Chapter)**

Hosted by

Indian Institute of Remote Sensing
Indian Space Research Organisation
Department of Space, Govt. of India
Dehradun

www.iirs.gov.in

National Seminar

on

Recent Advances in Geospatial Technology & Applications

(for Post-graduate Students and Research Scholars)

March 2, 2020

Dehradun



Proceedings

iirs

Jointly organised by



**Indian Institute of Remote Sensing
&
Indian Society of Remote Sensing
(Dehradun Chapter)**

Hosted by

Indian Institute of Remote Sensing
Indian Space Research Organisation
Department of Space, Govt. of India
Dehradun

www.iirs.gov.in

Dr. Prakash Chauhan
Director, IIRS



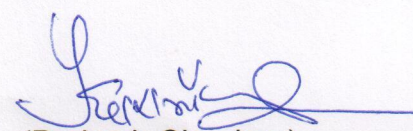
FOREWORD

It is with deep satisfaction that I am writing this foreword to the Proceedings of the National Seminar on “**Recent Advances in Geospatial Technology & Applications**” jointly organised by Indian Institute of Remote Sensing (IIRS) and Indian Society of Remote Sensing-Dehradun Chapter (ISRS-DC) on March 2, 2020. It was the unique initiative where the Institute (IIRS) and the Society (ISRS-DC) have come together to facilitate the young researchers to share, learn and gain experience. It has provided a forum where Post Graduate students and Research Scholars had opportunity to share their research work with the peers and furthermore to gain knowledge through interaction with experts in their discipline. The participants also learnt the data gaps and opportunities in Geospatial technologies & applications in the light of new challenges brought about by rapid urbanisation, depleting natural resources, climate change and so on and to bring resilience in the community.

I am hopeful that the research papers contained in this Seminar Proceedings shall be helpful for better understanding of the Earth and its environment and to devise suitable solutions using Geospatial Technologies. It will also encourage young researchers towards understanding the application potential of newer remote sensing data products.

We thank all authors and participants for their contribution.

Dated: June 30, 2020


(Prakash Chauhan)

Dr. S. K. Srivastav

Chairman, ISRS-DC (2018-20)



PREFACE

Indian Society of Remote Sensing - Dehradun Chapter (ISRS-DC) and Indian Institute of Remote Sensing (IIRS) jointly organised the National Seminar on “Recent Advances in Geospatial Technology & Applications” on March 2, 2020 for the postgraduate students and research scholars. It was one of the unique activities undertaken to provide an opportunity for young students and research scholars to showcase their research findings in front of their peers.

An overwhelming response was received from the student community, wherein total 72 participants attended the seminar. Total 64 papers were presented in the oral and poster sessions addressing various topics relevant to Earth observation, geospatial technology and their applications towards better understanding the Earth system processes and enhancing societal development. The papers presented were in general of high quality. The authors of a few select papers from both oral and poster sessions, as adjudicated by a panel of subject experts, were awarded by the ISRS-DC and IIRS. In addition, a few awards were also given away by the HEXAGON Geospatial.

I am happy to note that the organizing committee has brought out the proceedings of the seminar which consists of full papers presented by the young researchers. I congratulate all the authors for successfully presenting their research before the peers and experts and also thank them for writing the full paper for publication in the proceedings.

My appreciations to the organizing team for doing a commendable job in bringing out the proceedings. I am sure that it will serve as a good reference material for the researchers.

Dated: July 17, 2020


(S. K. Srivastav)

From Organising Committee (Core-team)

National Seminar on ‘Recent Advances in Geospatial Technology & Applications’ was jointly organised by Indian Institute of Remote Sensing (IIRS), ISRO, Dehradun and Indian Society of Remote Sensing-Dehradun Chapter (ISRS-DC) on March 2, 2020 at IIRS campus. It has provided a platform to Postgraduate Students and Research Scholars to participate and present their research work to geospatial community assembled at IIRS from all over the country. The Seminar has received huge response as large number of abstracts were received for presentation in the Seminar. The abstracts submitted were reviewed by an inter-disciplinary committee and accepted for presentation in the Seminar. Sixty-four papers were presented in six oral sessions: (i) Theme-1: Geospatial Technology & Recent Advances, ii) Theme-2: Geospatial Applications in Agriculture, Soils and Forestry Sciences, iii) Theme-3: Geospatial Applications in Atmospheric & Marine Sciences, iv) Theme-4: Geospatial Applications in Geosciences and Disaster Management, v) Theme-5: Geospatial Applications in Urban & Regional Development and vi) Theme-6: Geospatial Applications in Water Resources; and a multi-disciplinary Interactive Seminar Poster Session. Best papers presented in the Seminar were awarded by IIRS and ISRS-DC, and by a geospatial industry, M/S Hexagon Geospatial.

We express our deepest appreciation to all the abstract contributors, paper presenters, attendees and full paper authors for submitting abstracts/full papers and participation in the Seminar. It is because of their sheer hard work that we have been able to publish the Seminar Proceedings. The forty-four research papers contained in this Proceeding have not been peer reviewed and the authors were suggested to prepare their papers according to International Society for Photogrammetry and Remote Sensing (ISPRS) guidelines. We would like to thank all review committee members for their efforts in reviewing the abstracts. We are grateful to all the session chairs, co-chairs and rapporteurs for conducting the sessions. We would like to thank the Evaluation Committee for their efforts in evaluating presentations and selecting best papers from the seminar. We are grateful to the members of various Committees of this Seminar for their efforts. We express our sincerest gratitude to Dr. R. R. Navalgund, Honorary Distinguished Professor, ISRO and former Director, National Remote Sensing Centre (NRSC) and Space Applications Centre (SAC) for his kind presence and guidance to all of us. We are grateful to Dr. Prakash Chauhan, Director, IIRS, Dehradun and Dr. S.K. Srivastav, Chairman, ISRS-DC for providing guidance, infrastructure and financial support for organising the National Seminar on ‘Recent Advances in Geospatial Technology & Applications’ at IIRS Dehradun.

Pramod Kumar, Dr. Bhaskar R. Nikam and Ms. Asfa Siddiqui

INDEX

Sl. No.	Research Paper	Author(s)	Page no.
THEME-1: Geospatial Applications in Geosciences and Natural Hazards			
1.	Automatic Flood Mapping Using Sentinel-1 GRD SAR Images and Google Earth Engine: A Case Study of Darbhanga, Bihar <i>Antony Joh Moothedan, Pankaj R. Dhote, Praveen K. Thakur, Vaibhav Garg, S. P. Aggarwal, Manaruchi Mohapatra</i>		1
2.	Estimation of Soil Erosion Using Geospatial Tools: A Case Study of Indravati Basin, Chhattisgarh <i>Mohit Dipeshbhai Jani, Praveen K. Thakur, Arpit Chouksey, Bhaskar R. Nikam, S.P. Aggarwal</i>		5
3.	Applications of Remote Sensing and Photogrammetry Techniques in Landslide Investigation Around Guruda- Odisha <i>Lynette Dias, Yengkhom Kesorjit S.</i>		10
4.	Monitoring Forest Fire Progression During Fire Season in Parts of Tehri and Pauri District Using Normalized Burnt Ratio Index <i>Shailja Mamgain, Disha Chauhan, Krishna Das, Arijit Roy</i>		13
5.	Drought Monitoring Using Gravity Recovery and Climate Experiment over Marathwada Region <i>S. M. Bhere, G.K. Patil</i>		19
6.	Analysis of Uttarakhand Forest Fire with Landsat 8 Imagery for Years 2015 to 2019: A Case Study of Pauri District <i>Pooja Dobhal, Rishi Prakash and Nitin Mishra</i>		24
7.	Importance of Geographic Information System (GIS) to Evaluate Seismic Damage State and Damage Probability of RC Building Structure <i>P. Shil, A. Chourasia, S. Singhal, Rabindranatha</i>		31
8.	Inventory of Glacial Lakes & Detection of Potentially Dangerous Lakes for GLOF using Remote Sensing & GIS in Pithoragarh District of Uttarakhand, India <i>Sanjay Kumar Dwivedi, Arvind Pandey, Gaurav Joshi, Sachin Pandey, Nirmala Sharma</i>		36

Sl. No.	Research Paper	Author(s)	Page no.
THEME-2: Geospatial Applications in Urban & Regional Development			
9.	Reviewing the Importance of three Dimensional Mapping of Underground Utilities in Bihta, Bihar <i>Amit Kumar</i>		42
10.	Assessing the Thermal Behaviour of Urban Materials Using Hyperspectral Data in Ahmedabad City, India <i>Gautami Kushwaha, Asfa Siddiqui, Vinay Kumar</i>		45
11.	Study of Heat Waves and Urban Heat Island Interaction in a Single Frame Using Regional Climate Model: WRF-Urban <i>Priyanka Rao, Kshama Gupta, Arijit Roy, Ashutosh K. Jha, Prashant Kumar</i>		51
12.	Study of LST, NDVI and its Correlation with LULC For Urban Heat Island Analysis of Vadodara, Gujarat <i>Riddhi Joshi, Mithil Modha, Manik H. Kalubarme</i>		56
13.	Use of GIS for Study of Urban form of Historic Towns in Karnataka <i>M. Kashkari and T. S. Brar</i>		64
14.	Trends of Macro and Micro-Urbanization: A Case Study of Bhubaneswar-Cuttack Twin City <i>Srutisudha Mohanty, Jagabandhu Panda and Sudhansu S. Rath</i>		70
15.	Assessment of Water Resource in Gurugram - A Case Study of Areas Developed by Private Developers <i>R. A. Dehade, T. S. Brar, S. Singh</i>		76
16.	Impact of Changing Land use on Ground water: Case Study of Alwar Urban Area <i>Ila Pant, Nikhita Bajaj</i>		81
17	Accuracy Assessment of Open Accessible Digital Elevation Models in Urban Areas <i>Esther Metilda, Shweta Khatriker, Ashutosh Bhardwaj, Kshama Gupta</i>		88
THEME-3: Geospatial Technology & Recent Advances			
18.	Development of Web Based Framework for Health Disorder Analysis Using Open Data Kit: A Heath GIS Approach <i>Souvik Sankar Mitra, Abhinanda Saikia, Anuvi Rawat, Priyanka Rao, Shiva Reddy Koti</i>		94

Sl. No.	Research Paper	Author(s)	Page no.
19	Web Based Information System Using GIS for Rural Development <i>Ashish Mani, Dharmendra Kumar, Deepak Kumar</i>		98
20.	Analysis of Multiple Component Scattering Model Decomposition <i>Bhanu Prakash M. E., Shashi Kumar</i>		107
21.	Visualization of UNESCO World Heritage Site on Web Geoportal to Aid for Future Excavation <i>Chandan Grover, Esha Semwal, Saumyata Srivastava, Hina Pande, Poonam S Tiwari, S. Raghavendra, S. Agrawal</i>		111
22.	Analysis of Back-Scattering Coefficient of Novasar-1 S-Band SAR Datasets for Different Land Cover <i>Ojasvi Saini, Ashutosh Bhardwaj and R. S. Chatterjee</i>		116
23.	Scene Level Land-Cover Classification of Satellite Images Using Deep Learning <i>Shraddha P. Marbhal, Minakshi Kumar</i>		123
24.	Development of Web Based Co-registration Tool for Large Point Cloud Using WebGL Based Renderer <i>Souvik Sankar Mitra, Raghavendra S.</i>		127
25.	Implementation Of Semantic Segmentation on UAVSAR Data <i>Rajat Garg, Anil Kumar, and Shashi Kumar</i>		131
26.	Scientometric Review of Publications on Geospatial Technology <i>Rishabh Singh, Sudhakar Shukla</i>		134
27.	Performance Analysis of Terrestrial Laser Scanners for Point Cloud Integration <i>Saumyata Srivastava, Esha Semwal, Chandan Grover, Hina Pande, Poonam S Tiwari, S. Raghavendra, S. Agrawal</i>		138
THEME-4: Geospatial Applications in Water Resources			
28.	Optimal Location of Smart Water Meters & Hotspot Analysis of Excessive Water Consumption: A Case Study of IIT, Bombay <i>Ali Nasir Bandukwala, Sana Firdaus</i>		144
29.	Cloud-Based Approach for Continuous Monitoring and Assessment of Inland and Estuarine Water Environments Using Sentinel-3 OLCI Data		151

Sl. No.	Research Paper	Author(s)	Page no.
	<i>Chintan B. Maniyar, Abhishek Kumar, Deepak R. Mishra</i>		
30.	Vulnerability Assessment of Arsenic in Groundwater and its Occurrence in Districts of Bihar, India <i>S. Dhamija1, H. Joshi</i>		158
31.	Streamflow Modelling of Pindar River Basin, Central Himalaya using Remote Sensing Data and Temperature Index Model <i>Ningombam Prikash Meetei, Rajeev Saran Ahluwalia, S D Khobragade, Shushanta Sarangi, S.P Rai, Sanjay K Jain</i>		165
32.	Water Harvesting Systems of the Past- A Case Study of Badami, India <i>Mythrayi Harshavardhan, Kuili Suganya</i>		170
33.	Generation of Historic, Present and Future Snow Cover Datasets Using Modelling Approach <i>Vishal Sharma, Bhaskar R. Nikam, Praveen K. Thakur, S. P. Aggarwal, Vaibhav Garg, Vaibhav Shrivastava, Sachchidanand Singh</i>		176
34.	Impact Assessment of Meteorological Drought on Agricultural Parameters Using Google Earth Engine: A Case Study on Penna River Basin <i>Arunav Nanda, Bhaskar R. Nikam, S. P. Aggarwal</i>		182
35.	Delineation of Groundwater Potential Zone Using RS and GIS in Devanahalli Taluk, Karnataka <i>Sanath Kumar K. R, Sharanya Ram S. R</i>		187
THEME-5: Geospatial Applications in Agriculture, Soil and Forestry Sciences			
36.	Habitat Distribution Modeling for Medicinal Plant <i>Valeriana Jatamansi</i> in Shivalik Foothills of Doon Valley <i>A. P. Mishra, N. Rawat, M.P.S. Bisht</i>		193
37.	Recent Developments in Remote Sensing Cloud Computing to Assess Variations in Indian Forests from 2001 to 2018 <i>R. Gupta, L.K. Sharma</i>		198
THEME-6: Geospatial Applications in Atmospheric and Marine Sciences			
38.	Coral Reef Mapping Using Sentinel-2 MSI Data in Poshitra and Pirotan Islands, Gulf of Kachchh, Gujarat <i>Foram Jadeja, Jalpa Jadeja, P. C. Mankodi, Manik H. Kalubarme</i>		203

Sl. No.	Research Paper	Author(s)	Page no.
39.	Variation and Distribution of Total Ozone During Tropical Cyclones and the Exchange Process <i>Kishore Kowtham, K. Srinivasa Raju, D.Thirumalaivasan</i>		209
40.	Time Series Gridded Precipitation Prediction Using Long Short-Term Memory (LSTM) Model <i>Manaruchi Mohapatra, Bhaskar R. Nikam, Praveen K Thakur, S.P. Aggarwal, Antony Joh Moothedan</i>		212
41.	Persistency of Thermal Front and its Seasonal Cycle in the Northern Arabian Sea <i>Reba Mary Raju, R. K. Nayak</i>		217
42.	Seasonal and Inter-Annual Variability of Atmosphere CH ₄ Based Model and GOSAT Satellite Observations <i>Shaik Allahudheen, Rabindra K. Nayak, M. Krishna Priya, A. Bhuvana Chandra, M.V. Lakshmaiah</i>		221
43.	Spatial and Temporal Precipitation Variability Analysis Using Concentration Index for Uttarakhand <i>Tanisha Jaiswal, C.M. Bhatt & Arijit Roy</i>		226
44.	Detection and Classification of Marine Slicks through Decomposition and Supervised Classification Using POLSAR Data <i>Vaishali Chaudhary, Shashi Kumar</i>		233

AUTOMATIC FLOOD MAPPING USING SENTINEL-1 GRD SAR IMAGES AND GOOGLE EARTH ENGINE: A CASE STUDY OF DARBHANGAH, BIHAR

Antony Joh Moothedan ^{1*}, Pankaj R. Dhote ², Praveen K. Thakur ³, Vaibhav Garg ⁴, S. P. Aggarwal ⁵, Manaruchi Mohapatra ¹

¹ Student, Master of Technology, Water Resources Department, Indian Institute of Remote Sensing, Dehradun, India

² Scientist/Engineer-'SD', Water Resources Department, Indian Institute of Remote Sensing, Dehradun, India

³ Scientist/Engineer-'SF', Water Resources Department, Indian Institute of Remote Sensing, Dehradun, India

⁴ Scientist/Engineer-'SE', Water Resources Department, Indian Institute of Remote Sensing, Dehradun, India

⁵ Group Head, Water Resources Department, Indian Institute of Remote Sensing, Dehradun, India

*corresponding author – antonyjohm@gmail.com

KEY WORDS: Flood Mapping, GEE, Sentinel-1

ABSTRACT:

Bihar has been highly affected due to the catastrophic flood events occurring every year. Mapping near real-time flood inundation is a vital input for decision makers to take effective response. Remote sensing has shown outstanding potential in flood mapping in recent years. With increased availability of active microwave remote sensing data, the operational flood mapping at near real-time can be taken up to support the disaster management authorities. This study presents an automatic flood inundation mapping approach from Sentinel-1 synthetic aperture radar (SAR) data exploiting Google Earth Engine (GEE) platform. The backscattered product of SAR images after pre-processing from the GEE platform have been used in this study. The 2019 Bihar floods affected 13 districts of North Bihar, India. For mapping flood inundation the optimal threshold value of VV polarised backscatter image of Sentinel-1 is identified based on Otsu's method. In addition, degree of slope generated from ALOS PALSAR DEM is also considered in order to minimize the misclassification over back-slope regions of SAR data. Thus, this approach can be utilized exclusively for operational flood inundation mapping and monitoring.

1. INTRODUCTION

Flooding is the most widespread hydrological hazard worldwide that affects water management, nature protection, economic activities, and hydro morphological alterations on ecosystem services, and human health. The mitigation of the risks associated with flooding requires a certain management of flood zones, sustained by data and information about the events with the help of flood maps with sufficient temporal and spatial resolution. A river flood occurs when the river flow can no longer be contained within its bed, and over spills its banks. Flooding is a natural and regular reality for many rivers, caused by any pulse of overflowing water (heavy rainfall, peak seasonal rains, or seasonal snow melt) that overwhelms a river channel, which supports the most naturally dynamic ecosystems, modelling soil and re-distributing nutrients in associated alluvial lands (Muis et al., 2015). However, humans often perceive floods negatively due to damage and loss of life.

Remote sensing techniques are an effective source of information to discriminate bodies of water over large areas, and therefore, they can be used to map flooded surfaces with sufficient temporal and spatial resolution (Tehrany et al., 2014). In the case of multispectral images, water bodies can be easily discriminated because of their spectral behaviour in the visible and infrared spectrum because it is different from other land covers (Kim et al., 2019), but they only operate in natural daylight conditions and cloudless skies. Since severe flooding usually occurs as a result of heavy rainfall, they are not always useful for this purpose. In Spain, due to the physiographic characteristics of the basins and the Mediterranean climatic conditions, most floods are associated with periods of heavy rainfall. The validity of multispectral observations for this purpose is limited by clouds because unclear weather conditions

are common during floods events (Chini et al., 2019). However, the Synthetic Aperture Radar (SAR) is a form of radar that is used to create more useful images over a target region to provide fine spatial resolution (Pulvirenti et al., 2017), which can operate day and night and is unaffected by cloud cover, smoke, atmospheric water, or hydrometeors. Moreover, the signal can penetrate through foliage (wavelength dependent), and therefore can provide more complete information about the inundation state (Refice et al., 2013). SAR based flood mapping methods are usually more complex than those based on optical sensors because of the process added to mitigate the error propagated from one or more of the error sources (Refice et al., 2014).

Microwave remote sensing is widely used for the study of floods because of its time-independent and weather-independent operability. Microwave sensors are sensitive to the dielectric properties. Water can be identified in the SAR images with ease as the water appears black due to the fact that smooth water surface provides no return to SAR sensor. The SAR data can provide timely cloud free input even during severe weather conditions.

2. STUDY AREA AND DATASET USED

2.1 Study Area

The study area for the study is Dharbhanga district of Bihar, India. Darbhanga district is one of the thirty-eight districts of Bihar state in eastern India, and Darbhanga city is the administrative headquarters of this district and 6th largest city of Bihar as well. The rivers Kosi, Bagmati and Kamla flow through the Dharbhanga district. The river Kosi flows through

the eastern-most border of the district, while the river Bagmati flows through the western border. The river Kosi drains the northern slopes of the Himalayas in Tibet and the southern slopes in Nepal. From a major confluence of tributaries north of the Chatra Gorge onwards, the Koshi River is also known as Saptakoshi for its seven upper tributaries. The Koshi is 720 km (450 mi) long and drains an area of about 74,500 km² (28,800 sq mi) in Tibet, Nepal and Bihar. The Koshi River is known as the "Sorrow of Bihar" as the annual floods affect about 21,000 km² (8,100 sq mi) of fertile agricultural lands thereby disturbing the rural economy

The Kosi has an average water flow (discharge) of 2,166 cubic metres per second (76,500 cu ft/s). During floods, it increases to as much as 18 times the average. The greatest recorded flood was 24,200 m³/s (850,000 cu ft/s) on 24 August 1954. The Koshi Barrage has been designed for a peak flood of 27,014 m³/s (954,000 cu ft/s).

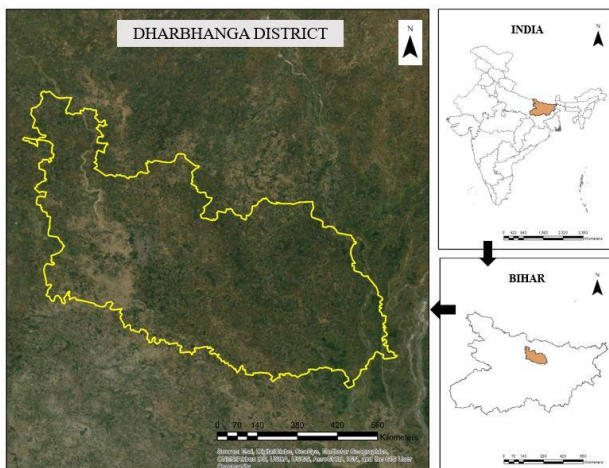


Figure 1: Study Area

2.2 Dataset Used

2.2.1 Sentinel-1 SAR Data

The GRD product of Sentinel-1 data was used for the study. Level-1 Ground Range Detected (GRD) products consist of focused SAR data that has been detected, multi-looked and projected to ground range using an Earth ellipsoid model. The ellipsoid projection of the GRD products is corrected using the terrain height specified in the product general annotation. The terrain height used varies in azimuth but is constant in range.

SPECIFICATIONS	
Observation Mode	Interferometric Wide Swath (IW) Mode
Band	C band (5.405 GHz)
Swath	250 Km
Polarization	Dual (VV+VH)
Spatial Resolution	5m x 20m

Table 1: Sentinel-1 Specifications.

Ground range coordinates are the slant range coordinates projected onto the ellipsoid of the Earth. Pixel values represent detected magnitude. Phase information is lost. The resulting product has approximately square spatial resolution and square

pixel spacing with reduced speckle due to the multi-look processing.

DATA	DATE
Sentinel-1 GRDH Data	25-08-2019
	03-09-2019
	06-09-2019
	15-09-2019
	18-09-2019
	27-09-2019
	30-09-2019
	03-10-2019
	06-10-2019
	15-10-2019

Table 2: Data Used

3. METHODOLOGY

In this study, the Sentinel-1 Level-1 Ground range Detected (GRD) data collection has been used. The pre-processing which involves thermal noise removal, radiometric calibration and terrain correction has been done using the Sentinel-1 toolbox which updates weekly in GEE data catalogue. Since, it is known that, like-polarization can better delineate flooded areas than cross-polarization, VV-backscatter has been utilized for effective flood inundation mapping.

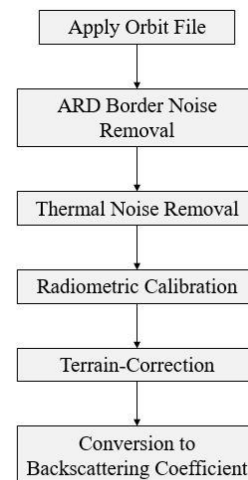


Figure 2: Pre-processing already done in GEE

According to theoretical knowledge, a typical bi-model nature of SAR backscatter histogram is expected over water abundant terrain. So, in this study, automatic thresholding based on Otsu's method (Bangare and Patil, 2016) is adopted to differentiate water and land from the image. The typical SAR backscatter is also influenced by topographic characteristics. As a consequence, part of the hilly terrain, particularly the back-slope regions receives low backscatter signal as in the case for water. Thus, the degree of slope generated from ALOS PALSAR2 RTC 12.5m has been used to minimise the errors. The study observed that the degree of the slope greater than 10° in back-slope regions are likely to appear as surface water due to increase in the local incidence angle. Thus, incorporating the

above factors, the final flood inundation layer for assessment is prepared.

► Otsu’s Method for Automatic Segmentation:

Otsu's thresholding method involves iterating through all the possible threshold values and calculating a measure of spread for the pixel levels each side of the threshold, i.e. the pixels that either fall in foreground or background. The aim is to find the threshold value where the sum of foreground and background spreads is at its minimum.

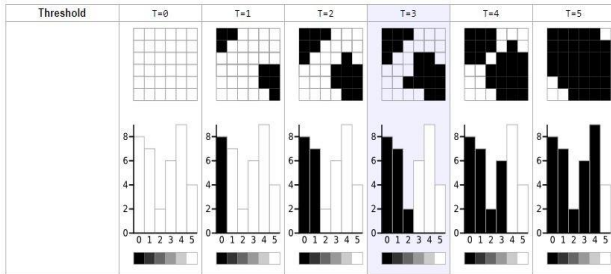


Figure 3: Different Iterations Otsu’s method.

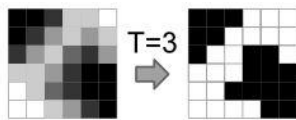


Figure 4: Greyscale to Binary conversion

The optimal threshold as defined by Otsu is the partition of the data that maximizes inter-class variance (equivalently, minimizes the sum of intra-class variances). Define inter-class variance as BSS/p , where BSS (between-sum-of-squares) is

$$BSS = \sum_{k=1}^p (\overline{DN}_k - \overline{DN})^2 \tag{1}$$

In the case of the project, there are two classes so $p=2$. Between-sum-of-squares (BSS) terminology to indicate the general method which describes the variance structure of a dataset. DN is the digital numbers of VV band, DN_k is the mean digital number of the entire dataset. The threshold value would be the one which minimizes the BSS . The thresholds are represented by the bins in the histogram. The advantage of the approach is that it only requires a single pass over the data. At each bin of the histogram, define class k as the pixels in that bin and lower.

4. RESULTS

The incessant rains during September, 2019 in Bihar has caused severe floods resulting in loos of lives, damage of crops and destruction of properties at a large scale. Many districts were affected by the flood with Dharbhanga being one of them due to the overflow of Kosi and Bagmati River.

The permanent water body pixels are reduced from the processed maps. The maximum flood was observed on 3th September, 2019 which covers an area of 324.85 km². After the particular date the flooded area decreased and on 15th October, 2019 the entire district was resettled to the previous state.

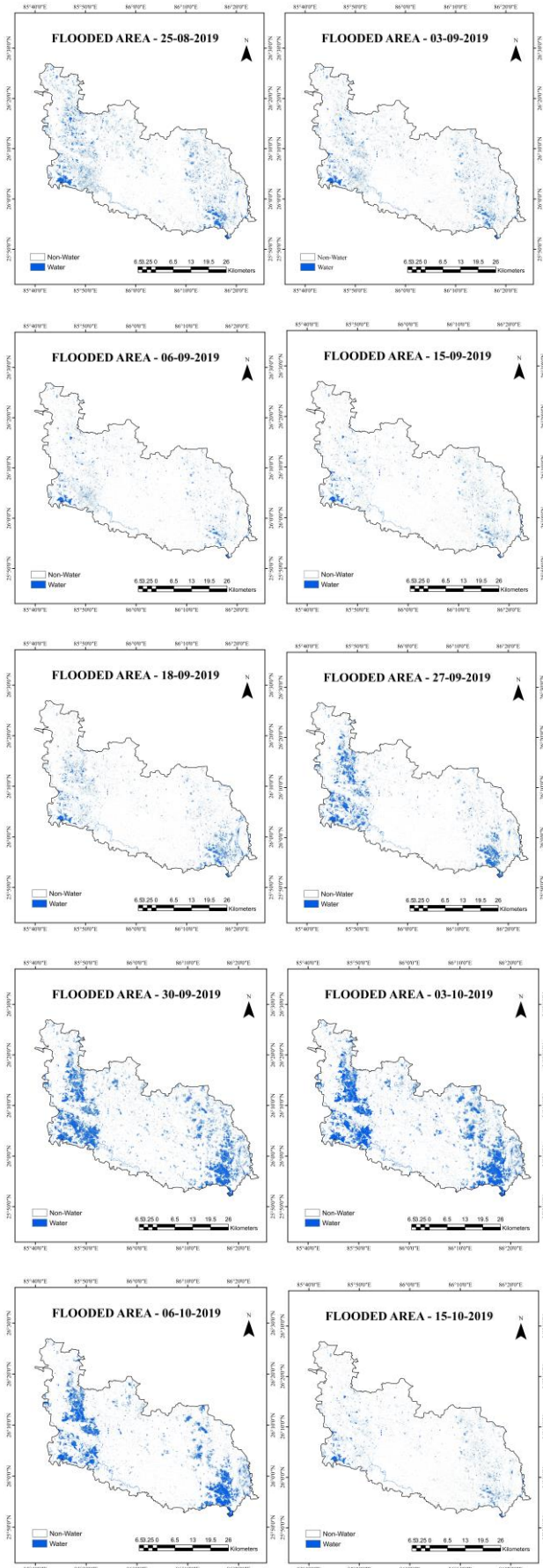


Figure 5: Processed Flood maps.

Date	Flooded Area (km ²)
25-Aug-19	126.7022
03-Sep-19	78.3927
06-Sep-19	36.4462
15-Sep-19	38.7928
18-Sep-19	65.8658
27-Sep-19	128.1133
30-Sep-19	279.2838
03-Oct-19	324.8447
06-Oct-19	222.0225
15-Oct-19	138.7928

Table 3: Flooded area at different dates

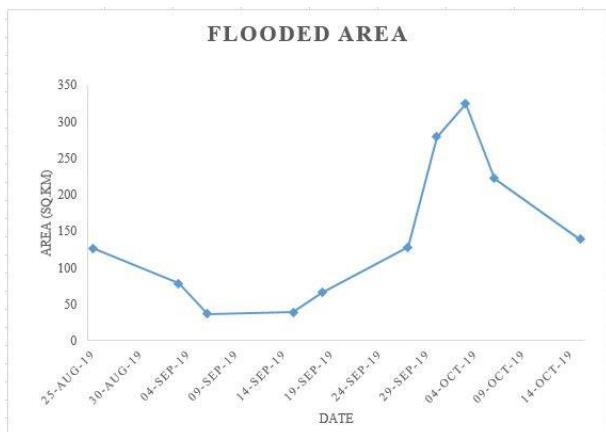


Figure 6: Flooded Area vs Date

5. CONCLUSION

In this study, a functional methodology was proposed for flood monitoring at a necessary spatial resolution derived from SAR images. Specifically, it aimed to highlight the potential use of the Sentinel-1 SAR data sets of the European Earth Observation mission for flood monitoring occurring in the middle course of the Kosi River (Bihar) in September 2019.

In SAR images, continental waters have strong contrast in the backscatter values due to their low or null roughness in the absence of waves, behaving like a specular surface that reflects the radar return signal in a direction opposed to the sensor position. However, they need a correction and filtering process (orbital parameters, radiometric, noise reduction speckle, and geometric geometric). Evaluating the different Sentinel-1 parameters, our analysis showed that the best results were obtained using VV polarization configuration.

Based on the results, it is concluded that the freely available Sentinel-1 SAR data has great potential for rapid flood inundation mapping and monitoring. Particularly, GEE platform which is a cloud-based computation environment can support operational activities for planning and disaster risk reduction purpose. In addition, it can effectively be used for flood damage assessment by land use/ land over information as well as embankment breach identification.

REFERENCES

Bangare, S., Patil, S., 2016. Reviewing Otsu ' s Method For Image Thresholding. Flood risk and adaptation strategies under climate change and urban expansion: A probabilistic analysis using global data. *Sci. Total Environ.* <https://doi.org/10.1016/j.scitotenv.2015.08.068>

Chini, M., Pelich, R., Pulvirenti, L., Pierdicca, N., Hostache, R., Matgen, P., 2019. Sentinel-1 InSAR coherence to detect floodwater in urban areas: Houston and hurricane harvey as a test case. *Remote Sens.* 11, 1–20. <https://doi.org/10.3390/rs11020107>

Kim, D.-E., Gourbesville, P., Liong, S.-Y., 2019. Overcoming data scarcity in flood hazard assessment using remote sensing and artificial neural network. *Smart Water* 4. <https://doi.org/10.1186/s40713-018-0014-5>

Muis, S., Güneralp, B., Jongman, B., Aerts, J.C.J.H., Ward, P.J., 2015. Flood risk and adaptation strategies under climate change and urban expansion: A probabilistic analysis using global data. *Sci. Total Environ.* 538, 445–457. <https://doi.org/10.1016/j.scitotenv.2015.08.068>

Pulvirenti, L., Chini, M., Pierdicca, N., Boni, G., 2017. Detection of flooded urban areas using sar: An approach based on the coherence of stable scatterers. *Int. Geosci. Remote Sens. Symp.* 2017-July, 5701–5704. <https://doi.org/10.1109/IGARSS.2017.8128302>

Refice, A., Capolongo, D., Pasquariello, G., Daaddabbo, A., Bovenga, F., Nutricato, R., Lovergine, F.P., Pietranera, L., 2014. SAR and InSAR for flood monitoring: Examples with COSMO-SkyMed data. *IEEE J. Sel. Top. Appl. Earth Obs. Remote Sens.* 7, 2711–2722. <https://doi.org/10.1109/JSTARS.2014.2305165>

Refice, A., Pasquariello, G., D’Addabbo, A., Bovenga, F., Nutricato, R., Capolongo, D., Lepera, A., Pietranera, L., Manfreda, S., Cantisani, A., Sole, A., 2013. Inundation monitoring through high-resolution SAR/InSAR data and 2D hydraulic simulations. *Proc. 33rd EARSel Symp.* 15–22.

Tehrany, M.S., Pradhan, B., Jebur, M.N., 2014. Flood susceptibility mapping using a novel ensemble weights-of-evidence and support vector machine models in GIS. *J. Hydrol.* 512, 332–343. <https://doi.org/10.1016/j.jhydrol.2014.03.008>

ESTIMATION OF SOIL EROSION USING GEOSPATIAL TOOLS: A CASE STUDY OF INDRAVATI BASIN, CHHATTISGARH

Mohit Dipeshbhai Jani ^{1*}, Praveen K. Thakur ¹, Arpit Chouksey ¹, Bhaskar R. Nikam ¹, S.P. Aggarwal ¹

¹ Water Resource Department, Indian Institute of Remote Sensing (IIRS-ISRO), 4 Kalidas Road, Dehradun, India – 248001

*corresponding author – mjani2197@gmail.com

KEY WORDS: Soil Erosion, RUSLE, GIS, Remote Sensing

ABSTRACT:

Soil erosion is a major issue for an agriculture dependent country like India causing the loss of top fertility soil. The quantitative assessment of soil erosion by geospatial method can help in designing control measures to reduce the erosion. In the present study, Revised Universal Soil Loss Equation (RUSLE) is adapted to calculate the annual loss of the soil from Indravati Basin, Chhattisgarh. The Indravati Basin is a northern tributary of the Godavari River spreading over 40634 km² area and observes the highest amount of erosion compared to other catchments of India. Inputs parameters RUSLE were derived using remote sensing and ground observed data. In the present study both magnitude and spatial distribution of erosion was calculated. The derived annual soil erosion map was classified into five zones varying from slight to severe soil erosion hazard. Further the soil erosion map is linked with different elevation and land use land cover zones to identify the area of conservation to reduce the soil loss. The average soil loss rate from the basin was found to be 9.2 tons/ha/year and the maximum soil loss rate was around 56 tons/ha/year. The sediment yield found at the outlet is around 24.50 million tons per annum which shows a surge compared to the average annual sediment yield (1992-2002) of 21.20 million tons from the observed value of Central Water Commission (CWC).

1. INTRODUCTION

Soil erosion and soil loss is one of the major agricultural hazards which impacts to environment and leads to the loss of fertility of soil and reduced agricultural production. Landslide like hazards also occurs due to soil erosion. Soil erosion in the basin area is also related to soil nutrient loss, making it more essential to estimate soil erosion. Climate and Land Use change is also dependent on soil erosion. Soil erosion can affect the soil depth (Wardle et al. 2004) and organic matter (Langdale et al. 1992). Soil loss due to erosion is a global problem, especially affecting natural resources and agricultural production (Littleboy et al. 1992). The estimated soil erosion throughout the world is estimated between 12 and 15 t ha⁻¹ yr⁻¹ (Den Biggelaar et al. 2003), means the land losses are about 0.90–0.95 mm per year (FAO 2015).

According to a study conducted by NBSS&LUP (National Bureau of Soil Survey & Land Use Planning) as much as 187 Million hector of geographical area is subjected to environmental degradation (Sehgal and Abrol 1994). For Indian context soil erosion by water is ridiculously high. A study published by Narayana and Babu (1983) states that India soil erosion rate is 16.35 t ha⁻¹year⁻¹. Soil erosion rate of more than 80 tons/ha/year is reported for the Siwalik Hills (Singh et al. 1992). To study and analyse erosion effectively, extensive information on erosion status and erosion condition is needed. This information can be derived to a large extent from satellite data (Vemu and Pinnamaneni 1994).

For estimation of the soil erosion and sediment yield several empirical models which are based on geomorphological parameters were developed in the past (Jose and Das 1982). The type of models are ranges to empirical models like USLE (Wischmeier and Smith 1978) or RUSLE (Renard et al. 1991)

to physical or process-based like MMF (Morgan et al. 1984), EUROSEM (Morgan et al. 1992), WEPP (Laften et al. 1991) and varies considerably in ramification and data input. The Universal Soil Loss Equation (USLE) has been useful in predicting the mean rate of soil loss due to water erosion from agricultural lands. In the early 1990s, the basic USLE was updated from its empirical form and computerized to create an erosion prediction tool called the Revised Universal Soil Loss Equation (RUSLE). The RUSLE represents how soil, climate, land use and topography affect rill and sheet soil erosion caused by raindrop impacts. RUSLE method is extensively used to estimate soil erosion loss and to guide development and conservation plans in order to control erosion under different land cover conditions, such as agriculture, urban and forest lands. (Milward and Mersey 1999).

2. STUDY AREA AND DATA USED

2.1 Study Area

The chosen study area for this erosion modelling is in Indravati River which flows from the three states Orissa, Chhattisgarh and Maharashtra as shown in Fig.1. Indravati River is northern tributary of the Godavari River. Indravati river's starts from the Ghats of Dandakaranya, range from a hilltop village Mardiguda of Thuamula Rampur Block in the Kalahandi district of the state of Odisha. Due to the amalgamation of three streams, The River follows a westerly path and enters Jagadapur in the state of Chhattisgarh. The river moves from here in a southern route, before eventually uniting with the Godavari at the borders of three states. They are the state of Chhattisgarh, Maharashtra and Telangana. The river at a variety of stages of its course forms the boundary between Chhattisgarh and Maharashtra. Most of the river course is through dense forests of Nabarangapur & Bastar.

The river flows for 535 kilometres and has a drainage area of 40634 km².

The mean annual rainfall in this area is about 1288 mm, most of which occurs between May and September. Average potential evaporation rates are 6.5 mm per day, while average minimum and maximum temperature are 13 and 39 °C, respectively. The major land covers in the catchment are forest (68%), followed by agriculture (22%) and rest is barren, uncultivable and grazing land.

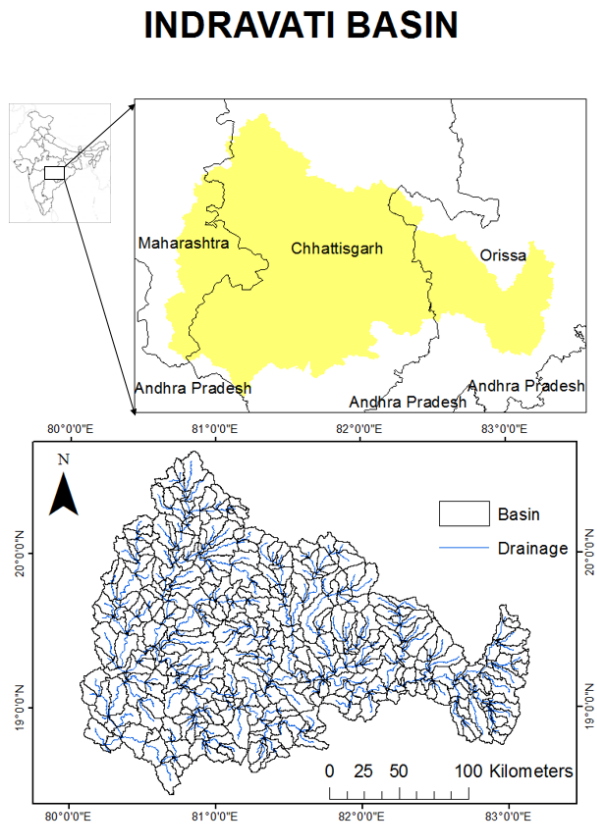


Figure 1. Indravati Basin

2.2 Dataset Used

2.2.1 Rainfall

The rainfall map used for the study is the climate normal dataset from IMD. These dataset provide the mean rainfall for each day and month as well as total rainy days for each month for the given year range. For this study it is from 1980 - 2010.

2.2.2 Land Use Land Cover Map

Land use and Land cover (LULC) classification products at 100-m resolution for India at decadal intervals for 2005. The data were derived from Landsat 4 and 5 Thematic Mapper (TM), Enhanced Thematic Mapper Plus (ETM+), and Multispectral (MSS) data, India Remote Sensing satellites (IRS) Resourcesat Linear Imaging Self-Scanning Sensor-1 or III (LISS-I, LISS-III) data, ground truth surveys, and visual interpretation. The data were classified according to the International Geosphere-Biosphere Programme (IGBP) classification scheme. (ISRO-IGBP 2005)

2.2.3 Soil Map

The soil texture has been recognized by NBSS&LUP (National Bureau of Soil Survey and Land Use Planning) map at 1:250000 scale in the study of soil type.

2.2.4 NDVI Map

The MOD13A1 V6 product provides a Vegetation Index (VI) value at a per pixel basis. There are two primary vegetation layers. The first is the Normalized Difference Vegetation Index (NDVI) which is referred to as the continuity index to the existing National Oceanic and Atmospheric Administration-Advanced Very High Resolution Radiometer (NOAA-AVHRR) derived NDVI. (Didan 2015)

2.2.5 Digital Elevation Model

In the present study MERIT (Multi-Error-Removed Improved-Terrain) DEM is used to get high accuracy global DEM at 3 arc second resolution (~90 m at the equator) by eliminating major error components from existing DEMs (NASA SRTM3 DEM, JAXA AW3D DEM, Viewfinder Panoramas' DEM). It is enhanced by separated absolute bias, stripe noise, and speckle noise and tree height bias using multiple satellite datasets and filtering techniques. (Yamazaki et al. 2017)

3. METHODOLOGY

The RUSLE model was used in the GIS platform in this study. The RUSLE was designed to compute the mean annual soil loss for ground slopes where flow convergence/divergence can be neglected, i.e., planar slopes, common in agricultural lands. The RUSLE is expressed by an equation, (angima et al. 2003),

$$A = [R] * [K] * [LS] * [C] * [P] \quad \dots (1)$$

Where, A = soil loss (t ha⁻¹ yr⁻¹), R = rainfall erosivity factor (MJ mm ha⁻¹ h⁻¹ yr⁻¹), K = soil erodibility factor (tons-year MJ⁻¹ -mm⁻¹), LS = slope-length and slope steepness factor (dimensionless), C = land management factor (dimensionless), and P = conservation practice factor (dimensionless).

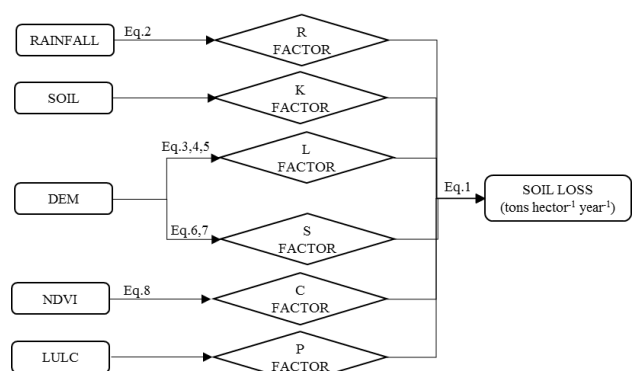


Figure 2. Framework for calculation of soil erosion by RUSLE

3.1 Rainfall and Run-off Factor

The rainfall erosivity factor (R) describes the erosivity of rainfall at a particular location based on the rainfall amount and intensity, and reflects the effect of rainfall intensity on soil erosion. The rainfall erosivity used in the RUSLE must quantify the effect of rainfall and explain the amount and rate of runoff associate with rainfall. (Wischmeier and Smith 1978)

Seasonal Relationship:

$$R_s = 71.9 + 0.361P_s \quad \dots (2)$$

R = average erosion index, P = average rainfall (mm) s stands for seasonal.

3.2 Soil Erodibility Factor

In RUSLE Erodibility factor is assumed to be constant throughout the year. Tables of K values are available in SCSO (Soil Conservation Service Offices) for most types of soil.

Soil Type	Erodibility Factor
Loamy	0.0671
Clay	0.0198

Table 1. Soil Erodibility Factor

3.3 Topographic Factor

The topographic factor or Slope Length and Steepness Factors (LS) was created from two sub-factors: a slope gradient factor (S) and a slope-length factor (L); both of which are determined from the Digital Elevation Model (DEM). Slope-length and gradient is the important parameter in the soil erosion modelling. (Morgan et al. 1984)

The L represents the effect of slope length on erosion. The soil loss per unit area increases as the slope length increases. The S represents the effect of slope steepness on erosion. (Ghansari and Ramesh 2016)

The L and S factors are calculated by using following equations.

$$L = \left(\frac{\lambda}{22.13} \right)^m \quad \dots (3)$$

$$m = \frac{\beta}{(1+\beta)} \quad \dots (4)$$

$$\beta = \frac{(\sin \theta / 0.0896)}{(3.0(\sin \theta)^{0.8} + 0.56)} \quad \dots (5)$$

Where, L = slope length factor, λ = slope length (m) (Flow Accumulation \times Grid size), m = slope-length exponent, β = Ratio of rill erosion to interrill erosion, θ = slope angle (Radian)

$$S = 10.0 \sin \theta + 0.03 \quad (\text{If } \tan \theta < 0.09) \quad \dots (6)$$

$$S = \left(\frac{\sin \theta}{\sin 5.143} \right)^{0.6} \quad (\text{If } \tan \theta \geq 0.09) \quad \dots (7)$$

Where, θ = slope angle (Radian)

3.4 Cover Management Factor (C)

The cover-management factor (C) is used to reflect the effect of cropping and other management practices on erosion rates. Vegetation cover is the second most important factor next to topography that controls soil erosion risk. The C factor ranges from 0 to approximately 1, where higher values indicate no cover effect and soil loss comparable to that from a tilled bare fallow, while lower C means a very strong cover effect resulting in no erosion. (Ercen et al. 2000)

$$C_i = 0 \quad (\text{if } NDVI \leq 0)$$

$$C_i = -\left(\frac{1}{NDVI_{max}} \right) (NDVI)_i + 1 \quad (\text{if } NDVI > 0) \dots (8)$$

3.5 Conservation Practice Factor (P)

Conservation practice factor indicates the rate of soil loss according to the various cultivated lands. There are contours, cropping, and terrace as its methods and it is important factor that can control the erosion (Shen et al. 2016)

To determine the conservation practice of the study area the LULC map is reclassified into four classes.

- 1 – Dense Evergreen Forest
- 2 – Mixed forest, Grass Land and Agriculture
- 3 – Barren Land and Waste Land
- 4 – Waterbodies

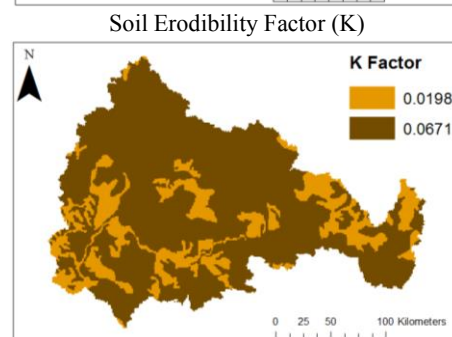
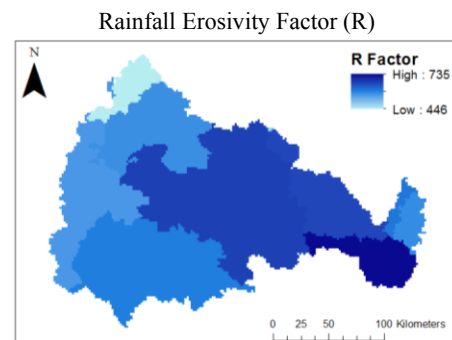
Reclass Value	Conservation Practice Factor (P)
1	1
2	0.9
3	0.5
4	0

Table 2. Conservation Practice Factor

4. RESULTS AND DISCUSSION

4.1 Derived Parameters

The input data were processed in ArcGIS and six factor maps: R, K, L, S, C and P were generated (Figure 2). These raster maps were integrated within the ArcGIS environment using the RUSLE relation to generate composite maps of the estimated erosion loss within the study area. Using a zonal statistics tool, we computed an area-weighted mean of the potential erosion rates for the physiographic regions and the basins of Indravati. Similarly, the erosion rates for slopes and LULC were generated. First, the slope map of Indravati Basin was generated from DEM in ArcGIS and then reclassified into 10 classes, then the LULC is reclassified into 4 classes. The erosion values for each class were thus obtained using zonal statistics. The results are presented in the form of maps and tables.



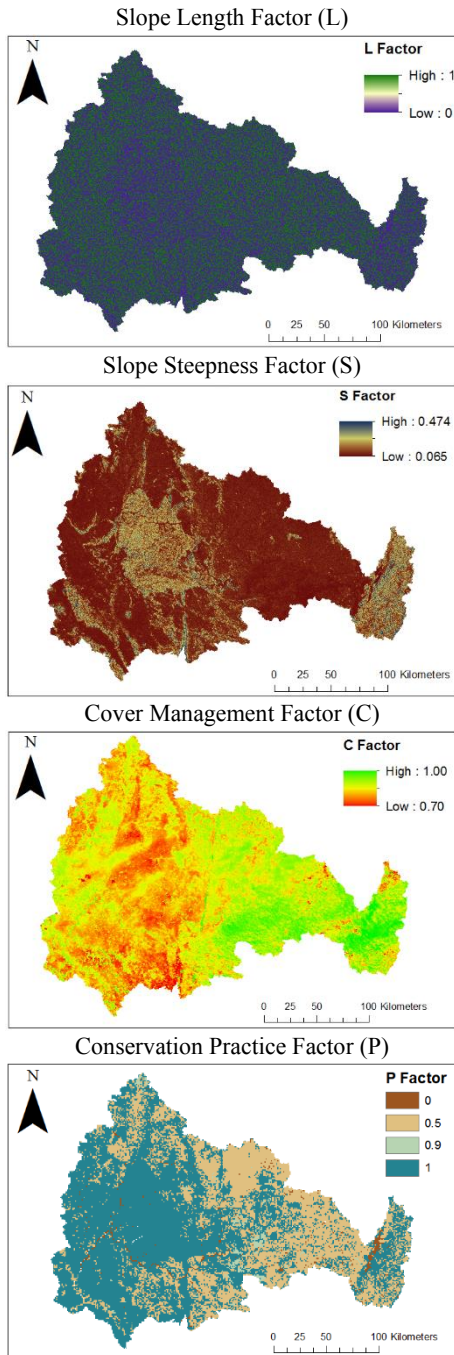


Figure 2. RUSLE Model Parameters

4.2 Soil Erosion Analysis

4.2.1 Average Annual Soil Loss by RUSLE

Computing all six factors of RUSLE, the Average annual Soil Erosion (1980-2010) map is generated. Which is divided into the watersheds of size 10 km². The watersheds are prioritized on five classes based on the severity. (Singh et al. 1992)

The maximum value of erosion found in the Indravati Basin is 56 tons/hectar/year and the average value of erosion found is 9.2 tons/hectar/year. The watersheds are classified into five classes. 1- Slight (<5), 2- Moderate (5-10), 3-High (10-20), 4-Very High (20-40), 5-Severe (40-80) tons/hectar/year. (Figure 3(a)).

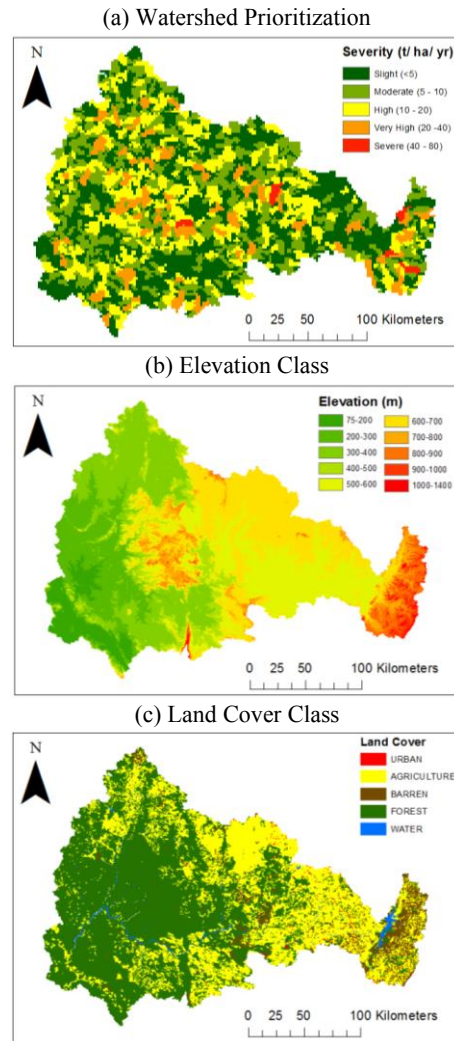


Figure 3. Basin Erosion Analysis

4.2.2 Soil Erosion by Elevation Class

The basin is divided into ten elevation classes ranges between 75 – 1400 m. The average erosion (tons/hector/year) and soil loss (million tons) is calculated and shown in Table 3.

Elevation Class (m)	Avg. Erosion (t/h/yr)	Soil Loss (Mil. tons)
75-200	4.8	0.89
200-300	5.7	2.43
300-400	5.9	3.93
400-500	7.4	2.62
500-600	6.0	4.57
600-700	6.4	5.20
700-800	9.0	2.20
800-900	8.5	1.49
900-1000	7.7	0.87
1000-1400	9.0	0.28

Table 3. Erosion Analysis by Elevation Class

4.2.3 Soil Erosion by Land Cover Class

The basin is divided into four Land Cover classes. The average erosion (tons/hector/year) and soil loss (million tons) is calculated and shown in Table 4.

LULC Class	Avg. Erosion (t/h/yr)	Soil Loss (Mil. tons)
URBAN	4.5	0.16
AGRICULTURE	5	7.86
BARREN	6.8	2.74
FOREST	6.6	13.71

Table 4. Erosion Analysis by Land Cover Class

5. CONCLUSIONS

The average annual soil loss (1980-2010) calculated for the basin is 24.48 Million Tons, which is showing surge compared to the average annual sediment yield (1992-2002) of 21.20 million tons from the observed value of Central Water Commission (CWC). (Vemu and Pinnamaneni 2011)

6. REFERENCE

Angima, S. D., Stott, D. E., O'neill, M. K., Ong, C. K., & Weesies, G. A. (2003). Soil erosion prediction using RUSLE for central Kenyan highland conditions. *Agriculture, ecosystems & environment*, 97(1-3), 295-308.

Didan, K. (2015). MOD13A1 MODIS/Terra Vegetation Indices 16-Day L3 Global 500m SIN Grid V006 [Data set]. NASA EOSDIS Land Processes DAAC. Accessed 2020-02-23 from <https://doi.org/10.5067/MODIS/MOD13A1.006>

Den Biggelaar, C., Lal, R., Eswaran, H., Breneman, V., & Reich, P. (2003). Crop yield losses to soil erosion at regional and global scales: Evidence from plot-level and GIS data. *Land Quality, Agricultural Productivity, and Food Security: Biophysical Processes and Economic Choices at Local, Regional, and Global Levels*, ed. Keith Wiebe, 262-279.

Erencia, Z., Shrestha, D. P., & Krol, I. B. (2000). C-factor mapping using remote sensing and GIS. A case Study of Lom Sak/Lom Kao, Thailand. *Geographisches Institut der Justus-Liebig-Universität Giessen and Intern Inst. for Aerospace Survey and Earth Sci.(ITC), Enschede, The Netherlands.*

Ganasri, B. P., and H. Ramesh. "Assessment of soil erosion by RUSLE model using remote sensing and GIS-A case study of Nethravathi Basin." *Geoscience Frontiers* 7.6 (2016): 953-961.

FAO, I. (2015). Status of the World's Soil Resources (SWSR)—technical summary. Food and Agriculture Organization of the United Nations and Intergovernmental Technical Panel on Soils, Rome, Italy.

Jose, C. S., & Das, D. C. (1982, November). Geomorphic prediction models for sediment production rate and intensive priorities of watersheds in Mayurakshi catchment. In Proc. of International Symp. On Hydrological Aspects of Mountainous Watersheds, School of Hydrology, UOR, Roorkee (Vol. 1, pp. 15-23).

Laflen, J. M., Lane, L. J., & Foster, G. R. (1991). WEPP: A new generation of erosion prediction technology. *Journal of Soil and Water Conservation*, 46(1), 34-38.

Langdale, G. W., West, L. T., Bruce, R. R., Miller, W. P., & Thomas, A. W. (1992). Restoration of eroded soil with conservation tillage. *Soil Technology*, 5(1), 81-90.

Littleboy, M.; Silburn, D.M.; Freebairn, D.M.; Woodruff, D.R.; Hammer, G.L. Impact of soil erosion on production in cropping systems. I. Development and validation of a computer simulation model. *Aust. J. Soil Res.* 1992, 30, 757-774.

Milward, A. A and Mersey JE, 1999. Adapting the RUSLE to Model Soil Erosion Potential in a Mountainous Tropical Watershed. *Catena*, 38(2), 109-129.

Morgan, R. P. C., Morgan, D. D. V., & Finney, H. J. (1984). A predictive model for the assessment of soil erosion risk. *Journal of agricultural engineering research*, 30, 245-253.

Morgan, R. P. C., Quinton, J. N., & Rickson, R. J. (1992). EUROSEM documentation manual. Silsoe College, Silsoe, Bedford, UK, 34.

Narayana, D. V., & Babu, R. (1983). Estimation of soil erosion in India. *Journal of Irrigation and Drainage Engineering*, 109(4), 419-434.

Renard, K. G., Foster, G. R., Weesies, G. A., & Porter, J. P. (1991). RUSLE: Revised universal soil loss equation. *Journal of soil and Water Conservation*, 46(1), 30-33.

Shen, H., Zheng, F., Wen, L., Han, Y., & Hu, W. (2016). Impacts of rainfall intensity and slope gradient on rill erosion processes at loessial hillslope. *Soil and Tillage Research*, 155, 429-436.

Singh, G., Babu, R., Narain, P., Bhushan, L. S., & Abrol, I. P. (1992). Soil erosion rates in India. *Journal of Soil and water Conservation*, 47(1), 97-99.

Sehgal, J. L., & Abrol, I. P. (1994). *Soil degradation in India: status and impact.* Oxford & IBH Publishing Co.

Vemu, S., & Pinnamaneni, U. B. (2011). Estimation of spatial patterns of soil erosion using remote sensing and GIS: a case study of Indravati catchment. *Natural Hazards*, 59(3), 1299-1315.

Wardle, D. A., Bardgett, R. D., Klironomos, J. N., Setälä, H., Van Der Putten, W. H., & Wall, D. H. (2004). Ecological linkages between aboveground and belowground biota. *Science*, 304(5677), 1629-1633.

Wischmeier, W. H., & Smith, D. D. (1978). Predicting rainfall erosion losses: a guide to conservation planning (No. 537). Department of Agriculture, Science and Education Administration.

Yamazaki D., D. Ikeshima, R. Tawatari, T. Yamaguchi, F. O'Loughlin, J.C. Neal, C.C. Sampson, S. Kanae & P.D. Bates A high accuracy map of global terrain elevations *Geophysical Research Letters*, vol.44, pp.5844-5853, 2017 doi: 10.1002/2017GL072874

APPLICATIONS OF REMOTE SENSING AND PHOTOGRAMMETRY TECHNIQUES IN LANDSLIDE INVESTIGATION AROUND GURUDA- ODISHA

Lynette Dias ¹, Yengkhom Kesorjit S. ¹

¹ School of Earth Ocean and Climate Sciences, Indian Institute of Technology Bhubaneswar, India-ld12@iitbbs.ac.in

KEY WORDS: Landslide susceptibility, Slope stability, Scoops3D, DEM

ABSTRACT:

Landslides are one of the most common natural disasters in mountainous/hilly regions all over India. According to a recent report of the Geological Survey of India on the landslide vulnerable zone, approximately 0.42 million square kilometers of land area in India is prone to landslides. However, landslide vulnerable hot spots in the Eastern Ghats remain unknown and do not appear in this figure. The primary trigger for landslides in hilly terrains is rainfall, which saturates the soil and lowers the stability of a slope. With the onset of climate change, such natural disasters have been intensified causing tremendous damage. The state of Odisha is frequently hit by severe storms and tropical cyclones, which trigger numerous landslides in the districts encompassing the Eastern Ghats. No detailed landslide studies have been carried out in this vulnerable region and neither does slope stability data exist, mainly due to the ruggedness of the topography, lack of infrastructure and manpower to physically survey the region. One of the alternative and low cost approaches for pilot study slope stability mapping terrain is using Remote sensing techniques. In this study, we highlight the outcomes of our pilot study on mapping and identification of landslide susceptible areas in an around Guruda in the Ganjam district of Odisha that suffered major landslides after cyclone Titli in October 2018. This was done by creating a digital elevation model (DEM) and carrying out slope stability analysis using Scoops3D. It enabled us to create a 3D model of the area, calculate the displaced volume, identify unstable slopes and calculate the factor of safety for each point which can also be presented as a map layer. This 3D model of slope stability can also help generate a landslide susceptibility map created with various other geofactors, for future studies in the region thereby providing information to the government and the locals about the risk prone areas to prevent loss of life and property

1. INTRODUCTION

1.1 Introduction

On October 12th 2018, a very severe cyclonic storm-cyclone Tilti hit the coast of Odisha, making landfall in the Ganjam district. The region experienced very high amounts of rainfall in a short span of time. This sudden downpour triggered numerous landslides in the district and in the study area, as slope instability due to rainfall infiltration can lead to deadly landslides since saturation decreases the soil's cohesion (Borja et al., 2010). This region has very steep slopes and is prone to cyclones, hence the probability of recurrence of landslides in the area is high. However no detailed studies have been carried out in this vulnerable region mainly due to the ruggedness of the topography, inaccessibility of certain slopes and lack of infrastructure and manpower to physically survey the region.

The relative ease of use of remote sensing methods due to advancing technological prowess has enabled it to be used to study and classify landslides (Scaioni et al. 2014). Landslide susceptibility maps are the main outcome of remote sensing studies and they are prepared using landslide susceptibility factors like slope stability, rainfall, rock characteristics (Cheng et al., 2013).

In this study we attempt to carry out a 3 dimensional slope stability analysis using the Scoops3D version 1.1 developed by the U.S Geological Survey (USGS). This program has been used in various studies to study landslides caused by volcano flank collapse (Ball et al, 2018; Reid, Brien, 2006).

1.2 Study Area

The study area lies in the Eastern Ghats near a village called Guruda, in the Ganjam district of Odisha [19.038°N; 84.39°E]. It is located along the Odisha-Andhra Pradesh border approximately 60km south of Berhampur and falls under Survey of India toposheet number E45A. It is accessible via National Highway 22.

2. METHODOLOGY

2.0.1 Scoops3D: Scoops3D is a program used to analyse slope stability in a digital terrain. The terrain data is fed into the system as a digital elevation model (DEM) and the program uses a three-dimensional method of columns limit equilibrium analysis to compute the stability of potential slope failures with a spherical slip surface. Scoops3D allows for the optional input of subsurface layer files as well as pore water pressures distribution files. However these are not mandatory and the program can give a fairly accurate analysis of slope stability without the need of them as seen in studies carried out to test the program (Reid et al., 2015).

The Bishop's simplified method (Bishop, 1955) of limit equilibrium analysis is chosen to calculate the F for each point of the DEM. This method was found to yield a simple yet accurate estimate of 3D F values for rotational sliding surfaces (Hung et al, 1989). The result that the program generates shows the global minimum factor of safety for potential slip surfaces affecting each DEM cell, as well as the volumes and areas associated with these potential slope failures.

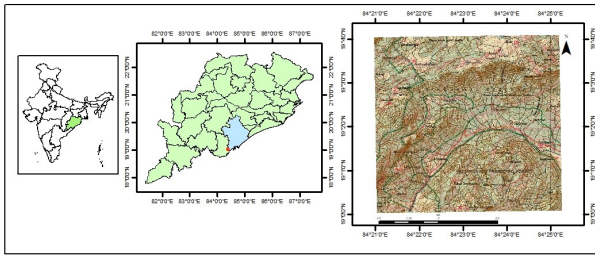


Figure 1. Study area, Survey of India toposheet number E45A

In addition to the DEM Scoops3D requires additional parameters to be set. These can be seen in table While the horizontal and vertical search resolutions can be determined based on the extent of the DEM points, soil characteristics like cohesion, angle of internal friction and unit weight were ascertained from other studies (Carter, Bentley, 1991; Gupta et al., 2007). The three dominant soil types in the study area were determined to be sandy loam, sandy clay and sandy clay loam based on remote sensing investigations in the Ganjam district (Srinivasan et al., 2018) and ground surveys (Sarkar, Sah, 2005). Input values can be seen in Table 1.

2.0.2 Digital Elevation Model (DEM): Scoops3D requires the input of a DEM with a high spatial resolution, 30m being the optimum resolution. For this study a DEM generated from the Indian Space Research Organization's Cartosat-1 satellite was used. The imagery was sourced from the National Remote Sensing Centre's web portal for the tile E45A. The DEM has a resolution of 1 arc sec (30m) and the imagery was taken three years before the cyclone, on 17/04/2015.

The DEM boundaries need to extend equally in both x and y directions and must be converted to Universal Transverse Mercator projection before they can be fed into Scoops3D. The DEM, which is downloaded as a geotiff file, has to be converted to an ascii file preferably Arc Ascii format. These modifications were done using Global Mapper v20.0. The input DEM is shown in Figure 2.

Parameter	Input
Cohesion(kPa)	140
Angle of internal friction(deg.)	30
Unit weight(kN/m ³)	18
Vertical extent of lattice:	
Minimum(m)	100
Maximum(m)	4000
Vertical resolution(m)	20
Radius increment	50
Horizontal extent of Lattice	match DEM
Horizontal Multiplier	1
Number of directions	1
Factor of safety cutoff	1.4

Table 1. Input data from Scoops3D analysis

2.1 Results

An analysis of 17,599,242 trial surfaces generated an output DEM with a large failure surface along the eastern part of the study area as shown in Figure 3. This region has the highest

elevation in the study area. Table 2 shows the output values obtained. The global minimum factor of safety was found to be 1.3756. This agrees with the cutoff factor of safety value of 1.4 set by us. The displaced volume was found to be 0.145 09 km³. An ascii file of the factor of safety values for each point was also generated.

Parameter	Value
3D factor of safety	1.3756
Volume removed(km ³)	0.14509
Slip surface area(m ²)	1318180
Weight removed(kg)	1.88117

Table 2. Output data from Scoops3D analysis

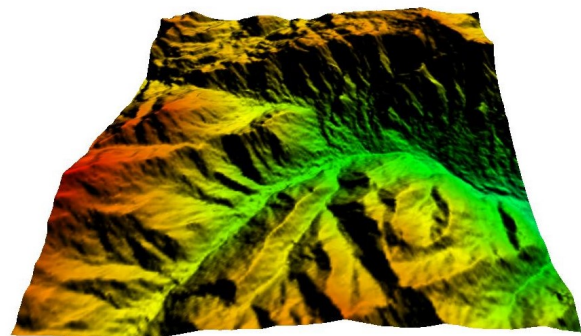


Figure 2. Input DEM

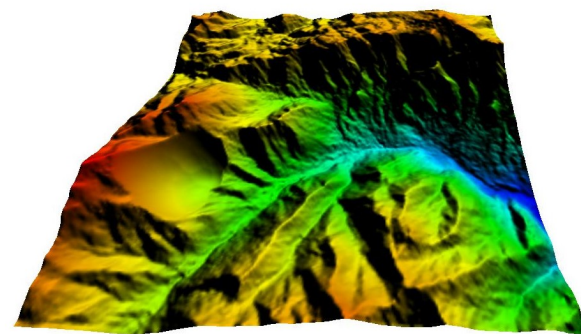


Figure 3. Output DEM

2.2 Discussion

High resolution satellite imagery taken from Google Earth for the study area before and after cyclone Titli (Figure 4,5) showed two landslides along the slope identified as unstable. This can be used as a rudimentary verification of the program's output. However to get a very high level of accuracy additional input files would be required.

There were no geophysical surveys carried out in the area and hence a subsurface profile could not be obtained although soil surveys in the district reported a soil cover of 10m (Sarkar, Sah 2005). This would affect the outcome of the study as the material underlying the soil cover is hard rock belonging to the Eastern Ghat Supergroup (GSI geological map).

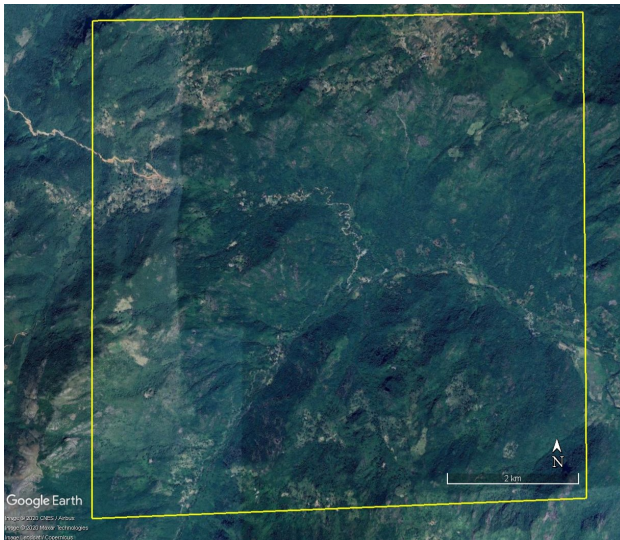


Figure 4. Study Area before the cyclone-March 2017



Figure 5. Study Area after the cyclone-November 2018

Structural features like faults are also not accounted for in this analysis. These parameters will have to be included to obtain a robust analysis of all potential failure slopes in the study area, as satellite imagery shows at least two other distinct zones where landslides have occurred that have not been identified by the program. A higher resolution DEM prepared from Unmanned Aerial Vehicle (UAV) imagery would also enhance the analysis as they can provide a spatial resolution of less than 5cm (Brooke,Merke, 2019).

CONCLUSION

A 3D model of the terrain post landslide was generated using Scoops3D and correlated with real landslides that occurred in the region. However a higher resolution DEM would yield more accurate results as will the provision of subsurface data, groundwater data, and lab tested soil parameters. The factor of safety values generated can be used to create a slope stability map, which can then act as one of the landslide susceptibility factors to prepare a landslide susceptibility map. This can help in disaster preparedness and management by the concerned authorities to prevent future loss of life and property.

REFERENCES

Ball, J. L., Taron, J., Reid, M. E., Hurwitz, S., Finn, C., Bedrosian, P., 2018. Combining multiphase groundwater flow and slope stability models to assess stratovolcano flank collapse in the Cascade Range. *Journal of Geophysical Research: Solid Earth*, 123(4), 2787-2805. <https://doi.org/10.1002/2017JB015156>

Bishop, A. W., 1955. The use of the slip circle in the stability analysis of slopes. *Geotechnique*, 5(1), 7-17. <https://doi.org/10.1680/geot.1955.5.1.7>

Borja, R. I., White, J. A., 2010. Continuum deformation and stability analyses of a steep hillside slope under rainfall infiltration. *Acta Geotechnica*, 5(1), 1-14.

Brook, M. S., Merke, J., 2019. Monitoring active landslides in the Auckland region utilising UAV/structure-from-motion photogrammetry. *Japanese Geotechnical Society Special Publication*, 6(2), 1-6.

C1-DEM-16b-2005-2014-v2r1-84E19N-e45a, National Remote Sensing Centre, ISRO, Government of India, Hyderabad, India.

Carter, M., Bentley, S. P., 1991. Correlations of soil properties. Pentech press publishers.

Cheng, C. T., Huang, C. M., Wei, L. W., Lee, C. F., Lee, C. T., 2013. Landslide Susceptibility Map. ICL Landslide Teaching Tools, ISBN: 978-4-9903382-2, 50-55.

Google: Google Earth Pro Version 7.3.2.5776 (64-bit). <https://www.google.com/earth/>

Gupta, S., Ranaivoson, A., Edil, T., Benson, C., Sawangsuriya, A., 2007. Pavement design using unsaturated soil technology.

Hungr, O., Salgado, F. M., Byrne, P. M., 1989. Evaluation of a three-dimensional method of slope stability analysis. *Canadian geotechnical journal*, 26(4), 679-686.

Reid, M. E., Brien, D. L., 2006. Assessing massive flank collapse at stratovolcanoes using 3-D slope stability analysis. In *Landslides from Massive Rock Slope Failure* (pp. 445-458). Springer, Dordrecht.

Reid, M.E., Christian, S.B., Brien, D.L., and Henderson, S.T., 2015, Scoops3D—Software to analyze 3D slope stability throughout a digital landscape: U.S. Geological Survey Techniques and Methods, book 14, chap. A1, 218 p., <http://dx.doi.org/10.3133/tm14A1>.

Scaioni, M., Longoni, L., Melillo, V., Papini, M., 2014. Remote sensing for landslide investigations: an overview of recent achievements and perspectives. *Remote Sensing*, 6(10), 9600-9652.

Srinivasan, R., Singh, S., Nayak, D., Mukhopadhyay, S., Kalaiselvi, B. (2018). Mapping of major soils in coastal Odisha: A remote sensing and GIS approach-A tool for land use planning.

MONITORING FOREST FIRE PROGRESSION DURING FIRE SEASON IN PARTS OF TEHRI AND PAURI DISTRICT USING NORMALIZED BURNT RATIO INDEX

Shailja Mamgain*, Disha Chauhan, Krishna Das, Arijit Roy

Disaster Management Studies Department, Indian Institute of Remote Sensing, ISRO, 4 – Kalidas Road, Dehradun 248001, India- shailja309@gmail.com*, dishachauhan18@gmail.com, miss.krishna10@gmail.com, arijitroy@iirs.gov.in

KEY WORDS: Sentinel, fire progression, NBR, forest fire, Uttarakhand.

ABSTRACT:

Forest fire is one of the major causes of the ecological degradation and biodiversity loss. Forest fires have social, economic and environmental impacts. It affects the flora and fauna of the region, livelihood of people depending on it, causes increase in the greenhouse gas emissions like CO₂ etc. The objective of this paper is to assess the forest fire progression during the fire season i.e. in the months of April and May (2019) and how this is affected by the vegetation type and density, topography, meteorological and anthropogenic factors in parts of Pauri and Tehri Garhwal districts of Uttarakhand. Sentinel 2A & 2B data is used to calculate Differenced Normalized Burnt Ratio (dNBR) to monitor and assess the progression of forest fire in the study area using datasets for approximately every 10 days interval. The results show that the area affected by fire was initially less in the beginning of April but within a month it increased upto ten times and covered an area of about 352 hectares. This study also concludes that the progression of the forest fire is observed more towards the higher elevation upto 4000m and as expected the proximity to the road and settlement plays an important role in the initiation of the fire. This study will help in understanding the fire behaviour for the planning of forest fire mitigation measures and restoration and rehabilitation activities.

1. INTRODUCTION

Forest is the most valuable natural resource and plays an essential role in the human life and the environment. Forest fire brings about incomplete or complete disintegration of vegetation cover thus spread along these lines changing the radiation balance by expanding the surface albedo, water runoff and increasing the soil disintegration (Darmawan, 2001). Under the Sendai framework for disaster risk reduction, forest fire is regarded as an important natural disaster. Every year about 55% of the forest cover is subjected to fires, not only adversely affecting the ecology but also causing an economic loss of over 440 crore (Gubbi, 2003). According to a report released by Forest Survey of India (FSI) in 2019, about 21.40% of forest cover in India is prone to fires (*India State of Forest Report, Forest Survey of India, 2019*) among which forests in the north eastern region and central India was found to be most vulnerable.

In India, maximum of the forest fires are accepted to be due to anthropogenic activities. Uttarakhand has about 38,000 sq. km of forest area which is about 63.41% of the state's geological area (*India State of Forest Report, Forest Survey of India, 2019*) and regularly shows forest fire action from February to June, with most severe in May and June. During the April 2016 occasion, forest fires were far reaching covering the vast majority of the forested districts of the state and the quantity of fires detected was abnormally high (Gupta et al., 2018; *India State of Forest Report, Forest Survey of India, 2016*). Forest fires in Uttarakhand have been steady and notable feature. It is one of the major disasters in the forests of Pauri and Tehri Garhwal. Every year due to forest fire, a huge loss of diversity of flora and fauna occurs and the ecosystem and environment get affected (Miller and Yool, 2002). Topography and vegetation plays an important role in understanding the progress of forest fire and in determining the severity of the fire (Cocke et al., 2005; Sunar and Özkan, 2001).

Interpretation on fires on a global scale has been mainly through the satellites (Veraverbeke et al., 2014). Active forest fire monitoring using satellite data has been carried out from 2006 as part of the Disaster Management Support Programme of ISRO (Jha et al., 2016). Many researchers over the world recommend that, the ratio between the near infrared and short wave infrared of the electromagnetic spectrum is more effective in burnt severity mapping because the burnt area shows higher reflectance in Short Wave Infra-red Region (SWIR) than the green vegetation (García and Caselles, 1991; Miller and Thode, 2007). The Normalized Burn Ratio (NBR) and the Normalized Difference Vegetation Index (NDVI) are the two techniques which are most repeatedly used to determine fire severity established by (Deering et al., 1975; Rouse et al., 1974), representing the radiation value and thus, the vitality of vegetation. Like NDVI, NBR takes values running between -1 and 1. In vegetated zones it takes positive values, while its negative values relate to uncovered soil. In consumed regions, NBR values decay simultaneously as the fire seriousness rises (Babu KV et al., 2018). Thus Normalized Burn Ratio is the difference between near-infrared (NIR) and middle-infrared reflectance divided by their sum (Key and Benson, 2006).

In this study, Sentinel 2A and 2B satellite datasets were used to map the progression of forest fire of the burnt area over some parts of Pauri Garhwal and Tehri Garhwal districts of Uttarakhand, India. Sentinel 2 satellite data is freely available and has higher spatial resolution of 10m and 20m. Therefore, the Sentinel 2A and Sentinel 2B dataset was used to generate the forest fire progression map in this study. This paper has attempted to assess the progression of forest fire during the fire season and the major factor which is responsible for forest fire. The study will help in understanding the behaviour of fire with respect to the various factors and their effects in the progression of the fire which will help in forest restoration and mitigation measures.

* Corresponding author

2. STUDY AREA

The study area is part of Pauri Garhwal and Tehri Garhwal districts in Uttarakhand, India located partly in the Gangetic plain and partly in the northern Himalaya. Pauri Garhwal lies between 29.8688° N latitude and 78.8383° E longitude having total area of 5,230 square km and Tehri Garhwal lies between 30.3012° N and 78.5661° E having 4,080 square km total area. Tehri Garhwal district is situated in North to Pauri Garhwal. Pauri town holds the headquarters of the district which is located at elevation of 1814 meters above sea level and elevation of Tehri Garhwal is 1524 meters. Topography of the region is mainly mountainous and it includes forests, meadows, savannah grasslands marshes and rivers. More than 50% of the districts are covered by forests which are found in various types due to variation in altitude, climate, rock and soil etc. The main forest types are Khair/ Sisso forests dominated by species of *Acacia catechu*, *Shorea robusta*, *Dalbergia sissoo*, *Bombax ceiba*, etc; Chir Pine forests consisting mainly of *Pinus roxburghii*; Oak forests with species such as *Quercus semecarpifolia*, *Rhododendron arboreum*, *Rhus panjabensis*, etc; and Deodar forests present at higher elevation consisting *Cedrus deodara* as dominating species and also *Pinus excelsa*, Silver fir and Spruce.

Due to demographic pressure the frequency of forest fire has increased which cause habitat loss of wildlife resulting in human-animal conflicts.

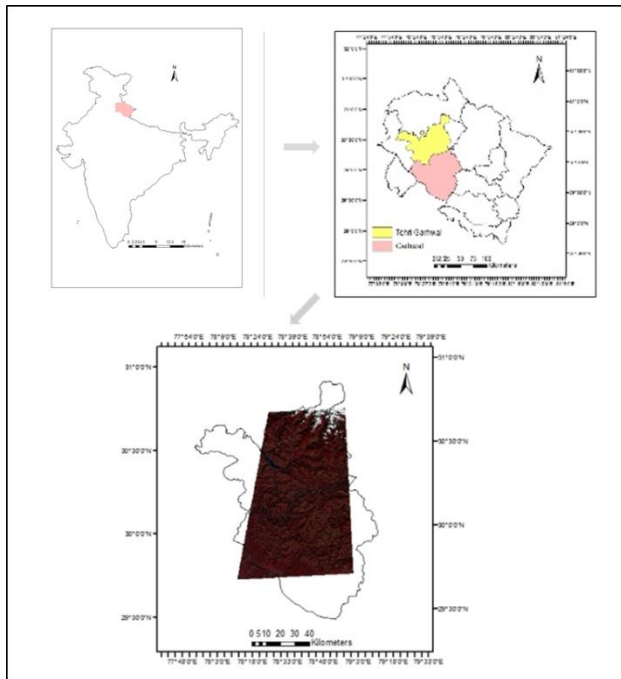


Figure 1: Study area map

3. MATERIAL AND METHODS

3.1 Datasets used

Sentinel 2A and 2B datasets are used for carrying out this study. The data has been downloaded for pre- fire season i.e. for January and for post- fire season i.e. for April and May for the year 2019. Post- fire season data is downloaded with

approximately 10- days interval to monitor the progression of the forest fire in the study area. CartoDEM version 2 data is used to derive the elevation, slope and aspect for the area. The shapefiles for roads and settlements is downloaded from Open Street Map (OSM). The details about the sentinel datasets used in this study are mentioned in table 1.

Table 1: Details of satellite images

Satellite data	Date of acquisition	Tile info
Sentinel 2A	17-01-2019	T44RKU
Sentinel 2B	02-04-2019	T44RKU
Sentinel 2B	15-04-2019	T44RKU
Sentinel 2A	27-04-2019	T44RKU
Sentinel 2B	05-05-2019	T44RKU
Sentinel 2A	10-05-2019	T44RKU
Sentinel 2A	27-05-2019	T44RKU

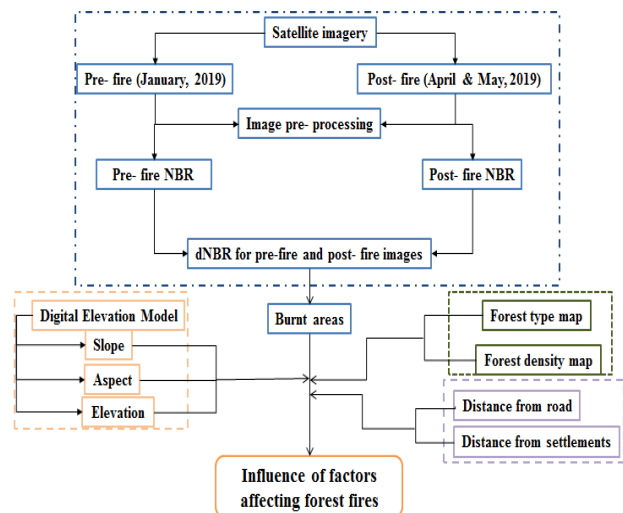


Figure 2: Methodology

3.2 Softwares used

QGIS plug-in called Semi- automatic classification is used for the atmospheric corrections using dark object subtraction method. ERDAS IMAGINE 2014 is used for stacking the layers of the dataset. ERDAS model maker is used to calculate the NDVI, NBR and dNBR for the study area and also reclassifying the outputs. ArcGIS 10.1 software is used to extract the burnt area pixels and calculating Euclidean distance from roads and settlements. Elevation, slope and aspect are derived from CartoDEM using ArcGIS software. Further statistical analysis and the maps composition are also done using ArcGIS software.

3.3 Pre-processing of data

The datasets of pre and post fire events contains 13 bands of different spatial resolution. Only the spectral bands which are required for calculation of NDVI and dNBR i.e. the green, red, near- infrared and short-wave infrared bands are pre- processed to get the atmospherically corrected TOA reflectance bands using dark- object subtraction method. These bands are then stacked together after resampling the short- wave infrared bands to 10m spatial resolution.

3.4 Standardization of Data

Based on the availability of the satellite images for required dates, only the north- west part of Pauri Garhwal district is considered in this study. The shapefiles of roads & settlements and all the data layers i.e. the Sentinel data and CartoDEM are then clipped for the study area.

3.5 Data Processing in GIS

Slope and aspect is derived from the DEM data of the study area. Forest type map and forest cover density map for the study area is prepared by classification techniques in ERDAS IMAGINE. Forest density map is prepared using NDVI slicing method. Euclidean distance is calculated from roads and settlements for the fire season and its correlation with the burnt areas is analysed. The correlation of burnt areas with other factors like slope, aspect, elevation, forest type and forest density is also analysed.

3.6 Burnt area detection

Burnt areas are extracted using an index called Differenced Normalized Burn Ratio (dNBR). Firstly, Normalized Burn Ratio is calculated using the formula stated below for pre- fire season (January, 2019) and for post- fire season i.e. for every 10 days interval data in the months of April and May, 2019 for the study area.

$$NBR = \frac{NIR-SWIR}{NIR+SWIR} \quad (1)$$

dNBR is the difference between the NBR of pre- fire and post- fire images. So, dNBR is calculated with NBR of January being constant as pre- fire NBR and different post- fire data to see the progression and rate of the forest fire in the study area. dNBR results have values ranging from -1 to +1. More the positive value, higher the severity of the burnt areas.

$$dNBR = NBR(pre) - NBR(post) \quad (2)$$

4. RESULTS AND DISCUSSIONS

4.1 Correlation with topographic features

a) Slope

The results show that the burnt areas are very large in the flat region which may be due to human intervention as there are more settlements. Then a gradual decrease in the fire is seen, with increase in slope upto 50 degrees after which no fire is observed with slope increment due to sparse vegetation.

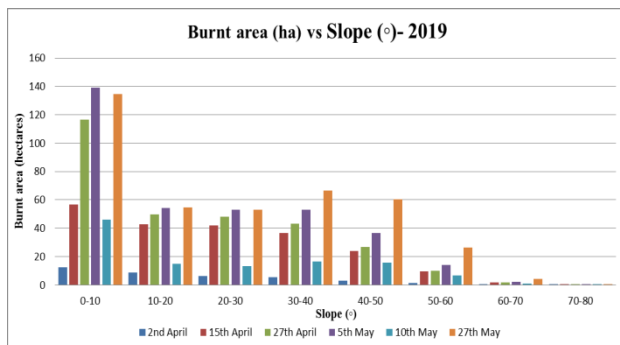


Figure 3: Graph of burnt area plotted against slope

b) Elevation

There is significant area under fire within 500 meters elevation due to the presence of human settlement in the region. With increase in elevation the fire is observed to be decreased up-to 2500 meters, after that a sudden onset is observed due to the presence of pine trees which are generally found in the elevation between 2500 to 3500 meters. Another reason for the increase in the fire progression is due to the upward movement of warm air resulting in moisture loss and elevated temperature in the higher region. The scrubs at lower altitudes as well as the isolated trees and the coniferous vegetation at higher altitudes catch fire easily due to low moisture content and high flammability (Gupta et al., 2018).

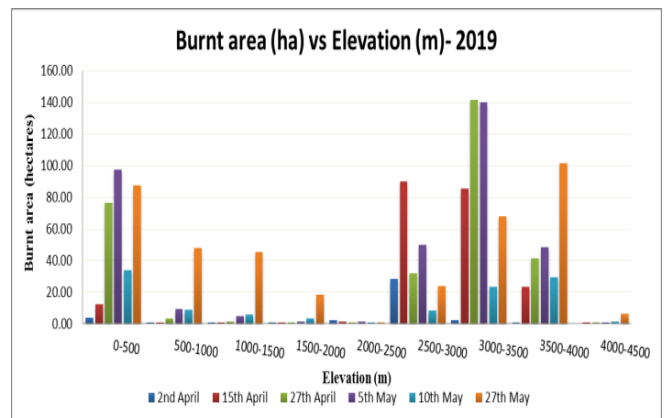


Figure 4: Graph of burnt area plotted against elevation

c) Aspect

The progression of forest fire is seen in both east and west direction which is due to the topography and the solar radiation condition of the region.

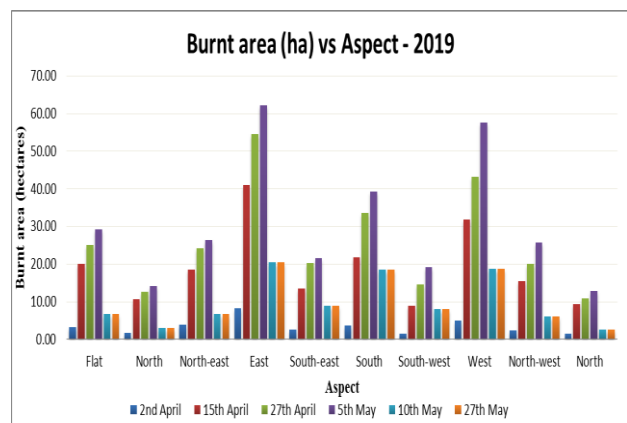


Figure 5: Graph of burnt area plotted against aspect

4.2 Correlation with anthropogenic factors

According to the results, anthropogenic activities are mainly responsible for initiation of the forest fire as the burnt areas are found closer than 500 meters to the roads and settlements. As the distance from the roads and the settlements increase, the fire progression decreases to a certain distance. After verifying from Google earth, it was found that there are some small villages which were not detected in the open street map data so their

effect on forest fire was not assessed. In the same way, some of the un-metalled roads were also not present in the open street data and thus their role in initiating and spreading the forest fire was not assessed.

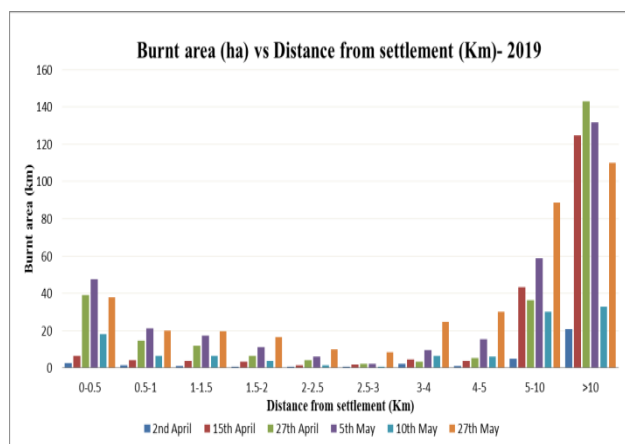


Figure 6: Graph of burnt area plotted against distance from settlement

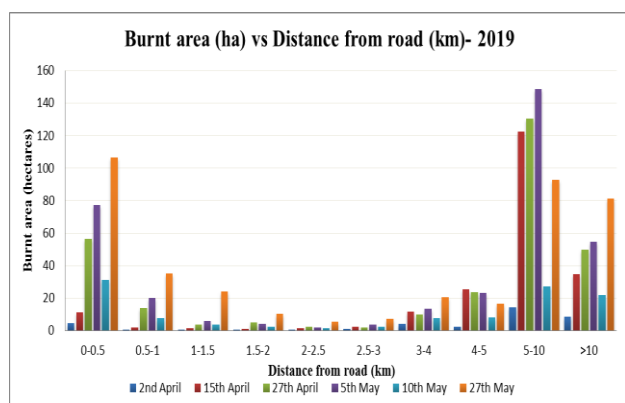


Figure 7: Graph of burnt area plotted against distance from road

4.3 Correlation with vegetation type and density

Species consisting of Oak, Sub-alpine and temperate coniferous are more prone to fire damage. The calorific value of Pine needles are high which adds to its combustibility but are least affected due to its high canopy (Bahuguna and Singh, 2002). In contrast Oak canopies are much lower than Pine making this species vulnerable to fire. However, the scars made in Chir Pine for resin extraction leave the plant susceptible for burning of the heartwood which consequently kills the tree (Koppmann et al., 2005). The results show that the forest fire spreads more in the less vegetation area or the areas where grasses are predominant.

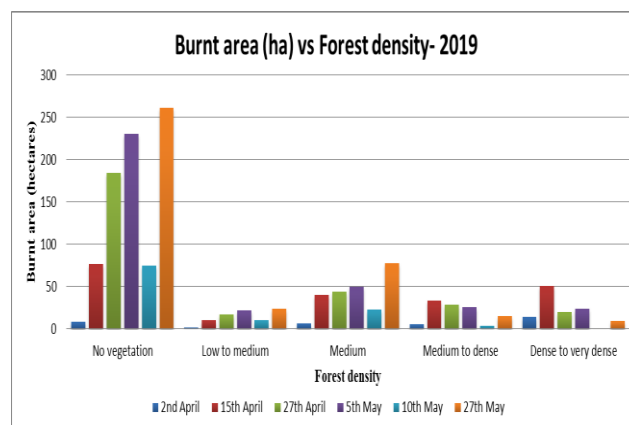


Figure 8: Graph of burnt area plotted against forest density

The table below shows the details of burnt areas within different forest type regions.

Table 2: Details of burnt areas with respect to different forest types

Vegetation type	Burnt areas (2019)					
	2nd April	15th April	27th April	5th May	10th May	27th May
Deodar	0.1	0.47	0.91	1.62	--	0.16
Dry evergreen scrub	0.17	0.75	0.51	0.5	0.08	0.61
Dry alpine scrub	0.95	5	3.65	2.79	0.92	1.01
Mixed plantation	1.21	4.27	5.74	6.1	1.14	2.35
Himalayan moist temperate	0.91	1.42	0.81	1.8	0.29	2.52
Eucalyptus	--	0.15	2.86	3.5	1.53	2.55
Degraded forest	0.19	0.27	1.23	2.29	2	3.11
Dry deciduous	--	0.17	0.8	2.24	1.42	4.95
Sal	0.13	0.26	0.17	1.16	1.96	5.31
Sal mixed moist deciduous	0.3	3.48	3.48	3.86	3.39	6.59
Temperate coniferous	3.22	19.19	9.8	13.52	1.68	9.96
Sub alpine	4.15	26.18	23.6	22.92	4.39	14.79

Oak	6.62	24.1	8.77	34.91	3.81	18.99
Dry deciduous scrub	1.02	0.83	1.02	2.69	2.26	29.32
Pine	0.66	0.85	1.64	3.87	4.91	38.88

4.4 Fire progression analysis

The burnt area is estimated to be about 37 hectares during the onset of the fire season i.e. on 2nd April, 2019. The fire gradually progresses and covers an area of more than 352 hectares i.e. 10 times within a month (5th May, 2019) due to high temperature and dry weather conditions (Bargali et al., 2017; Gupta et al., 2018). The results imply that with the proceeding of the fire season, there is a gradual increase in the fire progression. But during mid-May, there is a sudden decline in the fire progression which is due to the heavy rainfall in the region according to the weather report (also verified with TRMM data).

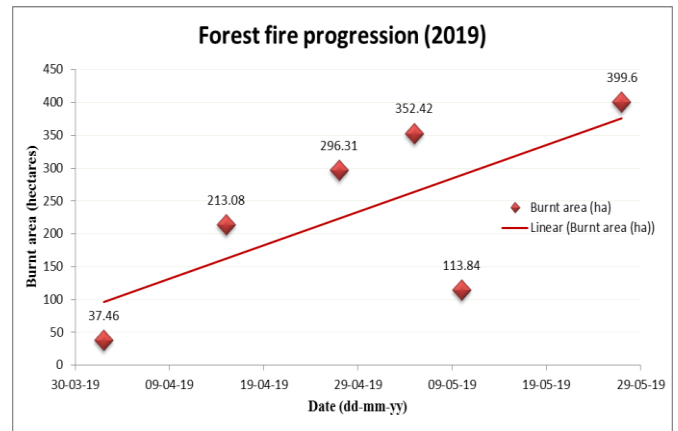


Figure 9: Graph showing the forest fire progression i.e. burnt areas plotted against time

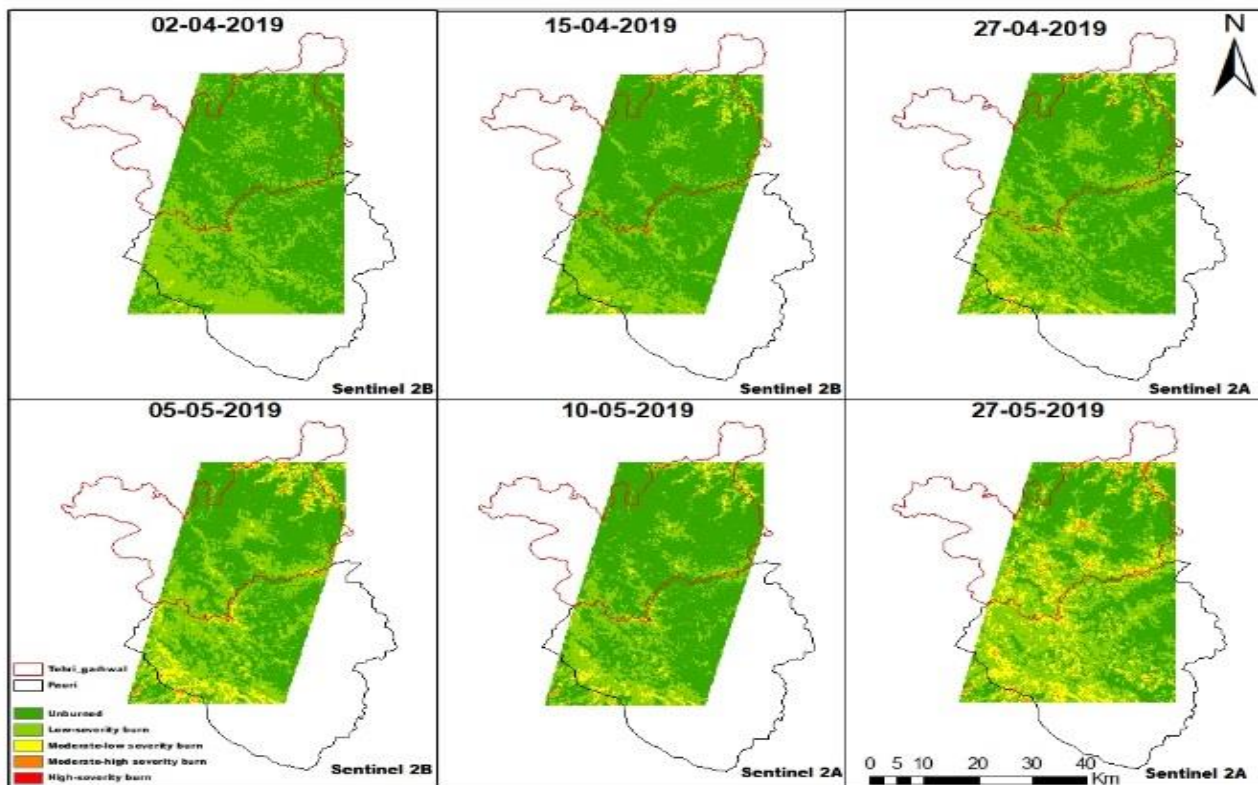


Figure 10: Map showing the forest fire progression with time in the study area

CONCLUSION

In this study datasets of Sentinel 2A and 2B were used to assess forest fire progression during the peak months of forest fire i.e. April and May. Various parameters such as slope, elevation and aspect, anthropogenic factors, vegetation type and density were considered. Anthropogenic factors including road and

settlements were found major factors for initiation of the fire. This was evident by the presence of more burnt area in the regions with the elevation and slope where there were more settlements. The Fire progression was in both East and West directions. Vegetation type also plays an important role in onset of the fire depending on the varied flammability of the different species. Thus, the study would be helpful to detect the most fire prone regions and in attempt to control the severity due to fire.

REFERENCES

- Babu KV, S., Roy, A., Aggarwal, R., 2018. Mapping of Forest Fire burned severity using the Sentinel datasets. XLII, 20–23.
- Bahuguna, V.K., Singh, S., 2002. Fire situation in India. *International Forest Fire News* 26, 23–27.
- Bargali, H., Gupta, S., Malik, D., Matta, G., 2017. Estimation of Fire Frequency in Nainital District of Uttarakhand State by Using Satellite Images. *Journal of Remote Sensing & GIS* 06. <https://doi.org/10.4172/2469-4134.1000214>
- Cocke, A.E., Fulé, P.Z., Crouse, J.E., 2005. Comparison of burn severity assessments using Differenced Normalized Burn Ratio and ground data. *International Journal of Wildland Fire* 14, 189–198. <https://doi.org/10.1071/WF04010>
- Darmawan, M., 2001. Forest Fire Hazard Model Using Remote Sensing and Geographic Information Systems: Toward understanding of Land and Forest Degradation in Lowland areas of East Kalimantan, Indonesia, in: 22nd Asian Conference on Remote Sensing. pp. 20–23.
- Deering, D., Rouse, J., Haas, R., Schell, J., 1975. Measuring forage production of grazing units from Landsat MSS data, in: Proc. 10th Int. Symp. Remote Sensing Environment. pp. 1169–1178.
- García, M.J.L., Caselles, V., 1991. Mapping burns and natural reforestation using thematic mapper data. *Geocarto International* 6, 31–37. <https://doi.org/10.1080/10106049109354290>
- Gubbi, S., 2003. Fire, fire burning bright! Deccan Herald, Bangalore, India. Available from <http://wildlifefirst.info/images/wordfiles/fire.doc>.
- Gupta, S., Roy, A., Bhavsar, D., Kala, R., Singh, S., Kumar, A.S., 2018. Forest Fire Burnt Area Assessment in the Biodiversity Rich Regions Using Geospatial Technology: Uttarakhand Forest Fire Event 2016. *Journal of the Indian Society of Remote Sensing* 46, 945–955. <https://doi.org/10.1007/s12524-018-0757-3>
- India State of Forest Report, Forest Survey of India, 2019.
- India State of Forest Report, Forest Survey of India, 2016.
- Jha, C.S., Gopalakrishnan, R., Thumaty, K.C., Singhal, J., Sudhakar Reddy, C., Singh, J., Vazeed Pasha, S., Middinti, S., Praveen, M., Murugavel, A.R., Yugandhar Reddy, S., Vedantam, M.K., Yadav, A., Srinivasa Rao, G., Parsi, G.D., Dadhwal, V.K., 2016. Monitoring of forest fires from space - ISRO's initiative for near real-time monitoring of the recent forest fires in Uttarakhand, India. *Current Science* 110, 2057–2060. <https://doi.org/10.18520/cs/v110/i11/2057-2060>
- Key, C.H., Benson, N.C., 2006. Landscape assessment: Remote sensing of severity, the Normalized Burn Ratio. FIREMON: Fire Effects Monitoring and Inventory System. General Technical Report, RMRS-GTR-164-CD 305–325. <https://doi.org/10.1002/app.1994.070541203>
- Koppmann, R., Czapiewski, K. V., Reid, J.S., 2005. A review of biomass burning emissions, part I: Gaseous emissions of carbon monoxide, methane, volatile organic compounds, and nitrogen containing compounds. *Atmospheric Chemistry and Physics Discussions* 5, 10455–10516.
- Miller, J.D., Thode, A.E., 2007. Quantifying burn severity in a heterogeneous landscape with a relative version of the delta Normalized Burn Ratio (dNBR). *Remote Sensing of Environment* 109, 66–80. <https://doi.org/10.1016/j.rse.2006.12.006>
- Miller, J.D., Yool, S.R., 2002. Mapping forest post-fire canopy consumption in several overstory types using multi-temporal Landsat TM and ETM data. *Remote Sensing of Environment* 82, 481–496. [https://doi.org/10.1016/S0034-4257\(02\)00071-8](https://doi.org/10.1016/S0034-4257(02)00071-8)
- Rouse, J.W., Haas, R.H., Schell, J.A., Deering, D.W., 1974. Monitoring vegetation systems in the Great Plains with ERTS, NASA SP-351, in: Third ERTS-1 Symposium, NASA, Washington, DC. pp. 309–317.
- Sunar, F., Özkan, C., 2001. Forest fire analysis with remote sensing data. *International Journal of Remote Sensing* 22, 2265–2277. <https://doi.org/10.1080/01431160118510>
- Veraverbeke, S., Sedano, F., Hook, S.J., Randerson, J.T., Jin, Y., Rogers, B.M., 2014. Mapping the daily progression of large wildland fires using MODIS active fire data. *International Journal of Wildland Fire* 23, 655–667. <https://doi.org/10.1071/WF13015>

The Proceedings of National Seminar on 'Recent Advances in Geospatial Technology & Applications', March 02, 2020, IIRS Dehradun, India

DROUGHT MONITORING USING GRAVITY RECOVERY AND CLIMATE EXPERIMENT OVER MARATHWADA REGION

S. M. Bhere¹*, G.K. Patil¹

¹Department of Civil Engineering, Government College of Engineering, Aurangabad, Maharashtra, India 431005.

KEY WORDS: GRACE, Drought, water deficit, Marathwada, Drought indices, NDVI, SPI, GRACE based Drought Index

ABSTRACT:

The Gravity Recovery and climate experiment (GRACE) is a very important tool to monitor the changes in water resources over the globe which was launched as a twin satellite in May 2002 in the lower earth orbit by NASA and German aerospace center. The objective of this work is to explore and study the scope of drought monitoring using gravity recovery and climate experiment (GRACE) in Marathwada, Maharashtra (India) and for validation, the 2009-2010 drought of Maharashtra is considered. The GRACE provides 250 gravity profiles per day and that leads to changes in water storage within the earth's surface. The data from GRACE as terrestrial water storage represents the combination of the surface as well as subsurface water and therefore it is an important tool to analyze the overall changes in terrestrial water storage that lead to a better understanding of drought. For drought, the terrestrial water storage data of GRACE from Jet Propulsion Laboratory (JPL) is used in the form of equivalent water thickness and the monthly average is calculated from the year 2002 to 2015 for determining the monthly deficit in terrestrial water storage by taking the difference between average water storage and the monthly values. The monthly deficit will represent the drought severity by multiplying the duration of deficit and its magnitude. The same approach can be used for analyzing flood by GRACE, in which the excess terrestrial water is calculated from its monthly average of GRACE terrestrial water storage anomaly. The data shows the average magnitude of 2009-2010 is -157.794 mm, the highest deficit in the GRACE series. The summer of 2010 also showed a deficit of about - 101.774 mm and the deficit can be observed as a negative value in the deficit curve from May 2009 to May 2010, a twelve-month drought duration. As GRACE is capable of providing the surface as well as subsurface water storage data, it can be a very powerful tool to analyze the drought than the other indices. For validation, the GRACE based drought index is then compared with the other conventional index and it shows a good correlation with the different indices in the different seasons. The GRACE based drought index is compared with the monthly SPI and NDVI based drought index for pre-monsoon, monsoon, and post-monsoon seasons. The study shows the GRACE based drought index includes all aspects of water storage deficit including groundwater and soil moisture which important for a region like Marathwada, as many farmers depend on groundwater resources.

1. INTRODUCTION

1.1 Drought characteristics

The World Meteorological Organization in 1986 says the drought is a persistent prolonged deficit of precipitation. Drought occurs in climatic zones where the relative precipitation is low and not only precipitation but factors like temperature, humidity, rainfall distribution, and its intensity during cultivation period of crops affect the characteristic, severity and duration of drought (Wilhite, 2000). The UN Convention to combat drought and desertification (UN Secretariat General, 1994) says drought as a phenomenon that causes serious hydrological imbalances due to significantly below normal precipitation and it affects the land resources and its production system. Food and Agriculture Organization (FAO 1983) of the UN defines the drought as a percent of year when crop lacks moisture. Drought in small agricultural fields can also be monitor by Streamflow when the observation of the annual value of daily streamflow is smallest (Gumbel, 1963). Maximum people are affected by drought than any other natural hazard as it affects the food chain which eventually harms the ecosystem. (Gumbel, 1963; Jomaa, Saab, Skaf, El Haj, & Massaad, 2019; Kay, Rudd, Davies, Kendon, & Jones, 2015) Drought can depend on the reduction in terrestrial water storage and can lead to crop failure and water quality deterioration. It also affects the socio-economic conditions of human habitats. (Swenson, Wahr, & Milly, 2003) and such complex hydraulic event may cause major economic damages (Peters et al., 2002) in the country like India where monsoon is predominant and more than 20% deficiency in southwest monsoon consider as a dry year which sometimes shows the reduction of 2 Mha in cultivation land like in 2009-2010. (Murthy, Chakraborty, Sai, & Roy, 2011) Soule and Mooley, 1980, used Standardized Precipitation Index (SPI) as a basic indicator for drought analysis and it is easy to

interpret and spatially invariant and its probabilistic approach may be useful to analyses risk (Tehrany, Pradhan, & Jebur, 2013) SPI gives a better representation of dryness and wetness than other Indices like PDSI but it may not give better picture of monthly water balanced based drought indices and it will only give the transformation of probability of observed precipitation. To study drought in India due to southwest monsoon from June to September, the Standardized Precipitation Index is used. (Pai, Sridhar, Guhathakurta, & Hatwar, 2011) Evaluation of drought requires specific time scale, it also helps to study its impact and it also helps to analyze active and break events in drought. (Pai et al., 2011)'s Study shows SPI is the better index for analyzing drought than Percent of Normal Precipitation for Marathwada.

Healthy vegetation and crops can be judged by satellite-based vegetation index for the signature of droughts on crops as it gives the spectral reflectance ratio between Near Infrared and Red spectrum of electromagnetic wave (Kogan, 1990). (Burgan & Hartford, 1993) studied relative greenness as the percent value of a pixel with reference of average historical greenness of pixel. Drought characteristic can be studied by Normalized Difference Vegetation Index (NDVI) based index as the deviation from mean as the reference of the standard deviation of a pixel for the selective period (Peters et al., 2002)

1.2 About GRACE

Gravity Recovery and Climate Experiment (GRACE) was launched by NASA and German Aerospace Center (DLR) for monitoring gravitational changes on earth with the help of K-band Microwave ranging sensor and global positioning system receiver (J. L. Chen, Rodell, Wilson, & Famiglietti, 2005; J. L. Chen, Wilson, Tapley, & Ries, 2004; Swenson & Wahr, 2002; Swenson et al., 2003). Change in gravity may lead to change in mass and it can further be converted into a change in water resources in equivalent water thickness. (J.

* Corresponding author
Sachin Bhere
studentsachinbhere@gmail.com

Chen et al., 2018; Feng et al., 2013; Hasan, 2009; Sharma, 2014) GRACE data is processed and corrected by Jet Propulsion Laboratory (JPL) by NASA, GFZ German Research Centre for Geosciences and Center for space research, university of Texas.(Swenson et al., 2003)

This paper discuss about the application of Gravity Recovery and Climate Experiment to analyze the extreme hydrological event. The paper is divided into the three sections, first section discuss about the data used to analyze the extreme hydrological event specially drought and flood. The next section discusses about the findings for analyzing drought by different drought index and compassion with the GRACE based drought index. This section also give a glimpse about the analysis of historical flood event based on the terrestrial water storage for the major basins in India like Indus, Ganges, Godavari, Krishna, Narmada and Mahanadi. The final section discusses about the future scope of the finding the conclusion. This section is also provides the insight about the application of the GRACE data for analyzing and prediction of the extreme hydrological events.

2. DATA AND METHODOLOGY

2.1 Study Area

The Marathwada is an administrative region of Maharashtra comprise of eight districts which expands from North latitude 17°5' to 20°5' and east longitude 70°5' to 78°5'. The total geographical area of Marathwada is about 64,000 sq. Km. The Marathwada is located at central Maharashtra and comes under semi-arid region with rainfall of 700 mm and maximum and minimum temperature is about 40° C and 6° C respectively. (Ramachandran et al., 2019) Marathwada have black cotton soil and with the relatively low humidity it makes good environment to cultivate cotton, sugarcane, wheat and other rainfall dependent crops.

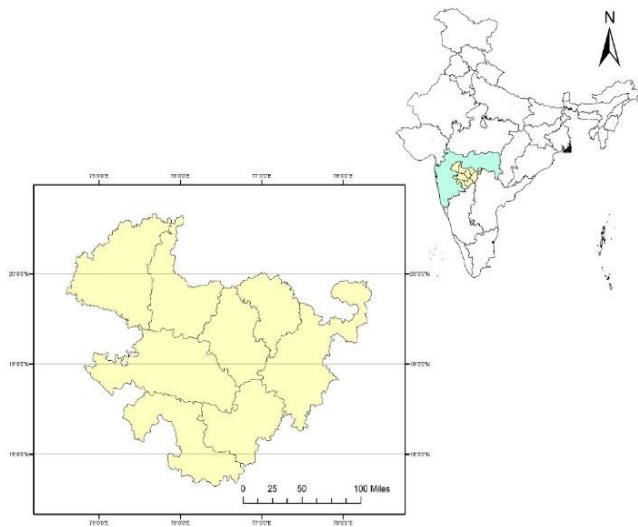


Fig 1. Location of Marathwada as a study area on Map of India and Maharashtra.

The rainfall pattern of Marathwada is changing throughout the year for last few decades. Data shows the decreasing trend of annual rainfall of Marathwada from 1901 to 2017. As the rainfall days and intensity for June and September is shrinking and opposite trend is observed in July and August. From the data we can state that the rainfall days are shrinking and that is affecting the total crop cultivation period. The crop production is mostly depending on rainfall and by decreasing trend one can say that the frequency of drought is increasing. From the data decreasing trend is observed in rainfall for month June from 1901 to 2017 and increasing trend is observed in mid monsoon months like August and July from 1901 to 2017.

2.2 Data and Methodology

The objective of this study is to find out the reliability of the GRACE-based drought index for Marathwada region. The drought in Marathwada is monitored by standardized precipitation index (SPI) as it gives the idea about precipitation deficit it fails to analyze the drought for Rabi or post-monsoon crops. The GRACE-based data can be used to determine the monthly terrestrial water storage (TWS). TWS can be used to represent the actual water availability throughout the year for the cultivation of crops.

This study includes the determination of standardized precipitation index (SPI), NDVI-based drought index and GRACE-based drought index for Marathwada region. The monthly GRACE based index is then compared with monthly SPI and NDVI- based drought index or Standardized vegetation index.

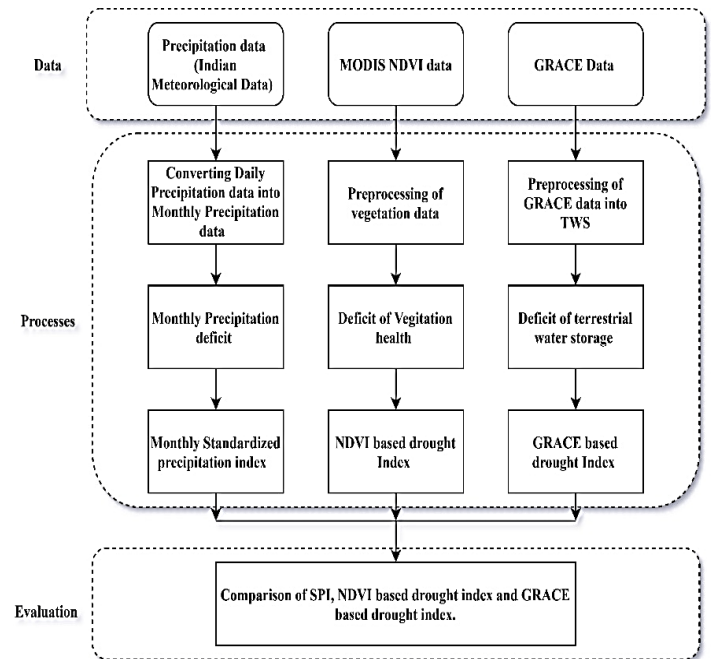


Fig 2. Flowchart of methodology for evaluating standardized drought index, NDVI based drought index and GRACE terrestrial water storage based drought index.

Figure represent the flow of methodology for evaluating different drought index along with GRACE based drought index. For calculating Standardized vegetation index the daily precipitation data form Indian meteorological department is used and then it was converted into monthly rainfall data form year 2002 to 20011. NDVI based drought index is calculated with the help of regional MODIS NDVI data (<https://glam1.gsfc.nasa.gov/>). The regional NDVI data is then used to calculate the monthly healthy vegetation deficit. The NDVI based drought index may be used to determine the agricultural condition of Marathwada. The GRACE based drought index is calculated for monthly terrestrial water storage. The data is obtained from the processing center of GRACE Website of Center for Space Research (CSR) of University of Texas at Austin. (<http://www.csr.utexas.edu/grace>). The monthly data is then used to determine the deficit of monthly terrestrial water storage and then the index is calculated. The GRACE's terrestrial water storage is comprise of different water resources so the drought index may replicate the total deficit of all water resources

2.2.1 Standardized Precipitation Index: The standardized precipitation drought index is calculated based on the average precipitation deficit. The SPI can be calculated in the monthly, 3-month, 6-month, 9-month and 12-month interval. In this study the monthly SPI is used. The SPI is easily calculated. The SPI gives the good interpretation of drought for monsoon season spatially and temporally. SPI gives a better representation of dryness and wetness

The Proceedings of National Seminar on 'Recent Advances in Geospatial Technology & Applications', March 02, 2020, IIRS Dehradun, India than other Indices like PDSI but it may not give better picture of monthly water balanced based drought indices and it will only give the transformation of probability of observed precipitation.

2.2.2 NDVI-based Drought Index:For calculating NDVI-based drought index Moderate resolution imaging spectroradiometer (MODIS) vegetation index product is used (Lan, Zhang, Lacey, Hoffmann, & Wu, 2009). NDVI is used to determine the condition of healthy vegetation. It ranges from -1 to 1. These values represent the health of vegetation. Values near one represent the healthy vegetation. It is calculated by taking ratios of spectral reflectance of NIR and Red spectrum of electromagnetic wave (Bechtel et al., 2012)

NDVI-based drought index is calculated by taking difference between NDVI values (NDVI_{ij}) of each Pixel with monthly average (\overline{NDVI}_{ij}) of each pixel and then it is divided by the standard deviation. For developing drought index, the deficit in vegetation health index (D_{VI}) is calculated.

$$D_{VI} = \frac{NDVI_{ij} - \overline{NDVI}_{ij}}{\sigma} \quad (1)$$

Vegetation drought index is then calculated by dividing the deficit vegetation health index by the monthly standard deviation of NDVI ($\bar{\sigma}$)

$$VDI = D_{VI} / \bar{\sigma} \quad (2)$$

By NDVI-based drought index, the drought severity is divided into five categories from very poor to very good. Following are the classification and NDVI- based drought index values(Peters et al., 2002)

NDVI-Based drought index range	Classes
0 – 0.05	Very Poor
0.05 - 0.25	Poor
0.25 – 0.75	Average
0.75 – 0.95	Good
0.95 – 1.00	Very good

Table 1. Classification based on the normal probability distribution of NDVI-based drought index into five classes.

The above classification is based on the normal probability distribution of NDVI. The classes very poor or poor represent the lower NDVI values than the average value of that month of year. Similarly the good and very good represent the high NDVI values than the average values of NDVI of that month in the year.

2.2.3 GRACE- based Methodology: Gravity recovery and climate experiment (GRACE) was launched as a joint mission by German space research agency and NASA to determine the change in gravitation field of earth. To determine the change in gravitational field of earth the two satellites with precise distant meter and GPS is launched in 2002. The change in distance between two satellites is then converted and downscaled into gravitational change of earth. Further the data is downscaled and processed to use as a change in terrestrial water storage. The Terrestrial water storage of GRACE data can is then converted into the equivalent water thickness to replicate the change in water storage, especially ground water. The change in terrestrial water storage shows not a single water resources but complex combination of different water resources and segregating these water resources may require different observed

data and other information. Proposed drought index involved the overall terrestrial water storage and the monthly deficit is calculated by taking difference between the monthly terrestrial water storage and monthly average terrestrial water storage. To form the index the terrestrial water deficit is then divided by the standard deviation of monthly GRACE data. The index is calculated based on the water storage deficit (D_{WS}). The water storage deficit is calculated by taking difference between the monthly values of terrestrial water storage (WS_{ij}) for ith month of jth year to the monthly average of series of terrestrial water storage (\overline{WS}_{ij}).

$$D_{WS} = WS_{ij} - \overline{WS}_{ij} \quad (3)$$

The GRACE based drought index (GDI) is then calculated by dividing water storage deficit (D_{WS}) by its standard deviation ($\bar{\sigma}$)

$$GDI = D_{WS} / \bar{\sigma} \quad (4)$$

The GRACE based drought index represent the actual deficit in the water storage and replicate the actual drought condition for year. The GRACE based drought index may be the actual measurement of the drought for post-Monsoon crops. The severity can be calculated by considering peak value of drought index and period can be calculated by considering the start and end of t6he negative graph which represent the values below average. The negative value of GRACE based drought index shows the drought period and positive value represent non-drought or average to good water storage condition.

3. Result and Discussion

3.1 2009 Marathwada drought analysis

Drought occur in 2009-2010 was one of the extreme drought of Marathwada and all over India and it was considered as the worst drought in 40 years by The Economic Times. In this study the severity of drought is calculated using change in GRACE terrestrial water storage data and drought index is formed as already discussed in methodology which include the calculation of monthly water deficit for Marathwada region. The GRACE based drought index gives the idea about the deficit in the total terrestrial water storage by considering the monthly average of GRACE 15 year series. For year 2009-2010 the negative value is observed from May 2009 to January 2010 and it drops again in March 2010. The negative value of GRACE based drought index shows the occurrence of drought in mid-May till next year monsoon. The values of GRACE based drought index is noted as -3.759 in September-October 2009.

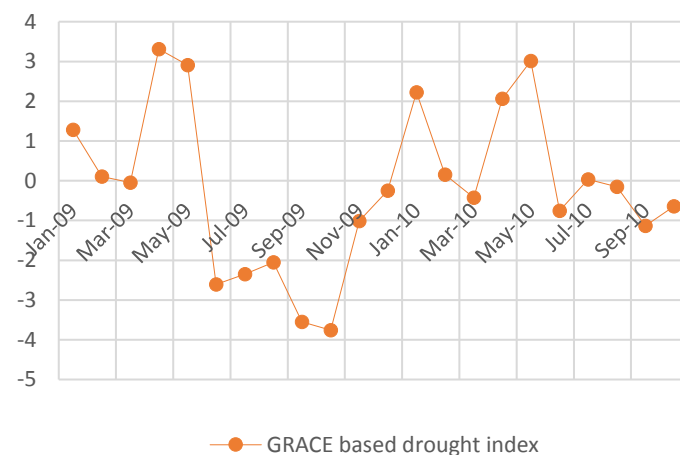


Fig 3. The GRACE based drought index for Marathwada

As GRACE terrestrial water storage include not only surface water but it includes soil moisture and ground water storage. Comparing GRACE based drought index with other conventional drought index like Monthly Standardized Precipitation Index (SPI-1) and NDVI based drought index, the GRACE based drought characterization is

validated. The monthly SPI shows the peak negative values in month of June 2009 as -1 which shows the historically low deficit in rainfall.

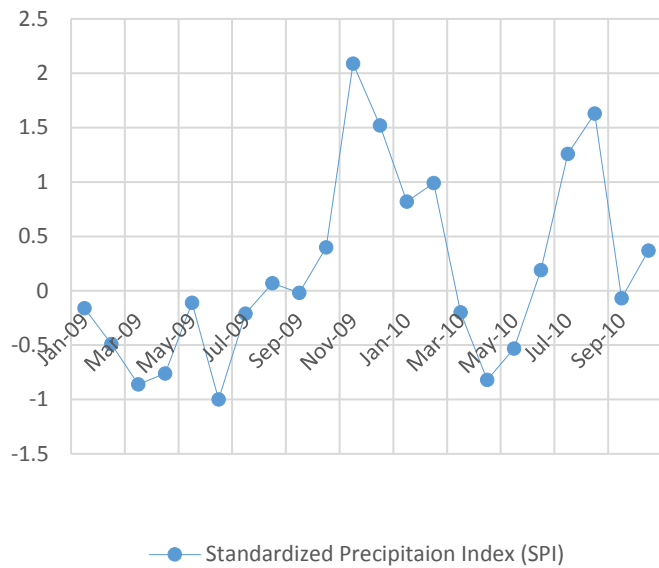


Fig 4. The Standardized Precipitation Index (SPI) for Marathwada

This low rainfall is going to affect the total terrestrial water storage throughout the year and it replicate in the drought index which is based on NDVI and GRACE. The NDVI based drought index shows the monthly vegetation health deficit. The NDVI based drought index shows the negative value in the post monsoon month as the low rainfall affect the vegetation health throughout the year. The GRACE based drought index shows the both scenario of SPI and NDVI based drought index as it covers the soil moisture, groundwater storage and surface water storage altogether. The NDVI based drought index shows relatively good values in monsoon period as the vegetation health is directly proportional to the availability of water into root zone of vegetation. The crop production can be judge by the NDVI based drought index.

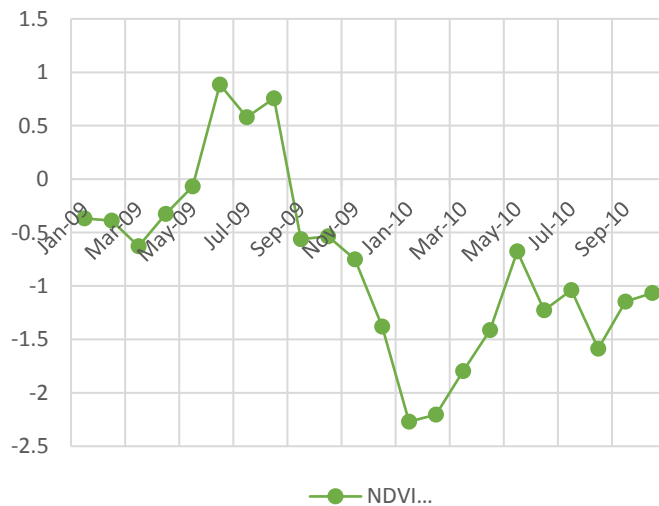


Fig 5. NDVI based drought index for Marathwada

The comparison of NDVI and GRACE based drought index shows the very good correlation for Monsoon season and relatively good correlation for post and pre monsoon seasons. The SPI shows the poor correlation with other drought index as it only shows the deficit of rainfall.

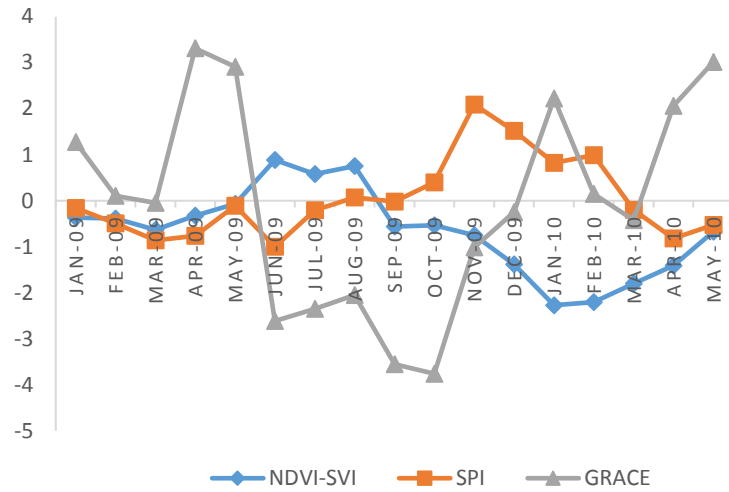


Fig 6. The line plot of different index for drought year 2009-2010

Indices	Pre-Monsoon	Monsoon	Post-Monsoon
NDVI and GRACE based drought index	0.5631	0.7973	0.6914
SPI and GRACE based drought index	0.0667	0.001	0.729
SPI and NDVI based drought index	0.5332	0.2273	0.1776

Table 2. Correlation of GRACE based drought index with NDVI based drought index and SPI for Pre-Monsoon, Monsoon and Post-Monsoon seasons for year 2009.

4. CONCLUSION AND SUMMARY

The study shows the GRACE based drought index include all aspects of water storage deficit including groundwater and soil moisture which important for region like Marathwada as many farmers depends on ground water resources like well and borewells. NDVI based drought index fails to show the monsoon drought condition but it can be used to for characterization of post monsoon drought as it shows the vegetation health index. The Standardized Precipitation index may show the rainfall deficit for monsoon season but it fails to recognize drought and its severity in post and pre monsoon period. As 2009 and 2004 drought shows significant correlation with GRACE based drought index and NDVI based drought index, one should adopt these indices for characterization of drought. The duration and severity can also be calculated by GRACE based drought index more accurately. The GRACE based drought index shows the reasonable precision for monthly drought analysis where the groundwater is the major source of water. Gravity recovery and climate experiment have a capability of providing monthly terrestrial water storage data. After 2017 the GRACE-FO is providing data with more accuracy so the real time drought characterization is possible for large area as the spatial resolution of GRACE is good. The prediction of drought can be possible with the help of GRACE mission as the terrestrial water storage is depends on the rainfall in the Marathwada as it is the only source of water. The GRACE is very string tool to understand the ground water changes in the region and it will help to policymaker to understand the drought condition and can plan the new agricultural pattern in Marathwada. The GRACE based drought index shows good correlation with NDVI based drought index which replicate the vegetation and crop health. The researcher may use GRACE based drought index to analyze the local condition of drought according to the use of different water resources. The

The Proceedings of National Seminar on 'Recent Advances in Geospatial Technology & Applications', March 02, 2020, IIRS Dehradun, India
Stream flow drought index (SFDI) will also use to judge the GRACE based drought index where the crop cultivation is depending on only single stream of water. The GRACE can also use to identify the basin performance by the historical terrestrial water storage analysis. The floods can be analyze by determining the above average trend of the GRACE index. The reliability of this drought index can be calculated by comparing different drought indices in the different categories like hydrological droughts, meteorological drought and agricultural drought.

ACKNOWLEDGEMENT

I would like to thank Government College of Engineering, Aurangabad for providing lab facility to analyze GRACE the data. I would also like to extend my gratitude towards Dilkap Research Institute of Engineering and Management Studies, Neral, Indian Meteorological Department, Pune and Dr. D. G. Regulwar for valuable help while processing and working on data.

REFERENCES

Bechtel, B., Langkamp, T., Böhner, J., Daneke, C., Oßenbrügge, J., & Schempp, S. (2012). Classification and Modelling of Urban Micro-Climates Using Multisensoral and Multitemporal Remote Sensing Data. *ISPRS - International Archives of the Photogrammetry, Remote Sensing and Spatial Information Sciences*, XXXIX-B8(September), 463–468.
<https://doi.org/10.5194/isprsarchives-xxxix-b8-463-2012>

Burgan, R. E., & Hartford, R. A. (1993). Monitoring vegetation greenness with satellite data. *General Technical Report - US Department of Agriculture, Forest Service*, (INT-297).

Chen, J. L., Rodell, M., Wilson, C. R., & Famiglietti, J. S. (2005). Low degree spherical harmonic influences on Gravity Recovery and Climate Experiment (GRACE) water storage estimates. *Geophysical Research Letters*, 32(14), 1–4.
<https://doi.org/10.1029/2005GL022964>

Chen, J. L., Wilson, C. R., Tapley, B. D., & Ries, J. C. (2004). Low degree gravitational changes from GRACE: Validation and interpretation. *Geophysical Research Letters*, 31(22), 1–5.
<https://doi.org/10.1029/2004GL021670>

Chen, J., Li, J., Zhang, Z., Ni, S., Senanayake, I. P., Dissanayake, D. M. D. O. K., ... Mansor, S. (2018). Overview of the Gravity Recovery and Climate Experiment (GRACE) Data and Applications. *Global and Planetary Change*, 7(1), 33–43.
<https://doi.org/10.5194/hess-15-2665-2011>

Feng, W., Zhong, M., Lemoine, J. M., Biancale, R., Hsu, H. T., & Xia, J. (2013). Evaluation of groundwater depletion in North China using the Gravity Recovery and Climate Experiment (GRACE) data and ground-based measurements. *Water Resources Research*, 49(4), 2110–2118. <https://doi.org/10.1002/wrcr.20192>

Gumbel, E. (1963). Statistical forecast of droughts. *International Association of Scientific Hydrology. Bulletin*, 8(1), 5–23.
<https://doi.org/10.1080/02626666309493293>

Hasan, S. (2009). *Terrestrial water storage change from temporal gravity variation*. Retrieved from http://www.hydrology.nl/images/docs/dutch/2009.04.27_Shaakeel_Hasan.pdf

Jomaa, I., Saab, M. T. A., Skaf, S., El Haj, N., & Massaad, R. (2019). Variability in Spatial Distribution of Precipitation Overall Rugged Topography of Lebanon, Using TRMM Images.

Atmospheric and Climate Sciences, 09(03), 369–380.
<https://doi.org/10.4236/acs.2019.93026>

Kay, A. L., Rudd, A. C., Davies, H. N., Kendon, E. J., & Jones, R. G. (2015). Use of very high resolution climate model data for hydrological modelling: baseline performance and future flood changes. *Climatic Change*, 133(2), 193–208.
<https://doi.org/10.1007/s10584-015-1455-6>

Kogan, F. N. (1990). Remote sensing of weather impacts on vegetation in non-homogeneous areas. *International Journal of Remote Sensing*, 11(8), 1405–1419.
<https://doi.org/10.1080/01431169008955102>

Lan, Y., Zhang, H., Lacey, R., Hoffmann, W. C., & Wu, W. (2009). Development of an Integration Sensor and Instrumentation System for Measuring Crop Conditions. *Agricultural Engineering International: CIGR Journal*, 0(0), 1–16.

Murthy, C. S., Chakraborty, A., Sai, M. V. R. S., & Roy, P. S. (2011). Spatio-temporal analysis of the drought of kharif 2009 and 2002. *Current Science*, 100(12), 1786–1788. Retrieved from <http://www.jstor.org/stable/24077547>

Pai, D. S., Sridhar, L., Guhathakurta, P., & Hatwar, H. R. (2011). District-wide drought climatology of the southwest monsoon season over India based on standardized precipitation index (SPI). *Natural Hazards*, 59(3), 1797–1813.
<https://doi.org/10.1007/s11069-011-9867-8>

Peters, A. J., Walter-Shea, E. A., Ji, L., Viña, A., Hayes, M., & Svoboda, M. D. (2002). Drought monitoring with NDVI-based Standardized Vegetation Index. *Photogrammetric Engineering and Remote Sensing*, 68(1), 71–75.

Ramachandran, A., Palanivelu, K., Mudgal, B. V., Jeganathan, A., Guganesh, S., Abinaya, B., & Elangovan, A. (2019). Climate change impact on fluvial flooding in the Indian sub-basin: A case study on the Adyar sub-basin. *PLoS ONE*, 14(5), 1–24.
<https://doi.org/10.1371/journal.pone.0216461>

Sharma, H. (2014). Evaluation of Groundwater Depletion Scenario and its Impacts in NW India by Geodetic Techniques and Modelling Approaches Evaluation of Groundwater Depletion Scenario and its Impacts in NW India by Geodetic Techniques & Modelling Approaches, 76.

Swenson, S., & Wahr, J. (2002). Methods for inferring regional surface-mass anomalies from Gravity Recovery and Climate Experiment (GRACE) measurements of time-variable gravity. *Journal of Geophysical Research: Solid Earth*, 107(B9), ETG 3-1-ETG 3-13. <https://doi.org/10.1029/2001jb000576>

Swenson, S., Wahr, J., & Milly, P. C. D. (2003). Estimated accuracies of regional water storage variations inferred from the Gravity Recovery and Climate Experiment (GRACE). *Water Resources Research*, 39(8).
<https://doi.org/10.1029/2002WR001808>

Tehrany, M. S., Pradhan, B., & Jebur, M. N. (2013). Spatial prediction of flood susceptible areas using rule based decision tree (DT) and a novel ensemble bivariate and multivariate statistical models in GIS. *Journal of Hydrology*, 504, 69–79.
<https://doi.org/10.1016/j.jhydrol.2013.09.034>

Wilhite, D. A. (2000). Chapter1 Drought as a Natural Hazard. *Drought: A Global Assessment*, 147–162.

ANALYSIS OF UTTARAKHAND FOREST FIRE WITH LANDSAT 8 IMAGERY FOR YEARS 2015 TO 2019: A CASE STUDY OF PAURI DISTRICT

Pooja Dobhal¹, Rishi Prakash² and Nitin Mishra³

^{1,3}Department of Civil Engineering, ²Department of Electronics and Communication Engineering
Graphic Era Deemed to be University, Dehradun, India
pujadobhal@gmail.com, dr.rishi.prakash@ieee.org

KEY WORDS: Forest fire, Fire detection, Landsat 8, MODIS, VIIRS, OLI data

ABSTRACT:

Forest fire is one of the disasters causing threat to biodiversity and it has various adverse effects on the environment. The burning can reduce the soil nutrients and makes it more vulnerable for soil erosion. The smoke and pollution release due to fire can cause various types of respiratory diseases. Therefore, it is vital to have accurate and timely information of fire. With the adoption of free data policies and advancement in instruments and technology, this life taking threat can be detected and managed timely. Though the ultimate goal is to protect our forests from this life taking threat, the main objective of this paper is to review the capability of existing fire detection algorithms on Landsat 8 data for Pauri Garhwal region of Uttarakhand, India. The studies have been conducted for the years 2015 to 2019 with the help of high spatial resolution (30 m) Landsat-8 imagery. The algorithms used to study the active fire were developed by Schroeder et al., 2016. The algorithm gives the active fire data, for which initial validation has been done with visual interpretation but the conformity has been done using fire points from existing fire detecting and monitoring instrument (MODIS and VIIRS) which provides real-time forest fire data regularly. The result of Landsat 8 fire detection algorithms shows the significant increase in the detection of small fires. This paper also suggests that combination of remote sensing and GIS tools can be the most promising technique to deal with such life causing threats.

1. INTRODUCTION

Forest fire in Uttarakhand region occurs very frequently. This region is more vulnerable for forest fire due to the presence of highly flammable Pine Trees and larch stands. In the summer season from April to May, fire incidents are at peak when both air and soil temperatures are high. When the temperature is high, the moisture content in atmosphere becomes low which results into easy ignition of the fire. This is the reason why fires are prevalent around the summer time (Hussin et al., 2008). Frequent occurrence of this hazard has been one of the major reasons for the depletion and extinction of most of our valuable plants and animal species. In spite of frequent occurrence of forest fire, there was no detailed and dependable information available (Chand et al., 2007). This scenario also results in a lot of underestimations of fire extent deriving from lack of detection system and monitoring of fire occurrence in inaccessible areas and high costs of the ground surveys. Without any reliable information about the extent fires, management to handle it is totally difficult.

To overcome from this problem, remote sensing is the only way that permits to capture the type of data that humans cannot sense such as near infrared and thermal part of electromagnetic spectrum (Chuvieco et al., 1989). This technology can assess the area which is inaccessible to us. It is even impossible to do ground survey of such areas and proper estimate can never be provided by such traditional methods.

Current trend of day by day increasing in the rate of forest fire events in the state, there is an urgent need of the technology which can efficiently detect fire on real time and manage it. Though more than a decade, a satellite remote sensing active fire data has been widely used to inform fire management systems (Rugumamu, 1995), but due to the coarser spatial resolution data availability it becomes difficult to locate the fire

spot. This can only be done with the help of high spatial resolution remote sensing imageries.

With the increase in open data policies and the availability of satellite images with high spatial resolution, detection and management of this threat become more efficient. These detections can be useful in many ways such as for identifying the fire prone areas (Giglio et al., 2003), to stop fire on time so that it cannot damage the environment and all the living forms, burnt area can be detected (Jha et al., 2016) and further techniques can be applied to reduce its impact. Similarly, numerous other applications such as air quality and carbon emission mapping methodologies have aided from point source information provided by satellite active fire detection and illustrating data set (Justice et al., 2002). The main aim of this paper is to review the capability of existing fire detection algorithms (Schroeder et al., 2016) on Uttarakhand area and to analyse five year's forest fires in this region.

2. STUDY AREA

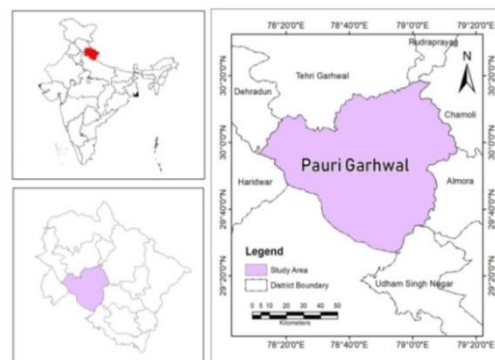


Figure 1. Study Area

The study area Pauri Garhwal is one of the districts of Uttarakhand, India, which is located partly in the Gangetic plain and partly in the northern Himalayas (Figure 1). It lies between the latitude 29° 45'N to 30°15' N and longitude 78° 24'E to 79° 23' E. It encompasses an area of 5329 sq. km and is located at a height of 1650 m. The Pauri Garhwal has generally sub-temperate to temperate climate and it remains pleasant in summers and cold in winters. The maximum temperature known in the month of June is 45°C at Kotdwar while at Dhuthatoli it only rises to 25°C. Temperature descends to a minimum of 1.3°C in January and average monthly temperature for the region ranges from 25°C to 30°C.

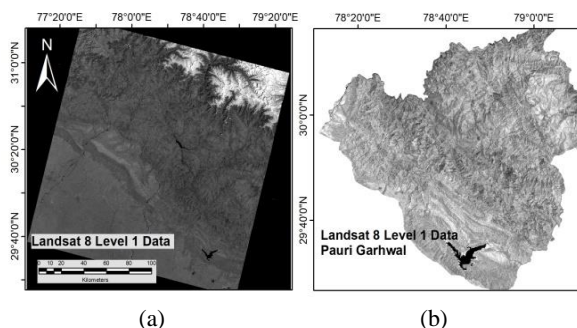


Figure 2. (a) Landsat 8 Level 1 Data (b) Clipped Pauri Garhwal Area

The hilly terrain with its densely forested slopes receives adequate rainfall generally commencing from mid- June up to mid- September. Occasionally rainfall is noted in winters. Average annual rainfall in the Pauri district is 218 cm, about 90 percent of which is generally concentrated over the monsoon. Relative humidity varies between 54 and 63 percent. In winters, many parts of Pauri receive snowfall when temperature drops to a freezing point. Besides Alaknanda, Nayar is the major river in the district and one of the major tributaries of Alaknanda, after the confluence of eastern and Western Nayar at Satpuli. Eastern and western Nayyars originate from Dudatoli range and drain their water to the south (Saklani P., 2008).

There is a huge considerable variation on the forest type in study area which are mainly based on altitude, climate, rocks, soil etc. Khair and Sisso Forests, which are also termed as Reverie forests, occur in areas of lower elevations while Chir Pine forests are the most extensively developed type in the Nayar catchments. These forests are found at the altitude which ranges between 900 m to 1500 m. Oak forests occur at an altitude ranging from 800 m to the highest elevations of Pauri Garhwal area. Deodar forests are confined to areas of higher elevation and one of the most beautiful types found in the Himalayan region. Individual trees may attain a height of over 35 m and a diameter of over 110 cm.

Pauri Garhwal area of Uttarakhand is selected for the study because it is highly susceptible to fire. This region has experienced forest fire every year in the months of April and May.

3. DATA USED

In this work Landsat-8 satellite data, shape file to extract study area and fire points from MODIS and VIIRS for validation have been used. Landsat 8 Level 1 images have been acquired from USGS Earth Explorer website. Landsat 8 data used for the

study listed in the Table 1. The Landsat-8 was designed by the National Aeronautics and Space Administration (NASA) carrying the Operational Land Imager (OLI) and Thermal Infrared Sensor (TIRS). It is placed on a sun-synchronous orbit at 705 km altitude and 10:00 am equatorial crossing time. It has 16 days Temporal Resolution. In this study, standard terrain corrected Level 1 T from OLI has been used. It has nine spectral channels with a spatial resolution of 30m (15m for Panchromatic Channel 8). It has 185 km x 180 km scene size. Shape file of Uttarakhand and India has been downloaded from ArcGIS and Info GIS MAP website respectively. MODIS C6 (Aqua and Terra) and VIIRS-1 (375m Spatial Resolution) Fire Points for validation have been downloaded from Fire Information for Resource Management System (FIRMS). VIIRS data and MODIS fire data are best complement to each other due to their increased temporal resolution. The improved spatial resolution of the 375 m data provides a greater response over fires of relatively small areas as compared to MODIS of 1 km spatial resolution.

Date	Data Id
17-04-2015	LC08_L1TP_146039_20150417_20170409_01_T1
19-04-2016	LC08_L1TP_146039_20160419_20170326_01_T1
05-03-2017	LC08_L1TP_146039_20170305_20170316_01_T1
25-04-2018	LC08_L1TP_146039_20180425_20180502_01_T1
28-04-2019	LC08_L1TP_146039_20190428_20190508_01_T1

Table 1. Landsat 8 Level 1 data used for the Study

4. METHODOLOGY

The main aim of this study is to apply the fire algorithms (Schroeder et al., 2016) in the study area to show that landsat can detect fire more accurately with better spatial resolution than the existing fire detecting sensors. Following steps explains the methodology for detection of fire pixels in Landsat Level 1 image and its validation. Figure 3 shows the flowchart of methodology.

Step 1: The study area from satellite image has been extracted using shape file of Uttarakhand (Figure 2).

Step 2: Conversion of DN into Reflectance data has been done using rescaling coefficients found in the metadata (MTL) file available with L1T data.

Step 3: The algorithm developed by Schroeder et al., 2016 has been used to detect fire pixel in the study area.

Step 4: Conversion of fire pixels into vector points has been done to locate the position and for validation purpose.

Step 5: Buffering of Landsat points, MODIS points and VIIRS points have been done according to their respective spatial resolution to validate the fire pixels obtained from Landsat images.

Landsat 8 provide images at a spatial resolution of 30 m whereas the fire product available from MODIS & VIIRS are at a spatial resolution of 1 km and 375 m respectively. Therefore with Landsat data more fine details can be obtained.

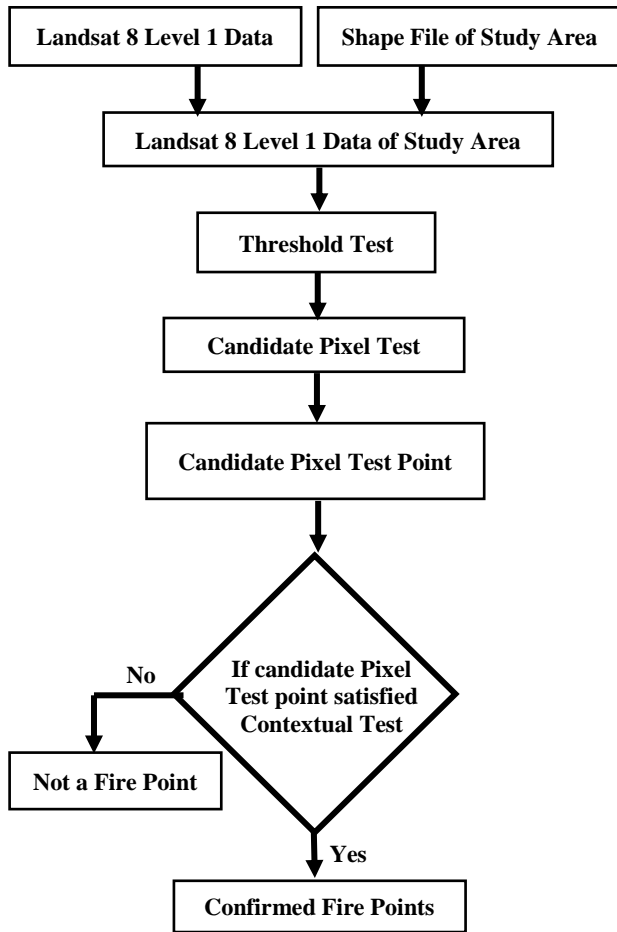


Figure 3. Flowchart showing methodology adopted to detect active fire pixel

5. RESULT AND DISCUSSION

The pixel values of Landsat 8 L1T data are in the form of digital number. The radiometric resolution of Landsat 8 L1T product is 16 bit, therefore the pixel values ranges from 0 to 65535. When the image is in the form of digital numbers it does not provide any direct relationship with physical property of land cover. The physical property such as surface temperature, atmospheric temperature, surface moisture, leaf water, and biomass are related to the spectral reflectance. Therefore, to determine the physical property of land use land cover, reflectance data is more powerful than digital number. The digital number provided in Landsat L1T product can be converted to the Top Of Atmosphere (TOA) reflectance (Figure 4) by using equation 1.

$$R = M \times DN + A \quad (1)$$

Where

R = TOA planetary spectral reflectance

M = Reflectance multiplicative scaling factor for respective band,

DN = L1 pixel value in DN

A = Reflectance additive scaling factor for respective band. Coefficients M and A can be obtained from the metadata file provided with Landsat L1T product.

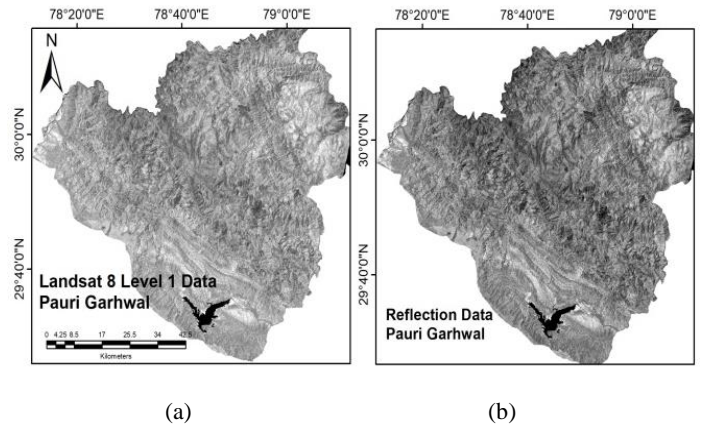


Figure 4. Conversion from DN to Reflectance.(a) Data in Digital Number (b) Reflectance Data

Then algorithms developed by Schroeder et al., 2016 have been applied in which initial algorithm is mainly based on the fire sensitive SWIR channel 7 data. This channel uses the emissive component of fires in the $2.2 \mu\text{m}$ spectral window. During the day time, the emissive fire component is mixed with the background which is dominated by the reflected solar component. In order to separate them, the NIR channel 5 data have been used that are mostly unresponsive to fire affected pixels. The algorithm-1 designed to identify potentially unambiguous active fire pixels which is given by equation 2.

$$\{R_{75} > 2.5 \text{ AND } R_7 - R_5 > 0.3 \text{ AND } R_7 > 0.5\} \quad (2)$$

Where

R_i = Reflectance of band i and

R_{ij} = Ratio between reflectance of band i and band j .

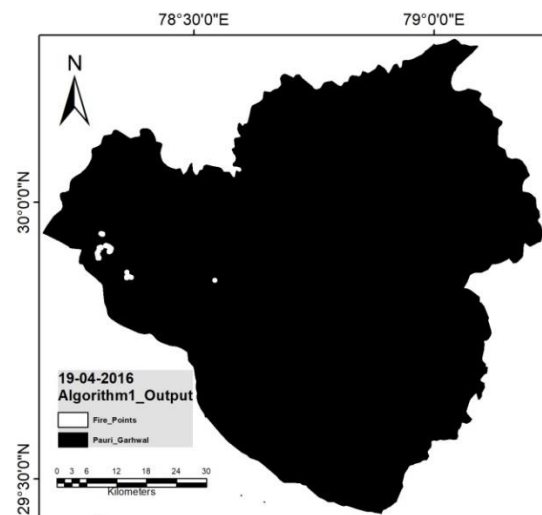


Figure 5. Algorithm 1 Output

To check the other candidate's fire pixels for further analysis, algorithm-2 applied which is given by equation 3.

$$\{R_{75} > 1.8 \text{ AND } R_7 - R_5 > 0.17\} \quad (3)$$

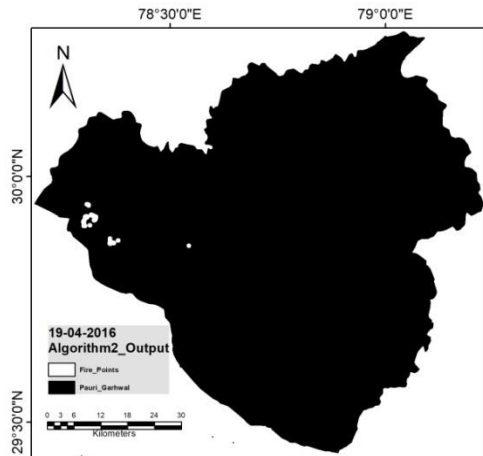


Figure 6. Algorithm 2 Output

Pixels satisfying algorithm 2 must need to satisfy the following set of contextual equations to be classified as fire pixels.

$$R_{75} > R_{75}^- + \max[3\sigma_{75}, 0.8] \quad (4)$$

AND

$$R_7 > R_7^- + \max[3\sigma_7, 0.8] \quad (5)$$

AND

$$R_{76} > 1.6 \quad (6)$$

Where

R_i^- and σ_i = mean and standard deviation for = Reflectance of band i and

R_{ij}^- and σ_{ij} = mean and standard deviation for the ratio between reflectance of band i and band j . The contextual test has been carried out using valid back ground pixels from a 61×61 window centered on the candidate pixel.

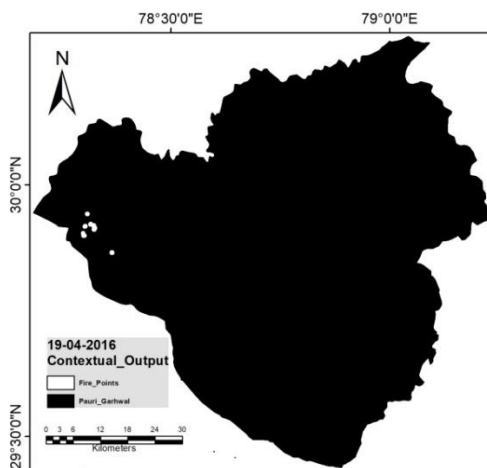
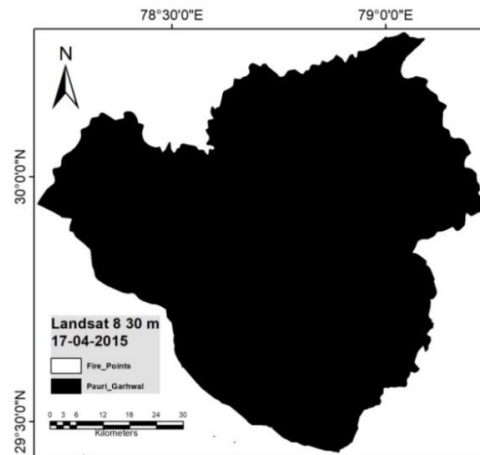


Figure 7. Contextual Test Output

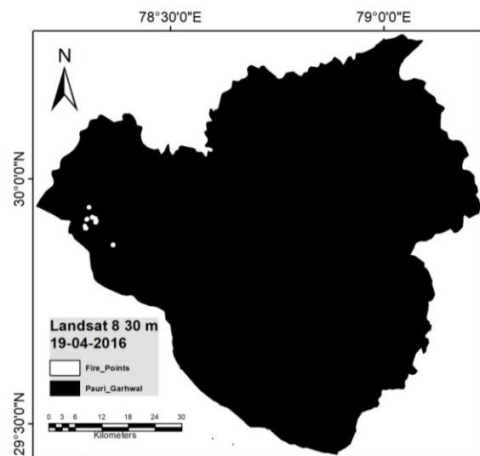
The fire affected pixel locations are visible in the figure 7. These pixels had been converted into vector points for validation purpose.

6. FIVE YEAR ANALYSIS

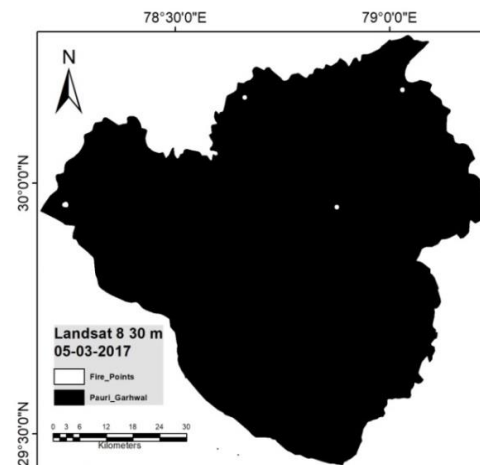
Forest fire detection has been carried out from the year 2015 to 2019 to analyse the fire locations. Figure 8 (a) to (e) shows the contextual output fire points for year 2015 to 2019 respectively.



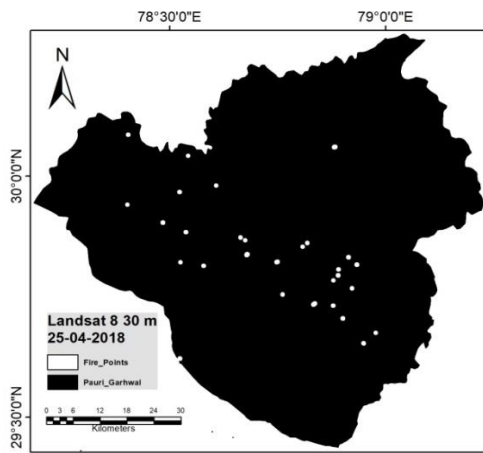
(a)



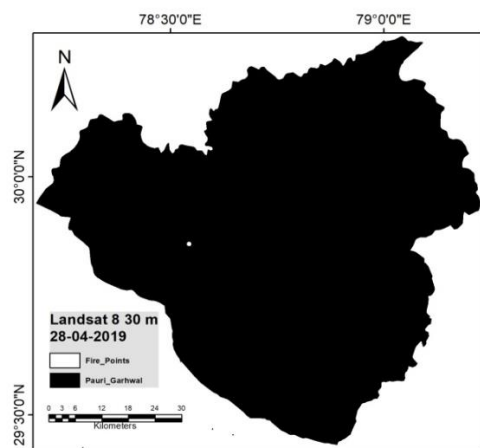
(b)



(c)



(d)

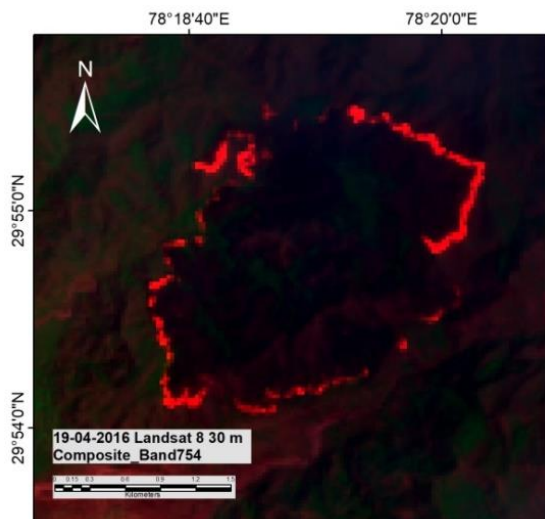


(e)

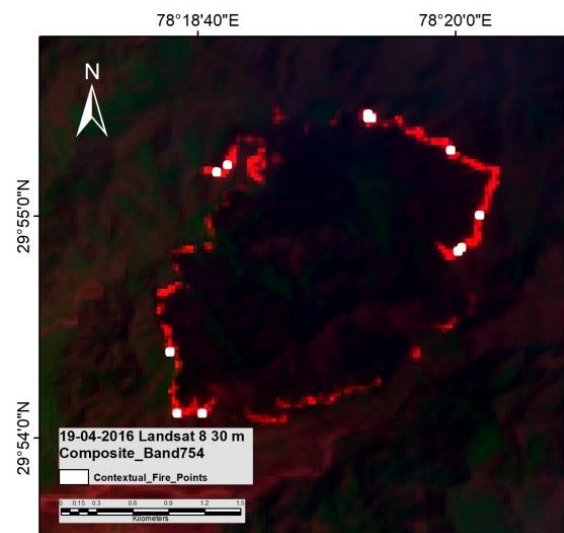
Figure 8. Contextual Output of fire point for year (a) 2015 (b) 2016 (c) 2017 (d) 2018 and (e) 2019

7. VALIDATION

Initially composite image of Band 7, Band 5 and Band 4 was generated for some basic visual interpretation (Schroeder et al., 2008), in which Landsat 8 fire points overlaps the bright pixels of composite image.



(a)



(b)

Figure 9. Validation of Landsat 8 Fire Points (a) Landsat 8 band 7, band 5 and band 4 composite (b) Landsat 8 Contextual test fire points.

The exact validation of fire pixels from the applied algorithms has been done using MODIS and VIIRS/SNPP (Schroeder et al., 2008) fire points downloaded from Fire Information for Resource Management System (FIRMS). Due to the difference in spatial resolution of all three satellites, it becomes difficult to match the exact fire locations and to validate the outcome of fire detection algorithms. To overcome this problem, buffering of fire pixels has been done according to their spatial resolution such as Landsat-8 has 30 m spatial resolution so 15 m buffering has been applied on it. Similarly 187.5 m and 500 m buffering has been done for VIIRS and MODIS data respectively. Figure 9 shows the methodology adopted for the validation of fire pixels.

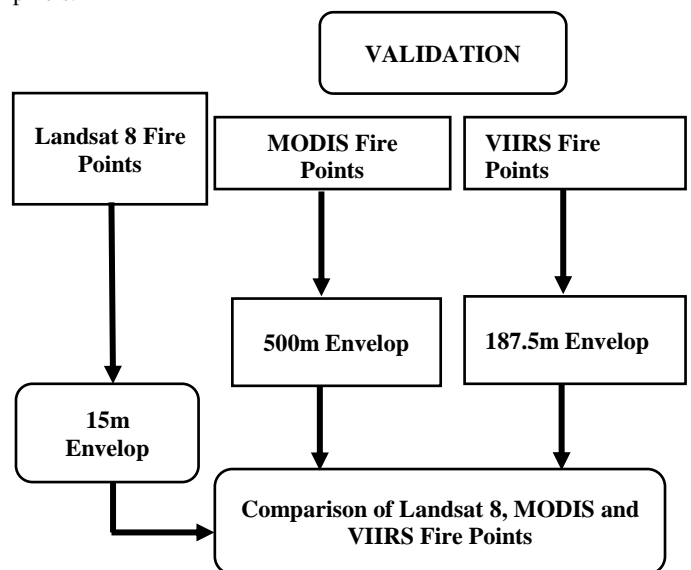
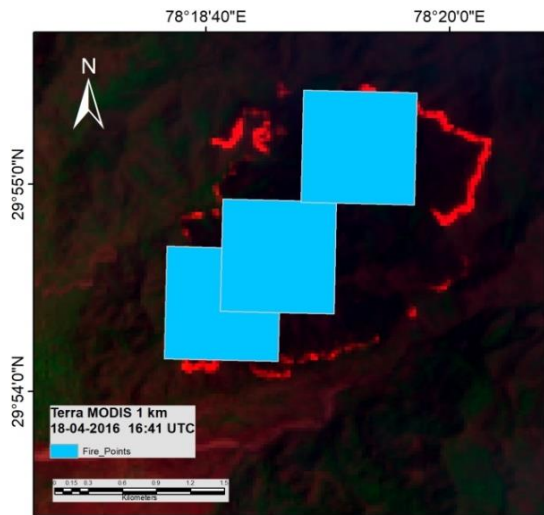


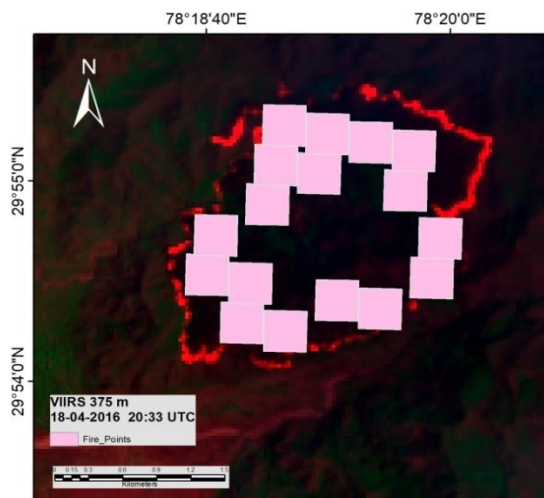
Figure 10. Flowchart showing methodology adopted for validation

The other major problem in validation of data is the huge time difference of satellite pass of MODIS and VIIRS comparative to Landsat 8, due to which it would be difficult to compare the

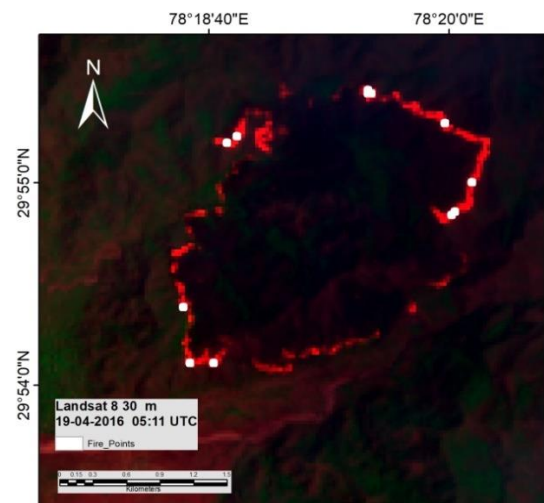
fire points of all these satellites. To overcome from this problem we took the fire points of previous day and analyse the fire pattern and its direction to validate the points.



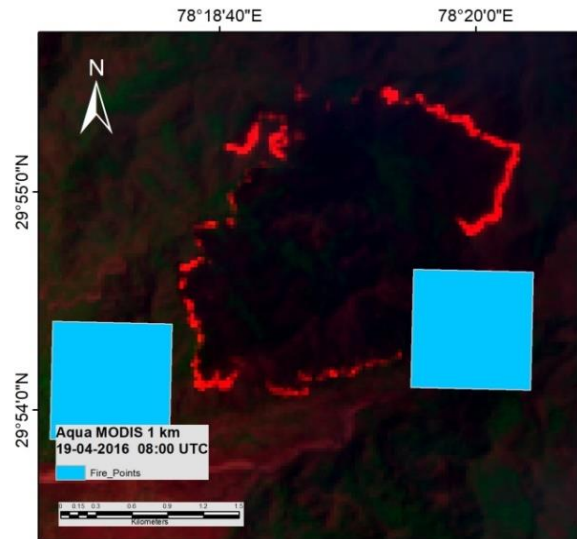
(a)



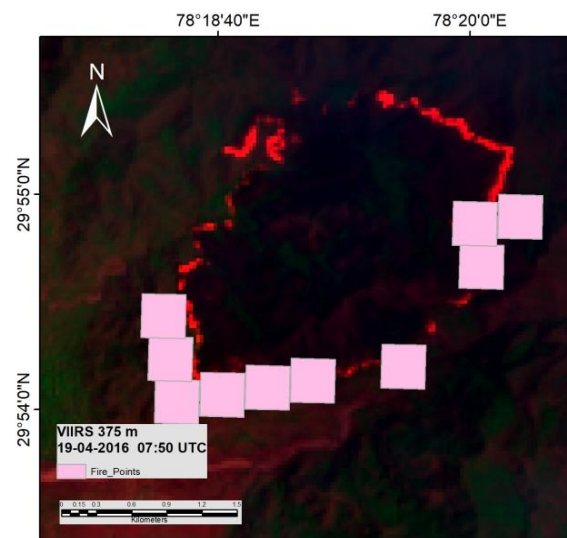
(b)



(c)



(d)



(e)

Figure 11: Comparison of active fire pixels from Landsat 8, MODIS and VIIRS for validation (a) MODIS previous day fire points (b) VIIRS previous day fire points (c) Landsat 8 19-04-2016 fire points (d) VIIRS same day fire points (e) MODIS same day fire points.

Active Fire Points from	No. of fire Pixels	
	Previous Day	Same Day
Landsat	12	
MODIS	3	2
VIIRS	17	10

Table 2. Active fire points from Landsat 8, MODIS and VIIRS

From the figure 11a and 11b, it has been observed that the fire points from MODIS and VIIRS are present in the inner rim. However the next day, the fire point has been shifted outward direction which is clearly visible from figure 11d and 11e. The pass timing of Landsat 8 lies between these consecutive passes. From the figure 11c, it can easily be seen that the fire points from Landsat 8 are lie between the fire points of these two passes which gives the conformity of fire observed from Landsat 8 algorithms. Table 2 shows the number of active fire pixels from Landsat 8, MODIS and VIIRS.

8. CONCLUSION

The algorithms developed by Schroeder et.al, 2016 have been applied in the Pauri region of Uttarakhand, India. It shows more significant small scale mapping of active forest fire. Landsat 8 has much finer spatial resolution (30m, Pan bands 15 m) than MODIS (>=1 km) and VIIRS/SNPP (375 m), due to which it provide more accurate detail of active fire area and reduce the false fire alarms. The capability of fire detection algorithm in the study area has been validate using the present fire detection system in the region (MODIS and VIIRS/SNPP).The validation with satellites having different spatial resolutions is difficult, which can be overcome with buffering of point data as per their respective spatial resolutions. Though due to the huge time difference of satellite passes the exact validation of fire points cannot be done, but with the help of MODIS and VIIRS previous and same day fire points pattern fire points from Landsat 8 can be easily concluded as fire points. From the results, it can easily be observed that the fire patterns recognized from all three satellites are almost same while giving more accurate location of fire due to finer resolution. With the help of Landsat 8 fire detection algorithm, the initial (or small) fire can be detected while the detection system based on existing satellites can only detect large fires. Due to which the control and management of fire can be difficult and huge loss of biodiversity can happen.

REFERENCES

Chand T.R.K., adrinath K.V.S., Murthy M.S.R., Rajshekhar G., Elvidge C.D., Tuttle B.T. (2007) Active forest fire monitoring in Uttaranchal State, India using multi-temporal DMSP-OLS and MODIS data, *International Journal of Remote Sensing*, 28:10,2123-2132. OI:10.1080/01431160600810609.

Chuvieco E., Congalton R.G. (1989), Application of Remote Sensing and Geographic Information System to Forest Fire Hazard Mapping. *Remote Sensing Environment* 29:147-159 (1989).

Giglio L., Descloitres J., Justice C. O., Kaufman Y. J., (2003) Enhanced Contextual Fire Detection Algorithm for MODIS, *Remote Sensing of Environment* 87 (2003) 273–28227.

Hussin Y. A., Matakala M., Zagdaa N., The Applications Of Remote Sensing And GIS In Modeling Forest Fire Hazard In Mongolia The International Archives of the Photogrammetry, Remote Sensing and Spatial Information Sciences. Vol. XXXVII. Part B8. Beijing 2008 .

Jha C. S., Gopalkraishnan R., Thummatry K.C., Singhal J., (2016) Monitoring of forest fires from space-ISRO's initiative for near real-time monitoring of the recent forest fires in Uttarakhand, India. *Scientific Correspondence*

Justice C.O., Giglio L., Korontzia S., Owensa J., Morisettec J.T., Roya D, Descloitres J, Alleaumed S, Petitcoline F., Kaufman Y. The MODIS fire products. *Remote Sensing of Environment* 83 (2002) 244–262

Rugumamu W., (1995) The use of Remote Sensing Technology in Combating Forest Fires.

Saklani P. Forest Fire Risk Zonation, A case study Pauri Garhwal, Uttarakhand, INDIA , January, 2008

Schroeder, W., Oliva, P., Giglio, L., Quale B., Lorenz E. & Morelli F., (2016) Active fire detection using Landsat-8/OLI data. *Remote Sensing of Environment*, 185(2016),210-220.

Schroeder W., Prins E., Giglio L., Csiszar I., Schmidt C., Morisette J., Morton D. Validation of GOES and MODIS active fire detection products using ASTER and ETM+ data.,

Schroeder W., Ruminski M., Csiszar I., Giglio L., Prins E., Schmidt C., Morisette J. Validation analyses of an operational fire monitoring product: The hazard Mapping System., *International Journal of Remote Sensing* ,29:20,6059-6066

Importance of Geographic Information System (GIS) To Evaluate Seismic damage state and Damage Probability of RC Building Structure

P. Shil¹, A. Chourasia², S. Singhal², Rabindranatha³

¹Manipal Institute of Technology, MAHE Manipal, Manipal - 576104, India, piyushshil2014@gmail.com

²CSIR- Central Building Research Institute, Roorkee - 247667, India

³Manipal Institute of Technology, MAHE Manipal, Manipal - 576104, India, ravi.nath@manipal.edu

Commission VI, WG VI/4

KEYWORDS: Geographic Information System (GIS), Spatial Data Infrastructure (SDI), Seismic Collapse Probability, Collapse Stages, Retrofitting, Remote Sensing (RS).

ABSTRACT:

The past study shown that since last few decades natural disaster intensity and frequency increased. As a result, worldwide every year loss of life and loss of assets rate also increasing. This study discussed importance of Geographic Information System (GIS) to identifying and quantifying seismic damage and damage probability of reinforced concrete building structure. To ensure lifeline and damage stage of any structural modal structural engineer using number of data and geological information, those are collected from different database website, such as PEER database. Using new technology like Geographic information system (GIS), Remote-sensing (RS), Geographic Information System (GIS) and Global Navigation Satellite System (GNSS) all database website updating their database system and represent in such a way that people can understand easily. In current study considered one G+5 reinforced concrete (RC) frame building model located in seismic zone V (IS 1893-2016). To evaluate seismic damage probability and damage stage of proposed structural model used time-history analysis. To performed time-history analysis, past earthquake database required those are recorded in systematic way and mapping properly done by GIS. GIS provides many facilities to collect seismic historical data such as Map Navigation, Legends, Layer control, Information viewer, Search, Routing etc. Using these information designers make better plane and view about the considerable place.

1. Introduction:

According to report published by world disaster management within last decade from 2001 to 2010 almost 4022 times natural disaster held in all over world, due to which approximate 1221332 peoples killed worldwide (Consuegra, Vitalini, 1995). Growth rate of population is increasing as well as population density increasing in high risk areas which may one of the main reasons to increasing loss of life during natural disaster. Also lack of planning and management is another reason to fail again and again against natural disaster like earthquake, tsunamis etc.

It is possible to mapping most frequent areas and mark as highly risk zone areas also possible to predict about disaster by using modern technologies and risk management tools such as Geographic Information system (GIS), Global Navigation satellite system (GNSS) and Remote-Sensing (RS) (Wu, Wang, 2010). But it is necessary to present of data and information to use of GIS and RS for risk and natural disaster management

The present study deals with uses of GIS to design earthquake resistance structure to reduced effect of earthquake in different structure. Recently structural engineer tries to design such kind of structure those have enough ability to resist any natural disaster like Earthquake, tornado etc. For that, before start analysis and design such kind of structure, engineer needs spatial data and historical information etc.

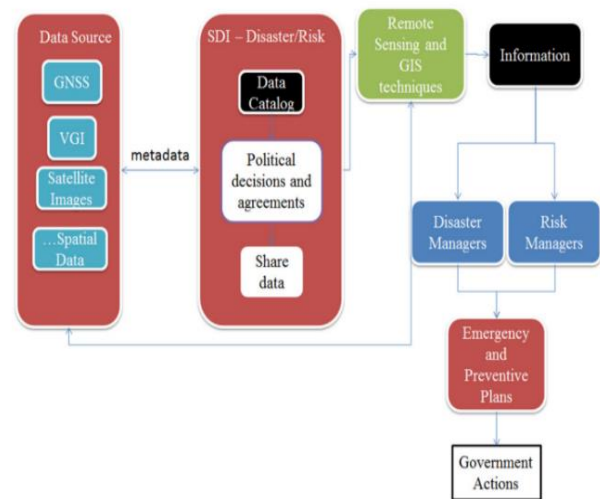


Figure 1. Scheme for space-based data use for risk and natural disaster management

In this study considered a RC building structure in Nepal. Which is comes under earthquake Zone V. Means the considerable place is highly earthquake prone Zone, therefore before design of any structure on that area it is very much necessary to collect proper information, historical data about previous natural disaster etc. To collect these entire data engineer follows different database those made by modern technologies like GIS, GNSS and RS etc.

2. Application of Satellite images, GIS, GNSS and RS for risk disaster management:

Due to natural disaster every year billion dollars infrastructure damage, huge number loss of life happening. Those are directly affecting on world economy. GIS, GNSS and remote sensing technique are continuously using to manage pre-disaster and post-disaster operation. Mitigation and preparedness efforts are generally related with pre-disaster activities (Roy et al. 2009). Response and recovery are generally related with post-disaster activities. To reduce vulnerability of societies due to disaster mitigation refers. Preparedness refers to operation that simplify arrangement for responding against natural disaster. Response and recovery are referring to short-term effect of disaster and process of restoring activity as pre-disaster condition like reconstruction and retrofitting.

GIS technique provides information permitting process and remote sensing, also it provides identification and relationships between standards and variables. Moreover, GIS gives various risk assessment information such as geomorphological, geological and climatological data for planning purpose (Yongmei, Chen, 2019) Recently during response and recovery phase SPOT image technique are frequently used to identify damage after natural disaster.



Figure 2. Although imagery typically has an accuracy statement, it is always a good practice to compare imagery against a map source with the same datum, projection, and coordinate system.

As per MODIS (Moderate Resolution Imaging Spectroradiometer) methodology time series imagery very much useful to detect changes before and after disaster. After flood disaster, uses of satellite image like ETM+ (Enhanced Thematic Mapper Plus) and UK-DMC (a satellite that is one, from several satellites in the Disaster Monitoring Constellation) are common to investigate.

Remote-sensing technique are now using all kind of natural disaster such as Flood, Earthquake, fires, tsunamis. And landslides etc. during post-earthquake phase (response and recovery) (IFRC. World Disaster Report 2011).

Immediately after natural disaster, quick-response methodology used to identify and quantify the changes due to disaster by using IKONOS and QUICKBIRD images. Those images given by FORMOSAT-2 satellite, which provide low-cost images and acquire timely to evaluating damages in different places by earthquake and tsunamis.

Beyond images, now a days for precise positioning out-After that analysis systematically for recorded data. To find damage stages of proposed building need to develop fragility curve based on HAZUS methodology and FEMA P695. For that intensity measured (IM) and damage measured (DM) must select. space technology using. GNSS and GPS (Global positioning System) is most popular among all. Data given by GPS are using to manage emergency moment, control the condition after natural disaster, monitoring geophysical phenomena specially landslide etc. The SNNs (Sensing Node Network System) using to detect slow mass movement like landslide. As an example, by monitoring GPS data station located in Taiwan it would make easy to collect characteristic and demonstrate of Chi-Chi earthquake (Japan). By recording Pre phase and post phases of the event generate complete database of earthquake displacement.

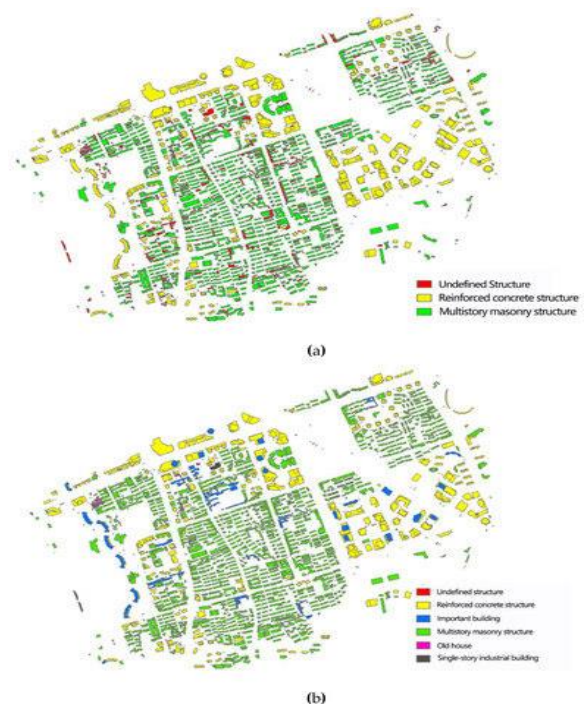


Figure 3. Distribution of structural types before and after pretreatment. (a) Distribution of structural types before pretreatment. (b) Distribution of structural types after pretreatment.

Japan Aerospace Exploration Agency (JAXA) sponsored one project about application of GIS and RS for disaster control point of view. Their main objective behind that project were assessment of Risk and vulnerability of different building structure for different magnitude of earthquake in Kathmandu valley. To get conclusion of their objective they followed HAZUS methodology developed US Federal Emergency Management Agency (FEMA). In the present study the main objective is assessment of risk probability of an RC structure using HAZARD map which is prepared by GIS.

3. Methodology:

3.1 Models and Ground Motion Records:

One RC Frame G+3 building modal were prepared in SAP2000 v20 computer software. All geometrical and structural details are shown in Table 1. Design of considering structural model done as per guideline suggest by IS 1893-2016. The model has fundamental time period of first mode is $T_1=0.826$ sec. At first need to perform static analysis next to conduct dynamic analysis (DA) need to select suitable ground motion. Current study suitable ground motion selected from PEER database those have magnitude 6.93.



Figure 4. Selecting the Monterey City Hall Record

In present study spectral acceleration at fundamental time-period for 5 percent damping, $S_a(T_1, 5\%)$ considered as an IM and inter-story drift ratio considered as a DM.

Details	Structure without precast shear wall	
Number of stories	G+3	
Height of building in meter	14	
Maximum Length along Transverse Direction (X-axis) (m)	15.5	
Maximum Length along Longitudinal Direction (Y-axis) (m)	9.5	
Beams size in mm	B ₁ ,B ₂ ,	250 x 250
Column size in mm	C ₁ ,C ₂ ,	350 x 350 450 x350
Loading	Dead load	3.5 kn/m ²
	Live load	
Software used	SAP2000 v20, Autocad, seismoSignals, SeismoMatch	
Ground motion	Selected from PEER	

Table 1. Architectural and Structural details.

3.2 Models and Ground Motion Records:

Hazus Method provide guidelines to prepared fragility curve as per data has been collected (Federal Emergency Management Agency., 2000). Based on fragility curve it is possible to find the structural damage stage and risk possibility of proposed building model.If P represent the probability of damage states for a particular spectral displacement,

$$P \left[\frac{ds}{S_d} \right] = \Phi \left[\frac{1}{\beta_{ds}} \ln \left(\frac{S_d}{\bar{S}_{d,ds}} \right) \right] \dots \dots \dots (1)$$

Where, $\bar{S}_{d,ds}$ =Threshold spectral displacement for particular damage state, ds.

β_{ds} = Standard deviation of the natural logarithm of spectral displacement for particular damage state, ds. It represents the combined variability of capacity property, demand and uncertainty in damage state threshold

Φ = the standard normal cumulative distribution function.

S_d =Spectral Displacement of the building.

Damage state	Spectral displacement
Slight damage	0.7 S _{dy}
Moderate damage	S _{dy}
Extreme damage	S _{dy} + 0.25(S _{du} -S _{dy})
Complete damage	S _{du}

Table 2. Damage state definition as per Barbat et al. (2006)

Description of building	Capacity control points		Damage state threshold values			
	S _{dy}	S _{du}	slight	moderate	extreme	collapse
RC Frame building	41	81.06	28.7	41	51.01	81.06

Table 3. Median damage state threshold for the RC school building from simulation.

Beta values	Medium rise building
Slight s1	0.55
Moderate s2	0.61
Extensive s3	0.68
Complete s4	0.74

Table 4. standard deviation values

4. Result and discussion:

By shearing GIS data and remote sensing (RS) information with various natural disaster and risk management organization present in all over the world, it is possible to

prepare emergency plane for any selected place, risk avoiding design of infrastructure and structural building.

To fulfil the selected objective in the present study performed nonlinear static analysis and developed nature of structural response against lateral force shown in figure 3.

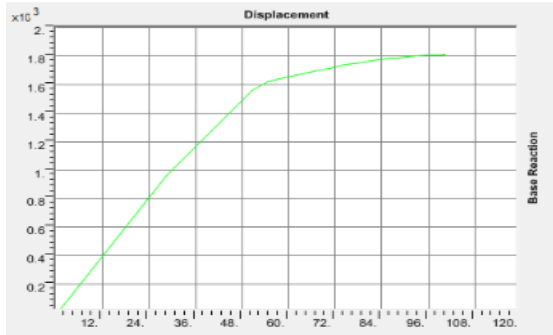


Figure 5. Displacement vs Base shear curve.

After that to get spectral displacement need to convert above relation into spectral form as shown in figure 4.

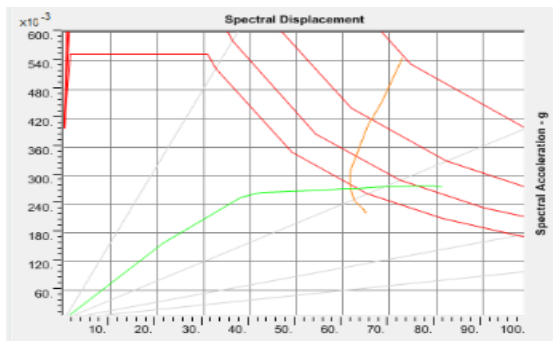


Figure 6. Spectral Displacement vs Spectral acceleration curve.

From the above relationship possible to find yield spectral displacement (S_{dy}) 41mm and ultimate spectral displacement (S_{du}) 81.06 mm and performance point at (273.03, 61.73).

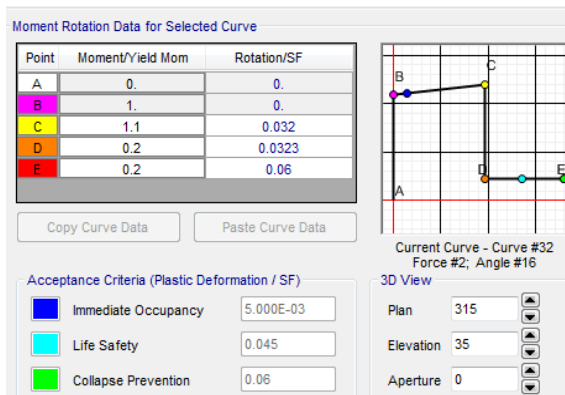


Figure 7. Limit state of proposed structural model.

This image shows the considerable structure comes under which stage. That check can be done pre-disaster and post-disaster condition. Based on this it is possible to categories which structure comes under which stage and prepared a map by the help of GIS software such as ArcGIS for various agencies for pre-disaster and post-disaster rectification activity.

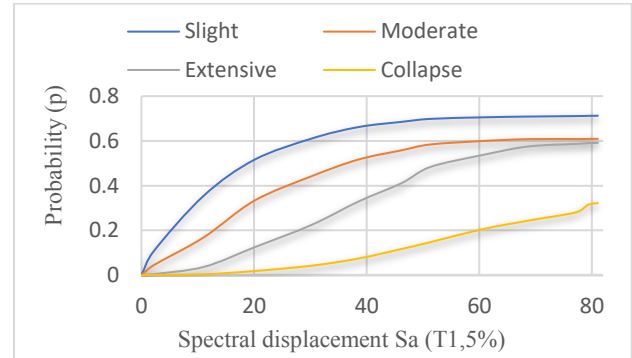


Figure 8. Collapse probability for various damage stage.

Above graph (figure 8) represent collapse probability of proposed structure with increasing earthquake intensity for various damage state classified by HAZUS manual. Graph shows probability to occur slight damage is more than moderate, extensive and collapse state.



Figure 9. Various building damage state based on HAZUS Methodology using ArcGIS Software.

Based on that collapse probability it is possible to represent by mapping through GIS software for easy to understand about various damage state for further research work. Also, easy to make disaster prevention planning for pre and post disaster activity like response and recovery.

5. Conclusion

In this present study, Application of Geological information system (GIS) and Remote sensing (RS) for planning and design of structural building and Infrastructure, both the pre and post disaster activity such as Response and Recovery are properly explained with an example of reinforced concrete (RC) frame building subjected to a real historical

earthquake ground motion. Conclusion of present study are as follows

- Analysis of structure based on GIS information provide advantage to smartly predict seismic damage, vulnerability assessment and retrofitting in pre-disaster and post-disaster condition. Which make the process planning and design more accurate and reliable.
- Orbital platform taking a vital role in Structural design and planning sector to prevent damage due to natural disaster. In addition to safe human life and economic loss due to structural and non-structural collapse.

References

- Amnani, H. H., Amiri, J. V., Rajabnejad, H., 2018.: Energy distribution in RC shear wall-frame structures subject to repeated earthquakes. *Soil Dynamics and Earthquake Engineering*, 107, 116-128.
- Biswal, A., Prasad, A. M., Sengupta, A. K., 2019: Study of shear behavior of grouted vertical joints between precast concrete wall panels under direct shear loading. *Structural Concrete*, 20(2), 564-582.
- Baker, J. W., 2015: Efficient analytical fragility function fitting using dynamic structural analysis. *Earthquake Spectra*, 31(1), 579-599.
- Consuegra, D.; Joerin, F.; Vitalini, F., 1995: Flood Delineation and Impact Assessment in Agricultural Land Using GIS Technology. In *Geographical Information Systems in Assessing Natural Hazards*; Carrara, A., Guzzetti, F., Eds.; Kluwer Academic Publishers: Dordrecht, The Netherlands, pp. 177-198
- Council, B. S. S., 2000: Prestandard and commentary for the seismic rehabilitation of buildings. Report FEMA-356, Washington, DC.
- Chopra, A. K., 2003: Theory and Applications to Earthquake Engineering, *Dynamics of Structures*, 45, 34-54.
- Codjoe, S. N. A., 2007: Integrating remote sensing, GIS, census and socioeconomic data in studying the population - land use/cover Nexus in Ghana: A literature update. *Afr. Developmt.* 32: 197-212.
- DeBy, R. A., 2001: Introduction to GIS. In *Principles of Geographic Information Systems. An Introductory Text Book*, pp 26-57 (DeBy, R. A. ed.). International Institute for Aerospace Survey and Earth Sciences, Enschede.
- Federal Emergency Management Agency., 2000: Prestandard and commentary for the seismic rehabilitation of buildings. American Society of Civil Engineers (ASCE).
- Herk, M. 2007: Modelling Habitat Suitability to Predict the Potential Distribution of Erhard's Wall Lizard *Podarcis erhardii* on Crete. M.Sc. Thesis, International Institute for Geo-Information Science and Earth Observation, Enschede
- IFRC. World Disaster Report 2011; International Federation of Red Cross and Red Crescent Societies: Geneva, Switzerland, 2011. Available online: <http://www.ifrc.org/> (accessed on 30 May 2012).
- Lee, S.; Choi, J., 2004: Landslide susceptibility mapping using GIS and the weight-of-evidence model. *Int. J. Geogr. Inf. Sci.*, 18, 789-814
- Lu, X., Wu, H., Zhou, Y., 2017.: Seismic collapse assessment of self-centering hybrid precast walls and conventional reinforced concrete walls. *Structural Concrete*, 18(6), 938-949.
- Melisse, A. M., Weng, O., Thenkabail, P. S. and Senay, G. B., 2007: Remote sensing sensors and applications in environmental resources mapping and modelling. *Sensors* 7: 3209-3241
- Ozkul, T. A., Kurtbeyoglu, A., Borekci, M., Zengin, B., Kocak, A., 2019: Effect of shear wall on seismic performance of RC frame buildings. *Engineering Failure Analysis*, 100, 60-75.
- Roy, S., Jena, S., 2009.: Earthquake Disaster Management Using GIS and Probabilistic Risk Assessment, *Geospatial world*.
- Vamvatsikos, D., Jalayer, F., & Cornell, C. A., 2003: Application of incremental dynamic analysis to an RC-structure. In *Proceedings of the FIB Symposium on Concrete Structures in Seismic Regions* (pp. 75-86).
- Wu, F., Yu, B., Yan, M.; Wang, Z., 2010: Eco-environmental research on the Wenchuan Earthquake area using Disaster Monitoring Constellation (DMC) Beijing-1 small satellite images. *Int. J. Remote Sens.*, 31, 3643-3660.
- Yongmei Z., Chen S., 2019,: GIS-Based Seismic Hazard Prediction System for Urban Earthquake Disaster Prevention Planning, Sustainability.

INVENTORY OF GLACIAL LAKES & DETECTION OF POTENTIALLY DANGEROUS LAKES FOR GLOF USING REMOTE SENSING & GIS IN PITHORAGARH DISTRICT OF UTTRAKHAND, INDIA

Sanjay Kumar Dwivedi¹, Arvind Pandey¹, Gaurav Joshi¹, Sachin Pandey¹, Nirmala Sharma¹

¹ Department of remote sensing and GIS, S.S.J. Campus Almora, Kumaun University, India

KEY WORDS: Global warming, Glacial lakes, GLOF, Spatial planning, Remote Sensing & GIS

ABSTRACT:

Global warming & changing temperature causing faster melting of glacial ice, resulting in formation of large number of glacial lakes. Glacial lake is a water mass existing in a sufficient amount and extending with a free surface in, under, adjacent to or before a glacier and originating from glacier activities and melting processes of a glacier. Glacial lake outburst floods (GLOFs) are sudden, fast-flowing release of glacial lake water that moves downslope as a result of lake dam failures. Some studies reported no glacial lakes in Uttarakhand are potentially dangerous, but on 17th June 2013, the Kedarnath GLOF event has created a need to update the analysis of glacial lakes & GLOF risk assessment. The present research using Remote Sensing & GIS techniques has been carried out in the Pithoragarh district of Uttarakhand, India. This study includes Inventory of glacial lakes using Sentinel 2 satellite data of 24 October 2019 to study characteristics of glacial lakes in district Pithoragarh. Lakes mapping has been carried out by semimanual digitization on the basis of visual interpretation along with NDWI and Google earth information. Potentially dangerous are detected with the help of their area, volume & slope information. In this study, 5 potentially dangerous lakes were detected. Potentially dangerous lakes are linked with their down streams & their flood risk zones are mapped. The result of the study can help in carrying out downstream flood risk assessment, betterment in spatial planning and better preparedness for future GLOF hazards.

1. INTRODUCTION

Changing climate of the twentieth century pronouncedly affected the glacier conditions of the Himalaya. The average surface temperature on the Earth's surface have been continuously increasing since the end of the Ice Age and has increased between 0.3°C to 0.6°C over the past hundred years (ICIMOD, 2007), (Neeraj Kaushal et al., 2016), because of this more glacial ice will melt and snow cover would decrease leaving behind many more glacial lakes in future. Outside the polar region, the Himalayas have the largest concentration of glaciers. Most of the Himalayan glaciers have retreated in recent past, leaving behind large number of glacial lakes. Burst or sudden release of huge volume of water along with mud and debris from these lakes causes glacial lake outburst flood in valley downstream give rise to massive destruction of infrastructure, natural resources and loss of human life. A glacial lake can form on the surface of the glacier itself (supraglacial), within the glacier ice (englacial), below the glacier ice (subglacial), in front of a glacier (proglacial), in side/surrounding of glaciers (periglacial) or in relict cirques (tarn or cirque) and also dammed by glacier moraine or ice (moraine-dammed or ice-dammed) (Rakesh Bhambri et al., 2015). The formation of supraglacial lakes and moraine dammed glacial lakes and glacial lake outburst flood is a major concern in countries such as Bhutan, China (Tibet), India, Nepal and Pakistan (Babu k. Govindha Raj et al., 2012). The sudden catastrophic discharge of large volumes of water from these lakes is a characteristic of many glaciated regions of the globe. Such glacial lake outburst flood (GLOF) can cause extensive damage to the natural environment, human property and lives as they can drain extremely rapidly and cause dramatic floods (Babu k. Govindha Raj et al., 2012). In the recent past, some of the glaciers have retreated due to climate warming, not only affecting water resources and hydrological processes, but

also causing the expansion of glacial lakes (Yao T. et al., 2010), (Sanjay K. Jain, 2012). The lakes located at the snout of the glacier are mainly dammed by the lateral or end moraine, where there is high tendency of breaching, such lakes could be dangerous as they may hold a large quantity of water; breaching and the instantaneous discharge of water from such lakes can cause flash floods enough to create enormous damage in the downstream areas (Campbell, 2005). In order to assess the possible hazards from such lakes, it is therefore essential to have a systematic inventory of all such lakes formed at the high altitudes. This is feasible by identifying them initially through satellite images (and aerial photographs, if available) and to assess their field setting subsequently, besides making a temporal inventory, a regular monitoring of these lakes is also required to assess the change in their nature and aerial extent. (Campbell, 2005), (Sanjay K. Jain, 2012).

In 2005, ICIMOD reported that there are no glacial lakes in Uttarakhand are potentially dangerous (Campbell, 2005). But Kedarnath GLOF event in 2013 creates a need to update the analysis of glacial lakes for understanding the future GLOF hazards that can help in carrying out risk assessment, and better preparedness for future.

2. STUDY AREA

The study area Pithoragarh district located in eastern part of Uttarakhand India, is one of the hilly district in Uttarakhand Himalaya. It lies between the latitudes 29°26' - 30°80'N and longitudes 79°82' - 81°04'E. The area has maximum extent of 93 km from East to West and 150 km from North to South. Total area of the state is 7110 sq. km with elevation ranging upto to 7368m m.s.l. Pithoragarh has almost area in hilly terrain and it is part of Kumaun division of Uttarakhand.

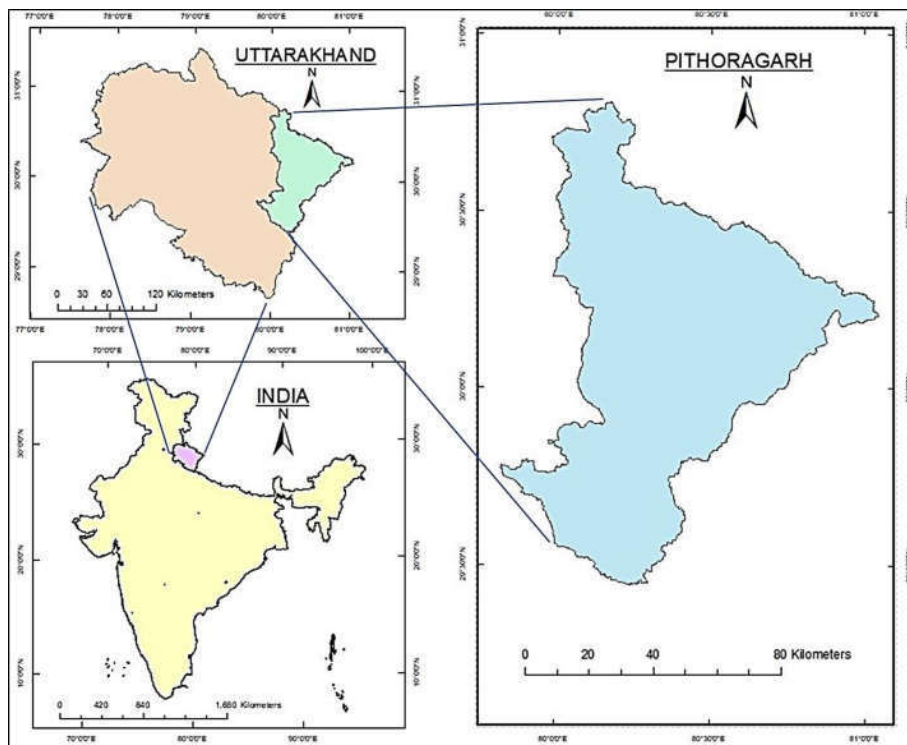


Figure 1: Study Area Map

3. DATA USED

For the present study, post monsoon multispectral data of was acquired. ASTER Digital Elevation Model (DEM) data was acquired for elevation, slope and drainage analysis. Ground control points were collected. SENTINEL-2 satellite image of Pithoragarh district were acquired. The image was of 24 October 2019 with a spatial resolution of 10 meters. The satellite images were downloaded from the ESA portal.

4. METHODOLOGY

4.1 NDWI: One of the significant ideas in the assurance of different object through remote sensing is that the items reflect vitality distinctively in various pieces of the electromagnetic range. This variety relies upon the properties of the articles under perception. By methods for this inalienable property of objects, we can detect them. Applying the idea of two spectral channels with maximum reflectance difference for an object (i.e. water), a blue channel (maximum reflectance of water) and a near-infrared (NIR) channel (minimum reflectance of water) were chosen (C. Huggel et al., 2002):

$$NDWI = \frac{B_{NIR} - B_{blue}}{B_{NIR} + B_{blue}} \dots\dots\dots (C. Huggel et al., 2002).$$

As a result of spectral reflection, some shadowed areas are misclassified as lakes. A threshold value of 0.35 was given to the NDWI layer to extract water bodies, As a result glacial lakes were extracted from the threshold method.

Threshold layer was converted into vector layer for analysing lakes and for map making. With Vector layer we can perform geometric operations regarding to the feature.

4.2 Volume Calculation: Determination of lake volume techniques have been developed to detect and map glacial lakes

using satellite images (C. Huggel et al.2002). Topographic maps for derivation of lake area often do not represent the current situation and hence, are generally less appropriate. The volume, V (in m³), of a glacial lake can then be expressed as a function of the area A (in m²) by using the empirical relationship from (C. Huggel et al., 2002), (Sanjay K. jain et al., 2012):

$$V = 0.104A^{1.42}$$

4.3 Criteria adopted for Potentially Dangerous Lake detection:

The criteria for identifying potentially dangerous glacial lakes are based on field observations, processes and records of past events, geomorphological and geotechnical characteristics of the lake and surroundings, and other physical conditions. Criteria such as area/volume of lake, breaching evidences, condition of lake and its surrounding have been investigated (Sanjay K. Jain et al., 2012).

The criteria adopted for detecting potentially dangerous lakes is listed below:-

4.3.1 Type of glacial lake

Moraine-dammed lakes have been found to produce larger outburst floods than glacier-dammed lakes for the same stored water volume or potential energy (Costa and Schuster, 1988), (Clague and Evans, 1994) unless a mechanical failure (nontunnel drainage) of an ice dam is involved (Walder and Costa, 1996), (C. Huggel et al., 2002).

4.3.2 Volume of the Lake

In general, the lakes, which have a volume of more than 0.01 km³ are found to have past events. A lake, which has a larger volume than this, is deeper, with the deeper part near the dam (lower part of lake) rather than near the glacier tongue, and has

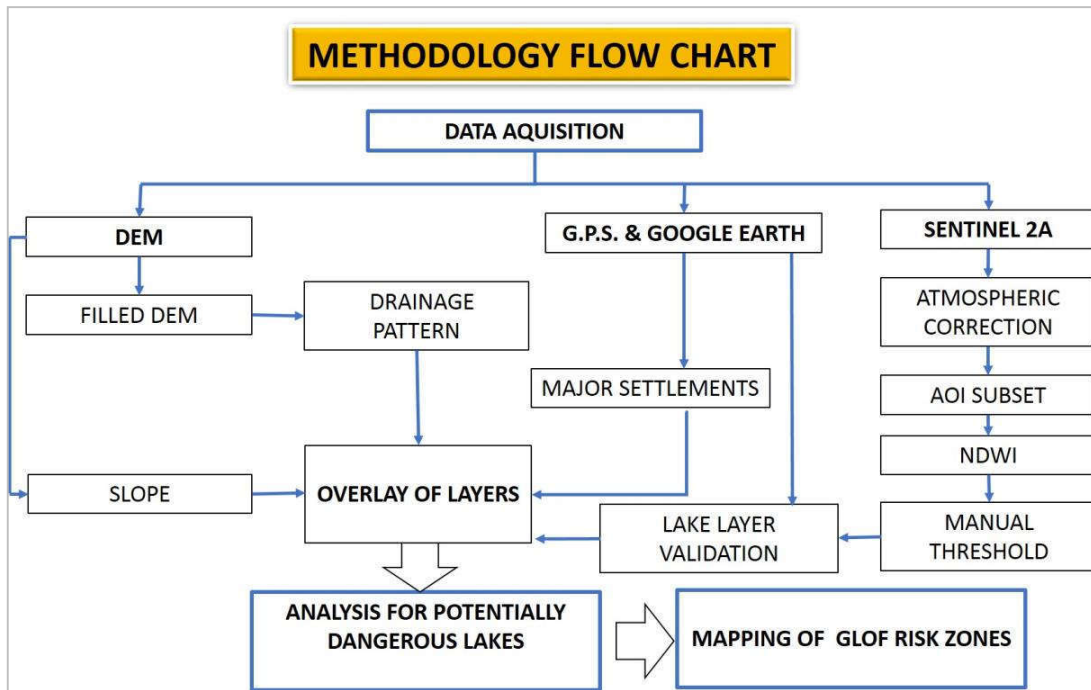


Figure 2: Methodology flow chart of the work

rapid increase in lake water volume is an indication that a lake is potentially dangerous (Campbell, 2005). But In 2013, Chorabari glacial lake was bursted whose total volume of water is estimated to be 0.71–0.72 million m³ (P. K. Champati Ray et al., 2015) and became a major disaster in the history of uttrakhand ,India. Therefore minimum lake volume threshold was defined considering the volume of Chorabari lake.

The magnitude of a flood caused by the failure of a glacier or moraine dam is relevant for further hazard analyses. A variety of empirical equations based on documented outburst events has been proposed to estimate the maximum discharge (Huggel, 2002).

$$Q_{\max} = 0.00077V^{1.017} \dots\dots\dots(Huggel, 2002)$$

Where, Q_{\max} = maximum possible discharge
 V = volume of the lake

4.3.3 Distance from mother glacier

The valley lakes with an area bigger than 0.1 km² and a distance less than 0.5 km from the mother glacier of considerable size are considered to be potentially dangerous, Cirque lakes even smaller than 0.1 km² associated (in contact or distance less than 0.5 km) with steep hanging glaciers are considered to be potentially dangerous; Even the smaller size steep hanging glacier may pose a danger to the lake (Campbell, 2005).

4.3.4 Slope of the associated terrain

High steepness in slope before lake can cause sudden debris or avalance strike in the lake which can cause lake dam failure and

a glacial lake outburst hazard may occur. High steepness in slope after the lake leads to fast erosion of water from the lake with very high velocity in the case of a glacial lake outburst.

5. RESULTS

5.1 Inventory Of Glacial Lakes:

In this study, glacial lakes have been delineated using remote sensing technique and manual delineation approach. The area of lakes varies from 493.76 m² to 225933 m² for the year 2019, lake area, volume and calculated maximum possible discharge is given in the lake inventory table given below. Most of the lakes are situated above 3,000m above sea level. The area of the biggest lake is 225933 m² (0.225 km²) and volume is 4165666.22 m³ situated at elevation of 4900m. Google earth and glacial lake inventory of uttarakhand (Rakesh Bhambri et al., 2015) were used in detecting glacial lake type.

5.2 Potentially Dangerous Lakes:

In the above study, 5 lakes are identified as potentially dangerous lakes to create a GLOF hazard, all five lakes are above an elevation of 4000 m above mean sea level. Lake 2, lake 7, lake 11, lake 13 and lake 16 are identified as the potentially dangerous lakes, they fulfilled the criteria adopted for a potentially dangerous lake. Characteristics of these lakes are shown in the profile graph below :-

Lake No.	Longitude	Latitude	Lake Area (m ²)	Lake Volume (m ³)	Maximum Possible discharge(m ³ /s)	Elevation (meters)	Type of the glacial Lake (Google Earth & Rakesh Bhambri et al., 2015)
1	80.515	30.456	29224.90	228245.72	216.76	5239	End-moraine dammed glacial lake
2	80.388	30.446	101940	1345496.93	1316.93	4343	End-moraine dammed glacial lake
3	80.511	30.409	5140.33	19348.25	17.61	4746	End-moraine dammed glacial lake
4	80.511	30.407	17308.40	108482.12	101.73	4742	End-moraine dammed glacial lake
5	80.422	30.401	4544.20	16241.37	14.74	4155	Recessional moraine dammed glacial lake
6	80.237	30.379	977.15	1831.39	1.60	3959	Recessional moraine dammed glacial lake
7	80.655	30.352	41605.89	376906.21	361.01	4508	End-moraine dammed glacial lake
8	80.073	30.336	5869.58	23359.11	21.34	4197	Recessional moraine dammed glacial lake
9	80.713	30.263	15806.09	95359.60	89.22	4530	Supra glacial lake
10	80.635	30.216	930.20	1707.70	1.49	3905	End-moraine dammed glacial lake
11	80.136	30.210	80137.39	956047.30	930.33	4361	Cirque lake
12	80.065	30.629	993.23	1874.34	1.64	4109	Lateral moraine dammed glacial lake
13	80.532	30.392	118367	1663492.50	1634.06	4766	Recessional moraine dammed glacial lake
14	80.076	30.515	1981.79	4998.67	4.44	4132	Supra glacial lake
15	80.082	30.504	1163.81	2347.39	2.06	4052	Supra glacial lake
16	80.176	30.563	225933	4165666.22	4156.32	4900	End-moraine dammed glacial lake
17	80.084	30.506	755.20	1270.24	1.10	4048	Lateral moraine dammed glacial lake
18	80.582	30.271	30370.5	241054.41	229.14	4882	Lateral moraine dammed glacial lake
19	80.240	30.38	733.07	1217.71	1.05	3979	Recessional moraine dammed glacial lake
20	80.239	30.379	493.76	694.74	0.59	3988	Recessional moraine dammed glacial lake
21	80.435	30.400	3686.26	12066.61	10.90	3884	Lateral moraine dammed glacial lake

Table 1: Glacial lake inventory

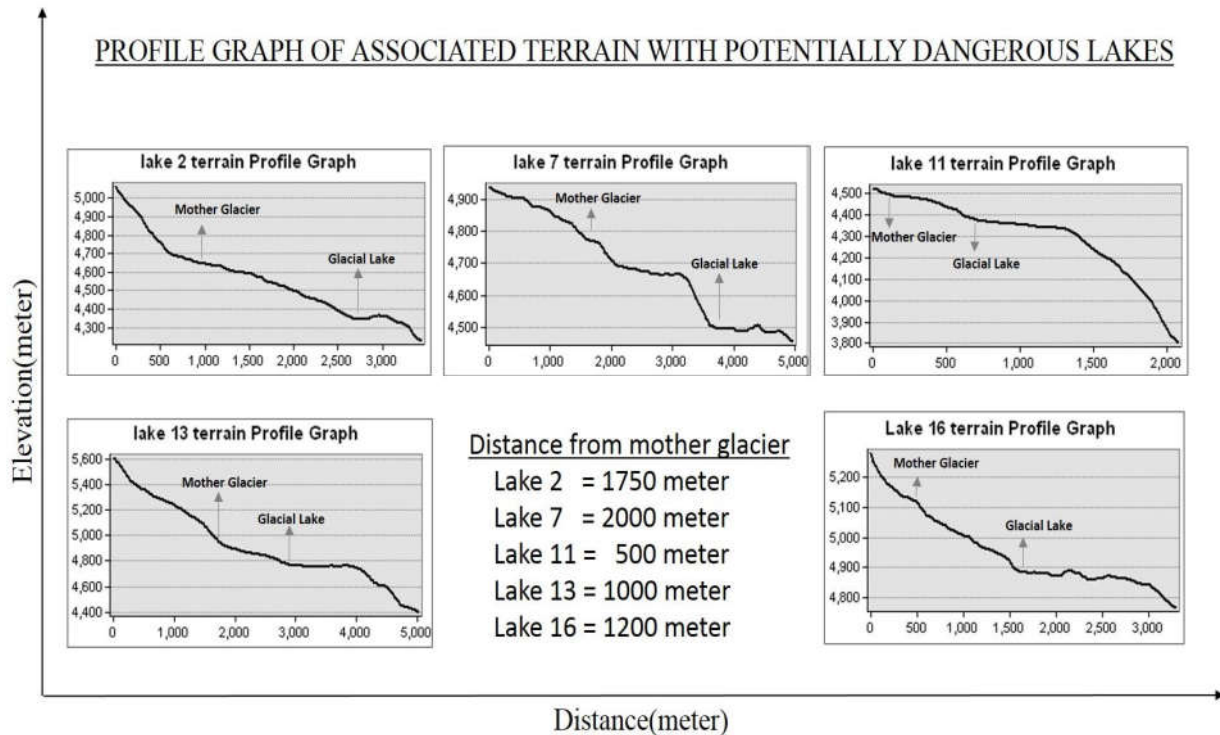


Figure 2: profile graph of the terrain in which potentially dangerous lakes are situated.

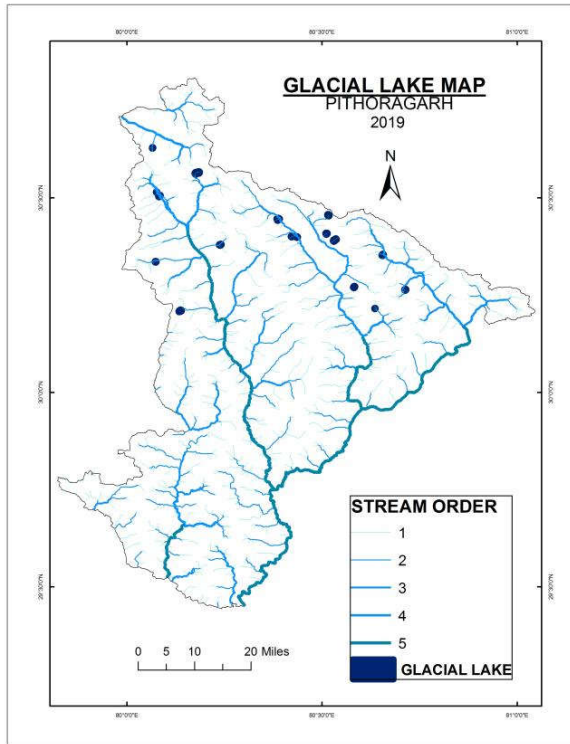


Figure 3: Glacial lake map

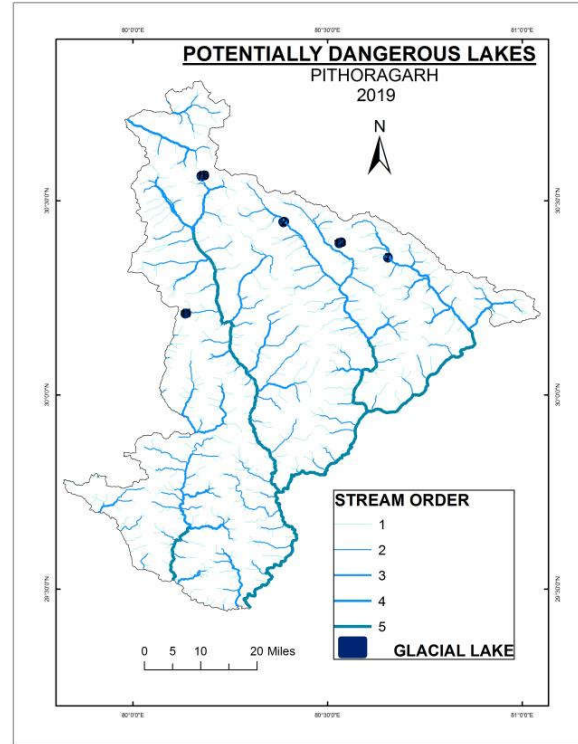


Figure 4: Potentially dangerous lakes map

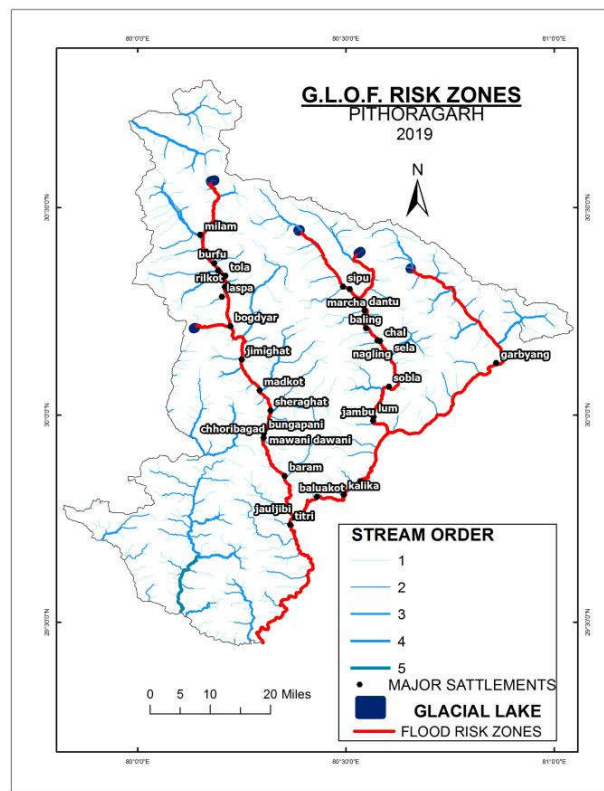
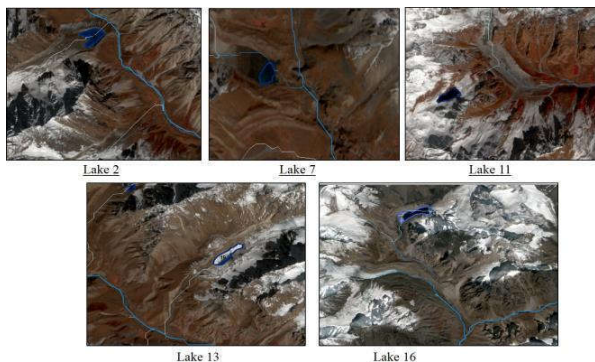


Figure 5: Map of Flood risk zones for possible GLOF events

6. CONCLUSION

In the present study, remote sensing and GIS techniques was used to make glacial lake inventory of the study area and potentially hazardous lakes was detected, those having potential to make a big glacial lake outburst flood event.

There are 21 lakes are identified from which 5 lakes are identified as potentially dangerous lakes a viz. lake 2, lake 7, lake 11, lake 13, lake 16 as in pictures shown below: -



Creating inventories and monitoring of glaciers and glacial lakes can be done quickly and correctly using a combination of satellite images supplemented by reference topographic information. The multi-stage approach of using remotely sensed data and field data will increase the accuracy of the work. The integration of visual and digital image analysis with a geographic information system (GIS) can provide very useful tools for the study of glaciers, glacial lakes, and Glacial Lake Outburst Floods (GLOFs). The integration of visual and digital image analysis with a Geographic Information System (GIS) can provide very useful tools for the study of glacial lakes and glacial lake outburst floods (GLOFs). It is essential to study a proper modelling approach for moraine breaching in order to assess the potential threat of hazard from the existing glacial lakes. Many studies have been done in past on GLOFs and on lakes prone to outburst, but there is a lack of systematic analysis of GLOF events and glacial lakes for their potential of hazard. It is crucial to study complex procedure of interacting with GLOF disasters.

REFERENCES

Babu K. Govindha Raj , Vinod K Kumar, Remya S.N.,2013: Remote sensing based inventory of glacial lakes in Sikkim Himalaya: semi-automated approach using satellite data. *Geomatics, Natural Hazards and Risk*, 4:3, 241-253. doi.org/10.1080/19475705.2012.707153

Campbell JG, 2005: Inventory of glaciers, glacial lakes and the identification of potential glacial lake outburst floods (GLOFs) affected by global warming in the mountains of India, Pakistan and China/Tibet Autonomous Region. Technical Report of APN Project 2004-CMY-Campbell, available online at http://ns.apn.gr.jp/en/products/project_reports/2004/Final%20Rport/2004_03_CMY_Campbell.pdf

Christian Huggel, Andreas Käab, Wilfried Haeberli, Philippe Teyssie, and Frank Pau, 2002: Remote Sensing Based Assessment of Hazards From Glacier Lake Outbursts: A Case Study in the Swiss Alps. *Canadian Geotechnical Journal*, 39(2): 316-330, doi.org/10.1139/t01-099

Clague J.J., and Evans S.G., 1994: Formation and failure of natural dams in the Canadian Cordillera. *Geological Survey of Canada Bulletin* 464, Ottawa.

Costa J.E., and Schuster R.L., 1988: The formation and failure of natural dams. *Geological Society of America Bulletin*, 7: 1054-1068.

ICIMOD, 2007: Impact of climate change on Himalayan Glaciers and Glacial Lakes: Case studies on GLOF and Associated Hazards in Nepal and Bhutan. International Centre for Integrated Mountain Development(ICIMOD)

Neeraj Kaushal, Kamal Kumar, 2016: Time Series Analysis of Glacial Lake in Western Himalayas Based on NDWI and MNDWI. *International Journal for Research in Applied Science & Engineering Technology (IJRASET)*, Volume 4, Issue III, ISSN: 2321-9653

P. K. Champati Ray, Shovan Lal Chatteraj , M. P. S. Bisht, Suresh Kannaujiya, Kamal Pandey, Ajanta Goswami, 2016: Kedarnath disaster 2013: causes and consequences using remote sensing inputs. *Nat. Hazards*, volume 81, 227-243 doi.org/10.1007/s11069-015-2076-0

Rakesh Bhambri, Manish Mehta, D.P. Dobhal, Anil K. Gupta, 2015: Glacier Lake Inventory of Uttarakhand. Wadia Institute Of Himalayan Geology, (An Autonomous Institute of Department of Science & Technology, Government of India) 33, General Mahadeo Singh Road, Dehradun 248001

Sanjay K. Jain, Anil K. Lohani, R. D. Singh, Anju Chaudhary, L. N. Thakural, 2012: Glacial lakes and glacial lake outburst flood in a Himalayan basin using remote sensing and GIS. *Journal of the International Society for the Prevention and Mitigation of Natural Hazards*, vol. 62(3), pages 887-899, July. doi.org/10.1007/s11069-012-0120-x

Walder J.S., and Costa J.E., 1996: Outburst floods from glacier dammed lakes: the effect of mode of lake drainage on flood magnitude. *Earth Surface Processes and Landforms*, 21: 701-723.

Yao, T., Li, Z., Yang, W. et al. Glacial distribution and mass balance in the Yarlung Zangbo River and its influence on lakes. *Chinese Science Bulletin*, 55, 2072-2078. doi.org/10.1007/s11434-010-3213-5

REVIEWING THE IMPORTANCE OF THREE DIMENSIONAL MAPPING OF UNDERGROUND UTILITIES IN BIHTA, BIHAR

Amit Kumar¹

¹Department of Urban and Rural Planning, Indian Institute of Technology Roorkee, Roorkee- 247667, India
Tel: +91-7979925919; Email: akumar4@iitr.ac.in

KEY WORDS: Underground Utilities, Ground Penetrating Radar, Geospatial Tools, GPS, 3D mapping.

ABSTRACT:

India's urban population is growing to see a manifold increase in the coming decades. With increasing load on urban management and infrastructure, one way to provide an efficient infrastructural facility will be through efficient urban infrastructure and utilities. Growing cities will create a need to utilise the underground or space below the stratum to ensure efficient infrastructure service delivery to all its end users. In order to ensure optimum performance and monitoring of the service, the utilities and infrastructures must be mapped in three dimensions. Both new and existing infrastructures must be mapped which will make the monitoring and maintenance efficient. This paper highlights the importance Geospatial applications in the development of 3-D utility maps in Indian scenarios, taking a specific case of the city of Bihta, Bihar. Several case studies from cities already using such maps have been studied to ensure establishing best practices in geospatial applications from across the globe in ensuring better mapping services. The intended outcome of the study is reliable information about the advantages of three dimensional utility and infrastructure mapping in Indian cities. This study can be of vital information for practical application by urban administrators and practitioners.

1. INTRODUCTION

As per the World Bank data, urban areas across the world, have seen huge expansion over the recent past in demographic terms, from 33.609% in 1960 to 55.271 in 2018. (*Urban population (% of total population) | Data*, no date) This expansion created additional pressure on service delivery like urban utilities and infrastructure. To meet the growing needs of this urban development, public infrastructure like services, urban utilities, roads and rail lines were moved to the underground spaces. Across the world, cities are already making attempts to create a system of smart and intelligent infrastructure. (Momin, 2018)

While addition of infrastructure and utility systems and further advancements in their management systems is definitely an imperative, it also brings along judicious location of the existing utilities underground and a better mapping of the ones to be established.

2. MAPPING OF THE UNDERGROUND UTILITIES

The urban underground is a complex web of various urban utilities like electricity, gas, telecommunication wires, water supply and waste water or traffic control. (Zarkhidze and Lemenager, 2004). Any addition or removal of utilities require exhaustive knowledge of the currently buried systems. Long stretches of modifications or additions can mean large interferences with existing systems. In order to lay the new pipe or utility, several elements have to be taken care to ensure best trajectory. (Zarkhidze and Lemenager, 2004). Recent developments in 3D GIS has opened ways for expanded representation of geospatial elements in 3D, which helps in storing the object characteristics such as shape, location, geometry etc. It also eases the processing and interpretation of such 3D datasets. On an advanced note, the benefits of this 3D mapping could be expanded by incorporating it pan city. (Saran et al., 2018)

Detection of the utilities buried underground can be done by several techniques such as:

- Visual Inspection (Closed circuit television)
- Pulsed Technology
- Electromagnetic and radio frequency technology
- Magnetic Technology
- Acoustic technology
- Resistivity Technology
- Sewer Scanner and evaluation technology

(Haoet al., 2012), (Rogers et al., 2009), (Geiger, 2006)

Out of the above the GPR or the Ground Penetrating Radar which is a sub-surface radio frequency investigation method, has shown its effectiveness over the others in the exploration and mapping of the underground utilities and infrastructures. (Cheng, Tang and Chan, 2013)

A few major countries have already implemented or at least setup the conceptual idea of 3D mapping of underground infrastructure and utility networks and their management in relation to the cadastral system. For instance, the city of Zurich, has developed its own utility plan since 1999 which has helped it establish a governance framework with various utility providers. (Yan et al., 2019)

3. CASE STUDIES

3.1 Use of Ground Penetrating Radar for mapping in Paris.

This case gives us an example of underground mapping done in an extremely dense location of Paris, with potentially several utilities lying underground in a complex matrix. The client demanded the installation of a new water pipe about 2.5 km in stretch in the centre of Paris about a mile away from the famous Eiffel Tower. A pipe of diameter 250 mm was planned to be laid down in the initial 1.5km which potentially had most of the pipelines. Over such a long course and in a highly populated area, a large number of sub-surface have to be avoided. Therefore, knowing accurately location and depth of all possible obstacles, on and around the planned path was a crucial step. It

also included ensuring that when many pipes were crossing perpendicularly the route of the future pipe, the acquisition of the images be done at 90 degrees angle.



Figure 1 Survey equipment for utility mapping, Paris
Source: (Zarkhidze and Lemenager, 2004)

This project also ensured that a high degree of accuracy was maintained when it came to the errors in the first 1m, limiting them to 10cm only. When it comes to 3D mapping, efficiency and precise positioning are essential. To address the efficiency aspect, a multi-antenna system, Mala Cart system was used, which is pushed by a light weight vehicle. This system is assisted by a precise and automated positioning system such as a GPS to ensure the data collected is correctly integrated with the local coordinates to create a spatial data. The acquisition path is one critical decision before the data is collected. Principally, it goes along the planned trajectory of the future pipe, mostly parallel.

Once, all the datasets generated were processed, they were created into a 3D visualisation by an appropriate tool. Finally the data was interpreted using various interpretation tools, the interpretation was verified and further merged with user data and the GPS coordinates. This study points out that the 3D ground penetrating radar was an efficient and accurate technology, to map sub-surface infrastructures and utilities, employing the appropriate methods. (Zarkhidze and Lemenager, 2004)

3.2 Use of Ground Penetrating Radar for mapping in Tunisia

This study presents the mapping of sewer lines in an urban region of the city of Tunis in Tunisia. The method employed was Ground Penetrating Radar (GPR) in combination with interpolation over the target area.

Tunisia faces the issue of damage of underground utilities by workers who dig in their nearby vicinities. These incidents caused harm to the workers as well as the utility systems. Damage of utility systems like water supply and storm water drainage also leads to several issues like pollution of potable water and the unwanted situation of material damage. This kept happening because of the absence of any knowledge about the presence of underground utility locations between the designed ones and the actual locations.

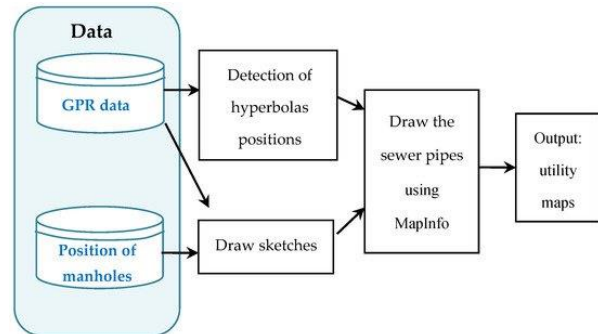


Figure 2 Flowchart of the major steps under the mapping activity in Tunisia

Source of the Image: (Ghozzi *et al.*, 2018)

The study area had several buried objects like electricity cables, optical fibres, metal ducts, gas pipes, underground tanks, plastic ducts, etc. In the study provided, only the mapping of the underground sewer lines was carried out using the GPR technique. A sketch diagram of the study area was prepared, in which the location of the manholes were marked. Then using both the sketches and the GPR radar grams, the direction of the buried lines of sewer were drawn using MapInfo.

Hence, with this brief study, the sewer pipe was mapped which may further be expanded to other underground utilities and their interdependencies and conflicts. (Ghozzi *et al.*, 2018)

3.3 The LADM-based 3D underground utility mapping in Singapore

Singapore is a city state with shortage of land resources and hence there is an intense requirement of optimization of land resources for social and economic development. Its underground spaces have been continuously used for various multi-layered overlapping infrastructures and utilities including transportation and city sewer systems. Hence, an in-depth spatial mapping of the underground space is important for smart and resilient city planning. Also, from the dynamic data collection point of view, a reliable digital 3D map of the underground space is important to connect data acquisition and usage.

The data collection was done by Pegasus: Stream, a mobile mapping platform which collects and captures above and underground data by the photo, GPR and laser technology. Based on the 3D underground utility data model LADM - Land Administration Domain Model, the new collected data was used with the existing cadastral and utility data for land administration.



Figure 3 The Pegasus: Stream captures both above-ground and underground data.

Source of the Image: (Van Son *et al.*, 2018)

The use of the mobile 3D platform for GPR possesses enormous potential for quick sub-surface data collection for the roads of large areas, with minimal disruption to traffic.(Yan *et al.*, 2019)

4. PRESENT SCENARIO IN INDIA

India as a country is now looking ahead at enormous growth in the urban areas. With increased load on infrastructure and utility demands, India is also taking up mapping of 3D utilities in different cities.

After the announcement to develop 100 smart cities and the introduction of AMRUT for improving the overall efficiency of the present cities, a detailed and comprehensive Asset and Utility management system is proposed that includes a set of exhaustive tools meeting the accurate digital asset mapping, monitoring and evaluation and planning requirements of the Municipal Corporations. To develop such comprehensive asset management systems, mapping of all assets, infrastructures and utilities both underground and above the ground are important. Possession of such accurate database and its understanding will save time, mitigate risk of injury, save money and increase user confidence. (Momin, 2018)

5. UTILITY MAPPING IN BIHTA

Bihta is a satellite town as proposed by the Patna Master plan 2031, in Bihar. Approximately 157.17 square km in area, its population is projected to increase to 188208 to 2031, as per the Patna Master Plan 2031. It is located along the river Son. It is planned as an educational and industrial hub of the Patna Metropolitan Area. It houses the IIT Patna, NSIT campus, NIT Patna campus, ESIC hospital and a separate Industrial area.

The development of Bihta and has paced up tremendously within the last decade. This calls for a good asset management system of the infrastructure which is going to be laid by the authorities in the coming near future. Available techniques include GPR combined with geospatial tools such as BIM, GIS, GPS, etc. to effectively map the underground utilities.

Also, the random and clustered development of various zones of Bihta implies a varied and unplanned underground utility presence. Hence, an appropriate 3D utility mapping for the city of Bihta with existing as well as the upcoming future utilities can help in creating an accurate 3D database which will lead to an efficient and cost-effective management systems.

6. CONCLUSION

This paper presenting the importance of the 3D mapping of the underground utilities briefly highlights the point that a 3D mapping of the underground utilities is a need of the hour. From the above 3 case studies ranging from a very dense and well-planned Paris to Tunisia to a very recent mapping exercise in Singapore, we can assess the immense benefits they have recorded after the three dimensional mapping of their utilities underground. Some of the benefits are: High degree of accuracy in mapping with GPR, Minimising the damages and time duration during the up gradation of existing utilities, Minimising conflicts of the new utility layers with the existing layers underground, Data collection and proper management of the asset systems underground can be carried out.

The above systems for mapping, hence must be used in Bihta as the city is emerging and early stage planning is crucial and will be beneficial in the longer run.

REFERENCES

- Bernold, L., Venkatesan, L. and Suvarna, S. (2002) 'A Multi-Sensory Approach to 3-D Mapping of Underground Utilities', in. doi: 10.22260/ISARC2002/0082.
- Cheng, N.-F., Tang, H.-W. C. and Chan, C.-T. (2013) 'Identification and positioning of underground utilities using ground penetrating radar (GPR)', *Sustainable Environment Research*, 23, pp. 141–152.
- Geiger, G. (2006) 'State-of-the-art in leak detection and localization', 32, pp. 193–198.
- Ghozzi, R. *et al.* (2018) 'Mapping of Sewer Lines Using GPR: A Case Study in Tunisia', *Data*, 3, p. 40. doi: 10.3390/data3040040.
- Hao, T. *et al.* (2012) 'Condition assessment of the buried utility service infrastructure', *Tunnelling and Underground Space Technology*, 28, pp. 331–344. doi: <https://doi.org/10.1016/j.tust.2011.10.011>.
- Momin, A. A. S. (2018) 'Mapping of the Assets and Utilities : A vision for the development of Smart Cities in India', in.
- Rogers, C. *et al.* (2009) 'Predictive Mapping of Soil Geophysical Properties for GPR Utility Location Surveys', in.
- Saran, S. *et al.* (2018) 'Utilities of Virtual 3D City Models Based on CityGML: Various Use Cases', *Journal of the Indian Society of Remote Sensing*, 46(6), pp. 957–972. doi: 10.1007/s12524-018-0755-5.
- Van Son, R. *et al.* (2018) 'A framework for reliable three-dimensional underground utility mapping for urban planning', in. Hannover: International Society for Photogrammetry and Remote Sensing (ISPRS) (International Archives of the Photogrammetry, Remote Sensing and Spatial Information Sciences), pp. 209–214. doi: 10.3929/ethz-b-000304140.
- Stoter, J., Ploeger, H. and van Oosterom, P. (2013) '3D cadastre in the Netherlands: Developments and international applicability', *Computers, Environment and Urban Systems*, 40, pp. 56–67. doi: <https://doi.org/10.1016/j.compenvurbsys.2012.08.008>.
- Urban population (% of total population) | Data* (no date). Available at: <https://data.worldbank.org/indicator/SP.URB.TOTL.IN.ZS> (Accessed: 28 February 2020).
- Yan, J. *et al.* (2019) 'THE LADM-BASED 3D UNDERGROUND UTILITY MAPPING: CASE STUDY IN SINGAPORE', *Int. Arch. Photogramm. Remote Sens. Spatial Inf. Sci.* Copernicus Publications, XLII-4/W15, pp. 117–122. doi: 10.5194/isprs-archives-XLII-4-W15-117-2019.
- Zarkhidze, A. and Lemenager, E. (2004) 'Case study - Use of 3D GPR technologies for utility mapping in Paris', in, pp. 375–378. doi: 10.1109/ICGPR.2004.180006.

ASSESSING THE THERMAL BEHAVIOUR OF URBAN MATERIALS USING HYPERSPETRAL DATA IN AHMEDABAD CITY, INDIA

Gautami Kushwaha¹, Asfa Siddiqui¹, Vinay Kumar¹

¹ Indian Institute of Remote Sensing, Indian Space Research Organization, Dehradun, Uttarakhand, India –
(gautamikush@gmail.com, asfa@iirs.gov.in, vinaykumar@iirs.gov.in)

KEYWORDS: urban heating, urban materials, hyperspectral remote sensing, land surface temperature

ABSTRACT:

With accelerating urbanization, natural landscapes are tremendously changing to urban landscapes and impervious built surfaces. This is leading to the degraded thermal environment in urban areas because of the higher thermal capacity and conductivity, solar radiation and absorption associated with the materials present. The heterogeneity in urban landscapes with different types of land-use/land-covers and surface materials plays a vital role in regulating the urban thermal environment within a city. The study focuses on the identification of major urban materials in Ahmedabad City through HSRS imagery and analyzing the role of different surface materials on the urban heating scenario in the study area. The hyperspectral imagery procured by Airborne Visible and InfraRed Imaging Spectrometer – Next Generation (AVIRIS-NG) during February 2016 was used to classify urban materials and Landsat-8 data was used to estimate land surface temperature (LST) through Radiative Transfer Model (RTM) for quantification of urban heating. Two classification techniques, Spectral Angle Mapper (SAM) and Support Vector Machine (SVM) were performed to classify the selected study area into five natural materials (water, bare soil, grass, crop, and trees) and six man-made materials (asphalt, PVC, marble, tin, concrete, china mosaic). The overall classification accuracy obtained through SVM (95.41%) was better than that obtained through SAM (70.68%). The highest mean LST of man-made urban material is observed for tin (29.68°C) followed by asphalt (29.49°C) and the lowest is observed for china mosaic (28.84°C). The range of LST of man-made surface materials is between 5-11°C, lowest LST values are observed in areas surrounded by vegetation and water and highest in areas surrounded by high heat absorption materials like asphalt and tin. This indicates that a material's heating behaviour is not only dependent on its thermal properties but also depends on the surrounding materials. The integration of information acquired from both HSRS and TIR shall add in understanding the relation of the urban thermal environment with urban surface characteristics.

1. INTRODUCTION

Urban population is continuously expanding around the globe with 55% of the world's population in 2018 to 68% expected in 2050 (Department of Economic and Social Affairs United Nations, 2018), which leads to extending urban boundaries by conversion of natural landscapes into concrete jungles. Urbanization has distinctly changed the natural landscapes to urban landscapes and impervious built-up materials, which are introducing anthropogenic sources of heat and pollution. Successively, this change in physical properties of a landscape is affecting the hydrological, thermal, radiative and aerodynamic properties, which in turn altering the heat exchange between the surface and the atmosphere (Jansson, 2006). This ultimately signifies that surface materials play a pivotal role in deviating 'urban climate' from its surroundings and that is one of the main reasons for urban heat island (UHI) effect. The urban landscapes are highly heterogeneous, it consists of a variety of surface elements like walls, roofs, roads, trees, water bodies, patches of grass and shrubs. Therefore urban environment has a wider range of surface properties in comparison to natural landscapes like forests and agriculture (Wang et al., 2017). Different materials in urban landscapes contribute differently to energy exchange in cities, which subsequently influence the climatic conditions such as air temperature and humidity in the near-surface atmosphere (Jansson, 2006). The heat is retained in the urban landscape during the day and released during the night due to the high heat capacity of construction materials

abundant in urban areas. Thus due to more impervious surfaces and lack of vegetation in urban areas, evapotranspirative cooling is reduced and as a result, turbulent latent heat flux is relatively small (Galli & Vallati, 2012).

Hyperspectral remote sensing (HSRS) data has been widely used in urban studies in many ways, including extraction of accurate impervious surfaces, roof and road types and corresponding age, source of pollution and changing landscape pattern (Ridd, 1995). In the domain of urban climate and environment studies, thermal infrared (TIR) satellite remote sensing data have been extensively used and it has made tremendous achievements, majorly for analyzing land surface temperature (LST) patterns and their relationships with surface characteristics and for understanding surface urban heat islands (SUHI) (Ren et al., 2015). The HSRS has not been so far extensively used for urban heating studies. The integration of information acquired from both HSRS and TIR shall add in understanding the relation of the urban thermal environment with urban surface characteristics.

The aim of the present study is to identify major urban materials through HSRS imagery and analyze the role of different materials on the urban heating scenario in the selected part of Ahmedabad City. For that, hyperspectral imagery procured by Airborne Visible and Infrared Imaging Spectrometer – Next Generation (AVIRIS-NG) was used to classify urban materials and Landsat-8 data was used to estimate land surface temperature (LST)

through Radiative Transfer Model (RTM) for quantification of urban heating. Two classification techniques, Spectral Angle Mapper (SAM) and Support Vector Machine (SVM) were performed to classify the selected study area into five natural materials (water, bare soil, grass, crop, and trees) and six man-made materials (asphalt, PVC, marble, tin, concrete, china mosaic). The LST of each urban material in various built setups is analyzed to understand their contribution to urban heating in the study area.

2. STUDY AREA

The study area is part of Ahmedabad city (Figure 1), which is the fifth-most populous city of India with a population of 55,77,940 in 2011 and the largest city of Gujarat state. It extends between 23°2'34.7064" N to 23°0'23.0184" N latitudes and 72°37'19.7328" E to 72°25'42.276" E longitudes encompassing an area of 70.90 km², which is 15% of total area of Ahmedabad city (466 km²) and it is at an altitude of 173 feet from mean sea level. Ahmedabad city is the industrial and financial growth engine of the Gujrat state and has emerged as an important economic and industrial hub in India, which is why it is undergoing rapid urban growth. Sabarmati River flows through the study area, dividing it into East Ahmedabad (old city) and West Ahmedabad (new city) and half part of Kankariya Lake is also present in the selected study area. The study area covers the old city, new city area and peripheral area of the city. The study area has heterogeneous urban materials including both natural (grass, vegetation, water, soil, etc.) and manmade (asphalt road, concrete, china mosaic, etc.) and encompasses both parts of the city core and peripheral area, which makes it suitable for the study. The study area has an arid steppe hot climate with a mean annual temperature is greater than 18°C and marginally less rain than required for a tropical savannah climate (Peel, Finlayson, & McMahon, 2007). The summers in Ahmedabad stays from March to June with highest temperature reaching 43°C and lowest 24°C, whereas winters are from November to February with the highest temperature reaching 30°C and lowest 13°C. The monsoon season generally occurs from June to September and the city records average annual rainfall around 782 mm. The average relative humidity is 60% with a maximum of 80% to 90% during the rainy season. Studies on the urban thermal environment of Ahmedabad city proved that it has been severely affected by heatwaves and urban heat island effect (Joshi et al., 2015; Mohammad, Goswami, & Bonafoni, 2019), which raised the need to crate Heat Action Plan for Ahmedabad City (Ahmedabad Municipal Corporation, 2016).

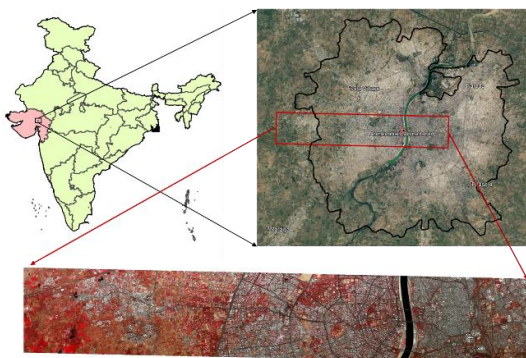


Figure 1 Study Area (Part of Ahmedabad City)

3. MATERIALS USED

The hyperspectral data of Airborne Visible Infrared Imaging Spectrometer-Next Generation (AVIRIS-NG) has been used for the classification of urban materials (natural and man-made) in the study area. The scene was acquired on 10th February 2016 at 8:01:29 am by Jet Propulsion Laboratory (JPL), National Aeronautics and Space Administration (NASA) under the Indian Space Research Organization (ISRO) – National Aeronautics and Space Administration (NASA) Airborne Hyperspectral Imaging (HySI) Programme. This dataset contains 425 bands with 8.1m spatial resolution, measuring the wavelength range from 380 nm to 2510 nm with 5 nm sampling.

Landsat-8 OLI (Operational Land Imager) and TIRS (Thermal Infrared Sensor) data (Row 44/Path 149) is used for estimation of NDVI and LST of the study area. The Radiative Transfer Model is used for the estimation of LST from band-10 (10.6 - 11.19 μm) having a 30 m spatial resolution. Dataset acquired on 4th February 2016 at 11:09 am is used in the study because it is closest to AVIRIS-NG data acquisition time and has 0.27 land cloud cover which makes it suitable for the study.

Surface parameters (temperature, relative humidity, and atmospheric pressure) of the study area are obtained from the Meteorological & Oceanographic Satellite Data Archival Centre (MOSDAC) website of SAC, ISRO. These records are acquired from the automatic weather station (AWS) in SAC, Ahmedabad for 4th February 2016 at 11:09 am. These parameters are used to extract atmospheric profiles (atmospheric transmittance, upwelling radiance, and downwelling radiance) from the Atmospheric Correction Parameter Calculator (ATM CORR) (<https://atmcorr.gsfc.nasa.gov/>).

4. METHODS

For the classification of urban materials, AVIRIS-NG's Level-2 processed product is used which is atmospherically corrected to recover the Lambertian surface reflectance. This stage of processing involves modeling the atmosphere, dynamically retrieving quantities such as water vapor content. This modeling is based on the ATREM algorithm (Thompson et al., 2015). The data processing and classification are performed in ENVI software. Bad band correction is performed in the data set and 71 noisy and no data bands were removed. This data is geometrically registered with respect to the Landsat-8 Panchromatic band which has a spatial resolution of 15m, closer to that of AVIRIS-NG (8.1m), with automatically generated and manually crosschecked 30 tie point and 0.42 RMS error. The spectral library for classification is generated by collecting ROIs on the basis of ground knowledge (Figure-2). Two classification techniques SAM and SVM are used in for classification of urban materials in the study area. Multiple values of maximum spectral angle are assigned for different land cover classes for SAM, while SVM classification is applied with default settings.

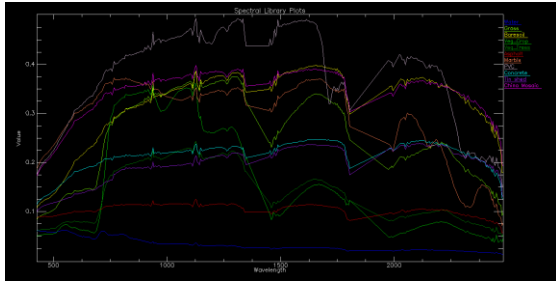


Figure 2 Spectral Library used for classification

The TIRS Band-10 (10.60-11.19µm) of Landsat-8 is utilized for estimation of land surface temperature (LST) using the RTE method due to its better performance as compared to TIRS Band-11 (Department of the Interior, 2019). Recent studies on LST estimation proved that the RTE method using Band 10 gives more accurate results as compared to other methods (Split window and single-channel algorithm) (Yu, Guo, & Wu, 2014). The LST estimated by RTE given by Yu et al., 2014 is as follows:

$$LST = \frac{C_1}{\lambda \cdot \ln \left\{ \frac{C_2}{\lambda^{5.1} \left[\frac{L_{10} - I_{\uparrow} - \epsilon_s(1-\epsilon)I_{\downarrow}}{\epsilon_s + \epsilon} \right] + 1} \right\}} \quad (1)$$

Where, $C_1 = 4387.7 \mu\text{m} \cdot \text{K}$, $C_2 = 1.19104 \times 10^8 \text{ W} \cdot \mu\text{m}^4 \cdot \text{m}^{-2} \cdot \text{sr}^{-1}$, λ = effective band wavelength (for TIRS Band 10 $\lambda = 10.896$), L_{10} is TOA spectral radiance (Watts/($\text{m}^2 \cdot \text{srad} \cdot \mu\text{m}$)) for TIRS band 10, I_{\uparrow} is upwelling atmospheric radiance (Watts/($\text{m}^2 \cdot \text{srad} \cdot \mu\text{m}$)), I_{\downarrow} is downwelling atmospheric radiance (Watts/($\text{m}^2 \cdot \text{srad} \cdot \mu\text{m}$)), ϵ is land surface emissivity and t is atmospheric transmittance.

The LSE is an intrinsic property of a material which is defined as the ratio of the radiance emitted by a body to the radiance emitted by a black body at an given wavelength and temperature (Li et al., 2013) and can be estimated from P_v and TOA reflectance of OLI red band (band 4) by using NDVI thresholds method:

$$\epsilon = \begin{cases} a_i \rho_{red} + b_i & NDVI < 0.2 \\ \epsilon_v P_v + \epsilon_s (1 - P_v) + C_i & 0.2 \leq NDVI \leq 0.5 \\ \epsilon_v + C_i & NDVI > 0.5 \end{cases} \quad (2)$$

Where, ϵ_v and ϵ_s is the emissivity of vegetation and soil respectively and C_i is a term that takes the cavity effect into account due to the surface roughness ($C = 0$ for flat surfaces). The values of ϵ_v and ϵ_s for Landsat-8 TIRS band-10 are 0.9668 and 0.9863 respectively (Yu et al., 2014).

The proportion of vegetation (P_v) (also referred to as fractional vegetation cover) is derived from NDVI, which was calculated from OLI red and near-infrared bands (band 4 and 5) of Landsat 8 after converting them to TOA reflectance:

$$NDVI = \frac{\rho_5 - \rho_4}{\rho_5 + \rho_4} \quad (3)$$

$$P_v = \left[\frac{NDVI - NDVI_{min}}{NDVI_{max} - NDVI_{min}} \right]^2 \quad (4)$$

Where ρ_5 and ρ_4 are TOA reflectance of band 5 and band 4 respectively. The NDVI represents the density of green in an area (Schinasi, Benmarhnia, & De Roos, 2018) whereas P_v depicts the amount and nature of vegetation

cover and modulates the proportions of vegetation and non-vegetated ground (e.g., bare soil) visible to a sensor (Weng, 2009).

The LST over classified land covers is analyzed for the study area by estimating zonal statistics (mean, maximum, minimum and range) of LST on each land cover. The effects of surrounding urban materials on the LST values of a particular material was assessed.

5. RESULTS AND DISCUSSIONS

Figure-3 illustrates the output of SVM and SAM classification technique showing eleven urban material classes. It can be observed by the visual interpretation of classification results in Figure-3 that SAM classification significantly overestimated the china mosaic and asphalt class and underestimated the tin and concrete class. Whereas, the SVM classification results are relatively accurate for all urban material classes. Shadow is classified as asphalt in both the classification techniques.

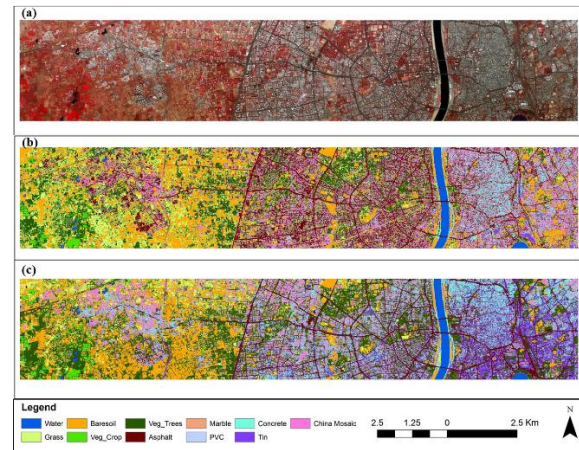


Figure 3 (a) FCC of study area, (b) Classification output from SAM and (c) Classification output from SVM

The Table-1 summarizes the results obtained from both the classifiers in terms of classification accuracy. The accuracy of classification results was estimated with 0.1% of the sample size. The SVM exhibited better Overall Accuracy (OA) of 95.41%, which is 24.73% more than that of SAM classifier (70.68%). Also, the Kappa coefficient (K) for the SVM classifier (0.948) is higher as compared to that of the SAM classifier (0.670).

Table 1 Classification accuracy from SAM and SVM

	SAM	SVM
Overall Accuracy	70.68%	95.41%
Kappa	0.6702	0.948

Furthermore, Figure-4 shows the Producer's accuracy and User's accuracy in all the classes for comparative analysis of both the classifiers. It is observed that the producer's accuracy of bare soil is highest for both SVM and SAM classification (i.e. 100% in both the cases) whereas Tin shed has lowest producer's accuracy for both i.e. 84.91% for SVM and 38.68% for SAM because of similar spectra to that of concrete (Figure-2). Apart from bare soil, trees and PVC gave 100% producer's accuracy which is the same in the user's accuracy also. But the user's accuracy

from SAM classification is 100% for water and agricultural vegetation. All the land-covers gave more than 80% user's and producer's accuracy from SVM classification, whereas the accuracies are ranging between 35-100% from SAM classification. That is why SVM classification results are used for further analysis.

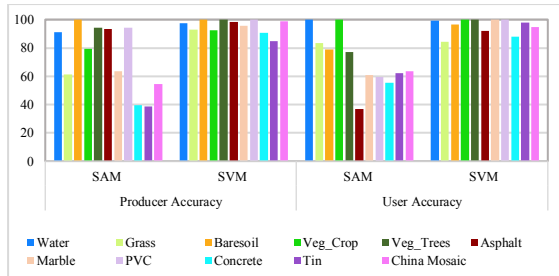


Figure 4 of Producer's and User's accuracy of SAM and SVM classification

Figure 5 shows the distribution of urban materials in different parts of the study area. The classification results show that the old city area (east of Sabarmati River) is high density (78.07%) built-up area with tin-shed (27.15%), concrete (24.04%) and asphalt (18.15%) as major surface materials. There are some buildings with china mosaic as roof material, around 8.25% of the area, but these are new buildings (5-8 years). The west of Sabarmati River has a comparatively less built-up density (60.19%) and since many buildings in this area are built in the last 20 years with china mosaic roofs instead of concrete, this region has more china mosaic (19.62%) roofs than old city area. The peripheral area (western part of the study area) has only 22.61% of the built-up surface. Majority of the land cover is natural in this region with 33.68% bare soil, 28.97% trees, and 11.06% grassland. China mosaic is the major building material in this part i.e. 10.20%.

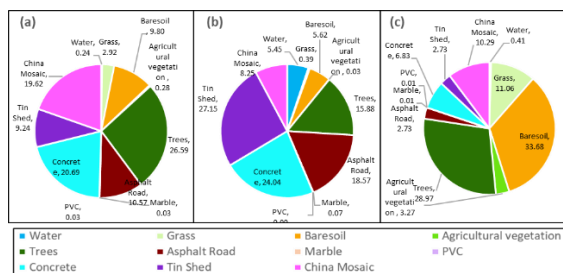


Figure 5 Land-cover distribution in (a) West of Sabarmati River, (b) East of Sabarmati River (Old City area) and (c) Peripheral area

The estimated LST in the study area ranges between 22.58°C -36.12°C (Figure 6). The old city area exhibits higher LST values as compared to the new city area. Higher LST values (29°C-36°C) are observed mainly in the old city area, while the new city area exhibits relatively lower LST values (25°C -29°C).

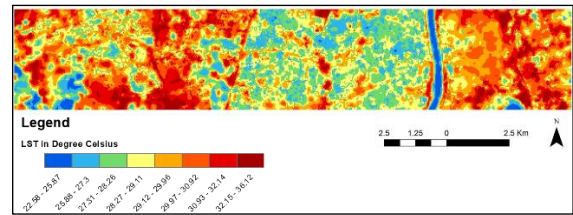


Figure 6 LST estimated for the Study Area

It is noticed that mean LST in the study area is highest in areas with land-cover bare soil (30.33°C), followed by grass (29.72°C), tin (29.68°C) and asphalt (29.49°C), whereas water exhibits lowest mean LST (25.89°C) as shown in Table-2. Amongst all building materials classified in the study area, china mosaic exhibits lowest mean LST i.e. 28.84°C because of its lower solar absorption and high thermal emittance, whereas tin shed exhibits highest mean LST i.e. 29.68°C due to high solar absorption and lower thermal emittance. The maximum LST in the study area is recorded for asphalt road (36.12°C) followed by tin shed (35.74°C) and bare soil (35.39°C) and minimum LST is recorded for natural land-covers i.e. agricultural vegetation (22.58°C), grass (23.52°C), bare soil (23.42°C), trees (23.32°C) and water (24.08°C). These statistics support the fact that urban materials like asphalt, tin shed and concrete contribute severely to the urban heating phenomenon by absorbing more solar radiation, whereas more reflective urban materials like china mosaic are effective in reducing urban heating.

Table 2 LST Statistics for the Study Area (Red shade demarcating the highest values and blue demarcating the lowest values in respective columns)

Value	Minimum LST	Maximum LST	Range	Mean LST
Water	24.080	31.033	6.953	25.887
Grass	23.523	33.086	9.563	29.724
Bare soil	23.425	35.388	11.963	30.327
Agricultural Vegetation	22.576	32.590	10.013	28.209
Trees	23.324	35.111	11.787	28.854
Asphalt	24.602	36.123	11.521	29.493
Marble	26.881	30.910	4.029	29.205
PVC	26.892	31.032	4.140	29.133
Concrete	25.571	34.697	9.125	29.202
Tin	25.988	35.736	9.748	29.677
China Mosaic	25.818	34.227	8.410	28.840

The urban materials in the study area have significant LST ranges, from 4°C to 12°C (Table-2). These differences between highest and lowest LST exhibited by particular materials support that heating effect by one material can be curbed by setting up cool materials in the surroundings. As shown in Figure 7 if asphalt road is surrounded by vegetation it has lower LST values (26.52°C) and if it is present in high-density built-up area and surrounded by materials like tin shed and concrete, it gives high LST value (35.84°C). Similar behavior can be observed for other materials (concrete, tin shed) also in Figure 7. These records intend for the heating and cooling effect of

neighboring land-cover and urban materials on the heating scenario of particular surface material.

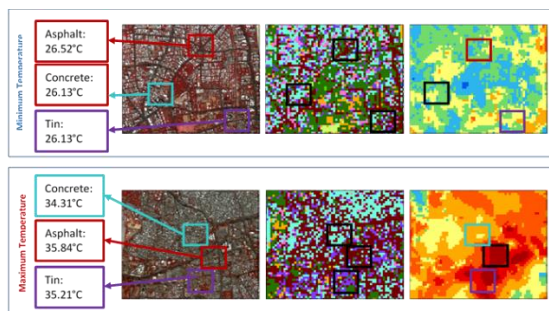


Figure 7 Variation in LST exhibited by built materials due to neighbor land-covers

6. CONCLUSION

The study of the urban thermal environment is incomplete without knowledge and understanding of the thermal properties of materials present in an urban landscape, both natural and man-made. The potential of hyperspectral remote sensing data in urban material classification enables the possibility of analyzing the urban thermal environment in detail. The present study utilized both hyperspectral and thermal remote sensing data to assess the contribution of different urban materials in urban heating in the selected part of Ahmedabad City. The SVM technique proved more accurate (95.41%) in the classification of urban materials in the study area as compared to SAM (70.68%). The major man-made materials in the study area are concrete, tin, asphalt and china mosaic and amongst them, tin and asphalt are the warmest materials followed by concrete and china mosaic has the lowest mean LST. The urban material classification and LST results of this study show that man-made materials like tin shed, asphalt and concrete have a major contribution in raising the temperature in the old city area of Ahmedabad City as compared to china mosaic, which is major roofing material in new city area and periphery of the city. The china mosaic is capable of bringing down LST by 1°C than urban materials having high solar absorption and lower thermal emittance. The evaporative cooling of vegetation and water bodies is observed to reduce the temperature by 3-8°C. The notable range (8-11°C) of LST values of built-up materials infer that materials' thermal properties are not the only reason for heating effect in an urban neighborhood but the density of material in that area and the heating behavior of surrounding materials also contribute to heating or cooling phenomenon.

However, assessment of the individual contribution of different urban materials in the heating and cooling of an urban landscape provides a strong background in understanding the urban thermal environment in the context of specific study areas. Application of hyperspectral thermal imagery data can also be explored for such studies which can enable the classification of urban materials on the basis of spectral as well as thermal properties.

REFERENCES

- Ahmedabad Municipal Corporation. (2016). *Ahmedabad Heat Action Plan 2016 - Guide to extreme heat planning in Ahmedabad, India*. <https://doi.org/10.1371/journal.pone.0091831>
- Department of Economic and Social Affairs United Nations. (2018). World Urbanization Prospects 2018. In *Webpage*. Retrieved from <https://population.un.org/wup/>
- Department of the Interior, U. S. G. S. (2019). LANDSAT 8 (L8) DATA USERS HANDBOOK Version 4.0 April 2019. In the *Department of the Interior, U.S. Geological Survey* (Vol. 4). Retrieved from https://prd-wret.s3-us-west-2.amazonaws.com/assets/palladium/production/atoms/files/LSDS-1574_L8_Data_Users_Handbook_v4.0.pdf
- Galli, G., & Vallati, A. (2012). Thermal Characteristics of Urban Surface Materials. *Advanced Materials Research*, 629, 443-447. <https://doi.org/https://doi.org/10.4028/www.scientific.net/amr.629.443>
- Jansson, C. (2006). *Urban microclimate and surface hydrometeorological processes*.
- Joshi, R., Raval, H., Pathak, M., Prajapati, S., Patel, A., Singh, V., & Kalubarme, M. H. (2015). Urban Heat Island Characterization and Isotherm Mapping Using Geo-Informatics Technology in Ahmedabad City, Gujarat State, India. *International Journal of Geosciences*, 06(03), 274-285. <https://doi.org/10.4236/ijg.2015.63021>
- Li, Z. L., Wu, H., Wang, N., Qiu, S., Sobrino, J. A., Wan, Z., ... Yan, G. (2013). Land surface emissivity retrieval from satellite data. *International Journal of Remote Sensing*, 34(9-10), 3084-3127. <https://doi.org/10.1080/01431161.2012.716540>
- Mohammad, P., Goswami, A., & Bonafoni, S. (2019). The Impact of the Land Cover Dynamics on Surface Urban Heat Island Variations in Semi-Arid Cities : *Sensors*, 19(17), 3701. <https://doi.org/10.3390/s19173701>
- Peel, M. C., Finlayson, B. L., & McMahon, T. A. (2007). Updated world map of the Köppen-Geiger climate classification. *Hydrology and Earth System Sciences*, 11(5), 1633-1644. <https://doi.org/10.5194/hess-11-1633-2007>
- Ren, P., Meng, Q., Zhang, Y., Zhao, L., Yuan, X., & Feng, X. (2015). An unmanned airship thermal infrared remote sensing system for low-altitude and high spatial resolution monitoring of urban thermal environments: Integration and an experiment. *Remote Sensing*, 7(10), 14259-14275. <https://doi.org/10.3390/rs71014259>
- Ridd, M. K. (1995). Exploring a V-I-S (vegetation-impervious surface-soil) model for urban ecosystem analysis through remote sensing: comparative anatomy for cities. *International Journal of Remote Sensing*, 16(12), 2165-2185. <https://doi.org/10.1080/01431169508954549>

- Schinasi, L. H., Benmarhnia, T., & De Roos, A. J. (2018). Modification of the association between high ambient temperature and health by urban microclimate indicators: A systematic review and meta-analysis. *Environmental Research*, *161*, 168–180. <https://doi.org/10.1016/J.ENVRES.2017.11.004>
- Thompson, D. R., Gao, B. C., Green, R. O., Roberts, D. A., Dennison, P. E., & Lundeen, S. R. (2015). Atmospheric correction for global mapping spectroscopy: ATREM advances for the HypsIRI preparatory campaign. *Remote Sensing of Environment*, *167*, 64–77. <https://doi.org/10.1016/j.rse.2015.02.010>
- Wang, Y., Di Sabatino, S., Martilli, A., Li, Y., Wong, M. S., Gutiérrez, E., & Chan, P. W. (2017). Impact of land surface heterogeneity on urban heat island circulation and sea-land breeze circulation in Hong Kong. *Journal of Geophysical Research*, *122*(8), 4332–4352. <https://doi.org/10.1002/2017JD026702>
- Weng, Q. (2009). Thermal infrared remote sensing for urban climate and environmental studies: Methods, applications, and trends. *ISPRS Journal of Photogrammetry and Remote Sensing*, *64*(4), 335–344. <https://doi.org/10.1016/j.isprsjprs.2009.03.007>
- Yu, X., Guo, X., & Wu, Z. (2014). Land surface temperature retrieval from Landsat 8 TIRS-comparison between radiative transfer equation-based method, split window algorithm and single-channel method. *Remote Sensing*, *6*(10), 9829–9852. <https://doi.org/10.3390/rs6109829>

Study of Heat Waves and Urban Heat Island Interaction in a single Frame using Regional Climate Model: WRF-Urban

Priyanka Rao¹, Kshama Gupta¹, Arijit Roy¹, Ashutosh K. Jha¹, Prashant Kumar²

¹Indian Institute of Remote Sensing, ISRO, Dehradun- priyanka123.iirs@gmail.com, (kshama, arijitroy, akjha)@iirs.gov.in

² Space Applications Centre, ISRO, Ahmedabad- prashant22@sac.isro.gov.in

KEY WORDS: Heat Waves, UHI, WRF-Urban, N-Down, Domain Configuration

ABSTRACT:

A heat wave is a short-term phenomenon. Severe heat waves have a negative impact on human health, increases the mortality rate (more in children and older age groups), water resources, agriculture etc. Therefore, it is important to study heat wave events, so that an adequate warning system can be introduced for the safety of common people. Currently, the analysis and illustration of heat waves in a comprehensible and manageable way is a critical challenge for climate services. The recognition of heat waves is based on high quantities of daily temperature distributions, and can be applied to any temperature series. The heat waves are indicated by their duration, frequency and intensity. Urban environments and heat waves interact synergistically and increase the thermal environment through the effect of the Urban Heat Island (UHI). The potential for a projected warmer future climate to compound heat waves in urban environments is a matter of concern.

In this case study, heat wave analyses has been done over the region of Delhi using WRF-urban model. Domain configuration has been done in the manner that regional phenomenon (heat wave) and local phenomenon (pre-existing UHI) both could be covered and heat wave variation in the core built up area due to presence of pre-existing heat island could be observed. The simulation has been carried out for six days of May 2016. As this study includes fine resolution domain, and performing 5 nested (online) model simulations need huge computational resources that can be reduced if major characteristics are observed from coarser resolution, before performing finer resolution WRF simulation. So, a very limited explored technique named nest down (n down) technique has been used in which the output of coarser domain has been used as input for finer domain and these simulations have been performed offline. NCEP GFS data at 0.25° has been taken for boundary and initial conditions and LSPs like LAI, Fapar, Albedo, etc., have been updated in the model. The results were validated through IMD data. Temperature and relative humidity correlation between model and IMD values at Delhi (for example) were observed as 0.95 and 0.72 respectively in domain3, 0.95 and 0.82 respectively in domain4, and 0.92 and 0.66 in domain5. These correlations when compared with the earlier studies using nested (online) simulation, it was found to be at comparable scales. Hence, nest down approach could be used to study the regional and local phenomenon that too with the low computational resources and time.

1. INTRODUCTION

Prolonged extreme temperature conditions are referred as heat waves. National Disaster Management Authority (NDMA) of India describes the heat wave as unusually high temperatures, more than normal peak temperatures in the north-western parts of India during the summer season (NDMA, n.d.). The peak period of heat waves in northern India has been observed between March and June but in some rare cases it may prolong till July (Nissan et al, 2017; Rohini, Rajeevan, & Srivastava, 2016). These extremes in temperature create thermal discomfort for the living beings in the region as it may result into heat stress and other major health issues which even leads to death in severe cases. Indian Meteorological Department (IMD), provides few criteria for defining the heat waves (NDMA, n.d.):

- Temperature is considered normal when it is recorded as 40°C or less for plains, and 30°C or less for hilly areas.
- When maximum temperature recorded is less than or equal to 40°C, 5°C to 6°C increase from normal is considered as heat waves and severe heat waves are being considered when temperature increases 7°C and beyond.

- When recorded maximum temperature is more than 40°C, temperature increase of 4°C to 5°C is considered as heat waves while temperature increase of 6°C and more is being declared as severe heat waves.
- When maximum temperature recorded is 45°C or more, then no other condition is being considered and directly heat waves are being declared.

Increasing temperature extremes is becoming a key disaster in the present scenario, responsible for the severe outcomes leading to destructive atmosphere, degradation in the natural resources and even death of living beings. Due to climate change this destruction is becoming more prominent. In the urban areas, because of complex built up, the heat increases more and more and the existing UHI effect gives a positive feedback loop to the heat waves and which ultimately contributes to the global warming. The different built up material, has different properties and depending on those properties buildings entrap the heat, which contributes in the UHI. Out of the most fatal 11 natural hazards in the continental United States, heat waves (including those associated with drought) represent a plurality of mortality (about 20 percent) (Borden & Cutter, 2008). The vulnerable section of the society especially elderly, children and poor people amongst the whole population are severely affected by the heat waves. Several number of deaths have been recorded in the region of Greece due to severe problem

of heat stroke and heat exhaustion (Theoharatos et al., 2010). Despite of the countless destructions caused by heat waves, to human life and natural resources, it has been taken for granted and as a result today it has become a major concern w.r.t. climate change. Future HW projections predict that intensity, duration and frequency of HW will increase in the twenty-first century (Meehl & Tebaldi, 2004). Numerical Weather Prediction (NWP) has been proven as valuable tool to analyse as short term forecasting tool as well as to predict heat wave conditions in future. (Giannaros et al., 2018). Various studies had utilised mesoscale NWP model, Weather Research and Forecasting (WRF) model to study and forecast the extreme temperature periods, outlining the land surface processes to produce and develop intense hot weather conditions (Chiriaco et al., 2014). The WRF model is based on the parameterisation of the physical mechanisms which is been done by land surface models (LSMs). The studies so far focus on heat wave and UHI separately and very less work has been done to analyse UHI and heat waves together and their impact on each other. The need of extensive computational resources due to necessity of capturing regional to local phenomenon through multiple domains is found to be one of the major reason. Since, this study aims to analyse the heat wave, which is a regional phenomenon, simultaneously with the local phenomenon called UHI, and also how they affect/influence each other. Hence, a less explored approach of WRF model, named nest down (n-down) has been evaluated in this study to overcome the limitations faced by earlier studies.

2. STUDY AREA AND DATASET USED

This section elaborates the details of study area and the dataset used for this study.

2.1 Study Area and Domain Configuration

The study area selected for this case study is Delhi (Figure 1). However, to study heat waves, which is a regional phenomenon, the domain configuration has been done in such a way so that the area besides and towards western India could be covered. For this purpose a total of five domains have been created with the spatial resolution of 40.5km, 13.5km, 4.5km, 1.5km and 0.5km, where the spatial extent of last domain covers Delhi and nearby area. Delhi has been assumed as one of the very fast growing cities of Indian subcontinent and the pace of increase in urbanisation is showing extruding results. Delhi masks about 1484 sq. km area, out of which 700 sq. km (approx.) comes under urban category which makes it the area wise largest city of the country. Because of the dense urban area and prominent existing UHI effect, the phenomenon could be easily studied in this area. All these characteristics, makes the study of UHI effect and its influence on heat waves and vice versa, over National Capital Region of Delhi.

2.2 Dataset Used

Data used in this study for WRF simulations consists of default geographic data which comprises of land use, DEM, etc. out of which Land Surface Parameters (LSPs) like albedo, vegetation fraction, LAI, Fapar and Fcover has been updated in the model for improved accuracy. Meteorological data used is NCEP GFS, which provides initial and boundary conditions for the configured domain extent. To validate the parameters like, temperature, relative humidity, wind speed, etc. IMD weather station data has been used. The details of the data resolution has been mentioned in table 1.

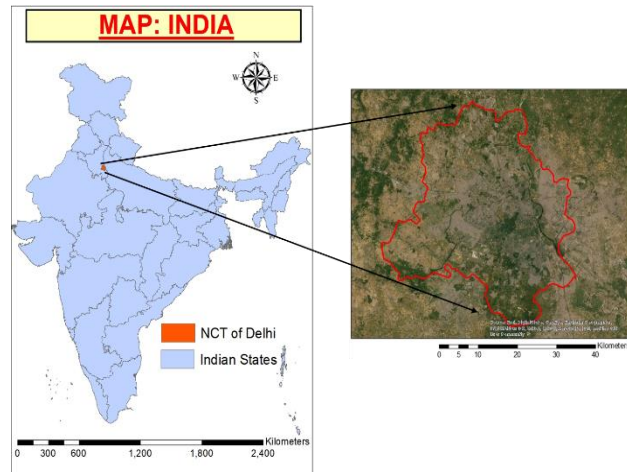


Figure 1 Study Area Map

Table 1 Data used for WRF model simulations

DATA	RESOLUTION
GTOPO30 Elevation	1KM
Albedo (Bhuvan)	1KM
Green Fraction (Bhuvan)	1KM
LAI, Fapar, Fcover (Copernicus)	1KM
NCEP GFS data at every 3 hours	0.25°
IMD Data (for validation)	Point location

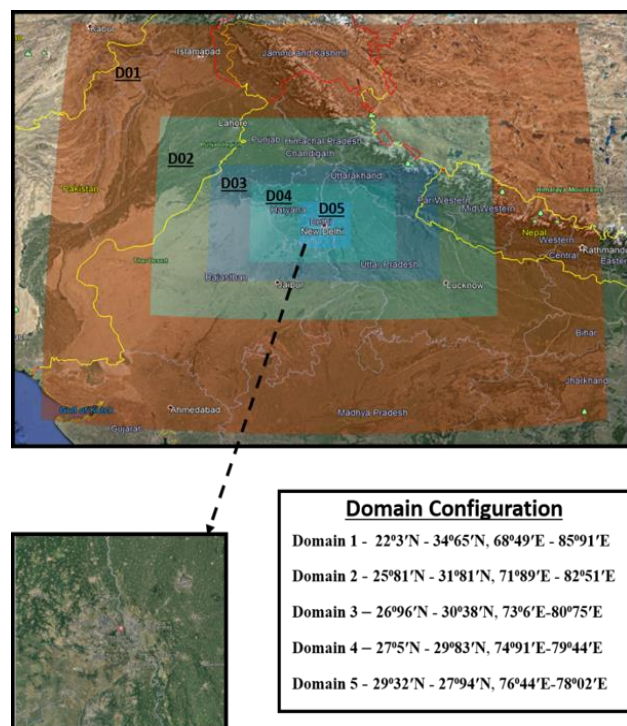


Figure 2 Domain Configuration for WRF simulations

3. METHODOLOGY

This section describes overall methodology adopted to achieve the objective.

Firstly WRF model setup, configuration and compilation has been done in the Linux environment. Domain creation has been done by considering the influence of local and regional phenomenon i.e., UHI and Heat Waves on each other. In total five domains have been created with outermost domain D01 having 40.5km spatial resolution and innermost domain D05 with 0.5km spatial resolution. Geographic data has been downloaded for the model and LSPs have been updated from Bhuvan and Copernicus. Meteorological data has been downloaded to provide the initial and boundary conditions. Time period selected for the heat wave simulation is May14, 2016 to May20, 2016 as this year has been found very warm in the last decade and also this time period faces extreme heat (World Meteorological Organization, 2017). Output at every 3 hours has been obtained. Simulation of multiple domains together, require heavy computational resources and time, that is why, a less explored approach named one way nested run using n-down has been used in this research work. This is basically an offline approach for WRF simulations. During online multiple domain simulations, the output of the coarser domain has been passed on to the inner domain as initial and boundary conditions, whereas, in offline nested run using n-down, output of coarser domain has been taken as input for the inner domain, and simulation for the inner domain is done offline. Here, domain D01, D02 and D03 has been simulated together using online nested run and then domain D04 has been run offline i.e., separately by taking outputs of domain D03 and similarly domain D05 has been simulated offline using output of domain D04. Finally validation has been performed w.r.t. IMD data. The overall methodology of the WRF simulation has been described in figure 2 while the detailed methodology of n-down has been explained in figure 3.

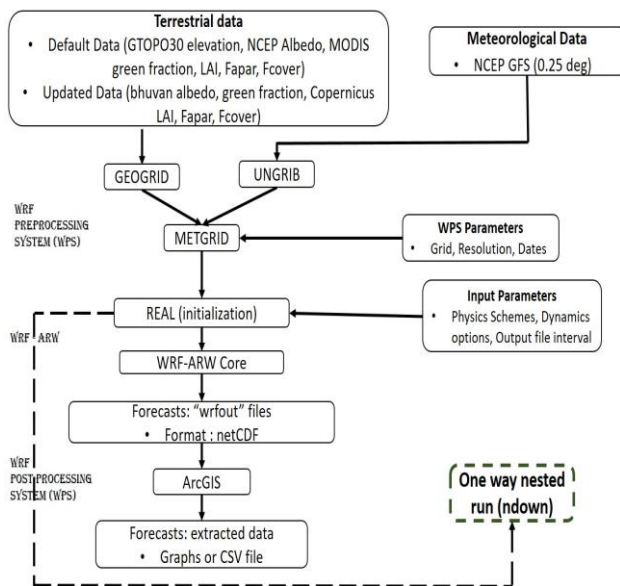


Figure 3 Flow chart of the methodology of WRF simulation

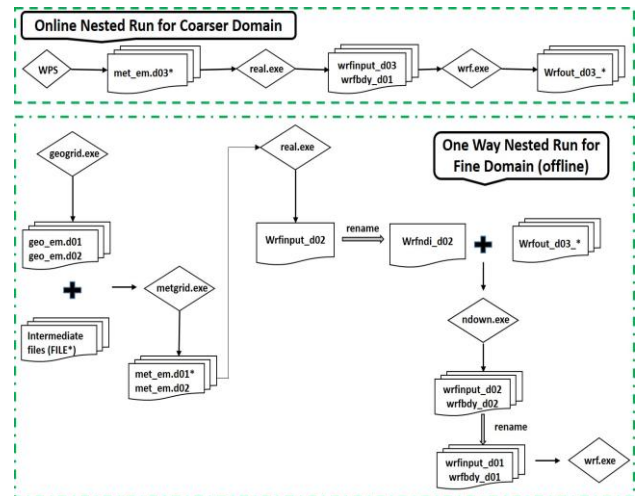


Figure 4 Detailed explanation of the n-down approach. Source (ARWUsersGuideV3.8)

To achieve the desired objective, parameterisation of the model has been done accordingly. The physics options appropriate for the heat wave simulation for present study has been detailed out in table 2.

After the successful WRF run, results of simulation were obtained in netcdf file format, which consists of several parameters. For analyses purpose, temperature at 2m was available readily, and other parameters like wind speed and relative humidity needs to be computed by applying the respective formulas. For example wind speed is a vector quantity and has two components called U2 and V2, which are used for the calculation of the wind speed. To validate the results IMD data has been used and statistical measures like Root Mean Square Error (RMSE), Mean Absolute Error (MAE) and Correlation (R) were computed.

Table 2 Physics Options used in the WRF model for present case study

Physics option	D01	D02	D03	D04	D05
Micro Physics	WSM6				
Long Wave Radiation Scheme	RRTMG				
Short Wave Radiation Scheme	RRTMG				
Surface Layer (sf_sfclay_physics)	Monin-Obukhov (Janjic Eta) Scheme				
Land Surface Physics (sf_surface_physics)	Unified Noah Land Surface Model				
PBL scheme (bl_pbl_physics)	Mellor-Yamada-Janjic scheme				
Urban Surface Physics (sf_urban_physics)	Nil			BEP+ BEM	BEP+ BEM
Cumulus Scheme	Betts-Miller-Janjic scheme				

4. RESULTS

Temperature, Wind Speed and Relative Humidity has been computed and according to the point location of the IMD stations, the data/values of all the parameters were extracted and analysed at every 3 hours w.r.t. IMD data. Figure 4 shows the spatial variation of Temperature, Relative Humidity and Wind Speed of domain D03 for May 17, 2016 at 14:30 hrs IST. Similarly for all the domains spatial analyses has been performed and from that, temperature, RH and wind speed values have been extracted at the point locations of IMD stations. The values obtained were plotted against the IMD values of corresponding station location. Figure 5 shows the variation in domain 3 between IMD data and the observed data from the model outputs at Dehradun point location. Figure 6 shows the correlation of the observed (model) outputs w.r.t. IMD values of domain 3. Statistical measures have been calculated at each point location of IMD weather station for each domain separately. For example, at New Delhi-Safdarjung station, it has been observed that for domain 3, the correlation for temperature is 0.95, for relative humidity it is 0.72 and for wind speed, it is 0.39; in domain 4, obtained correlation values were 0.95, 0.82 and 0.50 for temperature, relative humidity and wind speed respectively; similarly obtained correlation value of domain 5 were 0.92, 0.66 and 0.61 for temperature, relative humidity and wind speed respectively. These correlation values were obtained after removing the outliers from the results. The comparison depends on the subject to availability of the IMD data, as it was not available continuously for the desired time period and time interval. Hence, the statistical measures vary accordingly. Overall summary of statistical measures computed for all the IMD stations falling under each domain, has been compiled in table 3.

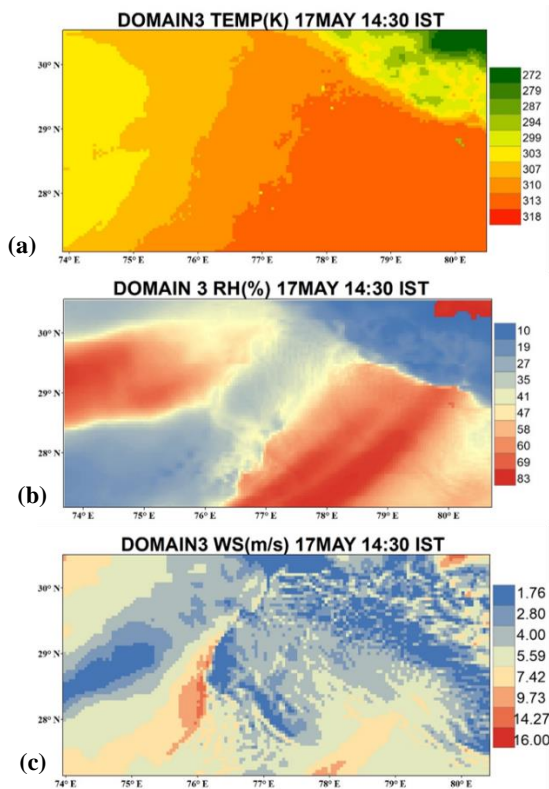


Figure 5 Spatial variation for domain D03 (a) temperature, (b) relative humidity, (c) wind speed, on May17 at 14:30 IST

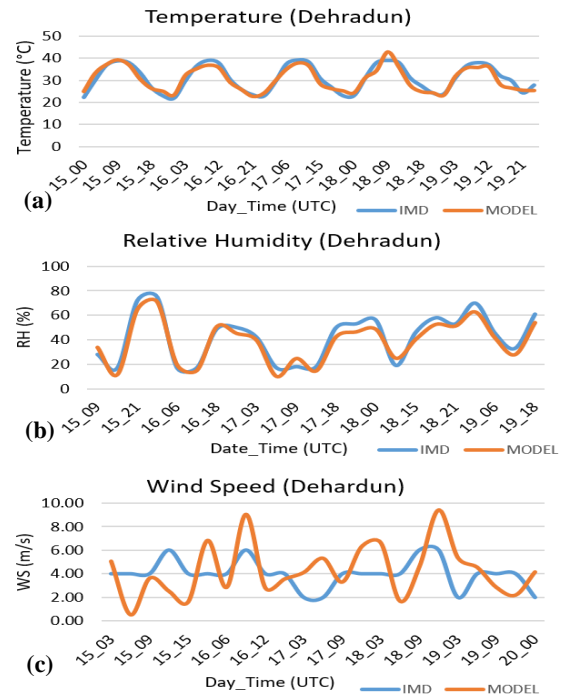


Figure 6 Variation of observed (model) value with the IMD values of (a) temperature, (b) relative humidity and (c) wind speed

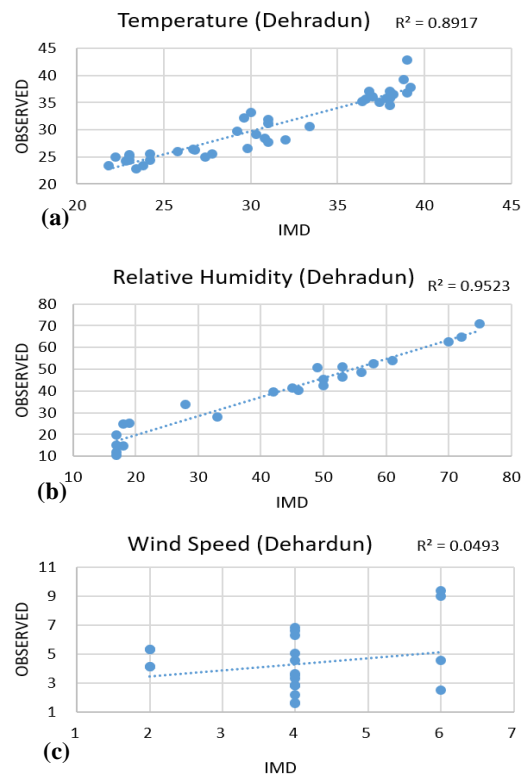


Figure 7 Graphical representation of the domain D03 for analysing correlation of observed (model) output w.r.t. IMD data, where (a) temperature, (b) relative humidity and (c) wind speed

Table 3 Compiled statistical measures' table consisting of Mean RMSE, Mean MAE and Mean Correlation of all IMD stations covered by domain D03

Variable	Mean RMSE	Mean MAE	Mean Correlation
Temperature	2.43	2.08	0.92
Relative Humidity	1.19	4.95	0.89
Wind Speed	3.29	2.78	0.31

5. DISCUSSION AND CONCLUSION

Heat waves are being affected by various factors mainly due to anthropogenic activities and regional wind patterns. However, in urban areas it exacerbated due to pre-existing UHI conditions. Heat waves are being studied now a days with keen interest as it is playing key role in climate change. Rapidly increasing urbanization is also playing a key role in amplifying the heat waves because of the positive feedback provided by UHI to heat waves. Mesoscale models are being explored at a very large scale to analyse this phenomenon at a fine sub-grid resolution level and also it helps in future prediction. To study heat waves and UHI, WRF-urban has been used widely at various platforms. To study heat wave and UHI together and to analyse their impact on each other, multiple domain configuration is needed as heat wave is a regional while UHI is a local phenomenon. However, multiple domains covering a wider and local region require extensive computational resources and time. Hence, in this study, 5 domains covering entire north Indian region till NCT Delhi at local scale have been created. To optimize the computational resources and time, less explored ndown methodology in WRF have been applied. The evaluation of results obtained from nested down (n-down) approach displayed high correlation in temperature values when compared with the IMD observations, whereas relative humidity also shows good correlation. However, correlation with the wind speed is low. These results when compared with the previous studies (Lalitha, 2018; Medisetti, Sankar, & Gupta, 2018), which were performed using multiple domains revealed comparable accuracies. Hence, one way nested down (offline) approach can be recommended as a substitute to the online multiple domain simulations which requires heavy computational resources and time.

6. REFERENCES

Borden, K. A., & Cutter, S. L. (2008). Saptial patterns of natural hazards mortality in the United States. *International Journal of Health Geographics*, 7(64). <https://doi.org/https://doi.org/10.1186/1476-072X-7-64>

Chiriaco, M., Bastin, S., Yiou, P., Haeffelin, M., Dupont, J. C., & Stéfanon, M. (2014). European heatwave in July 2006: Observations and modeling showing how local processes amplify conducive large-scale conditions. *Geophysical Research Letters*, 41(15), 5644–5652. <https://doi.org/10.1002/2014GL060205>

Giannaros, C., Nenes, A., Giannaros, T. M., Kourtidis, K., & Melas, D. (2018). A comprehensive approach for the simulation of the Urban Heat Island effect with the

WRF/SLUCM modeling system: The case of Athens (Greece). *Atmospheric Research*, 201(July 2017), 86–101. <https://doi.org/10.1016/j.atmosres.2017.10.015>

Government of India. (n.d.). National Disaster Management Authority, India. Retrieved February 26, 2020, from <https://ndma.gov.in/en/2013-05-03-08-06-02/disaster/natural-disaster/heat-wave.html>

Lalitha, A. (2018). *Multi-City Urban Weather Simulation Using Wrf Model*. Andhra University.

Medisetti, B., Sankar, G. J., & Gupta, K. (2018). *Improved urban parameters for urban micro climate modelling using WRF model*. Andhara University.

Meehl, G. A., & Tebaldi, C. (2004). More intense, more frequent, and longer lasting heat waves in the 21st century. *Science*, 305(5686), 994–997. <https://doi.org/10.1126/science.1098704>

Nissan, H., Burkart, K., de Perez, E. C., Van Aalst, M., & Mason, S. (2017). Defining and predicting heat waves in Bangladesh. *Journal of Applied Meteorology and Climatology*, 56(10), 2653–2670. <https://doi.org/10.1175/JAMC-D-17-0035.1>

Rohini, P., Rajeevan, M., & Srivastava, A. K. (2016). On the Variability and Increasing Trends of Heat Waves over India. *Scientific Reports*, 6(June). <https://doi.org/10.1038/srep26153>

Theoharatos, G., Panatavou, K., Mavrakis, A., Spanou, A., Katavoutas, G., Efstathiou, P., Mpekas, P., Asimakopoulos, D. (2010). Heat waves observed in 2007 in Athens, Greece: Synoptic conditions, bioclimatological assessment, air quality levels and health effects. *Environmental Research*, 110(2), 152–161. <https://doi.org/https://doi.org/10.1016/j.envres.2009.12.002>

World Meteorological Organization. (2017). WMO confirms 2016 as hottest year on record, about 1.1°C above pre-industrial era. Retrieved February 27, 2020, from press release website: public.wmo.int/en/media/press-release/wmo-confirms-2016-hottest-year-record-about-11c-above-pre-industrial-era

STUDY OF LST, NDVI AND IT'S CORRELATION WITH LULC FOR URBAN HEAT ISLAND ANALYSIS OF VADODARA, GUJARAT

Riddhi Joshi ¹, Mithil Modha ², Manik H. Kalubarme²

¹Department of Environmental Studies, Faculty of Science, The Maharaja Sayajirao University of Baroda, Gujarat-390002–jriddhij@gmail.com

² Department of Environmental Studies, Faculty of Science, The Maharaja Sayajirao University of Baroda, Gujarat-390002-modhamithil@gmail.com

²Bhaskarcharya Institute for Space Applications and Geo-Informatics (BISAG), Department of Science & Technology, Government of Gujarat, Gandhinagar, India- mhkalubarme@gmail.com

KEY WORDS: Urban Heat Island, Land Surface Temperature (LST), NDVI, LANDSAT, Land Use/Land Cover, Vadodara

ABSTRACT

Population and economic growth have escalated urbanization and thus fostered city expansion over the past few years at an alarming rate. Elevated temperatures within the city, increased urban-settlements, reduced urban green spaces, degrading air quality, thermal stress and discomfort are the environmental consequences noted due to the same. As per the EPA guidelines, the Urban Heat Island (UHI) refers to increased temperature of urban and suburban regions as compared to its rural surroundings. LST and NDVI are reliable indicators of UHI as they are closely associated with distinct LULC classes. NDVI determines the abundance and quality of vegetation whereas LST determines the temperature of LULC features with respect to its heat emissions, construction materials and geometry. The present study focuses on ward-wise analysis of Vadodara city for examining UHI intensities and to understand the trend by relating current scenario with past 20 years scenario. The results indicated negative correlation between LST and NDVI whereas it was further determined that its value is co-dependent with each distinct LULC class i.e. the values of LST and NDVI differ vividly with each specific LULC class. The present study finds its applications in identifying existing urban thermal hotspots of the city, proposing ideal land-use planning for future urban constructions and mitigating urban heat island effects and thus providing better urban environmental conditions.

1. INTRODUCTION

Urban heat islands often amplify the impacts of heatwaves in the city. The increase in heat morbidity and mortality is more profound in squatter urban settlements. In India, heatwave events and consequent deaths have been increasing since 1979 till date. Weather extremes cause significant impacts on human health. (IPCC, 2018)

As per the Environmental Protection Agency (EPA) guidelines, if the annual mean air temperature of a city with one million or more people increases by 1.8 to 5.4°F (1 to 3°C) i.e. warmer than its surroundings it can be termed as urban heat island.

Environmental Protection Agency (EPA) further classifies UHI into two categories namely, Surface Urban Heat Island (SUHI) and Atmospheric Urban Heat Island (AUHI).

Indirect measurement of UHI involves satellite data analysis using remote sensing and the study depiction in the form of thermal images. The intensity of UHI is variable to day and night time as well as to seasons. Land Use/Land Cover pattern significantly dominate the UHI intensity. Built-up areas, road pavements, open spaces dissipate more heat energy as compared to vegetative patches and waterbodies (Image: 1) this difference is mainly due to the evapotranspiration of vegetation and specific heat capacity of water.

Normalized Difference Vegetation Index (NDVI) gives a brief idea about the presence and health conditions of vegetation. This index helps in identifying the urban green spaces and natural vegetative surfaces. Whereas, Land Surface Temperature (LST) determines the temperature of various LULC features. These two indices help in identifying the potential heat emitting ground cover features and quantitatively determine its contribution in generating thermal discomfort.

However, micro-scale urban warming of a city duplicates macro-scale global warming phenomena, both in terms of consequences and need of immediate actions.

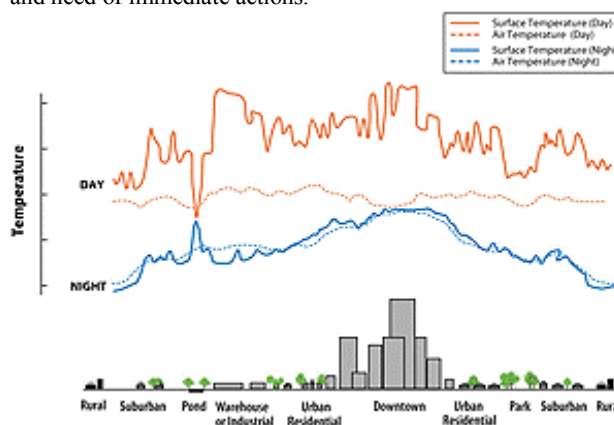


Image Source 1 <https://www.epa.gov/heat-islands/learn-about-heat-islands>

The ward wise analysis of a city helps in identifying accurate relationship between LST, NDVI and LULC as it enhances the assessment level.

Population and thus expansion of urban land are bound to occur in upcoming years. However, evaluating existing urban thermal zones and ideal thermal conductive zones can effectively aid in framing immediate mitigation steps for active vulnerable zones, management and maintenance of overall environmental conditions of the city.

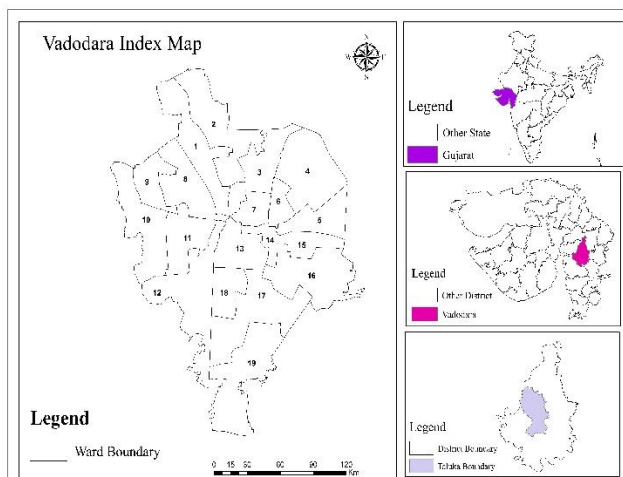
2. STUDY AREA

2.1 Vadodara

Vadodara is located on the banks of river Vishwamitri at an altitude of 39 meters. Vadodara city is also known as the cultural capital of Gujarat.

The climatic conditions of the city are semi-arid. The city has well-flourished and established industrial estates, transportation and communication networks, magnificent architectural monuments, well-developed residential/commercial areas and numerous waterbodies and gardens.

The city is home to a population of approximately 2 million people (Census, 2011). The city is divided into 19 wards and the governing body is Vadodara Municipal Corporation (VMC). The city has an average area of 235 square kilometres.



Index Map 1 Vadodara City Wards

3. METHODOLOGY

In this study, the UHI and LST of Vadodara city was analysed using LANDSAT data. The satellite digital data was downloaded from <https://earthexplorer.usgs.gov/> and was analysed using open source software QGIS.

LANDSAT 8 data for 2019-2020 with spatial resolution of 30 meters (visible, NIR, SWIR) and 100 meters (thermal) has been used.

LANDSAT-5 data for 1999-2000 with spatial resolution of 30meters (visible, NIR, SWIR) and 120 meters (thermal) has been used.

3.1 LULC Classification

Manual land use land cover analysis was carried out by layer stacking bands using semi-auto classification plug-in in QGIS 3.10

Bands 2, 3, 4 and 10 were used in case of LANDSAT-8 whereas bands 2, 3, 4 and 6 were used for LANDSAT-5.

Identified features were marked and grouped into pre-defined classes of vegetation, built-up, agricultural lands, waterbodies, open areas etc.

As the study areas is a metropolitan city, combination of two LULC features were also used pertaining to ease of classification and spatial resolution.

Area of each classified LULC class was calculated using field calculator.

3.2 Normalized Difference Vegetation Index (NDVI)

NDVI values range between +1 and -1. Healthy vegetation reflects more NIR and green light whereas unhealthy vegetation reflects more visible light.

$$NDVI = \frac{NIR - R}{NIR + R}$$

For LANDSAT-8 digital data,
NIR = Near Infrared = Band 5
R = Red Band = Band 4

For LANDSAT-5 digital data.
NIR = Near Infrared = Band 4
R = Red Band = Band 3

3.3 Land Surface Temperature (LST)

LST values quantitatively determine the temperature of LULC class. It incorporates mutli-step analysis using of thermal band and metadata files of the digital data (Avdan and Jovanovska 2016)

a) Top of Atmospheric Spectral Radiance

$$L_{\lambda} = M_L * Q_{cal} + A_L - O_i$$

Where, L_{λ} represents spectral radiance at sensor's aperture, M_L represents the band-specific multiplicative rescaling factor, Q_{cal} represents quantized and calibrated standard product pixel values, A_L is the band-specific additive rescaling factor, O_i is the correction for TIR band 10 (Landsat 8 OLI) and 6 (Landsat 5 TM)

Table 1: Top of Atmospheric Spectral Radiance

Sr. No.		Landsat-8 OLI	Landsat-5TM
01	M_L	0.000342	0.0055375
02	A_L	0.1	1.1
03	O_i	0.29	0.29

b) Brightness Temperature

$$BT = \frac{K_2}{\ln[(K_1/L_{\lambda}) + 1]} - 273.15$$

Where K_1 and K_2 are band specific thermal conversion constants available in metadata file

c) NDVI Method for Emissivity Correction

$$Emissivity = 0.004 * BT + 0.986$$

d) Land Surface Temperature

$$T_s = \frac{BT}{\{1 + [(\lambda BT/\rho) \ln \epsilon_{\lambda}]\}}$$

Here, BT = Brightness Temperature, λ = Wavelength of thermal band.

4. LULC, NDVI, LST MAPS

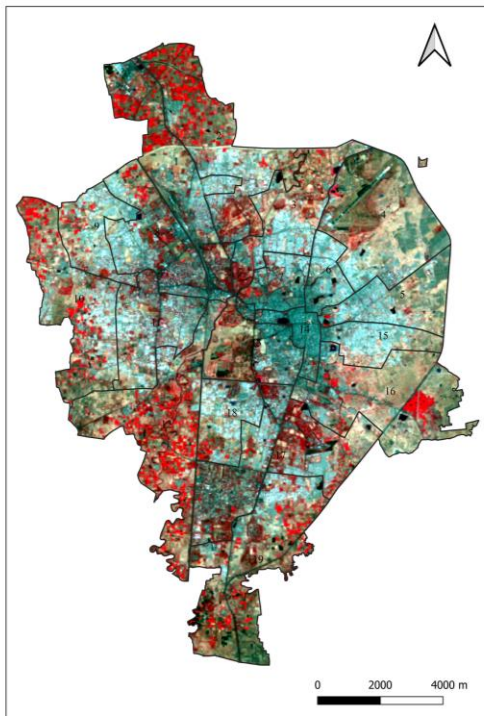


Figure 1 VADODARA FCC, APRIL 2019

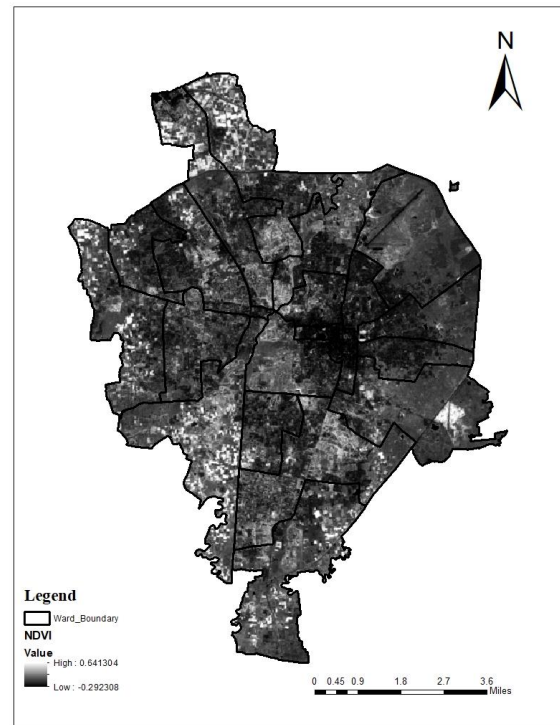


Figure 3 VADODARA NDVI, APRIL 2019

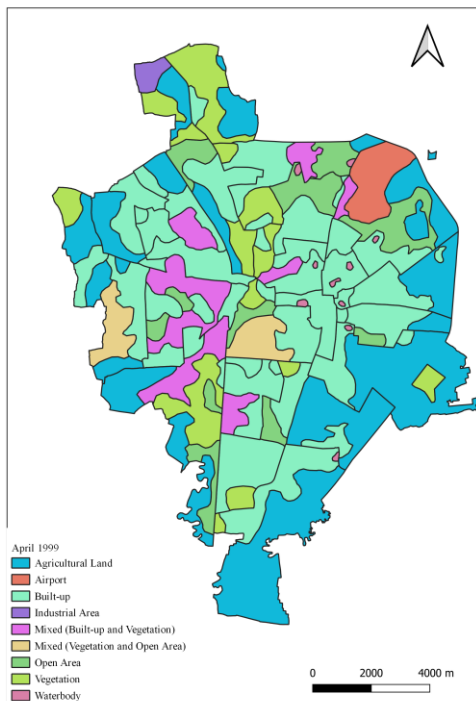


Figure 2 VADODARA LULC, APRIL 1999

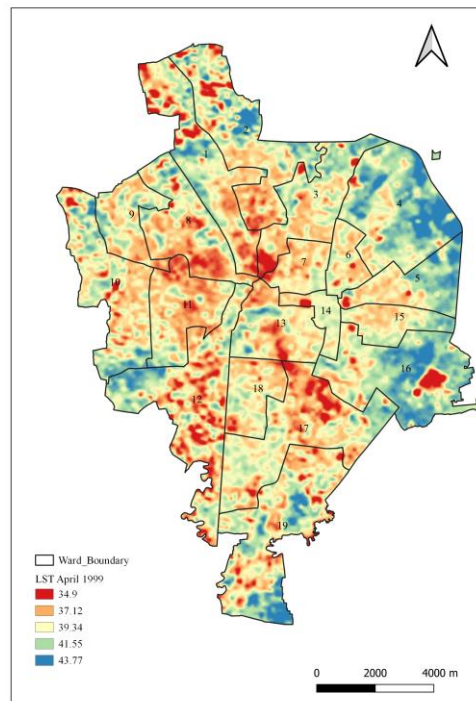


Figure 4 VADODARA LST, APRIL 2019

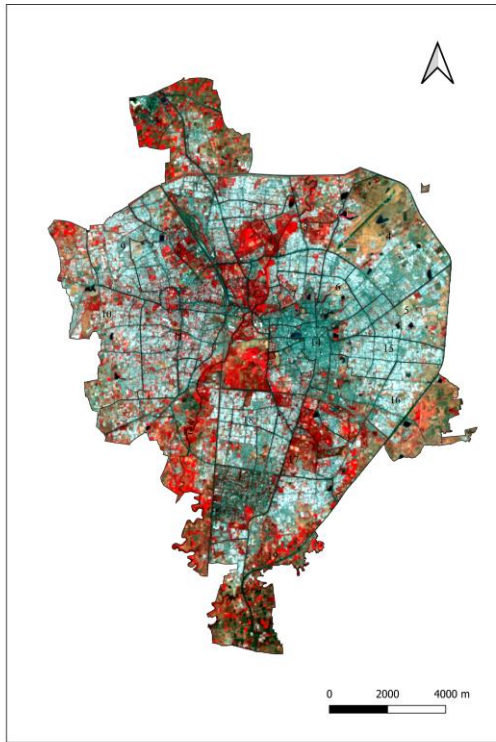


Figure 4 VADODARA FCC, APRIL 1999



Figure 6 VADODARA NDVI, APRIL 1999

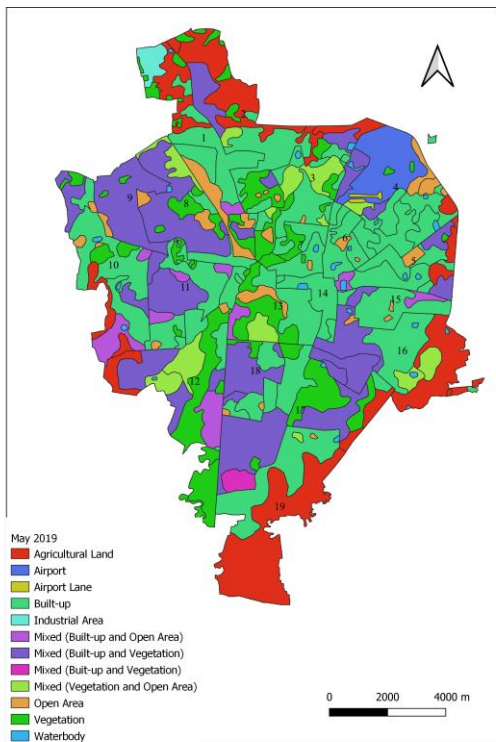


Figure 5 VADODARA LULC, APRIL 1999

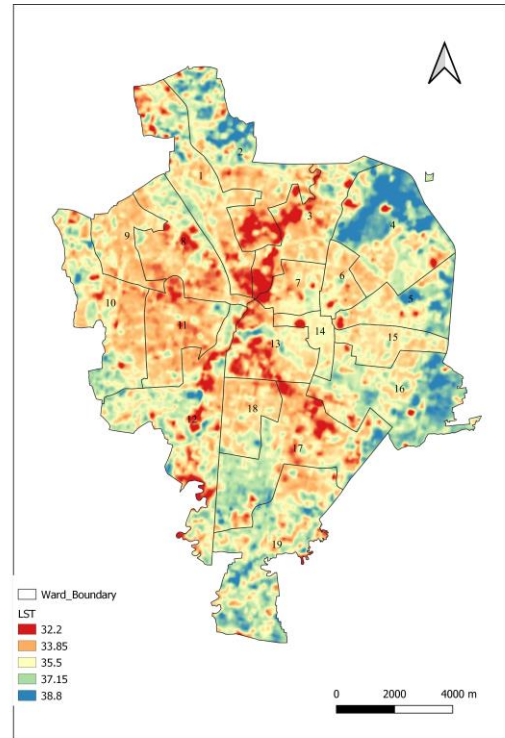


Figure 7 VADODARA LST, APRIL 1999

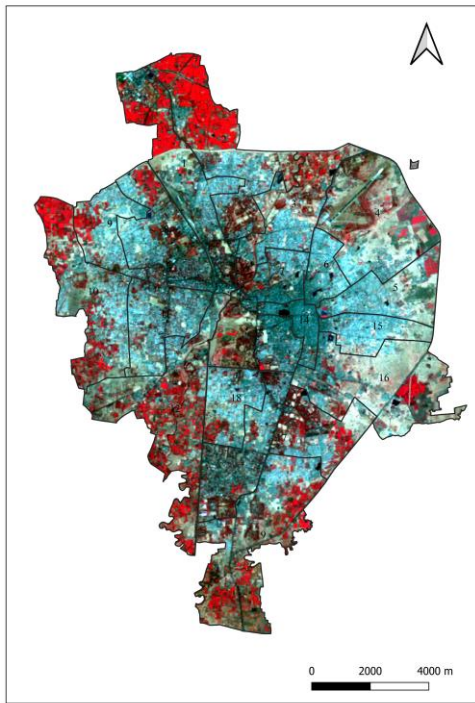


Figure 8 VADODARA FCC, JANUARY 2000

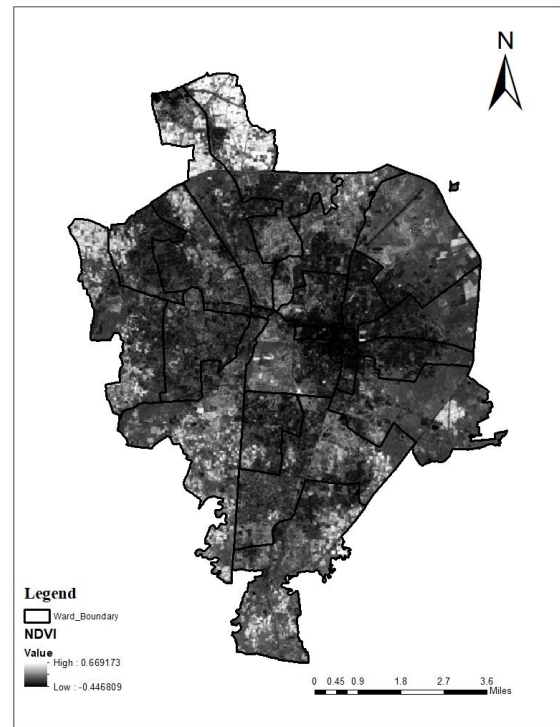


Figure 10 VADODARA NDVI, JANUARY 2000

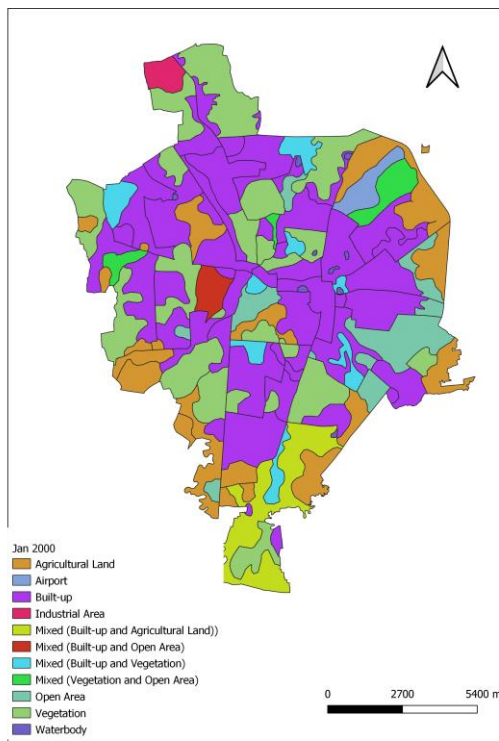


Figure 9 VADODARA LULC, JANUARY 2000

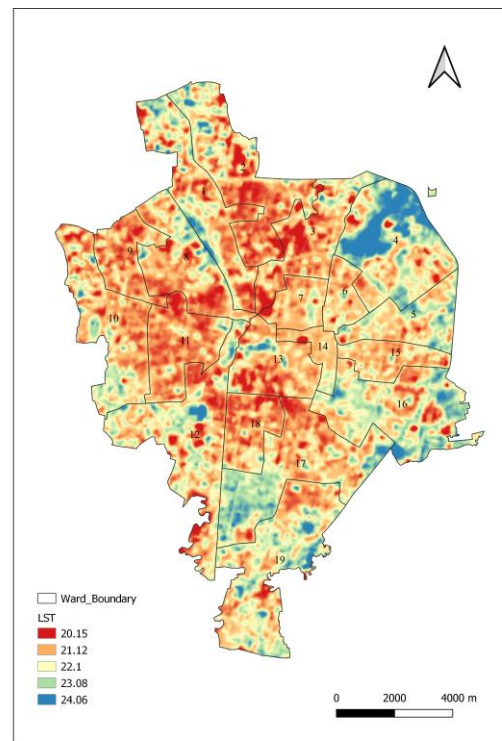


Figure 11 VADODARA LST, JANUARY 2000

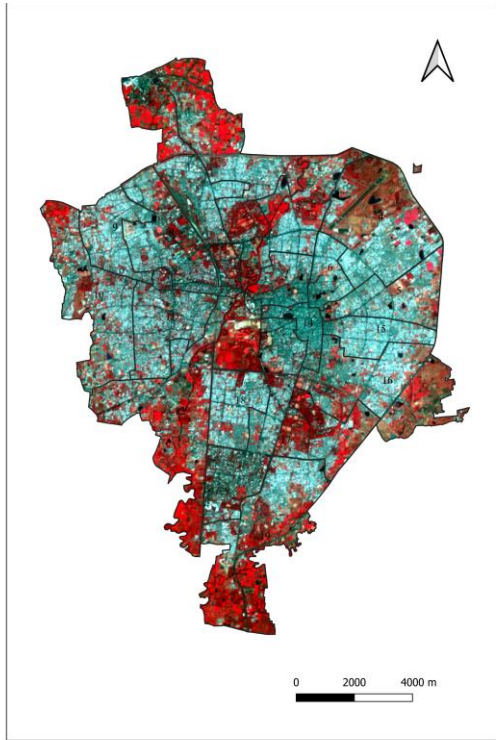


Figure 12 VADODARA FCC, JANUARY 2020



Figure 14 VADODARA NDVI, JANUARY 2020

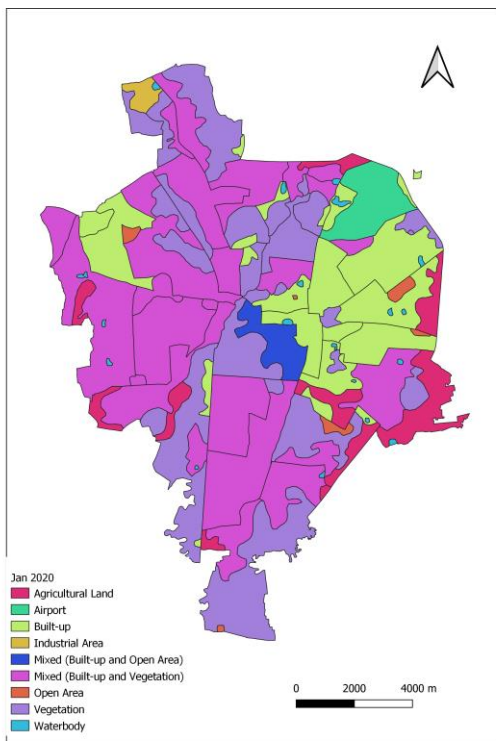


Figure 13 VADODARA LULC, JANUARY 2020

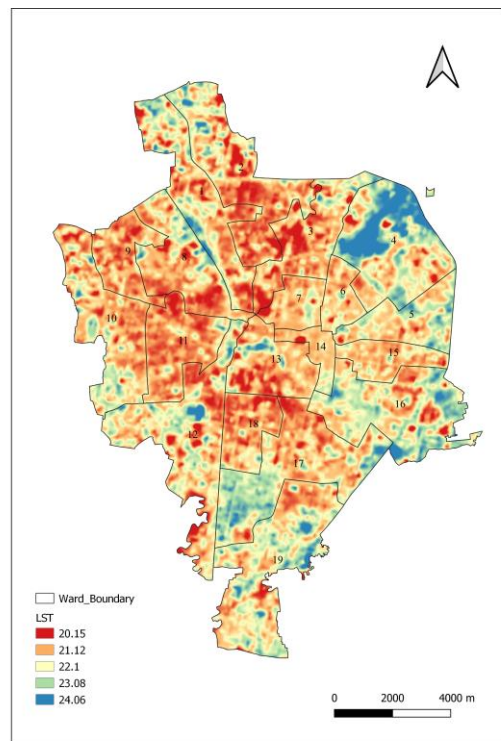


Figure 15 VADODARA LST, JANUARY 2020

5. RESULTS AND DISCUSSIONS

• Vadodara : Urban Heat Island

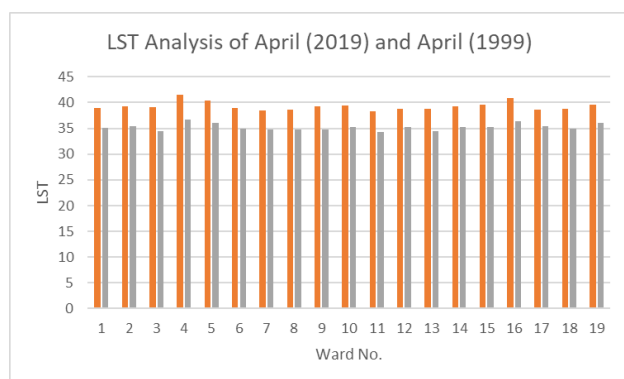
Vadodara fulfils the two conditions stated by EPA for UHI,

- 1) Population greater than 1 million
- 2) 1-3°C higher temperature than the rural surroundings

Table 2: Temperature in Vadodara city and Buffer areas:

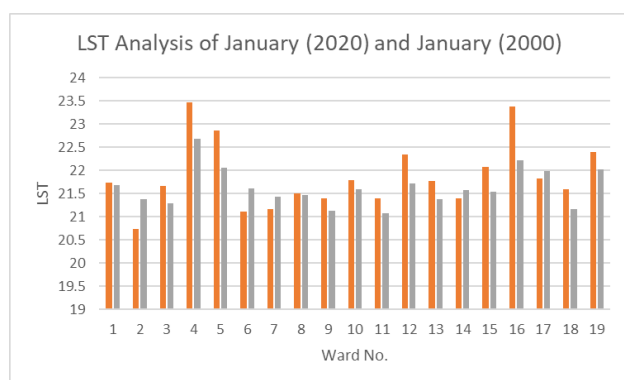
Vadodara City (Population approx. 2 million)	5 Km buffer from ward boundary	10 Km Buffer ward from boundary
36.21°C	35°C	35.14°C

• Ward- Wise Analysis for April (2019-1999)



As shown in the graph, highest value of LST is noted for ward no. 4 and comparatively lowest value is noted for ward no. 11. LULC features and their respective areas of ward no. 4 comprises of 31% Airport, 24% Built-up, 7% Agricultural Land, 17% Mixed (Built-up and Vegetation) and 21% Open Area. Whereas, for ward no. 11 LULC composition is as follows: 60% Mixed (Built-up and Vegetation), 20% Built-up, 19% Open Area.

• Ward-wise Analysis of January (2020-2000)



As shown in the graph, highest value of LST is noted for ward no.4, 5, 16, and 19 mainly due to the presence of airport and more open spaces. Whereas, the lowest value of approximately 21°C was noted for ward no. 1, 2, 3, 6, 7, 8, 9, 10, 11, 13, 15, 18 i.e. wards with waterbodies, mixed LULC classes comprising of built-ups, vegetation are marked.

The change in area in 20 years is noted to be an increase of 100,112 square meters. The results indicate, urban heat island phenomena is less intense during cold seasonal weather conditions i.e. during January and more effective during warm seasonal weather conditions i.e. during April.

The intensity of UHI during January 2000-2020 showed no major difference probably due to natural cool conditions. Whereas UHI intensity increased by 1-4°C during April 2019 as compared to April 2000. This increase might probably subjected to natural hot weather conditions and increasing urbanization.

NDVI and LST indicated negative correlation. Increase in LST values leads to linear decrease in NDVI values. Built-ups indicate higher LST values and lower NDVI values whereas vegetation indicated higher NDVI values and lower LST values. Waterbodies depict negative NDVI values.

It has also been noted that the pattern of urban settlements contribute majorly to the trend of elevated temperatures. The LULC classes with mixed features i.e. Built-up and Vegetation, Vegetation and Open Area, Waterbodies balanced the heat energy emitted from buildings, roads through the presence of urban green spaces to a certain extent and reduce the thermal discomfort in that particular ward.

Thus, urban expansion and development is bound to occur in near future but efficient planning and constructions can be implemented so as to reduce UHI intensity. Vadodara can be categorised as an emerging UHI as an increase of just 1% temperature is noted, hence it is viable enough to bring it down to negligible.

Existing features can be modified i.e. through increasing urban green spaces, vegetation, artificial waterbodies, cool pavements, cool roofs, reducing green-house emissions, improving and maintaining overall environmental conditions.

For future constructions, LULC features can be used as a base data to counteract the effects of new settlements via vegetation or waterbodies and thus reduce the overall thermal stress. Normally, expansion occurs at the loss of natural landscapes but with increasing demands there's no option of entirely curbing the development but smart planning and management can definitely minimize or eliminate the adverse effects.

ACKNOWLEDGEMENTS

The authors express their sincere gratitude to The Bhaskaracharya Institute for Space Applications and Geoinformatics and The Maharaja Sayajirao University of Baroda for their support and guidance during the conduct of study. We are very thankful to all the faculties at both the institutions for solving our queries and providing us with their valuable insights and highlighting the scope of improvement of the study.

REFERENCES

- 1) Akhtar, R. (2007). Climate change and health and heat wave mortality in India.
- 2) IPCC, 2018: Summary for Policymakers. In: Global warming of 1.5°C. An IPCC Special Report on the impacts of global warming of 1.5°C above pre-industrial levels and related global greenhouse gas emission pathways, in the context of strengthening the global response to the threat of climate change, sustainable development, and efforts to eradicate poverty [V. Masson-Delmotte, P. Zhai, H. O. Pörtner, D. Roberts, J. Skea, P. R. Shukla, A. Pirani, W. Moufouma-Okia, C. Péan, R. Pidcock, S. Connors, J. B. R. Matthews, Y. Chen, X. Zhou, M. I. Gomis, E. Lonnoy, T. Maycock, M. Tignor, T. Waterfield

- (eds.]. World Meteorological Organization, Geneva, Switzerland, 32 pp
- 3) EPA, R. U. H. I. compendium of strategies-Urban Heat Island basics.
 - 4) Avdan, U., & Jovanovska, G. (2016). Algorithm for automated mapping of land surface temperature using LANDSAT 8 satellite data. *Journal of Sensors*, 2016.
 - 5) Raj, S., Paul, S. K., Chakraborty, A., & Kuttippurath, J. (2020). Anthropogenic forcing exacerbating the urban heat islands in India. *Journal of Environmental Management*, 257, 110006.
 - 6) Lee, K., Kim, Y., Sung, H. C., Ryu, J., & Jeon, S. W. (2020). Trend Analysis of Urban Heat Island Intensity According to Urban Area Change in Asian Mega Cities. *Sustainability*, 12(1), 112.
 - 7) Joshi, R., Raval, H., Pathak, M., Prajapati, S., Patel, A., Singh, V., & Kalubarme, M. H. (2015). Urban heat island characterization and isotherm mapping using geo-informatics technology in Ahmedabad city, Gujarat state, India.
 - 8) Mehrotra, S., Bardhan, R., & Ramamritham, K. (2018). Urban informal housing and surface urban heat island intensity: exploring spatial association in the City of Mumbai. *Environment and Urbanization ASIA*, 9(2), 158-177.

USE OF GIS FOR STUDY OF URBAN FORM OF HISTORIC TOWNS IN KARNATAKA

M. Kashkari¹ and T. S. Brar^{1*}

¹SSAA, Ansal University, Gurugram, Haryana – monicakashkari@gmail.com, brartejwant@gmail.com

KEY WORDS: Urban Form, Historic Towns, Geographical Information System , Open Data Kit

ABSTRACT:

Urban form evolves constantly due its response to social, technological, economic and environmental policies and development. The study of urban form analyze complex result of historic constraints and how urban form was conceived, analyzed, built and modified over space and time. Karnataka is the 4th fastest urbanizing State in India, with about 34% of its population as urban. Located in the Southern region of India, Karnataka has a population of 61.09 million (Census 2011) making it India’s ninth most populous state. The Government of Karnataka has notified 6 settlements namely Kittur , Bidar, Bijapur, Mysore, Sri-Rangapatnam and Badami as historic settlements in Karnataka in 2005. 14 more in the next list of heritage cities including Gulbarga (Kalburgi). These historic towns trace their history to prehistoric times, having a number of archaeological sites in the near vicinities. The towns are dotted with heritage buildings and sites and predominantly present medieval character, though the towns might be having a number of layers of development. Geographical Information System along and Open Data Kit (ODK) which have come as great tools for efficiently collection of data and land use analysis, has been used to study of evolution of historic towns in Karnataka. ODK has been used for collection of primary data of these towns along with Geographic Coordinates and primary survey of the core of these towns. This data has been used to in QGIS along with imagery chronological of these towns from google Earth and historic and town and country planning records to study the growth of these towns and formulate policy for sustainable urban form of these towns.

1. INTRODUCTION

Urban form can be a 2-dimentional or a 3-dimentional representation. As urban areas metamorphize from being single to multi nuclei towns and to smart towns. Traditional urban fabric and its related infrastructure in these urban areas are unable to cope with these rapidly changing urban forms. As a result, the quality of life is being adversely affected. More so, if these urban areas have emerged from historic context and still have that legacy in form of historic buildings, features and way of life. This is evident in urban areas of the state of Karnataka where illustrious dynasties like Cholas, Rastrakutas, Vijayanagar kings have ruled over time to time. The state of Karnataka has a number of world heritage sites, prompting the state to notify certain settlements as the heritage towns. This research attempts to asks: What and whether there is a connect between urban form and sustainability? Whether traditional systems are affected by changes in urban form in these towns having historic context? What might be the impacts on sustainable urban development in these towns? This research focuses on the four towns notified by Government of Karnataka as heritage towns viz Badami, Bidar, Gulbarga, and Bijapura.

1.1 Objective of study:

Use of Geographical Information System along and Open Data Kit (ODK) for the collection of data and land use analysis, to study the evolution of urban form of historic towns in Karnataka.

1.2 Scope and limitation:

Scope of the study is limited to the four notified historic towns, viz Badami, Bidar, Gulbarga, and Bijapura, of Karnataka. The study is limited to the data collected from the open sources and primary surveys conducted using the ODK tools for Badami and Bijapur only.

1.3 Methodology:

The identification of secondary sources w.r.t. chronological evolution of the form of historic towns and subsequent collection of primary data of the historic core and water sources.

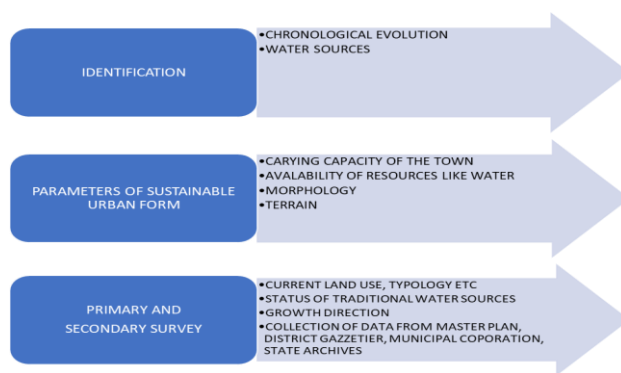


Figure 1. Methodology

* Corresponding author

2. LITERATURE REVIEW

Urban form refers to the visually perceptible features of the city, produced by structure in correlation with the surface, shape, space, structures and circulatory systems in defined natural setting. The characteristics determining the nature of form, as given by Kevin Lynch (1960, 1981), are:

- a) Typology of space: quality (appealing or not) and representative shape of space present like linear, radial etc.
- b) Quantity of space and flow: it is measure and size of adopted spaces i.e. what kind of overall effect is generated
- c) Grain: it is the differentiation and separation in spaces of the major activity and flow elements.
- d) Density: it is the intensity with which unit spaces of major activity and flow elements fill unit space.
- e) Focal organization: it is the spatial arrangement of the key points as they relate to one another and whole urban pattern. it is the relation of landmark with its surroundings.
- f) Space distribution: it is the gross pattern of space arrangement. it can be concentration at one point.

An Urban area and its development have been described as a work of the art, an instrument of communication, a historical artifact and correspondingly there have been many approaches to its planning and design. Urban areas can be seen as the junctions of flows of goods, people finance and information (Harris, 2003). The towns are competing with each other in attracting investments. As a result, urban economics are changing in their relations with the region from which they draw resources. The towns are thus experiencing lot of ecological concerns, congestions on communication networks, rise of essential items and social issues, which has rekindled the debate on understanding the relation between urban form and sustainability. The towns grow in an uncontrolled manner and the fringe areas are the worst effected, resulting into changed urban structure. Transportation networks and land use thus create such an interplay that are not conducive to an efficient and sustainable urban form nor provides desirable mobility solution to its inhabitants. (UN Habitat, 2013).

Traditionally, towns are found to have been situated next to rivers or water sources, which also determines the overall form of the settlement. Understanding the concept of Sustainability in case of urban settlements begins with an assessment of the site conditions to provide natural occurring resources, such as light, air, and water, and the extent to which the existing natural systems will be required to support the new development. This process is based on the concept of an interdependence, that would encompass the natural system interlinked with a series of interconnected geological, hydrological, topographical, ecological, climatological, and cultural attributes (NIUA,2011). The urban form cannot change the regional climate, but can moderate the microclimate and improve the conditions of the settlements and their inhabitants. The potential conflicts exist between compactness and passive solar design, because the higher densities associated with compactness would increase shading, thereby reducing solar access. There would also be trade-offs between compactness and ecological design, with

higher densities impinging on green space and other ecological aspects. The dependency of urban climate on urban form in tropical climatic region is immense. According to the studies, urban geometry is one of the factors to understand and mitigate negative impacts of urban climate based on understanding of thermal comfort in tropical and sub-tropical regions. Urban climate is analyzed on aspects like Spatial-temporal, the implication to urban planning and design etc. Also, certain age-old tradition knowledge system is available to be seen in the tropical climate like typical building designs, low density areas, courtyard houses, traditional water harvesting features, elaborate division of uses (both indoors and outdoors) etc.

Urban forms are changing with addition of activities, as urban areas metamorphize from being single to multi nuclei cities and to smart cities. This is particularly evident in towns and cities of developing economies. Traditional urban systems in these settlements are unable to cope with these rapidly changing urban forms . As a result, the quality of life in terms of adequate and accessible water supply, clean environment, connectivity and sustainability at large is being adversely affected. In the recent years, a close association and inter-relation has been found between urban areas and climate change. With the focus now on sustainable development goals (SDGs), urban planners and designer’s world over have been thriving to bring energy efficiency as a core parameter for planning the urban environs. Hence, concepts pertaining to quality of life and liveability index are also being used to explain sustainability or impacts of sustainable development. This research proposes to compare the traditional urban form of old historic settlements of Karnataka by applying basic principles of sustainability like density, Walkability, building energy etc and evaluated the carrying capacity of the settlement, availability of resources, morphology and terrain condition (Williams & Jenks,2000). With reference to the current literature available on the subject, the various features for analysis of sustainable urban form is density, land uses, built form, street patterns, open spaces, landmarks, building facades, mass space relationship, skyline, center-fringe relationships. Since most of this information can be collected along the roadside, accordingly, the parameters listed in Table 1 were taken up for the data collection in the historic towns of Karnataka.

S.No.	Parameter
1	Direction
2	Land use
3	Floor
4	Material used
5	Street furniture
6	Node
7	Landmark
8	Age of the building
9	Streetscape
10	Skyline
11	Drain flow
12	Drain size

Table 1. Parameter for analysis

3. HISTORIC TOWNS IN KARNATAKA

Karnataka is the 4th fastest urbanizing State in India, with about 34% of its population as urban. Located in the Southern region of India, Karnataka has a population of 61.09 million (Census 2011) making it India's ninth most populous state; the state has an area of 191,791 sq. km and accounts for 5.8 per cent of the country's total land area. The state is divided into 29 districts. Bengaluru is the capital city.

Karnataka historically was home to a number of powerful dynasties. The ruins of Vijayanagar at Hampi, temples at Pattadakal, Belur, Halebedu, Caves at Badami, Buddhist monasteries at Sannati and many more of such heritage sites and centres give the examples of state's legacy. The Government of Karnataka has notified 6 settlements namely Kittur, Bidar, Bijapur, Mysore, Sri- Rangapatnam and Badami as historic settlements in Karnataka in 2005. 14 more in the next list of heritage cities including Gulbarga (Kalburgi).



Figure 2.

Location of various historic towns in Karnataka.

Source: Current Study

3.1 Badami

The town of Badami was the capital city during the Chalukyan era in 6th century. Today, it is a well-known tourist destination in Karnataka. Natural landscapes having rocky terrain, intricate carvings in cave temples, vibrant older core of the settlement lends the place a unique character. Administered by Town Municipal Corporation, its Jurisdiction covers an area of 4.23 sq.km with a Population of the town is about 30943 as per 2011 census. Topography of Badami taluk the district is rugged and undulating. No river system passes near /through the town. Badami town is situated in the midst of the ravine between two rocky hills. An annual average rainfall is approx. 600mm with heavy rainfall experienced between the months of August to September. The town slopes gently towards the southern and

eastern side converting in the valley running along the periphery of the town. It ends in the river Mallaprabha on the eastern side at a distance of 8 Km. Agasthya teertha ,the natural water body is one of the earliest examples of how rainwater can be harvested to a scale that could feed an entire town.The tank is created by barricading the flow of monsoon waters in a location such that every drop of rain falling over the hills flows down to the tank, wherein the water was flowing into another valley, embankments have been created in such a manner so as to Figure 1 redirect the flow into the tank. The efficiency of the system is evident when you see the water level in this large tank going up nearly by a foot in just an hour's good rain. The tank holds sufficient water, and it normally doesn't run dry even in the summer months. It is perhaps the creation of Agasthya teertha that enabled dynasties of the past to survive even in this arid landscape.

3.2 Bijapur

On the other hand, Bijapur city is the district headquarters of Bijapur District of Karnataka state. It is also the headquarters for Bijapur Taluka. It is well known for its historical monuments built during the rule of the Adil Shahi dynasty. Bijapur is located 530 km from Bangalore, about 550 km from Mumbai, and 384 km from Hyderabad. Bijapur's urban population as per 2011 census is 3.26 lakhs. It is the 9th biggest city in Karnataka. The city was established in the 10th -11th Centuries by the Kalyani Chalukyas and was known as Vijayapura (City of victory). After which, the city passed to Yadava dynasty. In 1347, the area was conquered by the Bahmani Sultanate of Gulbarga. In 1518 when the Bahmani Sultanate split into five splinter states known as the Deccan sultanates. Bijapur became one of the five sultanates and was ruled by the kings of the Adil Shahi dynasty (1490–1686). Bijapur is well known for its historic water structures called bavdis, which brought water for the use of the inhabitants of this historic metropolis. Today, Bijapur has generated a lot of interest among foreign and domestic tourists as well as academicians alike to see and learn the architectural marvels created predominately during the Adil Shahis, however the overall settlement needs an urgent up gradation to its infrastructure and amenities as well upkeep of its heritage.

4. COLLECTION OF DATA

The methodology used for study of urban form of Historic towns of Karnataka is primarily utilizing the advances in the Geographic Information System. The chronological evolution of the town is captured through the temporal maps from the google earth and further collaborated with the archival data available with various agencies like, Urban Development Authority, Municipal Corporation, Gazetteer Department, archives etc.



Figure 3. Badami town, 2006 Source Google Earth



Figure 4. Badami town, 2009 Source Google Earth



Figure 5. Badami town, 2011 Source Google Earth



Figure 6. Badami town, 2014 Source Google Earth



Figure 7. Badami town, 2018 Source Google Earth

Figure 3 to Figure 7 gives the time series images of the Badami town from the Google Earth, which after further collaborating with archival and secondary data is further used for analysis of growth of the town, land use changes etc. Since the towns had to be extensively covered for primary data collection, based on the identified parameters for the study which were derived out from the literature review, the first and the foremost necessity was to create a format for the data collection. Since it was proposed to use GIS for the current research, the data form was created with appropriate shapefiles. The shapefile was made with the field names, type etc. The widget type had to be correctly mentioned i.e. whether, value, text or attachment After this the form so created was uploaded using the QRealttime Plugin. The form so created had to be synchronized from the database and the server. ODK collect app on the mobile phone was used for field survey. On the mobile app, blank form created using the QReal GIS plugin was downloaded from the server by clicking on the Get Blank form. All the available forms on the server were listed, the desired form as created earlier was selected.

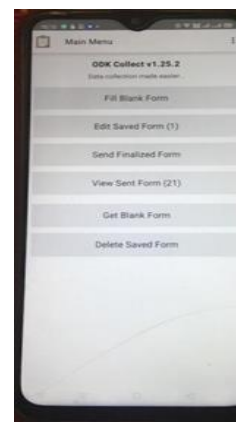


Figure 8. Screenshot of the ODK app Source: Current Study

The fill blank form as shown in the Figure 8 was selected and with this the data filling process was started as shown in the Figure 9 The first field to be filled was the geo-location. Further as per the format designed, other fields were filled on site. The photograph of the location could also be clicked and saved on the form. Once the filling process is completed, the form was saved and exited. The finalized form was uploaded to the server by clicking on the send finalized form on the app. The data so captured was synced and imported to the QGIS for further analysis.

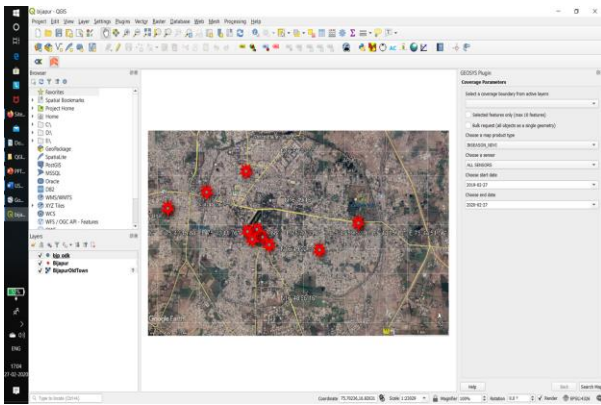


Figure 16. Screenshot of the QGIS for Bijapur Town
Source: Primary survey using ODK Collect app

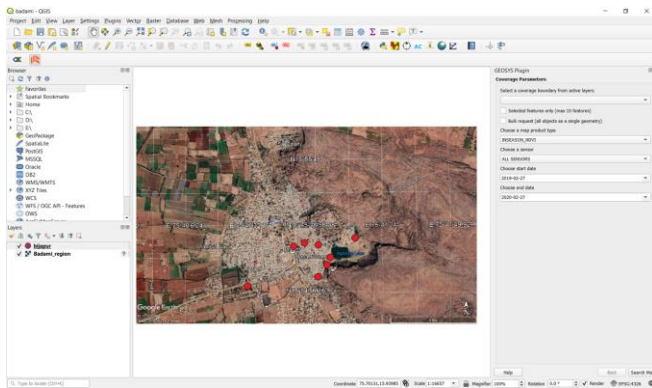


Figure 17. Screenshot of the QGIS for Badami Town
Source: Primary survey using ODK Collect app

While using ODK Collect app for the field survey, the possibility of taking pictures of the Data source and its surroundings is also possible. During the field survey for Badami and Bijapur, the pictures taken by the mobile app is shown in Figure 10 and 11. Further, Figure 12 and 13 gives the survey data downloaded on the QGIS for the historic town of Bijapur, the survey data could also be downloaded on Excel as shown in Figure 14 and 15 which could further enhance the analysis prospective of the data. The spatial information, location of the survey points with the related attribute data was available in QGIS as shown in figure 16 and 17 for further interpretation.

5. CONCLUSION

Urban form is a mean to measure and understand the formation as well as development of towns along with its physical environment over phases of its evolution. There are various ways by which the urban form can be described is based on the intricacies of the towns in question. Recent discussions in the field of urban planning has led to rethinking on the local climatic conditions and its adaptation in the town's planning and development, which in turn is strongly influencing the shape of the town as well as determine the its skyline and density concentrations. This research seeks to contribute to the development of a methodology to examine urban form in the

current context of sustainable development. The study could be used as a policy tool to set up guidelines and support a more integrated sustainable approach to urban regulation and decision-making.

Experience of use of ODK in the primary survey for collection of data can be summarised in the ease of work flow. The data collection and compilation became seamless and fast as no additional steps were required for the compilation process. Further, learning from the survey was to have a small data form and ensure that the image captured in ODK is of low resolution so as to have smaller size for faster synchronisation with the server. Thus, one should as far as possibly design the data collection form in such a manner that form is faster to fill on site and images per form not exceed 2 under normal circumstances. To sum up, the use of ODK, QGIS and QRealTime Plugin in primary data collection on account of its superior integration and cost effectiveness is one of the better ways to collect primary data.

ACKNOWLEDGEMENTS

We are thankful to Shri Shiva Reddy Koti, Shri Prabakar Alok Verma and Indian Institute of Remote Sensing, Dehradun for providing training and assistance, as and when needed to use QRealTime Plugin in QGIS and ODK Collect app.

REFERENCES

- Lynch, K. (1960). *Image of the City*. Cambridge: MIT Press.
- Lynch', K. (1981). *A Theory of Good City Form*. Cambridge: MIT Press.
- Williams, K., Jenks, M. Eds (2000), *Sustainable Urban Form*. Routledge: New York, NY, USA; pp. 19 – 29.
- National Institute of Urban Affairs, (2011), *Sustainable Urban Form for Indian Cities*, City Form India, Ministry of Urban Development.
- Rakodi, C. (2003). *Politics and performance: The implications of emerging governance arrangements for urban management approaches and information system*. *Habitat International*, 27 (4), pp. 549-573.
- UN-Habitat (2013). *Planning and design for Sustainable Urban Mobility*. UN-Habitat.
- QGIS Development Team, 2019. QGIS 3.6., Open Source Geospatial Foundation. grass.osgeo.org (20 September 2019).
- Koti, S.R. and Verma, P.A., 2019. Plugin QRealTime. QGIS Software, Version 3.8, Open Source Geospatial Foundation. <https://plugins.qgis.org/plugins/QRealTime/>
- ODK Development Team, 2019, ODK Collect v 1.27.1. <https://github.com/getodk/collect/releases/tag/v1.27.1>

TRENDS OF MACRO AND MICRO-URBANIZATION: A CASE STUDY OF BHUBANESWAR-CUTTACK TWIN CITY

Srutisudha Mohanty¹, Jagabandhu Panda^{1,*}, and Sudhansu S. Rath¹

¹ Department of Earth and Atmospheric Sciences, National Institute of Technology Rourkela, Odisha 769008, India
Email address: srutisudha80@gmail.com, jagabandhu@gmail.com, sudhansu.rath@gmail.com

KEY WORDS: Sustainable Development, Urban Morphology, Spatial Metrics, Entropy, Urban Expansion

ABSTRACT:

The eleventh sustainable development goal envisions creating an environmentally safe, economically strong and ecologically rich strengthened network of urban-peri urban-rural pockets with high resiliency. It demands special attention to the critical planning of sustainable cities at the regional level. In developing countries like India, the urban-related policies and schemes are biased for the megacities like Delhi, Mumbai and Kolkata, in which the growth rate has been dropped drastically in the last few years. On the contrary, small and medium-sized cities are growing exponentially with a burgeoning population and limited resources. Such kind of urban expansion affects the landscape at the macro as well as micro-level. The current study aims to evaluate the level of macro-urbanization in terms of the overall growth of the urban area in the temporal dimension and quantifying the urban morphological characteristics for assessing the micro-urbanization. Bhubaneswar-Cuttack urban complex is considered for the case study, which spread across 745 Km² area in between 20° 12' to 20° 23' N latitudes and 85° 44' to 85° 54' E longitudes on the eastern coastal plains of India. The BHUVAN land use and land cover data sets of the year 2005, 2010 and 2015 are used for the analysis and reclassified to 5 major classes i.e., built-up, waterbody, vegetation, agriculture and barren land. For a thorough understanding of spatial urban development, a multi-ring buffer technique is adopted and concentric rings of 5 km interval have been taken up for the study. The result shows that the Bhubaneswar-Cuttack urban complex experienced an increase of ~5% in built-up area cover since 2005. Arable land is found to be gradually converted to residential, industrial and commercial establishments. Shannon's entropy is found maximum in core city within 5 km buffer area and subsequently, the value declines up to 15 km followed by a parabolic rise within 30 km concentric circle. Dynamics at macro-level influences the pattern of micro-urbanization substantially and the rate of randomness is critically interrelated with the patch density. Micro-level dynamics are evaluated using spatial metrics and it depicts the size, edginess and fractality of the built-up patches in the urban complex. Although the city core is experiencing compact development due to infill growth, and re-urbanization, the peri-urban area suffers largely due to highly dispersed patch development. Therefore, a comprehensive analysis of rapidly growing cities like Bhubaneswar-Cuttack can provide valuable information regarding the growth pattern and urban dynamics, which will help the planners and policymakers for sustainable designing of the city.

1. INTRODUCTION

Urbanization not only deals with the conversion of rural land use (LU) to urban counterpart but also leads to a complex spatial expansion associated with varying socio-economic, socio-cultural as well as technological transformation. In developing countries, the rate of urbanization is increased dramatically in the last few decades, and the lack of proper planning and management practices may result in an unsustainable city environment. However, the statistics show that approximately 50 percent of the global urban dwellers reside in small and medium-size cities with less than 5 lakh inhabitants, which means only one in every eight-person lives in the 33 megacities with more than 10 million population (World urbanization prospects, 2018). United Nations projected that India alone might add up to 416 million urban dwellers to the world urban population considering its exponential rate of growth and having the largest pool of rural population in the world.

The pattern of growth and the characteristics of relatively smaller cities are well monitored and documented by researchers, intellectuals and relevant government bodies (Dutta and Das 2019; Chai et al. 2019) and reported that in India, most of the urban-related policies and projects are biased for the megacities like Delhi, and Mumbai, where the rate of development has been dropped drastically in recent years. According to the Census

report of India (2011), there are 3894 small and medium-sized cities, growing exponentially to accommodate the migrated population with their limited resources and emerged as a significant challenge for the urban planners. The process of urbanization in terms of fundamental change in the structural aspects of a city landscape and functionality within the same is more or less different than that of the megacities (Chai et al. 2019; Dutta and Das 2019). They lack the institutional support, necessary infrastructures, and amenities, and that hinders the growth and economy of the city. Hence, they are more prone to sprawlification, which may affect the quality of life. Such conditions push away the sustainability goal of the city and give rise to alleged negative impacts viz. traffic congestion, environmental pollution, energy consumption, and irreversible destruction of harmony between ecology and economy. Despite the urges, there are fewer studies that have been conducted over relatively smaller cities.

The urban expansion is a very complex phenomenon and occurs at a higher degree of spatio-temporal heterogeneity. The major drivers of urban land transformation at the macro-level are geographical location, topographical features, transportation networks, distance from the nearby city, and these conditions may vary case to case basis. Macro-urbanization is mostly represented as the spatial form of the urban area and how it

* Corresponding author

changes with time. It is usually delivered in terms of the compactness or scatteredness of the city. The compact city core depicts a densely developed urban patch with high connectivity, while sprawled growth patterns can be observed in the case of a fragmented city core. This study evaluates the macro-urbanization using Shannon's entropy approach and landscape-level spatial metrics. However, the spatial characteristics of urban patches indicating the patch density, edginess, fractal dimension, nuclearity represent the micro-dynamics of the urbanization, which can be quantified by the class and patch level spatial metrics. Combining both macro and micro-level urban expansion for a city can deliver a holistic knowledge about the process involved in the expansion of the urban area. Thus, the current study focuses on the intensive analysis of macro-pattern and micro-dynamics of the near-coastal twin city Bhubaneswar-Cuttack of Odisha, India during 2005-2015. The two primary objectives are (i) to monitor the spatial expansion of the urbanized area considering the whole city and assess the characteristics of growth pattern in the temporal dimension, and (ii) to evaluate the localized changes in the city landscape in terms of the composition and configuration of urban patches.

2. STUDY AREA

Bhubaneswar-Cuttack urban complex is the largest urban agglomeration of Odisha, India, located between 20°12' to 20°23' N and 85°44' to 85°54' E over an area of ~745 km² (Figure 1).

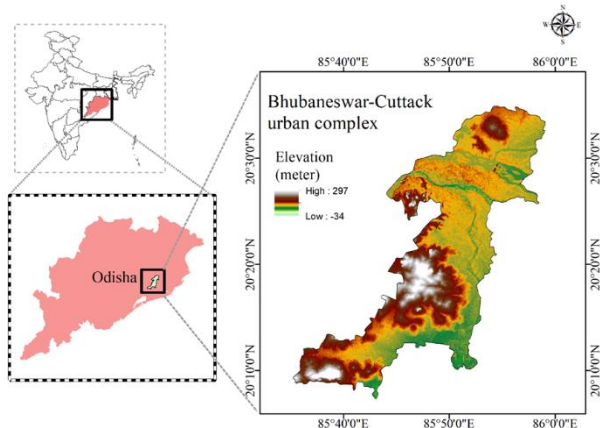


Figure 1: Geographic location of the study area

German architect Dr. Otto H. Königsberger initially planned the city Bhubaneswar. The city has emerged as the capital of Odisha and gradually converted into a modern city with tremendous scope for development. However, Cuttack has served its own time as the capital of the historical state of Odisha close to a thousand years, which makes the city culturally rich and traditionally developed over time. Most of the administrative offices, educational institutions and industries have been developed in and around the twin city, attracting a huge amount of population inflow. The idea of Bhubaneswar-Cuttack urban complex came into existence by the policymakers given the proximity between these two urban centers, the orientation of growth and economic co-dependency. The topography of the urban complex is mostly characterized by fluvial type, while a zone of hilly terrain is found in the western and south-western side of the city.

3. DATA AND METHODOLOGY

The data used for the current study include pre-processed remote sensing images from the BHUVAN portal (http://bhuvan.nrsc.gov.in/bhuvan_links.php) of National

Remote sensing Centre (NRSC), ISRO for the years 2005 to 2015. The overall classification accuracy of these data is found to be 90.07 %. The acquired images are pre-processed, masked according to the boundary of the city area, and reclassified into five major LU categories, i.e., built-up, water, vegetation, agriculture, and barren land as shown in the figure 2.

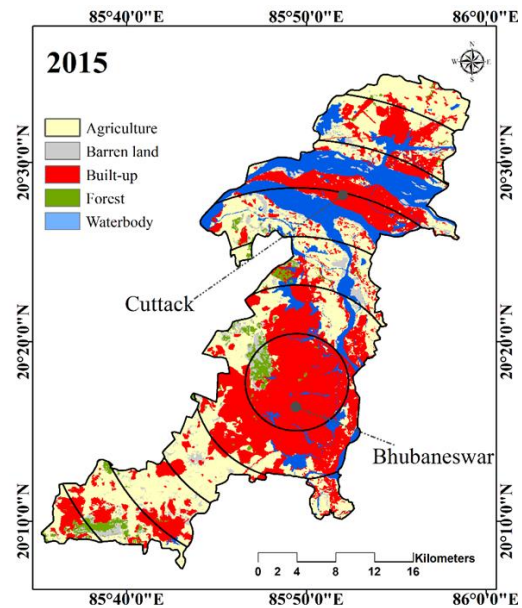


Figure 2: Land use land cover map of the twin city Bhubaneswar and Cuttack for the year 2015 showing buffer rings.

These thematic layers are used as base map for further analysis. To understand the spatial spread of the city, the built-up area cover is calculated for the study period using ArcMap. Further, Shannon's entropy is computed using a multi-ring buffer (MRB) approach considering 5 km interval for the whole duration as it can statistically summarise the macro-growth pattern of the city and provides the information regarding the degree of scatteredness in the city landscape (Jat et al. 2008). For a better understanding of the localized patch characteristics and the micro-dynamics of the city, five spatial metrics are selected. Those are patch density (PD), percentage of landscape (PLAND), edge density (ED), area-weighted mean fractal dimension (AWMFD), and aggregation index (AI).

4. RESULT AND DISCUSSION

4.1 Land use change during the study period

Areas around the urban agglomeration have witnessed a rapid and substantial amount of change in its land-use configuration (Figure 3). Such land-use changes are initiated mainly due to urbanization during the last decade. It has greatly affected fertile agricultural lands in the Mahanadi delta area.

The total built-up area cover of the urban complex is increased from 275.5 km² in 2005 to 289.9 km² in 2015, resulted in 5.2 percent rise in overall urban area. A higher rate of urban growth is found during 2005-2010, the latter five years shows a relatively slower growth rate. The northern part of the city, mainly covered by agricultural land, is gradually shifted to residential, industrial and commercial establishments. A prominent green cover earlier seen in the north and the north-western side of the core urban area has started to shrink with the expansion of the New Bhubaneswar area. The rigorous observation over the LU classified maps

makes it clear that from 2005 to 2015 (Figure 3), barren land and built-up area have changed significantly. The built-up area has increased at the cost of the decrease in vegetation, agricultural land, and river bed while barren land has converted to farm land and urban patches. The increased rate of built-up land implies that urban expansion to accommodate the burgeoning population and to meet the demand of the housing, job opportunities, medical facilities, educational institutions, theme parks and other amenities.

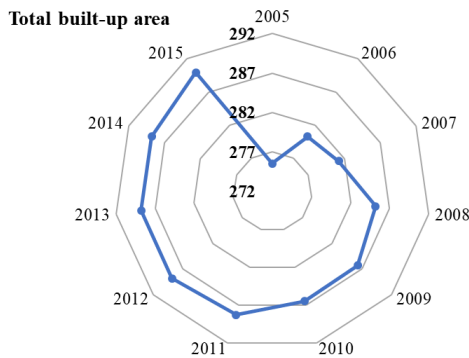


Figure 3: Spatial expansion of the total built-up area in Bhubaneswar-Cuttack urban complex during the 2005-15.

4.2 Identifying the spatial growth types

Three distinct spatial growth patterns are observed during 2005-2015 (Figure 4) over the urban complex. Those are infilling, edge expansion, and outlying development. Infilling growth occurred mainly within the free spaces of the main urban core, whereas edge-expansion takes place mostly adjacent to the compact landscape. It occurs due to the expansion of the existing industries, residential, or institutional areas over the years. The scattered outlying growth occurs far from the urban core along the major roads (national highway, state highway) and outside the core city. However, in the current case, only a small portion of the city has accounted for infilling and edge expansion type of growth. The increasing trend of dominant outlying growth generally results in the formation of sprawl, whereas infilling refers to the agglomerated growth type.

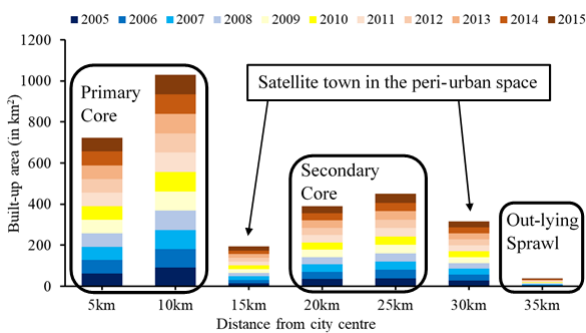


Figure 4: Expansion of urban land cover in the concentric buffer rings from the city centre towards periphery during the 2005-15

Although the built-up patch is dominant in the central zone of 5 km buffer of the urban complex, but in terms of net area coverage the subsequent zone of 10 km shows a higher value. It indicates the primary core area of the urban complex and its ever-rising growth pattern. Furthermore, another core is found in the 20-25 km buffer area, primarily located at Cuttack city and few

sprawled patches around the compact core of Bhubaneswar. Fringe and establishment of satellite township can be seen within the 15 and 30 km zone, whereas the outermost concentric ring reveals the occurrence of sprawl far from the core city.

4.3 Analyzing macro-pattern using Shannon's entropy

The pattern of urban growth depicts the sprawl characteristics in the study area. Using the LU layers, the study area is divided into seven buffer rings of 5 km for the computation of entropy value which is shown in Table 1.

Table 1. Shannon's entropy values for the Bhubaneswar-Cuttack urban complex for the selected years.

Year	Shannon's Entropy	Ln(n)
2005	1.69533	2.3979
2006	1.47512	
2007	1.69771	
2008	1.69535	
2009	1.69667	
2010	1.69664	
2011	1.69897	
2012	1.69890	
2013	1.69894	
2014	1.69892	
2015	1.70096	

The result shows that the overall trend of the study area for different time periods project a strong urban sprawl capability. It revealed that the degree of urban sprawl in the region gradually increases in recent years. The upper limit of entropy, Ln (n) is 2.3979, which indicates the highest possible randomness. The highest value of entropy is found in the year 2015 (i.e., 1.7), and the lowest (1.47) in 2006, characterized by an intermitting pattern of the dispersed urban area. The zone-wise distribution of entropy is portrayed by clustering and dispersion of urban LU patches over the selected city. Nevertheless, the entropy increases sharply in the same year (2006) for the buffer area of 10 km and shows minimum value throughout the other areas. This peculiar pattern depicts the rapidity of new patch establishments in the whole city at a macro-level. Among all the concentric rings, the 20 km buffer shows a declining trend whereas the 15 and 25 km concentric rings illustrate an increasing trend of entropy in the considered decade. For the central core of 5 km buffer, the result shows a very slowly varying but more stagnant pattern of entropy depicting the compact landscape dominated by infilled growth.

4.4 Spatial metrics-based analysis focusing micro-urbanization

For analyzing the urban dynamics, five spatial metrics have been chosen from the FRAGSTATS 4.2 package. They are Patch Density (PD), Percentage of Landscape (PLAND), Edge Density (ED), Area-weighted mean fractal dimension (AWMFD) and Aggregation Index (AI) and broadly divided into three categories such as area and edge metrics, shape metrics and aggregation metrics. The spatio-temporal pattern of the micro-dynamical characteristic is shown in figure 5. Bhubaneswar-Cuttack urban complex experiences a higher number of scattered urban patches in the year 2005, and it seems to decrease onwards 2010 by ~6%, creating an aggregated mass of built-up area in the city core. The metrics provide an important observation about the city that the urban patch is increasing as a compact entity in the first five years

and, in the later years, the fragmentation of the patches around the peri-urban area. The patches experience less connectivity due to dominant sprawled development

4.4.1 PD: The compositional metrics PD measures the density of urban patches in each buffer ring by comparing it with the total landscape area. Figure 5 (a) indicates that towards 2015, the maximum compactness is found in the central buffer of 5 and 10 km, but the value minimizes in the 15 km buffer ring. On the contrary, a higher fragmentation is found in 2005 from the city core to a 15 km circular patch. It specifies the gradual compaction of the core in due course with the rising built-up density resulting in infill growth patterns. For the buffer areas from 20 to 35 km, the declining trend of density is identified due to sprawled growth in the peri-urban area.

4.4.2 PLAND: This metric can provide information about the proportional abundance of like patches in the city landscape. The range of this metric is very large in the case of the Bhubaneswar-Cuttack urban complex. Despite the high standard deviation of PLAND from the core to the outer periphery of the city, a dominant trend is found for all the buffer rings, i.e., the area cover of urban land has been increased gradually and peaked in 2015. The city core is approximately 85 % covered by the urban patches, while the value drops up to 11 % in the peri-urban landscape. Besides the outer-most buffer ring, the minimum PLAND value for built-up patches is found in the 15 km buffer ring due to the extensive area coverage by the Mahanadi River.

4.4.3 ED: This metric computes the edge length of the urban patches per unit area, and the unit is meters per hectare. ED found to vary drastically in different years mainly around the city's primary and secondary core spreading across 5-10 and 20-25 km buffer rings and portrays a continuously declining pattern. Supporting the findings of PLAND metric, this configuration metric shows a trend of least values for the year 2015 in almost all over the landscape. This phenomenon indicates the lessening of the perimeter of the individual patches by clustering due to edge expansion and infill growth pattern. The higher value of ED obtained for a fragmented landscape with dispersed patches.

4.4.4 AWMFD: The degree of complexity of the natural, planar shapes is expressed in fractal dimension considering the relationship between the area and the perimeter of the concerned shape. A complexly shaped patch is more or less the result of unplanned development, and it may serve as the seed nuclei for sprawled growth. In the selected urban complex, the minimum AWMFD values are mostly obtained in 2015 for the concentric ring of 5, 10, 20, 25, and 30 km. The least fractality is found in 2006 for the 15 km circle and 2010 for 35 km circular area. The occurrence of infill development in those particular buffer rings accounts for lower complexity whereas the out-lying pattern may severely intensify the fractal dimension of the landscape. The rising values of fractal dimension in the outer buffer indicates that the complex process of urbanization has already started far from the core city and several new patches are coming up in the recent years. Those patches are mostly rural areas, gradually converting to small satellite townships due to the proximity to the major transportation networks connecting the urban complex.

AI: The degree of aggregation in terms of both dispersion and interspersions can be quantified using AI. This metric considers the total number of like adjacencies of a focal class placed next to each other in a landscape. Therefore, AI of the built-up patches in the given buffer ring can depict the maximally clumped landscape that is most likely found in 2015 over the whole city except the 35km buffer ring, and the least aggregation was seen

in 2005. AI can identify the spatial growth patterns; for instance, the index value increases with infill and edge development and declines with scattered sprawling.

5. CONCLUSION

The sustainable development goals focussing on the environmentally safe, economically strong and ecologically rich city can only be achieved if the correct planning and management manifest is prepared beforehand focusing on the sprawling. For that, intensive analysis of the growth pattern and changing morphological characteristics over the years need to be carried out carefully at both the city and patch level. Abundant literature is available for the megacities of India, but relatively fewer studies are found for small and medium-sized cities, which demand the focus to be shifted towards them. To fill that gap, this paper presents a comprehensive understanding of the macro-pattern and micro-dynamics of one of the rapidly growing agglomerations of India, i.e., Bhubaneswar-Cuttack urban complex.

An integrated approach of remote sensing and geographic information system (GIS) is shown to measure the urban growth patterns at the city (macro) level and patch (micro) level. The study revealed that the three major growth patterns i.e., infill, outlying, and edge-expansion are highly correlated with the micro-dynamics of the urban patches and can be measured using the class/patch level spatial metrics. In due course, the central primary core in Bhubaneswar city and the surrounding 5 km buffer area, is completely transformed into compact built-up LU. A similar pattern is observed in the 20 and 25 km zones due to the presence of secondary core in Cuttack city. Both the areas mentioned above indicate dominant infill growth as a result of re-urbanization. The outer area falling into 25-35 km concentric circles are giving a clear indication of out-lying fringes following the highways and isolated patch development. Several industrial townships and their residential colonies have been developed in those areas over the last decade. The 10 and 20 km zones area predominantly showing the edge expansion around the existing core, and those are mostly part of the planned urban complex. Characterizing different urban growth using the MRB method certainly highlights the pattern of urban expansion from the city center to the peripheral areas. It can also capture the composition and configuration aspects of the landscape at the patch level of the city. However, similar studies with high-resolution datasets such as IKONOS, Cartosat series, Worldview can increase the accuracy of the analysis to a great extent, and even smaller changes can be captured, which is not possible with medium or coarse resolution satellite products.

ACKNOWLEDGEMENTS

The Department of Science and Technology (DST), Government of India is sincerely acknowledged for partially funding this research through the project with file no. EMR/2015/001358. The NRSC of ISRO (http://bhuvan.nrsc.gov.in/bhuvan_links.php) is duly acknowledged for providing the LULC thematic datasets.

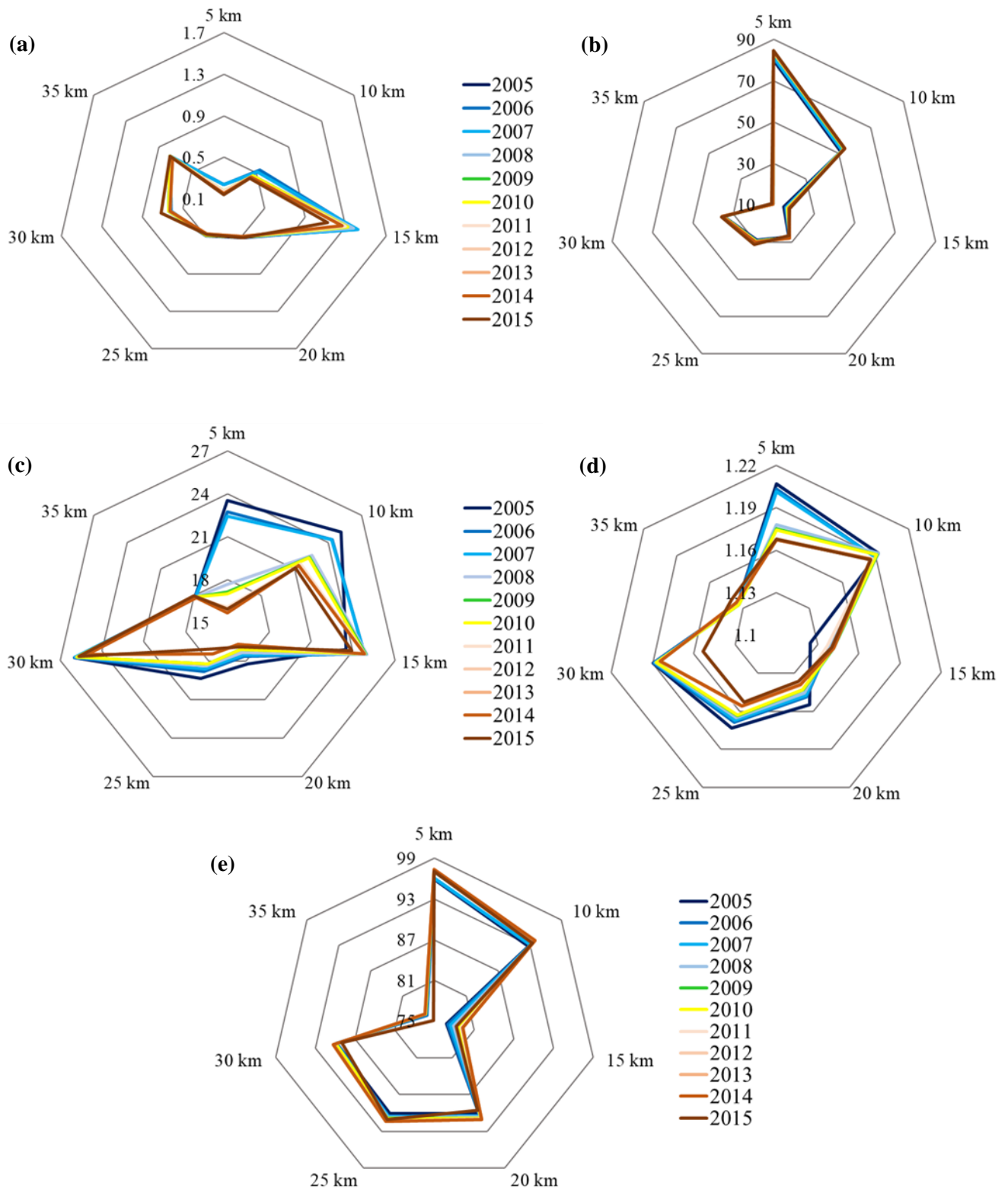


Figure 5. Class metrics for the Bhubaneswar-Cuttack urban complex (a) Patch density (PD), (b) Percentage of landscape (PLAND), (c) Edge density (ED), (d) Area weighted mean fractal dimension (AWMFD), (e) Aggregation Index (AI).

REFERENCES

- Aithal, B. H., & Ramachandra, T. V. (2016). Visualization of urban growth pattern in Chennai using geoinformatics and spatial metrics. *Journal of the Indian Society of Remote Sensing*, 44(4), 617-633.
- Chai, B., & Seto, K. C. (2019). Conceptualizing and characterizing micro-urbanization: A new perspective applied to Africa. *Landscape and Urban Planning*, 190, 103595.
- Dadashpoor, H., Azizi, P., & Moghadasi, M. (2019). Land use change, urbanization, and change in landscape pattern in a metropolitan area. *Science of The Total Environment*, 655, 707-719.
- Dutta, I., & Das, A. (2019). Application of geo-spatial indices for detection of growth dynamics and forms of expansion in English Bazar Urban Agglomeration, West Bengal. *Journal of Urban Management*, 8(2), 288-302.
- Hao, R., Su, W., & Yu, D. (2012, October). Quantifying the type of urban sprawl and dynamic changes in Shenzhen. In *International Conference on Computer and Computing Technologies in Agriculture* (pp. 407-415). Springer, Berlin, Heidelberg.
- Huang, X., Xia, J., Xiao, R., & He, T. (2019). Urban expansion patterns of 291 Chinese cities, 1990–2015. *International journal of digital earth*, 12(1), 62-77.
- Jiao, L. M., Tang, X., & Liu, X. P. (2017). SPATIAL LINKAGE AND URBAN EXPANSION: AN URBAN AGGLOMERATION VIEW. *International Archives of the Photogrammetry, Remote Sensing & Spatial Information Sciences*, 42.
- Jokar Arsanjani, J. (2019). Characterizing and monitoring global landscapes using GlobeLand30 datasets: the first decade of the twenty-first century. *International Journal of Digital Earth*, 12(6), 642-660.
- Li, S. (2018). Change detection: how has urban expansion in Buenos Aires metropolitan region affected croplands. *International Journal of Digital Earth*, 11(2), 195-211.
- Nong, D., Lepczyk, C., Miura, T., Fox, J., Spencer, J., & Chen, Q. (2014). Quantify spatiotemporal patterns of urban growth in Hanoi using time series spatial metrics and urbanization gradient approach.
- Pandey, B., Zhang, Q., & Seto, K. C. (2018). Time series analysis of satellite data to characterize multiple land use transitions: a case study of urban growth and agricultural land loss in India. *Journal of land use science*, 13(3), 221-237.
- Sapena, M., & Ruiz, L. A. (2015). Analysis of urban development by means of multi-temporal fragmentation metrics from LULC data. *The International Archives of Photogrammetry, Remote Sensing and Spatial Information Sciences*, 40(7), 1411.
- Shukla, A., & Jain, K. (2019). Critical analysis of spatial-temporal morphological characteristic of urban landscape. *Arabian Journal of Geosciences*, 12(4), 112.
- UNDESA. (2018). World urbanization prospects: 2018. *Nairobi (Kenya): United Nations Department for Economic and Social Affairs*.
- Weerakoon, K. G. P. K. (2017). Analysis of Spatio-Temporal Urban Growth Using GIS Integrated Urban Gradient Analysis; Colombo District, Sri Lanka.
- World urbanization prospects. (2014). *United Nations: San Francisco, CA, USA*.
- Xu, G., Jiao, L., Liu, J., Shi, Z., Zeng, C., & Liu, Y. (2019). Understanding urban expansion combining macro patterns and micro dynamics in three Southeast Asian megacities. *Science of The Total Environment*, 660, 375-383.
- Yang, C., Li, Q., Zhao, T., Liu, H., Gao, W., Shi, T., ... & Wu, G. (2019). Detecting Spatiotemporal Features and Rationalities of Urban Expansions within the Guangdong–Hong Kong–Macau Greater Bay Area of China from 1987 to 2017 Using Time-Series Landsat Images and Socioeconomic Data. *Remote Sensing*, 11(19), 2215.
- Zeng, Y., Xu, Y., Li, S., He, L., Yu, F., Zhen, Z., & Cai, C. (2012). Quantitative analysis of urban expansion in central china. *International Archives of the Photogrammetry, Remote Sensing and Spatial Information Sciences*, 39(B7), 363-366.

ASSESSMENT OF WATER RESOURCE IN GURUGRAM – A CASE STUDY OF AREAS DEVELOPED BY PRIVATE DEVELOPERS

R. A. Dehade¹, T. S. Brar^{2*}, S. Singh³

¹ Institute of Town Planners India, New Delhi – dehaderupali@gmail.com

² Sushant School of Art & Architecture, Ansal University, Sector – 55, Gurugram – brartejwnt@yahoo.com

³ Government of Karnataka, Vijayapura City Corporation – shail_singh@rediffmail.com

KEY WORDS: Urban Water Resource Management, Private Developers, Urban Water Cycle, ODK Collect, QGIS

ABSTRACT:

Water is a natural resource, fundamental to life, agriculture and sustainable development. The Haryana Sub-region is a water scarce, dependent to a large extent on surface water and sources located outside. The distribution of piped water to Gurugram began in year 1990, when city began drawing water from the Yamuna canal in Sonapat. Prior to this, the area was entirely dependent on the ground water as there was no other major source of surface water, such as river to draw from. The launch of city's first water treatment plant in Basai, helped augment the supply for the then developing sectors between Sector 1 – 57. Since then, these sectors were supposed to rely on the canal water. Despite that, the illegal ground water extraction continues in the privately developed areas. Geographical information System along and Open Data Kit (ODK), which have come as great tools for efficiently collection of data and land use analysis, has been used to study of evolution of water resource in Gurugram. ODK Collect has been used for collection of primary data of drainage network of Gurugram along with Geographic Coordinates and primary survey of the core of the sites surveyed. The data collected has been analysed in QGIS with imagery from Google Earth, Topographic Sheets of Survey of India and maps from Town and Country Planning Department, Haryana. These tools have also helped identify the morphological changes to this geography and giving insights into the impacts on water management. This study records the chronological development of water supply in Gurugram, and formulates policy for sustainable urban water resource management.

1. INTRODUCTION

1.1 Introduction

Water is a natural resource, fundamental to life, agriculture and sustainable development. The Haryana Sub-region is a water scarce, dependent to a large extent on surface water and sources located outside. A Functional Plan on Groundwater Recharge for National Capital Region (NCR) was prepared in 2009 by NCR Planning Board to assess groundwater resources in NCR and to guide the participating states on various aspects of ground water management in NCR.

According to Agricultural department of Ground Water cell, in five years, from 2014-2018, the ground water table in Gurugram district is reduced by two and a half meters. The district has overdrawn water reserves by a whopping 226%! Experts and Officials all have pointed to singular cause for these heavy losses: Vicious cycle of real estate and population growth.

1.2 Gurugram

Gurugram as a city can be classified in three major area:

1. The Old Gurgaon
2. The Erstwhile H.U.D.A. (Haryana Urban Development Authority – now HSVP) developed areas and now taken over by GMDA
3. The areas developed by Private developers like DLF, Ansals, Unitech etc. (Colonizers areas)

Most part of Colonised Area lies towards South- Eastern side of the NH-8. While Gurugram started off as Millennial City, built by Private builders like DLF and Ansal API and followed by

Unitech Pvt. Ltd, today, it stands as a parched city in dire need of the basic necessity like water.

Ownership Statistics	Area(HA)	Percentage
HUDA/GMDA	5601	53.03
Colonizers Area	1105	10.47
Industrial Area	1349	13
Defence Land	633	5.9
Corporation Area	1896	17.9

Table 1. Ownership pattern in Gurugram

1.3 Need Of Study

The distribution of piped water to Gurugram began in year 1990, when city began drawing water from the Yamuna canal in Sonapat. Prior to this, the area was entirely dependent on the ground water as there was no other major source of surface water, such as river to draw from. The launch of city's first water treatment plant in Basai, helped augment the supply for the then developing sectors between Sector 1 – 57. Since then, these sectors were supposed to rely on the canal water. Despite that, the illegal ground water extraction continued and currently there is a grave water supply shortage particularly in the privately developed areas.

The need to study arises as to understand the causes of the current situation which is so critical. This study can provide pointers to planning effective and efficient water infrastructure when newer areas are developed..

* Corresponding author

1.4 Objective

The study aims to understand the complexity of water management in the residential areas developed by private developers

1. To analyse the present water governance structure in Gurugram
2. To understand how the water supply was provided to the areas developed by a private developer in Gurugram.
3. To assess the water demand and supply and current situation of water management in these areas
4. To recommend planning strategies for better water management in the case study area

1.5 Methodology

Methodology for the research includes Literature Review to identify the parameters of the urban water cycle and how they are interrelated. Then collect the data of these parameters for study using ODK and Analysing this data using QGIS.



Figure 1. Methodology

2. PRELIMINARY UNDERSTANDING & DEVELOPMENT OF PARAMETERS

2.1 Literature Review and Theoretical Framework

Literature search has been done to clarify the concepts, definitions, development of cities with respect to water resources, measures adopted to integrate water resource planning with urban planning and norms and standards for infrastructure. This entire literature search has been carried out through books, journals and previous studies. The basic aim of this stage is to form a theoretical framework to identify parameters to examine Urban Planning and Development strategies with respect to water resources.

Over the last two decades there has been process of rapid urbanisation, this is especially true in class-I and II towns, which have increased both in number and size i.e. population.

The growth of cities had lead to increase in pressure on land and natural resources (water vegetation, drainage pattern) in cities. This had lead to acute shortage of amenities i.e. water supply sanitation, and drainage problems in newly developed areas of these cities as no consideration as given to site analysis (slope, drainage water resources, soil, climatic, etc. analysis). Hence to avoid these problems due to lack of integration of planning of natural resource availability, there is need to integrate site analysis as an integral part of comprehensive planning exercise along with the projections/ requirements of resources for the future

2.2 Urban Hydrological Cycle & its Components

Urban Hydrology is defined as the interdisciplinary science of water and its interrelationship with urban man (Jones, 1971), resulting in creation of large impervious areas, producing noticeable drainage problems, and urban hydrology was born out of the necessity to control these problems. The hydrologic cycle has been used to represent the continuous transport of water in the environment (Asano, 1998).

The urban hydrologic cycle comprises water supply, wastewater disposal, and stormwater runoff systems, making up the total urban water system. However, the history and fragmentation of the water industry has meant that current research is dominated by detailed modelling of only sub-components of the total water system (Newall et al., 1998).

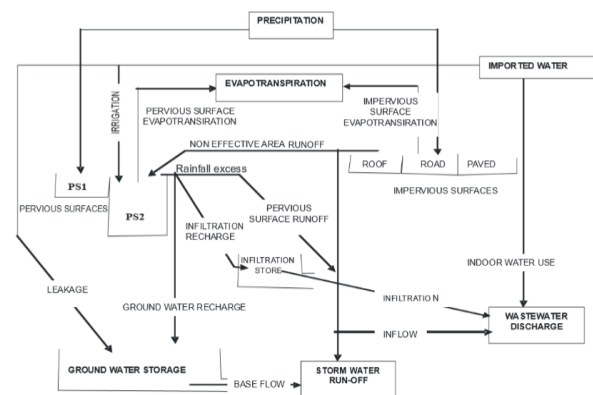


Figure 2. Structure of the Urban Water Cycle represented by Aquacycle

Particularly, the interaction between the potable water supply–wastewater discharge network, and the rainfall–stormwater runoff network, is rarely considered. In order to provide a complete picture of the spatial and temporal pattern of water demand and stormwater and wastewater supply, the water balance approach must be adopted along with the nature of urban development. The conceptual model developed to represent the urban water balance, known as Aqua cycle, is given in Eq. (2.1) & Figure. 2, also known as water balance model; arrows show the way in which water flows between the various surfaces and storages. The urban water cycle receives input both from precipitation and imported water, which together pass through the system and output in the form of evapotranspiration, stormwater, or wastewater. The state of the water stores is used to calculate the change in storage within the system.

$$P + I = E + R_s + R_w + US \quad \text{Eq. (2.1)}$$

P = Precipitation I = Imported Water E = Evapotranspiration
 S = Stormwater Runoff R_w = Wastewater Discharge
 US = Change In Storage

In thinking about sustainable development, one must view environmental capacity from a dynamic perspective and consider the time required for the restoration of the hydrological cycle. "Cycle capacity" refers to the time that nature needs to revive the hydrological cycle. The use of groundwater should be considered from the point of view of cycle capacity. Rain seeps underground and over time becomes shallow stratum groundwater. Then, over a very long period of time, it becomes deep stratum groundwater. For sustainable use of groundwater, it is necessary to consider the storage capacity for groundwater over time. If this is neglected and groundwater is extracted too quickly, it will disappear within a short time.

2.3 Present Status of Natural Drainage in Gurugram

There was a network of natural drains in Gurugram connecting the Aravalis to small lakes or Johards to drain the runoff generated from rain fall. The *Bundhs* of Gurgaon have been built on these drains to harness rainwater, maintain the water table, and regulate water management systems for the city. This can be seen in the Figure 3 which shows the Chakkarpur drain and Chakkarpur Wazirabad bandh. Unfortunately, over the years and with growing urbanisation, all these *bundhs* got encroached upon. Developers did not include them in the master plan for the city's expansion, and instead conducted heavy construction in the catchment. As a result, the bundhs eventually fell into disrepair and have been used as a place for defecation, for dumping debris, and became unsafe for use by citizens for movement across Gurgaon.

Running along the track is a storm water drain or *nullah* (Figure 4), which has also been cleaned and de-clogged into a smooth flowing water channel. Over 20 years of garbage dumped on the site has been cleared, including the removal of over 200 trucks of silt and plastic waste from the *nullah*. This extracted waste has been segregated and properly disposed of. Sewage flowing into the *nullah* has been stopped and diverted into sewage treatment plants. Further dumping of waste into the *nullah* has also been prevented. Over 6000 cu.m. of construction and demolition waste has been re-used in the construction of the Bundh.

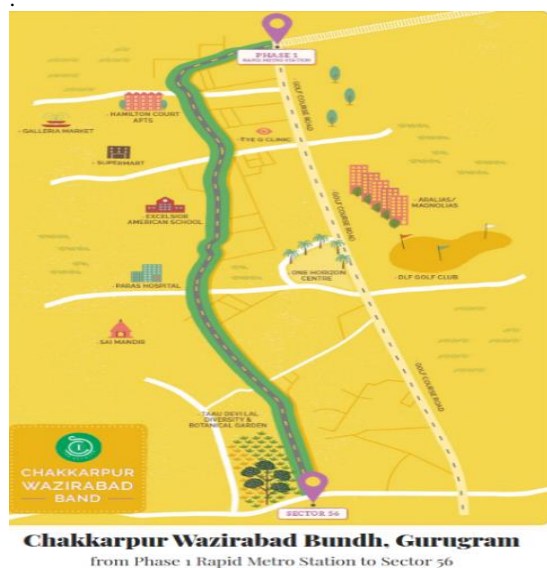


Figure 3. Chakkarpur Wazirabad Bundh, Gurugram

An integrated system for proper collection and discharge of rainwater has been constructed all along the Bundh. The collection and channelling of rainwater including recharge chambers, trenches, pits and laying of perforated pipes, ensure that rainwater flows in the right direction and recharges the groundwater table as well as the nallah

This one-of-a-kind project is a replicable example that showcases that clean and green public spaces and infrastructure for sustainable mobility can be made available in the heart of the city.



Figure 4. Chakkarpur Wazirabad Bundh, Gurugram

3. DATA COLLECTION AND ANALYSIS

3.1 Primary Data Collection using Open Data Kit App

The primary Data collection and survey of the area has been done using Open Data Kit (ODK) App and QRealTime – A QGIS Plugin. The point shape file with different parameters was prepared in QGIS and it was uploaded on Server and after survey was completed the data was downloaded and its analysis along with data from secondary sources has been done using QGIS.

Primary Data collection shows prominent morphological changes in Gurugram. These have been captured by physical survey done using the tool – Open Data Kit. In last 40 years, more than half of Gurugram's 519 water bodies have been encroached upon, in most cases, by the private builders/Land mafia. The primary survey of water bodies (New Gurugram) map shows the diminishing of natural nullahs and drains leading to flooding and obstructing the natural recharging of the water.

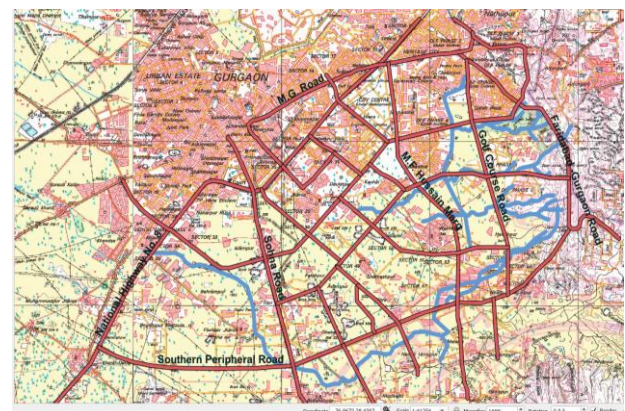


Figure 5. Streams & nallahs in 1984

The Badshahpur Jheel was concretized leading to it becoming a dumping ground and also preventing the ground water recharge. In the past ,these water bodies were a part of regular water supply and irrigation system.

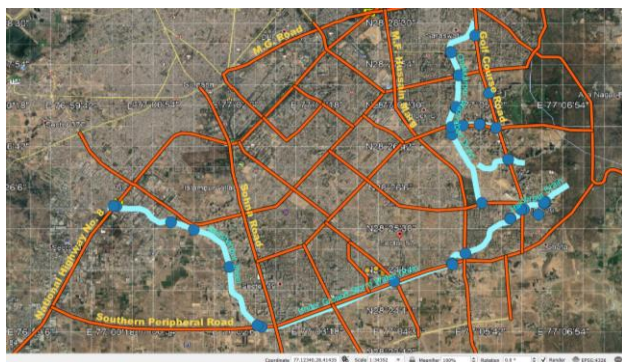


Figure 6. Streams & nullahs in 2020
Data collected Using ODK and applied in QGIS.

With over 100 nullahs, the city had a unique natural drainage system (Figure 5 and Figure 6). The natural drainage and recharge system of the area was revived by the British who built 118 check dams to control flooding



Figure 7. Extinct Water bodies
Source: Times of India – 14th June 2018

The four major water bodies – Ghata(50 ft. deep), Nathupur(30 ft. deep), Chakkarpur(12 ft. deep) and Jharsha(10 ft. deep) – used to store rainwater and recharge, thereby preventing water logging. The surplus would flow downstream, from these big water bodies to many smaller ones, through nullahs, serving the needs of the population throughout the year. And many of them have become extinct now due to uncontrolled development in these areas Figure 7.

3.2 Secondary Data Collection

The secondary source data has been collected from Google Earth Imagery, Gurugram Metropolitan Development Authority (GMDA).

3.2.1 Water Resource Management in Gurugram

Before 1990 Gurugram was entirely dependent on the ground water as there was no other major source of surface water – river or Reservoir. The distribution of piped water to Gurugram began in year 1990, when city began drawing water from the Yamuna canal in Sonapat. The launch of city’s first water

treatment plant in Basai, helped augment the supply for the then developing sectors between Sector 1 – 57.

Gurugram now has a water management network which consists of Water supply network, Sewerage network and Drainage network which is controlled and managed by Gurugram Meropolitan Development Authority (GMDA).. The details of which are given in Figure 8, Figure 9 and Figure 10.

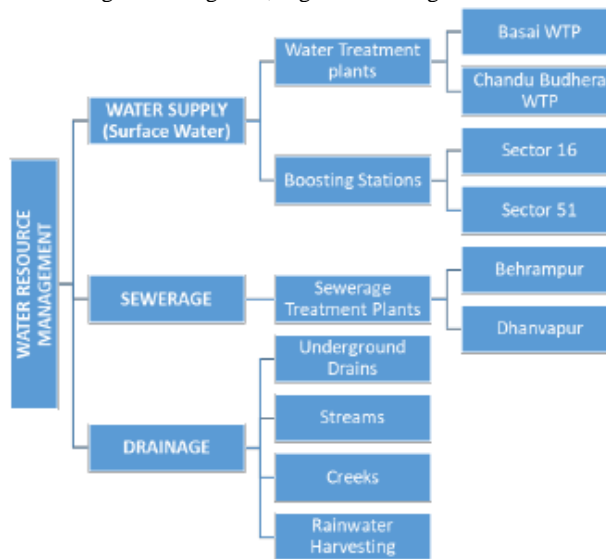


Figure 8. Water Resource Management, Gurugram

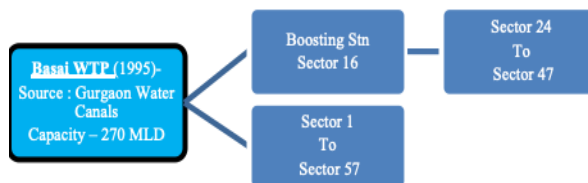


Figure 9 Water supply chain, from Basai WTP, Gurugram

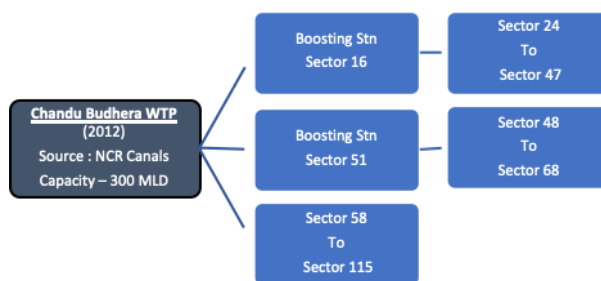


Figure 10. Water Supply Chain, from Chandu Budhers WTP, Gurugram

Type of Water	Water Filling Station	Uses of Water
Potable / Drinking Water	Waterworks - Basai Boosting Stn : Sec. 16 Boosting Stn : Sec. 51	Drinking
Raw/Canal Water	Waterworks – Chandu Budhera	Construction
Recycled water	STP - Dhawapur STP - Behrampur	Construction

Figure 11. Water Supply based on Usage, Gurugram

GMDA supplies water for constricton – Raw Water from its Water Treatment Plant (WTP) at Chandu Budhera and recycled

water from Sewerage Treatment Plants (STP) at Dhawalpur and Behrampur. GMDA also supplies water to colonies which are under construction or where water supply pipe lines have not been extended so far.

4. WATER RESOURCE MANAGEMENT PLAN FOR PRIVATE DEVELOPER AREAS IN GURUGRAM

4.1 Components of Water resource management plan

Water resource management plan for Gurugram will have three important components – Assessment and conservation of available water resources in Gurugram, Demand Management and Wastewater treatment and reuse. There is a need to have an integrated water resource management plan for new development sectors based on urban water cycle Figure 12.

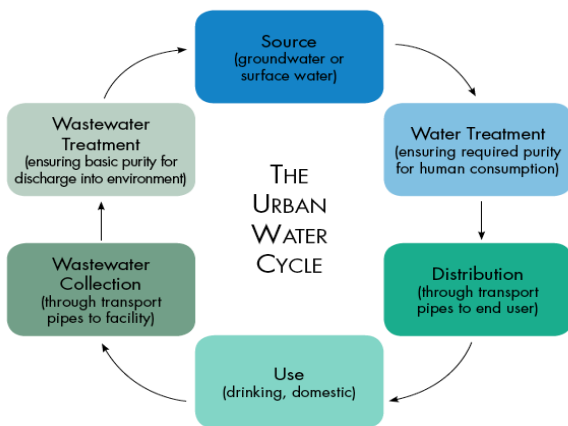


Figure 12. Urban Water Cycle.

4.1.1 Assessment and Conservation of water resources

Assessment of water resources can be done by:

- Total Precipitation in the area
- Water availability on the surface water resources
- Availability of ground water in the area
- Canal Water Availability
- Identifying waste water as resource and reuse it after recycling at the project site itself.

Conservation of water resources can be done by:

- Conserve the topography and drainage of the area. All the existing drains should be developed and protected to be part of the project.
- Identifying local surface water sources in the area like lakes Johars etc. and conserving them.
- Keep the surface runoff of the developed site to its original level before development by integrating rain water harvesting and ground water recharging in the projects.

4.1.2 Demand Management

Demand management has a major benefit that it leads to reduction in total cost of water to be imported from outside – especially the canal water. In the project site it can be done by adopting water saving / efficient fixtures and having two pipe plumbing system where treated waste water can be used for flushing of toilets and irrigation of landscaping areas. This can lead to reduction in demand of water supply by 35% i.e. from 135 lpcd to 90 lpcd

4.1.3 Wastewater Recycling and Management Techniques

Wastewater should be recognised as a resource and not as a problem. Also it is mandatory as per GMDA building byelaws to treat wastewater on site before disposal. At household level, i.e. waste water generated from bathing, washing of clothes, utensils, and flushing of toilets which is around 90 lpcd after treatment can be recycled for gardening, washing of courtyards and in some cases if proper care is taken for disinfecting it, can also be used for flushing thus reducing the overall per capita water demand by around 40 lpcd.

There are two type of technologies available for wastewater treatment – Mechanised wastewater treatment Plants and Nature Based Solutions and any one of them Should be adopted as per the availability of site and Quality of water required.

5. CONCLUSION

Rapid Urbanisation and Private developers encroached these areas throwing the entire water ecosystem in danger. This leads to flooding even with very little rain. Also, since this prevents the recharging, the ground water level has depleted drastically. These private developers also practice ground water extraction despite a ban to do so. The looming water shortage holds within it a seed of a larger ecological crisis.

About 80% water consumed domestically is released into drains and sewers as wastewater. In Gurugram, this will further pollute groundwater reserves, and even the Yamuna river. More wastewater also leads to more water borne diseases, such as common diarrhoea

6. ACKNOWLEDGEMENTS

We would like to express our deepest gratitude and thank Shri Shiva Reddy Koti, Shri Prabhakar Alok Verma and Indian Institute of Remote Sensing Dehradun for providing training and assistance, as and when required to use QRealTime Plugin in QGIS and ODK Collect app.

7. REFERENCES

- Jones, D.E., 1971, Where is Urban Hydrology Practice Today. Proc. Am. Soc. Civil Engg. Hydr. Div., 97 (HY2), 257-264 pp.
- Tanaka, H., Asano, T., Schroeder, E.D. and Tchobanoglous, G. (1998). Estimating the Safety of Wastewater Reclamation and Reuse Using Enteric Virus Monitoring Data. Water Environment Research, Vol. 70, No. 1, pp. 39–51
- Newall, B., Cameron, I., Lant, P., von Meunch, E., Olsson, G., 1998. Modelling sustainable urban water systems. In: Proceedings of the 11th IWSA-ASPAC Regional Conference, 1–5 November, Sydney, Australian Water and Wastewater Association Incorporated, pp. 550–556.
- QGIS Development Team, 2019. QGIS 3.6., Open Source Geospatial Foundation. grass.osgeo.org (20 September 2019).
- Koti, S.R. and Verma, P.A., 2019. Plugin QRealTime. QGIS Software, Version 3.8, Open Source Geospatial Foundation. <https://plugins.qgis.org/plugins/QRealTime/>
- ODK Development Team, 2019, ODK Collect v 1.27.1. <https://github.com/getodk/collect/releases/tag/v1.27.1>

IMPACT OF CHANGING LANDUSE ON GROUNDWATER, CASE OF ALWAR URBAN AREA

Ila Pant, Address: Sector- 12, Vrindavan Enclave, House No.- 63, Vasundhara, Ghaziabad, Uttar Pradesh-201012, e-mail ID- ilapant92@gmail.com
Sushant School of Planning and Development, Ansal University, Gurgaon.

Nikhita Bajaj, Address: WZ – 348, 3rd Floor, Street No. – 20, Shiv Nagar, New Delhi – 110058, E-mail ID – nikhitabajaj.mplan19@ansaluniversity.edu.in
Sushant School of Planning and Development, Ansal University, Gurgaon.

KEY WORDS: Alwar, urbanisation, Ground water, water resources, Landuse landcover, LandSAT, Geographic Information System, Remote sensing.

ABSTRACT:

Urbanisation is induced by human activities resulting in landuse –landcover change affecting the quality and quantity of water resources (Mukherjee, 2018). Groundwater being the most important resource, has depleted at the rate of 19.2 gigatons per year in northern India (Jain, 2018). Prime reason for groundwater depletion is cited as crop irrigation (Prasad 2018). The authors have explored the changing landcover and landuse in Alwar Urban area to decipher the reason, other than irrigation, for the depletion of groundwater.

Alwar, the study area lies in north eastern part of the desert state of Rajasthan, is a semi-arid climatic region. An effort is made to find reasons for depleting groundwater as in the current era of smart, it is pertinent that smart measures be adopted to maintain the water resources, especially in this age when cities are totally drying up.

Through this paper, landuse transformation in the region is mapped over a 30years timeline from 1991 to 2020 using LandSAT satellite images. Simultaneously, Groundwater levels are mapped for the same timeline using secondary as well as primary sources. A correlation is established between changing landuse and depleting groundwater using Geographic Information System and Remote Sensing tools.

1. INTRODUCTION

Alwar situated at 27° 34' North and 76° 36' East is 160kms distant from Delhi and 150 kms from Jaipur in National Capital Region. Alwar urban area of 8380 sq. km. at 268m from sea level, with Aravalli hills on the west and smalls hillocks all across the city, has the slope towards the south. In recent times apart from commercial importance, Alwar also emerged as promising tourist destination keeping its centrally placed location between Delhi and Jaipur. It has mesmerising scenic beauty, to which these lakes, forts, temples add physical, social and economic value.

The population in this urban area was 2,10,146 in 1991 which increased to 3,81,400 (including villages in the urban boundary). However, the estimated population as per master plan 2031 for Alwar is 5,35,000 for 2021, focusing more on industrial landuse. However, passing of National highway -8 from Alwar district changed the course of development and industrial settlements from Alwar city to Bhiwadi, Dharuheda, Shahjahanpur, Babal, Neemrana, Behror, etc.

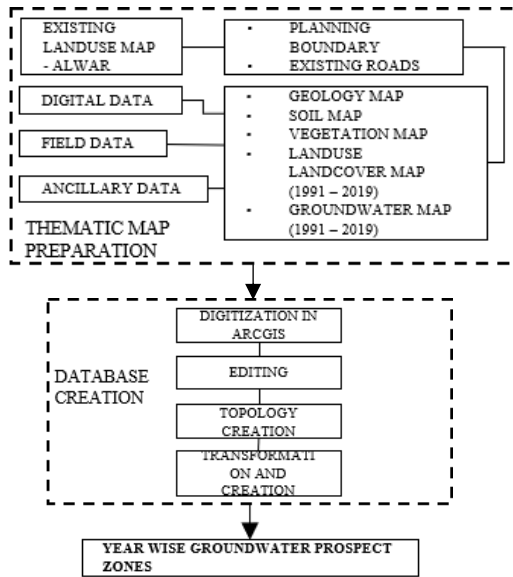
The urbanisation is very visible from the population counts which took a toll on groundwater of this area. Average rainfall in this area is 331mm (2017) which is also very indefinite. Saltwater (from oceans) constitutes around 97.2% of the global water resources and remaining 2.8% is available as fresh water. In this 2.8%, only 0.6% is groundwater and rest 2.2% is surface water (Wang,2011). Percentage of depletion in ground water is 8.69% from 1991 to 2019 in Alwar Urban area.

2. OBJECTIVES

- a. To study the groundwater evolution in the timeframe of 30years from 1991 to 2020 using landSAT satellite images.
- b. Study of landuse –landcover using satellite data from remote sensing.
- c. Generation of landuse –landcover maps of Alwar, Rajasthan on GIS.
- d. To find the reasons of depleting ground water in Alwar.

3. METHODOLOGY AND STUDY AREA

Study area for authors is the urban boundary of Alwar city in Rajasthan. This area is environmentally rich in presence of hills, forests, lakes and has great economical value (Hicks, 2007)



Working procedure for the preparation of maps.

3.1 Data collection

- i. Collection of existing data
- ii. Field investigations to complete data
- iii. Preparation of remote sensing maps

3.2 Data processing

- i. Preparation of basic maps
- ii. Vegetation
- iii. Geology
- iv. Soil
- v. Groundwater
- vi. Landuse Landcover

3.3 Printing

- i. Transferring data to digital format, using the GIS ARC
- ii. Printing of maps
- iii. Preparation of explanatory notes

4. RESULTS

4.1. Water Resources in Alwar

In Alwar, till census year 2011 drinking water provided to Alwar is through 183 tube wells of per day capacity 31 Mega Litre per Day. However, due to consistent depletion of ground water at the rate of 0.8 meter every year, only 26.8 Mega litre per day was possible. The water supply was 78 Litres per person per day. Along with tube wells, 261 handpumps also contribute to the water availability. As per Public Health Engineering Department (PHED) study of water quality shows it contains of Nitrate, Iron and other metals in excess (Master Plan 2031-Alwar) Water resources in Alwar administrative area includes:

Year 2017-2018			
S. No.	Water Resources	Total	In working condition
1	Wells	5268	184
2	Ponds	4	4
3	Tube Wells	4146	4146
4	Hand pumps	414	

Source: Statistical report 2017-2018

4.2. Geographic mapping

Following Geographic maps showing direct or indirect relation to groundwater of Alwar.

4.2.1 Vegetation Map

Produced from the LandSAT of Alwar urban area available in USGS¹ website (Figure 1). This map indicates:

- i. Vegetation Index

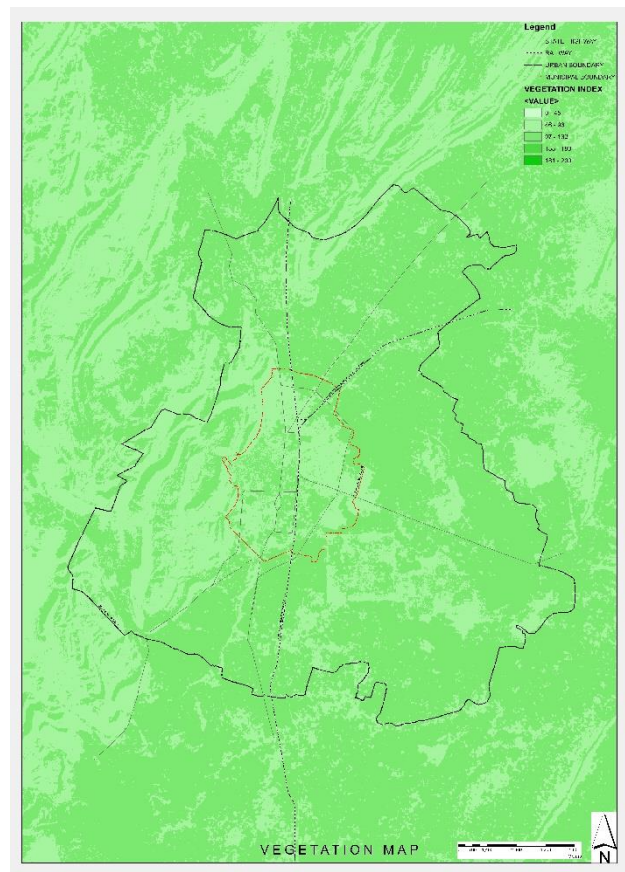


Figure 1. Vegetation map

4.2.2 Soil Map

Produced from the georeferencing of soil map (Figure 2) available in the district atlas of Rajasthan. Data obtained:

- i. Alluvial Soil – 62.3%
- ii. Red Grey Valley Soil – 37.7%

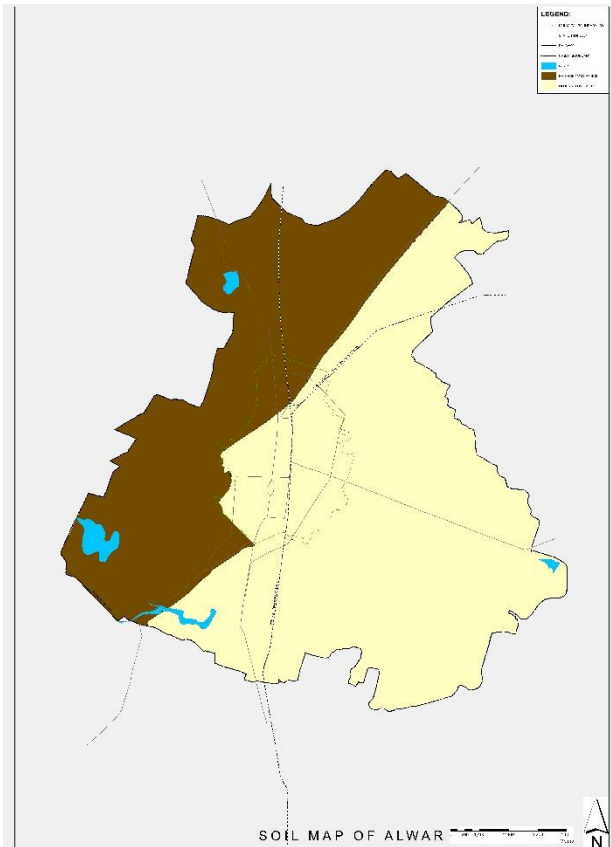


Figure 2. Soil Map

4.2.3 Geology Map

Produced from the georeferencing of geology map (Figure 3) available in the district atlas of Rajasthan. Data obtained:

- i. Alwar Group – 9.4%
- ii. Ajabgarh Group – 2.2%
- iii. Alluvium and wind-blown sand – 88.4%

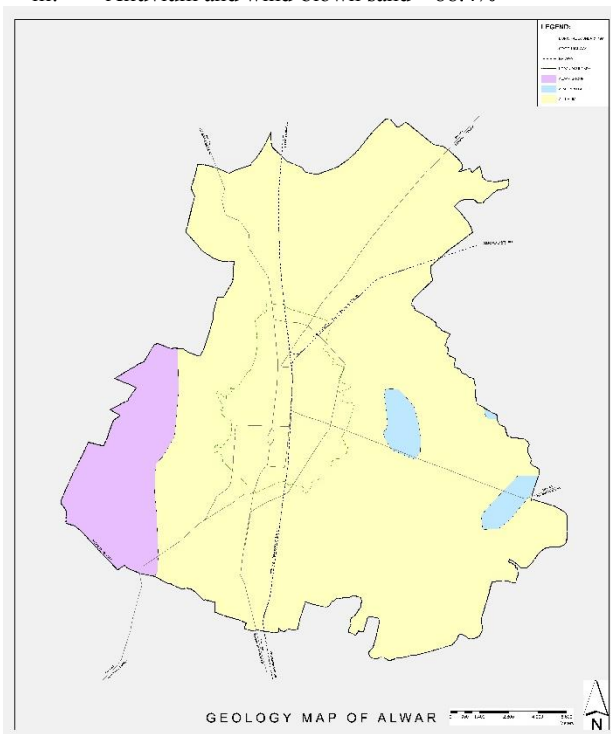


Figure 3. Geology Map

4.2.4 Slope Map

Produced from the Digital elevation model (DEM) files obtained from BHUVAN (Figure 4). Data obtained:

- i. Slope of alwar- 20 – 40 cm

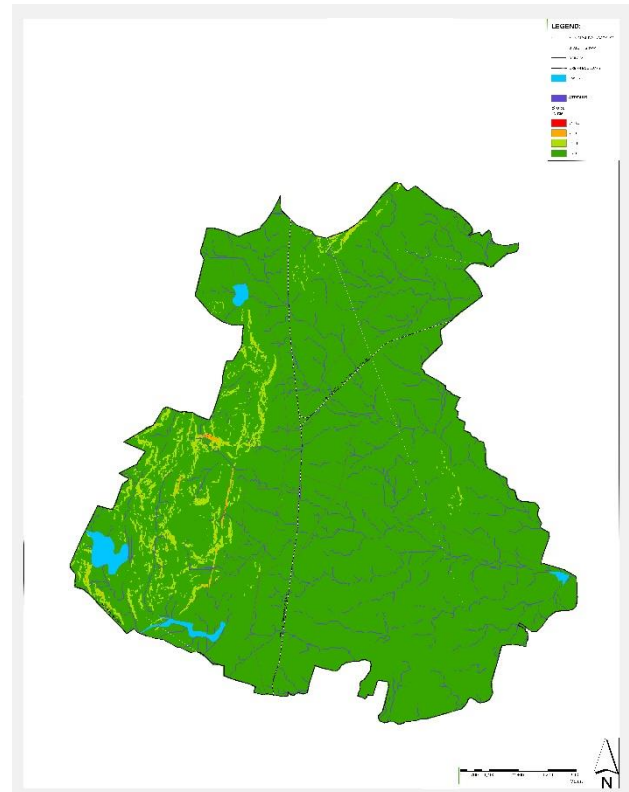


Figure 4. Slope map

4.3. Groundwater mapping in Alwar using Remote sensing and GIS

landuse –landcover map of Alwar urban area using Remote sensing tools and GIS

4.3.1 LULC Map of Alwar urban area – 1991

Produced from the LandSAT of Alwar urban area available in USGS website (Figure 5). This map indicates:

- i. Built Up - 15%
- ii. Surface water - 5%
- iii. Vegetation - 25%
- iv. Fallow Land - 0%
- v. Agriculture - 50%
- vi. Rocky field - 5%

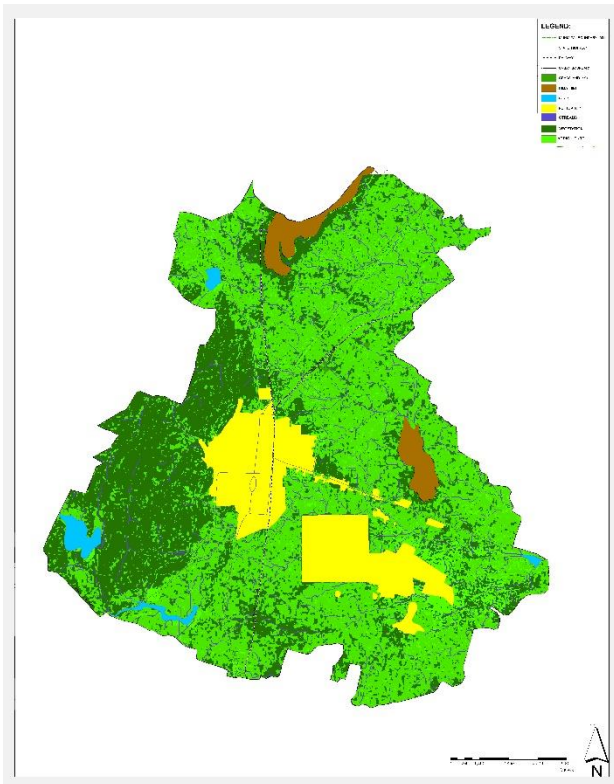


Figure 5. Landuse landcover map- 1991

4.3.2 Landuse Landcover Map of Alwar urban area – 2001

Produced from the LandSAT of Alwar urban area available in USGS website (Figure 6). This map indicates:

- i. Built Up - 16%
- ii. Surface water - 5%
- iii. Vegetation - 25%
- iv. Fallow Land - 4%
- v. Agriculture - 45%
- vi. Rocky field - 5%

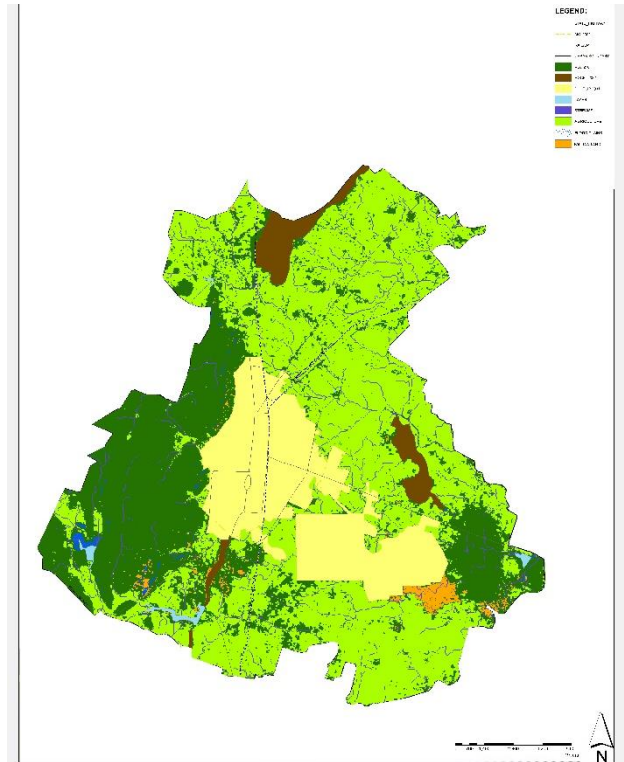


Figure 6. Landuse landcover map- 2001

4.3.3 LULC Map of Alwar urban area – 2011

Produced from the LandSAT of Alwar urban area available in USGS website (Figure 7). This map indicates:

- i. Built Up - 18%
- ii. Surface water – 1.5%
- iii. Vegetation - 25%
- iv. Fallow Land - 5%
- v. Agriculture - 40%
- vi. Rocky field - 5%

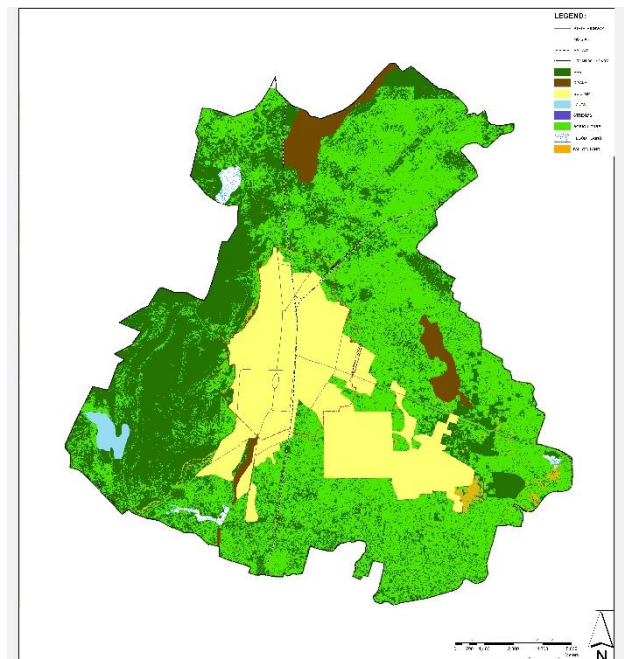


Figure 7. Landuse landcover map- 2011

4.3.4 LULC Map of Alwar urban area– 2019

Produced from the LandSAT of Alwar urban area available in USGS website (Figure 8). This map indicates:

- i. Built Up - 20%
- ii. Surface water - 3%
- iii. Vegetation - 25%
- iv. Fallow Land - 5%
- v. Agriculture - 40%
- vi. Rocky field - 5%

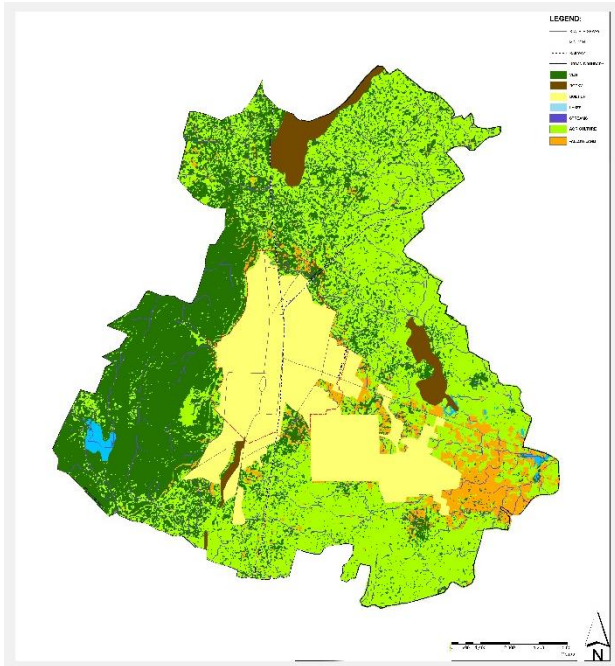


Figure 8. Landuse landcover map- 1991

4.3.5 Groundwater Map of Alwar urban area– 1991

Produced from the survey points available in IndiaWRIS website (Figure 9). This map indicates:

- i. Groundwater Range – 8-50 m(bgl)

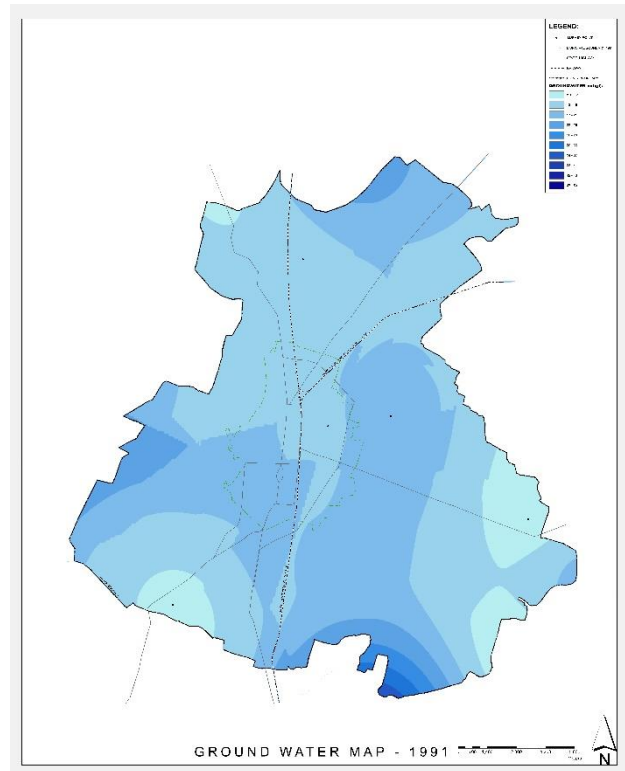


Figure 9. Groundwater map- 1991

4.3.6 Groundwater Map of Alwar – 2001

Produced from the survey points available in IndiaWRIS website (Figure 10). This map indicates:

- i. Groundwater Range – 4-22 m(bgl)

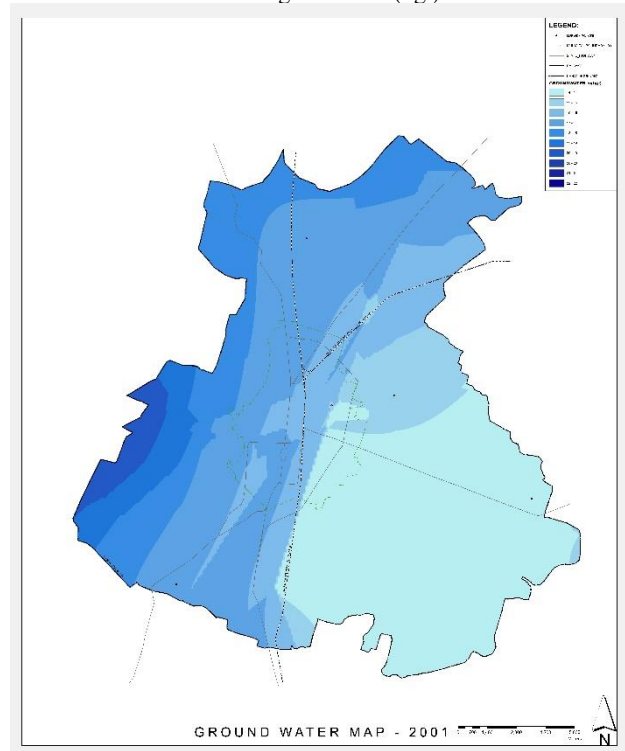


Figure 10. Groundwater map- 2001

4.3.7 Groundwater Map of Alwar – 2011

Produced from the survey points available in IndiaWRIS website (Figure 11). This map indicates:

- i. Groundwater Range – 7 – 46 m(bgl)

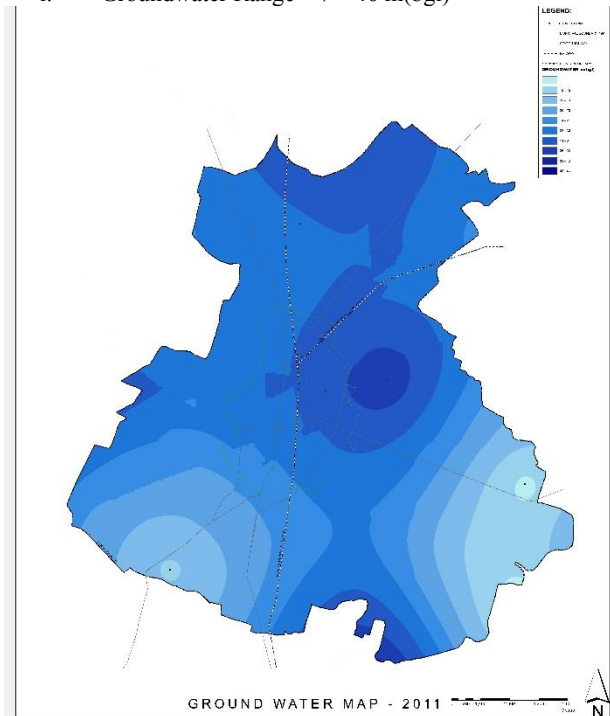


Figure 11. Groundwater map-2011

4.3.8 Groundwater Map of Alwar – 2019

Produced from the survey points available in IndiaWRIS website (Figure 12). This map indicates:

- i. Groundwater Range – 9-55 m(bgl)

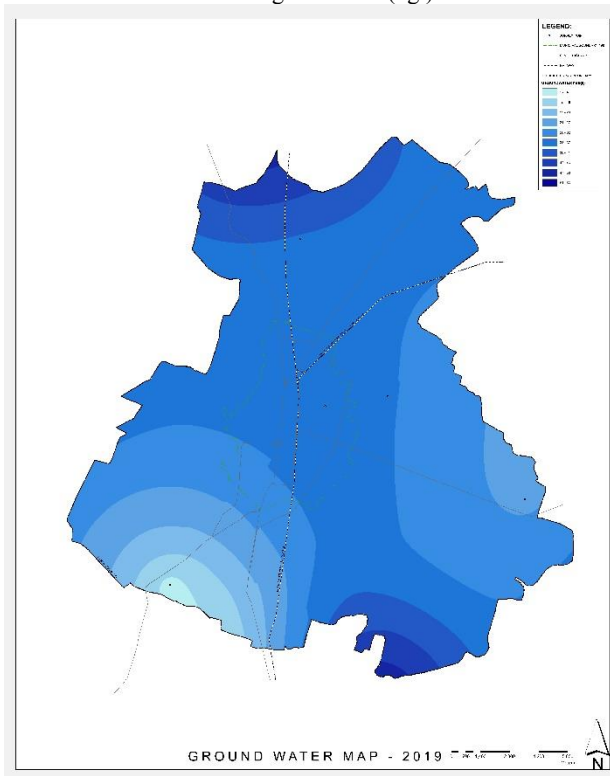


Figure 12. Groundwater map-2019

5. CONCLUSION

The boundaries area increasing so does the urbanisation, however, ground water level is on constant depletion. Groundwater is under tremendous pressure due the migration. Evident from Groundwater maps that after 2011 an increase in ground water is noticed which is under the programme of recharging of groundwater by Government of Rajasthan under vision 2025. Vision 2045 by Government of Rajasthan is to focus on sustainable development of water resources and optimum utilisation of natural water resources.

Important is to find a permanent solution of depletion of this limit resource by the government, policy makers, planners. Annual rainfall in 2011 as per mater plan 2031 of Alwar was 640mm which has reduced to 331mm in year 2017 as per the statistical report of 2017 for Alwar. Even after the conservation programme by Rajasthan government, the overall numbers showing groundwater level is negative.

Identification of this matter is concluded with a lot of studies, however, this is the time for some real time action with optimum use of Geospatial applications in urban and regional development.

ACKNOWLEDGEMENTS

The authors are thankful to their teaching faculty Dr. Prabh Bedi (professor) and Ar. Himanshu Panwar in the masters programme of Sushant School of planning and development in Ansal University, Gurgaon to guide through this manuscript.

REFERENCES

- Digital elevation model (DEM) files, BHUVAN.
- District Statistical report- 2018, Alwar Statistical Office.
- Gloria Hicks, 2007, getting at groundwater with gravity published in Sensing our Planet under Earth Science Data and Information System (ESDIS) Project.
- Groundwater points, IndiaWRIS
- LandSAT images, USGS website.
- Master Plan 2031, Urban Improvement Trust (UIT) website.
- Ming-Huang Wang et al, 2011, Research article published in water resources journals: A bibliometric analysis on Desalination and water treatment.
- Neha Jain, 2018, India's groundwater crisis, fuelled by intense pumping, needs urgent management, Mongabay, e-paper,

referring Dr. Matthew Rodell et al, 2018, Emerging trends in global fresh water availability.

R. Prasad, 2018, Groundwater depletion alarming in northwest, central India, The Hindu, e-paper

Salwa Farouk Elbeih, 2014, An overview of integrated remote sensing and GIS for groundwater mapping in Egypt.

Subham Mukherjee et al, 2018, Review on the Impacts of Land Use Land Cover Changes (1980–2014) on Urban Water security of Kolkata.

ACCURACY ASSESSMENT OF OPEN ACCESSIBLE DIGITAL ELEVATION MODELS IN URBAN AREAS

¹Esther Metilda, ²Shweta Khatriker, ^{*}Ashutosh Bhardwaj, Kshama Gupta

¹SRM Institute of Science and Technology, Kattankulathur

^{2,3,4}Indian Institute of Remote Sensing, Dehradun

ABSTRACT

Digital Elevation Model (DEM) represents the altitude of reflective surfaces of earth surface features. SAR Interferometry and Photogrammetric techniques are few of the techniques, which have been widely utilised to generate global DEMs. They are broadly used as a vital geospatial information sources for various geographic and multi criterion analysis. In the present context multitude of freely and openly accessible DEMs are available derived from varied microwave and optical remote sensing datasets. TANDEM-X DEM (TerraSAR-X add-on for Digital Elevation Measurement) has been derived from a SAR sensor at 90m spatial resolution with the main objective of creating precise 3D maps of earth features whereas SRTM (Shuttle Radar Topographic Mission) DEM is also derived from microwave dataset at 30m resolution. ALOS PALSAR RTC HR is a ALOS product derived from SAR data with 12.5 m spatial resolution and have been widely used in coastal area and land area mapping. CartoDEM V3 R1 at 30m resolution and ASTER GDEM V2 at 30m spatial resolution have also been used for landscape modelling, visualisation techniques etc. Three urban regions (cities) in different terrain conditions were chosen namely, Ahmedabad, Bhubaneshwar and Rishikesh with respect to GCPs collected through differential Global Positioning Survey (DGPS) survey. The presented study was mainly focused on the comparative assessment of these DEMs in which the TanDEM-X 90m is found to be of high accuracy with a RMSE of 1.78 m in Bhubaneshwar, 1.95 m in Ahmedabad and 3.33 m in Rishikesh.

Keywords: DEM, openly accessible, SRTM, TanDEM-X, ALOS PALSAR, Carto DEM

1. INTRODUCTION

A DEM is a 3 dimensional representation of the terrain surface. It serves as a primary input for various climatological, hydrological and geological applications. The quality of a DEM is a measure of how accurate the elevation is at each pixel and how accurately is the morphology presented and it depends on various factors like how the elevation data is collected, surface roughness etc. DEM datasets can be generated using various techniques such as photogrammetric and Light Detection and Ranging (LiDAR) methods, space-borne interferometry, radar altimetry, and conventional surveying techniques. There are many openly accessible DEMs available in the present context which can be downloaded freely by the user community for varied applications. TerraSAR-X add-on for Digital Elevation Measurements (TanDEM-X) is the recently launched DEM by Department of Land Resources (DLR) 90 m resolution. TanDEM-X is an earth observation radar mission that consists of a SAR interferometer built by two almost identical satellites flying in close formation. With a typical separation between the satellites of 120m to 500m a global Digital Elevation Model (DEM) has been generated (Bhardwaj, 2019). The horizontal as well as the vertical reference system (horizontal & vertical datum) of TanDEM-X DEM products is the WGS84 ellipsoid. CartoDEM Version 3 is also a freely downloadable DEM with a spatial resolution of 30 m by Indian Space Research Organisation. It is generated from stereo images acquired by Cartosat-1 (IRS P5) satellite in optical domain (Jacobsen, 2017). The DEM and subsequent ortho images generated facilitates large scale mapping and terrain modelling applications for entire country. Advanced Spaceborne Thermal Emission and Reflection Radiometer Global DEM (ASTER GDEM) (30 m) is now available from NASA's Land Processes Distributed Active Archive Center (LPDAAC) at 30 m resolution which is more refined and has a sharper imagery. ASTER DEM is available in Geo-tiff format

with signed 16 bits and is in geographic projection with latitude, longitude. SRTM DEM is derived from SAR Interferometric technique with a 1 arc-second, or about 30 meters sampling. (Elkhrachy, 2018) (Patel et al., 2016).

Many research observations have experimented with different open accessible DEMs and also with proprietary high resolution satellite DEMs which give varied results with respect to the spatial resolution and ground truth. The main objective of this paper is to analyse the open accessible DEMs in varied terrain and urban development conditions with respect to the GCPs taken by Differential Global Positioning System (DGPS) survey.

2. STUDY AREA

Three study areas have been selected for this analysis with different urban development and terrain conditions. The first study site selected is Ahmedabad city in Gujarat which lies between 23.0225° N, 72.5714° E where Sabarmati river partition the city into two regions and it has a very few undulating mild topography due to the presence of dunal landforms. The average elevation of the city is about 48 m above mean sea level. The second site selected is Bhubaneshwar city in Odisha which lies between 20.2961° N, 85.8245° E. It is in the eastern coastal plains along with Eastern Ghats Mountains and it has an average elevation of 45 m above mean sea level with coastal sand dunes and lateritic uplands. The third site was Rishikesh city in Uttarakhand state lies in 30.0869° N, 78.2676° E. This city is mainly known for its cultural heritage. It has an average elevation of 372 m and the sacred Ganges River flows through Rishikesh. It has highly undulating terrain and moderate urban development.

Specification	TanDEM-X	CartoDEM	ALOS PALSAR RTC HR	SRTM	ASTER GDEM
Acquisition Technique	Radar	Stereo imaging	SAR	Radar	Stereo imaging
Data Format	GeoTIFF	GeoTIFF	GeoTIFF	GeoTIFF	GeoTIFF
Vertical Datum	WGS 84 ellipsoidal	WGS 84	WGS 84	EGM96	EGM96
Spatial Resolution	90 m	30m	12.5m	30 m	30 m
Projection System	Geographic (lat/long)	Geographic (lat/long)	Geographic (lat/long)	Geographic (lat/long)	Geographic (lat/long)
Source	(https://tandemx-90m.dlr.de)	(https://bhuvan.nrsc.gov.in/)	(https://asf.alaska.edu/)	(https://earthexplorer.usgs.gov/)	(https://earthdata.nasa.gov/)

Table 1. Major Specifications of the Open Accessible DEM

3.MATERIALS & METHODOLOGY

TanDEM-X (90 m spatial resolution) provided by DLR (<https://tandemx-90m.dlr.de>) site. While, SRTM DEM have been downloaded from earth explorer (<https://earthexplorer.usgs.gov/>). ALOS PALSAR RTC was also a DEM derived from SAR data which is available from Alaska Satellite Facility vertex data (<https://asf.alaska.edu/>). CartoDEM data has been downloaded from National Remote Sensing Centre Bhuvan site (<https://bhuvan.nrsc.gov.in/>). Whereas, ALOS PRISM DEM has been obtained from <https://www.eorc.jaxa.jp/ALOS/en/aw3d30/index.htm> web location. The ASTER Global DEM has been downloaded from NASA explorer (<https://earthdata.nasa.gov/>)(Papworth et al., 2016).

As the accuracy of DEM relies upon the precision of the GCPs utilized in the study displaying during the acquisition of DEM, it calls for GCP directions to be clear, which can be collected through differential GPS (DGPS). Care was taken to distribute GCPs evenly throughout the study area and sufficient observations (45min – 1.5 hrs depending upon baseline distance) have been ascertained to precise values of GCPs locations.

The downloaded DEMs have been further evaluated with respect to Ground Control Points (GCPs) obtained through DGPS survey. The ground control points aids in calculating the absolute height error for the evaluation of these DEMs. (Shukla and Mintz, 1982)(Mahtab et al., 2003). In order to assess the DEMs, statistical errors like RMSE (Root Mean Square Error), Mean Absolute Error (MAE) and Standard Deviation in Error (SDE) have been calculated for assessment of absolute vertical accuracy. Linear error at 90% percentile (LE90%, confidence, LE90=1.6449* RMSE) (Khalid et al., 2016) is also used extensively for accuracy assessment of DEMs. The formulae used are given in equation 1 – 3. The values of LE90 was tabulated in table 1,2 and 3.

$$RMSE = \sqrt{\frac{\sum_{i=1}^n (z_1 - z_2)^2}{n}} \text{-----1}$$

$$MAE = \frac{\sum |z_1 - z_2|}{n} \text{-----2}$$

$$SDE = \sqrt{\frac{\sum_{i=1}^n (z_1 - z_2)^2}{n-1}} \text{-----3}$$

Where ‘n’ indicates the number of observations, Z₁ and Z₂ indicates the elevation values of DGPS survey and DEM respectively.

4. RESULTS & DISCUSSIONS

4.1 Qualitative Analysis

The GCPs from the DGPS survey are shown in figures 1, 2 and 3 respectively, for three sites at Ahmedabad (Gujarat), Bhubaneshwar (Odisha) and Rishikesh (Uttarakhand). Ahmedabad has a general elevation ranging from 0 to 48 m above mean sea level and the regions near Sabarmati river and the rural areas in this region has a very low terrain. Bhubaneshwar has a moderate rugged terrain with low steeped valleys. The elevation values ranges upto 59 m above MSL. Rishikesh has very high undulating terrain ranging from -327 m to 2186 m. Its valleys are highly dissected. TanDEM-X DEM (90m) shows clear and distinctive terrain for all the sites, Similarly CartoDEM recent version (30m) gives a better visual accuracy. ASTER Global DEM differs significantly visually for all three sites. InSAR DEMs (Khatraker et al., 2019), ALOS PALSAR and SRTM shows better accuracy when compared with ASTER GDEM but less in TanDEM-X DEM.

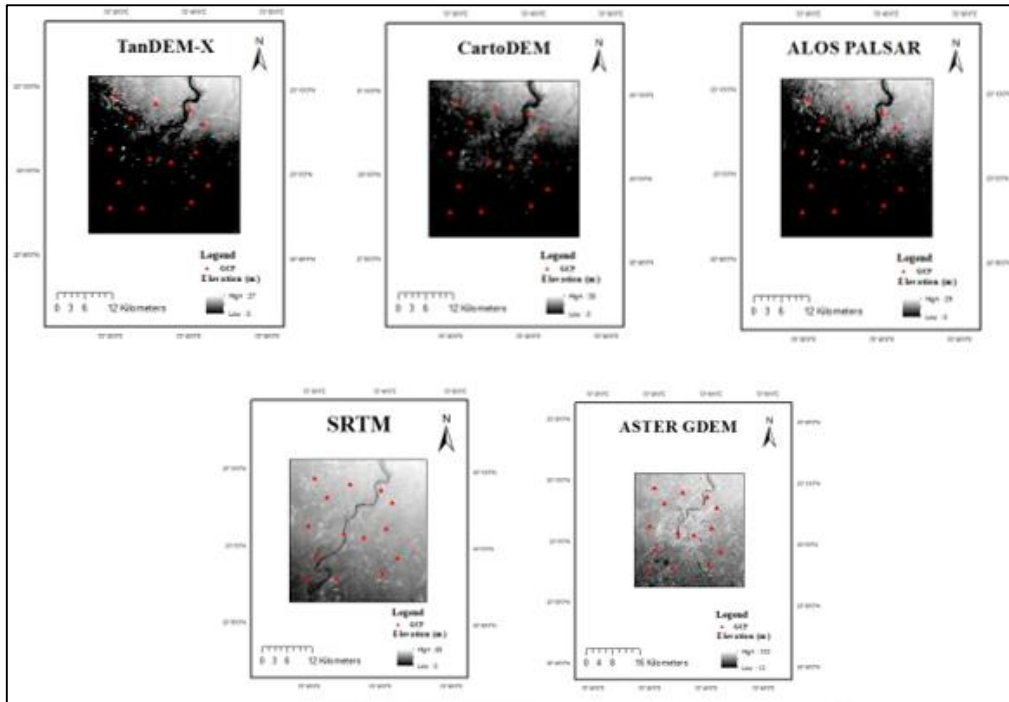


Fig.1 Digital Elevation Model for Ahmedabad region

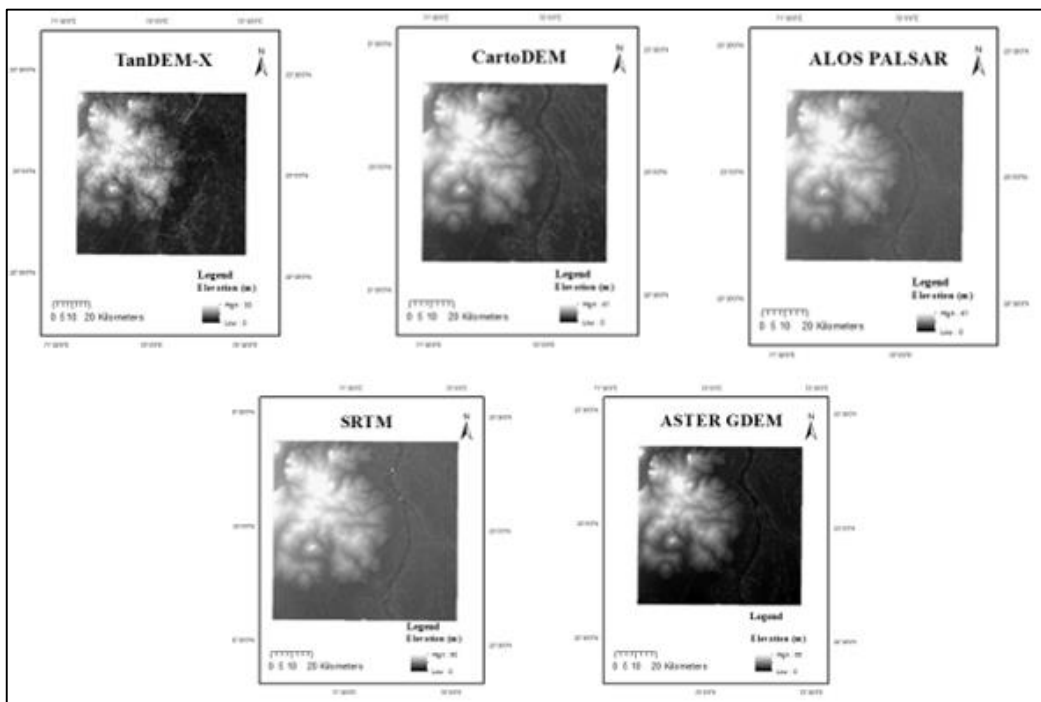


Fig. 2 Digital Elevation Model for Bhubaneswar region

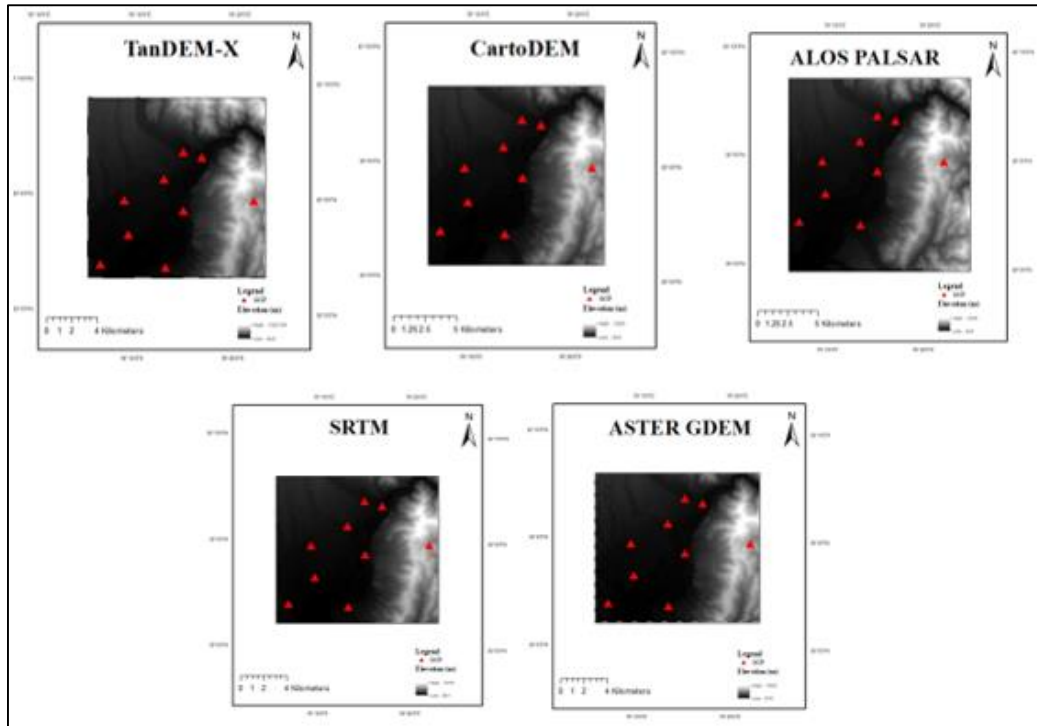


Fig.3 Digital Elevation Model for Rishikesh region

Errors	TanDEM	CartoDEM	ALOS PALSAR	SRTM	ASTER GDEM
RMSE	1.95	2.07	9.55	4.06	5.25
MAE	1.459	1.695	7.605	8.614	8.234
LE90	3.207	3.404	15.708	6.678	8.638

Table 2. Statistical Errors of the DEMs in Ahmedabad Region

Errors	TanDEM	CartoDEM	ALOS PALSAR	SRTM	ASTER GDEM
RMSE	1.081	3.695	3.062	31.479	29.105
MAE	0.831	0.066	2.707	24.667	22.801
LE90	1.78	6.082	5.04	51.814	47.908

Table 3. Statistical Errors of the DEMs in Bhubaneswar Region

Errors	TanDEM	CartoDEM	ALOS PALSAR	SRTM	ASTER GDEM
RMSE	3.33	3.13	5.514	6.88	8.62
MAE	2.29	2.39	3.571	3.917	6.120
LE90	5.477	5.14	9.069	11.316	14.179

Table 4. Statistical Errors of the DEMs in Rishikesh Region

4.2 Quantitative Analysis

Statistical errors like Root Mean Square Error (RMSE) and Mean Absolute Error (MAE) are calculated for the above DEMs. (Bolkas et al., 2016). The MAE for the experimental sites at Ahmedabad, Bhubaneswar and Rishikesh are 1.45 m, 0.831 m and 2.29 m for TanDEM-X DEM respectively. Both RMSE and MAE both depict normal model-execution errors, anyway RMSE gives more weight to errors, making MAE a progressively characteristic proportion of normal errors. Bhubaneswar has the lowest RMSE (1.08 m) and MAE (0.831 m) value when compared to Ahmedabad and Rishikesh with respect to all the DEMs. In Ahmedabad region, CartoDEM has the lowest RMSE value when compared to TanDEM-X and all other DEMs. The Mean Absolute Errors show significant variation in all the regions. The MAE (0.66 m) values of CartoDEM is higher in Bhubaneswar when compared to Ahmedabad and Rishikesh. Similarly, MAE (7.605 m) values of ALOS PALSAR showed higher in case of Ahmedabad as related to Bhubaneswar and Rishikesh. While, SRTM and ASTER Global DEM depicted lesser accuracy in Mean Absolute Errors in Bhubaneswar region when correlated with Ahmedabad and Rishikesh.

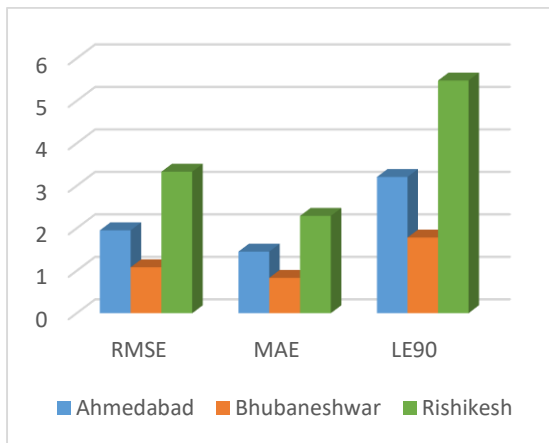


Fig. 4 TanDEM-X DEM Comparison of the Statistical Errors in all the Study Areas

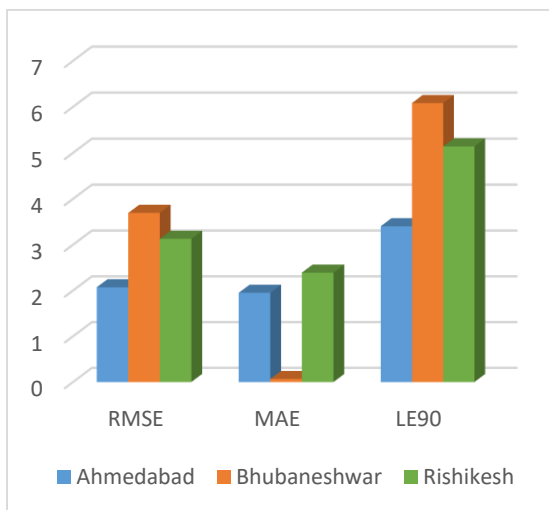


Fig. 5 CartoDEM Comparison of the Statistical Errors in all the Study Areas

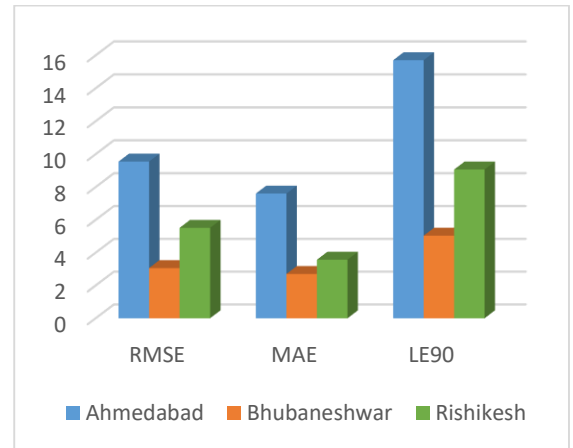


Fig. 6 ALOS PALSAR DEM Comparison of the Statistical Errors in all the Study Areas

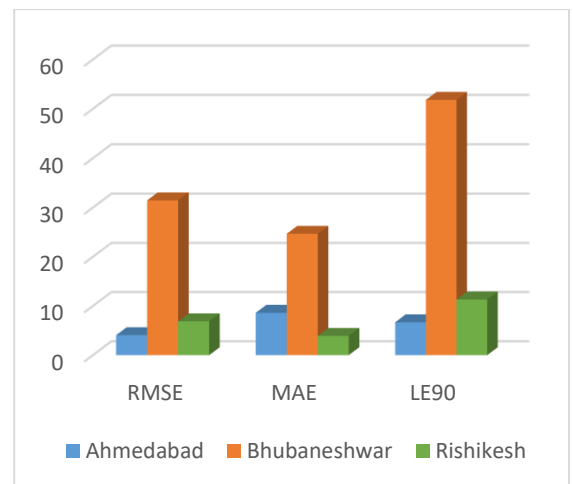


Fig. 7 SRTM DEM Comparison of the Statistical Errors in all the Study Areas

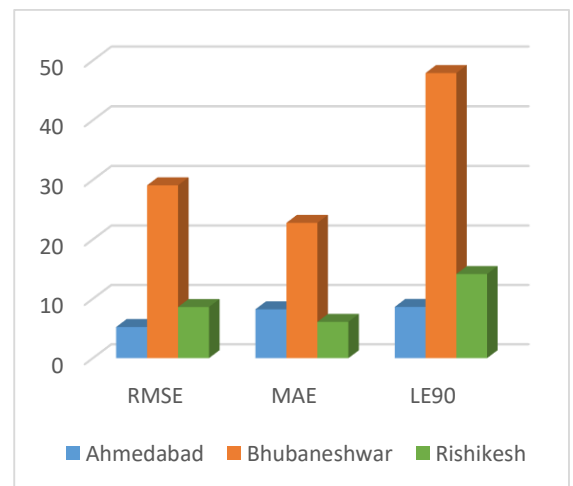


Fig. 8 ASTER GDEM Comparison of the Statistical Errors in all the Study Areas

5. CONCLUSION

The presented study was an attempt to make a comparative assessment for open accessible DEMs for performance evaluation. This evaluation covers three sites namely Ahmedabad, Bhubaneshwar and Rishikesh. For more precision and accuracy, the GCPs were collected through DGPS survey for accuracy assessment. TanDEM-X DEM (90 m) found to be most accurate above all DEMs

in Ahmedabad and Bhubaneshwar. However, CartoDEM showed better performance in Rishikesh region (RMSE= 3.13 m) as compared to Tandem-X. ALOS PALSAR with high terrain correction depicted reasonable accuracy in all the study areas. While, SRTM and ASTER Global DEM (RMSE=4.06, 5.25) displayed lesser accuracy as compared to TanDEM and CartoDEM. In future, various terrain parameters which can be extracted from DEMs can also be evaluated comparatively with respect to ground verification.

REFERENCES

- Bhardwaj, A., 2019. Assessment of Vertical Accuracy for TanDEM-X 90 m DEMs in Plain, Moderate, and Rugged Terrain. *Proceedings* 24, 8. <https://doi.org/10.3390/iecg2019-06208>
- Bolkas, D., Fotopoulos, G., Braun, A., Tziavos, I.N., 2016. Assessing digital elevation model uncertainty using GPS survey data. *J. Surv. Eng.* 142. [https://doi.org/10.1061/\(ASCE\)SU.1943-5428.0000169](https://doi.org/10.1061/(ASCE)SU.1943-5428.0000169)
- Elkhrachy, I., 2018. Vertical accuracy assessment for SRTM and ASTER Digital Elevation Models: A case study of Najran city, Saudi Arabia. *Ain Shams Eng. J.* <https://doi.org/10.1016/j.asej.2017.01.007>
- Jacobsen, K., 2017. Problems and limitations of satellite image orientation for determination of height models, in: *International Archives of the Photogrammetry, Remote Sensing and Spatial Information Sciences - ISPRS Archives*. International Society for Photogrammetry and Remote Sensing, pp. 257–264. <https://doi.org/10.5194/isprs-archives-XLII-1-W1-257-2017>
- Khalid, N.F., Din, A.H.M., Omar, K.M., Khanan, M.F.A., Omar, A.H., Hamid, A.I.A., Pa'Suya, M.F., 2016. Open-source digital elevation model (DEMs) evaluation with gps and lidar data. *Int. Arch. Photogramm. Remote Sens. Spat. Inf. Sci.* - ISPRS Arch. 42, 299–306. <https://doi.org/10.5194/isprs-archives-XLII-4-W1-299-2016>
- Khatriker, S., Gupta, K., Bhardwaj, A., 2019. Evaluation of Open Source SAR based Digital Elevation Models. *URSI Asia Pacific Radio Sci. Conf.* 248001.
- Mahtab, A., Narender, B., Ajai, 2003. Satellite derived Digital Elevation Model and terrain parameters - generation, accuracy assessment and validation. *J. Indian Soc. Remote Sens.* 31, 19–24. <https://doi.org/10.1007/BF03030748>
- Papworth, H., Ford, A., Welham, K., Thackray, D., 2016. Assessing 3D metric data of digital surface models for extracting archaeological data from archive stereo-aerial photographs. *J. Archaeol. Sci.* 72, 85–104. <https://doi.org/10.1016/j.jas.2016.05.005>
- Patel, A., Katiyar, S.K., Prasad, V., 2016. Performances evaluation of different open source DEM using Differential Global Positioning System (DGPS). *Egypt. J. Remote Sens. Sp. Sci.* <https://doi.org/10.1016/j.ejrs.2015.12.004>
- Shukla, J., Mintz, Y., 1982. Influence of land-surface evapotranspiration on the earth's climate. *Science* (80-.). 215, 1498–1501. <https://doi.org/10.1126/science.215.4539.1498>

DEVELOPMENT OF WEB BASED FRAMEWORK FOR HEALTH DISORDER ANALYSIS USING OPEN DATA KIT: A HEATHGIS APPROACH

Souvik Sankar Mitra¹, Abhinanda Saikia¹, Anuvi Rawat², Priyanka Rao³, Shiva Reddy Koti⁴

¹ M.Tech (Geoinformatics Department), Indian Institute of Remote Sensing, India- (souviksankar2013, nandaabhi01)@gmail.com

² M.Tech (Photogrammetry and Remote Sensing Department), Indian Institute of Remote Sensing, India – anuvirawat@gmail.com

³ M.Tech (Urban and Regional Studies Department), Indian Institute of Remote Sensing, India – priyanka.iirs@gmail.com

⁴ Scientist/Engineer – SE, Geoinformatics Department, Indian Institute of Remote Sensing, India – shiva@iirs.gov.in

KEY WORDS: HeathGIS, QRealTime, Open Data Kit, QGIS, Depression Analysis, PostgreSQL, IIRS

ABSTRACT:

Health disorder is an abnormal condition which negatively affects both physical and mental health. Currently, different factors like changed lifestyle, pollution etc. works as a catalyst for health disorder. But the main problem is people can't understand that he/she is suffering by any health issues or not. Sometimes they simply ignore some common symptoms thinking it as a simple health issue. According to World Health Organization (WHO), any health issue can be detected by some question answer method. This paper presents a web based framework for automatic health disorder analysis based on some predefined yes/no question using Open Data Kit (ODK). ODK community produces free and open-source software for collecting, managing, and using data in resource-constrained environments. It consists of several components like ODK-Collect, ODK-Build, ODK-Sensor, ODK-Briefcase, and ODK Aggregate.

According to doctor's advice, a questionnaire is made and published through ODK Build. Any user can fill and submit this questionnaire using ODK-Collect android app. The information is stored in ODK Briefcase server with GPS coordinates of the user. Using QRealTime Plugin in QGIS, the data is fetched and stored in PostGRE database. Also a list of specialized doctors about that problem is stored in that database. A website is developed where the client can check whether he is affected or not. If affected, then the coordinates of near doctors is shown on map. Also the shortest route is shown from the client's location to the nearest doctor's chamber so that the client can take quick action. This framework is scalable for any health disorder whether it is mental or physical. Also it makes people aware about its current health issue and intimate about nearest doctor.

1. INTRODUCTION

Mental disorders are significantly increasing worldwide leaving major negative impact on health and major changes in social, human rights and financial conditions of the people. (Mitchell et al., 2008). According to a report by the World Health Organisation, approximately 7.5% of Indians suffer from different types of mental health disorders. Statistical analysis predicts that by the year of 2020, roughly 20% of the Indian population will suffer from mental illness. The treatment gap is defined as the gap between the presence of aid available for mental disorder treatment and the prevalence of mental illness. One of the most common mental disorder is depression. It is estimated that depression affects nearly 264 million people worldwide (Steiner et al., 2016).

While the resources required for proactive healthcare and good disease surveillance are available more readily in developed countries, in developing countries like India, these are lacking and thus it compromises the quality of service provided. Collection of field data, its analysis and interpretation are key to a good healthcare service. Rapid growth of cell phone usage can help to fulfil the gap in data collection. Mobile data capture technology is efficient and cost-effective. (Maduka et al., 2017) Open data kit (ODK) is a similar kind of tool developed to provide an aid in data collection (Tridane et al., 2014)

ODK is an open-source set of tools designed to facilitate tasks at each stage of data collection. ODK provides three tools: Collect, Aggregate, and Build. Collect is a mobile client which

provides simple and user-friendly interfaces for collecting data. Aggregate is a data storage system hosted on a "cloud" based platform or on local servers. Build is a web-based form designer created to ease the process of creating digital forms (Hartung et al., 2012)

In this research work, a web based framework is presented, which will enable the user to analyse his/her mental health by answering the questions of the prepared questionnaire and locate the nearby health-care facility available. Incorporating all these components a website a dynamic website was prepared.

2. STUDY AREA AND DATA USED

The study area is located in Dehradun city which is part of Dehradun district and capital of Uttarakhand, a state in India. Located in the northern part of India, it lies 236 kilometres (147 mi) north of India's capital New Delhi and 168 kilometres (104 mi) from Chandigarh. Dehradun is located in the Doon Valley on the foothills of the Himalayas nestled between the river Ganges on the east and the river Yamuna on the west. The city is famous for its picturesque landscape and slightly milder climate and provides a gateway to the surrounding region. It is well connected to Himalayan tourist destinations such as Mussoorie and the Hindu holy cities of Haridwar and Rishikesh. Names of doctors and patients are used in this study with their consent.

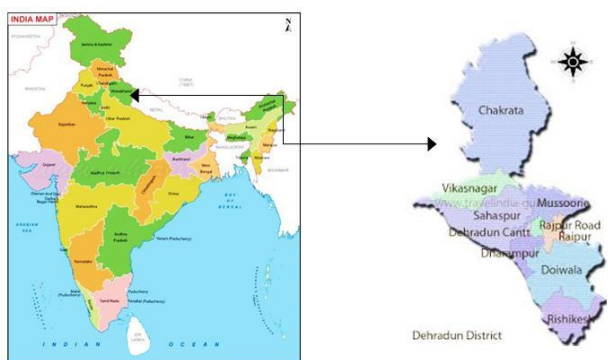


Figure 1: Study Area (source – openstreetmap.org)

The Open Data Kit (ODK) community produces free and open-source software for collecting, managing, and using data in resource-constrained environments. It allows the collection of data offline and submit the data, when internet connectivity is available. It allows communities to aggregate data with full control over the collected data and the servers, where the aggregated data is stored. Components of ODK are as follows -

2.1. ODK Build:

Component is used for designing a questionnaire for ODK. It works as a drag-and drop form designer for ODK XForms. It is used for data collection campaign e.g. for Health Sites

2.2. ODK-Sensor:

Used for Open data kit sensors for mobile data collection with wired and wireless sensors that submit the data to the mobile device and collect the data on the mobile device.

2.3. ODK-Briefcase:

ODK can collect the database records with GPS coordinates on a mobile device. ODK Briefcase is a Java application for fetching and pushing forms and their contents. With briefcase helps make billions of data points from ODK portable and use the data points e.g. for Decision Support Systems.

2.4. ODK Aggregate:

The ODK Aggregate is the backend of ODK infrastructure, receiving the data from the mobile devices. To be multiplatform it is designed as Open Source Java server that stores, analyses,

and presents survey data. Decision support is built on the collected data.

2.5. ODK Collect:

ODK Collect is an open source Android app that replaces paper forms used in survey-based data gathering. It supports a wide range of question and answer types, and is designed to work well without network connectivity.

ODK Collect renders forms into a sequence of input prompts that apply form logic, entry constraints, and repeating sub-structures. Users work through the prompts and can save the submission at any point. Finalized submissions can be sent to (and new forms downloaded from) a server.

3. METHODOLOGY

3.1 Making of Questionnaire

Based on WHO guidelines, total nine questions have been made to check the depression status of a patient. These questions cover different physiological, psychological state of a patient. It also covers details of daily life routine. The questions are –

- i. Do you feel depressed, irritable or hopeless?
- ii. Do you find difficulty in concentrating?
- iii. Do you feel trouble in falling asleep, staying asleep or sleeping too much?
- iv. Are you having poor appetite, weight loss or over eating?
- v. Do you feel tired or exhausted easily?
- vi. Do you feel bad about yourself?
- vii. Do you have trouble in speaking to your regular friends?
- viii. Do you have thoughts that you would be better off dead or of hurting yourself in some way?
- ix. Do you feel anxiety just after waking up in the morning?

To make this questionnaire online a vector layer is created in QGIS and different attributes which describes the patient such as name, age, gender, occupation, email has been added in it. Also each question is added as a separate attribute. Three options yes, no, don't know are added in the value map for these questions.

After creation of the layer, it is made online using QRealTime plugin of QGIS. An ODK server is created for storing inputs from clients and that server address is put as the QRealTime server to fetch the data directly from the server to QGIS.

3.2. Client Data Input

The client need to install the ODK Collect mobile application from Google Play Store to submit his/her answers. After installing, he should put the ODK server address where the form is stored. Then the form appears with the name that is given in the QGIS layer. The client need to fill the form and also answer the questions given. The location of client is automatically detected by the application. After submitting the form, the details have been stored in the ODK server with location details.

3.3. Acquire Doctor Details

An ODK form has been made to get the details of the existing doctors in the city. It make it scalable according to study area. The attributes present in the form are – Name, Email, Phone, Location, Appointment Time/Date, and Photo. The doctors have to fill the form using ODK Collect mobile application. The

location is automatically detected by this application. Based on that, the nearest doctor is chosen for a client.

3.4. Storing into Database

The client form and the doctor form both are stored in the ODK server. Through QRealTime plugin of QGIS, the doctor form is imported in QGIS as a vector layer. Also both forms are set to update in a specific time interval. If a new data is stored in the server, the plugin will automatically update the layers to their current version. Now using DB Manager, both layers are imported to PostgreSQL.

This PostgreSQL need to be PostGIS installed to support geospatial table. As two separate tables of client and doctor are created in the database, data is updated after specific time interval as discussed in previous section. In these tables, a geometry column is present to store the location details in hexadecimal format.

3.5. Web Client

As the clients fill up the questionnaire using application, they have to check the status whether he/she is suffering from depression or not. So a web client is made using HTML, JavaScript, and CSS. Here possible causes and different types of depression and how to avoid it is described. Clients can check their status by providing email. Based on their responses, a criteria is formed. Using that a SQL query execute in the database and a patient is marked as a depression patient if his/her response is higher than the criteria.

Then the nearest doctor details is retrieved from database comparing the client's location with all doctor's location and it is shown on map. Also using Leaflet API, the shortest route from the client's position to the doctor's chamber and the navigator is shown so that he/she can take immediate action. In this web client the location of all doctors is also shown so that anybody can reach to any of the doctors.

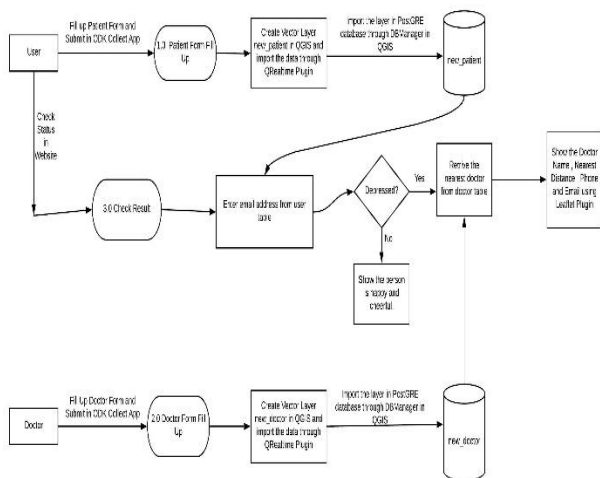


Figure 2: Data Flow Diagram

4. RESULTS AND DISCUSSION

The client need to install the ODK Collect web application and fill up the form. It includes Name, Age, Gender, Occupation, Email and the questionnaire. Similarly a separate form is made for doctors where Name, Phone Number, Email, Appointment Time, Photo is included.

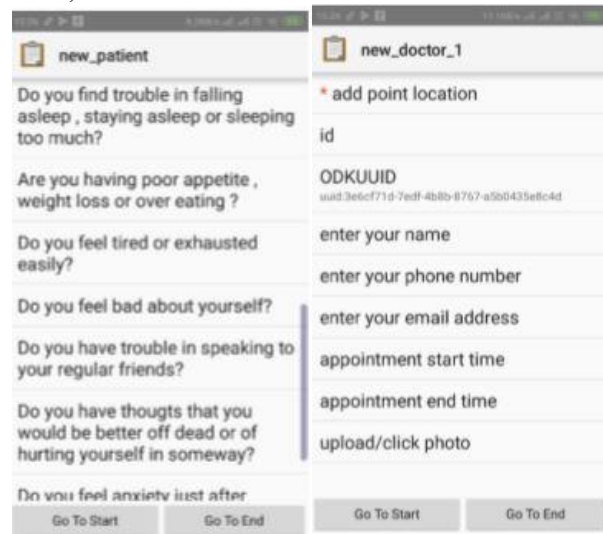


Figure 2: ODK Collect Patient and Doctor Form

The data stored in ODK server is imported in QGIS using QRealTime plugin. It is also getting updated when a new data is added in the server.

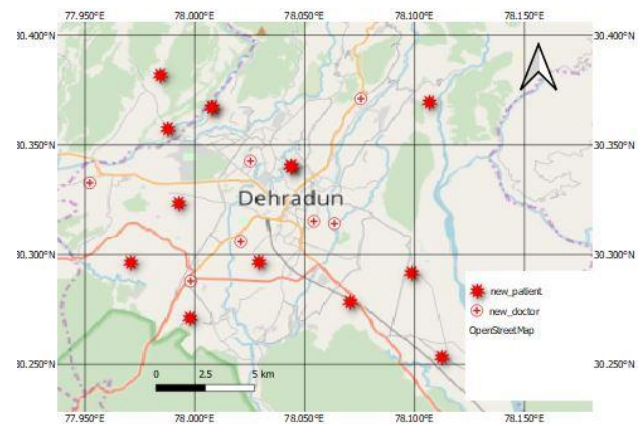


Figure 3: Map showing location of patient and doctors

A web client is developed to check the status of the client. The web client consists of different sections like depression types, how to avoid depression and check status.

WEB BASED INFORMATION SYSTEM USING GIS FOR RURAL DEVELOPMENT

Ashish Mani¹, Dharmendra Kumar², Deepak Kumar³

¹M.Sc. (GIS & RS), Student, Amity Institute of Geo-Informatics and Remote Sensing (AIGIRS), Amity University-Sector 125-NOIDA- 201303, Gautam Buddha Nagar, U.P., India. Phone No.: +91-9758502028. (e-mail: manishish6@gmail.com)

²Scientist/Engineer-SE, Indian Institute of Remote Sensing (IIRS), ISRO, 4 Kalidas Road Dehradun-248001. Phone No.: 0135-2524342 (e-mail: dharmendra@iirs.gov.in)

³Assistant Professor, AIGIRS, Amity University, Noida, 201303. Phone No.: +91-9448675499 (e-mail: deepakdeo2003@gmail.com)

KEY WORDS: Web GIS, Web Maps, Rural Development, Open Source Data, Web Designing & Database Management System

ABSTRACT:

"Web based geographic information system for rural development" is a GIS based application which gives comprehensive spatial information relating to demography, infrastructures, utilities and natural resources for a specific Village, City, Tehsil, District. Utilizing techniques of remote sensing and GIS on spatial domain, a spatial database is arranged, this database is then examined in a web GIS stage to make thematic maps. When the maps are prepared, they are distributed over Internet on an easy to understand interface. User can peruse through the interactive maps and get comprehensive spatial information. User can likewise make questions to get some explicit information, download maps, etc.

1. INTRODUCTION

1.1 Web Based Geographic Information System

Remote Sensing technology and Geographic Information System are unquestionable profitable instruments for assembling and investigating spatial data with remarkable pace [6]. Generally, these data innovations are not "open" to general users. That is, they are not in themselves ready to convey the data substance to a wide scope of users. For that we have to create application programming software tools available by means of intranet or web programs. This suggests some pre-processing of the data so it tends to be effectively exhibited, visualized, controlled and downloaded. As of late Internet has been getting the creative ability of mainstream researchers, which when converged with GIS has brought about the following technological advancement "Web GIS". This is a practical innovation in which the user does not need to spend on purchasing GIS programming and looking after them. Also, it has turned into a generally used instrument for simple access and spread of spatial and non-spatial data [5].

GIS based spatial planning is currently a generally acknowledged approach to deal with complex administration and decision-making issues of resource. The requirement for a sustainable information system is progressively being felt in every single natural resources and development activities, be these for urban or rural areas for sustainable planning.

The rise of Remote Sensing and Geographic Information System as an amazing tool for spatial examination and capacity has made computerization of the spatial information increasingly helpful. This new innovation can decrease the time and cost to the planners in arranging the information and arriving at exact resolution and choice. The sustainable development challenge is to advance regularly clashing requirements and demands.

1.2 Open Source Softwares (OSS)

Private venture or organizations are continually searching for approaches to save time and cut the working expense of their business. One approach to do this is by utilizing open source software (OSS) to maintain their business. Open Source Software (OSS) are the software that are freely available for public in the internet Firefox, Google Chrome etc. are the

popular examples of Open Source Software. In term of GIS (QGIS) is the popular example.

The Open Source GIS Software's are based on different base programming language. Three main groups of open source GIS in terms of programming languages are: 'C' Language, JAVA and .NET. Well known 'C' Language based Open Source GIS Software application incorporate GRASS and QGIS.

Uses of Open Source GIS Software:

1. Open Source GIS Software would enable analysts and solution developer entrance to a more extensive scope of devices than what is as of now offered by the business organizations.
2. Open Source GIS Software devices resolve the "Learning hole" during the time spent getting data from images and digital maps.
3. Open Source GIS Software save time and reduce the operating costs.

1.3 Web Maps

A Web based interactive map is known as web maps. A map created in one application is accessible and looks the same in other applications that implement the web map specification. Web maps can be invoked using a standard web browser by submitting requests in the form of Uniform Resource Locators (URL). The content of such URLs depends on which operation is requested. Now a day, web maps are used across many platforms in GIS field. It reduces development time without compromising a developer's flexibility.

1.4 Web Designing

Web designing is the way toward creating websites. It surrounds number of different features, including webpage layout, content creation, and computerization of visual things. The terms website designing and web development are regularly exchangeable but, in fact website designing is a subset of the more considerable class of web development. Hypertext Markup Language (HTML) are made for utilizing websites. Website designers excogitate site pages by bring into play HTML labels that characterize the materiality and metadata of each page. The structure and existence of the components inside a site page are ordinarily identified using (Cascading Style Sheets) CSS, or falling templates. Accordingly, many websites incorporate a

mix of HTML and CSS that specifies how each page will look in a program. Some website designers like to hand code pages (composing HTML and CSS from scratch), while others utilize a "WYSIWYG" editor like Adobe Dreamweaver. This kind of editor gives a visual interface to planning the website page format and the product consequently creates the compatible HTML and CSS code. Another prevalent method to design a website is with the content management framework like WordPress or Joomla. These administrations give different web layouts that can be utilized as a beginning stage for brand site. Website admins would then be able to include content and modify the design utilizing an online interface. While HTML and CSS are utilized to plan the appearance & layout of a site, pictures must be made independently. In this way, visual depiction may cover with website composition, since visual planners regularly make pictures for use on the Web. A few illustrations programs like Adobe Photoshop even incorporate a "Save for Web..." choice that gives a simple method to send out pictures in an arrangement upgraded for web distributing.

1.5 Database Management System

A database management system (DBMS) is framework software for making and controlling databases. The DBMS gives clients and developers a precise method to make, recover, update and oversee data or information.

A DBMS makes it feasible for end clients to make, read, update and erase information in a database. The DBMS basically fills in as an interface between the database and end clients or application programs, guaranteeing that information is reliably composed and remains effectively attainable.

The DBMS controls three critical things: the information, the database engine that enables information to be gotten to, bolted and altered - and the database construction, which characterizes the database's legitimate structure. These three central components help give simultaneousness, security, information uprightness and uniform organization strategies. Commonplace database organization errands upheld by the DBMS incorporate change management, execution observing/tuning and reinforcement and recuperation. Numerous database management systems are likewise in charge of robotized rollbacks, restarts and recuperation just as the logging and examining of movement.

1.6 Role of GIS in Web-Based Information System for Rural Development

Geographic Information System (GIS) is the propelled PC based strategy in geology as well as in all fields of science [3]. Web based GIS for rural development is a GIS application and is inadequate without the use of GIS and RS innovation. It is intended to store colossal information in computerized group and keep up databases identified with tehsils, towns and villages. The rise of RS and GIS as a useful asset for spatial investigation and capacity has basically eased the issue by computerization of the spatial information [4].

As we know GIS technology integrate normal database activities, for example, question and statistical analysis with the extraordinary representation and geographic analysis benefits offered by maps. There are different sources where we can use GIS in web-based information system.

1.6.1 Utility Mapping

1.6.1.1 Transportation Network

Different facilities like transportation networks, electricity, gas pipelines, health & education facilities are generally use for

utility mapping. One of the major components is transportation network or we can say that roads and railways are the lifeline of the city. It connects us from one facility to another. In urban planning or development transportation networks plays an important role. The major part of the economy is depending on the road and rail networks.

GIS is the suitable approach of the road mapping. Using latest satellite imagery or a base map user can easily digitize a roads and rails shapefile. These shapefiles can be helpful in creating a route map through which user can avail the information for urban and rural development.

1.6.1.2 Electricity Facilities

City growth by some means depends on the Electricity facilities. Good electricity network with latest power grids lines and more power stations can defines the city or village growth. The thematic map of these facilities can be created from the high-resolution satellite imagery and field survey.

1.6.2 Census Information

Census information web maps with graphs can be prepared based on data availability from the Census of India website that includes Total Population, Households, Literacy, Illiteracy, Working and Non-Workers Classification [1]. These information's are mandatory for the rural and urban development.

1.6.3 Land Use / Land Cover Mapping

Land use is an essential component of web-based information system for rural development which will be used as a basic unit in conjunction with other natural resources as well as socio-economic data for land and water resource development.

Land Use / Land Cover mapping can be done using satellite imagery. Visual Interpretation techniques and adequate verifications can be considered to identify various land use / land cover classes.

1.6.4 Watershed Mapping

Micro-Watershed is an essential unit for overall development of water resources of the particular area. A watershed encompasses information on all resources related to Geology, Geomorphology, Land, Water, Forests, Soil, Agriculture, etc. The Integration of these sets of information would aid the decision-makers and development process for systematic resources utilization and sustainable development of rural areas.

In watershed mapping, drainage map is going to be prepare with stream order. There are different sources where we can use GIS in web-based information system.

Slope and Aspect map can also be prepare under watershed mapping which tell user about the slope steepness / gentleness and direction of the slope.

1.6.5 Soil Mapping

Soil is an important land resource. Soil map can be prepared by using satellite imagery. Soil map is made and interpreted as per the user needs like soil irrigation classification, soil site suitability for different crops, soil fertility status, soil erosion status, and land capability classification.

1.6.6 Drainage Density Mapping

Drainage density is the complete length of the considerable number of streams in a basin divided by total area of the basin. It is a proportion of how well or how inadequately a watershed is depleted by stream channels. Drainage density relies on both atmospheric and physical characteristics of the basin. Through

mapping of drainage density, we can easily calculate the drainage density of a particular area. High drainage density suggests decrease in surface runoff, slope is gentle, high infiltration and also indicates greater flood risk where as low drainage density suggests increase in surface runoff, low infiltration, slope is steep and also indicates lesser flood risk

1.6.7 Ground Water Level Mapping

Groundwater is an essential natural resource beneath the earth surface. Groundwater levels are a marker of the measure of groundwater in aquifers and shallower water tables. Ground water level mapping helps in monitoring the ground water level of each dug well and tube wells.

The current work is tried to create a web based geographic information system which contain relevant information regarding rural development of different tehsils. In this work, there are different sources where we can use GIS as a web-based information system.

S. No	Sources
1	Census Information
2	Drainage Density
3	Ground Water Level
4	Land Use/Land Cover
5	Soil
6	Utilities Information
7	Watershed

Table 1. Sources for Web Based GIS

The web maps of these sources have been created in open source software for different tehsils. After which, an information system in a form of website has been arranged using HTML and CSS coding which contain GIS relevant information.

2. OBJECTIVE

1. Procurement of spatial and non-spatial data relevant to my study area.
2. To develop an interactive web map using free and open source GIS software (QGIS).
3. Display the web map as a web based geographic information system for rural development in a form of website using HTML, CSS coding.
4. Hosting the website on web.

3. STUDY AREA

The study area consists of two districts of Uttar Pradesh. First district Amethi lies at the latitude 26.1541° N and longitude 81.8142° E at an average height of 101 meters from mean sea level. The complete geographic area of Amethi district is around 3063 sq.km. The surface is commonly level, being broken just by gorges in the area of the streams. The main stream is Gomti, which goes through the focal point of the area. North side of this locale is limited by Faizabad District; South side is limited by Pratapgarh District. West side is limited by Bara-Banki District and Rai Bareilly District and the East side is limited by Sultanpur District. Amethi region has a wet and dry atmosphere with normal temperatures running between 23 °C to 28 °C. Another district Sultanpur lies at the latitude 26.2648° N and longitude 82.0727° E at an average height of 96 meters from mean sea level. The complete geographic territory of the areas is about 2672.89 sq.km. The surface is commonly level, being broken just by gorges in the area of the streams. The focal part is very developed, while in the south is across the board parched

fields and swampy bogs. Small rivers are the Kandu, Pili, Tengha and Nandhia. The area Sultanpur is limited by Faizabad locale in the north; Pratapgarh region in the south, Bara-Banki and Amethi Districts in the west and Azamgarh, Ambedkar Nagar and Jaunpur Districts in the East. The atmosphere of Sultanpur is semi-bone-dry with sweltering summer and similarly chilly winter season. Amid the late spring months for example May-June, the greatest temperature goes past 44 °C and in winter a long time of December and January, it is around 3-4 °C.

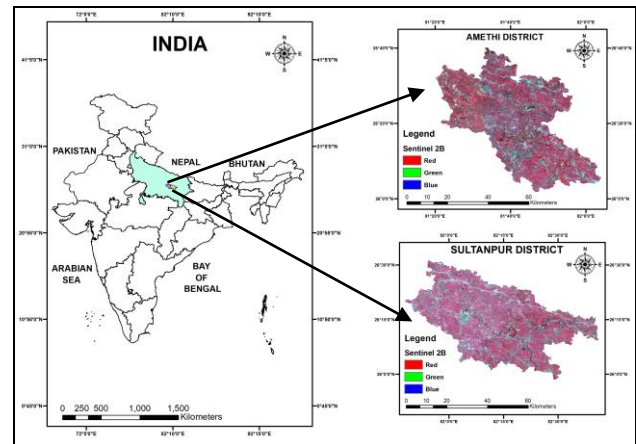


Figure 1. Study Area

4. METHODOLOGY

4.1 Collection of Data

(Table 2) below showing the collection of data from different source:

S No.	Data Category	Source
1	Census Information	http://censusindia.gov.in/
2	Watershed Delineation	DEM Data from https://earthexplorer.usgs.gov/
3	Ground Water Level	http://cgwb.gov.in/
4	Land Use and Land Cover	Sentinel 2B Data of date (19-01-2019) from https://earthexplorer.usgs.gov/
5	Soil Information	India Soil Shapefile provided by IIRS
6	Utilities Information	https://www.openstreetmap.org/
7	Drainage Density	DEM Data from https://earthexplorer.usgs.gov/

Table 2. Collection of Data

4.2 Import to Spatial Domain

The spatial domain is where a digital picture is characterized by the spatial directions of its pixels, means an image contain x, y coordinate or contains DN values for each pixel. After the invent of satellite imagery the use of satellite imagery is increasing day by day. This results in more and more use of GIS software. Now a days, there are so many GIS software like (Arc GIS, ERDAS Imagine, QGIS, Map info etc.). Here I have use Arc GIS, ERDAS Imagine and QGIS Software as per the requirement of my work.

All the spatial information and non-spatial information relevant to my study area has been imported to a spatial domain using an Arc GIS software. Census information excels and ground water level excels has been converted into software Supported (CSV) Comma Separated Value format. As we convert these .xls files into .csv files, the complete information of these files is opened in Arc GIS software which can be easily manipulated.

4.3 Process of Data Handling and visualization

After the data has been imported in spatial domain, the next step is data handling and visualization. Data Handling and visualization is directly related to the project objective. Here, my project objective is to create a web based geographic information system for two district Amethi and Sultanpur. So, I have to create separate maps and web maps from different sources for each tehsil in both districts. And then create an information system in a form of website.

S. No	Tehsil in Amethi	Sources
1	Amethi	Census Information, Watershed, Ground Water Level, LULC, Soil, Utilities and Drainage Density
2	Gauriganj	Census Information, Watershed, Ground Water Level, LULC, Soil, Utilities and Drainage Density
3	Musafirkhana	Census Information, Watershed, Ground Water Level, LULC, Soil, Utilities and Drainage Density
4	Tiloi	Census Information, Watershed, Ground Water Level, LULC, Soil, Utilities and Drainage Density

Table 3. List of Tehsil in Amethi with Sources

S. No	Tehsil in Sultanpur	Sources
1	Kadipur	Census Information, Watershed, Ground Water Level, LULC, Soil, Utilities and Drainage Density
2	Sultanpur	Census Information, Watershed, Ground Water Level, LULC, Soil, Utilities and Drainage Density

Table 4. List of Tehsil in Sultanpur with Sources

4.4 Database Creation

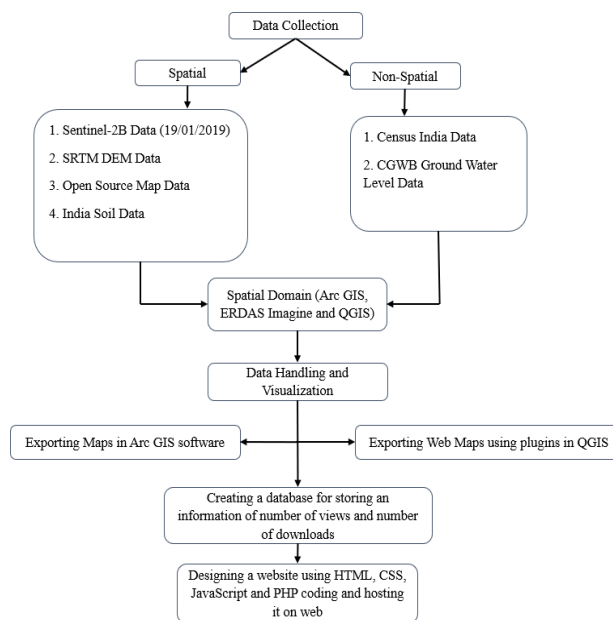
As we all know that database gives clients and developers a precise method to make, recover, update and oversee data or information. Here, a database with name “wbgis” has been created in MYSQL. This database has a table with name “Counter” which store all the information of number of persons who hit or view the website and download the maps. By creating this database viewer can be able to see the number of views in this website and number of maps has been downloaded.

4.5 Process of Designing and Developing a Website

Designing and developing a website is an interesting task. Both tasks needed patience which is a key and off course a good knowledge of programming language like HTML (Hypertext Markup Language), CSS (Cascading Style Sheets), JavaScript etc. There are different types of method to design a website. For example, designed your own website and develop a html code with our self or else design a website with the help of template like WordPress with contain its own code. The purpose of developing and designing a website for this project is to make an information system which collaborate all the relevant GIS information in a form of maps & graphs and the user who is viewing this website can download the maps and understand the use of GIS in rural development.

For this present study the website has been designed by my own website template which contain a coding of HTML, CSS and JavaScript. The coding of HTML, CSS has been developed by myself. A little but important use of PHP (Hypertext preprocessor) code also used to display a number of views in a website. Finally, to make the website live, hosting the web site on web.

4.6 Flow Chart of Following Methodology



5. RESULT AND DISCUSSION

After all the hard work completed above, finally a website (wbgis.co.in) has been developed which is showing the web based geographic information system for rural development.

5.1 Site Map for the website

A site map is a model of a site's substance intended to support both clients and web indexes explore the website. Site map is of many types for example a jpeg, a HTML page etc. Here, a jpeg of a site map has been created which is showing all the information of the website.

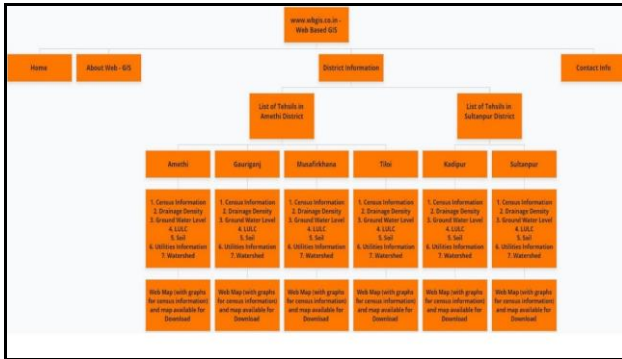


Figure 2. Site Map

5.2 Home page

The introductory page of a website, which have table of contents for the site. For this website there are 5 table of contents – Home, About Web-GIS, District Information, Contact Info and Site Map (which was already mentioned above). On clicking on home button user or viewer will return back to the home page.



Figure 3. Site Map

5.3 About Web-GIS page

This page is displaying the information about Web-GIS which include the role of GIS in developing rural areas and transforming them into an urban planned area.



Figure 4. About Web-GIS

5.4 Contact Info Page

This page contains the contact information of designer like mobile number, email and designer profile. Viewer can see that the number of profile viewers is increasing as the user is clicking on “click here” button.



Figure 5. Contact Info

5.5 District Information Page

This page contains the detailed information of all the tehsils present in both Amethi and Sultanpur District.



Figure 6. District Information

The District Information page contains two button which is named as “Amethi” and “Sultanpur”. On clicking on these buttons, the new page is open on same page on the right side of these buttons which contain list of tehsils in these two districts.



Figure 7. List of Tehsils

Now, click on any of these tehsils' buttons. The new page will open on new window which contain the information of different sources (Census Information, Drainage Density, Ground Water Level, LULC, Soil, Utilities Information and Watershed) in a form of Graphs (only for Census Information), Web Maps and Maps.

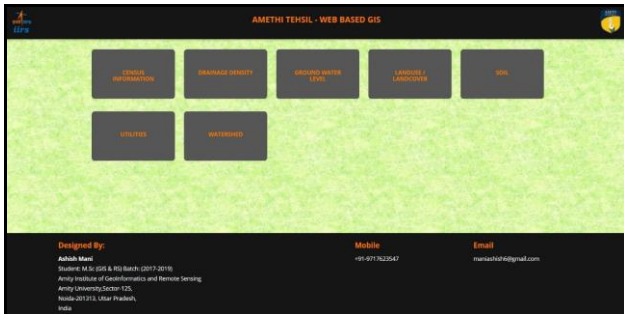


Figure 8. Amethi Tehsil

Different Web page of different tehsils is open on new windows which display the same information with different spatial information.

5.5.1 Amethi Census Information

Further clicking on census information button, the new page will open, which holds the web map of Amethi census information and graphs relevant to web map.

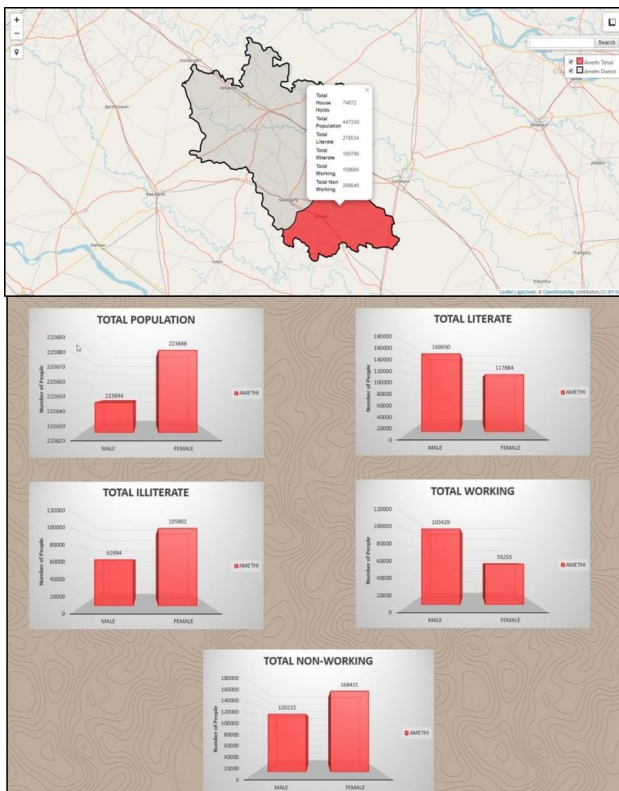


Figure 9. Census Information web map with graphs

The web map above on (Figure. 9), holds census information such as number of households, total population, total literate, total illiterate, total working and total non-working and also

holds graphical information which display web map information in gender (male & female) form. This web page helps the viewer to view Amethi tehsil census information in an easy and an interactive way as compare with the census information present in Census India official website. Side by side this web page also holds the graphical information which make this site more feasible. Similarly, web map with graphs also created for other tehsils.

5.5.2 Amethi Drainage Density

Next button holds spatial information of drainage density which will open on new page. This page has a web map of Amethi Drainage density with download button option.

The (Figure. 10) below, represents the Amethi drainage density web map which displaying the drainage density in three classes: low = green colour, medium = yellow colour & high = red colour and another map represents the drainage density map which can be downloaded from this web page and was created in Arc GIS software.

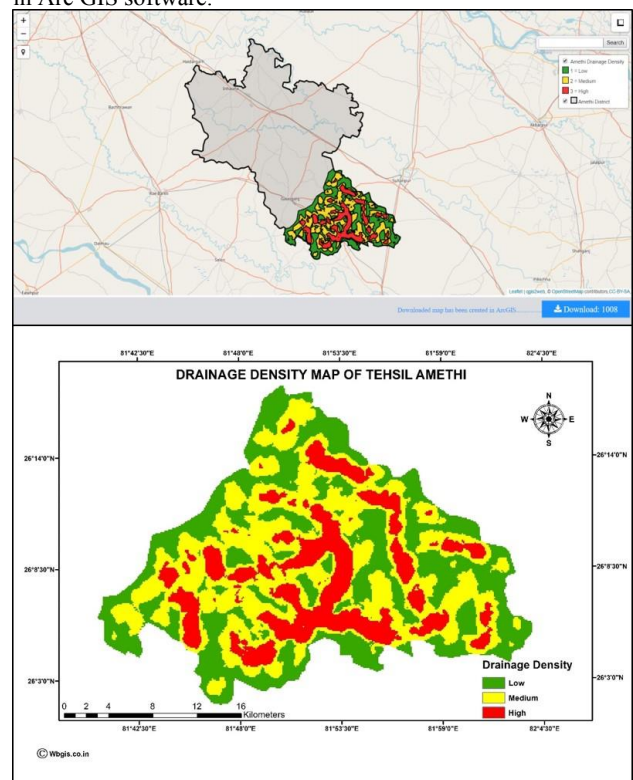


Figure 10. Drainage Density Web Map

Drainage density is the complete length of the considerable number of streams in a basin divided by total area of the basin. It is a proportion of how well or how inadequately a watershed is depleted by stream channels. Drainage density relies on both atmospheric and physical characteristics of the basin. Through mapping of drainage density, we can easily calculate the drainage density of a particular area. High drainage density suggests decrease in surface runoff, slope is gentle, high infiltration and also indicates greater flood risk where as low drainage density suggests increase in surface runoff, low infiltration, slope is steep and also indicates lesser flood risk. High drainage densities also mean a high bifurcation ratio. User can download drainage density map for the above purpose's like flood risk mapping, landslide prone area mapping etc. Similarly, drainage density web maps for other tehsils have been created

and also these web maps contain download option which contains drainage density map created in Arc GIS.

5.5.3 Amethi Ground Water Level

Next button holds spatial information of ground water level which will open on a new page. This page has a web map of Amethi ground water level with download button option.

The (Figure. 11) below, represents the Amethi Ground Water Level web map which displaying the Dug well information including ground water level and another map represents the ground water level map which can be downloaded from this web page and was created in Arc GIS software.

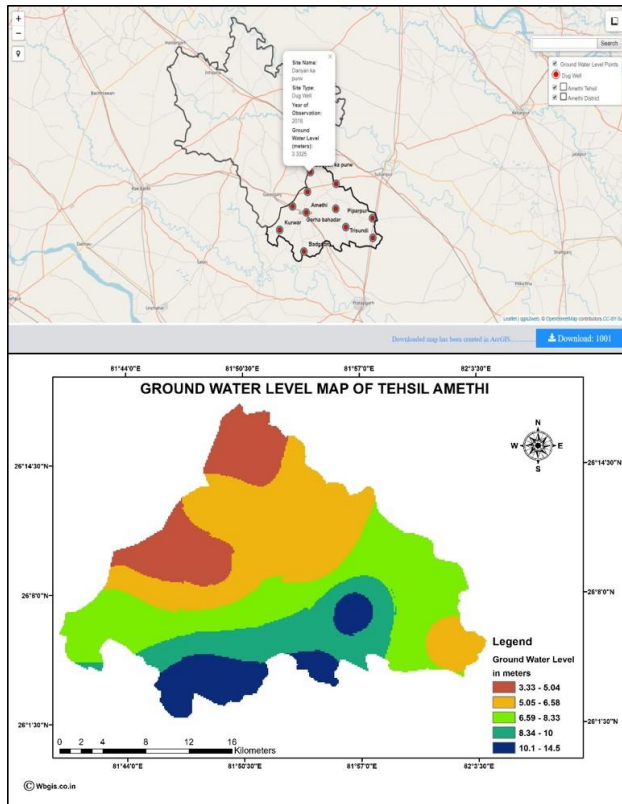


Figure 11. Ground Water Level Web Map

Groundwater is an essential natural resource beneath the earth surface. Groundwater levels are a marker of the measure of groundwater in aquifers and shallower water tables. Ground water level mapping helps in monitoring the ground water level of each dug well and tube wells. Through this web map we can easily see the Amethi tehsil dug well ground water level and through downloaded map we can easily view the ground water level in meters in whole Amethi Tehsils. Similarly, ground water level web maps for other tehsils have been created and also these web maps contain download option which contains ground water level map created in Arc GIS.

5.5.4 Amethi Land Use/Land Cover

Next button holds spatial information of LULC which will open on a new page. This page has a web map of Amethi LULC with download button option.

The (Figure. 12) below, represents the Amethi LULC web map which displaying the land use and land cover information and another map represents the LULC map which can be downloaded from this web page and was created in Arc GIS software.

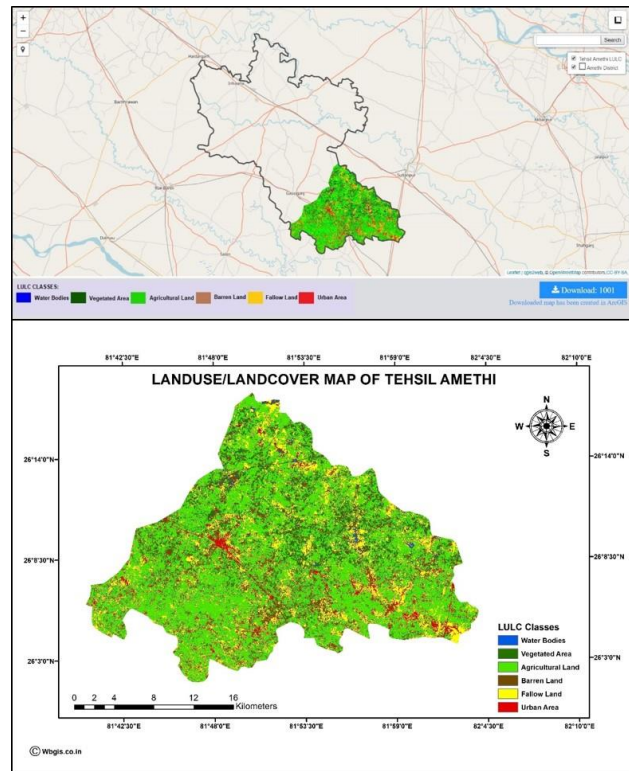


Figure 12. LULC Web Map

As we know that Land Use/Land Cover (LULC) are influenced by human intercession and characteristic phenomenon, such as agricultural interest and exchange, population development and utilization patterns, urbanization and economic advancement, science and innovation, and different variables. As an outcome, data about LULC is fundamental for any sort of natural resource management and action planning. This Amethi LULC map was classified into six classes (vegetated area, barren land, fallow land, agricultural land, urban area and water bodies). Similarly, Land Use/Land Cover (LULC) web maps for other tehsils have been created and also these web maps contain download option which contains LULC map created in Arc GIS.

5.5.5 Amethi Soil

Next button holds spatial information of soil which will open on a new page. This page has a web map of Amethi soil with download button option.

The (Figure. 13) below, represents the Amethi soil web map which displaying the detailed soil information and another map represents the soil map holds soil surface texture information which can be downloaded from this web page and was created in Arc GIS software.

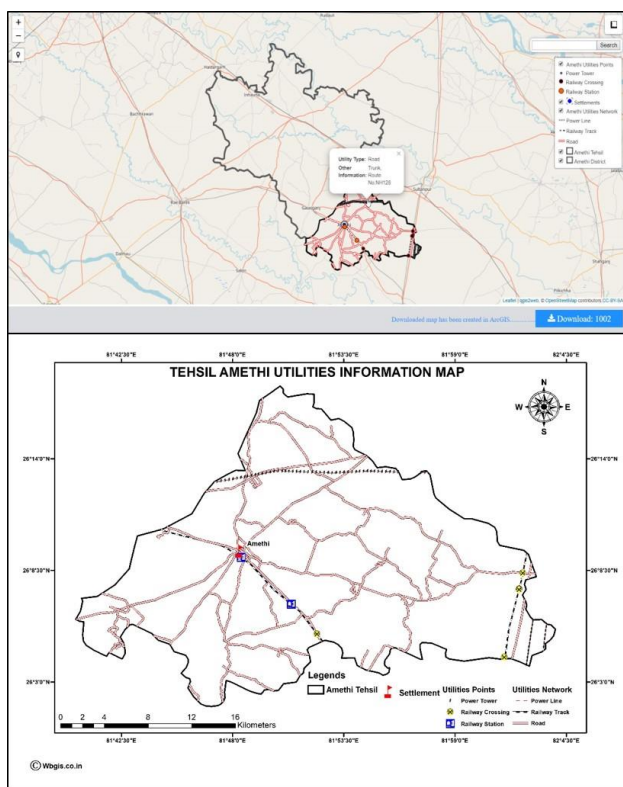


Figure 13. Soil Web Map

Soil is an important land resource. Soil map can be prepared by using satellite imagery. Soil map is made and interpreted as per the user needs like soil irrigation classification, soil site suitability for different crops, soil fertility status, soil erosion status, and land capability classification. This Amethi soil web map holds information of Soil characteristic. Similarly, Soil web maps for other tehsils have been created and also these web maps contain download option which contains soil map created in Arc GIS.

5.5.6 Amethi Utilities Information

Next button holds spatial information of utilities which will open on a new page. This page has a web map of Amethi utilities information with download button option.

The above (Figure. 14) below, represents the Amethi utilities web map which displaying the detailed utilities information and another map represents the utilities map which can be downloaded from this web page and was created in Arc GIS software.

A utilities maps demonstrates the positioning and distinguishing proof of streets and electricity links over and under the grounds. The system includes recognizing things like sewers, electric links, telecoms links, road burrows. Join this mapping procedure with a geological overview and the outcomes will give you a comprehensive detailed map of whatever is concealed underground or legitimately identified with any over the ground highlights. Utility maps are significant whenever you are getting things started as they show exact places of the utilities you will experience. It likewise prevents harming any utilities that may make hurt people in general or your workforce. This Amethi utilities web map and Amethi utilities map which was downloaded from download option shows the road network, electricity poles, electricity cables, railway station and railway crossing information of entire Amethi tehsil.

Similarly, utilities web maps for other tehsils have been created and also these web maps contain download option which contains utilities map created in Arc GIS.

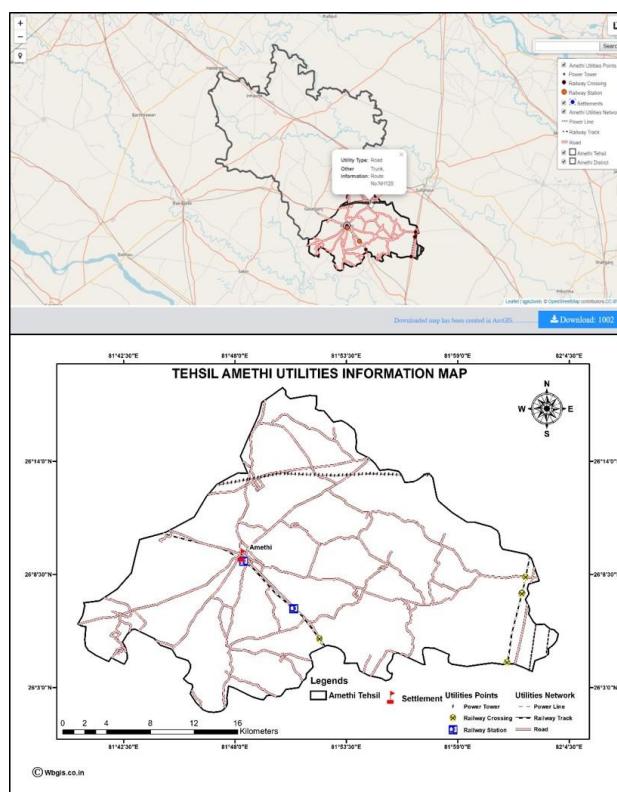


Figure 14. Utilities Information Web Map

5.5.7 Amethi Watershed

Next button holds spatial information of watershed which will open on a new page. This page has a web map of watersheds in Amethi with download button option.

The (Figure. 15) below, represents the Amethi watershed web map which displaying the detailed watershed information such as stream order, watershed basin and another map represents the drainage map with stream order which can be downloaded from this web page and was created in Arc GIS software.

Watershed is an essential unit for overall development of water resources of the particular area. The Integration of sets of information like soil, drainage, stream order, slope and aspect would aid the decision-makers and development process for systematic resources utilization and sustainable development of rural areas. Here the watershed web map of Amethi tehsil is displaying the stream order and stream length of each stream in entire Amethi tehsil. This information helps a decision-makers for systematic resource utilization and sustainable development of rural areas. They can also download the drainage map with stream order for their records.

Similarly, watershed web maps for other tehsils have been created and also these web maps contain download option which contains watershed map created in Arc GIS.

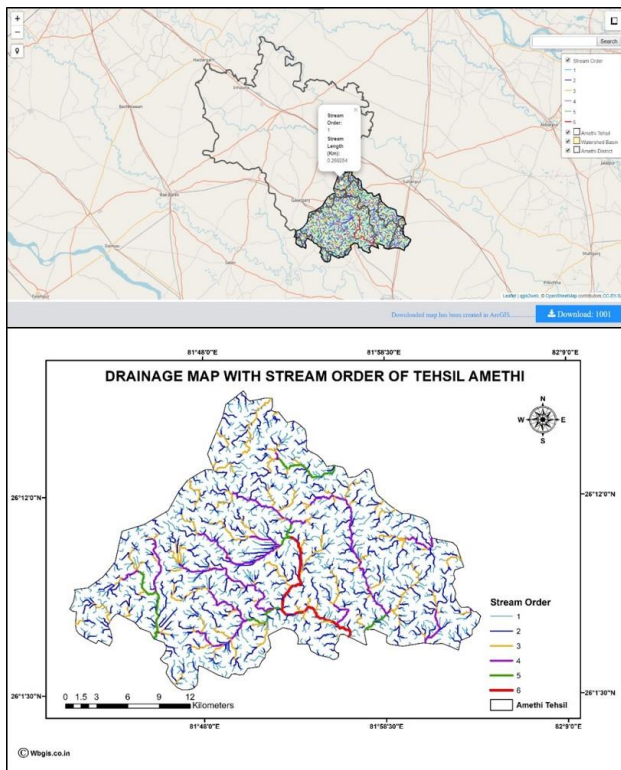


Figure 15. Watershed Web Map

6. CONCLUSION

The present study stresses the intensity of web-based GIS innovation which will help the leaders at tehsil level to more readily comprehend and assess spatial information by making realistic presentations utilizing data stored in the database. The geovisualization likewise gives the gap of facilities inside the topographical area and this investigation additionally proposed the required facilities for rural development.

A web-based Geographic information system will help the government in arranging, execution and observing of different rural development projects for advancement in various fields at a lot quicker rate which thus will make the tehsils, districts or even state innovatively more developed. This analysis has affirmed the requirement for spatial arranging, which can accomplish the ideal aftereffects of economic, social collaboration and overall improvement of a locale. This investigation includes a website which contains spatial information in a form of web maps for rural development.

This GIS database will be altered to meet the necessities of partner divisions/worried in giving the advanced asset databases and some other necessities of the tehsils, based on their issues/need/formative projects at village/ tehsil level.

This information can also be useful in future when a website might be planned exclusively to show all the information present in this website. Many of the ongoing projects can benefit from this, as a web map makes a site look more interesting and appealing to the visitors.

ACKNOWLEDGEMENTS

I want to give my special thanks to my faculty Assistant Professor Dr. Maya Kumari for her direction and her support in this project. I also want to give my true appreciation to Mr. Gaurav Chaurasia for helping me with the programming aspect.

REFERENCES

- [1] Censusindia.gov.in. (2019). Census of India: C.D. Block Wise Primary Census Abstract Data (PCA). [online] Available at: http://censusindia.gov.in/pca/cdb_pca_census/Houselisting-housing-UP.html [Accessed 10 February. 2019].
- [2] W3schools.com. (2019). HTML Tutorial. [online] Available at: <https://www.w3schools.com/html/> [Accessed 13 April 2019].
- [3] Simhachalam Alajangi, Kesava Rao Pyla, Amminedu Eadara, Prasad N S R. (2016). Web GIS based Information System for Rural Development. International Journal of Science and Research (IJSR), 5(5), pp.2469-2475.
- [4] M. Ozturan, B. Egeli, F. Bacioglu. (2004). Web-GIS based urban management information system: the case of satellite cities in Istanbul. WIT Transactions on information and communication technologies/32/14258.
- [5] Devalt.org. (2019). Web based Village Information System. [online] Available at: https://www.devalt.org/newsletter/jun10/of_3.htm [Accessed 7 January 2019].
- [6] Richard Scaria, Vijayan P. K. (2012). Sustainable rural development with the application of Spatial Information Technology and Mahatma Gandhi national rural employment guaranteed scheme. International journal of geomatics and geosciences Volume 2, No 4.
- [7] Gadm.org. (2019). GADM. [online] Available at: <https://gadm.org/> [Accessed 5 February 2019].
- [8] Diva-gis.org. (2019). Free Spatial Data | DIVA-GIS. [online] Available at: <http://www.diva-gis.org/Data> [Accessed 10 February 2019].
- [9] Survey, U. (2019). Earth Explorer - Home. [online] Earthexplorer.usgs.gov. Available at: <https://earthexplorer.usgs.gov/> [Accessed 4 February 2019].
- [10] Anon, (2019). [online] Available at: <http://jsac.jharkhand.gov.in/> [Accessed 13 April 2019].

APPENDIX

QR code of a website has been given below:



ANALYSIS OF MULTIPLE COMPONENT SCATTERING MODEL DECOMPOSITION

Bhanu Prakash M. E.^{1*}, Shashi Kumar²

¹Dept. of Photogrammetry and Remote Sensing, Indian Institute of Remote Sensing, Dehradun, India-
bhanuprakashme28@gmail.com

²Dept. of Photogrammetry and Remote Sensing, Indian Institute of Remote Sensing, Dehradun, India-shashi@iirs.gov.in

Commission VI, WG VI/4

KEYWORDS: Synthetic Aperture Radar (SAR), polarimetric SAR decomposition, cosine square distribution, multiple component scattering model, patch analysis.

ABSTRACT:

Polarimetric Synthetic Aperture Radar (SAR) decomposition is the process of extracting the characteristics of terrain features from the SAR data. Various polarimetric decomposition models have been proposed for the fully polarimetric SAR data but possesses many drawbacks. These include the ambiguities present in the representation of the actual scattering mechanism present in the terrain. Cosine squared distribution based multiple component scattering model (MCSM) is a five-component decomposition model including surface scattering, double-bounce scattering, volume scattering, helix scattering, and wire scattering. The scattering power contribution from the urban area is modeled as the sum of wire scattering, helix scattering and double bounce scattering in this model. The cosine squared distribution is used here to model the volume scattering power. In this work, the potential of cosine square distribution based MCSM is analyzed to assess the representation of the scattering mechanism of terrain objects. This model is implemented on multiple data sets of Radarsat-2, Gaofen-3, AIRSAR, and RISAT-1 acquired over the San Francisco area. The patch analysis is done by selecting small patches of urban area, vegetated area, and the water body to calculate the percentage of power contribution of surface, double-bounce and volume scattering. The patch analysis result is analyzed and compared with the Google Earth images to interpret the ambiguities present in the decomposition result. The result shows that the model performs well in representing the urban area by improving the double bounce scattering power with remarkably less volume scattering power. The dominance of volume scattering power in the forest and highly vegetated areas is also observed from the patch analysis result.

1. INTRODUCTION

1.1 Polarimetric decomposition

Synthetic Aperture Radar (SAR) is an active remote sensing technology for all-weather and all-time monitoring of terrain. The fully polarimetric SAR system captures images in four channels namely, horizontally transmitted and horizontally received (HH), horizontally transmitted and vertically received (HV), vertically transmitted and horizontally received (VH) and vertically transmitted and vertically received (VV). Polarimetric decomposition is used for characterizing the physical properties of terrain features from the SAR image. The fully polarimetric SAR image can be expressed using scattering matrix (S) and covariance and coherency matrices (C and T respectively) are order-three matrices which are derived from S. The coherent decomposition models are derived using S matrix and incoherent decomposition models are derived using the C or T matrices (Richards, 2009). The incoherent decomposition is preferred over coherent decomposition as it gives a better representation of the terrain (Pottier, 2012).

Freeman-Durden decomposition is a basic model based incoherent model in which the scattering contribution of each pixel of the SAR image is expressed as a linear combination of three basic physically interpretable scattering models (Freeman and Durden, 1998). The first order Bragg surface scatters (Surface scattering), canopy scatter from randomly oriented dipole (Volume scattering), double-bounce scatter are the three components considered in this technique. This technique assumes that there is no correlation between co-pol and cross-pol polarization channel intensities and the cross-pol term is only contributed by volume scatterer. This assumption helps for

directly deriving the volume scattering power from the cross-pol scattering power. Yamaguchi decomposition is developed by modifying the volume scattering model by considering the co-pol-cross correlation (Yamaguchi Yoshio, Toshifumi Moriyama, Motoi Ishido, 2005). Helix scattering is added as a fourth scattering mechanism that addresses the complex urban scatterers. The cross-pol power due to randomly oriented urban targets is also represented as volume scattering in the Freeman algorithm. This overestimation of volume scattering is being evaluated and replaced as helix scattering in this technique. The Freeman-Durden three-component decomposition model assumes that the co-polar and cross-polar components are uncorrelated and the cross-pol response can directly be interpreted as volume scattering. The validity of this assumption is ambiguous in highly complex urban areas. The multiple component scattering model (MCSM) decomposition model has been introduced with the assumption that the total backscatter from the urban area can be decomposed into the double bounce scattering, helix scattering and wire scattering (Zhang *et al.*, 2008).

1.2 Polarization Orientation Angle

The polarization orientation angle is defined as the angle between the major axis of polarization ellipse and the horizontal axis on the incident plane (Yamaguchi Yoshio, Toshifumi Moriyama, Motoi Ishido, 2005; Verma, 2012; Kumar *et al.*, 2019). The polarization angle is shifted by inclined terrain, oriented complex buildings, tilted linear bridges. The POA shift causes an increase in the cross-polarization channel intensity and thereby losing the symmetry property of coherency and covariance matrices. This makes the assumptions of zero co-pol and cross-pol correlation invalid hence creates ambiguity in the

identification of target scatterer. The POA shift can be corrected by rotating the coherency or covariance matrix using the rotation matrix (Lee and Ainsworth, 2010; Verma, 2012; Bhattacharya *et al.*, 2015; Singh and Yamaguchi, 2018). The POA compensation causes no change in the co-pol dependent elements in the coherency and covariance matrices while reduces the cross-pol dependent elements.

In this work, the multiple component scattering model decomposition is implemented on different space-borne and airborne datasets and the result is analyzed. The ambiguities present in the identification of scattering mechanisms are also addressed.

2. STUDY AREA AND DATASET

2.1 Study Area

The site selected for this work is the San Francisco area, the USA due to the presence of all types of scatterers within it including closely spaced buildings, linear features, highly vegetated areas, waterbody, etc.

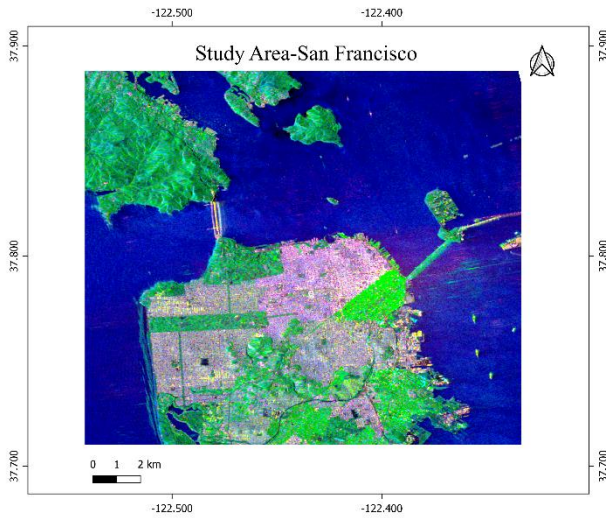


Figure 1. Yamaguchi decomposed the image for the San Francisco area. Red: double-bounce scattering, green: volume scattering, blue: surface scattering.

The area is been considered as a typical example for evaluating the potential of different polarimetric decomposition models.

Table 1. Specifications of the dataset used.

	Platform	Band	Date of Acquisition	Resolution
Radarsat-2	Space-borne	C	09-04-2008	4.73×9.65
AIRSAR	Air-borne	C	03-05-2003	9.26×3.3
Geofen-3	Space-borne	C	15-09-2017	0.44×0.62
ALOS PALSAR-1	Space-borne	L	22-01-2010	9.36×3.54

The Freeman-Durden and Yamaguchi decompositions give an overestimation of volume scattering from the closely spaced urban areas. This area is also famous for developing and testing of ship detection algorithms.

2.2 Datasets

The datasets used here to analyze the performance of the cosine square distributed MCSM decomposition are: Radarsat-2, AIRSAR, ALOS PLASAR-1, and Geofen-3. The details of the datasets is given in table 1.

3. MULTIPLE COMPONENT SCATTERING MODEL DECOMPOSITION

This decomposition model is derived using the coherency matrix calculated from the scattering matrix of fully polarimetric SAR data. This is a five-component model with elements surface scattering, double-bounce scattering, volume scattering, helix scattering, and wire scattering. The surface scattering component is modeled using the Bragg scatter from a moderately rough surface which is given by(Freeman and Durden, 1998):

$$T_S = \begin{bmatrix} |\beta|^2 & 0 & \beta \\ 0 & 0 & 0 \\ \beta^* & 0 & 1 \end{bmatrix} \quad (1)$$

The double bounce scattering component is modeled using even- or double-bounce scatter from a pair of orthogonal surfaces with different dielectric constants which are given by(Freeman and Durden, 1998):

$$C_D = \begin{bmatrix} |\alpha|^2 & 0 & \alpha \\ 0 & 0 & 0 \\ \alpha^* & 0 & 0 \end{bmatrix} \quad (2)$$

The volume scattering component is modeled using canopy scatter from a cloud of randomly oriented dipoles(Freeman and Durden, 1998)which is given by:

$$C_V = \frac{1}{4} \begin{bmatrix} 1 & 0 & 1/3 \\ 0 & 2/3 & 0 \\ 1/3 & 0 & 1 \end{bmatrix} \quad (3)$$

The helix scattering component is modeled as the correlation of co-pol and cross-pol intensities which is neglected in the Freeman-Durden decomposition (Yamaguchi Yoshio, Toshifumi Moriyama, Motoi Ishido, 2005). The model is given by:

$$C_H = \frac{1}{4} \begin{bmatrix} 1 & \pm j\sqrt{2} & -1 \\ \mp j\sqrt{2} & 1 & \pm j\sqrt{2} \\ -1 & \mp j\sqrt{2} & 1 \end{bmatrix} \quad (4)$$

The wire scattering component is proposed in (Zhang *et al.*, 2008) which is modeled as scattering from the linear structure and is given by:

$$C_W = \begin{bmatrix} |\gamma|^2 & \sqrt{2}\gamma\rho^* & \gamma \\ 2\gamma\rho^* & 2|\rho|^2 & \sqrt{2}\rho \\ \gamma^* & \sqrt{2}\rho^* & 1 \end{bmatrix} \quad (5)$$

The five-component model equation is given as:

$$C = F_S C_S + F_D C_D + F_V C_V + F_H C_H + F_W C_W \quad (6)$$

The methodology for conducting this research work is shown in the figure. 2. The fully polarimetric data is to be radiometrically calibrated to relate the intensity values present in the image to the radar backscattering. The multi looking is done to convert

the data from ground range to slant range and to convert it into square pixels.

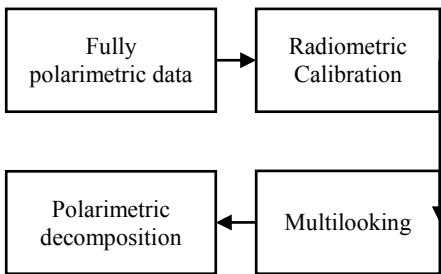


Figure 2 Methodology for the decomposition of the data.

The decomposition model is then applied to the pre-processed data.

3.1 Results

The Google Earth imagery for the study area is shown in figure 3. The different features present in the area is visible in the optical imagery. The decomposition results for the datasets are shown below. Among the five components generated from the MCSM decomposition model, the RGB image is generated with double-bounce scattering, volume scattering, and surface scattering respectively in red, green and blue channels. The MCSM decomposed Radarsat-2 data is shown in Fig. 4. The urban area is indicated by whitish pink color. The portion in the red rectangle is the area that shows the overestimation of volume scattering in the Yamaguchi decomposed image shown in the study area map. But this area is indicated in white color in figure 4 showing the reduction in the volume scattering power contribution.

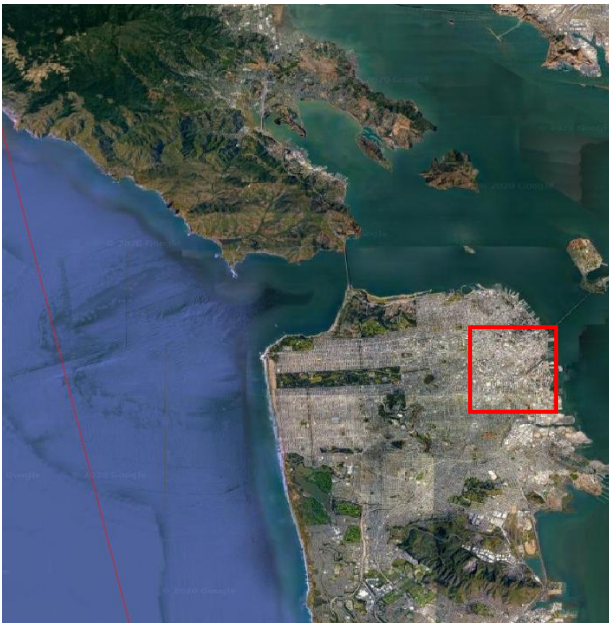


Figure 3 Google earth imagery of the study area.

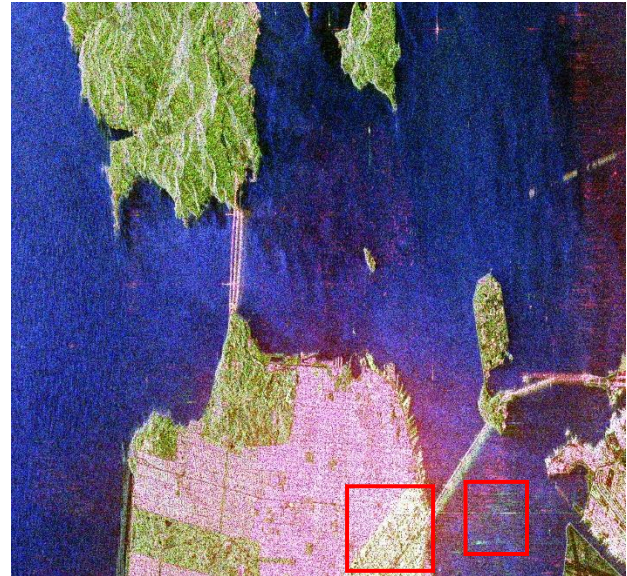


Figure 4. MCSM Decomposed image of Radarsat-2 data for the San Francisco area. Red: Double bounce scattering, green: volume scattering, blue: surface scattering.



Figure 5. MCSM Decomposed image of Geofen-3 data for the San Francisco area. Red: Double bounce scattering, green: volume scattering, blue: surface scattering.

In figure 5, the decomposed Geofen-3 image is given. The urban area is represented in pink color and the portion indicated in the red rectangle is represented by whitish pink color. This indicates the dominance of double bounce scattering in the urban area.

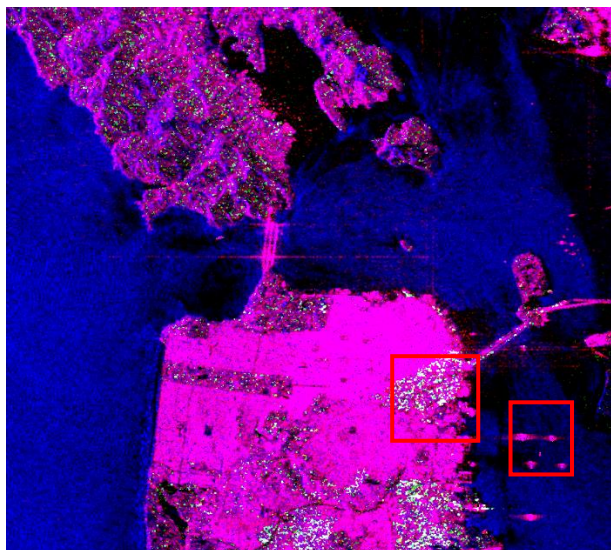


Figure 6. MCSM Decomposed image of ALOS PALSAR-2 data for the San Francisco area. Red: Double bounce scattering, green: volume scattering, blue: surface scattering.

The ALOS PALSAR-1 data decomposition result is shown in figure 6. It gives very high double-bounce scattering in the urban areas. But the double bounce scattering is overestimated in the vegetated area.

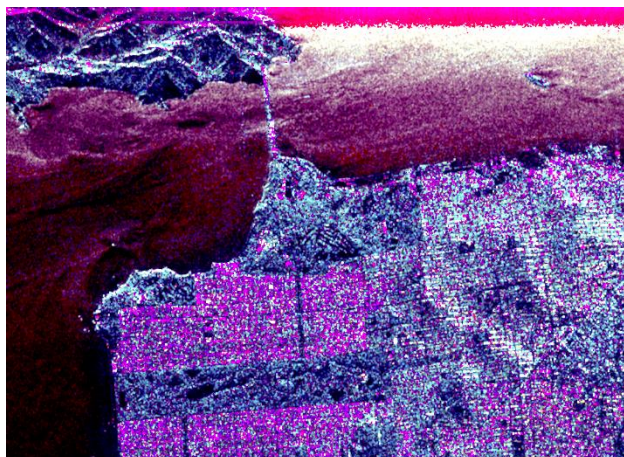


Figure 7. MCSM Decomposed image of AIRSAR data for the San Francisco area. Red: Double bounce scattering, green: Volume Scattering, Blue: Surface Scattering

The AIRSAR decomposed result is shown in figure 7. The urban area is indicated with a pink color which indicates the dominance of double bounce scattering. But the sea area is giving no dominant backscattering. The decomposition represents the sea area as a smooth surface. The vegetated area is indicated with green color in all the datasets except the L-band ALOS PALSAR-1 data.

4 Conclusion:

The multiple component scattering model decomposition is implemented in C-band Radarsat-2, AIRSAR, Geofen-3, and L-band ALOS PALSAR-1. The overestimation of volume scattering in the decomposition model is less in all the C-band datasets. But the L-band decomposition result overestimates the double bounce scattering in the vegetated area. This effect is due to the higher penetration power of the L-band radar wave.

REFERENCES

- Arii, M., Van Zyl, J. J. and Kim, Y. (2010) 'A general characterization for polarimetric scattering from vegetation canopies', *IEEE Transactions on Geoscience and Remote Sensing*. IEEE, 48(9), pp. 3349–3357. doi: 10.1109/TGRS.2010.2046331.
- Bhattacharya, A. *et al.* (2015) 'Modifying the Yamaguchi four-component decomposition scattering powers using a stochastic distance', *IEEE Journal of Selected Topics in Applied Earth Observations and Remote Sensing*, 8(7), pp. 3497–3506. doi: 10.1109/JSTARS.2015.2420683.
- Freeman, A. and Durden, S. L. (1998) 'A three-component scattering model for polarimetric SAR data', *IEEE Transactions on Geoscience and Remote Sensing*, 36(3), pp. 963–973. doi: 10.1109/36.673687.
- Kumar, S. *et al.* (2019) 'PolSAR-decomposition-based extended water cloud modeling for forest aboveground biomass estimation', *Remote Sensing*, 11(19), pp. 1–27. doi: 10.3390/rs11192287.
- Lee, J. Sen and Ainsworth, T. L. (2010) 'The effect of orientation angle compensation on coherency matrix and polarimetric target decompositions', *Proceedings of the European Conference on Synthetic Aperture Radar, EUSAR*. IEEE, 49(1), pp. 499–502. doi: 10.1109/TGRS.2010.2048333.
- Pottier, E. (2012) *Advanced Radar Polarimetry Tutorial*.
- Richards, J. A. (2009) *Remote Sensing with imaging radar: a review*, Springer. Verlag-Berlin Heidelberg: Springer. doi: 10.1007/978-3-642-02020-9.
- Singh, G. and Yamaguchi, Y. (2018) 'Model-Based Six-Component Scattering Matrix Power Decomposition', *IEEE Transactions on Geoscience and Remote Sensing*, 56(10), pp. 5687–5704. doi: 10.1109/TGRS.2018.2824322.
- Verma, R. (2012) *Polarimetric decomposition based on general characterisation of scattering from urban areas and multiple component scattering model*. University of Twente. Available at: http://www.iirs.gov.in/iirs/sites/default/files/StudentThesis/Verma_Ruchi_28154_Thesis.pdf.
- Yamaguchi Yoshio, Toshifumi Moriyama, Motoi Ishido, H. Y. (2005) 'Four-Component Scattering Model for Polarimetric SAR Image Decomposition based on Asymmetric Covariance Matrix', *Ieee Transactions on Geoscience and Remote Sensing*, 104(8), pp. 1699–1706.
- Zhang, L. *et al.* (2008) 'Multiple-component scattering model for polarimetric SAR image decomposition', *IEEE Geoscience and Remote Sensing Letters*, 5(4), pp. 603–607. doi: 10.1109/LGRS.2008.2000795.

VISUALIZATION OF UNESCO WORLD HERITAGE SITE ON WEB GEOPORTAL TO AID FOR FUTURE EXCAVATION

Chandan Grover^{1,*}, Esha Semwal¹, Saumyata Srivastava¹, Hina Pande¹, Poonam S Tiwari², S. Raghavendra¹, S. Agrawal¹

¹Photogrammetry and Remote Sensing Department, Indian Institute of Remote Sensing, Indian Space Research Organization, Dehradun (chandangrover32, esha.semwal1, saumyata.srivastava) @gmail.com, (hina, raghav, shefali_a) @iirs.gov.in

²Geoweb services, IT & Distance Learning Department, Indian Institute of Remote Sensing, Indian Space Research Organization, Dehradun (poonam@iirs.gov.in)

* Corresponding Author (chandangrover32@gmail.com, chandan@iirs.gov.in)

KEYWORDS: Heritage Site, Nalanda Mahavihara, Excavation, DEM, Cartosat, LISS-4, DGPS

ABSTRACT:

The ruins of Nalanda Mahavihara is a large and revered Buddhist monastery, in the historic city of Bihar in India. It is said that Nalanda was probably raided and destroyed by an army of the Mamluk Dynasty of the Delhi Sultanate under Bakhtiyar Khalji in the 13th century. The excavation of Nalanda ruins was initiated in the early 20th century by the Archeological Survey of India. ruins founded until now covered an area of about 12 hectare that includes stupas, chaityas, viharas, shrines, many votive structures and important artworks in stucco, stone, and metal. Archaeological stated that only 10% of the ruins is been excavated so far as Nalanda Mahavihara occupied a far greater area in medieval times. It is believed that other ruins are beneath the ground, hence DEM is essential to mark the extent of the ruins. In this paper, Cartosat-1 stereo pairs have been used for generating the Digital Elevation Model (DEM) of UNESCO Heritage Site i.e. Nalanda ruins, Bihar (India), using Ground Control Points that was later acquired by Differential Global Positioning System (DGPS). DEM of pixel size 3 x 3m is obtained. For better visualization purposes of the features of Nalanda ruins the LISS-IV data of 5.8m spatial resolution is draped on DEM. Many different Buddhist sculptures were found in these ruins during an excavation in the 20th century. Out of these, the location for some of the sculptures was accurately tracked and represented in the paper. This study could also help in finding the probable location of the next excavation.

1. INTRODUCTION

The History of Nalanda in 6thBC was about Lord Mahavira and Lord Budha. This is the birth and death place of Sariputra who was one of the loyal disciples of Lord Budha. The Region of Nalanda Mahavihara ruins, approximately 95 km southeast of Patna district of the ancient kingdom of Magadha (currently known as Bihar), India and about 82 km from UNESCO Heritage site Bodh Gaya that is also known as the birthplace of Buddhism. It is one of the earliest and largest institutes in the world from the 5th century for Buddhist culture and teachings up to when an army of the Mamluk Dynasty of the Delhi Sultanate under Bakhtiyar Khalji destroyed it in the 13th century.

Before its descent, it attracts foreign students to explore in the field of Religion, Science, Astronomy, Spiritualism, and Philosophy. One of the students was Xuanzang from China. After its deterioration, Nalanda was largely unremembered until Francis Buchanan-Hamilton surveyed the site in 1811–1812. The British army engineer Major General Sir Alexander Cunningham took an interest in the history and archaeology of India in the 19th century and was later appointed as Archaeological surveyor to the Government of India in 1861. With the newly formed Archaeological Survey of India (ASI), he conducted an official survey of Nalanda in 1861-62. The first phase of excavation was done in 1871, the second phase from 1915 – 38 and in the third phase from 1974 to 1982 excavation and restoration was done (Rajani, 2016). Before the execution of the first excavation the site was known as Baragaon, later on, a seal was discovered with the name 'Nalanda' engraved on it. So the site was named Nalanda. Many Buddhist sculptures were found during the excavation and the location for some of the sculptures was accurately traced. The resolution and scale of remote sensor data define the XYZ plane accuracy of DEM that

can be executed using photogrammetric methods. In the current study, DEM is generated from high-resolution cartosat-1 satellite stereo pairs using Ground Control Points (GCPs) that were acquired using the Differential Global Positioning System. Cartosat-1 carries two state-of-the-art panchromatic (PAN) cameras that take black and white stereoscopic pictures of the earth in the visible region of the electromagnetic spectrum. The swath covered by these high-resolution PAN cameras is 30 km and their spatial resolution is 2.5 meters. The GCPs were taken using Trimble SP80 Global Navigation Satellite System (GNSS), having two receivers: one was served as "Base" and another as a "Rover". Fifteen GCPs were taken around the site covers a perimeter of 115 km and an area of 828 square km. For better visualization purposes of the features of Nalanda ruins, the LISS-IV sensor image is enfolded on DEM. It is a multispectral high-resolution sensor having a spatial resolution of 5.8 m at nadir. It acquires data in three spectral bands (B2 520 – 590 nm, B3 620 – 680 nm, B4 770 – 780 nm) namely visible and near-infrared (Rossiter et al., 2014). The multispectral imagery covering a swath of 70 Km and has the additional feature of off-nadir viewing capability by tilting the camera by +/- 26 degrees.

2. STUDY AREA

The study was conducted in the Nalanda district of Bihar, India namely, Nalanda ruins located at 25° 8' 7.07176"N 85° 26' 32.79912"E. The Site was an inscription in the UNESCO World Heritage List in 2016. Nalanda prospered under the aid of the Gupta Empire in the 5th century. It was an ancient mahavihara and the largest Buddhist monastery in the ancient kingdom of Maghda. Presently, the ruins of Nalanda mahavihara spread over an area of 12 hectares. Study Area is shown in Figure 1.

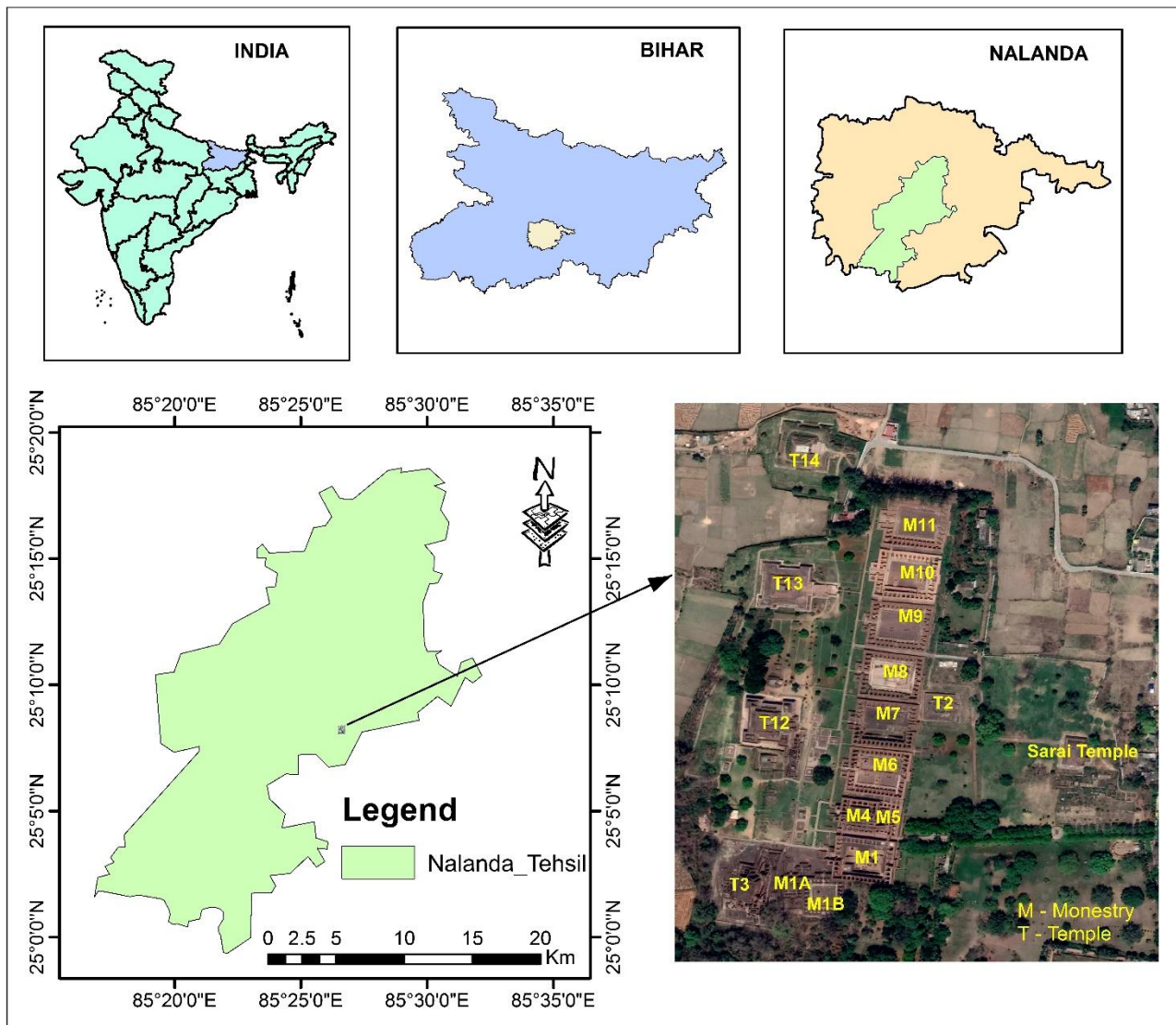


Figure 1. Representation of Study Area

3. METHODOLOGY

The workflow that was followed during the research is shown in Figure 2. The DEM is generated from high-resolution Cartosat-1 satellite stereo pairs. The extent of CARTOSAT-1 satellite data of ruins of Nalanda and relevant information of the study area are summarized in Table 1.

Image Properties	Nalanda
Latitude	25° 11' 40.2"
Longitude	85° 30' 16.56"
Path	572
Row	281
Date of Pass	30-Jan-19
Orbit number	74375

Table 1. Cartosat-1 data used

The Ground Control Points were acquired using Trimble GNSS SP80. 15 GCPs, collected on the ground using DGPS measurements for Nalanda. These were used as reference points while creating DEM. The Latitude and Longitude of GCPs are shown in Table 2.

Name	Latitude	Longitude
1	25° 8' 7.07"	85° 26' 32.8"
2	25° 8' 7.29"	85° 26' 32.8"
3	25° 8' 7.18"	85° 26' 32.62"
4	25° 12' 50.09"	85° 37' 5.08"
5	25° 11' 38.28"	85° 33' 13.66"
6	25° 14' 35.03"	85° 31' 2"
7	25° 17' 4.34"	85° 27' 35.67"
8	25° 6' 35.84"	85° 31' 33.37"
9	25° 5' 22.65"	85° 20' 56.93"
10	25° 5' 31.25"	85° 33' 56.79"
11	25° 10' 11.9"	85° 22' 2.5"
12	25° 17' 5.94"	85° 35' 51.19"
13	25° 18' 7.69"	85° 39' 48.69"
14	25.077803°	85° 26' 4.52"
15	25° 3' 9.93"	85° 34' 3.07"

Table 2. Acquired Ground Control Points

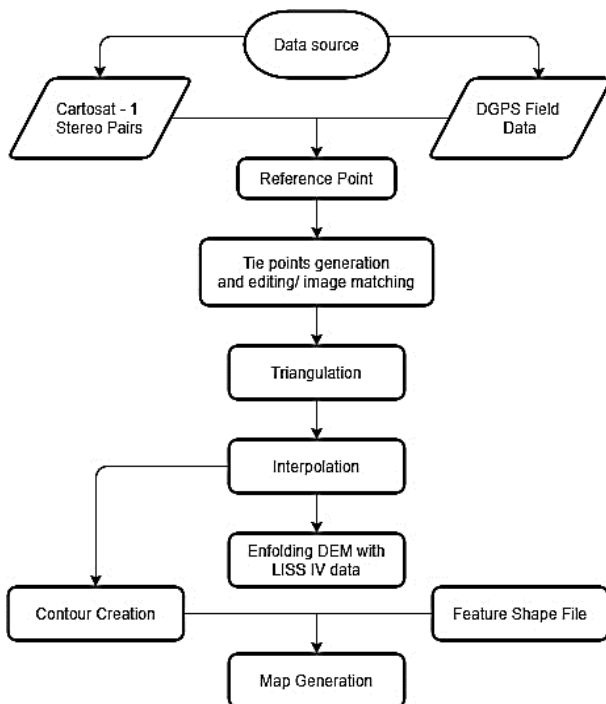
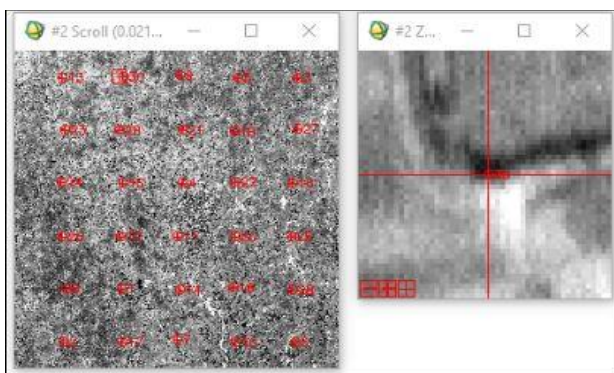
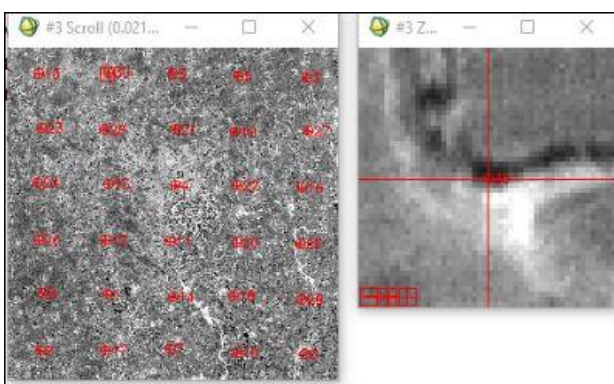


Figure 2. Flow chart representation of DEM and Map Generation of the study area

In overlapping areas of the stereo images, tie points are marked. These are those points whose coordinates are not known (Ahmed et al., 2007). In our study manual method of identifying tie points were employed in the regions under the urban area. A total 30 tie points were taken that shown in Figure 3.



(a)



(b)

Figure 3. (a) and (b) shows the tie points in Cartosat – 1 Stereo pairs

After the generation of tie points, the Cartosat-1 data were triangulated. Triangulation resolves the problem of finding the position of any given point in space (Giribabu et al., 2013) if its position on two images is known (Hartley and Sturm, 1996).

After generating the DEM, LISS – IV image having 5.8m resolution is enfolded on it. The extent of LISS-IV image data of the Nalanda area is summarized in Table 3. The final result is the generation of Map showing contour and feature shapefile using GIS Software.

Image Properties	Nalanda
Latitude	25° 15' 57.6"
Longitude	85° 14' 52.8"
Path	104
Row	54
Date of Pass	21-Apr-19
Orbit number	12291

Table 3. LISS - IV data use

4. RESULTS AND DISCUSSION

It is very beneficial to have a digital elevation model to visualize the elevation and other features of any area (Gruen et al., 2006). The Elevation model of the UNESCO area of Nalanda ruins of Bihar, India, using high-resolution Cartosat – 1 satellite stereo pairs and the pinpoint locations of two empty niches on the captured image of study site as shown in Figure 4. There, the three statues namely, Budha, Nagarjuna, and Samantabhadra once stood.

A contour map of the Nalanda area of 0.5m interval is created from DEM to understand the topography of the area shown in Figure 5. It shows the gradual change in elevation, nearby to the previously excavated area. This will give a clear indication that there may be many more monasteries, shrines, stupas, and viharas on the ground. For better visualization, the LISS – IV satellite image is enfolded on DEM and to digitize the important Monasteries, Stupas, and Temples (Shrines) a shapefile of ruins of Nalanda is draped on DEM. A stupa is a structure associated with the sacred life of Nalanda scholars. To devote the bodily remains of Sariputta (scholar) its construction was started in 3rd century BC and became continues for seven successive additions. In Nalanda, there is a relic type of stupas. The shrine is a holy or sacred site devoted to a specific saint, soul or similar figure of respect. There, the statues in shrines are made up of stucco, stone in varying size and shape (District and Value, 2015).

The area under ASI's buffer zone is 57.88 hectares and 23 hectares under the property line. But, to date excavation was done only in 12 hectares area only. Figure 6 shows the DEM along with the Archaeological Survey of India (ASI) boundary shapefile. In DEM, it can be clearly seen that there are some highly elevated areas near the remains of Nalanda Mahavihara and that area is non-excavated at present. And if that area is excavated in the future, it is very beneficial to know more about the history of Buddhism and Nalanda.

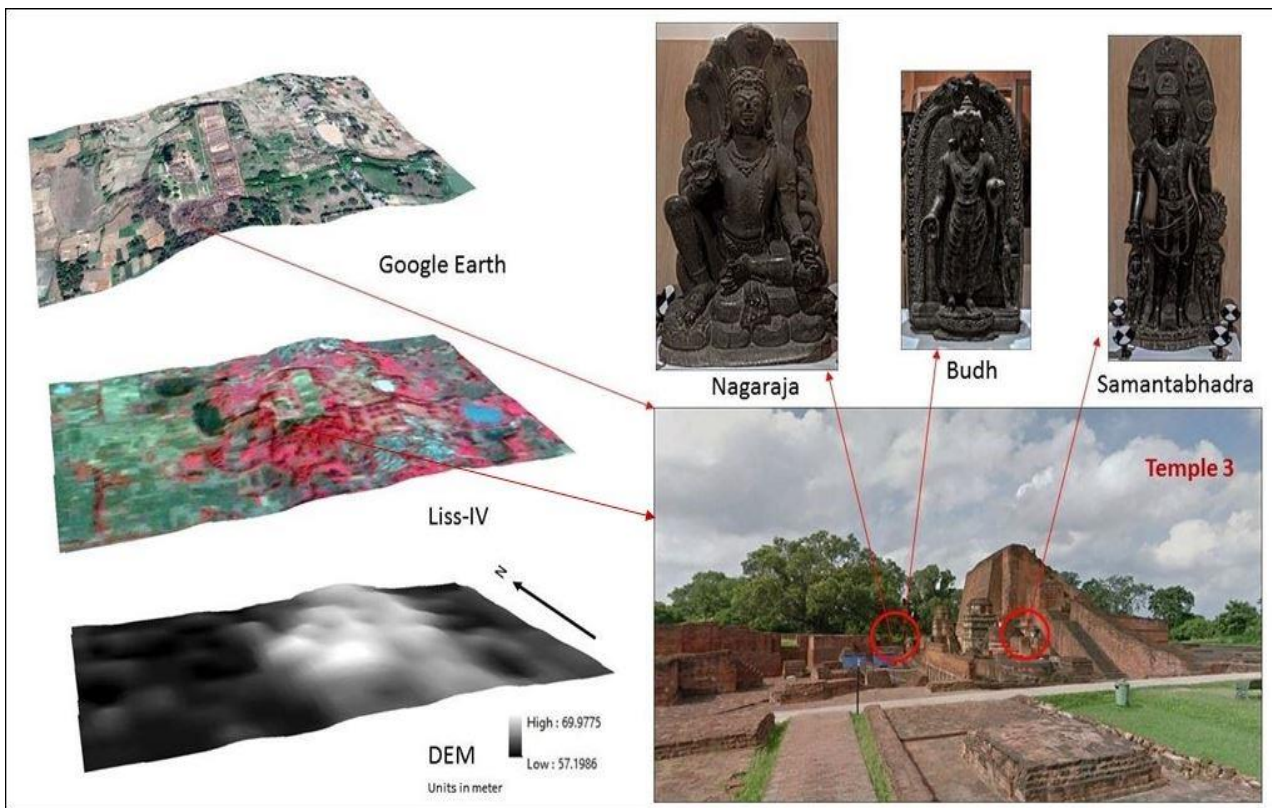


Figure 4. DEM generated from Cartosat - 1 satellite stereo pairs (bottom left), Wrapping of LISS - IV satellite image on DEM (middle left), Wrapping of Google Earth image on DEM (Top left) and the exact location of three statues Nagaraja, Budh and Samantabhadra on image captured during field survey (right).

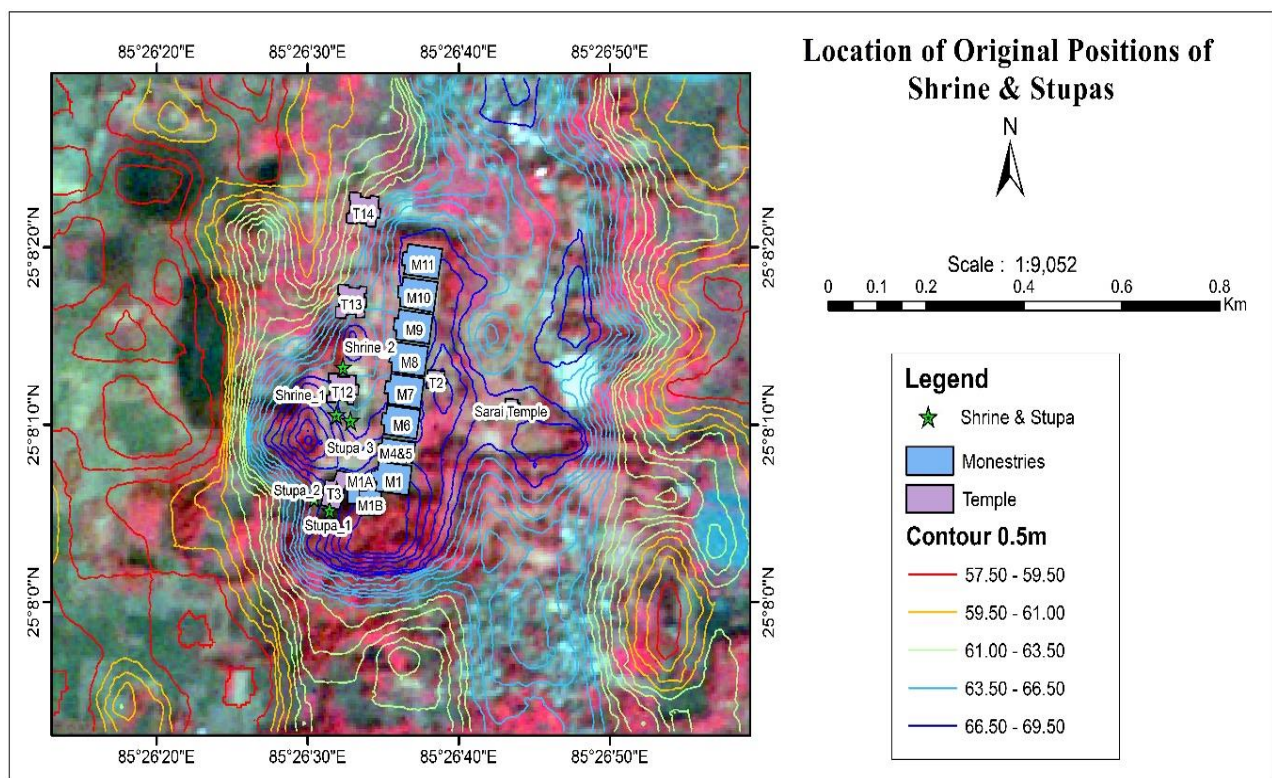


Figure 5. Visualization of Temples and Monasteries along with Stupas on contour generated from Cartosat-1 stereo pairs enfolded with LISS - IV satellite image

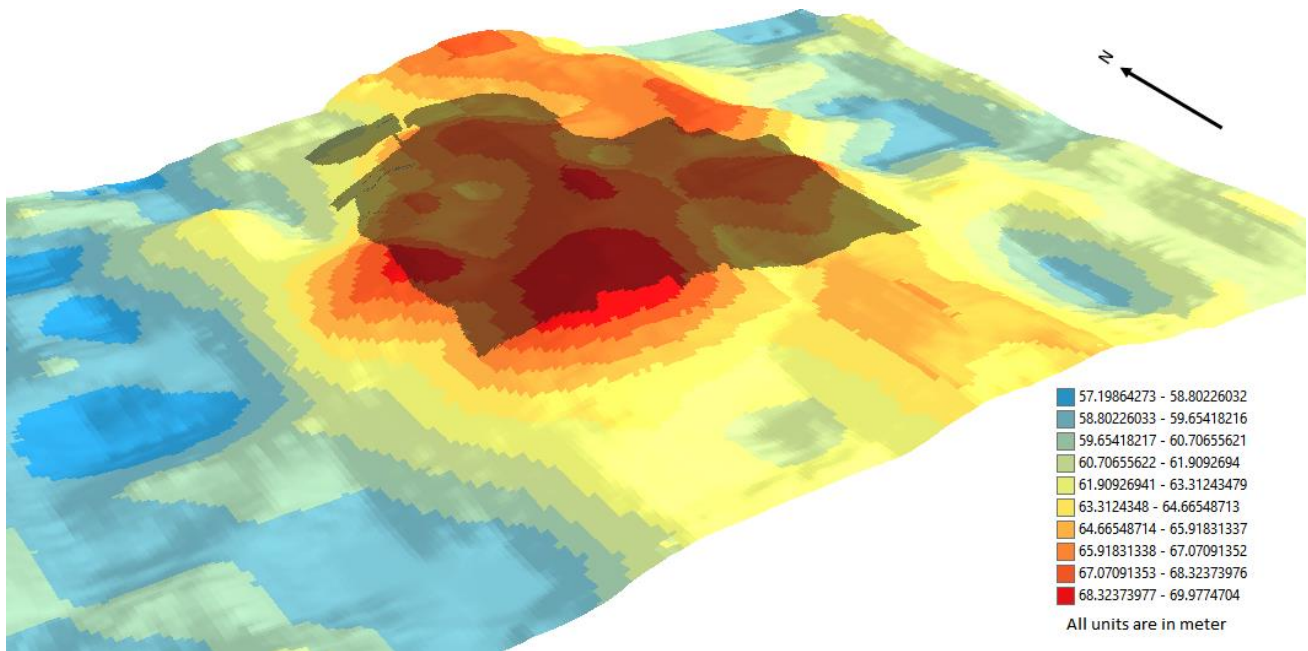


Figure 6. DEM (2.58m resolution) showing the elevation of the Nalanda area along with ASI boundary shapefile

5. CONCLUSION

From Literature and results obtained from the current study, it is expected that there are more monasteries, shrines, and stupas on the ground, which need to be excavated in the future. In addition, we can also relocate the sculptures to the actual positions that were traced during excavation through virtual reality in the future. That can be done by creating 3d models from high-density point clouds.

ACKNOWLEDGMENTS

The authors would like to thank Mr. Shankar Sharma, present Superintendent Archaeologist of ASI at Nalanda site for his corporation during data acquisition and sharing facts about the history of Nalanda and Dr. M. B. Rajani, a faculty member at the NIAS, Bangalore, for sharing the knowledge about the topography of the site. We also appreciate NRSC for providing Cartosat – 1 satellite stereo pairs and LISS – IV images.

REFERENCE

Ahmed, N., Mahtab, A., Agrawal, R., Jayaprasad, P., Pathan, S.K., Ajai, Singh, D.K., Singh, A.K., 2007. Extraction and validation of Cartosat-1 DEM. *J. Indian Soc. Remote Sens.* 35, 121–127. <https://doi.org/10.1007/BF02990776>

District, N., Value, U., 2015. Nalanda No 1502.

Giribabu, D., Kumar, P., Mathew, J., Sharma, K.P., Krishna Murthy, Y.V.N., 2013. DEM generation using Cartosat-1 stereo data: Issues and complexities in Himalayan terrain. *Eur. J. Remote Sens.* 46, 431–443. <https://doi.org/10.5721/EuJRS20134625>

Gruen, A., Remondino, F., Zhang, L., 2006. 3D modeling and visualization of Cultural Heritage sites from high-resolution satellite imagery. *Glob. Dev. Environ. Earth Obs. from Sp.* {611-

620}.

Hartley, R. and Sturm, P., 1996. Triangulation [CVIU]. *Image (Rochester, N.Y.)* 68, 957–966.

Rajani, M.B., 2016. The expanse of archaeological remains at Nalanda: A study using remote sensing and GIS. *Arch. Asian Art* 66, 1–23. <https://doi.org/10.1353/aaa.2016.0010>

Rossiter, A.G., Garbutt, S., D'Aoust, R.F., 2014. Resources. *Defin. Excell. Simul. Programs.* <https://doi.org/10.1097/01.cnj.0000306013.03983.e9>

ANALYSIS OF BACK-SCATTERING COEFFICIENT OF NOVASAR-1 S-BAND SAR DATASETS FOR DIFFERENT LAND COVERS

Ojasvi Saini^{1,*}, Ashutosh Bhardwaj² and R. S. Chatterjee³

¹ Photogrammetry and Remote Sensing Department, Indian Institute of Remote Sensing, 4, Kalidas Road, Dehradun-248001; ojasvi@iirs.gov.in, ojasvi21nov@gmail.com

² Photogrammetry and Remote Sensing Department, Indian Institute of Remote Sensing, 4, Kalidas Road, Dehradun- 248001; ashutosh@iirs.gov.in

³ Geoscience Department, Indian Institute of Remote Sensing, 4-Kalidas Road, Dehradun- 248001; rschatterjee@iirs.gov.in

* Correspondence: ojasvi@iirs.gov.in, ojasvi21nov@gmail.com; Tel.: +91-9416556074

KEYWORDS: NovaSAR-1; S-band; HH polarization; LULC; radar backscattering coefficient.

ABSTRACT:

NovaSAR-1 is a joint technology demonstration initiative of SSTL (Surrey Satellite Technology Ltd.), UK, and Airbus DS (former EADS Astrium Ltd, Stevenage, UK). The NovaSAR-1 minisatellite was launched on 16 September 2018 and it is operating on the S-band frequency range, which is less common in Spaceborne Synthetic Aperture Radar (SAR) systems. Both higher and lower SAR frequency bands (L-band & X-band SAR) have their advantages as well as limitations in different kinds of applications. High frequency (X-band) SAR systems are useful for top surface information extraction such as the DSM generation. However, at the same time, more noise and lesser coherence issues are also associated with high-frequency SAR systems. Low-frequency SAR (L-band) systems exhibit better ground penetration, high coherence, and low noise, but less precise scatterer level information. The S frequency band comes approximately in the middle of the X and L-band SAR frequency range and may be used as a trade-off between high and low-frequency SAR systems to overcome the limitations up to some extent. In this present study, the statistical analysis of the radar backscattering coefficient of HH polarization (Stripmap and ScanSAR) datasets of NovaSAR-1 S-band datasets corresponding to different land use and land covers (LULCs) has been done to analyse the potential of S-band data. The analysis was carried out at 4 experimental sites in parts of Jharkhand, West Bengal, Maharashtra, Odisha, and Chhattisgarh. The statistical analysis of σ^0 for four different sites of India for different LULCs, such as bare soil, forest, water, urban, cropland and concrete road has been carried out. The range for minimum and maximum mean σ^0 values for urban, bare soil, forest, water, cropland, and road features were found to be -5.45 to 4.76, -18.14 to -13.44, -17.17 to -14.34, -27.29 to -26.9, -16.88 to -13.31 and -26.64 to -14.98 respectively. Range of σ^0 pixel values of Calibrated datasets corresponding to different LULCs depicted that the data quality is good for the identification of various land covers. The separability analysis of the different land cover classes depicted that classes have good separability except for a few pairs such as road-water and crop-forest. With the availability of fully polarimetric as well as single look complex (SLC) interferometric data in the future, the polarimetric scattering behaviour and phase information along with the interferometric performance of the data may be analysed.

1. INTRODUCTION

NovaSAR-1 is a very low-cost small SAR satellite. The mission key features and instrument design of the NovaSAR-1 satellite have been designed to make it suitable for a range of applications, such as forestry, disaster monitoring (particularly flooding), agriculture and maritime observations (including ship and oil slick detection)[1]. An application-focused approach based on medium resolution applications and fulfilling the user's need in the most lucrative way has been used for the development of the NovaSAR-1 mission[2]. NovaSAR-1 SAR imagery is suitable for large and diverse kinds of applications from low-resolution environmental observations to the meticulous assessment of definite ground target areas. The specialty of the NovaSAR-1 mission is that its payload consists S-band SAR sensor, which is less common in Spaceborne SAR systems[3]. Operating between the SAR frequencies of X-band and L-band and near to C-band, S-band system (around 3.2 GHz) can be reasonably expected to serve a similarly wide range of applications to those demonstrated by systems currently operating in C-band[4]. S-band SAR may be expected to serve as a trade-off between high and low-frequency SAR systems to overcome the limitations of both high and low-frequency SAR systems up to some extent. Along with the selection of wavelengths, the capability of NovaSAR-1 to perform better in certain applications is also

dictated by other aspects including imaging geometry, resolution, coverage, revisit time to an area of interest and the delay between image acquisition and information delivery to a user. The following sections discuss the statistical analysis of the radar backscattering coefficient of HH polarization (Stripmap and ScanSAR) of NovaSAR-1 S-band datasets corresponding to different LULCs of the Indian region. Different surface features exhibit different scattering characteristics. For example, urban areas exhibit very strong backscatter, Forest area shows intermediate backscatter, calm water (smooth surface) looks very dark (low backscatter) and rough sea display increased backscatter due to wind and current effects. The radar backscattering coefficient σ^0 provides information about the imaged surface. It is a function of several parameters: (frequency f , polarisation p , the incidence angle of the electromagnetic waves emitted, roughness, geometric shape and dielectric properties of the target)[5]. The range values for minimum and maximum mean σ^0 for urban, bare soil, forest, water, cropland, and road features were found and separability analysis for different land covers was done.

2. EXPERIMENTAL SITES AND DATA SOURCES

The four different data swaths of NovaSAR-1 with Stripmap (6 m ground resolution) and ScanSAR (20 m ground resolution) modes acquired in HH polarization over the regions (West Bengal, Maharashtra, Jharkhand, Odisha, Chhattisgarh, and Uttar Pradesh) of India as shown in the figure 1 have been studied for the statistical analysis of radar back-scattering coefficient of

different land use and land covers. The study sites include urban areas (such as cities of Kolkata, Ranchi), forest area, Crop Land, water bodies, barren land, and bare soil land covers. The data properties (such as operational mode, polarization, resolution, and calibration constant) of the different NovaSAR-1 datasets acquired on different study sites and used in the study are shown in table 1 below.

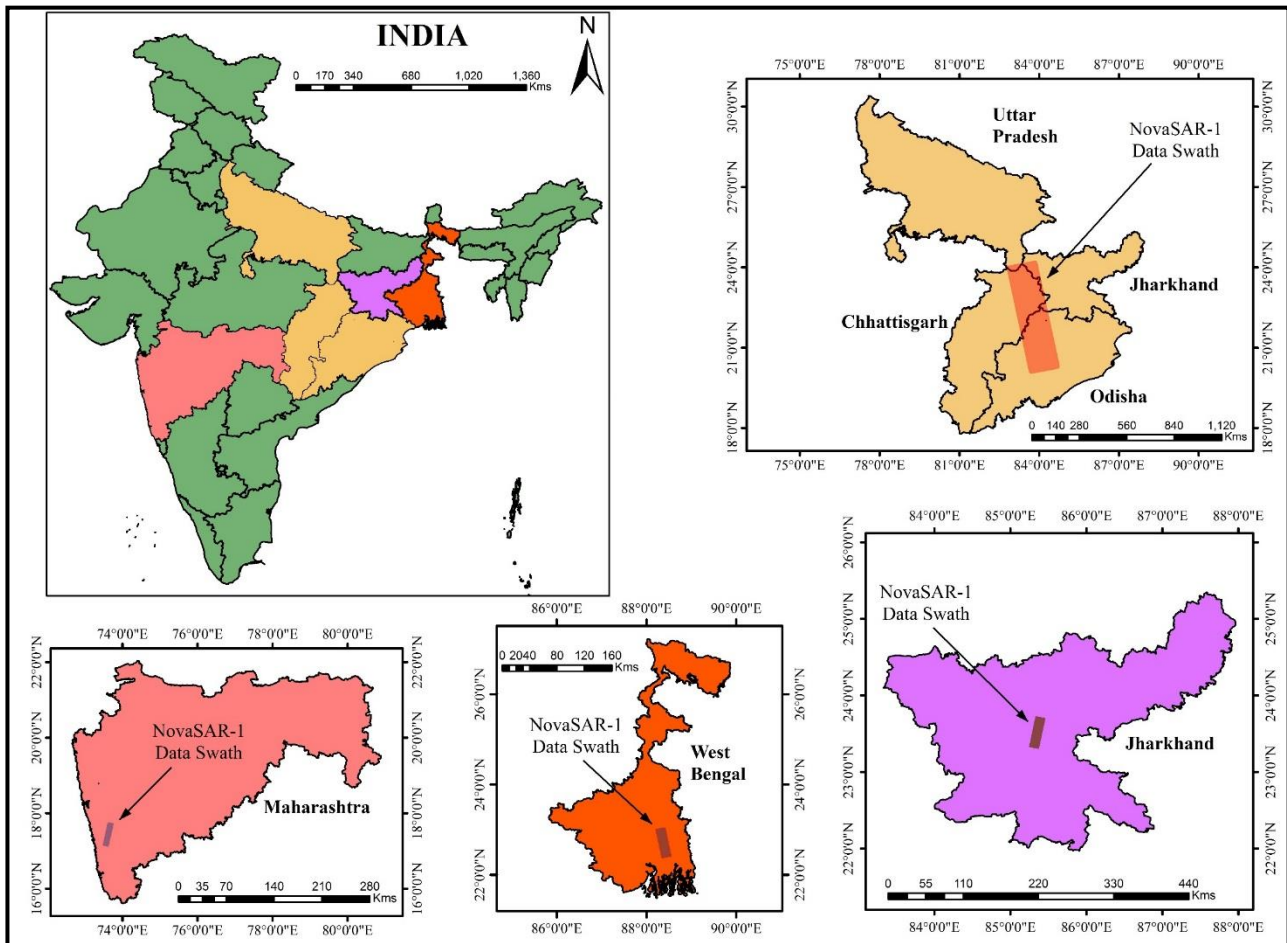


Figure 1. Locations for NovaSAR-1 Swaths over different experimental sites in India.

Table 1. Properties of NovaSAR-1 datasets used for different experimental sites

Data Properties	Maharashtra	West Bengal	Chhattisgarh & Odisha	Ranchi, Jharkhand
Operational Mode	6m_Stripmap_HH_5	6m_Stripmap_HH_F8	20m_ScanSAR_HH_H1-5	6m_Stripmap_HH_G5
Polarization	HH	HH	HH	HH
Product Type	GRD	GRD	SCD	GRD
Range Resolution	5.90 m	5.83 m	18.28 m	5.91 m
Azimuth Resolution	6.04 m	6.04 m	19.83 m	6.04 m
Calibration Constant (Linear scale)	7.98E+05	7.98E+05	3.99E+06	1E+05

3. METHODOLOGY

3.1 Radar Backscattering Coefficient (σ^0):

The radar backscattering coefficient σ^0 provides information about the imaged surface. It is a function of several parameters (sensor & ground target parameters) such as frequency, polarisation, the incidence angle of the electromagnetic waves emitted, roughness, geometric shape and dielectric properties of the target[5].

The four different data swaths of NovaSAR-1 with Stripmap (6 m ground resolution) and ScanSAR (20 m ground resolution) modes acquired in HH polarization over the experimental sites (West Bengal, Maharashtra, Jharkhand, Odisha, Chhattisgarh, and Uttar Pradesh) in India were processed according to the methodology given in flowchart figure 2. The NovaSAR-1 datasets were analysed and visually interpreted in SNAP software using a SNAP plugin named "NovaSAR Product Reader". The back-scattering coefficient (σ^0) for each of the images was generated using Equation (1) described in an Airbus technical report[6].

$$\sigma^0 = 10 \log_{10} (DN^2) - K_{cal}$$

Where, σ^0 is back-scattering coefficient, DN is pixel value in amplitude image and K_{cal} Calibration constant given in the metadata file.

The sigma nought (σ^0) generated images were filtered to reduce the speckle effect inherent in the SAR images. Region of interest (ROI) samples for different LULCs were selected from the sigma nought images for the statistical analysis of back-scattered pixel values for different land covers such as, for urban, bare soil, forest, water, cropland, and road features.

3.2 Separability Analysis:

The separability analysis of the different land cover classes has also been assessed on the basis of Transformed divergence distance among selected land cover classes. The transformed divergence (TDiver_{cd}) between two class c & d may be expressed as[7]:

$$TDiver_{cd} = 2000 \left[1 - \exp\left(\frac{-Diver_{cd}}{8}\right) \right] \quad (2)$$

Where, Diver_{cd} is the degree of divergence of separability between class c & d and may be expressed as:

$$Diver_{cd} = \frac{1}{2} \text{Tr}[(V_c - V_d)(V_d^{-1} - V_c^{-1})] + \frac{1}{2} \text{Tr}[(V_c^{-1} + V_d^{-1})(M_c - M_d)(M_c - M_d)^T] \quad (3)$$

Where, $\text{Tr}[\bullet]$ is the trace of matrix, V_c and V_d are the covariance matrices for the two classes c and d under investigation, and M_c and M_d are the mean vectors for the classes c and d.

This statistic gives an exponentially decreasing weight to the increasing distance between the classes. It also scales the divergence value to lie between 0 and 2000. A transformed divergence value of 2000 suggests an excellent separation between classes. Above 1900 provides good separation, while below 1700 is poor[7].

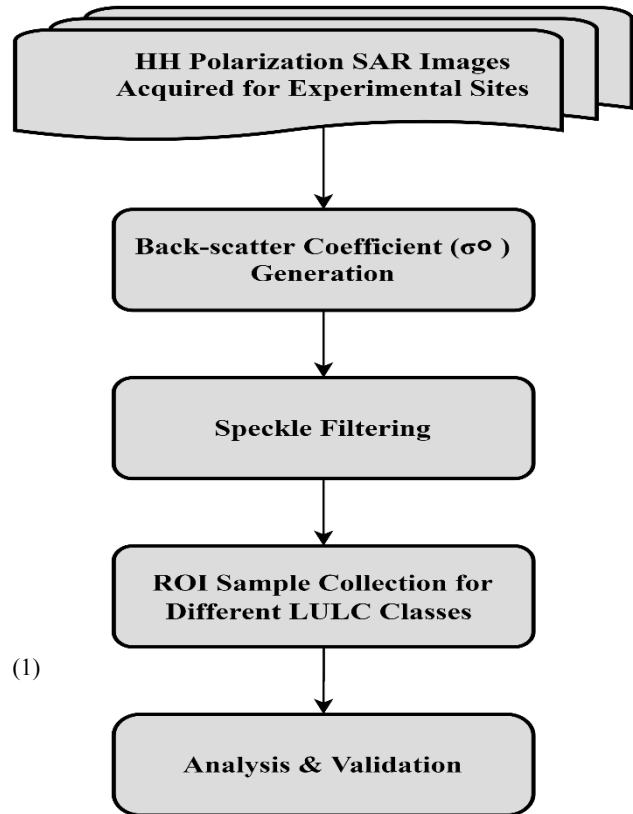


Figure 2. Flowchart of the methodology adopted for the study.

4. RESULTS AND DISCUSSION

4.1 Results for Mean σ^0 (West Bengal Site)

Only for the "Urban_Builtup" class, the mean σ^0 value was found to be positive (3.84 dB). All the other classes showed negative mean σ^0 values as shown in figure 3.

4.2 Results for Mean σ^0 (Maharashtra Site)

All the land cover classes depicted negative mean σ^0 values. The "Urban" class exhibited the highest mean σ^0 value (-3.23 dB) and the "Water_Body" class representing minimum mean σ^0 value (-26.9) as shown in figure 4.

4.3 Results for Mean σ^0 (Chhattisgarh Site)

The "Urban_Builtup" class exhibited the highest mean σ^0 value (-5.45 dB). In this image. Two different types of signatures were found for water bodies. The signature of "Water_Body_Turbid" with mean σ^0 value -14.05 dB was brighter than the signature of "Water_Body_Smooth" with mean σ^0 value -27.29 dB as shown in figure 5. The visuals of both the water classes are shown in figure 9.

4.4 Results for Mean σ^0 (Jharkhand, Ranchi Site)

The "Urban_Builtup" class is the only class among the all exhibiting positive mean σ^0 value (4.76 dB). The turbid water class is showing -17.5 dB mean σ^0 value, which is minimum among mean σ^0 values of all other classes as shown in figure 6.

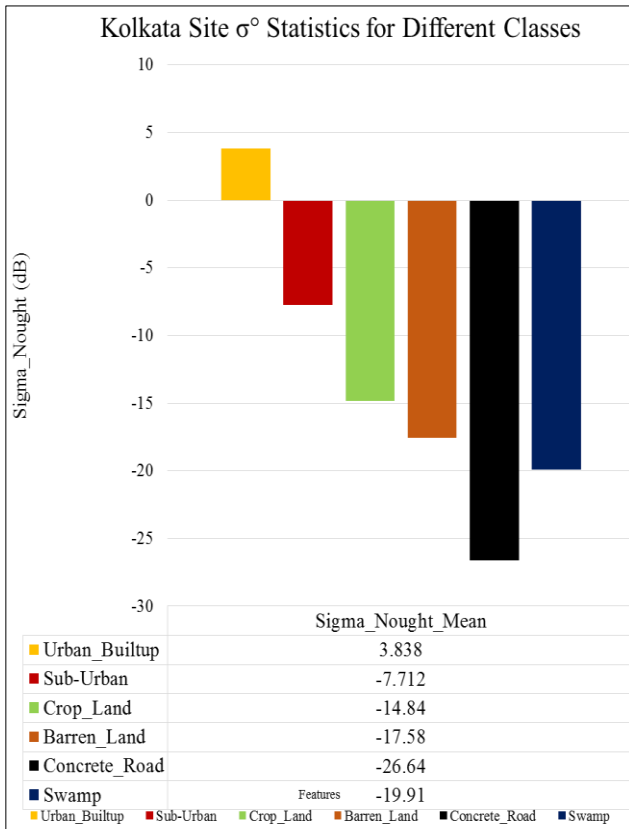


Figure 3. Mean σ^0 Statistics for Different Classes (Kolkata Site)

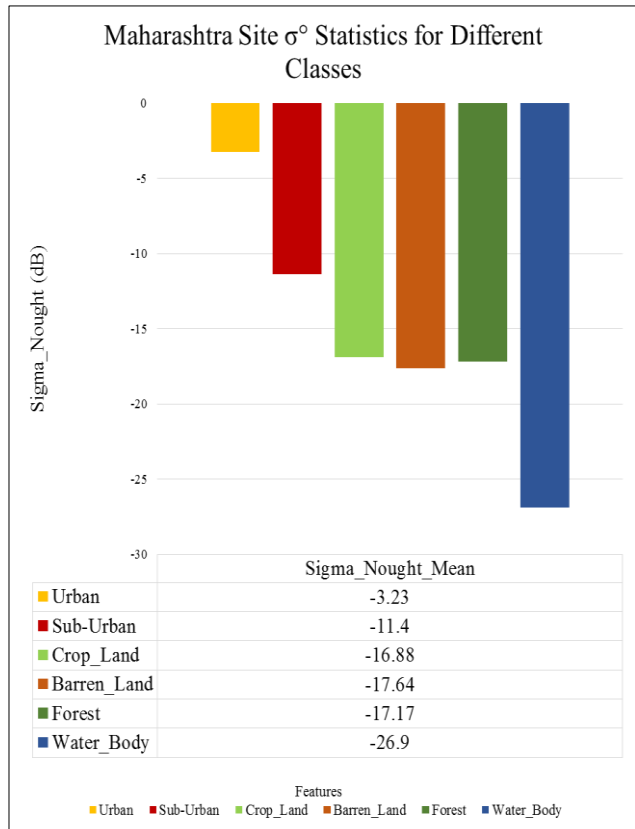


Figure 4. Mean σ^0 Statistics for Different Classes (Maharashtra Site)

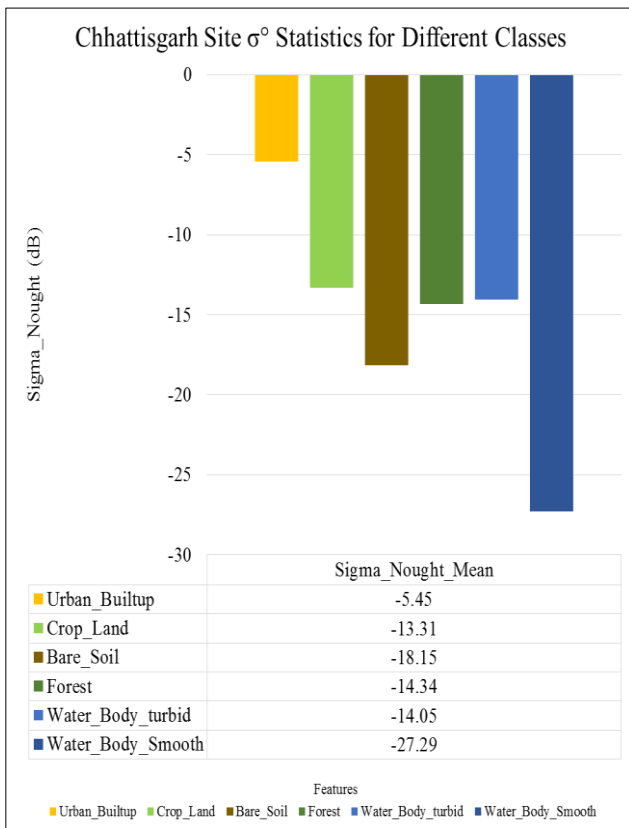


Figure 5. Mean σ^0 Statistics for Different Classes (Chhattisgarh Site)

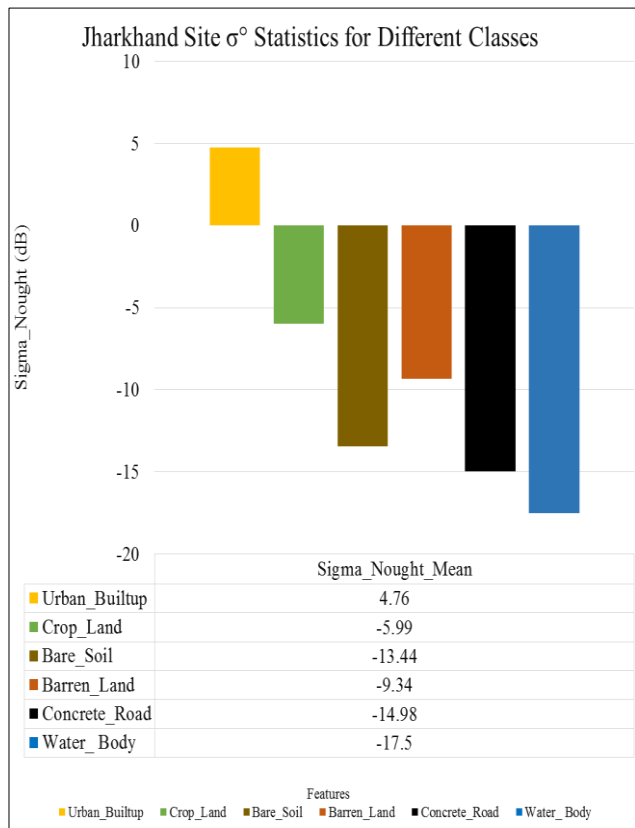


Figure 6. Mean σ^0 Statistics for Different Classes (Jharkhand Site)

4.5 Comparative Mean σ^0 Analysis of Different Land-Covers for Different Experimental sites

The plot of the mean σ^0 value for each class in all the experimental sites has also been generated for the comparative analysis of the back-scatter behavior of each class in every experimental sites. In all the experimental sites

“Water_Body_Smooth” class is showing the minimum mean σ^0 value and the “Urban_Builtup” class is giving maximum back-scattering signature. The mean σ^0 value for all the classes in “Jharkhand” site is comparatively higher than the mean σ^0 value for other experimental sites as clearly visible by blue bars in figure 7.

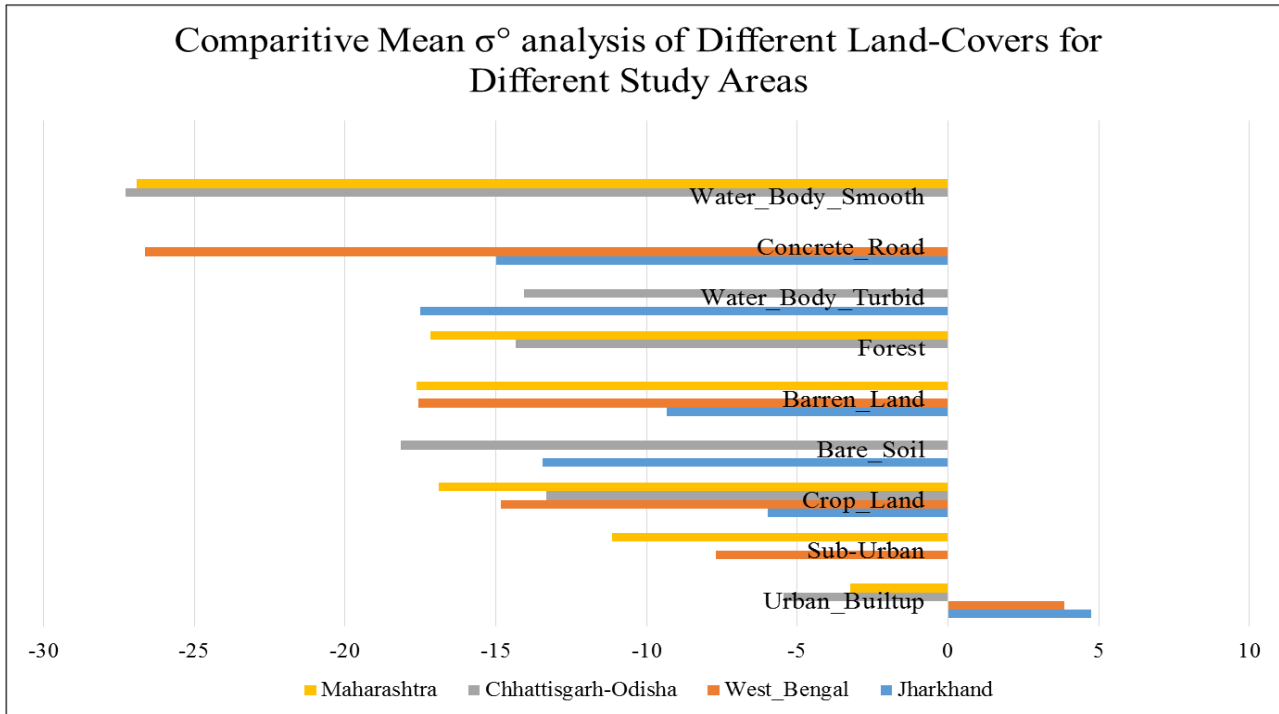


Figure 7. Comparative Mean σ^0 analysis of Different Land-Covers for Different Experimental sites

4.6 Separability Analysis of Different Classes Using Sigma Nought NovaSAR Image

The range of mean σ^0 values of Calibrated datasets corresponding to different LULCs depicted that the data quality is good for the identification of various land covers. The separability analysis of the different land cover classes depicted that some pairs of classes have good separability and some pairs of classes do not have much better separability. A transformed

divergence value of 2000 suggests an excellent separation between classes. Above 1900 provides good separation, while below 1700 is poor. Other than the pairs “Water_Body_Turbid” & “Crop_Land”, “Water_Body_Turbid” & “Bare_Soil”, “Water_Body_Turbid” & “Barren_Land”, “Water_Body_Smooth” & “Concrete_Road”, “Crop_Land” & “Barren_Land” and “Bare_Soil” & “Barren_Land”, every other pairs have good separability as shown in figure.

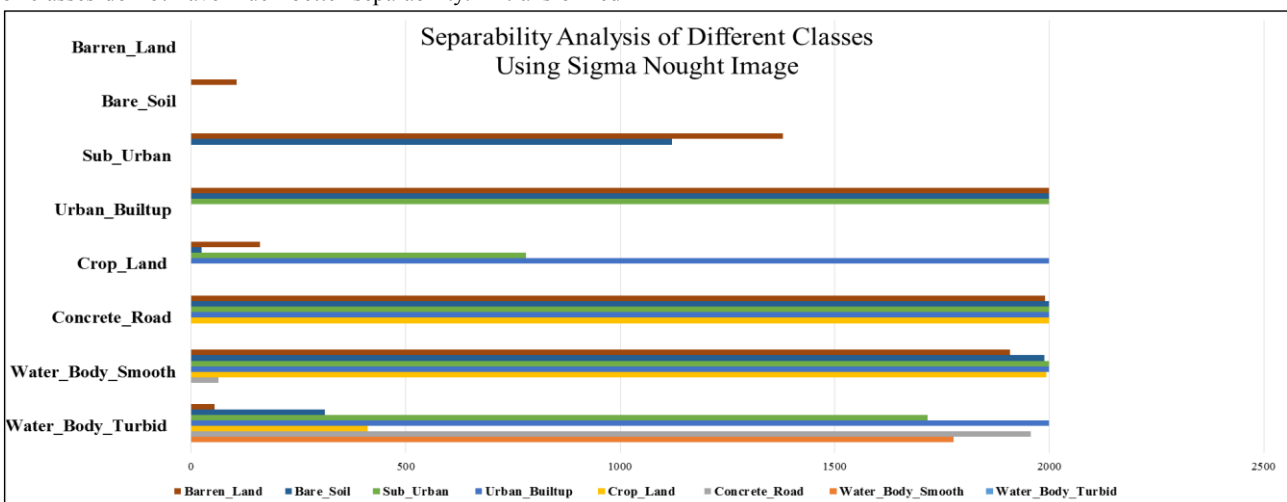


Figure 8. Separability analysis of different classes using sigma nought image

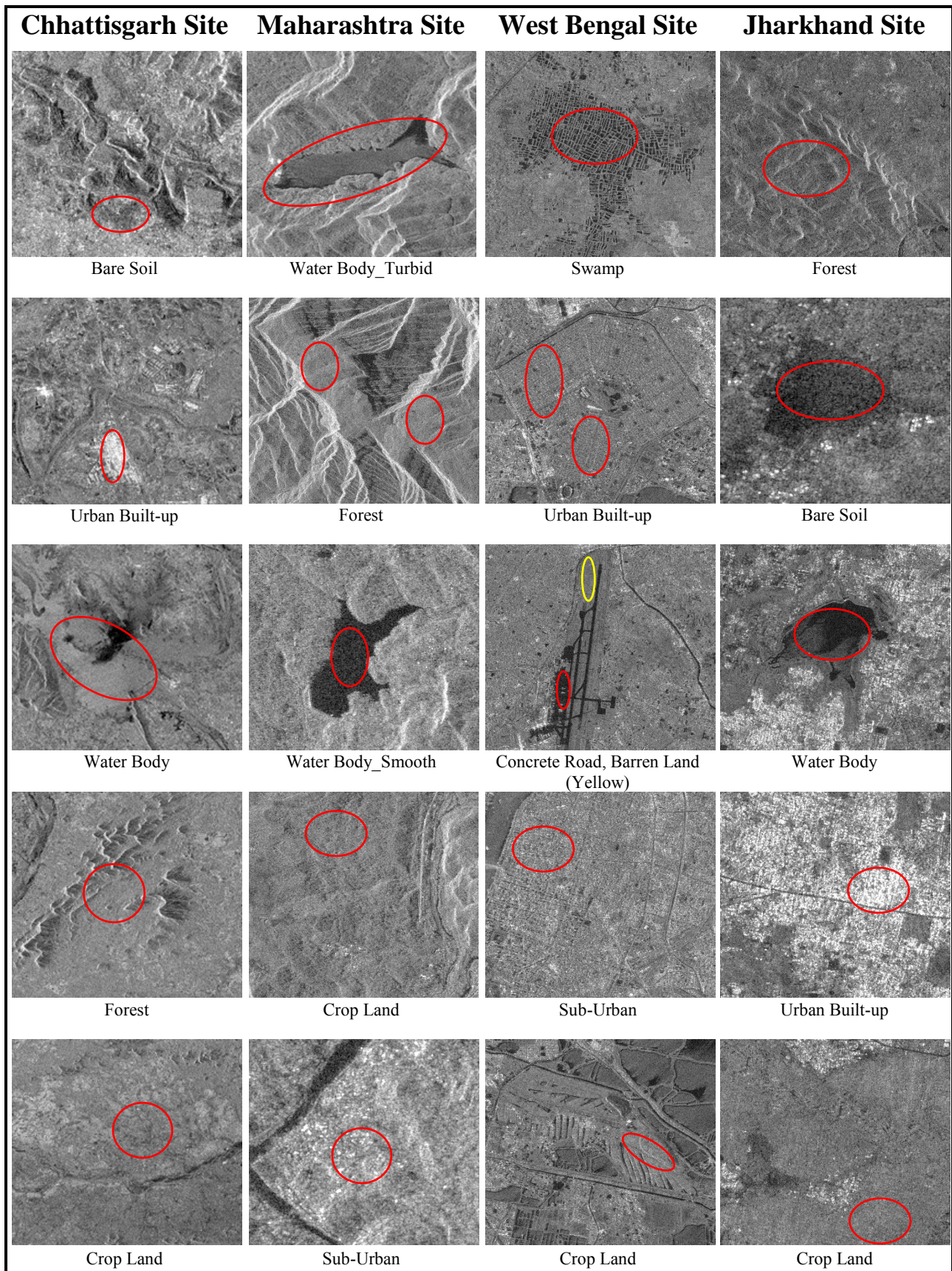


Figure 9. The visual representation of various land use and land cover classes from NovaSAR-1 data acquired on experimental sites

5. CONCLUSIONS

Range of σ^0 pixel values of Calibrated NovaSAR-1 S-band HH polarization datasets corresponding to different LULCs depicted that the data quality is good for the identification of various land use and land cover classes. As two different signatures of the water body were found in the back-scattering analysis of σ^0 images, this data is very much sensitive to the roughness water surface. The texture information of the targets was found clearly visible in 6m spatial resolution datasets. The separability analysis of the different land cover classes depicted that classes have good separability except for a few pairs of land cover classes. With the availability of fully polarimetric as well as single look complex (SLC) interferometric data in the future, the polarimetric scattering behaviour and phase information along with the interferometric performance of the data may be analysed.

ACKNOWLEDGEMENT

Authors would like to thank SSTL (Surrey Satellite Technology Ltd.), UK, Airbus DS (former EADS Astrium Ltd, Stevenage, UK) and Indian Space Research Organization (ISRO) for their insights and support through data sharing platforms. This study was made possible with the resources of Indian Institute of Remote Sensing (IIRS), Indian Space Research Organization (ISRO) Dept. of Space, India. Thanks are given to Director, IIRS for their support which is highly valuable and critical in the presented study.

REFERENCES

- [1] R. Bird, P. Whittaker, B. Stern, N. Angli, M. Cohen, and R. Guida, "NovaSAR-S: A low cost approach to SAR applications," *Conf. Proc. 2013 Asia-Pacific Conf. Synth. Aperture Radar, APSAR 2013*, pp. 84–87, 2013.
- [2] M. Cohen, D. Hall, and P. L. Semedo, "NovaSAR-S low cost SAR Payload," *Proc. Eur. Conf. Synth. Aperture Radar, EUSAR*, pp. 939–942, 2016.
- [3] P. Iervolino, R. Guida, and P. Whittaker, "Novasar-S and maritime surveillance," *Int. Geosci. Remote Sens. Symp.*, pp. 1282–1285, 2013.
- [4] A. Natale, R. Guida, R. Bird, P. Whittaker, M. Cohen, and D. Hall, "Demonstration and analysis of the applications of S-band SAR," *2011 3rd Int. Asia-Pacific Conf. Synth. Aperture Radar, APSAR 2011*, pp. 167–170, 2011.
- [5] B. W. Barrett, E. Dwyer, and P. Whelan, "Soil moisture retrieval from active spaceborne microwave observations: An evaluation of current techniques," *Remote Sens.*, vol. 1, no. 3, pp. 210–242, Sep. 2009.
- [6] R. Ningthoujam *et al.*, "Airborne S-Band SAR for Forest Biophysical Retrieval in Temperate Mixed Forests of the UK," *Remote Sens.*, vol. 8, no. 7, p. 609, Jul. 2016.
- [7] J. R. Jensen, *Introductory Digital Image Processing: A Remote Sensing Perspective*, 2nd ed. USA: Prentice Hall PTR, 1995.

SCENE LEVEL LAND-COVER CLASSIFICATION OF SATELLITE IMAGES USING DEEP LEARNING

Shraddha P. Marbhal¹, Minakshi Kumar²

¹M.Tech (EE) student at Dept. Of Technology, Savitribai Phule Pune University, Pune- shraddhamarbhal@gmail.com,

²Scientist/Engineer-SG, Indian Institute of Remote Sensing, Dehradun- minakshi@iirs.gov.in

KEYWORDS: CNN, Deep learning, Scene-level, Supervised learning techniques

ABSTRACT

The Satellite remote sensing technology gathers data/images at regular intervals. The quantity of received data is very large and is increasing rapidly with the growing technology. The task of classification in remote sensing is usually achieved on a pixel level, object level or scene level. Land cover classification of satellite images using deep learning technique aims to achieve uniform categorisation of landforms. In this paper, a supervised learning technique- convolutional neural network (CNN) model for satellite image classification was developed. High resolution satellite imagery datasets of 0.5 m resolution is used to classify the satellite images into semantic categories. An approximate 97% accuracy of classification is achieved. Furthermore, the study will be extended to resolution of 1m satellite images. Also a brief study of different CNN models used in satellite image classification is shown. The scene level classification classifies images into semantic categories such as forest, commercial area, residential area, etc. It is also observed that scene level classification has the potential to overcome some limitations of pixel and object level classifications. This demonstrates how use of scene-level classification in CNN can assist in improving classification accuracy.

1. Introduction

The Satellite remote sensing technology gathers data/images at regular intervals. The quantity of received data is very large and is increasing rapidly with the growing technology. The task of classification in remote sensing is usually achieved on a pixel level, object level or scene level (Y. Shendryk et al., 2019).

This paper includes a brief survey of pixel level, object level and scene level classification, a brief study of two CNN architectures-VGG and ResNet. Three datasets were used for classification of satellite images, two of which are publicly available dataset and rest one is the proposed high resolution satellite image dataset of a part of Chandigarh area, which is situated in north-west part of India.

2. Survey of pixel level, object level and scene level classification

Scene level classification is the process of labelling images or parts of images, often referred as ‘scenes’ into semantic categories such as forest, agriculture, water-body, etc.. Scene classification is a large, popular and significant area of research especially in the field of high resolution satellite remote sensing. Various study shows that for the use of deep learning approach in image classification, scene level classification provides multiple advantages over pixel and object level classifications. Both pixel and object level classification methods carry little semantic meanings (Cheng et al., 2017), and underperform when classifying ‘obscure’ classes such as haze, cloud shadows etc; in satellite imagery, as their properties could be similar to other land cover types e.g. cloud shadows signal is significantly affected by background features and is usually confused with water and dark vegetation signal (Hughes and Hayes, 2014)). The wealth of any machine learning based image classification problem predominantly depends on the size and quality of the training dataset. Thus in this respect, it is usually faster and easier to generate a training dataset for a scene level classification as compared to a pixel or object level classification. Also, scene level classification tends to have

higher generalization ability, as the contextual information of the whole scene is taken into account in the learning process (Zou et al., 2015).

To do a scene level classification problem, different supervised learning techniques (e.g. random forest, support vector machines, etc.) were studied, with convolutional neural network (CNN) based approaches which commonly shows the most accurate results (Ji et al., 2018).

3. Study of CNN architectures: VGG and ResNet

3.1 VGG architecture: VGG16 is a convolutional neural network model proposed by K. Simonyan and A. Zisserman from the University of Oxford in the paper “Very Deep Convolutional Networks for Large-Scale Image Recognition”.

The architecture depicted below in Figure 1 is of VGG16.

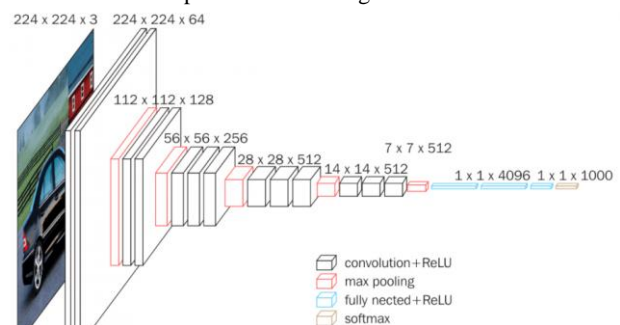


Figure 1: VGG16 architecture

The input to conv1 layer is of fixed size 224 x 224 RGB image. The image is passed through a stack of convolutional (conv.) layers, where the filters were used with a very small receptive field: 3x3 (which is the smallest size to capture the notion of left/right, up/down, centre). In one of the configurations, it also utilizes 1x1 convolution filters, which can be seen as a linear transformation of the input channels (followed by non-linearity). The convolution stride is fixed to 1 pixel; the spatial

padding of conv. layer input is such that the spatial resolution is preserved after convolution, i.e. the padding is 1-pixel for 3×3 conv. layers. Spatial pooling is carried out by five max-pooling layers, which follow some of the conv. layers (not all the conv. layers are followed by max-pooling). Max-pooling is performed over a 2×2 pixel window, with stride 2.

Three Fully-Connected (FC) layers follow a stack of convolutional layers (which has a different depth in different architectures): the first two have 4096 channels each, the third performs 1000-way ILSVRC (ImageNet Large Scale Visual Recognition Challenge) classification and thus contains 1000 channels (one for each class). The final layer is the soft-max layer. The configuration of the fully connected layers is the same in all networks.

All hidden layers are equipped with the rectification (ReLU) non-linearity. It is also noted that none of the networks (except for one) contain Local Response Normalisation (LRN).

There are two major drawbacks with VGGNet:

1. It consumes more time for training images.
2. The network architecture weights themselves are quite large (concerning disk/bandwidth).
3. Due to its depth and number of fully-connected nodes, VGG16 is over 533MB. This makes deploying VGG a tiresome task.

VGG16 is used in many deep learning image classification problems; however, smaller network architectures are often more desirable (such as ResNet, GoogLeNet, etc.). But it has very well equipped building blocks for learning purpose and is easy to implement.

3.2 ResNet: ResNet50 is short-form of Residual Network, a classical neural network. There are many variants of ResNet architecture i.e. same concept but with added layers. There is ResNet-18, ResNet-34, ResNet-50, ResNet-101, ResNet-152 etc. Refer Figure 2. The name ResNet followed by a two or more digit number simply implies the ResNet architecture with a certain number of neural network layers.

In this paper, ResNet-50 is used for classification of high resolution satellite images which is also one of the most vibrant networks on its own.

The architecture of ResNet50 has 4 stages as shown in the diagram below. The network can take the input image having height, width as multiples of 32 and 3 as channel width. For the sake of explanation, we will consider the input size as 224 x 224 x 3. The ResNet architecture performs the initial convolution and max-pooling using 7×7 and 3×3 kernel sizes respectively. Afterward, Stage 1 of the network starts and it has 3 Residual blocks containing 3 layers each. The size of kernels used to perform the convolution operation in all 3 layers of the block of stage 1 are 64, 64 and 128 respectively. The curved arrows refer to the identity connection. The dashed connected arrow represents that the convolution operation in the Residual Block is performed with stride 2, hence, the size of input will be reduced to half in terms of height and width but the channel width will be doubled. As we progress from one stage to another, the channel width is doubled and the size of the input is reduced to half. As ResNet-50 is a deeper network, bottleneck design is used in it. For each residual function F, 3 layers are stacked one over the other. The three layers are 1×1, 3×3, 1×1 convolutions. The 1×1 convolution layers are responsible for reducing and then restoring the dimensions. The 3×3 layer is left as a bottleneck with smaller input/output dimensions.

Finally, the network has an Average Pooling layer followed by a fully connected layer having 1000 neurons (ImageNet class output).

layer name	output size	18-layer	34-layer	50-layer	101-layer	152-layer
conv1	112×112	7×7, 64, stride 2				
		3×3 max pool, stride 2				
conv2.x	56×56	$\begin{bmatrix} 3 \times 3, 64 \\ 3 \times 3, 64 \end{bmatrix} \times 2$	$\begin{bmatrix} 3 \times 3, 64 \\ 3 \times 3, 64 \end{bmatrix} \times 3$	$\begin{bmatrix} 1 \times 1, 64 \\ 3 \times 3, 64 \\ 1 \times 1, 256 \end{bmatrix} \times 3$	$\begin{bmatrix} 1 \times 1, 64 \\ 3 \times 3, 64 \\ 1 \times 1, 256 \end{bmatrix} \times 3$	$\begin{bmatrix} 1 \times 1, 64 \\ 3 \times 3, 64 \\ 1 \times 1, 256 \end{bmatrix} \times 3$
conv3.x	28×28	$\begin{bmatrix} 3 \times 3, 128 \\ 3 \times 3, 128 \end{bmatrix} \times 2$	$\begin{bmatrix} 3 \times 3, 128 \\ 3 \times 3, 128 \end{bmatrix} \times 4$	$\begin{bmatrix} 1 \times 1, 128 \\ 3 \times 3, 128 \\ 1 \times 1, 512 \end{bmatrix} \times 4$	$\begin{bmatrix} 1 \times 1, 128 \\ 3 \times 3, 128 \\ 1 \times 1, 512 \end{bmatrix} \times 4$	$\begin{bmatrix} 1 \times 1, 128 \\ 3 \times 3, 128 \\ 1 \times 1, 512 \end{bmatrix} \times 8$
conv4.x	14×14	$\begin{bmatrix} 3 \times 3, 256 \\ 3 \times 3, 256 \end{bmatrix} \times 2$	$\begin{bmatrix} 3 \times 3, 256 \\ 3 \times 3, 256 \end{bmatrix} \times 6$	$\begin{bmatrix} 1 \times 1, 256 \\ 3 \times 3, 256 \\ 1 \times 1, 1024 \end{bmatrix} \times 6$	$\begin{bmatrix} 1 \times 1, 256 \\ 3 \times 3, 256 \\ 1 \times 1, 1024 \end{bmatrix} \times 23$	$\begin{bmatrix} 1 \times 1, 256 \\ 3 \times 3, 256 \\ 1 \times 1, 1024 \end{bmatrix} \times 36$
conv5.x	7×7	$\begin{bmatrix} 3 \times 3, 512 \\ 3 \times 3, 512 \end{bmatrix} \times 2$	$\begin{bmatrix} 3 \times 3, 512 \\ 3 \times 3, 512 \end{bmatrix} \times 3$	$\begin{bmatrix} 1 \times 1, 512 \\ 3 \times 3, 512 \\ 1 \times 1, 2048 \end{bmatrix} \times 3$	$\begin{bmatrix} 1 \times 1, 512 \\ 3 \times 3, 512 \\ 1 \times 1, 2048 \end{bmatrix} \times 3$	$\begin{bmatrix} 1 \times 1, 512 \\ 3 \times 3, 512 \\ 1 \times 1, 2048 \end{bmatrix} \times 3$
	1×1	average pool, 1000-d fc, softmax				

Figure 2: ResNet layers

Key Features of ResNet:

1. ResNet uses Batch Normalization at its core. The Batch Normalization adjusts the input layer to increase the performance of the network. The problem of covariate shift is mitigated.
2. ResNet makes use of the Identity Connection, which helps to protect the network from vanishing gradient problem.
3. Deep Residual Network uses bottleneck residual block design to increase the performance of the network.

4. Study area

A high resolution satellite image data was used for study purpose. A part of Chandigarh area situated in Punjab state (north-west part of India) was selected from high resolution satellite image data having 0.5m resolution and 90 images in RGB format each of 256x256 pixels were used for further analysis and classification. Refer Figure 3.

Also, two publicly available datasets- NWPU-RESISC45 (Cheng et al., 2017) and PatternNet (Zhou et al., 2018) were used for land cover classification using CNN architecture.



Figure 3: High resolution satellite image of a part of Chandigarh

5. Result

The capability of CNNs for satellite remote sensing imagery classification at the scene level have been extensively investigated on multiple publicly available datasets- NWPU-RESISC45 (Cheng et al., 2017), PatternNet (Zhou et al., 2018). In this respect, convolutional neural network were found to be very robust and accurate method for satellite and aerial imagery classification at the scene level.

It is also found that the above mentioned datasets could be classified using CNNs with accuracies of up to 97%.

It was also noted that pre-training helps to avoid over-fitting and reduce design time of CNN models, while an ensemble of CNN models applied to scene classification generally leads to improved accuracy.

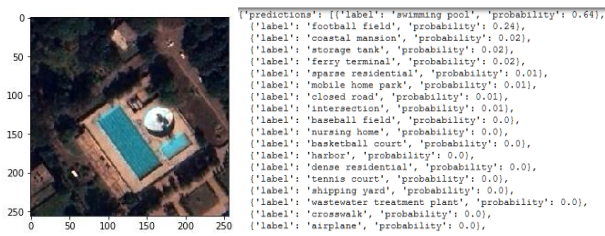


Figure 4: A visualized image from high resolution dataset of Chandigarh area (left) and predicted output of the same (right)

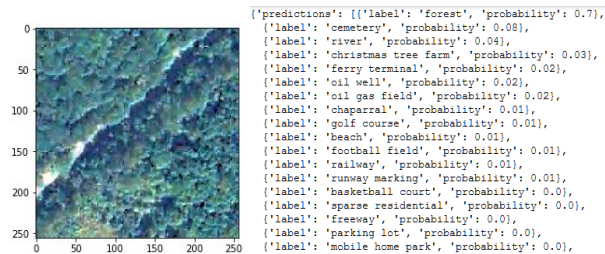


Figure 5: A visualized image from high resolution dataset of Chandigarh area (left) and predicted output of the same (right)

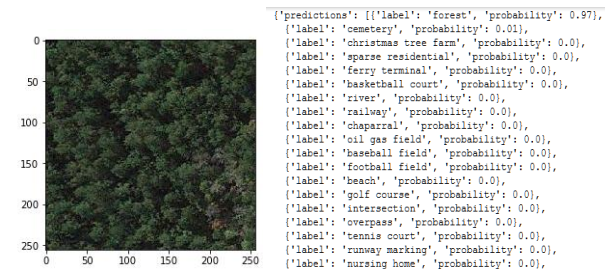


Figure 6: A visualized image from NWPU-RESISC45 dataset (left) and predicted output of the same (right)

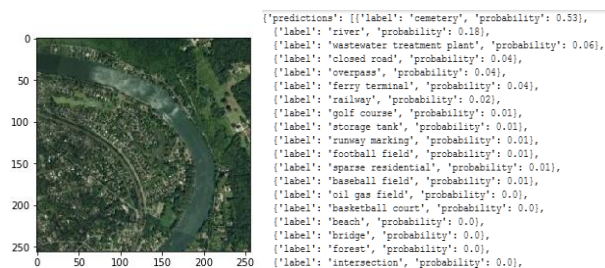


Figure 7: A visualized image from NWPU-RESISC45 dataset (left) and predicted output of the same (right)

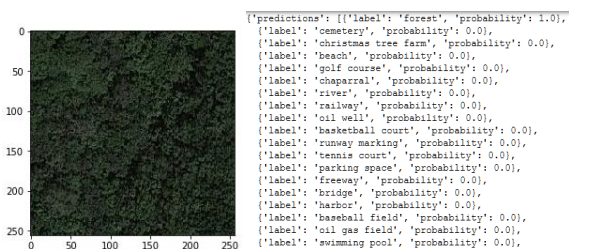


Figure 8: A visualized image from PatternNet dataset (left) and predicted output of the same (right)



Figure 9: A visualized image from PatternNet dataset (left) and predicted output of the same (right)

All datasets were visualized and outputs were predicted completely using python programming language which includes various libraries and pre-trained CNN models viz; ResNet-50 model, keras library, tensorflow library mainly.

A brief comparison of different datasets used for classification of satellite images is depicted in a table. Refer Table 1.

Table 1: Comparison of different datasets used for classification

S. N o.	Dataset	Cl ass es	Image s	Images/ class (approx.)	Resol ution (m)	Size
1	Propose d dataset	3	90	25	0.5	256x256
2	NWPU 45	45	31500	700	0.2-30	256x256
3	Pattern Net	38	30400	800	0.062-4.693	256x256

6. Conclusion

In this paper, a comparative study of various CNN models was done and it was found that even though ResNet-50 architecture is deeper than VGG-16/19 architectures, ResNet-50 has lower time complexity, while training image datasets and is also easy to optimize.

Also the majority of the studies utilizing the above mentioned publicly available datasets, address scene classification as a single-label problem (i.e; each scene is annotated with one class), while the real-world images usually contain multiple labels (i.e. classes could co-exist within a scene).

Furthermore, study will be extended for 1 m resolution of proposed datasets.

REFERENCES

G. Cheng, J. Han, X. Lu. Remote Sensing Image Scene Classification: Benchmark and State of the Art. Proceedings of the IEEE.

Gómez-Chova, L., Tuia, D., Moser, G., Camps-Valls, G., 2015. Multimodal classification of remote sensing images: a review and future directions. Proc. IEEE 103 (9), 1560-1584. <https://doi.org/10.1109/JPROC.2015.2449668>.

Hughes, M.J., Hayes, D.J., 2014. Automated detection of cloud and cloud shadow in single-date Landsat imagery using neural networks and spatial post-processing. Remote Sens. 6 (6), 4907-4926.

Ji, S., Zhang, C., Xu, A., Shi, Y., Duan, Y., 2018. 3D convolutional neural networks for crop classification with multi-temporal remote sensing images. *Remote Sens.* 10(1), 75.

M. Ahmadlou, M. R. Delavar, A. Basiri, M. Karimi. A Comparative Study of Machine Learning Techniques to Simulate Land Use Changes. *Journal of the Indian Society of Remote Sensing* (January 2019) 47(1):53-62

Mark Pritt, Gary Chern. Satellite Image Classification with Deep Learning. 2017 IEEE

Y. Shendryka, Y. Rista, C. Ticehurst, P. Thorburn. Deep learning for multi-modal classification of cloud, shadow and land cover scenes in PlanetScope and Sentinel-2 imagery. *ISPRS Journal of Photogrammetry and Remote Sensing* 157 (2019) 124-136

Zhou, W., Newsam, S., Li, C., & Shao, Z. (2018). PatternNet: A benchmark dataset for performance evaluation of remote sensing image retrieval. *ISPRS Journal of Photogrammetry and Remote Sensing*, 145, 197-209.

Zou, Q., Ni, L., Zhang, T., Wang, Q., 2015. Deep learning based feature selection for remote sensing scene classification. *IEEE Geosci. Remote Sens. Lett.* 12 (11), 2321-2325.

DEVELOPMENT OF WEB BASED CO-REGISTRATION TOOL FOR LARGE POINT CLOUD USING WEBGL BASED RENDERER

Souvik Sankar Mitra ¹, Raghavendra S ²

¹ M.Tech (Geoinformatics Department), Indian Institute of Remote Sensing, India - souviksankar2013@gmail.com

² Scientist/Engineer – SD, Photogrammetry and Remote Sensing Department, Indian Institute of Remote Sensing, India – raghav@iirs.gov.in

KEY WORDS: LiDAR, Potree, Point Cloud Co-Registration, WebGL, Web Visualization

ABSTRACT:

Point clouds are three-dimensional models that consist of points rather than the more widely-used triangle models. They are most commonly obtained as a result of scanning the real world through various scanning methods, such as laser scanning and photogrammetry. Point clouds can be used in various field of study like changes in urban, forest or other types of landscapes, the generation of three-dimensional assets for games and movies etc. In order to present these models to clients or an interested audience, it was traditionally necessary to transfer large amounts of data and to install third-party applications to view. But with limited resources it creates a bottleneck for any client machine. . With the release of WebGL, 3D content distribution over web browsers has become increasingly popular. It has evolved into a standard that is natively supported by all major browsers, on desktop and even mobile devices. Registration is a fundamental task in image processing used to match two or more pictures taken, for example, at different times, from different sensors, or from different viewpoints. These techniques have been independently studied for several different applications, resulting in a large body of research. Potree is a free open-source WebGL based point cloud renderer for large point clouds. It consists of different tools like measurement tool, clipping tool etc. But for two differently aligned point clouds there is no tool to co-register themselves. In this paper, a co-registration tool has been developed in Potree which can co-register two unaligned point clouds. Iterative Closest Point (ICP) algorithm has been used for registration. Through ICP, translation, rotation and scaling parameters have been calculated and one point cloud is moved onto other. Also an error metric i.e. Root Mean Square Error (RMSE) is calculated to find the dissimilarity between actual and co-registered point cloud. This tool will be beneficial for any two point clouds of same region coming from two different sources to co-register themselves.

1. INTRODUCTION

Point clouds are three-dimensional models that consist of points rather than the more widely-used triangle models (Scheiblauer et al., 2014). They are most commonly obtained as a result of scanning the real world through various scanning methods, such as laser scanning and photogrammetry.

Use cases include the generation of three-dimensional maps and globes (e.g. Google Maps, Caesium JS), keeping track of building progress or changes in urban, forest or other types of landscapes, the generation of three-dimensional assets for games and movies, or to capture movement and poses. In many use cases, the point clouds are treated as raw data, which is then refined by converting it into triangle models or two-dimensional images.

In order to present these models to clients or an interested audience, it was traditionally necessary to transfer large amounts of data and to install third-party applications to view it. Sometimes, the data has to be transferred by sending hard disks by mail, due to the large amount of space they require. With the release of WebGL, 3D content distribution over web browsers has become increasingly popular. It has evolved into a standard that is natively supported by all major browsers, on desktop and even mobile devices (Zhu et al., 2018)

To display enormous unprocessed point clouds at interactive rates without requiring long post processing, several algorithms

have been developed. In some algorithm, any assumptions about sampling density or availability of normal vectors for the points is neglected (Wimmer et al., 2006). Also an out-of-core editing system for point cloud is presented which allows selecting and modifying arbitrary parts of a huge point cloud interactively (Scheiblauer et al., 2014). Several sorting algorithms are compared to sort points which decrease point cloud creation time (Leimer, 2015).

Potree is a free open-source WebGL and JavaScript based point cloud renderer for large point clouds, developed at the Institute of Computer Graphics and Algorithms, TU Wien (Schuetz et al.,2016). Potree integrates previous works to build a web visualization system with different measurement tool like height measurement, volume measurement, building height profile etc.

Co-Registration is a fundamental task in image processing used to match two or more pictures taken, for example, at different times, from different sensors, or from different viewpoints (Brown et al., 2003). Similarly point cloud registration is needed to align two point clouds of same region taken by two different instruments by calculating translation, scaling and rotational parameters (Elhabian et al.,2016). Iterative Closest Point (ICP) Algorithm is one of the most used for point cloud co-registration (Ayder et al., 2012). It calculates the spatial transformation parameters as well as measure of error as root mean square error (RMSE). Potree covers various sampling

and filtering operations on point cloud but it lacks point cloud registration. This project involves the development of co-registration tool in potree toolbox using ICP algorithm.

2. STUDY AREA AND DATA USED

The study area is one of the oldest monument in Delhi, the capital of India. Humayun's Tomb is the tomb of the Mughal Emperor Humayun. The tomb was declared as UNESCO World Heritage Site in 1993. Besides the main tomb of humayun, several tombs and pathways are there. It was designed based on Persian architecture and was also the first structure to use red sandstone at such a scale.

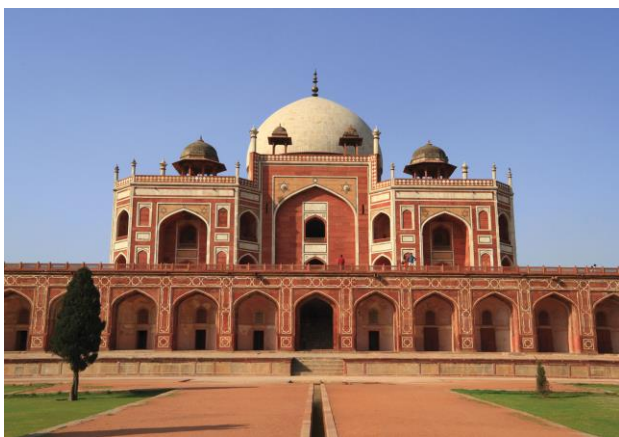
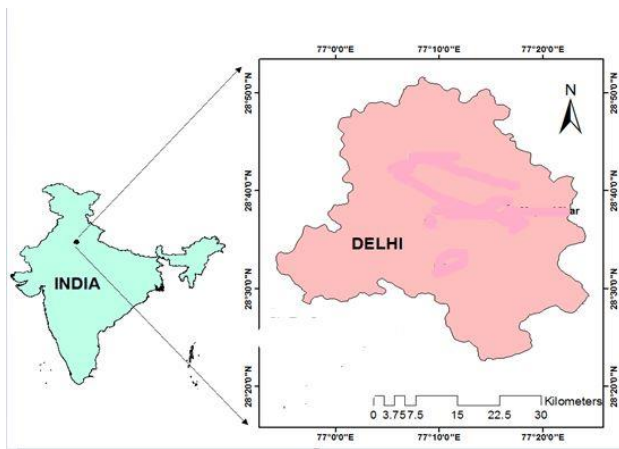


Figure 1: Study Site

Terrestrial Laser Scanner (TLS) is used to take point cloud. FARO FocusS 350 is the most compact, lightweight and intuitive TLS designed by FARO. It is designed for short, medium and long range applications and extensively used in the field of Architecture, Engineering, Construction, Public Safety and Forensics or Product Design.

Providing onsite registration during on-site data capture, the laser scanner immediately transmits scan data wirelessly providing efficiency and time savings. In this project, this function was disabled to get non registered point cloud.

Cloudcompare software is used to pre-process the point cloud before feeding it to potree. Potree JavaScript library is used to sample the point cloud for smooth visualization in browser.

XAMPP server is used for hosting the whole potree system in local server.

3. METHODOLOGY

3.1 Data Capture

A part of the study area is scanned with TLS keeping resolution as 1:16. This part is automatically co-registered within the TLS. Also keeping the automatic registration disabled, a small monument besides the main tomb is scanned. These two point clouds are used for validation of the co-registration algorithm.

3.2 Pre-processing

Generally, TLS does not visualize any colour in the raw scan. FARO FocusS 350 stored the colour information of every point by taking photographs after scanning. But to visualize the colour pre-processing is necessary. Also during scan along with location information some redundant information is also stored. So using Cloudcompare software these are removed, RGB information is retrieved and the point cloud is exported as ASCII text file.

3.3 Point Cloud Sampling

Using the potree converter this point cloud is converted to a subsampled one. Also corresponding html page and required javascript libraries are also installed. As different subsamples of the point cloud is generated it results smooth rendering of point in any system irrespective of processing and memory capacity.

An apache web server has been setup to host the subsampled point cloud on the web. Through the web server these point clouds can be accessed by any other system.

3.4 Iterative Closest Point Algorithm

Iterative closest point (ICP) algorithm is used to align two partially overlapping meshes given initial guess for relative transform. . It consists of a model shape which can be represented as Point Sets, Line Segment Sets, Implicit Curves, Parametric Curves, Triangle Sets, Implicit Surfaces and Parametric Surfaces. Given a scene shape which is represented as a point set, the scene shape may correspond to the model shape. The algorithm is –

- i) Begin with initial rotation, translation and scaling (initial value for registration parameters).
- ii) Fix the model shape and start moving the scene shape by applying the initial registration parameters. i.e. scale, rotate and then translate.
- iii) Compute the error metric that reflects the dissimilarity of the scene shape from the model shape.
- iv) If the error is minimum, we have correctly aligned the scene shape to the model shape, return with the aligned scene shape.
- v) Else calculate the new values for the registration parameters and go back to ii) with the new parameter values.

3.5. ICP in Potree

In Potree, minimum three reference point correspondences need to be selected in the model shape and scene shape. Given two points p_i in scene point and m_i in model point the Euclidean distance can be computed as follows –

$$d(p_i, m_k) = \|p_i - m_k\| = \sqrt{(p_{xi} - m_{xk})^2 + (p_{yi} - m_{yk})^2 + (p_{zi} - m_{zk})^2} \quad (1)$$

Given a scene point p_i and a model point set M , the Euclidean distance between p_i and M can be found as,

$$d(p_i, M) = \min_{k=1, \dots, N_M} d(p_i, m_k) = \min_{k=1, \dots, N_M} \|p_i - m_k\| \quad (2)$$

The final transformation equation would be like,

$$Y = sR(P) + t \quad (3)$$

Where, s = scale factor

t = Translation offset

$R(P)$ = rotated version of a scene point P

So using the correspondence points scale factor, translational offset and rotated vector is calculated. Then equation (3) is applied on every scene point.

Root Mean Square Error (RMSE) is calculated as error metric.

$$\sqrt{\frac{1}{N_p} \sum_{i=1}^{N_p} (y_i - (sR(P_i) + t))^2} \quad (4)$$

Where, N_p = Total number of scene points

y_i = Actual co-ordinate of scene point

4. RESULTS AND DISCUSSION

Using Potree Converter the point cloud is subsampled and visualized in browser using local server. Two point clouds are taken separately for running the co-registration tool. One is used as scene shape and one is model shape.

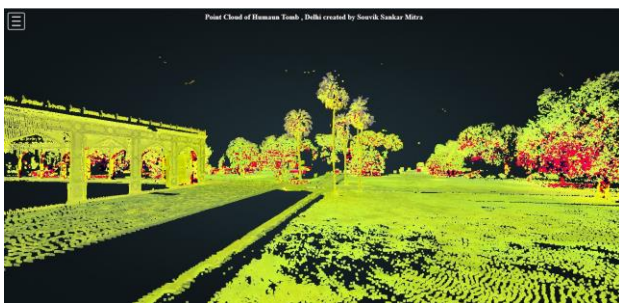


Figure 2: The Model Shape



Figure 3: The Scene Shape

Using javascript the algorithm is implemented and a button for the new point cloud registration tool is generated.



Figure 4: Point Cloud Registration Tool

Now three points are selected on the scene shape and the model shape. Then by clicking the tool, the scene shape is transferred onto its aligned position with model shape. The corresponding value is shown as javascript alert box.

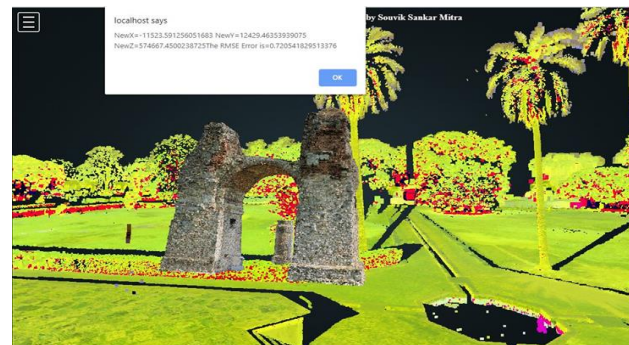


Figure 5: The co-registered point cloud

The root mean square error is found to be in between 0.5 to 0.7.

5. CONCLUSIONS

This study shows an effective way of visualizing large point cloud through web using Potree WebGL renderer irrespective of system's processing power. Also it shows development of co-registration tool in Potree to align to point clouds of same area. ICP algorithm is used in this purpose. The RMSE coming can be improved by taking some measurements. Potree has many measuring and aligning tool in its toolbox but it lacks some functions. In future, different tools like co-registration tool can be developed in Potree toolbox.

REFERENCES

- Aydar, U., Altan, M. O., Akyılmaz, O., & Akca, D. (2012). Co-Registration of 3D Point Clouds By Using an Errors-in-Variables Model. *ISPRS - International Archives of the Photogrammetry, Remote Sensing and Spatial Information Sciences*, XXXIX-B5(September), 151–155. <https://doi.org/10.5194/isprsarchives-xxxix-b5-151-2012>
- Elhabian, S., Farag, A., & Farag, A. (2009). A Tutorial on Rigid Registration Iterative Closed Point (ICP). (March).
- Gottesfeld, L. (1992). A Survey of Image Registration. (4).
- Scheiblauer, C. (2014). *Interactions with Gigantic Point Clouds*. 2014.
- Scheiblauer, C., & Wimmer, M. (2011). Out-of-Core Selection and Editing of Huge Point Clouds. 43(1).
- Schuetz, M. (2016). Potree : Rendering Large Point Clouds in Web Browsers, Science, B. O. (n.d.). External Sorting Of Point Clouds.
- Wimmer, M., & Scheiblauer, C. (2006). *Instant Points : Fast Rendering of Unprocessed Point Clouds*.
- Zhu, Q., Wu, J., Hu, H., & Xiao, C. (2018). Applied sciences LIDAR Point Cloud Registration for Sensing and Reconstruction of Unstructured Terrain. <https://doi.org/10.3390/app8112318>

IMPLEMENTATION OF SEMANTIC SEGMENTATION ON UAVSAR DATA

Rajat Garg⁽¹⁾, Anil Kumar^{*(1)}, and Shashi Kumar⁽²⁾

¹ University of Petroleum and Energy Studies, Dehradun, India – rajat.garg@ddn.upes.ac.in, anil.kumar@ddn.upes.ac.in

² Indian Institute of Remote Sensing, Indian Space Research Organization, Dehradun, India - shashi@iirs.gov.in

KEYWORDS: Deep learning, SAR, Semantic Segmentation, G4U decomposition.

ABSTRACT:

Simultaneous advances in the fields of deep learning and SAR based remote sensing has opened doors to plethora of research opportunities in a multi-disciplinary field of SAR data analytics. With recent developments in SAR sensors, we can capture high resolution data which can be used for better feature identification and thus highly accurate classification of SAR images. In this research, we have implemented a deep learning model for segmentation of every pixel present in our target area. We have chosen UAVSAR data of Houston City because it covers wide variety of features (Urban, Forest, Water Bodies and Grassland). For target decomposition, we have used G4U decomposition and the output of target decomposition is used for creating training dataset for our deep learning model. We have created a synthetic dataset consisting of 4000 images (size - 500*500 pixels each) and corresponding masks for training and we have done prediction on a small cropped image taken from original full image (size- 3300*24151 pixels). We are using Deeplab V3 model available in Tensorflow library in Python for implementing Semantic Segmentation on SAR data. The coordinates of UAVSAR data used are- Upper Left Latitude & Longitude = 30.451693023°, -95.870641693°; Upper Right Latitude & Longitude = 30.554906778°, -95.673900697°; Lower Left Latitude & Longitude = 29.107619024°, -94.943386924°; Lower Right Latitude & Longitude = 29.210412641°, -94.746501515°.

Initial experiments on this SAR data set has given promising results with overall accuracy of 99.16% on synthetic data and 80% on original image data. For further improvement, we are annotating actual images in addition to working with synthetic data. The benefit of using synthetic data is that it can be created within minutes by running a python code while creating real dataset requires manual annotation of hundreds of images which is very cumbersome and time consuming task. Thus, we can quickly create synthetic dataset as per requirement for training our model and we can make predictions on both synthetic and real data from that trained model. The scope of this paper will be limited to the discussion of methodology followed and results obtained by training on synthetic dataset only.

1. INTRODUCTION

The emergence of Deep Learning technologies has taken every industry by storm and SAR based remote sensing is no exception. The possibilities in this multi-disciplinary domain have further increased with availability of high resolution SAR data from various airborne and spaceborne missions like UAVSAR by NASA, Sentinel by ESA.

The UAVSAR data is made freely available for open access by NASA. We have downloaded a scene of Houston city and the data is available as covariance matrix. This covariance matrix is used as an input for target decomposition. While there are many algorithms available for target decomposition, we have chosen G4U decomposition [1] since it gives good results in regions containing diverse features. The image obtained from target decomposition is used for creating dataset for training our deep learning model Deeplab V3 [2].

Semantic segmentation is one of the key applications of deep learning. It involves linking every pixel of an image to a class label. Recently, many machine learning algorithms have been proposed to achieve this task and Convolutional Neural Network (CNN) based models have performed the best. The traditional machine learning algorithms were manually designed whereas a CNN based algorithm learns automatically through backpropagation. The presence of large number of convolution layers provide for better non-linear fitting. A fully convolutional network (FCN) was proposed by Long [3] which preserves spatial information by utilizing upsampling operation, replacing fully connected layers. The subsequent models have followed the same idea.

2. METHODOLOGY

In this work, a deep learning model Deeplab V3 has been implemented for semantic segmentation of PolSAR data. Figure 1 shows flow diagram of the process followed.

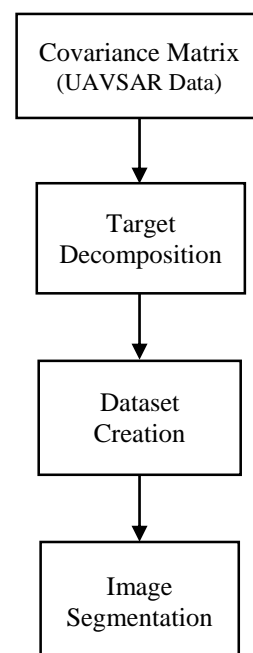


Fig.1 shows the flow chart of the work.

The UAVSAR dataset used for the analysis has 2m resolution and the scene chosen has a dimension of 3300*24151 pixels. The covariance matrix has 9 elements and model-based target decomposition methods tries to account for maximum of these elements.

2.1 TARGET DECOMPOSITION

Target decomposition is a process of classifying the SAR data scene into different classes based upon the backscatter from the surface feature. A successful and widely accepted model-based decomposition algorithm was proposed by Freeman and Durden [4] in 1998 which is used as a base for almost all the subsequent algorithms proposed. Another model based on four scattering components was proposed by Yoshio Yamaguchi [5] in 2005 which was able to enhance the urban features and thereby reduce the misclassification of urban features as forest. Another four-component model was proposed by Gulab Singh with unitary rotation of Coherency Matrix which is one of the most accurate models available. This G4U model has been implemented in this work with help of Python programming. The output of G4U decomposition is saved as a tiff image.

2.2 DATASET CREATION

We create small patches of 500*500 from the full image and crop 100 samples each of water, ground, residential, commercial and forest. These feature classes are used as foregrounds and a black image is used as background for creating synthetic dataset. Foregrounds are selected randomly within our python script and pasted on the black background to create a synthetic image. This process is repeated in the for loop till the desired number of images are created. We have created 4000 images using this script and used them for training and we have tested our model on 2 images, one synthetic image and one actual image.

2.3 IMAGE SEGMENTATION

Image segmentation has brought a revolution in the field of image processing, machine vision and related applications. One of the important tasks is Semantic Image Segmentation which gives pixel level information. While there are many models available for achieving the same, we have chosen Deeplab V3 which is one of the recent models and gives highly accurate results. A pre-trained model based on Xception architecture is used for transfer learning which is available on tensorflow’s github repository. We have ignored the logits so that model can learn on our own custom dataset which has different number of classes compared to PASCAL VOC dataset. The dataset needs to be converted to tfrecord file format before it can be passed on to the model for training. So, after preparing training and test sets, we convert them into compatible tfrecord format and the script for the same is available in Deeplab itself.

3. RESULTS

Deeplab V3 comes with a visualization code that can be used for obtaining predictions on test set. Initially we have done prediction on two images only, one from synthetic dataset and one from original dataset.

The synthetic image and its corresponding prediction is shown in figure 2(a) and figure 2(b) respectively. We have obtained an overall accuracy of 99.16% on synthetic dataset.

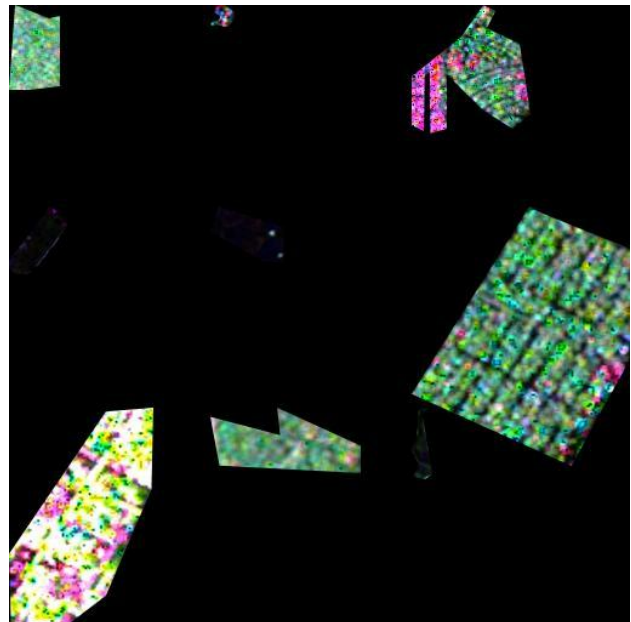


Fig. 2(a) Synthetic dataset image containing samples from Forest, Residential, Commercial and Field fixed on a black Background.

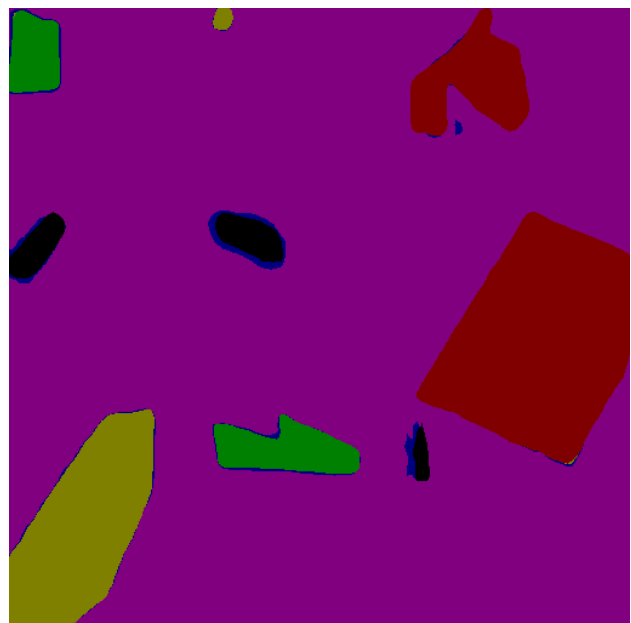


Fig. 2(b) Predictions on Synthetic image. Red = Residential, Green = Forest, Black = Field, Pink = Background.

Table 1. Truth Table of Synthetic data

Class	Forest	Residential	Commercial	Field	BG
Forest	3	0	0	0	1
Residential	0	15	0	0	0
Commercial	0	0	7	0	0
Field	0	0	0	2	0
BG	0	0	0	0	92

*BG= Background

The original image and its corresponding prediction is shown in figure 3(a) and figure 3(b) respectively. We have obtained an overall accuracy of 80% on original dataset.



Fig. 3(a) An image snippet (500*500 pixels) from original data having variety of features – Water, Residential, Commercial, Forest, Field.

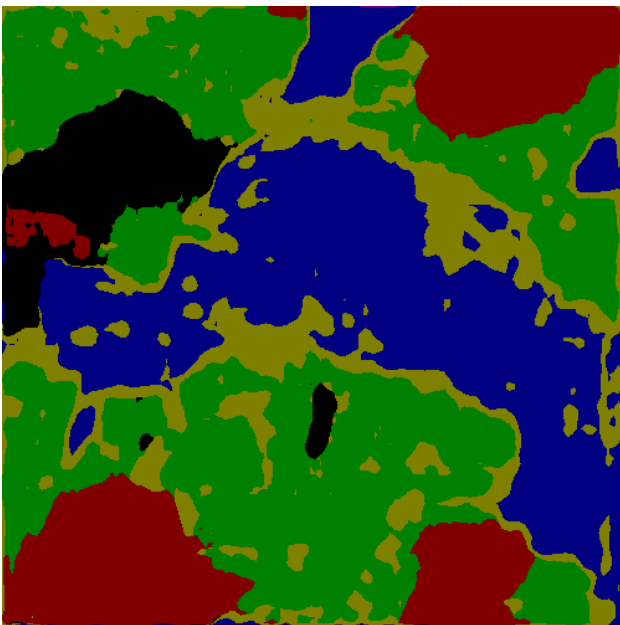


Fig. 3(b) Fig. 2(b) Predictions on Synthetic image. Red = Residential, Green = Forest, Black = Field, Blue = Water.

Table 2. Truth Table of Original data

Class	Forest	Residential	Commercial	Field	Water
Forest	11	0	0	0	0
Residential	13	23	1	0	0
Commercial	3	0	14	0	0
Field	4	0	0	7	3
Water	0	0	0	0	41

4. CONCLUSION

In this paper, Deeplab V3 has been implemented with Exception as base architecture for doing semantic segmentation on UAVSAR fully polarimetric data after implementing G4U decomposition. The initial experiments done on synthetic dataset have given promising results and we can extend this work by training on original dataset for getting highly accurate segmentation at pixel level. Also, fine tuning of hyper parameters and selection of custom filters for SAR data can further enhance the performance of the model.

ACKNOWLEDGEMENT

The authors would like to thank UAVSAR team for making SAR data available.

REFERENCES

Gulab Singh et. al., 2013: General Four-Component Scattering Power Decomposition with Unitary Transformation of Coherency Matrix, IEEE Transactions on Geoscience and Remote Sensing, Vol. 51, No. 5, May 2013.

Liang-Chieh Chen et. al., 2017: Rethinking Atrous Convolution for Semantic Image Segmentation.

Long et. al., 2015: Fully convolutional networks for semantic segmentation, Proceedings of the IEEE conference on Computer Vision and Pattern Recognition, Boston, MA, USA, 7-12 June 2015, pp. 3431-3440.

Anthony Freeman, 1998: A Three-Component Scattering Model for Polarimetric SAR Data, IEEE Transactions on Geoscience and Remote Sensing, Vol. 36, No. 3, May 1998.

Yoshio Yamaguchi et. al., 2005: Four-Component Scattering Model for Polarimetric SAR Image Decomposition, IEEE Transactions on Geoscience and Remote Sensing, Vol. 43, No. 8, Aug 2005.

Anirban Mukhopadhyay et. al., 2009: Unsupervised Satellite Image Segmentation by Combining SA Based Fuzzy Clustering with Support Vector Machine, Seventh International Conference on Advances in Pattern Recognition, 4-6 Feb. 2009, doi:10.1109/ICAPR.2009.50.

Jie Geng et. al., 2017: Deep Supervised and Contractive Neural Network for SAR Image Classification, IEEE Transactions on Geoscience and Remote Sensing, doi: 10.1109/TGRS.2016.2645226.

Lifu Chen et. al., 2019: A New Deep Learning Algorithm for SAR Scene Classification Based on Spatial Statistical Modeling and Features Re-Calibration, Sensors, MDPI, 30 May 2019, doi: 10.3390/s19112479.

Yinjie Xie et. al., 2019: A Novel Convolutional Neural Network Architecture for SAR Target Recognition, Advanced Sensor Technologies in Geospatial Sciences and Engineering, doi: 10.1155/2019/1246548.

Lifu Chen et. al., 2019: A New Deep Learning Algorithm for SAR Scene Classification Based on Spatial Statistical Modeling and Features Re-Calibration, Sensors, MDPI, doi: 10.3390/s19112479.

SCIENTOMETRIC REVIEW OF PUBLICATIONS ON GEOSPATIAL TECHNOLOGY

Rishabh Singh¹, Sudhakar Shukla¹

¹ Remote Sensing Applications Centre, Lucknow, Uttar Pradesh, India- 226021- er.rishabh.singh@outlook.com

KEY WORDS: Geospatial Technology, Scientometrics, Geographic Information System, Remote Sensing, Global Positioning System

ABSTRACT:

In the present study, a Scientometrics study was done on the literature present on Web of Science for “Geospatial Technology”. Geospatial technology is a booming area of research which refers to the acquisition of data through different technologies such as Geographic Information system, remote sensing, and global positioning system followed by its evaluation to interpret the results. The evaluation and interpretation include raw data processing, analysis, modelling, simulation, visualization and its interpretation. The main objective of this study was to find out research trend in the field of geospatial technology. The result of the search on web of science yielded 242 results. It was found that the highest number of publications were published in 2019 and almost an increasing trendline observed since the year 2000. In terms of document types, research articles were recorded as highest with 214 publications. The country leading in terms of publication in “geospatial technology” is USA followed by India, China, Australia and Canada. The leading journal in terms of publication is Remote Sensing followed by Computers and Electronics in Agriculture and Applied Geography. The leading research areas in which the geospatial technology is applied environmental sciences ecology followed by geology and then remote sensing. From this study it can be concluded that the geospatial technology is highly applied in the field of Environmental Sciences Ecology while its use in the field of agriculture and engineering should be emphasized to meet the sustainable development goals.

1. INTRODUCTION

Geospatial technologies are used to describe Mapping of Earth and its' features using modern technologies. It has been evolving since prehistoric times when first maps were drawn. In 1800's the use of cartography and mapmaking together with aerial photography developed. Remote sensing is one form of technology of geospatial technology focused on interpretation of aerial photographs through analysis of images from the satellites followed by its digital computing in the latest developments. Geospatial technology can also be used in assessing various key parameters in agriculture which help develop better methods for enhanced crop yields. With the advent of advanced technologies and increasing focus towards resolving issues of remote areas the practical application of geospatial technology has stretched arms. Apart from its application in remote sensing (Dar et al., 2011) it is also used fields such as agriculture (Rafoss et al., 2010), engineering (Nugent et al., 2010), and even psychology (Metoyer and Bednarz, 2017).

With increasing importance of the research on geospatial technology a scientometric evaluation of its work would help the scholars gain metric insights about the field. It will also help assessing the importance of technology in major research areas as well as the preferred journals which cover the works related geospatial technology. Though there have been scientometric studies on different related topics (Olawumi and Chan, 2018; Biljecki, 2009) but that on geospatial technology remains missing. Therefore, to highlight the importance of geospatial technology and its importance in different field along with the assessment of level of development, this study has been performed.

2. REVIEW OF LITERATURE

A similar kind of study was performed by Papadimitriou and Kidman (2012), in which they analyzed statistic and scientometric features of articles published in the journal,

‘International Research in Geographical and Environmental Education. They covered years of publications and performed several statistical tests. Another study by Olawumi and Chan (2018), highlighted the importance of sustainability research through similar type of study. They reviewed 2096 bibliographic records from web of science database and analyzed the same. They used techniques such as co-author, co citation and cluster analysis to obtain finding based bibliographic details. A selective journals study was performed by Biljecki (2016), in which he analyzed 12,436 papers published in 20 GIScience journals in 15 years duration. They analyzed publication patterns and trends. Their study focused on output volume, respective countries output, followed by collaboration statistics and altmetrics. An interesting study by Liu and Gui (2016), mapped transport geography research quantitatively through intellectual structures and its dynamics. They analyzed 4840 articles published during 33 years of time.

3. METHODOLOGY

The study consists of Scientometrics review of publications in the field of geospatial technology. The study was conducted after the collection of data from Web of Science database. The data was downloaded using the following specifications: “geospatial technology”, “all fields” followed by no other filter. The data collected was then downloaded and analysed, followed by the interpretation of the results.

The primary objectives of the study include the analysis of publication performance in the field of “geospatial technology”. Specifically, it aims to shed light upon:

- The year-wise publication trend in recent years
- The major countries leading the publications and consequently research

- The major research areas in which the publications are done
- The leading journals for selected for the publications
- The leading organizations contributing towards publication through research

4. RESULTS AND DISCUSSION

4.1. The year-wise publication trend in recent years

It has been analysed that an increasing trend in the number of publications has been observed in the recent years. The most productive year is 2019, followed by years 2018, 2017 and 2015 (fig 1). The year 2019 saw a rapid rise in the number of publications and considering the trend it can be inferred to be increasing in the year 2020 as well. From the observation, it can also be concluded that the research in the field of geospatial technology is in its early stages.

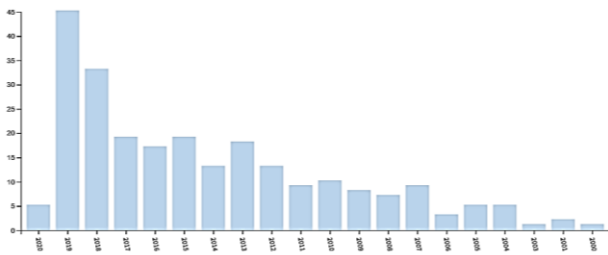


Fig 1. Year wise growth of publications in the field of geospatial technology

4.2. The major countries leading the publications and consequently research

A graph for the countries with leading number of publications was obtained and it can be observed that USA holds the top rank with highest number of publications while India and China have been placed on the second and third spot respectively (fig 2). There are many developed and developing countries in the list suggesting they are working the field of geospatial technology. But as is observed from the graph first three bars collectively account for majority of publications. Conclusively, it can be observed that these three countries combined account for the majority of the research with more than 50% of the total publication in the area combined.

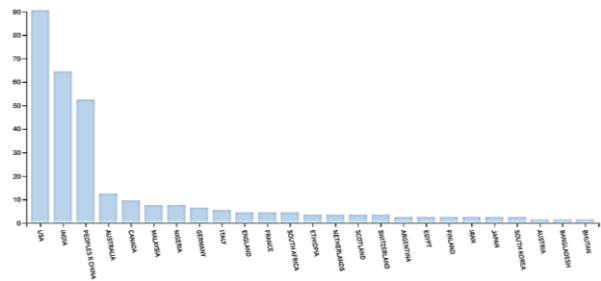


Fig 2. Country wise number of publications in the field of “geospatial technology”

4.3. The major research areas in which the publications are done

The major research areas in which the articles have been published are the ‘environmental science’, ‘geology’, and ‘remote sensing’. These three research areas account for the majority of work done in the field of geospatial technology (fig 3). Other areas include agriculture, computer science, forestry, chemistry, food science and health care, engineering, chemistry and even psychology. This goes to show that the application of geospatial is diverse and research is being carried out with multidisciplinary approach. Its use in agriculture, engineering and urban studies is well known, but its use in chemistry and psychology attracts some attention.

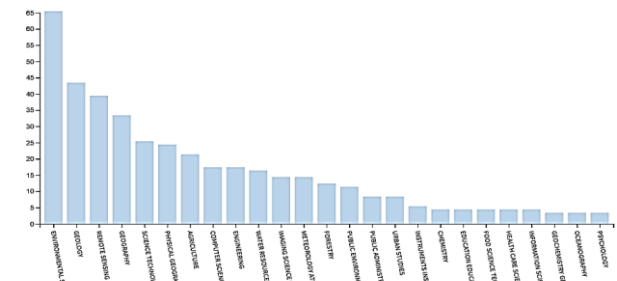


Fig 3. Major research area wise the number of publication in the field of “geospatial technology”

4.4. The leading journals preferred for the publications

The leading journals preferred for publication observed is ‘Remote Sensing’ (Q1: 4.1) followed by ‘Computer and Electronics in Agriculture’ (Q1: 3.17), ‘Applied Geography’ (Q1: 2.56) and ‘Journal of Geography’ (Q2: 1.26). Other journals such as ‘Journal of Forestry’ (Q1: 1.98), ‘Current Science’ (Q2: 0.75), ‘Geospatial Health’ (Q1: 1.42) and ‘Plos One’ (Q1: 2.776) have also been selected as journals for the publications (fig 4). Further analysing the credentials of journals it was observed that the most of the journals preferred for publication were best quartile journals with impact factors (The values mentioned in the form of Q represent quartiles followed

Olawumi, T. O., and Chan, D. W., 2018. A scientometric review of global research on sustainability and sustainable development. *J. Clean. Prod.*, 183, 231-250.

Papadimitriou, F., and Kidman, G., 2012. Statistical and scientometric analysis of international research in geographical and environmental education. *International Research in Geographical and Environmental Education*, 21(1), 11–20.

Rafoss, T., Sælid, K., Sletten, A., Gyland, L. F., and Engravslia, L., 2010. Open geospatial technology standards and their potential in plant pest risk management—GPS-enabled mobile phones utilising open geospatial technology standards Web Feature Service Transactions support the fighting of fire blight in Norway. *Comput. Electron. Agric.*, 74(2), 336-340.

PERFORMANCE ANALYSIS OF TERRESTRIAL LASER SCANNERS FOR POINT CLOUD INTEGRATION

Saumyata Srivastava^{1*}, Esha Semwal¹, Chandan Grover¹, Hina Pande¹, Poonam S Tiwari², S. Raghavendra¹, S. Agrawal¹

¹Photogrammetry and Remote Sensing Department, Indian Institute of Remote Sensing, Indian Space Research Organization, Dehradun (saumyata.srivastava, , esha.semwal1, chandangrover32) @gmail.com, (hina, raghav, shefali_a) @iirs.gov.in

²Geoweb services, IT & Distance Learning Department, Indian Institute of Remote Sensing, Indian Space Research Organization, Dehradun (poonam@iirs.gov.in)

* Corresponding Author

KEYWORDS: Terrestrial Laser Scanner, TLS, Lidar, Leica, Faro, accuracy assessment.

ABSTRACT

Nowadays, there are various type of Terrestrial Laser Scanner (TLS) scanners with their respective accuracy and product quality. Thus, accuracy assessment is a requisite step if we need accurate result while integrating those scans into one. Precision valuation of multi-data integration is also essential as point cloud density vary with distance and elevation. The current study emphases on accuracy assessment of two terrestrial laser scanners. The laser scanning systems used for this study are Faro Focus350 and Leica P50. In this paper, the individual as well as comparative study of both the scanners is done, keeping the environment constant in which scans are been acquired. The intensity data was studied for the diagnostics of a building and other structures. The point cloud variation is studied on increasing the elevation of the sample while keeping its XY coordinates constant. In accordance with the result, the RGB value of data obtain from Leica P50 Canon EOS 60D camera differ from Faro Focus350 integrated colour camera. Thus, the final product from these two scanner may show variation when view in true colour composite. But there is not much difference in their point cloud density, so they are compatible with each other. Though point cloud obtain from Faro scanner shows more detail features for small distance.

1. INTRODUCTION

There has been a remarkable increase in the application of terrestrial laser scanners in the last few decades because of its capability to generate highly precise, realistic and three dimensional point cloud datasets of complex environments and geometries. Since the launch of first commercial terrestrial laser scanner in 1998, The hardware part of terrestrial laser scanner has experienced frequent improvement, marked by reduction in size, weight and price and as well as constantly increasing spatial resolution, improved accompanying of digital imagery and faster scanning. At present, a large variety of terrestrial scanners are available in the market with their respective accuracy and product quality. The overall performance of a laser scanning system should be tested in comparison with other laser scanning systems, in order to see, if the system fulfils the user requirements for specific applications. Thus, accuracy assessment is a requisite step if we need accurate result while integrating data from different scanners.

In present work the scanning systems used were FARO FOCUS 350 and LEICA P50. Both the scanners use time-of-flight method and near infrared wavelength for scanning. The Laser Scanner FocusS350 series offers advanced functionality in addition to increased distance, angular accuracy, and range they ensures high-quality measurements. The Leica ScanStation P50 delivers highest quality 3D data and HDR imaging at an extremely fast scan rate. Its range and angular accuracy paired with low range noise and survey-grade dual-axis compensation

form the foundation for highly detailed 3D colour point clouds mapped in realistic clarity. Along with laser scanner, we have also used Total Station and Global Navigation Satellite System (GNSS) for measuring the distance and coordinates of certain points on ground which were visible in scans.

2. DATA ACQUISITION

2.1 TLS systems used

For scanning of our site we have used two Terrestrial Laser Scanner (TLS). Thus, point cloud data is acquired from TLS Faro S350 and Leica P50. Moreover, Leica P50 has its own Survey setup functionality, it could orient itself and back sight the target at the time of georeferencing. The ScanStation P50 is generally used for large distance scanning and outdoor laser scanning projects where high data quality is a must, but with a focus on longer distances to be covered. (Leica Geosystems AG, 2017) This ranges from capturing tall buildings and large infrastructure objects such as skyscrapers, dams and bridges, to the 3D documentation of big pit mines. Unreachable sites like hillside slides can also be scanned from a remote and safe position. The FARO laser scanner is characterised by its arrangement, it has single laser unit comprised of laser, mirror and integrated camera. (FARO, 2019) Faro Focus S350 is usually used for short distance scanning or for indoor scanning for which detailing is essential, as maximum range for this scanner is 350 meter. Comparison for both the data has been done in this study. Table 1 shows the general specification of both the instruments.

		
Name	Faro S350	Leica P50
Range Accuracy	± 1mm	1.2 mm + 10ppm over full range (120 m / 270 m mode) 3 mm + 10ppm over full range (570 m / >1 km mode)
Angular accuracy	19 arcsec for vertical/ horizontal angles	8” horizontal; 8” vertical
Wavelength	1550nm	1550 nm (invisible) / 658 nm (visible)
Resolution:	Up to 165 megapixel color	4 megapixels per each 17° × 17° colour image; 700 megapixels for panoramic image
Field-of-View:		
Horizontal	360°	360°
Vertical	300°	290°
GPS	Yes	No
Compass	Yes	Yes
Height Sensor	Yes	No
WLAN	Yes	Yes
Data storage capacity	SD, 256GB card	256 GB internal solid-state drive (SSD) or external USB device

Table 1 : Comparison of Specification of both TLS system

2.2 Other Hardware Used

For the location of Scanscations and coordinates of sites the Global Navigation Satellite System (GNSS) system used is SP80. While for measuring the distance, for further comparison of positional accuracy, we have used Total station Leica TS07.



Figure 1: Representation of GNSS SP80 (left) and total station Leica TS07 (right)

3. STUDY AREA

The area of study for our research work is IIRS Campus at coordinates A(30° 20' 27.68" N, 78° 2' 37.80" E), B(30° 20' 28.41306" N, 78° 2' 37.52311" E), C(30° 20' 28.25207" N, 78° 2' 37.47559" E) and D(30° 20' 28.11584" N, 78° 2' 37.73677" E). Coordinates of these locations are measured using DGPS.

4. METHODOLOGY

4.1 Similar Environment during Scan

In this study, similar environment was created while collecting data, workflow of which is represented in figure 2. On keeping the similar environment it was found that the time taken for a single scan, along with the photo capture view, was more in Leica P50 as compared to taken for a single scan from Faro Focus S350.

Height of Instrument – 1.54 m

Faro S350	Leica P50
Profile – outdoor > 20m	Profile – 120m
Image resolution – HDR off	Image resolution – 1920*1920
Quality – 3x	Sensitivity – High
Mpts – 176	Scan rate – 1 million pts/sec
Resolution – 3.1mm/10m	Resolution – 3.1mm@10m
Scan Size – 11378*8533 pts	No. of Points – 9520*8099 pts
Time – 17min 33sec	Time - 23 min 50 sec

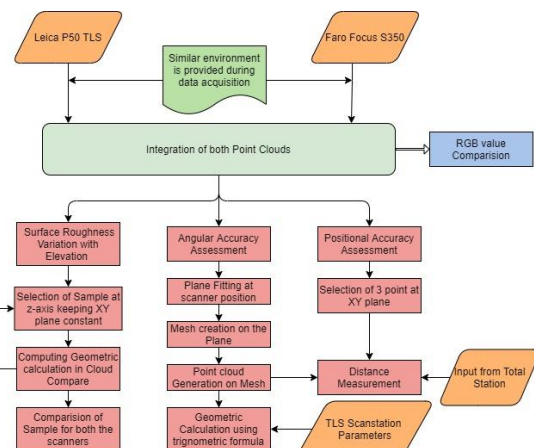


Figure 2: Workflow for Comparative Analysis of two Terrestrial Laser Scanner



Figure 4: RGB View of point cloud data in Leica P50 scanner (left) and Faro S350 scanner (right)

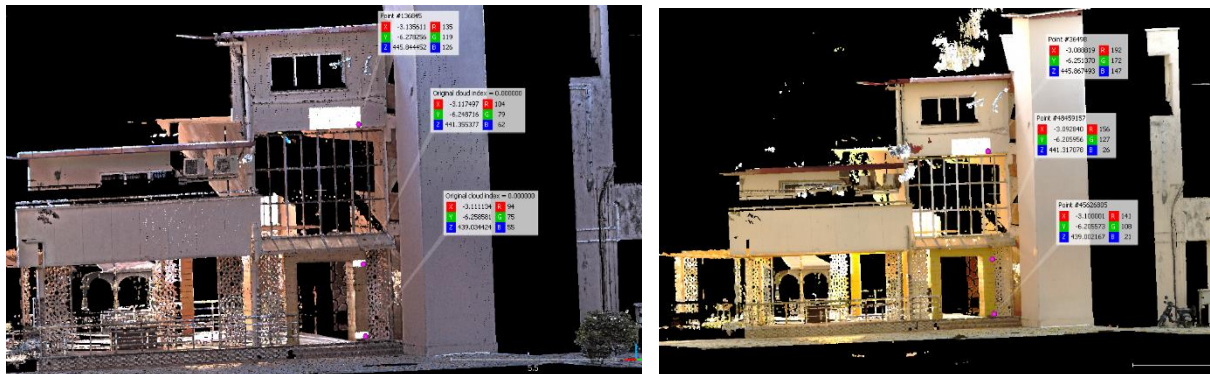


Figure 3: RGB value variation for similar points in Leica (left) and in Faro (right)

5. RESULTS AND DISCUSSIONS

5.1 Comparison in RGB view

The terrestrial laser scanner recorded digital photographs of the same area that is being scanned (Figure 3) and extract the RBG colour values from the photographs (Figure 4) and attach them to laser scans. (Walsh et al., 2017) When compared both the data in RGB view, it was found that both the scanners give different value for same point cloud and in the same environment.

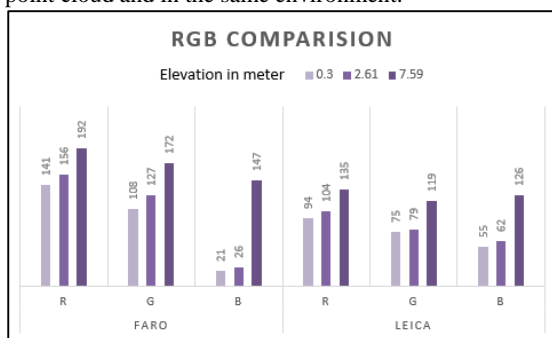


Figure 5: Graph showing comparison in RGB value of the sample sets from two scanners captured at different elevation on the same XY plane.

RGB value of both the scanners when visualized for different points at different elevation keeping the XY

coordinates constant, it was found that they vary at different rate on increasing altitude. From Figure 5, one can conclude that RGB value of faro is overall higher than the RGB value of LeicaP50. Though the rate of change of value is same for both the instrument. As there is difference in pixel value thus one can identify both the scan individually after their merging.

5.2 Integration of both Point Clouds

The scan taken from FARO FOCUS 350 was processed and its point cloud was created in SCENE software. Similarly CYCLONE software was used for processing and point cloud generation of scan taken from LEICA P50 scanner. Since the point cloud generated by SCENE software and CYCLONE software were in different formats, so they were first exported to E57 format. The integration and further analysis of these point cloud data was done in CLOUD COMPARE software. The registration of both the point clouds into one was done using 14 tie points. Final RMSE after combining both the data came out to be 0.144413m. The integrated scan in Figure 6 when viewed in grayscale, the merged point cloud appears to be a single point cloud but when viewed in RGB the difference in point clouds is clearly visible. In RGB view one can easily identify both the point clouds separately.

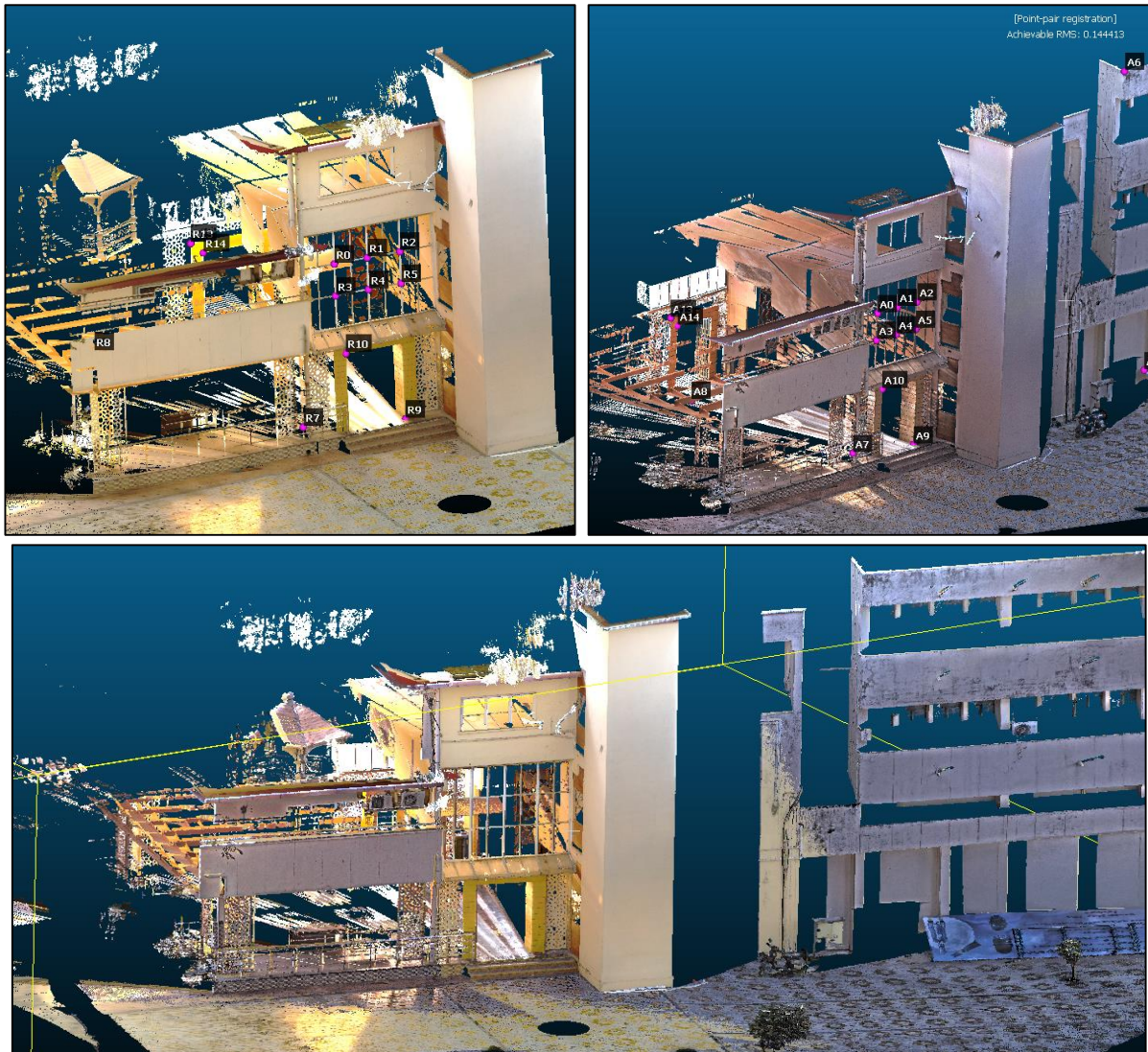


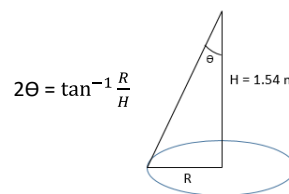
Figure 6: Representation of Tie Points on Faro scan (Top Left) and Leica Scan (Top Right). Merged scans from both the scanner (Bottom image)

5.3 Angular and Positional Accuracy

In this study we have examine the vertical field of view covered by both the scanners and also the RMSE distance in point cloud, to find out which one is better for our work.

5.3.1 Angular Accuracy

Faro focus Scanner claims to cover 300 degree vertical field of view. While on the other hand, Leica Scan Station P50 claims to cover 290 degree field of view. Both the scanners do not scan the area under them and that place appears as black coloured circular gap in the point cloud. For checking the angular accuracy first, we have attached a plane on the gap where scanner was placed on both the scans. Then we have generated the mesh to fill the gaps. This has been done because points could not be picked in the gap space. Then point clouds are been generated on those mesh to carry out geometric calculations.



Height of the instrument was 1.54m while radius in Faro came out to be 0.895635 m and in Leica it was 1.070855 m. On applying tangent equation, the value of 2θ came out to be 299.637048° for FaroS350 and 290.3735682° in Leica P50.

5.3.2 Positional Accuracy

In order to check which scanner provide more precise results for long range data collection we examined different points on the same XY plane, locations are represented in Figure 8 In this study we marked three points on the ground which was clearly visible in the scans. The distance of these points from the scanner was

measured using Total Station. The distance of these points was then measured in point cloud. The results of the measurement are show in the table below.

Points	Total Station	Leica	Faro
A	12.055	12.041582	12.095987
B	5.935	5.922274	5.942020
C	4.233	4.245021	4.258093

The variation of error in distance for Leica does not vary with distance, as can be seen in Figure 7, for short range while it varies drastically in Faro scanner when it scans at an angle.

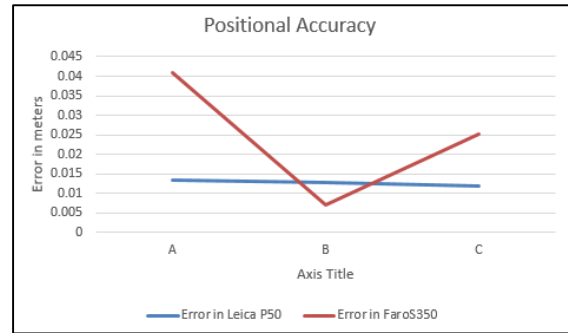


Figure 7: Error variation in distance measurement when compared with distance measured from Total Station.

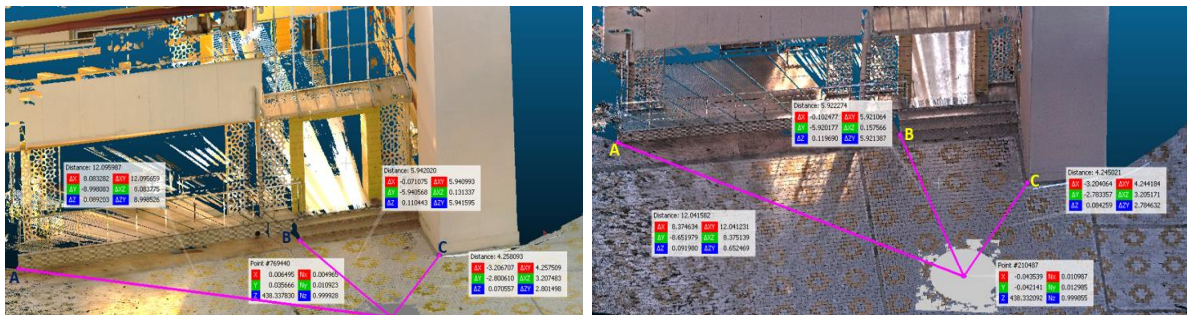


Figure 8: Representation of XYZ distance of points measured from scan station position

5.4 Surface Roughness Variation with Elevation

Point cloud distribution of three samples are compared keeping XY coordinates constant and increasing the elevation. In cloud compare, roughness is estimated for each point, their result is elaborated in Table 2, such that the 'roughness' value is equal to the distance between this

point and the best fitting plane computed on its nearest neighbours. If there's not enough neighbours to compute a LS plane (i.e. less than 3) an invalid scalar value (NaN) is set for this point.

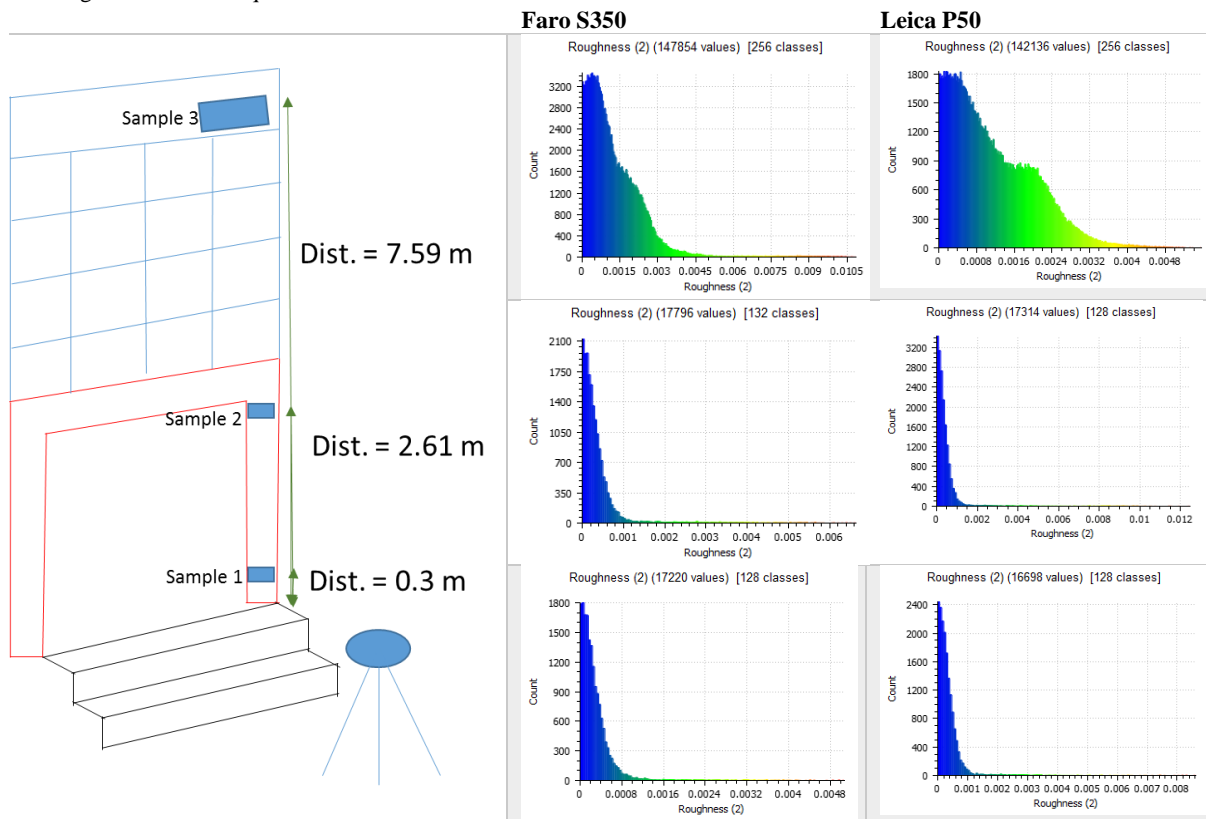


Table 2: Variation of Roughness with increase in elevation on sample plane is represented for both TLS.

6. CONCLUSIONS

The result shows the different impact of the instruments in data filtering (scan quality settings) at acquisition time and of additional software import filters on the point cloud quality of two selected scanner models (Wunderlich et al., 2013). All systems showed advantages and disadvantages in the hard-ware and software components for this specific application (Sternberg and Kersten, 2007) such as there is vast variation in RGB view of the scans though the data is captured at the same environment with the difference of about 20 minutes. This variation may affect the final integrated data when 3D model is created. While angular accuracy is compared with the specification claimed by their respective industries and it was found that they are more or less accurate. Though there is difference in positional accuracy when sample points are taken at different surface (planner and edge surface).

7. REFERENCE

- FARO, 2019. FARO Focus Laser Scanner 2.
- Leica, 2014. Leica ScanStation P20 2.
- Leica Geosystems AG, 2017. Leica ScanStation P30 / P40 Because every detail matters 2.
- Mechelke, K., Kersten, T., Lindstaedt, M., 2007. Comparative investigations into the accuracy behaviour of the new generation of terrestrial laser scanning systems, Optical 3D Measurement Techniques VIII.
- Sternberg, H., Kersten, T.P., 2007. Comparison of terrestrial laser scanning systems in industrial as-built-documentation applications. Opt. 3-D Meas. Tech. VIII Vol. I, 389–397.
- Walsh, S.J., Page, P.H., Brewington, L., Bradley, J.R., Mena, C.F., 2017. A beach vulnerability framework for the galapagos islands: Fusion of worldview 2 imagery, 3-d laser scanner data, and unmanned aerial vehicles, Comprehensive Remote Sensing. Elsevier. <https://doi.org/10.1016/B978-0-12-409548-9.10438-5>
- Wunderlich, I., Ohlmann-Lauber, J., Schäfer, T., Reidl, F., 2013. Objective Specifications of Terrestrial Laserscanners–A Contribution of the Geodetic Laboratory at the Technische Universität München, Metrica.Gr.

Optimal Location of Smart Water Meters & HOTSpot Analysis of Excessive Water Consumption: A Case Study of IIT Bombay

Ali Nasir Bandukwala ¹, Sana Firdaus ²

Centre of studies in resource engineering, Indian Institute of Technology (IIT) Bombay, 400076, Mumbai, Maharashtra

¹ a.nasir0001@gmail.com, ² firdaus.sana91@gmail.com

KEY WORDS: IOTs, HOTSPOTS, AHP, Smart water system, SCADA, weighted overlay

ABSTRACT:

Water stress is posing a great threat to the people. With increase in population the demand of water has increased, calling out for more number of water supply networks. These supply systems connects raw water sources to consumers through a gigantic infrastructure, which includes buried water mains, service connections, metering systems and thousands of other networking parts. However, these supply networks cause huge wastage of water because of leakages, pipe bursts, fraud and manipulation etc. This wastage accompanied by traditional metering system sometimes goes as high as 40% of the total water supply. To address these issues, recently a new technology in the form of real-time smart water meters has emerged, which is based on the Internet of Things (IoT) concept. This can be used to monitor the water usage both by water supply providers and users. This research aims at development of smart water metering network by integrating IoT and Geographical Information System (GIS).

1. INTRODUCTION

1.1 Current Scenario

Currently water conservation is one of the biggest issues that owes to traditional metering system where it is more or less like a guess estimate to get a track of our real water usage and wastage. Also traditional metering system involved manual recording of meter's reading which is time consuming, inaccurate and susceptible to corruption and theft. However all these problems can be solved by incorporating smart water meters which enables automatic meter reading (AMR) in some pre-defined topology (smart grid) [1]. The real time reading can then be communicated to a database station and further to the consumers through the concept of Internet of Things (IOT).

1.2 Literature Study

Various studies have been done initially where in smart water meters have been deployed using IOT in successful manner [2]. Koo et al. (2015) talked about sustainable water supply using big data collection and internet of things. Cominola et al. (2015) have concluded in their paper that for reliable water supply and reduced water utilities cost, implementing effective water management system is very important. Al-Ali et al. (2015) have presented the idea of IoT and smart grid technology in their research study. However very few researches have been carried out on smart water meters using IOT and Geographical Information Systems (GIS). Since sensor is having a location associated in itself so incorporation of spatial coordinates always give more reliable results. One more example is of The

IoT based Smart Water Meter system which provides real-time visibility over water consumption to consumers and Utilities. The system is designed to generate 22 alerts on conditions/anomalies such as over consumption of water resource, billing, and leakage detection to name a few. The system features two-way communication between Cloud Service and CDMA based water meters with communication time locked at 200-300 millisecond. The VN Server and Azure Storage serves as the meter data management system (MDMS) for the VN system. It was developed by Saviant consultants which gave us idea how to integrate the GIS system with dashboards and APIs to get real time value.

The objective of this research is to deploy smart water meters in some predefined topology using IoT and GIS. Here the methodology has been proposed for IIT Bombay hostels and residential areas.

2. WORK FLOW

2.1 Aim

To increase the efficiency of water distribution and management system by optimally locating the position and installing smart water system.

2.2 Methodology

2.2.1 Existing water meters:

The supply networks cause huge wastage of water because of leakages, pipe bursts, and manipulation etc. This wastage accompanied by traditional metering system sometimes goes as high as 40% of the total water supply. To address these issues, a new technology in the form of real-time smart water meters needs to be incorporated with an integration of GIS.

The primary source of drinking for IIT Bombay is Brihanmumbai Municipal Corporation (BMC) pipeline. This water is used for various purposes in the campus by various uses - residential, hostels, academic and hospitality uses, laboratory uses, by swimming pool, used for landscaping/gardening, for construction, by hospital and fire purposes, etc.

BMC pipeline first goes to pump house and then directly to hostel areas and elevated storage tank (ESR). The water from ESR is further distributed to hill side and lake side area (including academic area) as shown in fig 1.

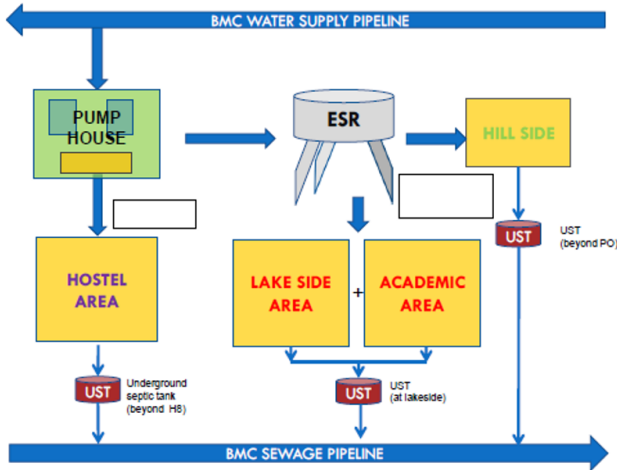


Figure 1: Water Supply Lines of IIT Bombay

2.2.2 Site Selection:

For the purpose of study and preparation of prototype, one of the hostels was selected whose water consumption and population (588) was known.

As per the experimental studies done by CTARA department of IIT Bombay the water consumption per head per day for hostel 12 came out to be 232.925 litres (table 1) which is way higher than the ideal consumption allowance of 135 litres as per URDPFI.

Table 1: Consumption of water by Hostel 12.

Sl. no	Water Usage	Lpcd
1	Mess Usage (cooking)	17.415
2	Flushing usage (does not use BMC water)	48.78
3	Domestic usage (drinking, showers, cleaning)	129.24
4	Laundry usage	37.49
5	Total usage	232.925

2.2.3 Flow diagram:

This Project was done to increase the efficiency of water distribution and management system by optimally locating the

position and installing smart water system. It was done in three stages as shown in fig 2: the first stage was ZONE IDENTIFICATION which was performed by using various parameters like Distance from hostels, existing water and sewerage network etc. Then the land suitability analysis was carried by giving weightage to these parameters according to the AHP (Analytical Hierarchy Process) method of normalization. Thus this weightage analysis gave the suitable locations for installation of water meters. The second stage was Installation of water meters in cost efficient manner and connecting it to the SCADA system for centrally controlling and making effective use of IoT. The third stage was the key element of the system. In this we did the HOTSpot analysis of the installed water meters to find out the hot (excessive) and cold (least) spots of the water consumption in the campus. GETIS ORD Gi* statistics was used for the purpose and the consumption of water meters was compared with the existing standards of CPCEED guidelines. These hotspots were spatially located in the campus and could be centrally monitored and regularized. A certain code block was written in python scripting to generate the HOTSpot without user feed in the central system. Based on the meter readings this code block would automate the process and regularly generate the spatial map for the users. The user interface of this can be made available Through AI application of ArcGIS. Thus, the residents of the campus can easily access the information of their daily consumption of water through this meter readings available on their smart phones. Further, the system would help to analyse the meter criticality index and the loss of centrally control the usage of excessive water in a single building. The administration can detect water leakage and excess consumption and can function accordingly. User can easily detect any leakage or water wastage in the household through emails or messages. User can get real time data of their usage through a dashboard or an android app. This technology will save water as well as change consumer behaviour. The NRW loss can be controlled.

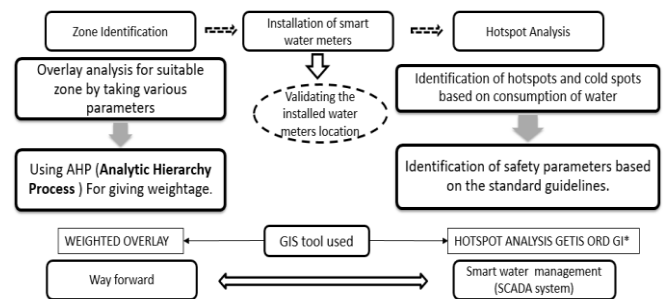


Figure 2: Work Flow Diagram

2.3 Identification of Suitable Zones

The first step is to identify the suitable zones or the optimal locations where the water meters need to be installed. This would be done by GIS technique called weighted overlay (fig 3) or suitability analysis.

In this technique few parameters are selected like proximity details, effective use etc. of certain things based on which the suitable land is identified. For the identification purpose it is necessary to give score or weightage to these parameters.

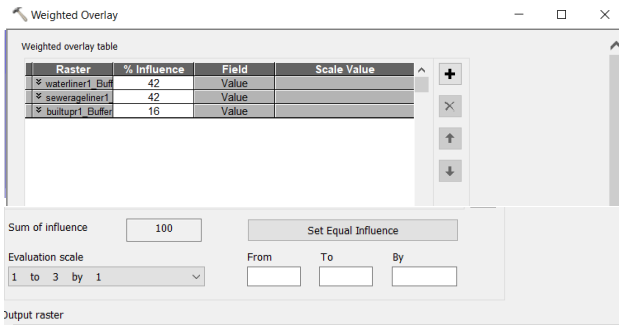


Figure 3: Weighted overlay toolbox

2.3.1 Weighted Overlay:

The tool combines the following steps: **a.** Reclassifies values in the input rasters into a common evaluation scale of suitability or preference, risk, or some similarly unifying scale. **b.** Multiplies the cell values of each input raster by the rasters' weight of importance. **c.** Adds the resulting cell values together to produce the output raster. The tool only accepts integer rasters as input, such as a raster of land use or soil types. Continuous (floating-point) rasters must be reclassified to integer before they can be used.

The three parameters chosen for the weighted Overlay (figure 3) are as shown in the figure 4, 5, and 6.

- Proximity to water network
- Proximity to Sewerage network
- Proximity to Built-up area.

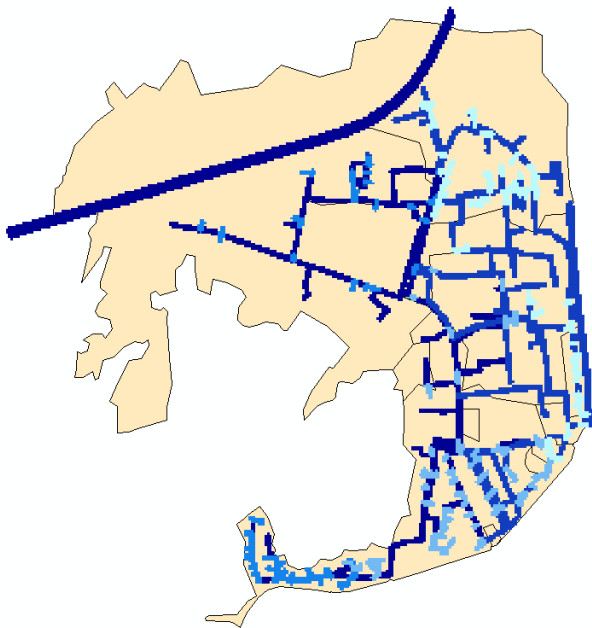


Figure 4: Raster of water network

Water network lines were selected and a buffer of 1 m on both the sides was taken which was then converted to raster form.

Sewerage network lines were selected and a buffer of 1 m on both the sides was taken which was then converted to raster form.

Built-up were selected and a buffer of 60 m on all the sides was taken which was then converted to raster form.



Figure 5: Raster of Sewerage network

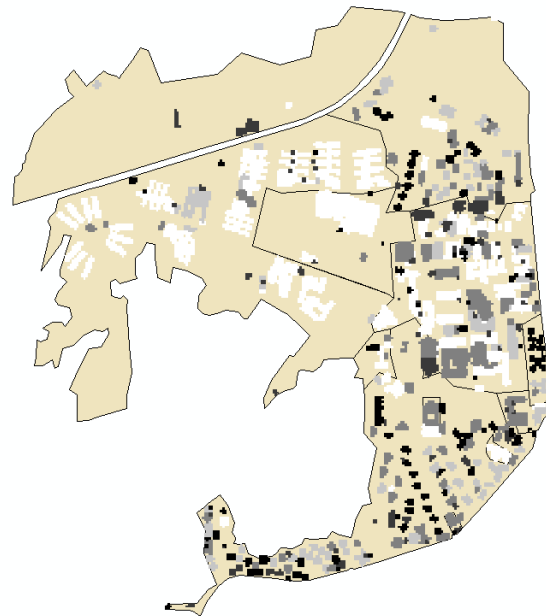


Figure 6: Raster of Built-Up

2.3.2 AHP (Analytical Hierarchical Process)

An $n \times n$ matrix is assembled, where n is the number of alternatives. Considering a given criterion, matrix A is supplemented with values a_{ij} , where i is a base alternative for comparison, corresponding to row i , and j is the alternative being compared with i . If the contribution of i to the criterion being considered is of strong importance relative to j , a_{ij} assumes the value of 5 (table 2), which can be considered a dominance of i over j . Intermediate values between those shown can also be considered.

The procedure presents some important relationships in the matrix:

$$a_{ji} = 1/a_{ij}$$

In the case of consistent evaluations:

$$a_{jk} = a_{ik}/a_{ij} \text{ where } k \text{ and } j \text{ are two alternatives being compared to } i.$$

Table 2: Fundamental Scale of SAATY

Intensity of importance	Definition
1	Equal importance
3	Moderate importance
5	Strong importance
7	Very strong importance
9	Extreme importance

After the matrix is complete, the process searches for a vector that expresses the priority of each alternative for the considered criterion. For Saaty, this vector of priorities x is obtained by starting from the relation between matrix A , its greater eigenvalue λ and the corresponding vector x .

$$Ax = \lambda x.$$

Comparisons are made between each alternative against each criterion and between each criterion at one level against the higher-level criterion to which it is associated. Finally, each criterion of the first level is compared against the objective. The comparison is made by assembling matrices in the same way and with the same scale as presented in table 7. The priorities of the criteria are used as weights to calculate the priorities of the alternatives in each criterion until the priorities of the alternatives against the overall objective have been calculated.

Thus the three parameters selected to prepare the prototype had been given score and the normalized weights respectively (table 3, 4) which was then used to apply the weighted overlay analysis in order to identify the optimal locations.

Table 3: Relative Scoring

	water line	Sewerage line	Building
water line	1	1	3
Sewerage line	1	1	3
Building	0.33	0.33	1
	2.33	2.33	7

Table 4: Weightage after Normalization

	Normalization				Weightage %	
	water line	Sewerage line	Building	SUM TOTAL	Sum 100/3	*
water line	0.429184549	0.429185	0.428571	1.286941	42.89802	42
Sewerage line	0.429184549	0.429185	0.428571	1.286941	42.89802	42
Building	0.141630901	0.141631	0.142857	0.426119	14.20396	16

After feeding the data in GIS the weighted overlay maps were prepared to find the locations suitable for installation of water meters and smart water grid as shown in figure 8.

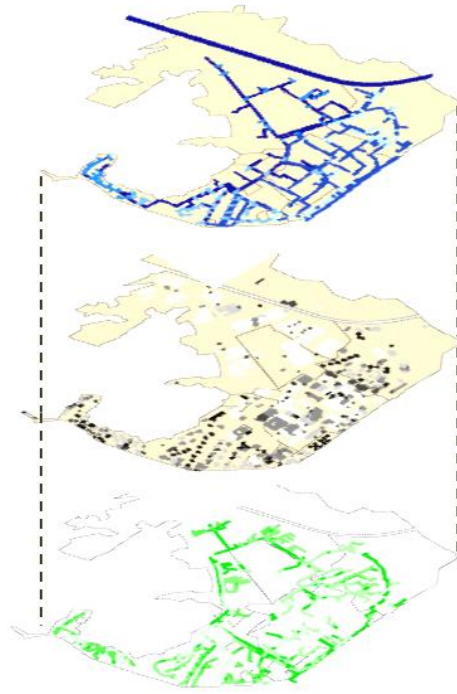


Figure 7: Overlapping the maps

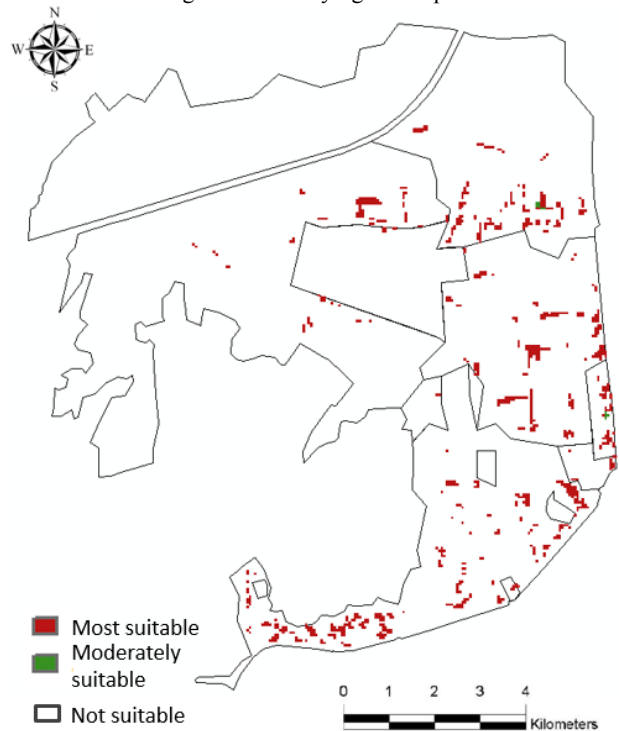


Figure 8: Optimal locations for water meter installations

After finding the suitable locations the water grid has to be installed in that locations. The next step is to connect it with IoT.

2.4 Smart metering grid

Smart Water Metering is a comprehensive approach to automatic meter reading (AMR) that collects data remotely and

automatically. This device allows a quick and effective management of the supply network to detect any damage or leakage of the system. Unlike traditional water metering systems, smart meters has the following benefits: **a.** Exhaustive control of consumption, **b.** Leak and breakdown detection, **c.** Fraud and manipulation detection, **d.** Efficient management of water resources, **e.** Secure data transfer, **f.** Financial conversion of consumption. For this research project smart water meters are proposed to be installed at some predefined smart metering grid or topology and further making them enable to communicate with each other using IoT.

As shown in fig. 9 a star network is used for an arbitrary network of water meters with a central data processing server. A cluster- tree network involves an additional router devices which acts as intermediaries between devices and hence increase the range of the network by creating clusters. A mesh (peer-to-peer) network has one coordinator and peer devices can communicate with each other directly.

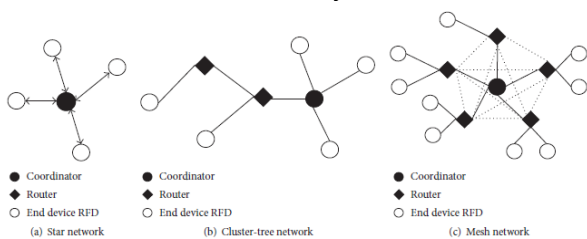


Figure 9: Topology examples

In the different types of topology examples shown in figure 9, the overall network management is done by the coordinator. Each network has exactly one coordinator which performs the following functions: 1. Start the network, 2. Assign how addresses are allocated to nodes or routers, 3. Permits other devices to join or leave the network, 4. It holds a list of neighbours and routers, 5. Transfers application packets.

A router is used in tree and mesh topologies to expand network coverage. The function of a router is to find the best route to the destination over which to transfer a message. A router performs all functions similar to a coordinator except the establishing of a network.

An end device can be a reduced functionality device (RFD). It also operates at low duty cycle power, meaning it consumes power only while transmitting information. The end device performs the following functions: Joins or leaves a network and transfers application packets.

In this study star network topology is being proposed as for each wing in Hostel 12 coordinators can work independently without affecting rest of the network.

2.5 IoT Sensors

After finding the appropriate grid for smart water meters it is necessary to deploy required sensors which will be able to communicate by IoT concept i.e. it can capture meaningful data, and communicate that data over a wireless network to a computer in the cloud for software to analyse in real time and help determine action steps. A smart device is associated with each object which provides the connectivity and a unique digital identity for identifying, tracking, and communicating with the object. IoT involves many, many things interacting with each other to produce actionable information as shown in figure 10.

For the current case study each sensor will monitor a specific condition or set of conditions such as temperature, pressure, water quantity, water quality, leakages etc. The sensor

information then could be transmitted to the coordinator using wifi or internet connection which would be further transferred to the base station through IOT gateway. An IoT gateway is a physical device or software program that serves as the connection point between the cloud and controllers, sensors and intelligent devices. All data moving to the cloud, or vice versa, goes through the gateway, which can be either a dedicated hardware appliance or software program.

In the base station data will be analysed online, on daily basis and the insights captured would be conveyed to both utilities and the users. For getting insights out of the humungous data, cloud based IoT and real-time data analysis is done. It's also referred as edge analytics where the physical world is connected to the world of computation. The edge computing applications do filtering, pre-processing and aggregation of data which further gives back feedback, support decisions and actions about and on the physical world.

In this study consumers can be alerted by email or messages if there is some water wastage or leakages. Similarly providers will be informed if there is any leakages or pipeline burst in the hostel or residential area. Here users or consumers are being referred to the faculty and students for Ananta building and Hostel 12 respectively. Also the providers here are the hostel administration/warden or the residential security offices which supervises the water supply need. An android app can also be developed and both the users and providers can have the real time track of water usage and wastage.

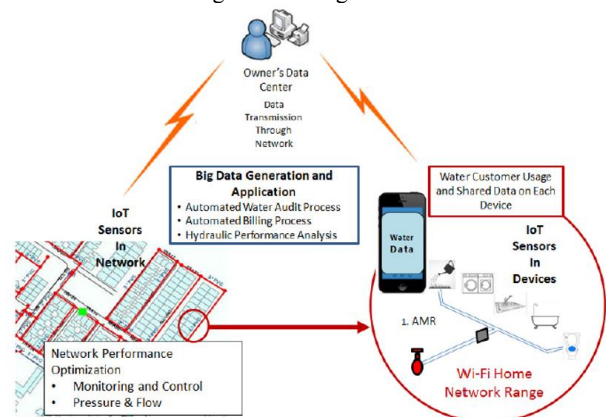


Figure 10: Working of IoT sensors

2.5.1 Installation of SCADA (Supervisory Control and Data Acquisition)

SCADA systems are crucial for industrial organizations since they help to maintain efficiency, process data for smarter decisions, and communicate system issues to help mitigate downtime.

The basic SCADA architecture begins with programmable logic controllers (PLCs) or remote terminal units (RTUs). PLCs and RTUs are microcomputers that communicate with an array of objects such as factory machines, HMIs, sensors, and end devices, and then route the information from those objects to computers with SCADA software

Goals of SCADA:

The major goals of SCADA are –

- ❑ Establishment of clusters with centralized control, allowing IITB to rationalize/reduce pump operators.
- ❑ Control Centre for 24/7 monitoring of flows and pressure
- ❑ Integrate clusters and Control Centre
- ❑ Link data to GIS database with it

- ❑ Provide training for staff in utilization of SCADA technology.

With the installation of this now the system is centrally regularized. In case of any leakage or overuse the defective meters can be stopped without manually looking for the flaw. This will also help in control of pressure in the buildings were the excessive use of waters is there. Now the question arise, how to find the excessive use?

2.6 Comparison with standards

The Consumption of the water per day will be fed in the water meters which will be monitored in the central system. These usage of waters will be compared to the service level benchmarks and the excessive use will be identified as the threat zone and immediate action will be taken against it. To automate the process GIS is a helpful tool.

2.7 Hotspot Analysis

This tool identifies statistically significant spatial clusters of high values (hot spots) and low values (cold spots). It creates a new Output Feature Class with a z-score, p-value, and confidence level bin (Gi_Bin) for each feature in the Input Feature Class.

The z-scores and p-values are measures of statistical significance which tell you whether or not to reject the null hypothesis, feature by feature. In effect, they indicate whether the observed spatial clustering of high or low values is more pronounced than one would expect in a random distribution of those same values.

2.7.1 Process of Hotspot Analysis

Hotspot Analysis is being done using the readings received from IoT sensors installed at the optimal locations. These readings are stored into the SCADA monitoring system. These readings are then feed into ArcGIS. For this project, we have considered the readings of IITB water meters to implement the concept of hotspot analysis. These readings give water usage for individual person when divided by population of the respective building. A safety parameter showing the levels of water usage is calculated defined by URDPFL. To calculate it, a python script (Fig.11) has been written to categorise the water usage from 1 to 5, 1 being the least usage areas and 5 being the areas showing high water intake.

```
Python Expression: assignValues(!Safety!)
Code Block:
def assignValues(Safety):
    if (readings >= 0 and Safety <50):
        return 1
    elif (readings >= 50 and readings <100):
        return 2
    elif (readings >=100 and readings<150):
        return 3
    elif (readings >=150 and readings <200):
        return 4
    elif ( readings > 200)
        return 5
```

Figure 11. Python Script

2.7.2 Generating Hotspot map

For the calculated values of safety parameters, hotspot analysis is using Getis-Ord G_i^* statistics. Getis-Ord G_i^* returns a z-score for every feature in dataset. For a positive z-score, the larger the z-score value, the more intense the clustering of high value

(hotspot).For negative value of z-score, the smaller the score ,the more intense is the clustering of low values(cold spots). We have used Hotspot Analysis tool (Fig.12) of ArcGIS, giving the input field as 'safety'.

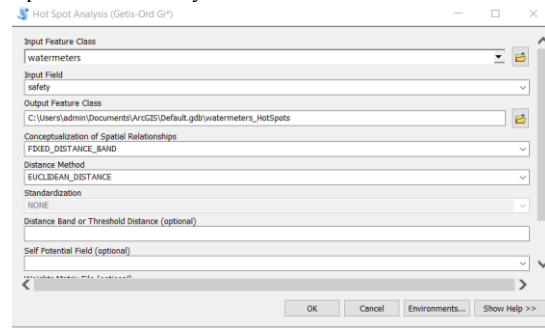


Figure.12 Hotspot Analysis Tool

Figure.13 shows the map generated based upon the hotspot analysis.

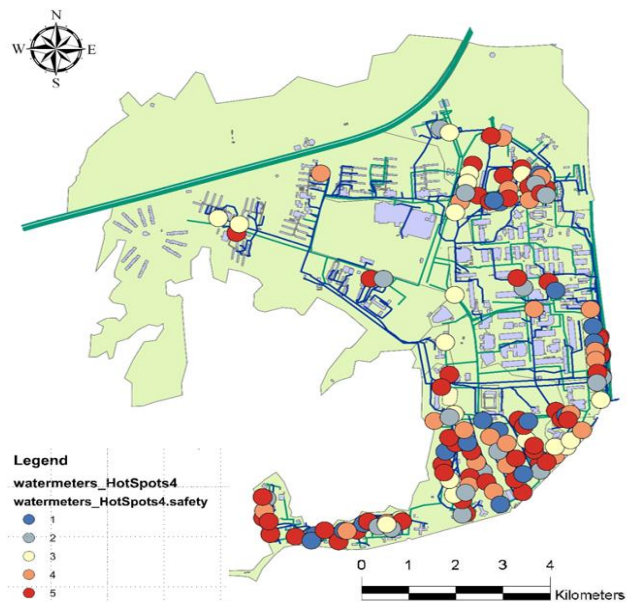


Figure.13 Hotspot Map

2.8 User Interface

Hotspot analysis is a critical step in finding the usage of water and regulating the supply. It is much more useful when the consumers can themselves see the daily usage and control the water loss. To better visualize the map and provide it to consumers, we have used the online platform of ArcGIS, which allows user to publically host a map. Figure.14 shows the map of water usage in IITB Campus hosted on ArcGIS online.

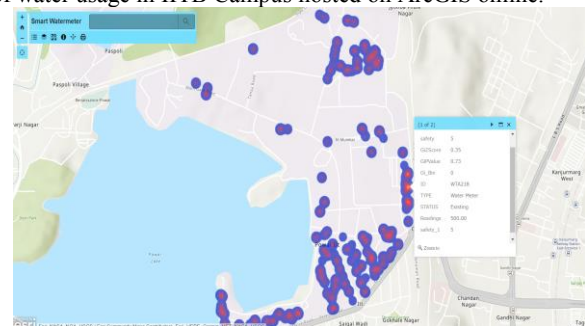


Figure 14.IITB Campus water usage

(<https://www.arcgis.com/apps/View/index.html?appid=0f430e3a2a324969b9a58acf9a9a877b>).

Any person can monitor the water consumption by the help of the above link.

3. WAY FORWARD

To provide day-to-day data to the users, applications can be developed which will be linked to ArcGIS. A dashboard showing the information like daily usage, monthly patterns, and bills can be created.

It can further be used to determine the:

- **Big Data Analysis**

Mass analysis

Assist decision-making

- **Guide user behavior**
- **Cost Efficient**
- **Water Quality Test**

Real-time water quality data

Ensure secure water

- **User Friendly**
- **Block Metering Area (BMA)**

Timely control of water distribution system

Maximized profitability

- **Pump Station Monitoring**

Intelligent scheduling

Real-time device operation monitoring

- **Pipeline Monitoring**

Leakage locating

Non-revenue water (NRW) reduction

Further these data can be used to analyse the **probability of meter failure, meter criticality, meter risk reduction** etc. In determining criticality and probability of failure, the method as applied by Schultz (2012) can be adopted. It can therefore be deduced that as meters age, their probability of failure increases. In this study, the probability of meter failure can be estimated by a Meter Failure Index. This index is computed by applying a formula adopted by Schultz (2012). Schultz (2012) computed the probability of pump failure by dividing the age of the pump by the design life of a pump.

4. CONCLUSIONS

The administration can detect water leakage and excessive consumption etc. and can function accordingly. With the help of IoT sensors and installation of SCADA the service providers can easily detect any leakage or water wastage in the respective buildings, thus controlling the NRW loss. Any user can get real time data of their usage through a dashboard or an android app. This technology will save water as well as change consumer behavior.

ACKNOWLEDGEMENTS

We would like to thank Prof. S. Durbha from CSRE IIT Bombay for giving us technological guidance for the completion of the project. We would like to specially thank Mr. Rajat Shinde for guiding us through the research work. We would also like to thank Ms. Neha Nande for giving us the relevant data as well as background support to carry out this research.

REFERENCES

Marais, J., Malekian, R., Ye, N., & Wang, R. (2016). A Review of the Topologies Used in Smart Water Meter Networks: A Wireless Sensor Network Application. *Journal of Sensors*, 2016.

Koo, D., Piratla, K., & Matthews, C. J. (2015). Towards sustainable water supply: Schematic development of big data collection using internet of things (IoT). *Procedia engineering*, 118, 489-497.

Retrieved from: <http://www.informit.com/articles/article.aspx?p=1409785&seqNum=3>

Retrieved from: <https://www.wateronline.com/doc/water-and-the-internet-of-things-0002>

Cominola, A., Giuliani, M., Piga, D., Castelletti, A., & Rizzoli, A. E. (2015). Benefits and challenges of using smart meters for advancing residential water demand modeling and management: A review. *Environmental Modelling & Software*, 72, 198-214.

Al-Ali, A. R., & Aburukba, R. (2015). Role of internet of things in the smart grid technology. *Journal of Computer and Communications*, 3(05), 229.

Retrieved from: <http://www.govtech.com/fs/Smart-Water-Meters-a-Critical-Tool-in-California.html>

TD 390, supervised learning study, project report on "Know your campus", water supply and waste water management, Indian Institute of Technology Bombay

Retrieved from: <https://timesofindia.indiatimes.com/city/bengaluru/iot-enabled-smart-meter-helps-hourly-water-tracking-at-apartments/articleshow/62500517.cms>

M.lapevaski. (2014) *_analytical_hierarchical_process_ahp_method_application_in_the_process_of_selection_and_evaluation*

Retrieved from: <https://www.smartcitiesdive.com/news/high-cost-of-smart-water-meters-keeps-adoption-rates-low/443905/>

Retrieved from: <https://smarterhomes.com/>

Retrieved from: <https://www.saviantconsulting.com/azure-case-studies/water-utilities-multi-tenant-saas-portal-development.aspx>

Asset Management: Integrating GIS as a Decision Support Tool in Meter Management in National Water and Sewerage Corporation/Gilbert_Akol_ECHELAI_GISMO1.pdf

February 2020

CLOUD-BASED APPROACH FOR CONTINUOUS MONITORING AND ASSESSMENT OF INLAND AND ESTUARINE WATER ENVIRONMENTS USING SENTINEL-3 OLCI DATA

Chintan B. Maniyar^{1,*}, Abhishek Kumar², Deepak R. Mishra²

¹Photogrammetry and Remote Sensing Department, Indian Institute of Remote Sensing (ISRO), India

²Centre for Geospatial Research, Department of Geography, University of Georgia, GA, USA

KEY WORDS: Water quality, cyanobacterial algal blooms, Sentinel-3, Lake Utah, Lake Okeechobee, Lake Chilika

ABSTRACT:

In the recent past, concentrations of Cyanobacterial Harmful Algal Blooms (CyanoHABs) in inland and estuarine water bodies have been increasing not only in India but throughout the world. Lake Chilika in India, lakes Utah and Okeechobee in the US are few of the many water environments that suffered heavy algal blooms in 2018. CyanoHABs or blue-green algae are amongst the first of prokaryotes that are increasingly becoming a health hazard, as they are capable of producing various toxins that can potentially affect human and aquatic life. The consequences of water quality degradation include and are not limited to a decline in aquatic life, animal and human health due to toxic water and sea-food consumption, hampering recreational activities, ultimately being detrimental to the country's economy. This demands a robust solution to monitor and conserve the water quality for inland and estuarine water environments. This study presents a cloud-based infrastructure developed on the open source Google Earth Engine (GEE) platform using the Sentinel 3 Ocean and Land Color Imaging (OLCI) sensor data, for near-real-time monitoring of such inland and estuarine water environments. The GEE dashboard developed in this study uses the level-1 Sentinel-3 OLCI data available in GEE, enables the user to import the data according to date range and cloud cover range, performs automatic correction for Rayleigh scattering before providing different visualizations of the data such as true color composite and false-color composite. It also generates heat maps for the suspended sediment concentration, chlorophyll-a (Chl-a) concentration, cyanobacterial cell density, and phycocyanin concentrations as water quality parameters, for the selected waterbody. Moreover, the spectra for any pixel can also be visualized by simply clicking on that pixel. This helps in continuous spatial and temporal analyses and monitoring of the water environments in a simplified way, particularly for CyanoHAB detection – since the phycocyanin component in the blue-green algae absorbs light at 620nm, which is a distinct band (band 7) in Sentinel-3. Since the dashboard is essentially a cloud based infrastructure, no computationally expensive resources are required – an active internet connection and a browser are sufficient for operation, hence making it inexpensive and user-friendly. The observations and results of the analyses thus performed can be insightful in detecting and identifying the occurrence of such algal blooms. This data can then be shared with the respective water management authorities for the amelioration of water quality.

1. INTRODUCTION

With every passing day, the amount of data is only increasing - so much so that the whole Earth has now been digitized - social networks, IOT and every other intelligent device constantly produces a stream of data (Chi et al., 2016). Remote Sensing (RS) domain thrives on data being gathered from sensors and phenomenon all over the world and a lot of times even in space, which is then used for many different applications such as natural hazard monitoring, global climate change, urban planning etc. (Chi et al., 2016). We have entered an era of high resolution Earth Observation (EO) (Ma et al., 2015). Every day, a large number of EO space borne and airborne sensors produce massive all sorts of data in various forms (Chi et al., 2016) with increase in RS data as high as several terabytes per day for a single satellite data center (Gamba et al., 2011). This voluminous data in the RS domain can be termed as RS big data (Guo et al., 2017). With such an increase in the rate of generation of RS data, a proper methodology to organize, structure, process (pre-processed, cleaned to remove error and noise) and manage becomes imperative (Mather, 2004). By continuously incorporating new and effective data processing methodologies and powerful computing architectures, big data analysis becomes highly efficient in terms of time and effort, when it comes to handling the RS data (Chi et al., 2016). A number of real world problems such as oil spill detection, content based image retrieval from hyperspectral data repositories (Chi et al., 2016) have been effectively addressed using big data in RS.

Cyanobacterial Harmful Algal Blooms (CyanoHABs) or blue-green algae, Earth's oldest photoautotrophs, are a major water quality issue in inland waters and estuarine environments. Typically composed of cyanobacteria species, these adversely affect the public health and the aquatic life of the waterbody (D. Mishra et al., 2018) by causing fish kills, animal deaths, human health risks, increase expenses of treatment for public water supply (Ibelings et al., 2014; Stumpf et al., 2016) and hamper recreational activities and ultimately affect the economy of a country in an adverse manner. Moreover, rising global temperatures and changing precipitations stimulate CyanoHABs because they are adapted to hot conditions (Paerl & Otten, 2013), and as a result they are becoming increasingly common in lakes, water supply reservoirs, and rivers and large water bodies from varying climatic regions (Page et al., 2018) throughout India and around the world, potentially affecting aquatic, animal and human health via toxic contamination due to the impact of cyanotoxins. The collective effect of CyanoHABs results into a distortion of the aquatic ecological cycle. The past year alone, there have been a lot many reports regarding CyanoHABs proliferations in various Indian waterbodies and reservoirs such as Barghi Dam in Madhya Pradesh, Ukai Dam in Gujarat, Stanley Reservoir in Tamil Nadu and many more. This makes it imperative to have a robust and consistent monitoring system to evaluate the spread of CyanoHABs in inland waters.

Satellite remote sensing is more effective and efficient for monitoring the CyanoHABs as compared to the other methods. It has been used to map several cyanoblooms in many areas around the world with great success (Pettersson & Pozdniakov, 2013), since times as early as the 1990s, for eg. electro-optical satellite platforms, Landsat 2 with the Coastal Zonal Color Scanner (Dupouy et al., 1988; Ulbricht, 1983), relating local increases in surface temperatures to the accumulations of cyanobacteria (Kahru et al., 1993). These early works resulted in expansion of research using satellite remote sensing to map cyanobacteria (Cullen et al., 1997). These methods include working on the satellite images of the waterbodies, which require robust architectures to process the data to achieve near-real time monitoring of CyanoHABs. Google Earth Engine (GEE) is a cloud based platform for planetary-scale geospatial analysis that brings together Google’s massive computational capacities (Gorelick et al., 2017) and its large storage. GEE can be accessed through an internet accessible application programming interface (API), which provides a very interactive environment with multi-petabyte analysis-ready geospatial data catalogue comprising of data from variety of satellite and aerial imaging systems in both optical and non-optical wavelengths, weather and climate forecasts, land cover, topography, co-located with the console (Gorelick et al., 2017), featuring the whole archive of Landsat, the first three Sentinel missions, and full Moderate Resolution Imaging Spectrometer (MODIS) (Traganos et al., 2018).

The overall objective of this study was to develop a near real-time cloud based infrastructure for quick and rapid monitoring of CyanoHABs and their temporal and spatial distribution. Study sites spread across India have been chosen to analyse the cyanoblooms. Satellite image based analysis was followed to achieve the objective, using the Sentinel 3 OLCI level-1 imagery. Phycocyanin pigment present in a cyanobloom absorbs light strongly at 620nm wavelength. Out of all the functional non-commercial satellites, only Sentinel 3 OLCI has a dedicated 620nm band (Band 7), hence enabling an effective detection of the presence of phycocyanins in the reflectance spectra and consequently a cyanobloom. GEE cloud based platform, which has attracted many environment scientists by its unique features, was used to develop a dashboard for analysis and visualization of data as it also allows easy sharing of code and results/alerts to the water managers. GEE provides level-1 data for Sentinel 3 OLCI, however, there is no satellite metadata in the GEE repository for the same. Apart from developing a GEE dashboard, other specific objectives of this study include estimating rayleigh corrected reflectance from the Sentinel 3 OLCI radiance in the GEE dashboard itself, developing indices for chl-a, cyanobacterial cell density, phycocyanin cell density, sediment cell concentration to quantify the presence of cyanobacteria in the waterbody, and also to be able to perform water quality analysis in a wider aspect. This dashboard not only allows near real-time satellite imagery analysis to monitor CyanoHABs, it also has a lot of on the fly interpretation and visualisation features such as on-click reflectance spectra for any pixel of the image, on-click values of various indices such Normalized Difference Vegetation Index (NDVI), Normalized Difference Chlorophyll Index (NDCI) etc., various masks for subtracting cloudy pixels and non-water pixels. Integration of all these features in the said GEE dashboard would help in an effective monitoring and analysis of CyanoHABs and general water quality as well, by providing timely updates.

2. METHODOLOGY

The overall methodology including data, processing steps, and final product is shown in Figure 1. Details about each component has been described in the following subsections:

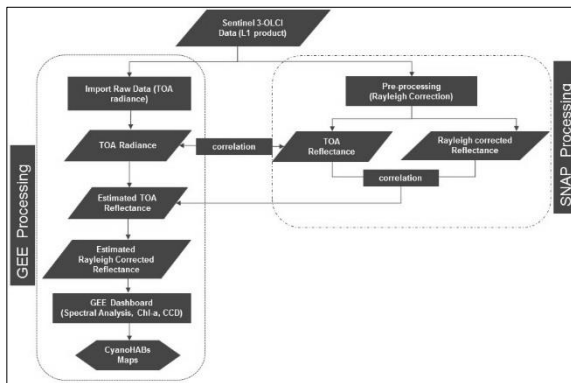


Figure 1. Overall methodology including data, processing platforms (GEE: Google Earth Engine and SNAP Toolbox), and various processing levels to derive final Cyanobacterial Harmful Algal Blooms (CyanoHABs) maps. The abbreviations used in the flow chart are as follow: TOA=Top of Atmosphere; Chl-a=Chlorophyll-a; CCD=Cyanobacteria Cell Density.

2.1 Satellite Data and Processing Platforms

The Level-1 (L1) Sentinel 3-OLCI Earth Observation Full Resolution (EFR) dataset corresponding to various inland and coastal waterbodies were downloaded from Copernicus Online Data Access (CODA: <https://codas.eumetsat.int/#/home>) for various sensing period and varying seasons. These dataset contains top-of-atmosphere (TOA) radiances at 21 spectral bands with center wavelengths ranging from the visible to the near-infrared (400 to 1029 nm) and at spatial resolution of 300m with worldwide coverage every ~2 days. The two data processing platform used in this study include GEE and ESA’s Sentinel Application Platform (SNAP) software (<http://step.esa.int/main/toolboxes/snap/>). As a multi-mission remote sensing toolbox, SNAP provides support for many satellite platforms including Sentinel-1, 2, 3, MERIS, Landsat, and others. GEE is a web-based platform that provides easy access to various satellite mission data (no need to download the data) and high computational speed.

2.2 TOA Radiance and TOA Reflectance Correlation

The OLCI data available in GEE is level-1 (L1) product. These products contain total radiance (L_t) ($mW \cdot m^{-2} \cdot Sr^{-1} \cdot nm^{-1}$) values measured by the sensor at the top of atmosphere (L_t^{TOA}) (Eq. 1). Further, the measured L_t^{TOA} include signals from the surface (that is being sensed, e.g. water in this study, L_w), and from the atmosphere (L_{atm}) (Eq. 1). It is important to mention that water leaving radiance (L_w) contributes only up to 10% of the signal received in the spectral bands from the blue to red (typically 400 nm – 670 nm) at the TOA and rest 90% of the signals are noise from the surrounding atmosphere (Gordon et al., 1997; D. R. Mishra et al., 2005; Page et al., 2018). Therefore, in water remote

sensing, to estimate any bio-optical parameters, first we need to remove the atmospheric noise (L_{atm}) from the L_t^{TOA} to derive L_w . Again, it is well known that L_t^{TOA} is sensitive to sun-sensor viewing and zenith angle, illumination, orientation, and position of the target etc (Gossn et al., 2019). Therefore, there is another parameter that is less affected by above factors, called surface reflectance (r_λ), is used frequently in remote sensing. r_λ is the ratio of the amount of light leaving a target to the amount of light falling onto it at a specific wavelength (λ). It is unitless parameter that overcomes the issues related to sun-sensor viewing and zenith angle, and represents property of the material being sensed. Typically, r_λ^{TOA} value is estimated using Equation 2 (Eq. 2). However, due to the lack of availability of OLCI metadata in GEE, r_λ^{TOA} value cannot be estimated using the Eq. 2. Therefore, we found an alternative method, i.e. by correlating L_t^{TOA} (available in GEE platform) with r_λ^{TOA} , that was derived after processing satellite images in SNAP software (Eq. 3).

$$L_t^{TOA} = L_w + L_{atm} \dots \dots \dots [1]$$

$$r_\lambda^{TOA} (SNAP) = \pi * L_\lambda^{TOA} * d^2 / ESUN_\lambda * \cos u_s \dots \dots \dots [2]$$

$$r_\lambda^{TOA} (GEE) \approx r_\lambda^{TOA} (SNAP) = m * L_t^{TOA} (GEE) + c \dots \dots \dots [3]$$

Where; r_λ^{TOA} = Top of atmosphere reflectance at specific wavelength (λ), L_λ = spectral radiance, d = Earth-Sun distance in astronomical units, $ESUN_\lambda$ = Extraterrestrial solar irradiance, u_s = Solar zenith angle; $r_\lambda^{TOA} (SNAP)$ and $r_\lambda^{TOA} (GEE)$ are TOA reflectance derived using SNAP and GEE platform respectively; m is correlation slope between $r_\lambda^{TOA} (SNAP)$ and $L_t^{TOA} (GEE)$ and c is intercept.

2.3 Rayleigh Correction

2.3.1 Rayleigh Correction in SNAP: In a satellite image, removing atmospheric perturbation is necessary in order to make an accurate analysis. Rayleigh correction is an important initial part of the atmospheric correction process, and requires satellite image metadata for accurate results. There are various tools and software that can be used for atmospheric correction of a satellite image such as ERDAS Imagine, ENVI, SeaDAS, SNAP etc. However, SNAP is an open-access software that is especially designed for Sentinel platform (Sentinel 1, 2, 3) sensors. Therefore, we used SNAP for Rayleigh correction. The input imageries for Rayleigh correction hold per-pixel data, which comprises of ground coordinates, uncorrected radiance for each band of the instrument, satellite metadata including the date and time of sensing, zenith angle, azimuth angle, and extra-terrestrial solar irradiance. The additional parameters provided by users include sea level pressure (SNAP default value: 1013.25 hPa) and ozone concentration in DU (SNAP default value: 300 DU). The output parameters include Rayleigh optical thickness bands, bottom of Rayleigh reflectance bands (r_{BRR}), gaseous absorption corrected TOA reflectance bands, TOA reflectance (r_{TOA}) bands and air mass. However, we were particularly interested in two output parameters, i.e. r_{TOA} and r_{BRR} . Therefore, r_{TOA} and r_{BRR} values were extracted corresponding to water pixels for various waterbodies post-Rayleigh correction. These values were further utilized in Rayleigh correction of same OLCI images using GEE platform.

2.3.2 Rayleigh Correction in GEE: The difference (Diff) between r_{BRR} (SNAP) and r_{TOA} (SNAP) extracted from water pixels corresponding to various waterbodies across different seasons was averaged (Diff_{Avg}) for each spectral band of OLCI sensor and applied to estimated r_{TOA} (GEE) (Eq. 3) to derive r_{BRR} in GEE (Eq. 4 & 5).

$$Diff_{Avg} = \sum_{i=1}^n Diff[i] = \sum_{i=1}^n r_{BRR} (SNAP)[i] - r_{TOA} (SNAP)[i] \dots \dots \dots [4]$$

Where; n = Number of pixels pin-pointed for each site; Diff [i] = The difference between r_{BRR} (SNAP) and r_{TOA} (SNAP) for i^{th} pixel; and Diff_{Avg} = Average of difference between r_{BRR} (SNAP) and r_{TOA} (SNAP) for all water pixels.

Hence, for a particular band with central wavelength (λ):

$$r_{BRR} (\lambda) (GEE) = r_{TOA} (\lambda) (GEE) - Diff_{Avg}(\lambda) \dots \dots \dots [5]$$

Where; $r_{BRR} (\lambda) (GEE)$ and $r_{TOA} (\lambda) (GEE)$ are estimated Rayleigh corrected reflectance and estimated TOA reflectance in GEE platform at central wavelength (λ); Diff_{Avg}(λ) is the average of difference between r_{BRR} (SNAP) and r_{TOA} (SNAP) for water pixels corresponding to a particular band with central wavelength (λ).

The estimated $r_{BRR} (\lambda) (GEE)$ was compared with respective $r_{BRR} (\lambda) (SNAP)$ (as reference) for each band and percentage normalized root mean squared error (%NRMSE) was estimated using Equations 6 and 7 (Eqs. 6 & 7). In addition to individual bands, %NRMSE was estimated for an index known as normalized difference chlorophyll index (NDCI) (derived from band combination; Eq. 8; (S. Mishra & Mishra, 2012)), that has been used as proxy for Cyanobacteria in past studies (Feng et al., 2014; Shi et al., 2017; Watanabe et al., 2015). The error propagation was also estimated for Chl-a (Eq. 9; S. Mishra & Mishra, 2012) and Cyanobacteria Cell Density (Eq. 10; Page et al., 2018) parameters, which are derived from NDCI.

$$RMSE = \sum_{i=1}^n \sqrt{[p_i(SNAP) - p_i(GEE)]^2} / n \dots \dots \dots [6]$$

$$\%NRMSE = \frac{RMSE}{Range} * 100 = \frac{RMSE}{p(max) - p(min)} * 100 \dots \dots \dots [7]$$

$$NDCI = \frac{r_{BRR} (709) - r_{BRR} (665)}{r_{BRR} (709) + r_{BRR} (665)} \dots \dots \dots [8]$$

$$Chl a = 194.325 * NDCI^2 + 86.115 * NDCI + 14.039 \dots \dots \dots [9]$$

$$CCD = 4989.5 * Chl a - 131742 \dots \dots \dots [10]$$

Where; RMSE = root mean squared error; P_i (SNAP) = parameter of interest ($r_{BRR}(\lambda)$, NDCI, Chl-a, CCD) derived using SNAP for pixel i ; p_i (GEE) = parameter of interest (e.g. $r_{BRR}(\lambda)$, NDCI, Chl-a, CCD) derived using GEE for pixel i ; n = total number of pixels; %NRMSE = percentage normalized root mean squared error; NDCI = normalized difference chlorophyll index; Chl-a = Chlorophyll-a; CCD = cyanobacteria cell density

2.4 Implementation of Rayleigh Correction Models in GEE

A GEE dashboard was developed by Weber (2017), which is a user-friendly interface that could map Chl-a and CCD concentrations for waterbodies anywhere in the world using Sentinel 2-MSI data. In this dashboard a user can either select a pre-determined waterbody from a dropdown menu, or zoom to their location of interest, then selects a cloud cover threshold, and as a result, the dropdown menu populates with all qualifying Sentinel 2-MSI images of that area (Weber 2017). However, Sentinel 2-MSI data lacks 620 nm spectral band that is needed for accurate detection of cyanobacteria. Therefore, previous GEE dashboard (by Weber 2017) was tuned in this study for Sentinel 3-OLCI data, which possess an additional 620 nm spectral band for accurate detection of CyanoHABs at increased revisit frequency (~daily) compared to five days temporal resolution of Sentinel 2-MSI. The functionalities developed in this new dashboard facilitate a focused analysis of a targeted waterbody by masking out the clouds (using short wave Infrared band) as well as the non water areas. The dashboard provides many visualizations such as NDCI, Chl-a, CCD by incorporating equations (Eqs. 3, 5, 8, 9, and 10) as JavaScript code in GEE platform. In addition to visualizations, the dashboard also facilitates analysis in terms of all the aforementioned parameters. For example, when a pixel of the satellite image is clicked upon, the index value (NDCI) or concentration (Chl-a or CCD) is displayed for that pixel. Apart from this, clicking on any pixel of the satellite image generates a spectra of the $r_{BRR}(\lambda)$ across the wavelengths of the 21 bands of OLCI. This spectra can be analyzed to detect an ongoing harmful algal bloom, or even the presence of cyanobacterial cells in the waterbody at a specific location pertaining to the pixel that was clicked upon.

3. RESULTS AND DISCUSSION

3.1 Correlation observed between Radiance and TOA Reflectance

As a result of analyzing level 1 Sen3 OLCI data (<https://scihub.copernicus.eu>) in SNAP and converting TOA radiance to TOA reflectance (rTOA) for each band, a high correlation was observed between TOA radiance and rTOA (Figure X; Table X). This correlation was seen for the selected study sites affected by CyanoHABs (marked in different colors on scatter plot in Figure X) across India. A seasonal bias was observed in correlation coefficients for these selected sites which diminished towards bands of longer wavelengths (>560nm).

To quantify the proxies of CyanoHAB including chl-a (Eq. X), pc (Eq. X), and CCD (Eq. X), we need the reflectance data mainly from 4 bands of Sentinel 3 – Band 7 (620nm), Band 8 (665nm), Band 11 (708.75nm) and Band 16 (778.75nm). These bands showed limited seasonal bias (Tables 3, 4, 5, 6). A significant correlation was observed between radiance and SNAP corrected reflectance of the 4 higher wavelength bands (Figure 2). Figure 2 shows the scatter only for the months of September and October as Indian waterbodies suffer from algal blooms in this time of the

year. The slopes for the best fit curve of all study sites increase towards higher wavelength bands since the amount of noisy signal is less in higher wavelengths. Moreover, the slopes for the best fit curve of all study sites tend to vary for different months according to the seasonal atmospheric conditions as well as the location of the study site. Thus obtained empirical relation in terms of “ $rTOA = radiance * gain + bias$ ” was implemented in GEE to obtain rTOA from level 1 radiance data.

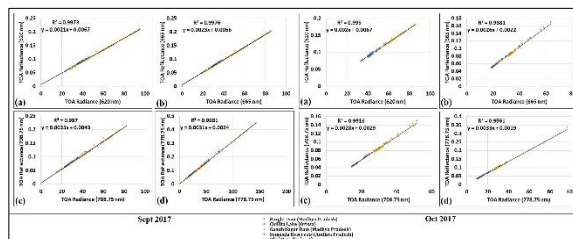


Figure 2. Scatterplots showing R2 value and best fit equation as obtained from the correlation between radiance and rTOA for the four high wavelength bands used for quantifying CyanoHAB and its constituents, as observed in Sept 2017 and Oct 2017

The error approximation in the estimation of rTOA was carried out by NRMSE (Eq. 7). Figure 3 shows the error bars of rTOA estimation for all the 21 bands of Sentinel-3 OLCI, with the maximum, minimum and average error among all sites for each band for September 2017. The error margin in rTOA decreased generally moving towards bands of longer wavelengths (Figure 3). This is because the higher wavelengths penetrate more and scatter less, hence there is comparatively less noise institution. However, the higher error in bands of shorter wavelength is not an alarming concern, since the longer wavelength bands (after Band 5 of Sentinel 3- OLCI) are used for estimating the Chl-a, PC and CCD (Eqs. x, y, z). Table 7 shows the %NRMSE in rTOA estimation for Bands 7, 8, 11 and 16 across selected CyanoHABs affected sites in India for September 2017.

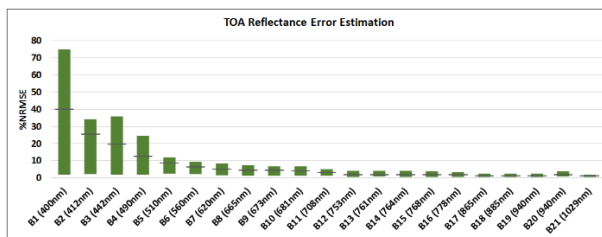


Figure 3. %NRMSE error bars in estimation of rTOA from radiance for all 21 bands of Sentinel 3, for September 2017. It can be observed that the error is generally decreasing towards the bands of higher wavelengths

Higher Wavelength Bands	%NRMSE in rTOA estimation				
	Barghi Dam	Chilika Lake	Gandhisagar Dam	Somasila Reservoir	Ukai Dam
Band 7 (620nm)	8.503	6.270	1.532	4.426	5.955
Band 8 (665nm)	7.284	5.515	1.360	3.695	5.881
Band 11 (708.75nm)	5.163	5.096	1.291	3.510	1.683
Band 16 (778.75nm)	2.113	3.628	1.062	2.019	0.605

Table 1. NRMSE in rTOA estimation of higher wavelength bands for September 2017

3.2 Correlation observed between TOA Reflectance and Bottom of Rayleigh Corrected Reflectance

Once rTOA was obtained, it was necessary to perform Rayleigh correction to remove the Rayleigh scattering effect in the recorded reflectance. On analyzing the rTOA and rBRR values obtained from SNAP, a high correlation was observed between the two for the same four bands (Figure 4). However, a significant seasonal bias was not observed in this case, since the conversion of radiance to rTOA normalized the bias across all months. Figure 4 shows the scatter plots for the same two months of September and October. Thus obtained empirical relation was implemented in GEE in terms of “rBRR = rTOA*gain + bias”.

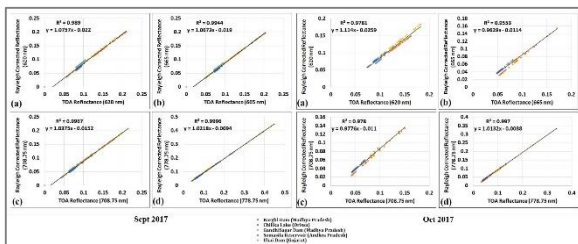


Figure 4. Scatterplots showing R² value and best fit equation as obtained from the correlation between rTOA and rBRR for the four high wavelength bands used for quantifying CyanoHAB and its constituents, as observed in Sept 2017 and Oct 2017

The error approximation in the estimation of rBRR was also carried out by the NRMSE (Eq. Y). Figure 5 shows the error bars of rBRR estimation for all 21 bands of Sentinel-3 OLCI, with the maximum, minimum and average error among all sites for each band, for September 2017. In this case too, the error margin in rBRR decreased generally towards bands of higher wavelength. The bands of shorter wavelengths showed significantly high error. This is because rBRR estimation is essentially correction for Rayleigh scattering, and shorter wavelengths undergo more amount of Rayleigh scattering. Moreover, the correlation coefficients were obtained by averaging the slope and intercept for all sites, and the scattering and aerosol properties vary according to the location and nature of the sites (inland and freshwater). However, in this case too, the higher error in the bands of shorter wavelengths is not an alarming concern as we use the bands of higher wavelength with reasonably lower NRMSE (Table 8) to quantify the CyanoHABs and its constituents.

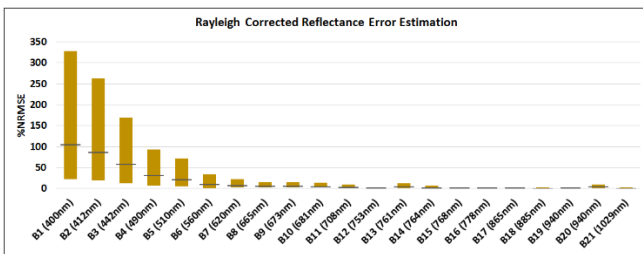


Figure 5. %NRMSE error bars in estimation of rBRR from rTOA for all 21 bands of Sentinel 3, for September 2017. It can be observed that the error is generally decreasing towards the bands of higher wavelengths

Higher Wavelength Bands	%NRMSE in rBRR estimation				
	Barghi Dam	Chilika Lake	Gandhisagar Dam	Somasila Reservoir	Ukai Dam
Band 7 (620nm)	23.004	8.520	3.694	2.246	3.394
Band 8 (665nm)	15.820	4.959	2.747	2.327	3.474
Band 11 (708.75nm)	9.205	4.208	2.116	3.044	1.212
Band 16 (778.75nm)	2.066	2.370	1.256	1.981	0.299

Table 2. NRMSE in rBRR estimation of higher wavelength bands for September 2017

3.3 Implementation of GEE Sentinel 3 Dashboard as Cloud-based Infrastructure

A GEE dashboard was developed as a part of this study, using the Sentinel 3 OLCI data available as an asset dataset in GEE. This is a user-interactive dashboard with a lot of customizable functionalities. To choose a location, the users can either browse through the dropdown list of selected waterbodies (Figure 6 (a)) or can center the map at a desired location. The user then has to provide a date range (Figure 6(c)) and may also choose to mask the cloudy pixels and non-water pixels (Figure 6(b)). Satellite imagery is imported according to the date range and automatically corrected for Rayleigh scattering before being displayed on the map-view panel (Figure 6(f)). Satellite images captured at different dates in the said date-range can be browsed from the dropdown in Figure 6(d). This dashboard also provides various visualizations of the satellite imagery such as Natural Color, False Color, NDCI, NDVI, Phycocyanin-3 (PC-3), Chlorophyll-a (Chl-a), Suspended Sediment Concentration (SSC) and Cyanobacterial Cell Density (CCD) as shown in Figure 6(e).

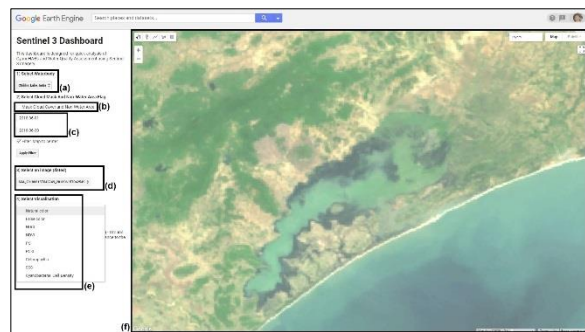


Figure 6. Snapshot of the proposed GEE dashboard with a Sentinel-3 satellite image of the Chilika Lake as captured on June 15, 2018 loaded in the map-view panel, along with all the interactive user functionalities in the panel on the left

Figure 7(a) shows the True Color Composite (TCC) or Natural Color Image as formed by the bands 8, 6 and 4 of the Sentinel-3 OLCI sensor. Figure 7(b) shows the false color composite image as formed by the bands 17, 8 and 6 of the Sentinel-3 OLCI sensor.

Figure 7(c) and Figure 7(d) show the TCC and FCC images respectively with the cloudy and the non-water pixels masked. Figure 7(e) shows the Chl-a concentration map (S. Mishra & Mishra, 2012), and Figure 7(f) shows the CCD concentration map (Page et al., 2018).

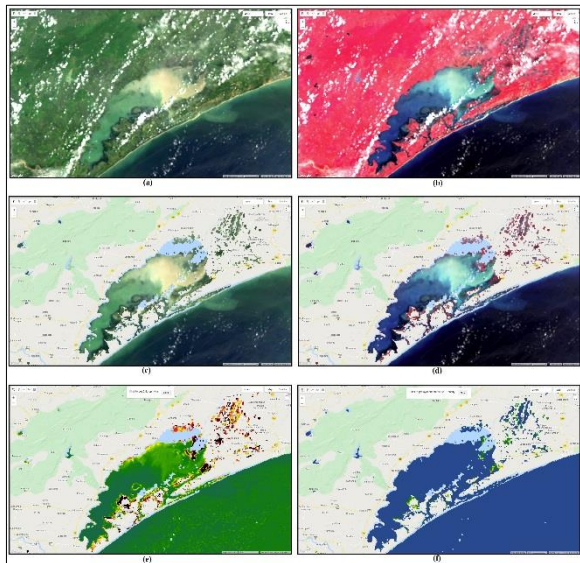


Figure 7. Different visualizations provided by the GEE dashboard for Sentinel-3 imagery of Chilika Lake as captured on Sept 10, 2017

Moreover, the dashboard also allows the analysis of spectral profiles – the user can click on anywhere within the image and the spectra of that pixel will be generated as shown in Figure 8(a). This is particularly helpful in detection of CyanoHABs since they possess the phycocyanin component which absorbs light at 620nm. Sentinel 3 OLCI’s band 7 also function at 620nm, and hence the spectra of a pixel inside a waterbody can be analyzed for detecting the bloom. Figure 8(b) shows the spectra of a pixel of Chilika Lake for an ongoing bloom wherein the absorption at 620nm can be observed. Whereas for the same waterbody, for the spectra of a pixel in a non-bloom area (Figure 8(c)), no absorption at 620nm is seen.

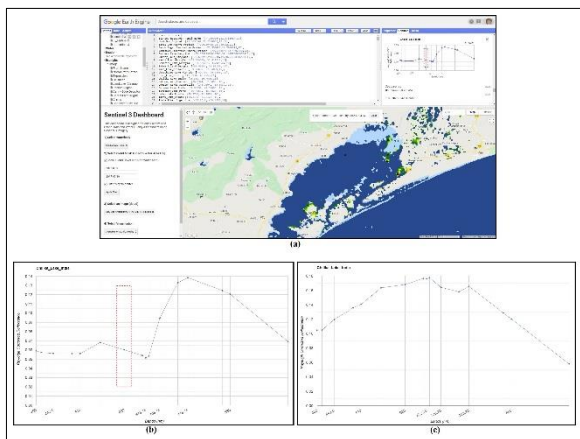


Figure 8. The on-click spectral feature generation feature of the GEE dashboard (a) showing the spectra of Chilika lake at bloom location(b) and non-bloom location(c)

4. CONCLUSION

A GEE dashboard was developed for quick detection of CyanoHABs and near-real-time monitoring of inland and coastal water bodies for water quality. This dashboard is easy to use and share, making it easy for the resource managers to effectively detect and visualize the bloom-affected regions in waterbodies. It is also helpful in planning field trips to such sites and executing timely management strategies. Moreover, this dashboard is a completely cloud-based platform so only a browser and an active internet connection are needed to use it. This makes it computationally inexpensive and increases the availability and accessibility of the dashboard. Five study sites as CyanoHAB affected waterbodies from India were analyzed as a part of this study. This dashboard uses empirical methods to estimate reflectance from radiance and to correct reflectance for Rayleigh scattering. It is evident from the NRMSE of the rBRR that this method is not robust for all bands but is suitable for our study since GEE provides level 1 Sentinel 3 data only, and the bands used for CyanoHAB detection show reasonably low NRMSE. There is a lot of scope for improving the accuracy in the quantification of cyanobacterial cell density and phycocyanin pigments by integrating data from multiple and diverse waterbodies. A similar dashboard for CyanoHAB detection and monitoring can be developed in the future with a robust model that integrates data from multiple sensors (Sentinel-2, Landsat 8, etc.).

REFERENCES

Kahru, M., Leppanen2, J.-M., & Rudl, O. (1993). II Cyanobacterial blooms cause heating of the sea surface. In *MARINE ECOLOGY PROGRESS SERIES Mar. Ecol. Prog. Ser* (Vol. 101).

Chi, M., Plaza, A., Benediktsson, J. A., Sun, Z., Shen, J., & Zhu, Y. (2016). Big Data for Remote Sensing: Challenges and Opportunities. *Proceedings of the IEEE*, 104(11), 2207–2219. <https://doi.org/10.1109/JPROC.2016.2598228>

Cullen, J. J., Ciotti, Á. M., Davis, R. F., & Lewis, M. R. (1997). Optical detection and assessment of algal blooms. *Limnology and Oceanography*, 42(5 II), 1223–1239. https://doi.org/10.4319/lo.1997.42.5_part_2.1223

Dupouy, C., Petit, M., & Dandonneau, Y. (1988). Satellite detected cyanobacteria bloom in the southwestern tropical pacific: Implication for oceanic nitrogen fixation. *International Journal of Remote Sensing*, 9(3), 389–396. <https://doi.org/10.1080/01431168808954862>

Feng, L., Hu, C., Han, X., Chen, X., & Qi, L. (2014). Long-Term Distribution Patterns of Chlorophyll-a Concentration in China’s Largest Freshwater Lake: MERIS Full-Resolution Observations with a Practical Approach. *Remote Sensing*, 7(1), 275–299. <https://doi.org/10.3390/rs70100275>

Gamba, P., Du, P., Juergens, C., & Maktav, D. (2011). Foreword to the Special Issue on “Human Settlements: A Global Remote Sensing Challenge.” *IEEE Journal of Selected Topics in Applied Earth Observations and Remote Sensing*, 4(1), 5–7. <https://doi.org/10.1109/JSTARS.2011.2106332>

- Gordon, H. R., Du, T., & Zhang, T. (1997). Remote sensing of ocean color and aerosol properties: resolving the issue of aerosol absorption. *Applied Optics*, 36(33), 8670. <https://doi.org/10.1364/ao.36.008670>
- Gorelick, N., Hancher, M., Dixon, M., Ilyushchenko, S., Thau, D., & Moore, R. (2017). Google Earth Engine: Planetary-scale geospatial analysis for everyone. *Remote Sensing of Environment*, 202, 18–27. <https://doi.org/10.1016/j.rse.2017.06.031>
- Gossn, J. I., Ruddick, K. G., & Dogliotti, A. I. (2019). Atmospheric correction of OLCI imagery over extremely turbid waters based on the red, NIR and 1016 nm bands and a new baseline residual technique. *Remote Sensing*, 11(3), 1–24. <https://doi.org/10.3390/rs11030220>
- Guo, H., Liu, Z., Jiang, H., Wang, C., Liu, J., & Liang, D. (2017). Big Earth Data: a new challenge and opportunity for Digital Earth's development. *International Journal of Digital Earth*, 10(1), 1–12. <https://doi.org/10.1080/17538947.2016.1264490>
- Ibelings, B. W., Backer, L. C., Kardinaal, W. E. A., & Chorus, I. (2014). Current approaches to cyanotoxin risk assessment and risk management around the globe. *Harmful Algae*, 40, 63–74. <https://doi.org/10.1016/j.hal.2014.10.002>
- Ma, Y., Wu, H., Wang, L., Huang, B., Ranjan, R., Zomaya, A., & Jie, W. (2015). Remote sensing big data computing: Challenges and opportunities. *Future Generation Computer Systems*, 51, 47–60. <https://doi.org/10.1016/j.future.2014.10.029>
- Mather, P. M. (2004). *Computer processing of remotely sensed images: an introduction*. John Wiley & Sons.
- Mishra, D. R., Narumalani, S., Rundquist, D., & Lawson, M. (2005). Characterizing the vertical diffuse attenuation coefficient for downwelling irradiance in coastal waters: Implications for water penetration by high resolution satellite data. *ISPRS Journal of Photogrammetry and Remote Sensing*, 60(1), 48–64. <https://doi.org/10.1016/j.isprsjprs.2005.09.003>
- Mishra, D., Ramaswamy, L., Kumar, A., Bhandarkar, S., Kumar, V., & Narumalani, S. (2018). A multi-cloud cyber infrastructure for monitoring global proliferation of cyanobacterial harmful algal blooms. *International Geoscience and Remote Sensing Symposium (IGARSS)*, 2018-July, 9272–9275. <https://doi.org/10.1109/IGARSS.2018.8519144>
- Mishra, S., & Mishra, D. R. (2012). Normalized difference chlorophyll index: A novel model for remote estimation of chlorophyll-a concentration in turbid productive waters. *Remote Sensing of Environment*, 117, 394–406. <https://doi.org/10.1016/j.rse.2011.10.016>
- Paerl, H. W., & Otten, T. G. (2013). Harmful Cyanobacterial Blooms: Causes, Consequences, and Controls. *Microbial Ecology*, 65(4), 995–1010. <https://doi.org/10.1007/s00248-012-0159-y>
- Page, B. P., Kumar, A., & Mishra, D. R. (2018). A novel cross-satellite based assessment of the spatio-temporal development of a cyanobacterial harmful algal bloom. *International Journal of Applied Earth Observation and Geoinformation*, 66(November 2017), 69–81. <https://doi.org/10.1016/j.jag.2017.11.003>
- Pettersson, L. H., & Pozdniakov, D. V. (Dmitrii V. (2013). *Monitoring of harmful algal blooms*. Springer.
- Shi, K., Zhang, Y., Zhou, Y., Liu, X., Zhu, G., Qin, B., & Gao, G. (2017). Long-Term MODIS observations of cyanobacterial dynamics in Lake Taihu: Responses to nutrient enrichment and meteorological factors. *Scientific Reports*, 7(1), 1–16. <https://doi.org/10.1038/srep40326>
- Stumpf, R. P., Johnson, L. T., Wynne, T. T., & Baker, D. B. (2016). Forecasting annual cyanobacterial bloom biomass to inform management decisions in Lake Erie. *Journal of Great Lakes Research*, 42(6), 1174–1183. <https://doi.org/10.1016/j.jglr.2016.08.006>
- Traganos, D., Poursanidis, D., Aggarwal, B., Chrysoulakis, N., & Reinartz, P. (2018). Estimating satellite-derived bathymetry (SDB) with the Google Earth Engine and sentinel-2. *Remote Sensing*, 10(6), 1–18. <https://doi.org/10.3390/rs10060859>
- Ulbricht, K. A. (1983). &title>Image Processing Of Remotely Sensed Phenomena</title> In A. J. Oosterlinck & A. G. Tescher (Eds.), *Image processing techniques*, (Advisory Group for Aerospace Research & Development, Neuilly-sur-Seine) (Vol. 0397, pp. 34–54). International Society for Optics and Photonics. <https://doi.org/10.1117/12.935279>
- Watanabe, F., Alcántara, E., Rodrigues, T., Imai, N., Barbosa, C., & Rotta, L. (2015). Estimation of Chlorophyll-a Concentration and the Trophic State of the Barra Bonita Hydroelectric Reservoir Using OLI/Landsat-8 Images. *International Journal of Environmental Research and Public Health*, 12(9), 10391–10417. <https://doi.org/10.3390/ijerph120910391>

VULNERABILITY ASSESSMENT OF ARSENIC IN GROUNDWATER AND ITS OCCURRENCE IN DISTRICTS OF BIHAR, INDIA

S. Dhamija^{1*}, H. Joshi²

¹Research Scholar, Department of Hydrology, Indian Institute of Technology Roorkee, Uttarakhand, India – sanadhamijaynr@gmail.com

²Professor, Department of Hydrology, Indian Institute of Technology Roorkee, Uttarakhand, India – himanshujoshi58@gmail.com

KEYWORDS: Groundwater Arsenic Vulnerability, Arsenic Vulnerability Index, Multi-Criteria Decision Making (MCDM), Analytical Hierarchy Process (AHP), Geographic Information System (GIS), Central Ground Water Board (CGWB).

ABSTRACT:

Groundwater Arsenic vulnerability is an essential aspect of the determination of groundwater vulnerable zones and for the development of management options to preserve groundwater quality. CGWB investigated and marked ten states of India, including Bihar as Arsenic Hotspots. As there is no proof regarding arsenic contamination in groundwater and yet to establish. Hence, the present study aims to provide a spatial and statistical analysis of the prevailing subsurface, hydrogeochemical parameters, and environmental conditions for arsenic occurrence in the groundwater. Secondary data usage by reviewing and analyzing proved to provide a cost-effective way of conducting the correlation studies and helped in portraying the present scenario. The arsenic vulnerability index has been developed with attempts to prepare a multipurpose database in GIS environment by applying Analytic Hierarchy Process (AHP) approach of Multi-Criteria Decision Making (MCDM) model under prevailing conditions. Maps created by ArcGIS to find out the groundwater arsenic vulnerable zones for twelve As affected districts of Bihar lying on Ganga Basin. The integrated vulnerability map exhibits high risk imposed on the northwestern parts of Patna and Bhojpur along with the central parts of Munger, Bhagalpur, and Vaishali districts due to the existence of shallow groundwater with low elevation accompanying high silicate and iron contents in the region. Validation performed against arsenic concentration of the state and by evaluation of the importance of each covariate for vulnerability. Groundwater vulnerability maps may assist in decision making and future planning for sustainable water resource development.

1. INTRODUCTION

The surface water is generally at high risk of getting contaminated due to industrial, municipal, and agricultural discharge, whereas groundwater remains relatively unaffected. Therefore, dependency on groundwater has increased, resulting in over-exploitation of groundwater resources. Consequently, water quality reduces and making it susceptible to pollutants. Arsenic toxicity is one of the significant groundwater concerns globally, adversely affecting humans, even at low concentrations. CGWB, 2015 reported ten states of India as Arsenic hotspots. Nowadays, flood plains of Ganges and Brahmaputra contaminated by arsenic. There is no absolute proves regarding arsenic emissions in groundwater, but several hypotheses suggest the geogenic release of arsenic from weathered igneous and sedimentary rocks. Anthropogenic activities such as mining, smelting, refining, and industrial processes may also contribute arsenic in groundwater. Microorganisms transfer arsenic through bioaccumulation and biotransformation, serves as biogenic sources (Matschullat, 2000; Nordstrom, 2002; Kumar, 2015; Jang et al., 2016). Arsenic exists in both organic and inorganic forms. Inorganic arsenic (iAs), widely distributed on the earth's crust in association with iron and sulfides. iAs exists in the oxidation states of arsines (As^{3-}), elemental arsenic (As^0), arsenite (As^{3+}), and arsenate (As^{5+}). Inorganic forms arsenite (As^{3+}) and arsenate (As^{5+}) are highly toxic and mobile, among which arsenite (As^{3+}) is ten times more toxic (Wang and Mulligan, 2006). Microorganism plays a crucial role in the processes of

oxidation, reduction, methylation, and demethylation of arsenic species for the microbial transformations between 3 and 5 oxidation states and in turn, affects its mobility and speciation in the environment (Lloyd and Oremland, 2006; Paez et al., 2009; Chatterjee et al., 2017). In oxygenated water, arsenic is mostly present as arsenate (+5) while under reducing conditions (<200mv), it is present as arsenite (+3) (Kim et al., 2011). Drinking water is one of the main pathways of exposure to people. Therefore, the acceptable limit of Arsenic in drinking water is 0.1 mg/l (BIS, 2012). CGWB report assured the groundwater arsenic contamination in fifteen districts of Bihar with the magnitude of contamination to be 0.18 mg/l. This paper deals with twelve districts of Bihar state lying on the Ganga River declared arsenic affected by CGWB. There are a few reasons behind selecting specific districts of the state for the research. Firstly, it forms a major part of the Middle Ganga Plain (MGP), especially lying on the main Ganga River. Secondly, it is highly productive and irrigated by the contaminated water. Lastly, being densely populated helps to gather evidences for the effects of arsenic. Application of MCDM method for prioritization and ranking using AHP approach, integrated with GIS, is an effective way for handling large datasets along with allocation of weights and ratings. This two steps evaluation criteria help in the prediction of arsenic vulnerable zones for groundwater quality. MCDM methods are capable of showing a realistic picture, even for secondary data (Agarwal et al., 2015). For remediation and prevention against spreading, the most important thing is to identify the extent of the problem; this

* Corresponding author

study focus on arsenic occurrence in the subsurface environment and attempts had made to categorize the districts of Bihar state in terms of high and low arsenic vulnerable zones considering hydro-geological and chemical factors using GIS.

2. FRAMEWORK AND METHODOLOGY

2.1 Study Area

Arsenic contamination in groundwater in Bihar first detected in 2002 (Chakroborti et al., 2011). Bihar, located on the eastern region of the largest Ganga basin between 24°20'10" N ~ 27°31'15" N and longitude 82°19'50" E ~ 88°17'40" E (GOI, 2015). Subsequent investigations marked a wide occurrence of arsenic in the Gangetic plain of Bihar, affecting 57 blocks of 15 districts (M/o WR and &GR, 2014). The current study based on twelve arsenic affected districts with Ganga main stem, covering an area of 26,558 sq. km (Fig 1). It has transitional climate, economy, and culture as it is positioned mid between humid and sub-humid states, West Bengal and Uttar Pradesh, respectively. Ganga River flows through southern Bihar from west to east. It is the fertile state with a variety of cereals and crops grown in the sub-tropic region under temperate zone with annual rainfall 100- 150 cm.

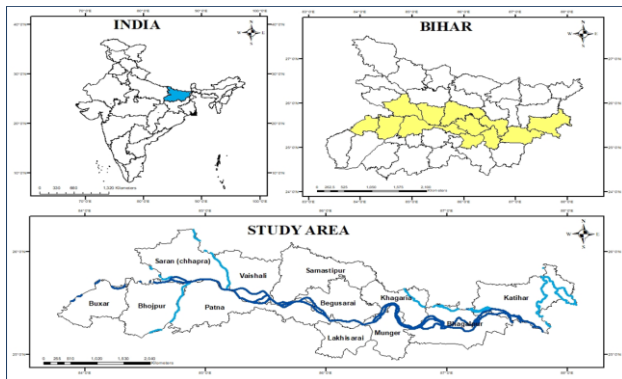


Figure 1. Study Area – Bihar, India

2.2 Methods

Schematic methodology applied is represented in Fig 2. and is divided into two main themes:

2.2.1 Data Procurement: Data procurement included secondary data collection, based on which effective covariates selected for mapping arsenic vulnerable zones. The selection of covariates based on the existing information and undertaken analysis reviewed in the comprehensive literatures related to arsenic contamination. Relevant secondary information and data available (i.e., depth to groundwater, Geomorphology, DEM images, and groundwater quality parameters) in official documents and reports prepared by various academic/research institutes as well as government and non-government organizations and reported in websites were collected (Table 1). Statistical correlation between arsenic and selected covariates predicts the linkage between them.

2.2.1.1 Data Preparation: Data preparation includes GIS processing of procured datasets. GIS provides an easy platform for analyzing large and complex groundwater datasets. It can enter, store, manipulate, process, analyze, and, most importantly, represents data in 2D and 3D surfaces with suitable map projections. These days GIS is widely used for problem-solving and decision-making processes.

S.no.	Covariate	Data Source	Format	Year
1.	Depth to Water level	Water Resource Information System (WRIS)	Tabular	2015
2.	Elevation	United State Geological Survey (USGS)	SRTM DEM Imagery	2015
3.	Geomorphology	Geological Survey of India (GSI)	Map	2007
4.	Groundwater Quality Parameters	Central Ground Water Board (CGWB)	Tabular	2015

Table 1. Selected Covariates and the Data Sources

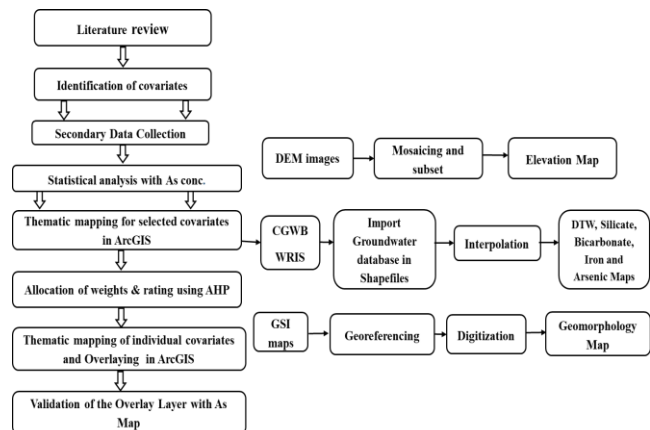


Figure 2. Schematic Flowchart of Methodology

Geomorphology map prepared from district resource map of the state obtained from Geological Survey of India (GSI) by georeferencing and digitizing it in ArcGIS v. 10.6.1. software. Shuttle Radar Topography Mission (SRTM) data of 30-meter resolution downloaded from United States Geological System (USGS) was used to map surface elevation. The study area covered in 10 SRTM images of September 2015 available in TIF format. Single DEM was obtained after Mosaicing, followed by image enhancement. The groundwater level data and Groundwater quality databases were procured from Indian Water Resources Information System (WRIS) and CGWB, respectively.

To assess spatial variation in arsenic concentration across the region total of 162 sample concentrations for arsenic validation were gathered and interpolated using the Ordinary Kriging statistical tool in ArcGIS. Correlation analysis among arsenic and quality parameters represented a strong correlation of Silicate, Bicarbonates, and Iron and hence, selected as covariates. Maps prepared for covariates are represented in Figure 3.

2.2.2 Analysis and Modelling: Analysis and modeling performed in ArcGIS software version 10.6.1 with application

of AHP approach of MCDM model. The final vulnerability map was generated by overlay analysis with proper validation.

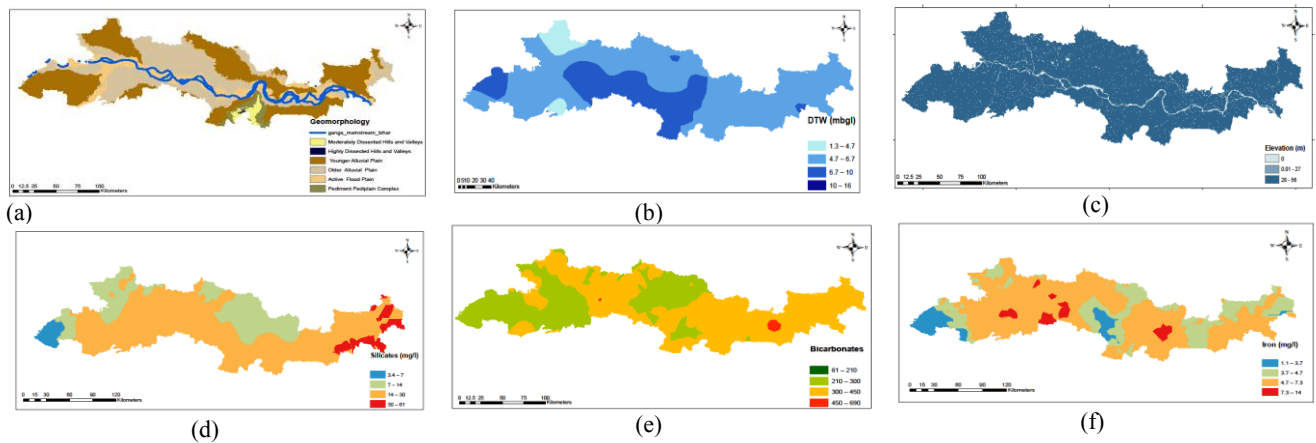


Figure 3. Thematic layers of (a) Geomorphology; (b) DTW; (c) bicarbonates; (d) elevation; (e) silicates; (f) iron of the study area.

2.2.2.1 Multi-Criteria Decision Making (MCDM):

MCDM is an algorithm which openly assesses multiple conflicting criteria in decision making. It is generally used for monitoring the alternatives by combining the site-specific information with expert’s judgment by prioritizing and ranking the alternatives to recommend the best one (Keshavarz-Ghorabae et al., 2018). It has a wide application for the last few decades for determining the groundwater potential zones across the world because it allows improvements in old methods and development of new ones (Gupta et al., 2010).

2.2.2.2 Analytical Hierarchy Process (AHP):

AHP is a multi-criteria decision method that uses hierarchical structures to represent a problem and then develop priorities for alternatives based on the judgment of the user (Saaty, 2008). It is an organized way to make decisions based on their priorities. It facilitates decomposition and pair-wise comparison, reduces inconsistency, and calculates priority vectors. The AHP procedure involves following steps (Lee et al., 2008): (1) Define the unstructured problem; (2) Develop the hierarchical framework according to selected covariates; (3) Construct the pair-wise comparison Matrix between input factors; (4) Evaluate the relative importance of factors by assigning the weight at each level of hierarchy, based on Saaty’s scale (Table 2) with the use of eigenvalue technique (Mann 1990); (5) Perform the judgement for pair-wise comparisons to obtain the relative importance of the alternatives (based on literature review); (6) Perform the consistency verification. CR must be less than 0.1(Saaty, 2008); (7) Repeat the steps from 3-6 for all levels in the hierarchy; (8) Develop the overall priority ranking and select best alternative.

For determination of rate and weightage for each covariate, rating comparison questionnaires were prepared and filled for the study area, based on literature surveys. Consistency Ratio (CR) check was performed after evaluation of eigen values, by following equations:

$$CR = CI / RCI \quad (1)$$

where CR= Consistency Ratio
CI= Consistency Index
RCI= Random Consistency Index

CI, here is obtained as:

$$CI = (\lambda_{max} - n) / (n-1) \quad (2)$$

where CI= Consistency Index
 λ_{max} = Maximum Eigen value of the matrix
n = number of groundwater affecting covariates

Intensity of Importance	Definition	Explanation
1	Equal importance	Two activities contribute equally to the objective
3	Weak importance of one over another	Experience and judgment slightly favor one activity over another
5	Essential or strong importance	Experience and judgment strongly favor one activity over another
7	Demonstrated importance	An activity is strongly favored and its dominance is demonstrated in practice
9	Absolute importance	The evidence favoring one activity over the another is of the highest possible order of affirmation
2,4,6,8	Equal importance	When compromise is needed

Table 2. Saaty’s Ratio Scale for Pair-Wise Comparison

2.2.2.3 Arsenic Vulnerability Index and Mapping:

Arsenic vulnerability Index is a dimensionless quantity that applies to perform the groundwater vulnerability mapping in an area. Groundwater arsenic vulnerability determines the ease of arsenic contamination in groundwater of specific areas, considering al hydrogeochemical characteristics (Hadžić et al., 2015). By combining the groundwater vulnerability map with elevated levels of arsenic in the state estimates risk potential zones. The weighted linear combination (WLC) technique was applied to determine the Arsenic Vulnerability Index (AVI). AVI was computed as the sum of the product of weights and ratings assigned to each of the covariates considered and is calculated by equation (3):

$$AVI = G_rG_w + D_rD_w + E_rE_w + S_rS_w + B_rB_w + F_rF_w \quad (3)$$

where G = Geomorphology
D = Depth
E = Elevation
S = Silicate
B = Bicarbonate

F = Iron
r = rating
w = weightage

Grouping of AVI values under three classes of low, moderate, and high vulnerability using ArcGIS equal interval classification method performed. Once all the four parameters were assigned weights and rates, the layers were combined into a single map to provide an Arsenic Vulnerability map to visualize which areas in the state are more vulnerable to arsenic concentration than others.

2.2.2.4 Data Validation: Validation is an important process of modeling to determine the accuracy of the model. Hence, it is important to validate the resultant AVI. Validation was carried out firstly by comparison of the weighted overlay thematic layer with the groundwater arsenic database interpolated in ArcGIS. Few simple techniques such as changes in classification classes, intervals, and single-layer techniques found to be suitable for validation. These methods also states about the sensitivity of model indirectly with each covariate.

3. RESULTS AND DISCUSSION

The exact reason behind arsenic contamination in the groundwater of Ganges has yet to establish, but common belief and various hypotheses proved that contamination is due to various natural and anthropogenic sources. The most accepted theory for the occurrence of arsenic in groundwater is due to geogenic sources, as rocks are the major reservoir of arsenic, containing arsenic bearing minerals. The sediments derived from the Himalayas are the main source of arsenic in groundwater of Ganga- Meghna- Brahmaputra plains (Chakroborti et al., 2011).

In Bihar, arsenic contamination is deliberated by geogenic causes as it exists in the solid phase and under a redox controlled environment gets released to groundwater. Organic carbon-rich clay beds also facilitate Arsenic dissolution. Elevated arsenic found in a new alluvial belt along the Ganges (Saha et al. 2009). This contamination is confined to sand, sandy clay, and silty clay layers of 50 m thickness, threatening the drinking water supply of the inhabitants. In the south and northern Ganga plains, low arsenic concentrations were observed (>0.05 mg/l). Aquifer characteristics govern about being shallow and unconfined aquifer.

3.1 Assessment of arsenic occurrence:

Arsenic occurrence was evaluated by spatial and statistical relationship of arsenic with covariates and presented graphically (Figure 4). The spatial relationship was examined by overlaying the groundwater As concentration thematic layer for the shallow aquifers with geomorphology, water table, elevation, and groundwater quality parameters. As per BIS 2012 and WHO, the maximum permissible limit for Arsenic is 50ppb. Therefore, the arsenic concentration has been categorized into three classes, i.e., < 50 ppb, 50-100 ppb, and >150 ppb, to draw out the relationship with various covariates. The statistical analysis determines the relationship of arsenic with its covariates. Hence, histograms were prepared to obtain the percentage of arsenic occurrence. Calculation of arsenic occurrence percentage concerning the area covered by each covariate represented in Fig 4.

Geomorphology reveals the geology of the state, which represents the geogenic evidences for arsenic contamination. The state is mostly covered with alluvial plains (younger, older,

and flood plains), which are composed of sand, silt, and clay (soil types) in varying proportions with the sediments deposited from the river Ganges and its tributaries. Since 42% of the area covered by younger alluvium, therefore, arsenic contamination has anticipated the younger alluvium plains of the state. The groundwater quality of older alluvium is much better than the younger alluvium. Arsenic distribution pattern in the state bears a considerable relationship with the Quaternary Sediments (geology) of alluvial stratigraphy (Bhattacharya et al., 1997; Das et al., 1995). Mineralogical composition of those sediments consists of quartz, feldspars, illite, and kaolinite, and the fine-grained over bank feces are rich in organic matter (Nickson et al., 1998). Deep flood plains enrich with organic matter, and active flood plains with high arsenic concentrations mostly have curvilinear depressions enclosing water bodies, where the sedimentation process is going on, resulting in arsenic release in groundwater. Bar graph between the area percentage (according to AHP mathematical model) and percentage occurrence of arsenic (depending upon the number of sites in each class) shows the high percentage of arsenic occurrence in the region of younger alluvium because it did not get oxidized in nature and is rich in organic matter (Fig 4 (a)). Most environmental arsenic problems, recognized so far, are the result of mobilization under natural conditions. Thus, the occurrence of arsenic in groundwater of the state got recognized as the geological evidence with spread out resulting from the mobilization under natural hydro-geologic conditions.

The depth to water level is considered as water level depth below ground level. In the middle Ganga plains of Bihar, potential aquifers are found at shallow depths with shallow water level <10 m (Fig 4 (b)). Hence, a high concentration of arsenic is observed in shallow aquifers, while concentration decreases with depth (Saha et al., 2010). The hand pumps for drinking water supply in rural and semi-urban areas are of depth range 20-40 m only, restricted the availability of groundwater samples beyond this depth indicated high arsenic. The reason for high concentration of Arsenic at shallow aquifers is by release from Arsenic rich iron sulfide minerals due to oxidation. Heavy pumping for irrigation from an aquifer leads to the compactness of surrounding clay and water expel as land sinks, which may contain arsenic, force it in deep aquifers.

As per the spatial relationship of arsenic with surface elevation, most of the considered area is low lying and has high arsenic concentration. Low surface elevation within the water level at deep depths, makes easy accumulation of finer sediments with arsenic adsorbing minerals. Areas with low slope retain water for a long duration, which allows greater infiltration, increase in water recharge, and a greater potential for groundwater contamination. Similarly, an area with steep slopes does not retain water, more runoff, and less infiltration, are less vulnerable to groundwater contamination. Topography ensures the duration of contaminant on the surface to infiltrate into the groundwater. High percentage of arsenic occurrence was observed in relatively flat areas, which suggests that the accumulation of finer sediments in low lying areas leads to high arsenic infiltration into deep aquifers (Fig 4 (c)).

The correlation was recognized between arsenic and other groundwater quality parameters obtained from CGWB, which displayed a strong correlation of arsenic with silicate, bicarbonates, and iron. Arsenic-contaminated groundwater is near-neutral and dominated by silicates, iron, and weak acid (HCO_3^-). Hydrogeochemical characteristics of Newer Alluvium indicated a higher load of (HCO_3^-). Hence, the presence of arsenic in the state largely depends upon geomorphology and groundwater quality of the area.

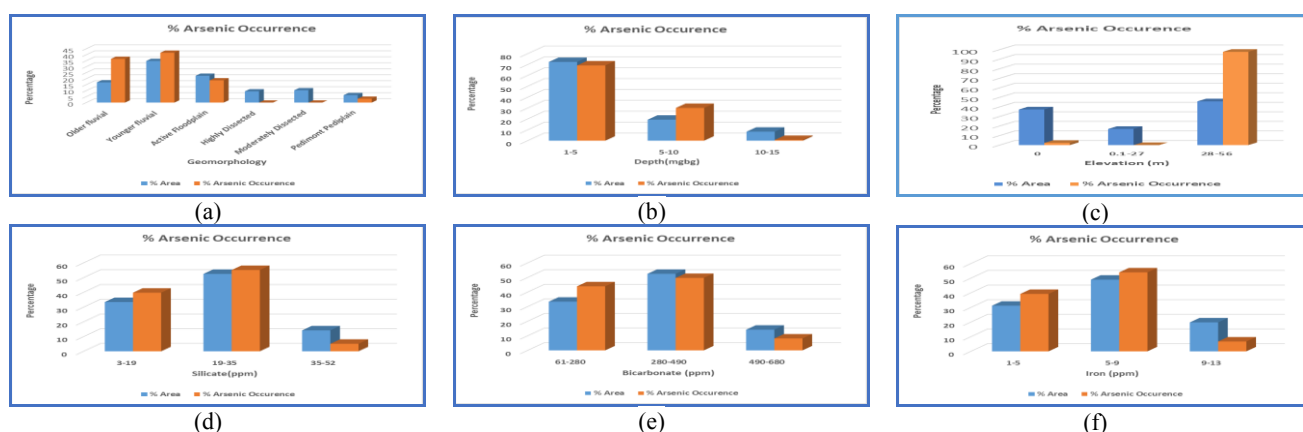


Figure 4. Percent of Arsenic Occurrence by covariates w.r.t. (a) Geomorphology; (b) DTW; (c) Elevation (d) Silicates; (e) Bicarbonates; (f) iron for the study area.

Higher silicates were reported in the districts Bhojpur, Bhagalpur, Buxar, Patna and Munger ranging from < 20mg/l; also the highest concentration of arsenic was reported in the same districts (<50ppb). Also, these districts lie in the region of newer alluvium plains and active flood plains, which is responsible for creating reducing conditions in the aquifer. Silicates being bulk of sediments upon leaching at high pH and low redox potential releases arsenic during silicate mineral dissolution (Alam et al., 2014). Hence, high silicate content accelerates more silicate mineral dissolution with high arsenic release (Fig 4 (d)).

Higher bicarbonate was reported in the central and northeastern districts of the state (<300ppb) and also most of the data points at this location represents a high concentration of arsenic (<50ppb). High percentage of arsenic occurrence found in the regions with bicarbonate concentration ranging from 280-490 ppm suggesting that bicarbonate ions can extract arsenic from sediment samples in both oxic and anoxic conditions (Fig 4 (e)). Bicarbonates can efficiently extract arsenic from arsenic adsorbed iron oxyhydroxides, imitating mobilization of arsenic from iron and manganese oxyhydroxides in sediments that are abundant in the subsurface core. HCO₃⁻ ions have an affinity to form complexes on the surface sites of iron hydroxide and substitute arsenic from the surface of minerals and sediments, resulting in the release of arsenic to groundwater.

Higher iron was reported uniformly in the state except for some central part of the state such as Bhojpur, Patna, Begusarai and Lakhisarai (< 4.7 mg/l) and also most of the data points at these location represents a high concentration of arsenic (<50ppb) (Fig 4 (f)). Weathering of clay sediments in the dry season remains less mobile iron for long durations, resulting in the release of mobile arsenic due to its strong affinity with pyrites. Similarly, Fe-Mn oxyhydroxides are a minor component of sediments but are larger reservoirs of arsenic (Alam et al., 2014). Reductive dissolution of Fe-bearing minerals releases As-oxyanions into the groundwater (Bennett et al., 2011). The release of As and Fe in the aqueous phase is due to oxidation of arsenic bearing sulfide minerals, which is supported by positive correlation between them. The organic carbon stimulates microbial respiration and triggers the reductive dissolution of As and Fe in the solid phase (Neidhardt et al., 2014).

3.2 Arsenic Vulnerability:

Arsenic vulnerability was computed by assigning weights and ratings based on AHP model considering the correlation coefficient value of arsenic with each covariate and within the classes of each covariate (Table 3). Overall Consistency Ratio

evaluated was 0.049 (0.049 < 0.1, hence accepted). After pairwise comparison, the thematic layers of each covariate after reclassification combined into a single map by overlay analysis tool of ArcGIS (Fig 5 (a)). Arsenic Vulnerability map helps to visualize which areas in the state are more vulnerable to arsenic concentration. The vulnerability index was computed as the sum of the product of weights and ratings assigned to each of the covariates considered for the study. The index value ranges from 100-292 in the study area. Northern regions of Bhojpur have displayed the highest index value, Patna and Munger districts with the southern part of Begusarai and Vaishali represents more vulnerability. Most of the districts show low and moderate arsenic vulnerability where all regions lie in channel alluvium zone with the shallow water level. Regions near to flood plains fall under the high vulnerable zone, which requires more attention regarding future land use patterns, keeping in mind the increasing arsenic pollution effects among the inhabitants.

Covariates	G	D	E	Si	B	Fe	Weightage
Geomorphology (G)	1	1	2	0.5	0.5	0.5	0.119599
Depth (D)	1	1	2	0.5	2	0.5	0.150648
Elevation (E)	0.5	0.5	1	0.3	0.5	0.5	0.0790951
Silicate (Si)	2	2	3	1	3	0.5	0.246319
Bicarbonate (B)	2	0.5	2	0.3	1	0.5	0.13046
Iron (Fe)	2	2	2	2	2	1	0.27388

CR= 0.049 < 0.1

Table 3. AHP Pairwise comparison for Bihar districts.

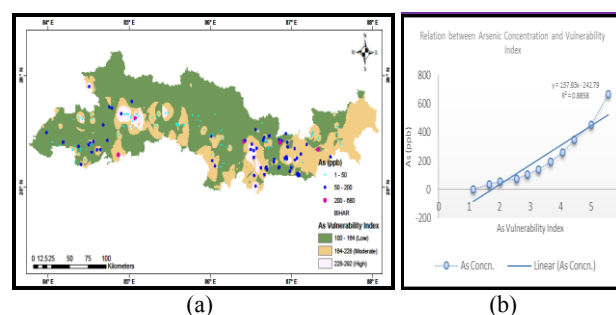


Figure 5. (a) Arsenic Vulnerability Index for Bihar and (b) Index validation by correlation. Validation was performed by assessment of spatial and statistical relation of vulnerability index with arsenic

concentration obtained from CGWB (Fig 5 (b)), change in classes and single-layer technique was used for validation. All these ways found out the most sensitive covariate responsible for arsenic contamination in groundwater as each covariate thematic layer is playing an essential role for final AHP decision making. It demonstrated the successful application of AHP model for the state. The results obtained from the vulnerability index are realistic, and the relation among covariates proves representative of the actual situation in the field. It represented geological evidences towards the release of arsenic in groundwater.

4. CONCLUSIONS

This paper attempted to determine the groundwater arsenic vulnerability using AHP method for 12 districts of Bihar state and looked out to be a successful methodology. Multi-Criteria Decision Making (MCDM) method used to provide a hierarchical quantitative framework and a process of comprehensive integration of diverse components. The extent of contribution of each indicator to overall vulnerability is different; therefore, different weights assigned to covariates using Analytical Hierarchy Process (AHP) method. Four covariates were selected to gather about the possible sources for the occurrence of arsenic in the subsurface environment. The state contamination is distressing the shallow aquifer (>50 m bgl), which is the source of hand pump based drinking water supply for many rural and semi-urban regions. Elevated arsenic concentrations confined in the flood plains, both in the active (flood-prone) and the older-younger plain of the Ganga River. Arsenic distribution marked with wide spatial variability resulting in patchiness in distribution across the state. The Arsenic affected aquifers represent young groundwater as the older alluvium supports the less permeable nature of the middle clay, holding the deeper aquifers under semi-confined to confined conditions (CGWB 2014). Groundwater in these aquifers can develop for community-scale water supply through deep tube wells where T remains > 5000 m²/day and is arsenic-free dep aquifers (Saha et al., 2009).

ACKNOWLEDGEMENTS

The authors are grateful to Indo-UK FAR-GANGA project, CGWB, Patna, Geological Survey of India, United States Geological Sciences, Indian Water Resource Information System, Ministry of Jal Shakti for providing secondary data for smooth research work. Maps throughout the paper created by Software ArcGIS® and ArcMap™ v 10.6.1, intellectual property of Esri, and used under license with Copyright © Esri. Financial support from IITR is appreciated.

REFERENCES

Agarwal, R., Garg, P., 2015: Remote Sensing and GIS-Based Groundwater Potential & Recharge Zones Mapping Using Multi-Criteria Decision Making Technique. *Water Resources Management*, 30.

Alam, M.S., Wu, Y., Cheng, T., 2014: Silicate Minerals as a Source of Arsenic Contamination in Groundwater. *Water Air and Soil Pollution*, 225.

Bennett, B., Dudas, M., 2011: Release of arsenic and molybdenum by reductive dissolution of iron oxides in soil with enriched levels of native arsenic. *Journal of Environmental Engineering and Science*, 2, 265-272.

Bhattacharya, P., Mukherjee, A., Mukherjee, A.B., 2011: Arsenic in Groundwater of India, *Encyclopedia of Environmental Health*, 150-64.

BIS, 2012: Bureau of Indian Standards.

CGWB, 2015: Arsenic Hot Spot in Ground Water in India.

Chatterjee, S., Moogoui, R., Gupta, D., 2017: Arsenic Contamination in the Environment, *Arsenic Contamination in the Environment*, Cham, Springer International Publishing, 13-35.

Chakroborti, D., Das, B., Murrill, T.M., 2011: Examining India's Groundwater Quality Management, *Environmental Geology*, 27-33.

GOI, 2015: Bihar State Profile.

Gupta, M., Srivastava, P., 2010: Integrating GIS and remote sensing for identification of groundwater potential zones in the hilly terrain of Pavagarh, Gujarat, India. *Water International*, 35, 233-245.

Hadžić, E., Lazović, N., Mulaomerović-Šeta, A., 2015: The Importance of Groundwater Vulnerability Maps in the Protection of Groundwater Sources. Key Study: Sarajevo Polje, *Procedia Environmental Sciences*, 25, 104-111.

Jang, Y., Somanna, Y., Kim, H., 2016: Source, Distribution, Toxicity and Remediation of Arsenic in the Environment – A Review, *International Journal of Applied Environmental Sciences*, 11 (2), 559-581.

Keshavarz-Ghorabae, M.A., Maghsoud, Zavadskas, E., Turskis, Z., Antucheviciene, J., 2018: Simultaneous Evaluation of Criteria and Alternatives (SECA) for Multi-Criteria Decision-Making, *Informatica*, 29.

Kim, K.W., Chanpiwat, P., Hanh, H.T., Phan, K., Sthiannopkao, S., 2011: Arsenic geochemistry of groundwater in Southeast Asia, *Frontiers of Medicine in China*, 5 (4), 420-433.

Kumar, C.P., 2015: Status and Mitigation of Arsenic Contamination in Groundwater in India, *The International Journal of Earth & Environmental Sciences*.

Lee, A.H.I., Wen, C.C., Ching, J.C., 2008: A Fuzzy AHP and BSC Approach for Evaluating Performance of IT Department in the Manufacturing Industry in Taiwan, *Expert Systems with Applications*, 34 (1), 96-107.

Lloyd, J., Oremland, R., 2006: Microbial Transformations of Arsenic in the Environment: From Soda Lakes to Aquifers, *Elements*, 2, 85-90.

Mann, S.H., 1990: An evaluation of the eigenvalue approach, 35, 295-301.

Matschullat, J., 2000: Arsenic in the Geosphere - A Review, *Science of the Total Environment*, 249 (1-3), 297-312.

M/o WR, & GR RD., 2014: Occurrence of high arsenic content in groundwater committee on estimates.

Nandimandalam, J.R., 2012: Evaluation of Hydrogeochemical Processes in the Pleistocene Aquifers of Middle Ganga Plain,

Uttar Pradesh, India, *Environmental Earth Sciences*, 65 (4), 1291–1308.

Neidhardt, H., Berner, Z., Freikowski, D., Biswas, A., Majumder, S., Winter, J., Gallert, C., Chatterjee, D., Norra, S., 2014: Organic carbon induced mobilization of iron and manganese in a West Bengal aquifer and the muted response of groundwater arsenic concentrations, *Chemical Geology*, 367.

Nordstrom, D.K., 2002: Worldwide occurrence of arsenic in groundwater, *Science*, 296, 2143-2145.

Paez E.D., Tamames, J., Lorenzo, V., Cánovas, D., 2009: Microbial Responses to Environmental Arsenic. *Biometals, an international journal on the role of metal ions in biology, biochemistry, and medicine*, 22, 117-30.

Saaty, T.L., 1980: *The Analytic Hierarchy Process: Planning, Priority Setting, Resource Allocation*, McGraw-Hill, New York, NY, 437.

Saaty, T.L., 2008: Decision Making with the Analytic Hierarchy Process, *International Journal of Services Sciences*, 1(1), 83.

Saha, D., Dwivedi. S.N., Sahu, S. 2009: Arsenic in Ground Water in Parts of Middle Ganga Plain in Bihar-An Appraisal, *Bhujal News Quarterly Journal*.

STREAMFLOW MODELLING OF PINDAR RIVER BASIN, CENTRAL HIMALAYA USING REMOTE SENSING DATA AND TEMPERATURE INDEX MODEL

Ningombam Prikash Meetei^{1*}, Rajeev Saran Ahluwalia¹, S D Khobragade², Shushanta Sarangi³, S.P Rai⁴, Sanjay K Jain²

¹Centre for Glaciology, Wadia Institute of Himalayan Geology, Dehradun (pksangom, raahluwalia05)@gmail.com

²National Institute of Hydrology, Roorkee (sdkhobragade@yahoo.com, sjain.nihr@gov.in)

³Department of Applied Geology, Indian Institute of Technology (Indian School of Mines), Dhanbad (shushanta@iitism.ac.in)

⁴Department of Geology, Banaras Hindu University, Varanasi (sprai1966roorkee@gmail.com)

*Corresponding author

KEY WORDS: Pindar River Basin, MODIS. Snow cover area, SNOWMOD.

ABSTRACT:

Assessment of snow cover area (SCA) is important for snow/glacier melt runoff, glacier mass balance study and other hydrological studies. Snow/glacier melt is a vital component of the river flow for the Himalayan river system. The major river system of India i.e., the Indus, Ganga and Brahmaputra River systems originated from the Himalayan region, are considered the lifeline of the Indian continent. The main source maintaining the flow of Himalayan rivers are snow/glacier melt runoff, rainfall runoff and base flow. The present study is to find out the variation of Snow-Covered Area (SCA) and streamflow modelling in the Pindar River Basin which is originated from Pindari Glacier in the central Himalaya using MODIS Terra (MOD10A2) data for the study period from 2005-2016. The annual mean SCA is found to be maximum (21.25%) in the year 2014 while it is minimum (12.85%) in 2016. On the basis of 12 years average analysis, January, February and December are found maximum SCA, while minimum is observed in August. Snowmelt runoff modelling has been carried out using the SNOWMOD model, and the snow/glacier melt runoff contribution is estimated to be ~33 %, while rainfall runoff and base flow contribution is to be estimated ~24 % and ~43 %, respectively.

1. INTRODUCTION

Fresh water resources are at a severe risk all over the globe as a significant consequences of climate change. The water contributes during summer period from the river originated from the Himalayan is mainly from the snow and glacier melt. Agriculture based economy of India depends largely on the irrigation water supply, provided by the Ganga River in north Indian states through Ganga Basin Irrigation system. Snowmelt is the process of converting the snow and ice into water. It requires energy to convert snow and ice into water. Snowmelt is the main component source of water supply in central Himalayan during summer time (Rai et al. 2009). Two widely used snowmelt models are temperature index model and energy balance model (Jain et al. 2010). The data required to run energy balance model are air temperature, albedo, solar insolation, wind speed and vapour pressure, which is rarely available in Himalayan region (Singh and Jain 2003). Air temperature is widely available in the Himalayan region. In the present study, temperature index model (SNOWMOD) is used to estimate the different

component in Pindar River and study the variation of snow cover area in Pindar river basin central Himalaya.

2. STUDY AREA

Pindar River originate from the Pindari Glacier at an elevation of 3820 m above sea level, which is located at central Himalaya in Bageshwar District of Uttarakhand, India. The glacier is 5 km long, the snout is about 6 m high and 2.5 m wide above the snout. The Pindar River Basin lies between Nanda Devi and Nanda Kot peaks and lie at 30°0'4.20"N - 30°19'5.099"N and 79°5'41.13"-80°5'37.69". The Pindar River confluences with Alakananda River at Karanprayag. The elevation range of the Pindar River Basin vary from 740 m to 6843 m. The basin area of Pindar River basin is 1860 km² up to Karanprayag (Figure 1). This is 5th stream order and one of the main tributary of Alaknanda River. The lithology of the glaciated valley is dominated by the Higher Himalayan crystalline rocks belonging to the Pindari formation of the Vaikrita Group (Valdiya, 1973). The terrain has preserved diverse glacio-geomorphological features, both erosional and depositional. This include the U-shaped glacial trough of trunk and tributary glaciers.

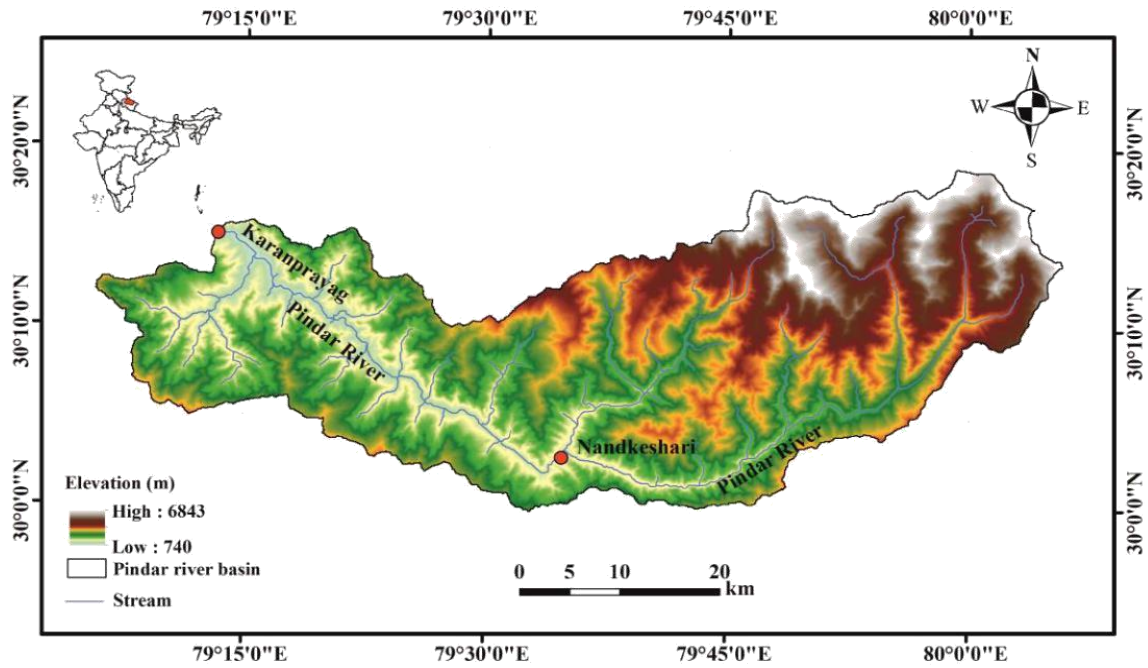


Figure 1: Study area of the Pindar river basin up to Karanprayag.

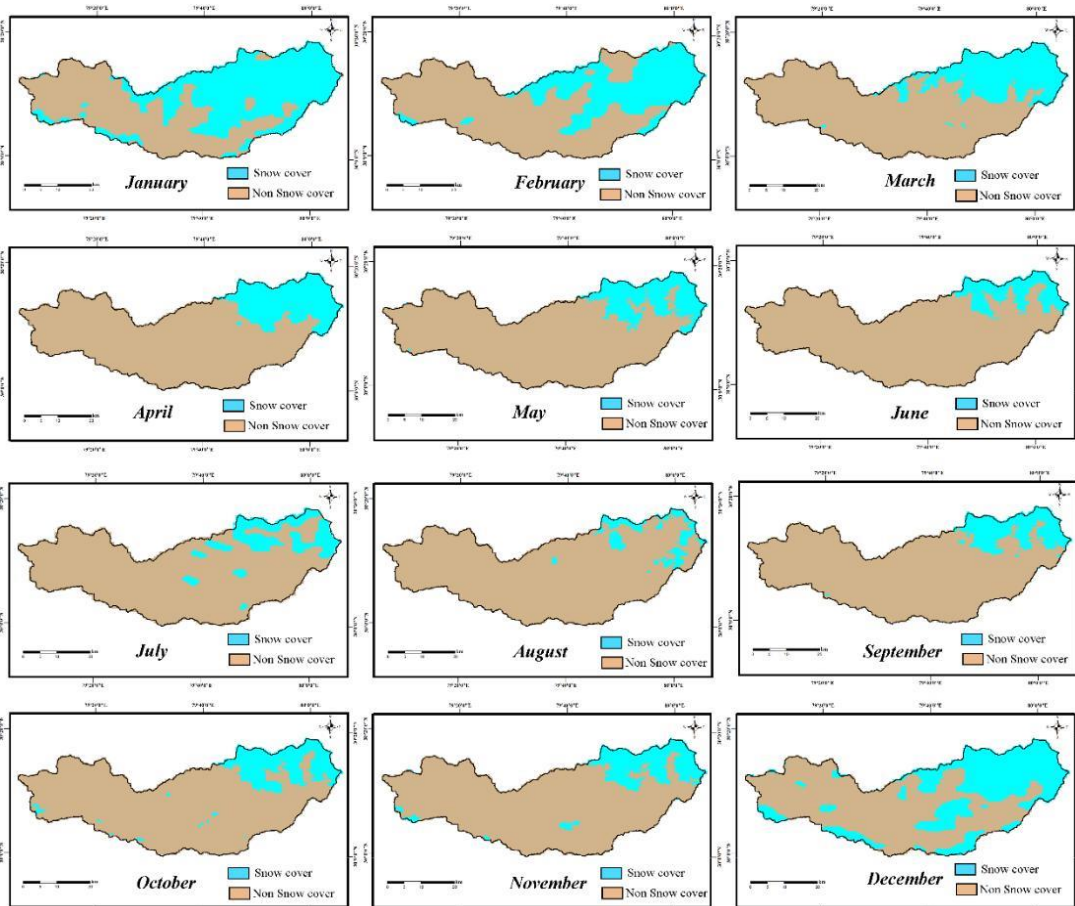


Figure 2: Snow cover map of Pindar River Basin by using MODIS 8 snow product from January to December for the year 2005

3. METHODOLOGY AND DATA USED

3.1 Digital Elevation Model (DEM)

ASTER DEM of 30 m resolution is downloaded from <https://earthexplorer.usgs.gov> and used to study the topography of the study area. Delineation of the basin area and 13 elevation zones with 500 m equal interval is classified by using Arc GIS 10.3 from ASTER DEM. Singh et al (2018) found that the accuracy of ASTER DEM is better than SRTM DEM in Himalayan regions.

3.2 Snow cover area (SCA)

SCA is the main input for simulation of snowmelt runoff model. MODIS/Terra Snow Cover 8-Day L3 Global 500 m Grid (MOD10A2) snow products were used in the present study to estimate the snow cover area of the Pindar River Basin over the time period of 2005–2016. MOD10A2 products provide for 8-day period maximum snow cover extent (Hall *et al.*, 2002) with a spatial resolution of 500 m. Mapping of snow cover from remote sensing data were explained by Dozier 1989, Hall et al. 1995. In rugged terrain such as Himalaya, Modis snow cover product give better result for estimation of SCA (Jain et al. 2008; Panday et al. 2014; Zhang et al. 2014). Various researchers such as Ahluwalia et al 2013; Maurer et al. 2003; Jain et al. 2008; Panday et al. 2014; Zhang et al. 2014 used MODIS snow cover product for stream flow modelling in the hilly region.

The sinusoidal projection of Modis snow product is reprojected to WGS 1984 UTM zone 44 and extracted the study area by using ERDAS Imagine software .The classified images are shown in the figure 2.

3.4 Temperature index model (SNOWMOD)

For the simulation of streamflow of Pindar River Basin, a temperature index model (SNOWMOD) is used to find the different component (snow/glacier melt runoff, rainfall runoff and baseflow) of Pindar River Basin. The generation of streamflow used the input data from snowmelt and rain and finally converted into runoff. The model performed three operation steps at each time. Firstly the available meteorological data are extrapolated in different elevation zones. The snowmelt rate is calculated at different point. Finally, the snowmelt runoff from snow cover area and rainfall runoff from non-snow cover area are integrated and routed separately with proper accounting of baseflow at the outlet of the basin.

4. RESULTS AND DISCUSSION

While analysis the MOD10A2 from the year 2005-2016, the annual mean SCA is found to be maximum (21.25%) in the year 2014 while it is minimum (12.85%) in 2016. On the basis of 12 years average analysis, January, February and December are found maximum SCA while the minimum is observed in August (Figure 3).

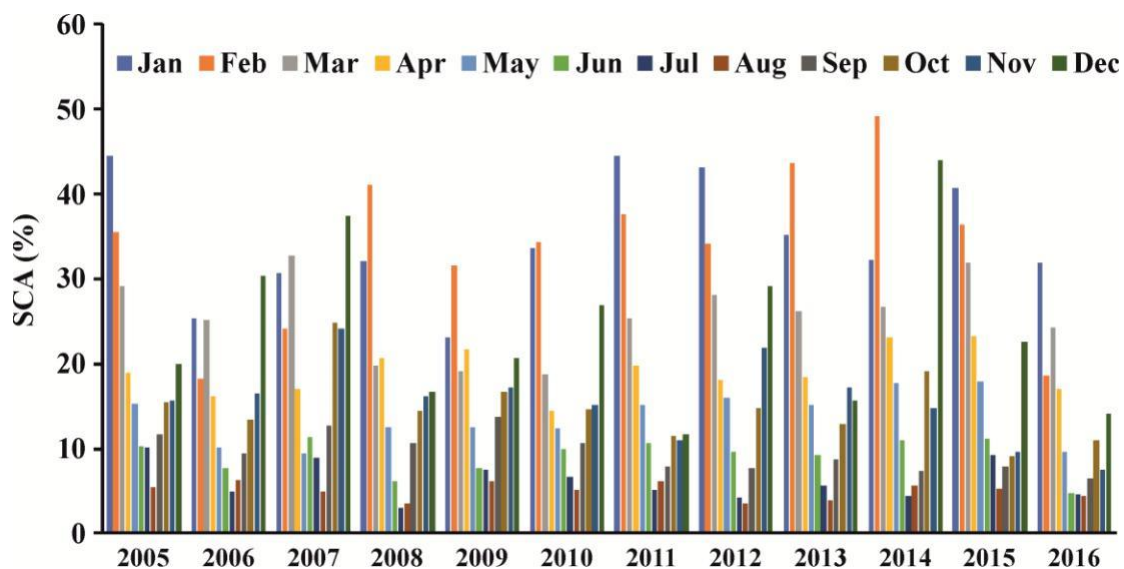


Figure 3: Distribution of SCA percentage from the year 2005-2016

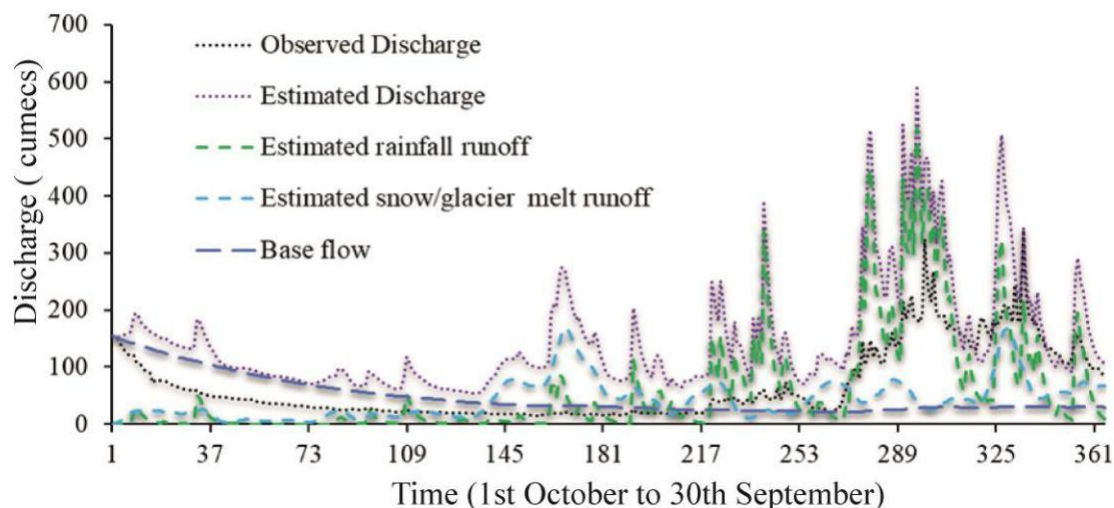


Figure 4: Observed and simulated daily streamflow for the Pindar river basin at Karanprayag for the 2005-2006

The snowmelt runoff model SNOWMOD has been applied for simulating the daily flows for the Pindar River at Karanprayag. The flow data for the year 2005 and 2006 have been considered for calibrating and validating the model. The efficiency of the model has been computed based on the daily simulated and observed flow.

The values of the model efficiencies are 82%, 80% for Pindar at Karanprayag. The performance of the model in preserving the runoff volume of entire year has been tested based on the criteria computed as percentage difference in observed and simulated runoff. The model has capability to separate out the contributions of rainfall, snow and glacier melt and base flow from the simulated flows. From hydrograph as shown in Figure 4, it has been observed that the model has simulated also the daily flows reasonably well showing generally a good matching with the daily observed flows. The trends and peaks of the daily flow hydrographs for the year are very well simulated by the model. As per the results for the contribution of the snowmelt runoff comes out to be ~33% and ~31% in the year 2005 and 2006 respectively. On an average, the contribution of snowmelt runoff is ~32% in Pindar River at Karanprayag.

Acknowledgement:

This study was supported by National Mission for Sustaining the Himalayan Ecosystem (NMSHE) funded by Department of Science and Technology, Government of India, New Delhi under the Research Project

(Research Project ID number 9). Authors have used MODIS products in this study and acknowledge the data providers. RSA and NPM is thankful to the Director, Wadia Institute of Himalayan Geology, Dehradun, India for supporting this research and permission to publish this work. The help extended by the Director, National Institute of Hydrology, Roorkee is also gratefully acknowledged.

REFERENCES

Ahluwalia, R. S., Rai, S. P., Jain, S. K., Kumar, B., & Dobhal, D. P. (2013). Assessment of snowmelt runoff modelling and isotope analysis: a case study from the western Himalaya, India. *Annals of glaciology*, 54(62), 299-304.

Dozier, J. (1989). Spectral signature of alpine snow cover from the Landsat Thematic Mapper. *Remote sensing of environment*, 28, 9-22

Hall, D. K., Riggs, G. A., & Salomonson, V. V. (1995). Development of methods for mapping global snow cover using moderate resolution imaging spectroradiometer data. *Remote sensing of Environment*, 54(2), 127-140.

Hall, D. K., Riggs, G. A., Salomonson, V. V., DiGirolamo, N. E., & Bayr, K. J. (2002). MODIS snow-cover products. *Remote sensing of Environment*, 83(1-2), 181-194.

Jain, S. K., Goswami, A., & Saraf, A. K. (2008). Accuracy assessment of MODIS, NOAA and IRS data in snow cover mapping under Himalayan conditions.

International Journal of Remote Sensing, 29(20), 5863-5878.

Jain, S. K., Goswami, A., & Saraf, A. K. (2010). Snowmelt runoff modelling in a Himalayan basin with the aid of satellite data. *International Journal of Remote Sensing*, 31(24), 6603-6618.

Maurer, E. P., Rhoads, J. D., Dubayah, R. O., & Lettenmaier, D. P. (2003). Evaluation of the snow-covered area data product from MODIS.

Hydrological Processes, 17(1), 59-71.

Panday, P. K., Williams, C. A., Frey, K. E., & Brown, M. E. (2014). Application and evaluation of a snowmelt runoff model in the Tamor River basin, Eastern Himalaya using a Markov Chain Monte Carlo (MCMC) data assimilation approach. *Hydrological Processes*, 28(21), 5337-5353.

Rai, S. P., Kumar, B., & Singh, P. (2009). Estimation of contribution of southwest monsoon rain to Bhagirathi River near Gaumukh, western Himalayas, India, using oxygen-18 isotope. *Current Science*, 240-245.

Singh, D. K., Gusain, H. S., Mishra, V., & Gupta, N. (2018). Snow cover variability in North-West Himalaya during last decade. *Arabian Journal of Geosciences*, 11(19), 579.

Singh, P., & Jain, S. K. (2003). Modelling of streamflow and its components for a large Himalayan basin with predominant snowmelt yields. *Hydrological sciences journal*, 48(2), 257-276.

Valdiya, K. S. (1973). Lithological sub-divisions and tectonics of the Central Crystalline Zone of Kumaon Himalaya. In *Proc. Symp on Geodynamics of the Himalayan region: Hyderabad, India*. National Geophysical Research Institute (pp. 204-205).

Zhang, G., Xie, H., Yao, T., Li, H., & Duan, S. (2014). Quantitative water resources assessment of Qinghai Lake basin using Snowmelt Runoff Model (SRM). *Journal of Hydrology*, 519, 976-987.

Water Harvesting Systems of the Past- A Case Study of Badami, India

Authors- Mythrayi Harshavardhan¹ and Kuili Suganya¹

¹ National Institute of Advanced Studies, Indian Institute of Science Campus, Bengaluru, Karnataka 560012

mythrayi.h@gmail.com

kuilisuganya@gmail.com

KEYWORDS: ancient water systems, Malaprabha, Badami, GIS, remote sensing

ABSTRACT:

Badami, also known as Vatapi in the ancient times, was the regal capital of the Early Chalukyan Kingdom, founded Pulakesi I in 544 CE (Michell, 2011). The settlement of Badami sets a good example to discuss the water harvesting systems engineered in the past for sustenance of the settlement with an understanding of the topographical conditions.

This paper explores Badami and its fortification area, by the various applications of geospatial technology to identify and document the various water harvesting systems (like tanks, wells, and aqueducts) that functioned as crucial water resources in the region. An understanding of the water harvesting systems has been achieved by studying and analysing old geo-referenced maps, satellite imagery (Google Earth, BHUVAN, Cartosat1 and Corona imagery). Furthermore, analysing topographical models generated using stereoscopic space imagery with Geographic Information Systems (GIS) tools and techniques, like the Digital Elevation Model (DEM) and anaglyphs. These GIS tools have helped in the visualisation of the landscape, study the terrain, and conduct various hydrological analysis (like, recognising the stream networks and extract catchment areas). This led to identifying one of the catchments that gathered water into a rocky cistern, which in turn distributed water in two ways: 1) *Agastya Tirtha*- a large reservoir amidst the settlement and 2) an aqueduct that supplied water to the fort area. The geospatial analysis of the region is further validated by field study and ground-truthing.

The findings have helped assess the historic landscape and the role of water harvesting systems in the hot semi-arid region of Malaprabha river valley mainly focussing on Badami and its immediate environs. This study contributes to a body of knowledge in the realm of ancient water systems in Malaprabha valley through understanding the interrelationship between human, water systems and the environs, and creating digital output. This would further enable us to conduct a comparative analysis of other such settlements across the region.

1. INTRODUCTION

1.1 Context

The river Malaprabha meanders through red sandstone rocky outcrops, a geological formation in the Deccan Plateau that has resulted from thousands of years of erosion. This unique yet magnificent landscape has some of the most ancient and iconic sites scattered across the region. The rivers and streams cutting across this idyllic landscape that has ravines, rock overhangs, haphazardly formed boulders, and precariously balanced stones creating a dramatic setting like no other. The landscape is a showcase of many historic settlements spread across the terrain that existed since the Early Chalukyan (5th Century) era. Some of the well-known historic settlements are Badami, Aihole,

Pattadakal, Mahakuta, and Banashankari that are home to monuments exhibiting impressive architecture in sandstone. Malaprabha flows north- eastwardly at a low gradient and hemmed by the rock formations of Kaladgi Basin in the North and granitic-gneiss in the South. The region has natural advantages of the river flowing across the landscape and surrounded by cliffs making it suitable for habitation (Michell, 2011). Apart from the river, there are various natural springs, tanks, wells, rocky cisterns and other water harvesting systems that are sources of water in this hot semi-arid belt. The prehistoric remains discovered in the region, are evidence of human habitation from the earliest times. (Michell, 2011)

Badami, the former capital of the Early Chalukyas, is located in the north-eastern part of the Malaprabha River Basin, in Karnataka, India. The settlement overlooks a large reservoir, *Agastya Tirtha*, (a main source of water). Badami is nestled in a ravine surrounded by red sandstone cliffs forming a majestic

horseshoe feature around the settlement. It has some of the most iconic monuments carved into the cliff faces and some perched on the rocky summits. The strategic value of the locale was appreciated and exploited by the former rulers, such as the Early Chalukyas, Rashtrakutas, Later Chalukyas, emperors of the Vijayanagara dynasty, Adil Shahi Sultans, the Marathas, Tipu Sultan, and the British. This Chalukyan capital was not only a centre for temple building activities, but also witnessed the construction of fortifications and watchtowers since the Early Chalukyan times, and consequently, developments made during Vijayanagara and Tipu Sultan's reign (Michell, 2011). This historic settlement exhibits certain planning characteristics and water harvesting features that are influenced by the local landscape. By setting the context and the topographical conditions of the locale, one is able to comprehend the landscape. This paper discusses the ancient water harvesting systems that were vital sources of water to the settlement, which is in the hot and dry climatic zone. Using geospatial techniques and tools, we were able to produce results after identifying and documenting the water resources. The applications of geospatial technology in this field of study has been discussed in the paper.

2. STUDY AREA



(a) Muttalgeri Kere



(b) Sidanna Kolla



(c) Rocky cistern in the fort area



(d) Reservoir (Agastya Tirtha)

2.1 Water Harvesting Systems

2.1.1 Overview: The River Malaprabha originates in the Sahyadri mountain range in the Western Ghats, at Kanakumbi. It flows from an altitude of 792.4 m through a landscape with sparse vegetation. Its confluence with the river Krishna is at a much lower altitude of 488m, at a place called Kudalasangama (Sunkad, 2013). The region predominantly has Black cotton soil (Agarwal & Narain, 1997). It is a relatively dry region with an average rainfall as low as 500-600mm annually, making it a major rainfall deficit area in the state (Joshi, 1955) (Madur, 2016).

However, we observed that there are various water harvesting systems, which were devised in the past to sustain settlements across this region and provide water for irrigation, drinking, and other domestic purposes. Water harvesting systems found in this valley are- tanks (locally known as *kere*¹) (Figure 1a), natural springs (also known as *kollas*²) (Figure 1b), streams (called *hallas*³) (Figure 1c), rocky cisterns (Figure 1d), wells, reservoirs (Figure 1e), aqueducts⁴, and *Tirthas*⁵ (Figure 1f) (Agarwal & Narain, 1997). Many of these structures, used even today, are centuries old and are interlinked hydrologically even though they were dispersed spatially (Shah, 2003).

¹ *Kere*- is a Kannada term for tanks, which were the main source of irrigation in Central Karnataka Plateau (Agarwal & Narain, 1997)

² *Kolla*- Natural springs in Kannada are known as *Kollas*. These springs feed water cisterns and man-made tanks. *Kollas* don't dry up and provide water even in the hottest months of the year. Some of them are scared places worshipped by some Hindus, for this reason. (Michell, 2011)

³ *Halla*- a Kannada term used for a tributary or a seasonal drainage channels that supplied water from the river. (Shah, 2003)

⁴ *Aqueduct*- a conduit like structure to carry water across a hollow or valley. (Britannica, 2019)

⁵ *Tirtha*- It is a Kannada term for tanks. *Tirthas* are tanks that are sacred and worshipped by some Hindus. They are usually in close proximity to a temple or a group of temples and can be of different types. One type of *Tirtha* is a reservoir that is mainly rain fed while the other type is fed by a natural spring that is trapped in a rectangular or square shaped tank. (Michell, 2011)



(e) Tirtha at Mahakuta

Figure 1: Types of water harvesting Systems in Malaprabha River Valley

- (a) Muttalgeri Kere (b) Sidanna Kolla (c) Rocky cistern near Upper Shivalaya (d) Reservoir (Agastya Tirtha) (e) Arali Tirtha

2.1.2 Case Study of Badami and the Geospatial Study: In the 5th Century, Badami was the seat of power to the Early Chalukyas. The natural defences and an ideal location made the site suitable to set-up a capital (Michell, 2011). The fortifications were built along the edge of the cliffs, while the settlement remained at a lower altitude, overlooking *Agastya Tirtha*, a large reservoir. The reservoir has steps descending down to the water.

The 1870 gazetteer discusses two sources that fed the reservoir and this was validated from our field study (Campbell, 1884, p. 561). One of the sources on the east, is a surface runoff in the form of a waterfall, which occurs only during a heavy spell of rain. The other source is a channel in the north that drains water into the Tirtha. The initial elevation profile of the drainage line generated from a 30m SRTM DEM (USGS, 2000) (using a threshold value of 200Sqkm in ArcHydro (ArcMap, Ver. 10.3.1)), in correlation with Google Earth and Survey of India (SOI) maps of different time periods (ranging from 1930 to 2003 publication) helped to determine the natural drainage channel that drains

rainwater into the *Tirtha* from its eastern catchment area. With respect to the northern channel, a closer observation of the Google Earth imagery of the area, enabled us to determine the location of a rocky cistern a few hundred metres to the north of the *Agastya Tirtha*, which was part of the neighbouring catchment (Figure 2). This cistern was found to be at an elevation of 671m. The overflow from this cistern flowed through the channel into the *Tirtha*, making it the second source of water for *Agastya Tirtha* at 581m.

About a few hundred metres from the Bhutanatha group of temples at the rear end of *Agastya Tirtha*, a rocky path leads to a rock shelter at *Aralitirtha*. The site is not easily accessible and it has an overhang above a rocky cistern that is fed by rainwater. The rock shelter has inscriptions and carvings of deities that existed since the Marthia Period (Michell, 2011). This site was identified from 1930 SOI maps, and is a part of the eastern catchment.



Figure 2: Google Earth image showing the rocky cistern north of *Agastya Tirtha*

Badami fort (North Fort) rises over 200m above the settlement. The vestiges of the fort complex indicated that the enclosure housed various structures like mandapas, temples, dargah, granaries, watchtowers, and rock cut cisterns. The cisterns are rain-fed and functioned as sources of water for the fort. (Michell, 2011). A field study of the site enabled us to observe the locations of the cisterns, and get a better understanding of the topography and geology of the place, as these are points where large amounts of surface run-off is collected. Mansour Shqjarat et. al (2010) studies the rocky cisterns in the region of Udruh in southern Jordan, which also has similar climatic and geological conditions (arid to semi-arid), as Badami and its surrounding region. It discusses that these cisterns may have formed from natural cavities in the rock strata, which could have either been enlarged artificially by cutting into the native rock. We can draw parallels to the rocky cisterns that are found in our study area.

A sketch of Badami Fort and the Pettah region drafted by John Jeffrey O'Donnoghue, a military engineer of The British army (Nanda & Johnson, 2015), shows an aqueduct connected to the north-eastern corner of the fort into a cistern. On studying google earth maps, DEM and a thorough ground validation of this area, we inferred that it, in fact, is an aqueduct and the source of water for the aqueduct is the same rocky cistern (at elevation 671m) (ref. Figure 3a & 3b) whose excess runoff flows into Agastya Tirtha. This aqueduct connects the higher cistern at 671m to fort cistern at a lower elevation of 622m causing the water to flow by gravity. The structure, which we inferred to be an aqueduct has a

thick layer (6") of lime plaster that is a typical construction technique for aqueducts and could date back to the Vijayanagara Period. (Figure 4a) At various places along its length, there are remnants of the vertical members that form a trough of the aqueduct, also have a thick coating of lime plaster. (Figure 4b) We also noticed that there were no bastions along the length of the structure which determines that it is an aqueduct. Furthermore, we noticed that in some of the stones used in the construction of the aqueduct (along with lime plaster remains), were rectilinear wedge marks, see (Figure 4c). Menon's (2018) work on wedge marks in the stones used for construction helped to substantiate that the aqueduct belonged to the Vijayanagara Period. Evidently, these wedge marks were used for construction in the Vijayanagara period, and the wedge holes were made to split the stones (Menon, 2018). Detailed photo documentation with geo-tagging of the photos and recording the various points of the structure helped process data and generate an elevation profile of the aqueduct.

The above discussion we infer that the former rulers of Badami, particularly of the Vijayanagara Period (1335-1570 AD) were pioneers in building intricate water networks systems, which were engineered to utilise natural catchment areas efficiently. The catchment areas of the waterbodies were enlarged by water drains or channels through a cascading system or overflow mechanism, which was in place. There were channels cut into the hard strata for excess water to run-off into a tank or a reservoir as discussed by Agarwal & Narain (1997).



Figure 3a: A rocky cistern that is the source of water for the aqueduct connecting to the fort

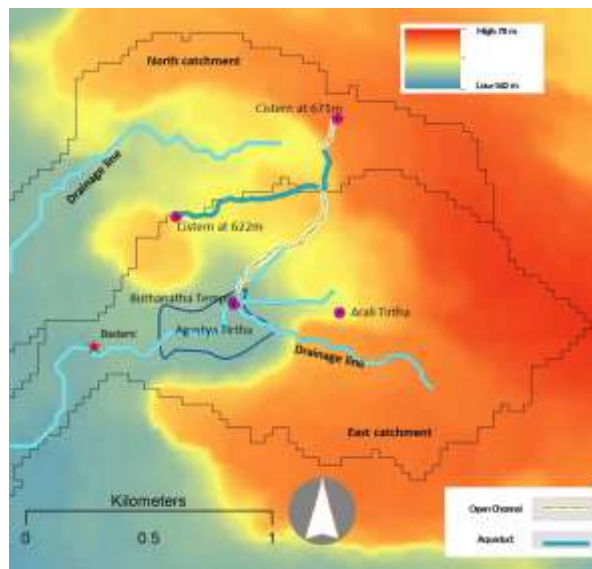


Figure 3b: CARTOSAT-1 DEM (10m resolution), generated from stereo pairs

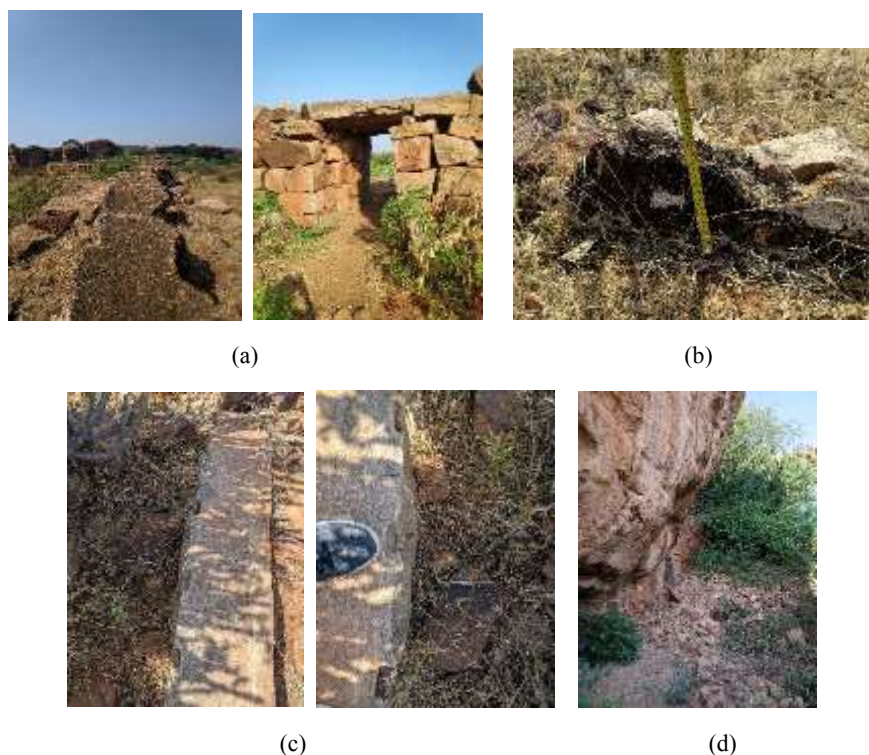


Figure 5: Images showing vestiges of the Aqueduct

(a) Aqueduct (b) Vertical members on either side forming a trough of the aqueduct (c) Rock showing angular wedge marks (d) Part of the aqueduct joining the fort

2.2 Geospatial Analysis of the Water Resources in the region

Badami has proved to be an interesting case study due to the topography and rocky landscape. We have used remote sensing techniques and GIS tools to acquire and analyse spatial data of the region. Digital maps, satellite imagery, and elevation models help visualise and study the landscape in detail. (Mandyam B. Rajani, 2009). Collecting this spatial data on Badami and its environs, set a precursor for the field trips we conducted thereafter. These layers of information in the study area have revealed some interesting features related to water harvesting system that existed from ancient times.

Spatial and temporal data obtained from satellite imagery and maps published by the Survey of India, of the study area in the scale of 1:50000, of different time periods (1930s, 1970s and 2000s), has helped identify and document important features. Field points and tracks obtained from short-range remote sensing instruments, on field trips validates these features such as parts of the fort and hydrological components that once supplied water to the fort. This has facilitated in generating thematic maps and adding vector data (points and polygons) as kml or shp files. A detailed inventory of the features of interest was also created. A digital elevation model of the study area was generated for further analysis of the terrain. DEM is a tool used in GIS to produce digital relief maps. This model is used to see terrain parameters, like slope, contours, elevation, and drainage pattern. It also helps in terrain modelling, simulation of the landscape, geomorphological analyses, and orthorectification of satellite imagery (Mandyam B. Rajani, 2009). Use of SRTM 30m dataset proved useful in this study as we could visualise the slope and

drainage patterns that supplied water to the different catchment points in the region. Overlaying the field points of the aqueduct on the DEM helps retrace the structure on the visualised landscape high resolution DEM and anaglyphs generated from CARTOSAT-1 stereo pairs created using ERDAS's Leica Photogrammetric Suit for visualisation.

3. CONCLUSION

The inferences drawn from the present study are that remote sensing combined with GIS tools and techniques, aid in a better spatial and temporal understanding of Badami and its environs. Some areas that were inaccessible could be traced through satellite imagery and remote sensing, without coming in physical contact with the area/ object (Muhammad Jehanzeb Masud Cheema, 2017). Various sources of literature and study of the Malaprabha river Valley chronicled by researchers reveal the efforts made by the rulers and planners of the past, who had harnessed nature and natural resources and built an extensive water network to meet the demands for agriculture, drinking and domestic purposes. A noteworthy feat of engineering was in place and it is commendable that many of these systems are still in use (M.G. Shivakumar, 5 April, 2016). The study of ancient water management systems in Badami and its immediate surroundings has helped uncover various structures, especially of the Vijayanagara Period, which was previously unknown. This is made possible by combining various datasets obtained from the geospatial analysis. A multidisciplinary approach has enabled us

to create a comprehensive and unique output using the GIS platform.

This study would add to the emotional value "the identity" (Feilde, 1989) of a society which "ensures the survival sense of place and its very character in a globalizing environment". It would bring together the information to the digital world, eventually contributing to creating awareness and improve the quality of the environment both globally and locally. Understanding the ancient water management systems would help with future explorations and planning level decisions while making sustainable developmental plans.

ACKNOWLEDGEMENTS

This study is undertaken as a part of a project under the Indian Heritage in Digital Space (IHDS) of Interdisciplinary Cyber-Physical Systems (ICPS) Programme is funded by the Department of Science and Technology (DST). We thank Principal Investigator of the project Dr. M. B. Rajani for her support and guidance on this study. We thank NIAS for the institutional support in carrying out the study.

REFERENCES

- Agarwal, A. & Narain, S., 1997. *Dying Wisdom- Rise Fall and Potential of India's Traditional Water Harvesting Systems*. New Delhi: Centre for Science and Environment.
- Blore, 2016. *Badami cave Temple, badami, Bagalkot .karnataka.india*. [Online]
Available at: <http://www.dronestagr.am/badami-cave-temple-badami-bagalkot-karnataka-india-2/>
[Accessed 23 February 2020].
- Britannica, the Editors of Encyclopaedia., 2019. *Aqueduct Engineering*. [Online]
Available at: <https://www.britannica.com/technology/aqueduct-engineering> [Accessed 22 February 2020].
- Campbell, James. M., 1884. *Gazetteer of the Bombay Presidency- Bijapur, Vol 23*. Bombay: Government Central Press.
- ERDAS (2014) ERDAS Imagine 2014. Hexagon Geospatial, Peachtree Corners Circle Norcross.
- Feilden, Bernard., 1989. *Guidelines for Conservation*. New Delhi: Indian National Trust for Art and Cultural Heritage.
- Joshi, Ramchandra Vinayak, 1955. *Pleistocene Studies in the Malaprabha Basin*. Poona; Dharwar: Deccan College Postgraduate and Research Institute; Karnataka University.
- M.G. Shivakumar, R. Cheluvraju., 5 April, 2016. *Ancient irrigation systems of Karnataka*. New Delhi, International Commission on Irrigation and Drainage.
- Madur, 2016. *Rainfall in Karnataka*. [Online]
Available at: <https://www.karnataka.com/profile/rainfall/>
[Accessed 20 February 2020].
- Mandyam B. Rajani, Sumanta K. Patra, Mamta Verma, 2009. Space observation for generating 3D perspective views and its implication to the study of the archaeological site of Badami in India. *Journal of Cultural Heritage*, December, 10(1), pp. e20-e26.
- Mansour Shqiarat, Fawzi Abudanah, Saad Twaissi., 2010. Water Management and Rock-Cut Cisterns with Special Reference to the Region of Udhrum in Southern Jordan. *Research Gate*, July, IV(02), pp. 205-227.
- Menon, Meghana Kuppa and Srikumar M., 2018. Stories from Silent Stones: On the Shape of Wedge Marks as a Diagnostic of Stone-Craft of Different Periods. *Heritage: Journal of Multidisciplinary Studies in Archaeology*, Volume 6, pp. 438-486.
- Michell, G., 2011. *Badami, Aihole, Pattadakal*. Mumbai: JAICO Publishing House.
- Muhammad Jehanzeb Masud Cheema, W. B. M Bastiaanssen, 2017. *Remote Sensing and GIS Applications in Water Resources Management*. s.l.:s.n.
- Nanda, V. & Johnson, A., 2015. *Cosmology to Cartography- A Cultural Journey of Indian Maps: from the Collections of Kalakriti Archives, Hyderabad and National Museum*. New Delhi: National Museum.
- NRSC, 2014. *CARTOSAT-1 Stereopair*, Hyderabad: National Remote Sensing Centre.
- Shah, Esha., 2003. *Social Designs- Tank Irrigation Technology and Agrarian Transformation in Karnataka, South India*. 1st ed. New Delhi: Orient Longman Private Limited.
- Sunkad, B.N., 2013. Water Quality of Malaprabha River With Reference to the Physio- Chemical Factors near Khanapur Town of Belgaum District. *International Journal of Innovative Research in Science, Engineering and Technology*, Vol. 2, Issue 4, April, 2(4), pp. 930-936.
- USGS, 2000. *Earth Explorer*, s.l.: United States Geological Survey.
- QGIS, 2015. QGIS Geographic Information System. Open Source Geospatial foundation Project. <http://qgis.osgeo.org>

GENERATION OF HISTORIC, PRESENT AND FUTURE SNOW COVER DATASETS USING MODELLING APPROACH

Vishal Sharma^{1*}, Bhaskar R. Nikam¹, Praveen K. Thakur¹, S. P. Aggarwal¹, Vaibhav Garg¹, Vaibhav Shrivastava¹, Sachchidanand Singh¹

¹ Water Resources Department, Indian Institute of Remote Sensing (IIRS-ISRO), 4 Kalidas Road, Dehradun, India – 248001.

*vishal.iirs@gmail.com

KEY WORDS: Snow Cover, VIC, CORDEX, Snow line, Temperature anomaly

ABSTRACT:

Snow cover maps play an important role in the study and impact of climate change in the mountainous region which receives snowfall. The snow line shift has been observed in the recent time at an alarming rate due to the rapid increase in temperature. Traditional snow cover maps are generated from ground based or space-based observations. These observations have limitations in terms of spatio-temporal coverage; resolution; repetitivity, etc. Snow cover maps can also be generated using physically based distributed land surface models. In the current study the Variable Infiltration Capacity (VIC) model, a semi-distributed land surface model is used for generation spatio-temporal dynamics of snow cover of Jhelum Basin at $0.025^\circ \times 0.025^\circ$ spatial resolution. The Jhelum Basin receives ample amount of snow fall during winter season. The dataset used in setting up of land surface model are digital elevation model, land use/ land cover map (ISRO-GBP- LULC Project), soil map (FAO) and other land surface parameters derived from remote sensing data. The model simulations are created using Era-Interim and CORDEX dataset for the period 1979 to 2018 and 2019 to 2099, respectively. Model calibration and validation is done for the winter season using the discharge data observed at Asham and Sangam outlet by the Irrigation and Flood Control Department, Kashmir. The model generated snow cover is validated for the time period 2000 to 2018 using the MODIS eight daily maximum snow cover product (MOD10A2). The historic snow cover maps are generated from the time period 1979 to 2000 and present maps are generated for the time period 2001 to 2018. The future snow cover maps are also generated for the period 2019 to 2050. The maximum snow cover area for the months of December, January and February is also plotted for the time period and it shows very high decrease in the snow cover area in the future time period. The snow cover area has shown tremendous turbulence in the curve due to increase in the extreme events in the near future time period. Snow cover products (in GeoTIFF format) generated in this study will be made available to other researchers for validation and further utility through web based data dissemination portals of IIRS, ISRO.

1. INTRODUCTION

Climate change over the North Western Himalaya is very crucial in the recent time and is always a topic of worry for the sub-continent region as it contains largest deposit of snow-glacier ice in the world besides the polar region. Snow cover is directly linked with the hydrology of the lower region as snow melt is the major contribution in discharge of the Himalayan Rivers. Jhelum River, a major river flowing through the Kashmir Valley, is home to a number of culturally and geologically sites having historical and scientific importance.

1.1 Snow Cover

Snow cover extent, snow depth, snowfall and snow water equivalent play an important role in the global energy and water cycles (Brown & Robinson, 2005). The snow cover area plays a vital role in understanding the changes in the local climate, hydrology of the region and also the downstream areas (Rathore et al., 2018). The change in the snow area over a period of time signals the effect due to climate change. As snow melt contributes directly as the runoff in the ablation period, its significance becomes very high in the downstream areas. Snow cover act as a buffer controlling river discharge and associated environmental processes. (Barnett et al., 2005; IPCC, 2007). The spatio-temporal snow cover variation over a period of time is quite important for climate monitoring of the region (Brown & Robinson, 2011; Nikam et al., 2017).

1.2 Model based Snow Cover

From the early 1960s, the various numerical and mathematical models are been used to simulate and to compute the snow accumulation and snow ablation processes. These involves various mathematical equations for illustrating relationships between various environmental processes. (Armstrong and Brun, 2008). The satellite-based snow cover products are available for a specific time period. Also due to the cloud cover and temporal resolution of the satellite there is limitation in obtaining daily products which can further be used in understanding the impact and changes in the daily snow cover area of the region. The modelling approach can be much more beneficial in generating the daily snow cover area along with other parameters i.e. Snow Water Equivalent (SWE), Snow density etc. The model utilized in the current study is Variable Infiltration Capacity (VIC) model, a macro scale semi-distributed hydrological model. (Liang et al., 1994; Liang, 1994; Liang et al., 1994, 1998; Liang, et al., 1996a; Liang, et al., 1996b; Xu Liang & Xie, 2001; Lidén & Harlin, 2000) The model is setup for the study area i.e. Jhelum. The model is first calibrated and validated with the observed discharge data. The discharge data observed at Asham and Sangam outlet is taken for model calibration and validation. The calibrated model is then utilized in generating the daily snow cover area. The daily snow cover area is again validated using the 8-daily maximum snow cover of the Modis data. Modelling is done to generate historic snow cover maps from the time period 1979 to 2000 and present maps are generated for the time period 2001 to 2018. The future snow cover maps are also generated for the period 2019 to 2050. The monthly analysis is then done for obtaining the changes in the study time period.

2. STUDY AREA AND DATASETS USED

2.1 Overview of the Study Area

The Jhelum River basin located in Himalaya stretches between 73.0–75.62 °E and 33–35 °N, as shown in Fig. 1. The Jhelum River, the second biggest tributary of the Indus River system. The basin with drainage area of 33466 km² is stretched between the elevations ranging from 214 to ~ 6280 m. River Jhelum is a major tributary of river Chenab which itself is a tributary of river Indus. The study area comprises of the Jhelum basin located in the state of Jammu and Kashmir, India (Mahmood et al., 2015). The average elevation of Jhelum basin is about 1830 metres above mean sea level. Jhelum river originates from the Verinag’s spring in the north-west side of Pir Panjal and from there it moves parallel to the Indus River. It also flows along the area of about 5956.973 km² alluvial soil of Kashmir Valley. The North side of the Kashmir valley contains large sources of glaciers which also contribute to Jhelum River discharge. In the north-west direction it joins the Dal and Wular lakes near Baramulla. After Baramulla it flows through a long gorge and ends in a confluence with the Chenab. The major city of the valley Srinagar is settled on both sides of the River Jhelum. It covers almost all the physiographic divisions of the Kashmir Valley and is drained by the most important tributaries of river Jhelum.

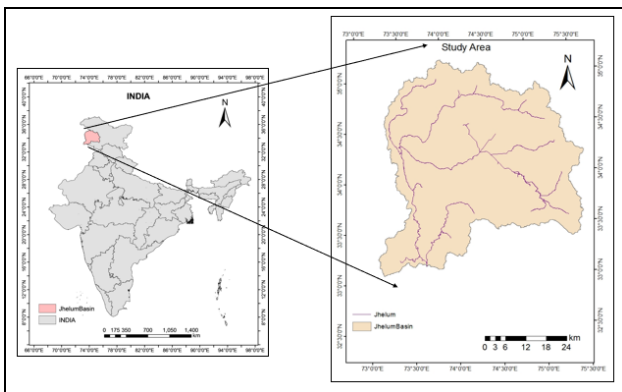


Figure 1 Study Area

2.2 Physiography of the region

The elevation profile and land use Land Cover of the basin is shown in Fig. 2. It is clear from the elevation map that most of the region of the basin lies at high altitude region and hence quite favourable conditions for the snow fall. The land use land cover is also shown below along with all the major classes present in the study area.

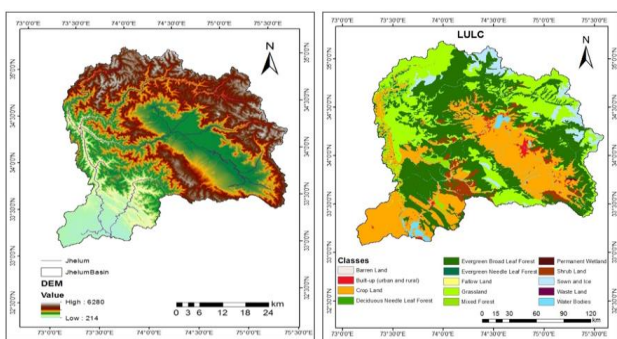


Figure 2 DEM and LULC

2.3 Datasets used in the study

The details of datasets used in the present study are provided in Table1.

Table 1 Datasets Used

A.	Remote Sensing datasets	Resolution	Source /Product
	DEM	30m X 30m	ASTER
	LULC	100m x 100m	ISRO-GBP
	8-Daily Modis Snow Cover	500m X 500m	MOD10A2
B.	Hydro-meteorological datasets	Resolution	
	Era-Interim	0.5° X 0.5°	ECMWF
	CORDEX	0.5° X 0.5°	www.cordex.org
C.	Secondary datasets		
	FAO-HWSD Soil Data	100m x 100m	FAO-HWSD
	Observed Discharge data	Monthly	Irrigation and Flood Control Department, Kashmir
D.	Software and Tools Used		
	ArcGIS, QGIS		
	VIC Tool, Python		
	VIC Model		

3. METHODOLOGY

The methodology adopted in carrying out the study is shown in the Fig. 3.

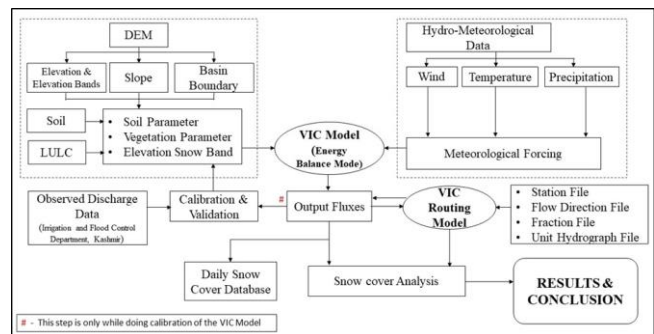


Figure 3 Methodology

3.1 Model Setup

The Variable Infiltration Capacity (VIC) model is setup at 2.5km X 2.5 km grid resolution for the Jhelum basin using the above shown flow chart. ASTER 30m Digital Elevation Model (DEM) is utilised in the basin delineation and in the input parameter file generation. The soil parameter is generated using the FAO-Soil map. The ISRO-GBP Land use Land Cover is utilised in preparation of the vegetation file. The hydrometeorological dataset used for the model simulation is ERA-Interim for present and historic time period and CORDEX for future time period. The ERA-Interim is a reanalysis product and its accuracy is suitable under the North Western Himala region (Sharma et al., 2018). The model is then calibrated and validated using the observed discharge obtained from the Irrigation and Flood control Department, Kashmir.

3.2 Snow Cover Validation

The snow cover fluxes obtained from the model simulation run of the calibrated model is then utilised in the validation of the snow cover area. The snow fluxes is then converted to georeferenced image file using the python scripts (inhouse developed). The daily files are then utilised in the generation of the 8-daily snow cover product. The 8-daily maximum snow cover product of MODIS (MOD10A2) is then used for validation of the simulated snow cover area.

3.3 Snow Cover Analysis

The daily snow cover products are then utilised for the analysis. As the snow cover occurs mainly in the months of December, January and February, the analysis is done for these months over three time period i.e. historic (1979-2000), present (2001-2018) and future (2019-2050). The maximum snow area for the month is calculated for each year and then the inter-comparison is done on the different time period in order to understand the impact of climate change on the river basin and its effect on the maximum snow cover area.

4. RESULTS

4.1 Calibration and Validation

The observed discharge data for Jhelum Basin is available for two stations (Asham and Sangam) for the time period of 2005 to 2013. The observed discharge is plotted against the model discharge and is shown in figures. The Nash-Sutcliffe efficiency and Coefficient of determination (R^2) are calculated for both the calibrated and also for the validated model.

4.1.1 Calibration

The data considered for calibration is of the time period from 2005 to 2009 years. The calibration plot between simulated and observed discharge data is shown in Figure 4 and 5.

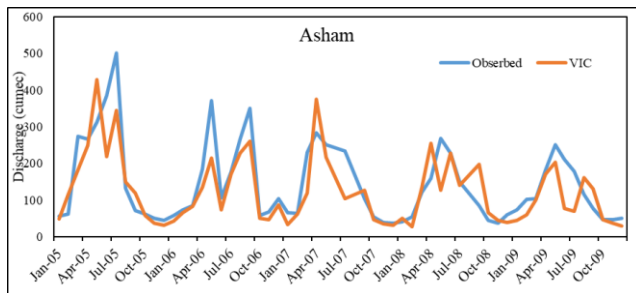


Figure 4 Calibration Plot at Asham outlet

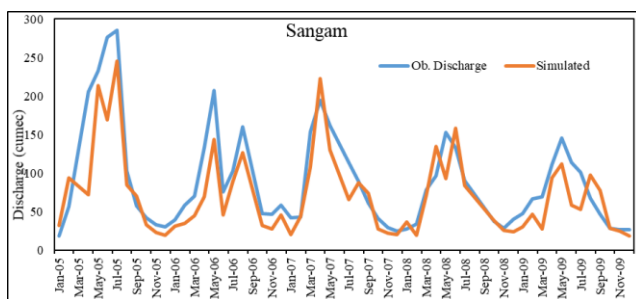


Figure 5 Calibration Plot at Sangam outlet

The scatter plot between the simulated and observed discharge is shown in the Figure 6.

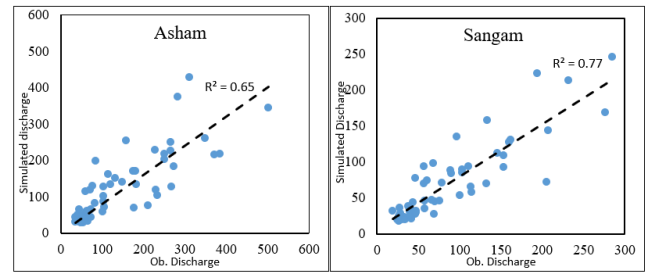


Figure 6 Scatter Plot at Calibration period

4.1.2 Validation

The discharge data is then validated for the time period of 2010 to 2013. The plot of discharge is shown in Figure 7 and 8. The simulated discharge for the validation period follows the same pattern as followed by the observed discharged.

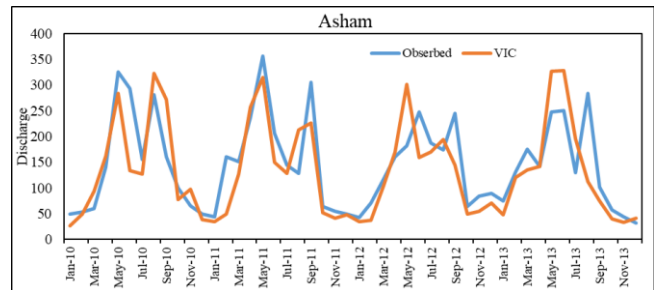


Figure 7 Validation Plot at Asham outlet

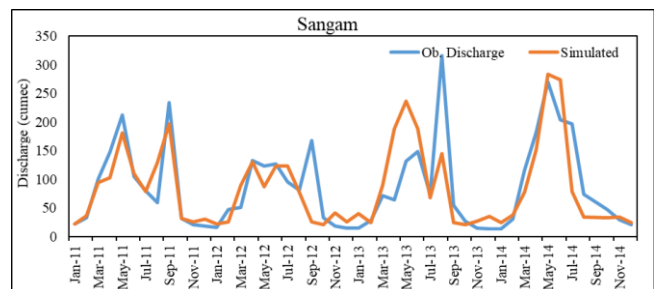


Figure 8 Validation plot at Sangam outlet

The scatter plot are also generated for the validation period at both the outlet and is shown below in the Figure 9.

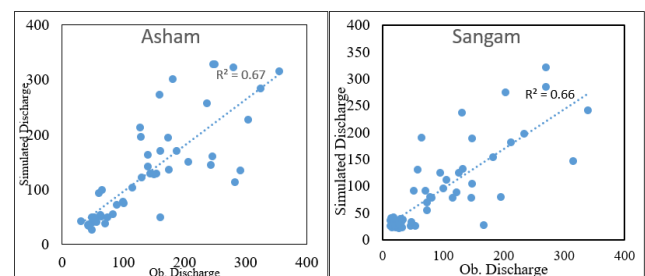


Figure 9 Scatter Plot at Validation Period

4.1.3 Statistical parameters

The Nash-Sutcliffe efficiency and the coefficient of determination (R^2) for the VIC hydrological model at calibration and validation period is shown below in the Table 2.

Table 2 Statistical Parameters

Basin Name	Parameter	Calibration	Validation
Asham	Nash-Sutcliffe efficiency	0.66	0.65
	Coefficient of Determination (R ²)	0.65	0.67
Sangam	Nash-Sutcliffe efficiency	0.70	0.67
	Coefficient of Determination (R ²)	0.77	0.66

4.1.4 References from Websites

4.1.5 References from Research Data: References from research data should be cited like (Dubaya et al., 2017).

4.1.6 References from Software Projects: References to a software project as a high level container including multiple versions of the software should be cited like (GRASS Development Team, 2017).

4.2 Snow Cover Validation

The Jhelum receives a huge amount of snowfall and the snow melt contributes to the runoff in the ablation period when there is very less rainfall. The snow cover area is validated for the accumulation period and early ablation period of snow i.e. from the months of November (initiation of snowfall) till April. The graph shown below shows the validation of 8 - daily snow cover area over the Jhelum basin. The total snow cover area is plotted against the snow cover area derived from the VIC model. The Figure 10 shows that the snow cover area is well calibrated with the observed snow cover area.

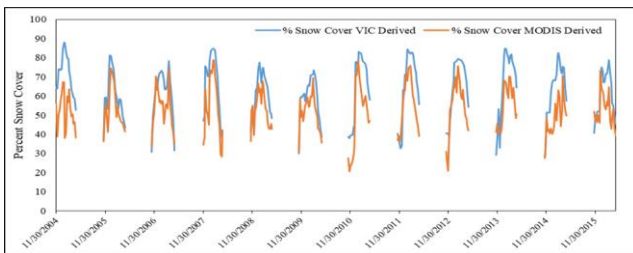


Figure 10 Snow Cover Area of Jhelum basin from VIC simulation and MODIS Snow Cover

The scatter plot is also generated for the given time period and is shown in Figure 11. The coefficient of determination came out to be 0.65.

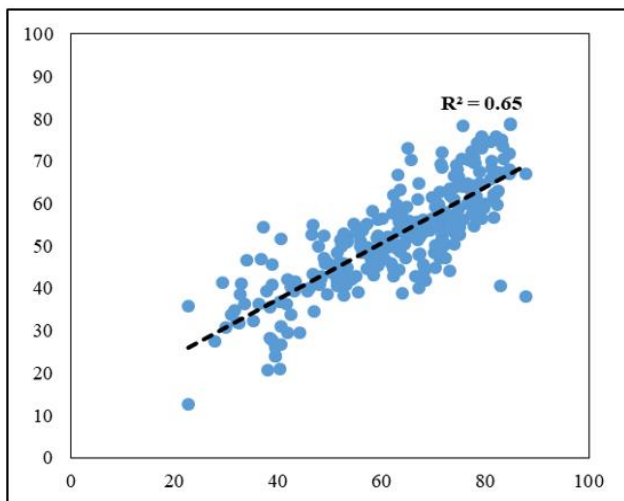


Figure 11 Scatter Plot of Snow area covered under VIC vs MODIS Snow Cover

Moreover, further validation of the simulated snow cover is observed by generating maps of the same date for which MODIS snow cover product is available and is shown in Figure 12, 13, and 14.

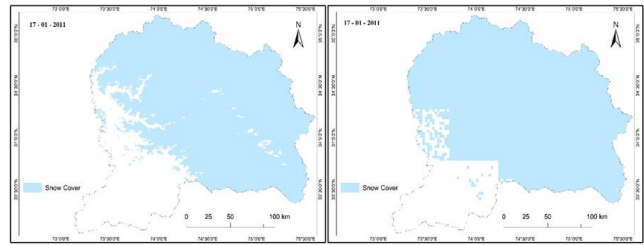


Figure 12 8-Daily maximum Snow Cover Area dated 17-01-2011

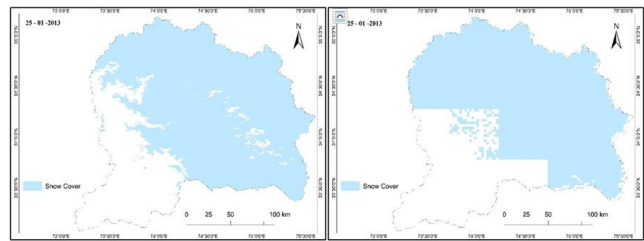


Figure 13 8-Daily maximum Snow Cover Area dated 25-01-2013

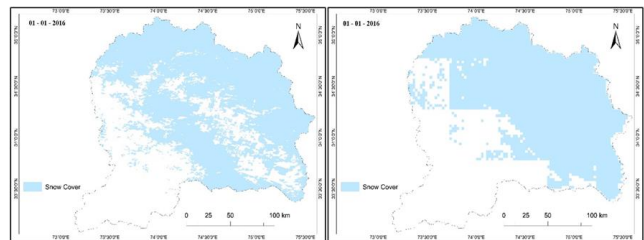


Figure 14 8-Daily maximum Snow Cover Area dated 01-01-2016

4.3 Snow Cover Change Analysis

The snow cover change is observed for the months of December, January and February. The monthly maximum snow cover area is calculated for each year from the products generated for all study time period i.e. historic (1979-99), present (2000-2018) and future (2019-2050).

4.3.1 January

The maximum snow cover area plots for the month of January is shown in the figure 15, 16 and 17. It has been observed that the in the historic time the maximum snow covered area remains almost constant but decrease in area is observed in the present time period and also tremendous decrease is observed in the future time period.

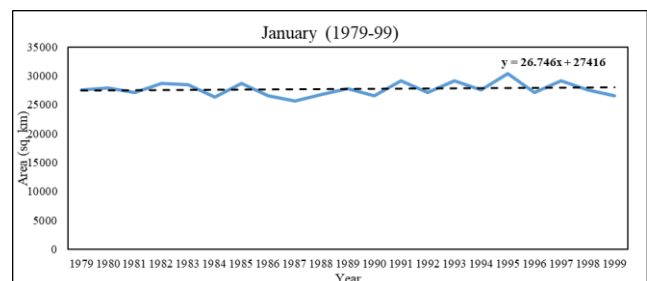


Figure 15 January Snow cover area (maximum) for Historic time period

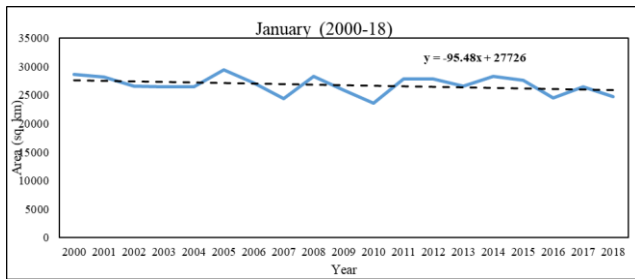


Figure 16 January Snow Cover (maximum) for Present time period

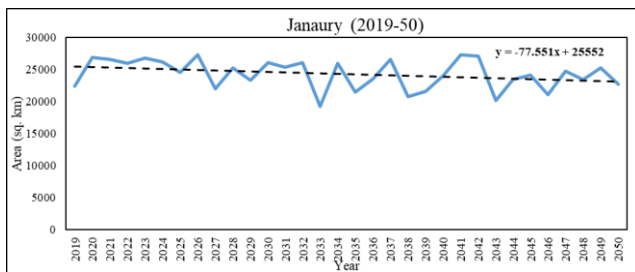


Figure 17 January Snow Cover (maximum) for Future time period

4.3.2 February

The maximum snow cover area plots for the month of February is shown in the Figure 18, 19 and 20. It has been observed that the in the historic time period, the maximum snow cover area shows the decreasing trend. In the present time period it has shown very less decreasing trend. But as observed in the month of January, the maximum snow cover area has shown very high decreasing trend in the future time period.

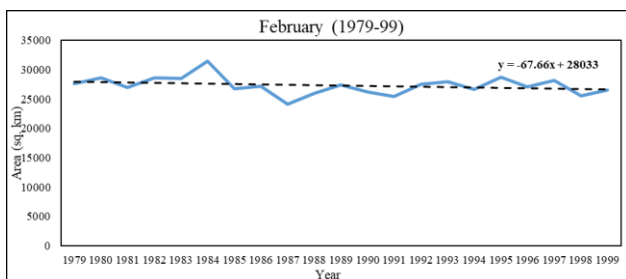


Figure 18 February Snow Cover area (maximum) for the Historic time period

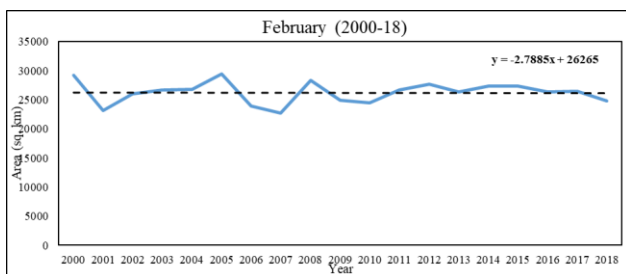


Figure 19 February Snow Cover area (maximum) for the Present time period

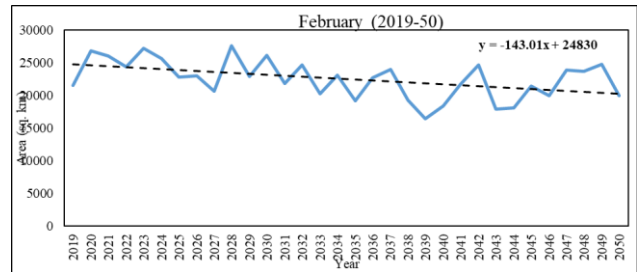


Figure 20 February Snow Cover area (maximum) for the Future time period

4.3.3 December

The maximum snow cover area plots for the month of December is shown in the Figure 21, 22 and 23. It has been observed that the in the historic time period, the maximum snow cover area shows the increasing trend. In the present time period it has shown little increasing trend. But the maximum snow cover area has shown decreasing trend in the future time period.

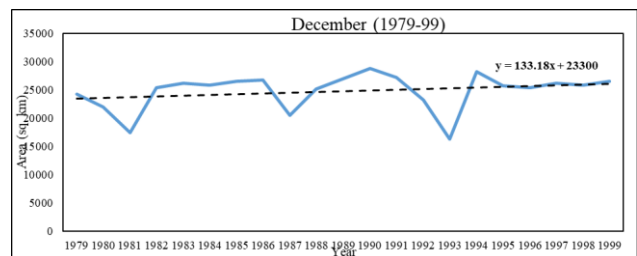


Figure 21 December Snow Cover area (maximum) for the Historic time period

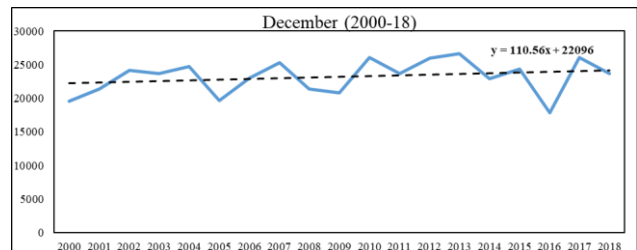


Figure 22 December Snow Cover area (maximum) for the Present time period

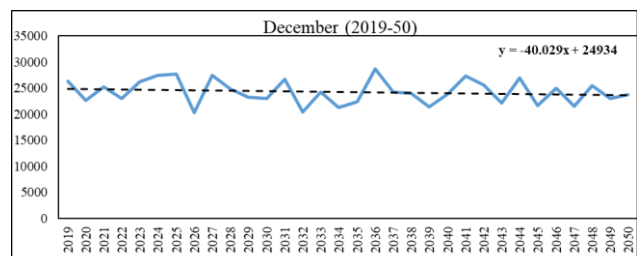


Figure 23 December Snow Cover area (maximum) for the Future time period

4.4 Snow Cover Daily Product

The snow cover for the entire Jhelum basin is generated for the historic (1979-2000), present (2001 – 2018) and future (2019 – 2050). The products generated will be made available to other researchers as per requests and also through web based data dissemination portals of IIRS-ISRO.

5. CONCLUSION

It has been observed that high accuracy in the snow cover can be achieved from the modelling approach. The snow cover area when plotted against the Modis snow cover, it has shown high accuracy. Also the plot generated between the total snow cover area for the snow accumulation period also that the trend follows the same pattern as observed in the MODIS snow cover area. The coefficient of determination (R²) obtained is 0.65. The modelling based daily snow cover area product can further be utilized in understanding the impact of climate change on the region. It has been observed that there is tremendous decrease in the snow cover area for the future time period. The snow cover has also shown increase in the month of December which indicates the shift in the winter climate towards the December month. As the climate is changing the snow line is shifting towards the upper altitude which signals the decreases in the snow cover area as observed from the snow cover product. It is a matter of concern for all the people residing along with the government to cater and plan as per the future changes.

REFERENCES

- Barnett, T. P., Adam, J. C., & Lettenmaier, D. P. (2005). Potential impacts of a warming climate on water availability in snow-dominated regions. *Nature*, 438(7066), 303–309. <https://doi.org/10.1038/nature04141>
- Brown, R D, & Robinson, D. A. (2011). Northern Hemisphere spring snow cover variability and change over 1922–2010 including an assessment of uncertainty. *The Cryosphere*, 5(1), 219–229. <https://doi.org/10.5194/tc-5-219-2011>
- Brown, Ross D, & Robinson, D. A. (2005). *Snow and Snow Cover BT - Encyclopedia of World Climatology* (J. E. Oliver (ed.); pp. 658–663). Springer Netherlands. https://doi.org/10.1007/1-4020-3266-8_187
- IPCC. (2007). *Climate Change 2007: Impacts, Adaptation, and Vulnerability* — IPCC. August. <https://www.ipcc.ch/report/ar4/wg2/>
- Liang, X., Lettenmaier, D. P., Wood, E. F., & Burges, S. J. (1994). A Simple hydrologically Based Model of Land Surface Water and Energy Fluxes for GSMs. *J. Geophys. Res.*, 99(D7), 14415–14428.
- Liang, X. (1994). *A Two-Layer Variable Infiltration Capacity Land Surface Representation for General Circulation Models*.
- Liang, Xu, Lettenmaier, D. P., & Wood, E. F. (1996a). One-dimensional statistical dynamic representation of subgrid spatial variability of precipitation in the two-layer variable infiltration capacity model. *Journal of Geophysical Research: Atmospheres*, 101(D16), 21403–21422. <https://doi.org/10.1029/96JD01448>
- Liang, Xu, Lettenmaier, D. P., Wood, E. F., & Burges, S. J. (1994). A simple hydrologically based model of land surface water and energy fluxes for general circulation models. *Journal of Geophysical Research: Atmospheres*, 99(D7), 14415–14428. <https://doi.org/10.1029/94JD00483>
- Liang, Xu, Wood, E. F., & Lettenmaier, D. P. (1996b). Surface soil moisture parameterization of the VIC-2L model: Evaluation and modification. *Global and Planetary Change*, 13(1–4), 195–206. [https://doi.org/10.1016/0921-8181\(95\)00046-1](https://doi.org/10.1016/0921-8181(95)00046-1)
- Liang, Xu, Wood, E. F., Lettenmaier, D. P., Lohmann, D., Boone, A., Chang, S., Chen, F., Dai, Y., Desborough, C., Dickinson, R. E., Duan, Q., Ek, M., Gusev, Y. M., Habets, F., Irannejad, P., Koster, R., Mitchell, K. E., Nasonova, O. N., Noilhan, J., ... Zeng, Q. (1998). The Project for Intercomparison of Land-surface Parameterization Schemes (PILPS) phase 2(c) Red-Arkansas River basin experiment.: 2. Spatial and temporal analysis of energy fluxes. *Global and Planetary Change*, 19(1), 137–159. [https://doi.org/https://doi.org/10.1016/S0921-8181\(98\)00045-9](https://doi.org/https://doi.org/10.1016/S0921-8181(98)00045-9)
- Liang, Xu, & Xie, Z. (2001). A new surface runoff parameterization with subgrid-scale soil heterogeneity for land surface models. *Advances in Water Resources*, 24(9), 1173–1193. [https://doi.org/https://doi.org/10.1016/S0309-1708\(01\)00032-X](https://doi.org/https://doi.org/10.1016/S0309-1708(01)00032-X)
- Lidén, R., & Harlin, J. (2000). Analysis of conceptual rainfall–runoff modelling performance in different climates. *Journal of Hydrology*, 238(3), 231–247. [https://doi.org/https://doi.org/10.1016/S0022-1694\(00\)00330-9](https://doi.org/https://doi.org/10.1016/S0022-1694(00)00330-9)
- Mahmood, R., Babel, M. S., & JIA, S. (2015). Assessment of temporal and spatial changes of future climate in the Jhelum river basin, Pakistan and India. *Weather and Climate Extremes*, 10, 40–55. <https://doi.org/https://doi.org/10.1016/j.wace.2015.07.002>
- Nikam, B. R., Garg, V., Gupta, P., Thakur, P. K., Kumar, A. S., Chouksey, A., Aggarwal, S., Dhote, P. R., & Purohit, S. (2017). *Satellite-Based Mapping and Monitoring of Heavy Snowfall in North Western Himalaya and its Hydrologic Consequences*.
- Rathore, B. P., Singh, S. K., Jani, P., Bahuguna, I. M., Brahmabhatt, R., Rajawat, A. S., Randhawa, S. S., & Vyas, A. (2018). Monitoring of Snow Cover Variability in Chenab Basin Using IRS AWiFS Sensor. *Journal of the Indian Society of Remote Sensing*, 46(9), 1497–1506. <https://doi.org/10.1007/s12524-018-0797-8>
- Sharma, V., Pandey, K., Thakur, P. K., Aggarwal, S. P., Nikam, B. R., Dhasmana, M. K., Shrivastava, V., & Singh, S. (2018). Seasonal Comparison of Era-Interim Precipitation Dataset for Entire Indian Region. *ISPRS - International Archives of the Photogrammetry, Remote Sensing and Spatial Information Sciences*, XLII(November), 20–23. <https://doi.org/10.5194/isprs-archives-XLII-5-567-2018>

IMPACT ASSESSMENT OF METEOROLOGICAL DROUGHT ON AGRICULTURAL PARAMETERS USING GOOGLE EARTH ENGINE: A CASE STUDY ON PENNA RIVER BASIN

Arunav Nanda^{1*}, Bhaskar R. Nikam², S. P. Aggarwal³

¹Water Resource Department, Indian Institute of Remote Sensing, Dehradun

²Scientist-SF, Water Resource Department, Indian Institute of Remote Sensing, Dehradun

³Group Head, Water Resource Department, Indian Institute of Remote Sensing, Dehradun

*corresponding author – arunavnanda7@gmail.com

KEY WORDS: Google Earth Engine, NDVI, Anomaly, GIS, Remote Sensing

ABSTRACT:

Understanding precipitation-vegetation interaction is of great importance to implementing adaptation and mitigation measures for terrestrial ecosystems. Many studies have explored the spatial pattern of precipitation-vegetation correlation along the precipitation amount gradient. While the impacts of other precipitation characteristics remain poorly understood. Here, we provided a comprehensive investigation of spatiotemporal patterns of vegetation response to precipitation anomalies in Penna river basin, using satellite-derived vegetation index and multi-source climate datasets. Vegetation productivity is directly influenced by weather characteristics such as precipitation and temperature. The response is not basically immediate but with a time lag period between the weather anomaly and the vegetative response. This study basically focuses on the response of the vegetation to the precipitation and soil moisture anomaly. The procedure basically consisted of comparing several timescales of NDVI (Normalised Differential Vegetation Index) and soil moisture with respect to precipitation. It was found that the correlation of soil moisture with respect to NDVI improved with 1- month lag.

1. INTRODUCTION

Sustained increase in Earth's temperature driven by anthropogenic emissions of greenhouse gases is projected to alter patterns of global atmospheric circulation and hydrologic regimes. The intensity of precipitation events and the frequency of extreme events have already increased across the globe and are expected to further increase. These various kinds of climate fluctuations have triggered ongoing changes of terrestrial ecosystems, with implications for both the ecosystem structure and function.

Vegetation, playing a significant role in the exchange of energy, water and carbon between

the land surface and atmosphere, is the main component of the terrestrial ecosystem. Substantial evidences suggest that the distribution, structure, composition, and diversity of vegetation populations and communities have been gravely impacted by global climate change. Growing scientific and public concerns about the dramatic changes in vegetation cover resulting from climate change have thus incited a focus of researchers on the assessment of vegetation response to changes in air temperature, precipitation, solar radiation, and sea surface temperature (SST). Among aforementioned climatic variables involving in vegetation-atmosphere interactions, precipitation variability is extraordinarily responsible for vegetation change due to the

dominant role that precipitation plays in water availability which has been generally considered as the principal factor controlling ecosystem structure/dynamics and driving biological processes in over 40% of Earth's vegetated surfaces. In general, altered precipitation patterns have critical effects on vegetation communities, especially in terms of vegetation growth and development, although effects vary among different ecosystems and species.

With the development of satellite observation technology since the 20th century, remotely sensed vegetation indices (VIs) from satellite data have been widely recognized as the effective approach to characterize vegetation dynamics at a larger spatiotemporal scale. There has been a general consensus among scholars that vegetation response to precipitation

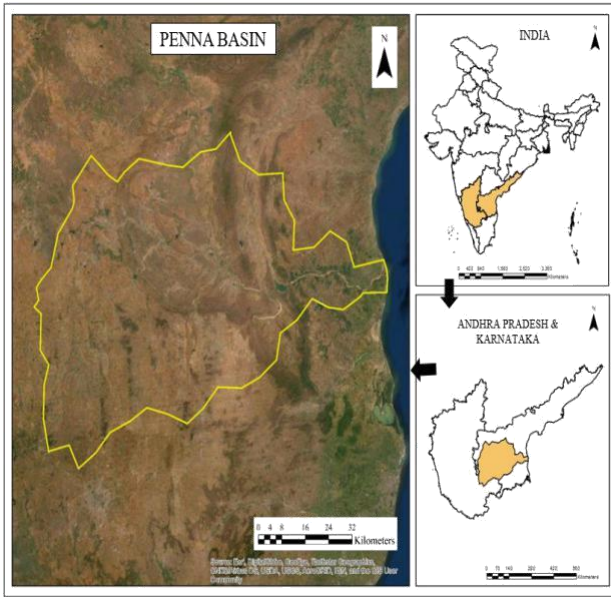
variability exhibits tremendous spatial heterogeneity. Considerable efforts have therefore focused on the interpretations for this phenomenon. The dynamic response of terrestrial vegetation to precipitation perturbations over an area depends on a variety of topographic attributes such as elevation, slope and aspect[1]. It was also found that the great spatial variability of relationship between vegetation growth and precipitation can be attributed to distinct vegetation types[2]. The correlations between NDVI and precipitation fluctuations at the inter-annual time scale in eastern and southern African savannah, and discovered that mean annual precipitation (MAP) plays an active role in determining spatial distributions of vegetation sensitivity to altered precipitation regimes[3]. Recently, in order to more comprehensively analyse the spatial pattern formation of vegetation response to precipitation variability, several studies tried to simultaneously consider the impacts of multiple external factors. The response of NDVI to precipitation variations in tropical Africa and detected that the spatially heterogeneous response of vegetation to precipitation is closely associated with MAP, vegetation type and soil properties[4]. The precipitation-vegetation relationship over East Africa based on an environmental effect model and demonstrated that vegetation sensitivity to

precipitation variability is mainly controlled by MAP, vegetation type and elevation[5].

2. STUDY AREA AND DATASETS USED

2.1 Study Area

The chosen study area for this study is the Penna river basin. The Penna River basin covers an area about 55,213km² and lies in between 10⁰ and 16⁰ North latitude and 77⁰ and 81⁰ East longitude. The river originates in northern part of Karnataka state in Nandi hills and passes through the Anantapuram, Kadapah, Chittor, Kurnool, Prakasam, Nellore and some talukas of Karnataka state and empties into Bay of Bengal, 30km NE of Nellore after passing through the Penna delta of Nellore district. The average annual rainfall of the Penna basin is 732.11mm. The average minimum temperature is about 18⁰C and the average maximum temperature is about 42⁰C. The basin enjoys semiarid, dry sub-humid and wet sub-humid types of climate. Most of the rainfall is provided by the moisture-bearing southwest monsoon, which provides rain to most of India between June and September. The Penna basin lies in the rain shadow of the high Western Ghats ranges, which prevents much moisture from reaching the region. Post-monsoon cyclonic storms in the coastal region produce additional rain during September and October. The winter northeast monsoon, which provides rain between December and March, provides little rain to the upper basin and slightly more to the lower basin.



2.2 Datasets used

2.2.1 Precipitation

The precipitation data used for this study is the TRMM 3B43 data which provides 3 hourly daily rainfall data by merging microwave data from multiple satellites, including SSMI, SSMIS, MHS, AMSU-B and AMSR-E, each inter-calibrated to the TRMM Combined Instrument. The monthly composite rainfall was computed for each month. All of the global precipitation datasets have some calibrating data source, which is necessary to control bias differences between contributing satellites. The multi-satellite data are averaged to the monthly scale and combined with the Global Precipitation Climatology Centre's (GPCC) monthly surface precipitation gauge analysis.

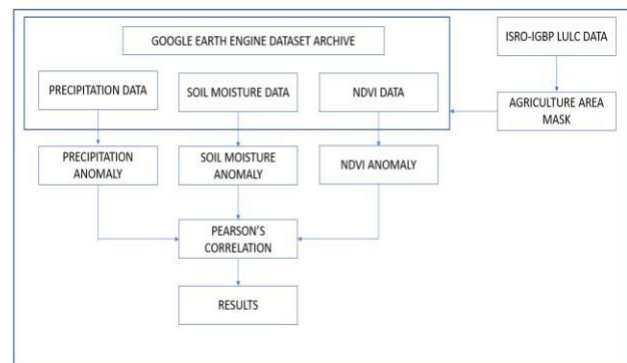
2.2.2 Normalized Difference Vegetation Index (NDVI)

The Normalized Difference Vegetation Index is generated from the Near-IR and Red bands of each scene and ranges in value from -1.0 to 1.0. This product is generated from the MODIS/006/MOD09GA surface reflectance composites.

2.2.3 Soil Moisture

The NASA-USDA Global soil moisture and the NASA-USDA SMAP Global soil moisture datasets provide soil moisture information across the globe. This dataset is generated by integrating satellite-derived Soil Moisture Ocean Salinity (SMOS) Level 2 soil moisture observations into the modified two-layer Palmer model using a 1-D Ensemble Kalman Filter (EnKF) data assimilation approach. The assimilation of the SMOS soil moisture observations helped improve the model-based soil moisture predictions.

3. METHODOLOGY



For this study, the above datasets were collected for the study period i.e., (2010-2018) from Google Earth Engine data repository. The datasets which were in different units and scales were converted to the same scale by applying correction factors. The ISRO-IGBP Land use land cover map was used to create a mask which only contained the cropping areas in the study area. This mask was applied on the datasets to extract the cropping areas. Then the above datasets were converted to monthly mean scale and the anomaly was computed for each parameter. The anomaly is basically calculated by:

$$AP_i = P_i - P_{(avr)i}$$

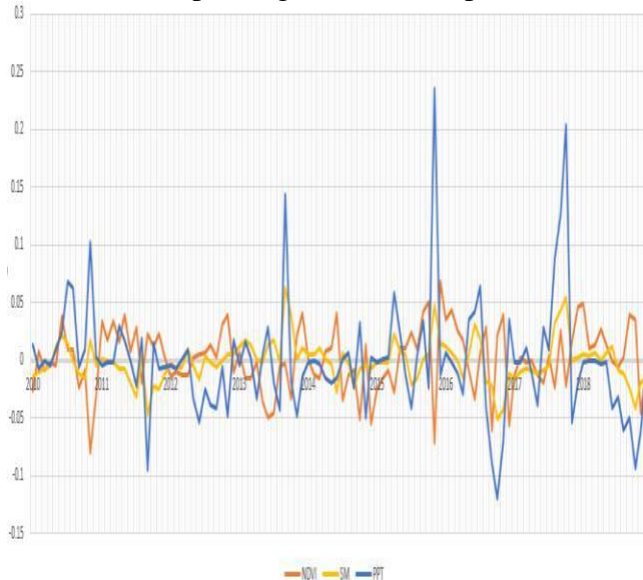
where AP_i is the anomaly in the day or month i , P_i is the value of a parameter of the day, or month i , and $P_{(avr)i}$ is the average of the entire data set.

After computation of anomaly for each month, a 1-month time lag was applied over the entire

dataset and the values of each parameter were computed. Then, these values were correlated with respect to each other and the results were computed.

4. RESULTS AND DISCUSSIONS

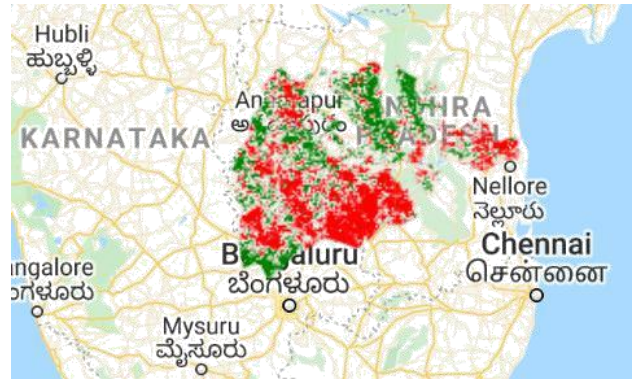
The anomalies were computed from the study time period and the following graph was obtained after plotting the different parameters.



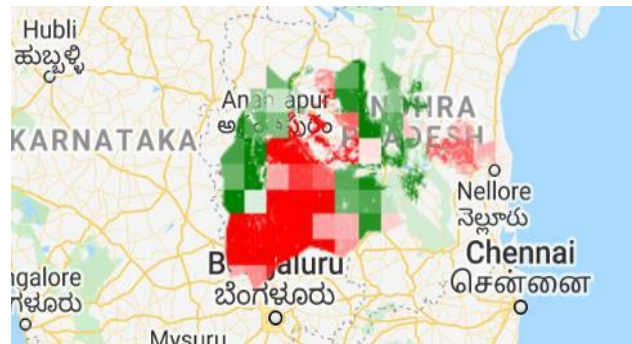
The Pearson correlation coefficient were computed by comparing different parameters and the following table was obtained:

Parameters	Correlation
SM vs NDVI	-0.2263
SM_lag vs NDVI	0.1607
Ppt vs SM	0.7334
Ppt vs SM_lag	0.3792

It can be seen that the correlation between soil moisture and NDVI is low when considered for the same month. But when a lag of 1 month is applied over the soil moisture, then the correlation suddenly improved. Similarly, in case of correlation between precipitation and soil moisture, it was high when considered for the same month, while it deteriorated when a lag of 1 month is applied.



NDVI vs Soil Moisture Anomaly



Precipitation vs Soil Moisture Anomaly

In the above figures, the Pearson correlation maps for the study area are shown. These were computed by the help of Google Earth Engine API. These outcomes clearly point to the fact that the red pixels denote negative correlation while green pixels denote positive correlation. The areas which have negative correlation are basically the rainfed cropping area while the positive correlation area are irrigated areas.

Thus, by the help of geospatial technology, one can be able to access the vegetation health and type along with the impact of various parameters on it.

5. REFERENCES

[1] A. B. White, P. Kumar, and D. Tchong, "A data mining approach for understanding topographic control on climate-induced inter-annual vegetation variability over the United States," *Remote Sens. Environ.*, vol. 98, no. 1, pp. 1–20, Sep. 2005.

- [2] P. A. Propastin, M. Kappas, and N. R. Muratova, "Inter-annual changes in vegetation activities and their relationship to temperature and precipitation in Central Asia from 1982 to 2003," *J. Environ. Informatics*, vol. 12, no. 2, pp. 75–87, Dec. 2008.
- [3] S. Chamaillé-Jammes and H. Fritz, "Precipitation–NDVI relationships in eastern and southern African savannas vary along a precipitation gradient," *Int. J. Remote Sens.*, vol. 30, no. 13, pp. 3409–3422, Jul. 2009.
- [4] P. Camberlin, N. Martiny, N. Philippon, and Y. Richard, "Determinants of the interannual relationships between remote sensed photosynthetic activity and rainfall in tropical Africa," *Remote Sens. Environ.*, vol. 106, no. 2, pp. 199–216, Jan. 2007.
- [5] P. Hawinkel *et al.*, "Vegetation response to precipitation variability in East Africa controlled by biogeographical factors," *J. Geophys. Res. Biogeosciences*, vol. 121, no. 9, pp. 2422–2444, Sep. 2016.

DELINEATION OF GROUNDWATER POTENTIAL ZONE USING RS AND GIS, IN DEVANAHALLI TALUK, KARNATAKA

Sanath Kumar K. R and Sharanya Ram S. R*

*Department of Civil Engineering, Nagarjuna College of Engineering & Technology Mudugurki Village, Venkatagirikote Post, Devanahalli taluk, Bangalore district - 562164 Karnataka. - sanathkumar18@gmail.com
sharanyaram108@gmail.com

KEY WORDS: Aquifer, Water, Drought Management, Gneiss terrain.

ABSTRACT:

Groundwater is the major source of water in the Bengaluru Rural as the city progresses due to the developmental activities the demand for water is also increasing. Groundwater is a portable form of water that can be used without treatment for domestic purposes. Identification of aquifer is a complicated task that can be executed by integrating various thematic maps such as drainage map, geomorphology map, slope map, aspect map, land-use/land cover map and validated with in-situ Borehole data by using Remote sensing and GIS. The Satellite imagery IRS-LISS-III is used for map water bodies. The data are having the 23 m spatial resolution, a swath width of 142 km, temporal resolution one year and spectral resolution of 3 bands from 0.52 to 0.86 μ m are used to prepare thematic maps. Devanahalli taluk is a severely drought-affected area in the recent past with hard Gneissose terrain which again does not hold good for the groundwater. Lineaments are another geological structure that can yield a good quantity of water.

Terrain belongs to the hard rock runoff is more and infiltration is very less. Northern part of the terrain has very little groundwater as it contains the high slope and hilly terrain. Southern part of the study area is having good potential zones of groundwater as it has more tanks and 7th order drainages. Slope and aspect of the area reveals that the southern part of the study area has a gentle slope. East and West part of the study area have moderate groundwater potential zones, as they have moderate slopes.

1. INTRODUCTION

Remote sensing and GIS are useful tools to map the potential groundwater zones as it is quick and reliable with less cost and manpower than conventional techniques (M. Sedhuraman et al. (2014)). To meet the demands of the Industrial and domestic water requirements, surface water is insufficient to fulfill the demand. Hence, there is a need for groundwater exploration. The water stored underneath the earth's surface in aquifers is referred to as groundwater (Govindaiah.S et.al (2017)). Identification of the groundwater is not an easy task, and at the same time, it's very difficult as the Aquifers provide small hints for its presence. When the terrain belongs to hard rock and the aquifer is at greater depth, then it cannot be confirmed by Groundwater potential zone mapping with the surface layers only, for this reason, borehole depth plays a key role in the aquifer identification. Many times, in the shallow aquifers are identified by the clusters of Vegetations. In addition, quantitative morphometric parameters of the drainage basin also play a major role in evaluating the hydrological parameters, which in turn helps to understand the groundwater situation (Krishnamurthy and Srinivas1995). Along with Morphometric parameters lineaments the large-scale linear features which are surficial expressions of underlying geological structural features like faults or joints also act as a source of groundwater in hard rock terrain (Chandra. S et al. (2006), Mondal. N. C. et.al (2008)). The high run-off controls the groundwater resources potentiality as it depends on the lithological characteristics of the terrain (Ghosh.P et al. (2015)). Terrain characteristics like weathering grade, fracture

extent, permeability, slope, drainage pattern, landforms, land use/land cover and climate which has potential command over the Groundwater storage (M. Sedhuraman et al. (2014), (Chandra.S et al. (2006), Govindaiah.S et.al (2017)). Groundwater storage begins with rainfall that infiltrates into the ground. The quantity of water that infiltrates into the ground varies according to the type of land surface cover and Infiltration into the ground is also strongly influenced by the season of the year (Dilip Kumar and Premendra Dev (2014)). However, it is important to note that the degree of influence of factors on groundwater occurrence varies and this may depend on space and time (Mallick. J et al. (2014)).

The conventional methods of exploration such as field-based hydrogeological and geophysical resistivity investigations do not always take into account the diverse factors that control the occurrence and movement of groundwater (Jaiswal R. et al. (2003)). Systematic integrated synoptic view approach is a necessary requirement in the field of Groundwater exploration. Delineation of groundwater potential zones by the integration/overlaying of thematic maps by weighted overlay method from the satellite data that is useful to identify the depth of unconfined aquifers and confined aquifers to semi-confined aquifers. (A. S. Jasrotia et al. (2013), Ghosh.P et al. (2015)), (Kesana Sai Teja and Dinesh Singh (2019)). Meteorological parameters like precipitation also have a major role in Groundwater recharge, Water in the basin arrives in the form of precipitation as part of the hydrologic cycle (Dilip Kumar and Premendra Dev (2014)). Groundwater potential

* Sanath Kumar K. R and Sharanya Ram S. R

zones in skewed rainfall distribution area are identified by climatological aspects and multi thematic layer approach by Weighted index overlay analysis method (Gumma M. K and Pavelic.P (2012)). Rough sets were coupled with Lineaments data and Modified DRASTIC models with an information-analytic technique are used to understand the aquifer vulnerability characteristics in the GIS environment (Khan. A et.al (2014)). Analytic Hierarchy Process and multi-criteria decision making (MCDM) techniques are also useful for Groundwater identification in semi-arid and hard terrain (Machiwal.D et. al., (2011)). The geomorphology and hydrogeological effects of the basin and the Multi-Criteria techniques are used for the analysis of groundwater potential zones (Dilip Kumar and Pramendra Dev (2014), Ghosh.P et al. and Machiwal.D et al. (2011)).

GIS have the capability to handle the larger remote sensing data sets, provide the facilities for the analysis of larger data sets and ground truth check is helpful for the further validation of results (Govindaiah.S et.al (2017)). Generating various thematic maps through remotely sensed data and their Analysis through GIS have proved that many thematic layers have direct or indirect control over groundwater occurrence (Jaiswal R. et al. (2003)). Applications of Remote Sensing and GIS for the exploration of groundwater potential zones are carried out by a number of researchers around the world but prospective groundwater zones are poorly defined in the hard rock terrain (Ghosh.P et. al. (2015)). The integrated approach of subsurface studies show magnet, SP and resistivity method reveals that lineaments are major groundwater resources in hard rock terrains Chandra.S et.al (2006) along with-it valley fill, valley flat alluvial plain are the target area for groundwater Preeja K. R. et. al., (2011). The borehole data are used for cross-validation Gumma M et.al., (2012).

Groundwater is the major source for domestic and household needs in the semi-arid regions of Rural India. (Chandra.S et al. (2006)). Development in various fields such as agriculture, industry, and urbanization in different countries, particularly in India. This has led to an increase in the demand for water supply mostly from the exploration of groundwater resources (Dilip Kumar and Premendra Dev (2014)). The proper management of both surface and groundwater resources through systematic inventory, conservation, and proper planning is essential for the economic and social development of any country (Jaiswal R. et al. (2003)). Due to depletion and uneven distribution of rainfall, nonexistence of adequate surface water, lack of water management techniques and the speedy progressive activities of society growth finally lead to the over exploitation of groundwater resources (Govindaiah.S et.al (2017)). In drought-prone areas micro- watershed-based development strategy may be considered as a best practice for integrated development, as the basic principle of watershed management is to conserve and develop water resources for land resource development (Ghosh.P et al. (2015)).

2. STUDY AREA

Aquifer zone identification and subsurface mapping are done in Devanahalli taluk, Bangalore Rural district, Karnataka. It is covering an area of 450 sq. km. Devanahalli taluk is located between north latitude 13.0 06'44.0" and 13.0 21'53.7" & East longitude 77.0 33'26.7" and 77.0 50'04.4". Devanahalli taluk is bounded by Chikballapur district on the North, Bangalore

Urban district on the south, Hoskote taluk on east and Doddaballapur taluk on the western side. Location map of Devanahalli taluk of Bangalore Rural district is presented in fig. 1.

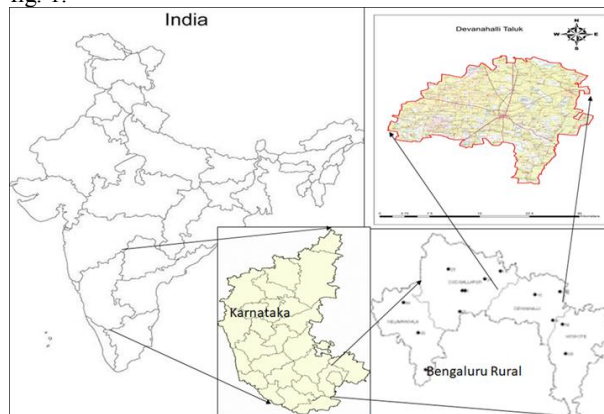


Figure 1. Devanahalli Taluk Map.

The area falls under the Eastern dry agro-climatic zone of Karnataka state and is categorized as drought-prone. The normal annual rainfall in Devanahalli taluk for the period 1981 to 2010 is 804 mm. Seasonal rainfall pattern indicates that a major amount of (447 mm) rainfall was recorded during South-West Monsoon seasons, which contributes about 56% of the annual normal rainfall, followed by North-East Monsoon season (216 mm) constituting 27% and remaining (140 mm) 17% in Pre-Monsoon season.

Geomorphologically, the taluk area is covered with uplands on Gneisses and Granites, which are ideal for agriculture. Physiography of the entire area is in the southern median region, characterized by an undulating landscape with broad valleys, where the elevation ranges from 700 to 1338 m above MSL with a good degree of slope. The eastern part of the taluk is covered by prominent hill ranges which are the continuation of Nandidurga hill ranges running almost North-South direction and is the provenance for the sediment and drainage of Pennar. The remaining portion is having rolling topography undulating and gently sloping lands and valleys.

In Devanahalli taluk, there are no perennial rivers. There are a few streams that rise in the hills and feed the number of tanks. The drainage pattern of the area can be described as drainage pattern which is dendritic to sub-dendritic (S. Srinivasa Vittala et al. (2008)). The drainage patterns are described as sub-rectangular due to the marked influence of geologic structures and more or less similar lithological characteristics.

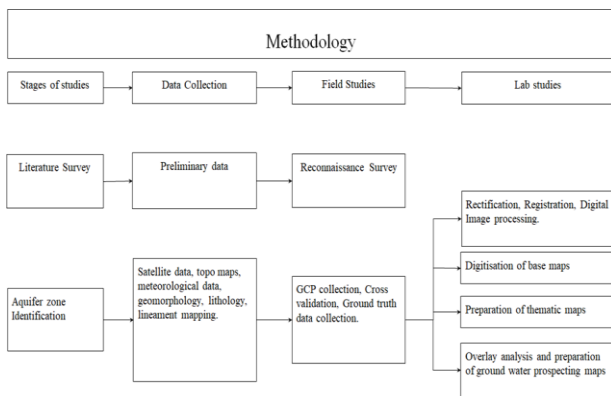
Devanahalli taluk is covered by four classes of soils that are clayey, clayey mixed, loamy skeletal and rocky land. The soil at the surface in this area are medium to coarse-grained texture, sub-surface soils are deep and heavily textured (S. Srinivasa Vittala et al. (2008)).

Geologically, the rocks in the study area belong to the Dharwar Supergroup of Archean Era. They are mainly composed of granite and granitic gneisses that are exposed in small hillocks. Devanahalli is a Gneissose terrain that contains confined aquifers. The hydrogeological parameter is essential to investigate the availability of potable water from aquifer Gail P et. al. (2011).

3. MATERIALS AND METHOD

1. Satellite data from IRS LISS-III are collected from the Bhuvan portal.
2. Topo Maps that are collected from the Survey of India are scanned and rectified using ArcGIS.
3. The geomorphology map is prepared using the toposheets.
4. Lineament mapping is prepared using the pre-existing map of the study area from NRSC website.
5. Digital image processing is carried out for the satellite data from LISS-III to get LU/LC maps in ERDAS Imagine.
6. Digitization is carried out in order to get required thematic maps using base maps collected from various sources.
7. Lu/Lc, Drainage, Lineament, Digital Elevation Model, Geomorphology, and Borehole depth data are used as raster data to carry out weighted overlay analysis to explore the potential zones of groundwater.

Table 1. Flowchart showing Methodology



4. RESULT AND DISCUSSION

4.1 Drainage

In this area 1st order to 7th order drainages are present and which have major influence on the infiltration and runoff. Total length of the drainages is 1206887.77 m and total number of different order of drainages are 3376.

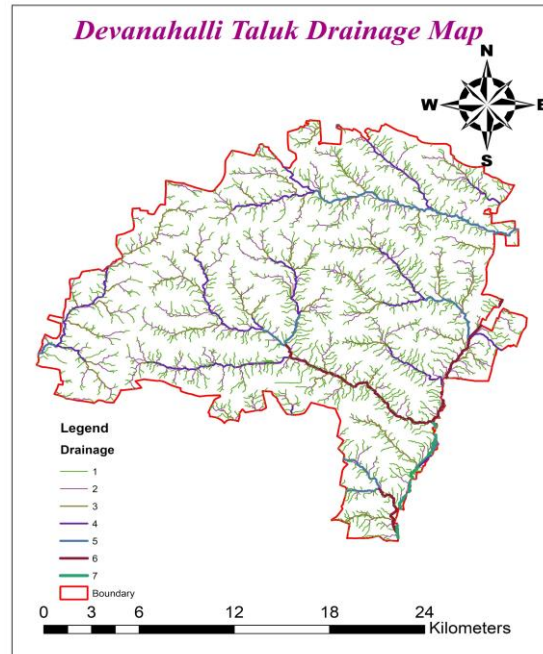


Figure 2. Drainage Map of Devanahalli Taluk.

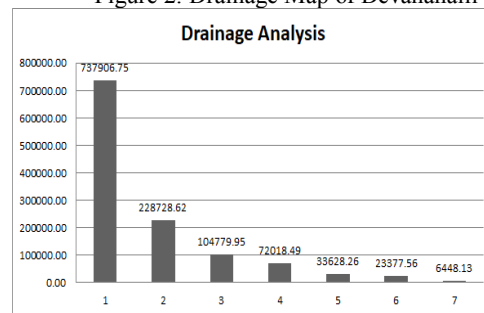


Figure 3. Showing the Drainage Analysis graph of Devanahalli Taluk

4.2 Lineament

Devanahalli taluk has 126 lineaments and a total length of 9906 m distributed throughout the taluk. Most of them are minor lineaments in their shape and size and have good quantities of water bearing capacity.

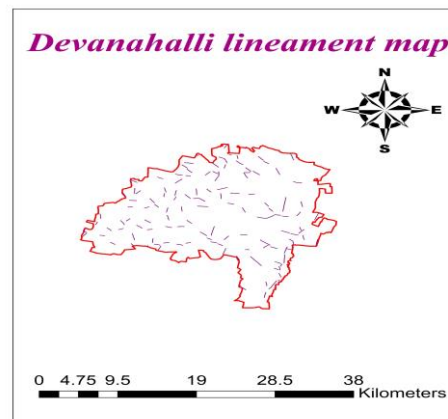


Figure 4. Lineament Map of Devanahalli Taluk

4.3 Digital Elevation Model

Digital Elevation Model shows that area have minimum elevation of 764m, maximum of 1004m and elevation difference in the area is 240m. Northern side of the study area is covered with the hills, have maximum elevation and have gently sloping elevation in east, west and southern part of the study area.

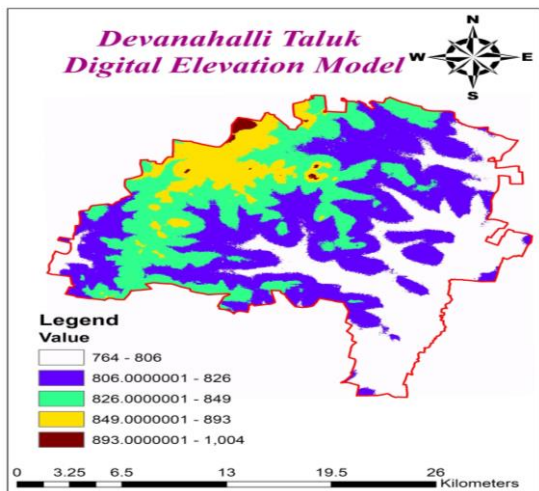


Figure 5. DEM Map of Devanahalli Taluk

4.4 Land Use/Land Cover

Lu/lc are classified into 10 classes most of the area is utilised for human settlement and to a certain extent is covered with surface tanks which holds most of the water in the taluk.

Table 2. Showing Land use/ Land cover classes and their areas

Sl.No	Classes	Area
1	Road	34323455.77
2	Vegetation	58983670.42
3	Dry Vegetation	51197679.91
4	Patterned Vegetation	47954735.47
5	Thin Vegetation	18994190.45
6	Residential Area	66853867.84
7	Dry Land	53362844.97
8	Thick Vegetation	14115683.62
9	Uncultivated Land	75104928.37
10	Built Up Area	27431441.49

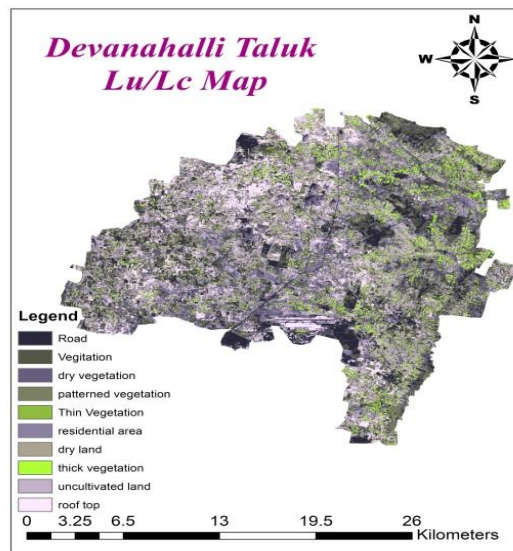


Figure 6. Lineament Map of Devanahalli Taluk

4.5 Geomorphology

Table 3. Showing Geomorphological Units and their areas

Sl. No.	Geomorphological Units	Area
1	Antropic Terrain	2836244.94
2	Antropic Origin	644667.61
3	Denudation Hills	2839880.00
4	Denudation Pedi plain	446542000.00
5	Water Body	22017083.71

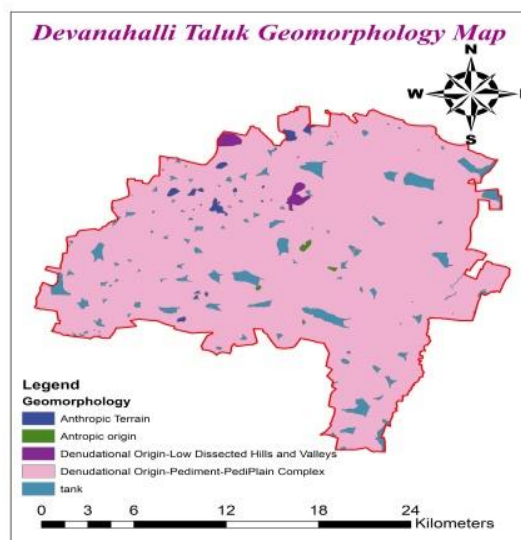


Figure 7. Geomorphology Map of Devanahalli Taluk

4.6 Overlay Analysis

Overlay analysis is carried out with the weighted overlay method classified with 4 classes Excellent, Good, Moderate and Poor.

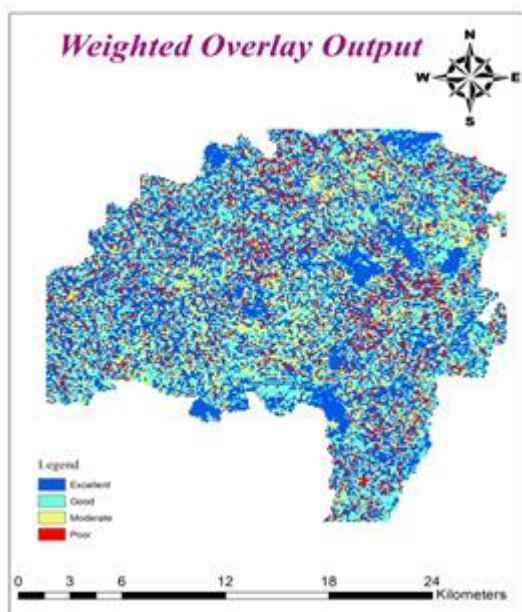


Figure 8. Overlay Analysis Output Map of Devanahalli Taluk

5. CONCLUSIONS

Overlay analysis draws the conclusion as follows:

Maximum areas which can hold a Moderate quantity of water and floodplain areas are the good potential zones of GW. Terrain belongs to the hard rock runoff is more and infiltration is very less hence tanks constructed across the stream to store the water. Northern part of the terrain has very little groundwater as it contains the high slope and hilly terrain. Southern part of Devanahalli Taluk is having good potential zones of groundwater as it has more tanks and 7th order drainages. Slope and aspect of the area reveals that the southern part of Devanahalli Taluk has a gentle slope compared with the northern part of the study area. The East and West part of Devanahalli Taluk have moderate groundwater potential zones, as they have moderate slopes. International airport is located at the southern part of the study area which needs more quantity of water. Rainwater harvesting is the only solution to recharge the aquifer, presently which is getting depleted due to the overexploitation of groundwater. Output is validated with the Borewell depth data which reveals that, borewell depth in few cases mainly depends on the Lineament and apart from this water is available at the Greater Depth around 1200ft. From the meteorological data it reveals that the source of Groundwater in Rainfall if failure in the seasonal rainfall hits directly the storage of GW intern results in the draught. Decrease in the water levels of the tanks are due to the highest evaporation rate in the study area in the peak summer.

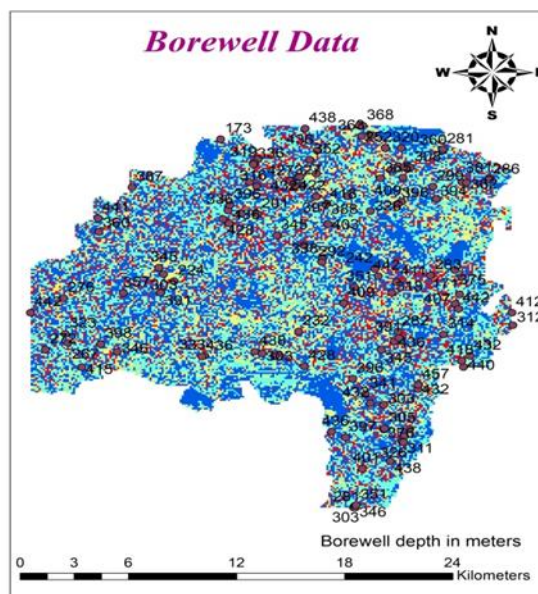


Figure 9. Bore well data overlaid on the groundwater potential zone image

6. ACKNOWLEDGEMENTS (OPTIONAL)

We would like to Acknowledge NRSC and Bhuvan ISRO for Providing LISS-III and DEM images to Carry Out this work. We would like to thank the Survey of India for Providing Toposheets required for the present study. We would also like to Thank USGS for Providing LANDSAT images. We would like to express our gratitude to NCET for giving the opportunity to pursue our Education and for continuous encouragement.

7. REFERENCES

1. A.S.Jasrotia, A., Bhagat, B., Kumar, A. and Kumar, R. (2012). Remote Sensing and GIS Approach for Delineation of Groundwater Potential and Groundwater Quality Zones of Western Doon Valley, Uttarakhand, India. *Journal of the Indian Society of Remote Sensing*, 41(2), pp.365-377.
2. Carter, G., Miskewitz, R., Isukapalli, S., Mun, Y., Vyas, V., Yoon, S., Georgeopoulos, P. and Uchrin, C. (2011). Comparison of kriging and cokriging for the geostatistical estimation of specific capacity in the Newark Basin (NJ) aquifer system. *Journal of Environmental Science and Health, Part A*, 46(4), pp.371-377.
3. Chandra, S., Rao, V., Krishnamurthy, N., Dutta, S. and Ahmed, S. (2006). Integrated studies for characterization of lineaments used to locate groundwater potential zones in hard rock region of Karnataka, India. *Hydrogeology Journal*, 14(6), pp.1042-1051.
4. De Menezes Travassos, J. and de Tarso Luiz Menezes, P. (2004). GPR exploration for groundwater in a crystalline rock terrain. *Journal of Applied Geophysics*, 55(3-4), pp.239-248.
5. Dilip kumar and premendra dev (2014) "Groundwater Potential Zone Identification of Karwi Area, Mandakini River Basin, Uttar Pradesh Using Remote Sensing and GIS Techniques." *International Journal of Engineering Science Invention* ISSN (Online): 2319 – 6734, ISSN (Print):

2319 – 6726 www.ijesi.org || Volume 3 Issue 11 || November 2014 || PP.10-19

6. Ghosh, P., Bandyopadhyay, S. and Jana, N. (2015). Mapping of groundwater potential zones in hard rock terrain using geoinformatics: a case of Kumari watershed in western part of West Bengal. *Modeling Earth Systems and Environment*, 2(1).
7. Gumma, M. and Pavelic, P. (2012). Mapping of groundwater potential zones across Ghana using remote sensing, geographic information systems, and spatial modeling. *Environmental Monitoring and Assessment*, 185(4), pp.3561-3579.
8. Govindaiah.S et.al., "Delineation of groundwater potential zones of Tumkur-Gubbi watershed of Shimsha river basin, Karnataka, India, by using remote sensing and GIS techniques". *Journal of international academic research for multidisciplinary*. Impact factor 3.114, ISSN: 2320-5083, Volume 5, Issue 3, April 2017.
9. Jaiswal, R., Mukherjee, S., Krishnamurthy, J. and Saxena, R. (2003). Role of remote sensing and GIS techniques for generation of groundwater prospect zones towards rural development--an approach. *International Journal of Remote Sensing*, 24(5), pp.993-1008.
10. K.A. Mogaji et. al., "Mapping of lineaments for groundwater targeting in the basement complex region of Ondo State, Nigeria, using remote sensing and geographic information system (GIS) techniques." *International Journal of Water Resources and Environmental Engineering* Vol. 3(7), pp. 150-160, August. ISSN 1991-637X ©2011.
11. Khan, A., Khan, H., Umar, R. and Khan, M. (2014). An integrated approach for aquifer vulnerability mapping using GIS and rough sets: study from an alluvial aquifer in North India. *Hydrogeology Journal*, 22(7), pp.1561-1572.
12. Karung Phaisonreng (2018) et. al., "Geospatial Technology Based Groundwater Potential Zone Mapping In Parts of Noyyal Basin, Tamil Nadu, India." © 2018 IJSRST | Volume 4 | Issue 2 | Print ISSN: 2395-6011 | Online ISSN: 2395-602X
13. Kesana Sai Teja and Dinesh Singh and Dinesh Singh (2019) "Identification of Groundwater Potential Zones using Remote Sensing and GIS, Case Study: Mangalagiri Mandal." *International Journal of Recent Technology and Engineering (IJRTE)* ISSN: 2277-3878, Volume-7, Issue-6C2, April 2019.
14. M. Sedhuraman (2014) et. al., "Integration of Geology and Geomorphology for Groundwater Assessment using Remote Sensing and GIS Techniques." *International Journal of Innovative Research in Science, Engineering and Technology (An ISO 3297: 2007 Certified Organization)* Vol. 3, Issue 3, March 2014.
15. Machiwal, D., Jha, M. and Mal, B. (2010). Assessment of Groundwater Potential in a Semi-Arid Region of India Using Remote Sensing, GIS and MCDM Techniques. *Water Resources Management*, 25(5), pp.1359-1386.
16. Mondal, N., Das, S. and Singh, V. (2008). Integrated approach for identification of potential groundwater zones in Seethanagaram Mandal of Vizianagaram District, Andhra Pradesh, India. *Journal of Earth System Science*, 117(2), pp.133-144.
17. Mallick, J., Singh, C., Al-Wadi, H., Ahmed, M., Rahman, A., Shashtri, S. and Mukherjee, S. (2014). Geospatial and geostatistical approach for groundwater potential zone delineation. *Hydrological Processes*, 29(3), pp.395-418.
18. Preeja K. R., Joseph, S., Thomas, J. and Vijith H. (2011). Identification of Groundwater Potential Zones of a Tropical River Basin (Kerala, India) Using Remote Sensing and GIS Techniques. *Journal of the Indian Society of Remote Sensing*, 39(1), pp.83-94.
19. Rai, B., Tiwari, A. and Dubey, V. (2005). Identification of groundwater prospective zones by using remote sensing and geoelectrical methods in Jharia and Raniganj coalfields, Dhanbad district, Jharkhand state. *Journal of Earth System Science*, 114(5), pp.515-522.
20. S. Srinivasa Vittala et. al., (2008) "Prioritization of sub-watersheds for sustainable development and management of natural resources: An integrated approach using remote sensing, GIS and socioeconomic data". *Current Science*, vol.95, no. 3, 10 August 2008, pp.345-354.
21. Sankar, K. (2002). Evaluation of groundwater potential zones using Remote Sensing data in upper Vaigai river basin, Tamil Nadu, India. *Journal of the Indian Society of Remote Sensing*, 30(3), pp.119-129.
22. Savita, R., Mittal, H., Satishkumar, U., Singh, P., Yadav, K., Jain, H., Mathur, S. and Davande, S. (2018). Delineation of Groundwater Potential Zones using Remote Sensing and GIS Techniques in Kankanala Reservoir Subwatershed, Karnataka. *International Journal of Current Microbiology and Applied Sciences*, 7(1), pp.273-288.
23. Senthilkumar, M., Gnanasundar, D. and Arumugam, R. (2019). Identifying groundwater recharge zones using remote sensing & GIS techniques in Amaravathi aquifer system, Tamil Nadu, South India. *Sustainable Environment Research*, 29(1).
24. Siddan Anbazhagan et. al., "Remote sensing in delineating Deep Fractured Aquifer Zones". *Geoinformatics in Applied Geomorphology*. Pp 204-229.
25. Singh, A., Panda, S., Kumar, K. and Sharma, C. (2013). Artificial Groundwater Recharge Zones Mapping Using Remote Sensing and GIS: A Case Study in Indian Punjab. *Environmental Management*, 52(1), pp.61-71.
26. Siva, G., Nasir, N. and Selvakumar, R. (2017). Delineation of Groundwater Potential Zone in Sengipatti for Thanjavur District using Analytical Hierarchy Process. *IOP Conference Series: Earth and Environmental Science*, 80, p.012063.
27. Subramani, T. and Santhi, D. (2018). Groundwater Potential and Recharge Zone Mapping for Namakkal Town Using RS & GIS. *International Journal of Engineering & Technology*, 7(3.10), p.155.
28. Yammani, S. (2007). Groundwater quality suitable zones identification: application of GIS, Chittoor area, Andhra Pradesh, India. *Environmental Geology*, 53(1), pp.201-210.
29. Youssef, A., Pradhan, B. and Tarabees, E. (2010). Integrated evaluation of urban development suitability based on remote sensing and GIS techniques: contribution from the analytic hierarchy process. *Arabian Journal of Geosciences*, 4(3-4), pp.463-473.

HABITAT DISTRIBUTION MODELING FOR MEDICINAL PLANT *VALERIANA JATAMANSI* IN SHIVALIK FOOTHILLS OF DOON VALLEY

A. P. Mishra ^{1*}, N. Rawat ¹, M. P. S Bisht¹

¹ Uttarakhand Space Application Centre, Dehradun, Uttarakhand, India – arunpratap7371@gmail.com

¹ Uttarakhand Space Application Centre, Dehradun, Uttarakhand, India – neel2406@gmail.com

¹ Uttarakhand Space Application Centre, Dehradun, Uttarakhand, India – mpbisht@gmail.com

KEY WORDS: *Valeriana jatamansi*, MaxEnt Algorithm, Bioclim, Habitat Modelling, Doon Valley

ABSTRACT:

Valeriana jatamansi is one amongst the most important medicinal plant species is distributed in subtropical to temperate region between 1000 to 3000 m in Himalaya. It is well known for its medicinal and other ethnobotanical properties. Due to overharvesting from the wild, its population is decreasing at an alarming rate and this species is placed in the Endangered categories. The present study depicts the potential distribution of *V. jatamansi* in Shivalik foothills of doon valley. The Worldclim bioclimatic variables, slope, aspect, elevation, and the forest types (based on IRS LISS-IV) data and 58 spatially well-dispersed species occurrence points were used to predict the potential distribution of *V. jatamansi* in 1164.23 km² study area. The suitable habitat for *V. jatamansi* was recorded 207 km² in the study area. Jackknife test was used to evaluate the importance of the environmental variables for predictive modeling. Maxent model was highly accurate with a statistically significant AUC value of 89. The result showed that temperature (31%) and precipitation (15%) is the key influential factor that affect its distribution. Our findings can be applied in various ways such as the identification of additional localities where *V. jatamansi* may already exist, but has not yet been detected, this approach could be promising in predicting the potential distribution of medicinal plant species and thus, can be an effective tool in species restoration and conservation planning.

1. INTRODUCTION

The Himalaya has a great wealth of medicinal plants and traditional medicinal knowledge. The Indian Himalaya is home to more than 8000 species of vascular plant. Out of total species of vascular plant, 1748 species have medicinal properties (Samant, 2003). India is one of 17 mega- biodiverse countries in the world with only 2.4 percent of the earth's land area, it accounts for 7-8 percent of the world recorded species including plant genetic diversity with medicinal properties has the potential of becoming a major global player in market for medicinal plant based herbal formulation, medicines and products. Uttarakhand is hilly state in Indian Himalayan region. Due to its unique geographic location and different climatic conditions, it has a rich biodiversity and variety of plant species. Local people of this region are basically depended upon medicinal plants for their primary health care system, health which are easily available around their hills, less expensive and no side effect as compare to modern medicine (Nazir and Pala, 2010).

V. jatamansi is one of the most imperative medicinal plant belongs to the family Valerianaceae. It is also known as *V. wallichii*. It is dispersed in subtropical and temperate Himalayan region in the middle of 1000 to 3000 m asl. Commonly it prefers hilly slants, clammy places, damp woods, trenches and alongside the streams. Due to its medicinal and other ethnobotanical properties, it has been used in Ayurvedic and Unani medication systems since ancient times. The roots or rhizome of this species are well known for the treatment of obesity, dermatitis, epilepsy, insanity and snakebite (Prakash, 1999) moreover, it acts as a natural source of sedative or tranquilizing compound viz. valepotriate (Violon

1983). Valerenic acid and valepotriates has been selected as a marker compounds which are derived from the rhizome of *V. jatamansi* and *V. officinalis* (Singh et al. 2006). In India, the species is included in the list of 178 medicinal plants with high volume trade/ consumption between 100 and 200 MT (metric tonnes). Further, the estimated annual consumption of the species in India is 123 MT with a price range of Rs. 95-100/ kg rhizomes with root (Ved and Goraya 2008). The estimated demand for *V. jatamansi* in India during the year 1999-2000 was 71.7 tonnes and 111.5 tonnes in 2001-2002 which further increased up to 216.2 tonnes during 2004-2005. At present uncontrolled amputation of plants from the wild mainly for pharmaceutical purposes has resulted in the rapid depletion of the stock from the natural habitats and the species placed in the endangered category in India (Samant et al. 1998). Hence conservation and sustainable utilization of this species are extremely important.

Habitat degradation and fragmentation, invasion of alien species, over-exploitation, and an ever-increasing human population are some of the critical factors answerable for the species loss all through the world (Barnosky et al. 2011), bringing about one-5th of the plant species on the threat of extinction (Brummitt and Bachman, 2010). Species habitat recovery is one of the success ecological engineering measures for the species rehabilitation and habitat conservation (Polak and Saltz, 2011). A detailed expertise on the modern distribution of species is often a pre-requisite to rehabilitate the species in any surroundings (Barik and Adhikari 2011).

Since past couple of decades, exploitation of this species has suddenly become a flourishing business for illegal collectors. This uncontrolled exploitation along with several other factors like destruction of habitats, overgrazing and tourism

* Corresponding author

interference are responsible for the dwindling status of this valuable species especially from higher altitudes. Over 90% of the market demand for this species is met from the wild. To get 1 kg of dry weight of *V. jatamansi* plant, as many as 400 to 500 individual plants are uprooted. Due to narrow distribution range, small population size, high use value and increasing demand, the species figured among the 58 identified as top priority species for conservation and cultivation in Doon Valley. Indiscriminate, unscientific harvesting and lack of organized cultivation of the plant has threatened its status in wild and listed as endangered species by International Union for conservation of Nature and Natural Resources. *V. jatamansi* assigned endangered status in J&K and Himanchal Pradesh. While its status in Uttarakhand was declared as critically endangered by NMPB (National Medicinal Plant Board).

Extend and availability of this important medicinal plants becomes necessary and therefore, present study is designed for predicting the potential habitat distribution of *V. jatamansi* in Dehradun District, Uttarakhand using Maxent modelling.

1.1 STUDY AREA

The study area, Dun valley is located in the Lesser Himalayan foothills falling in Dehradun district of Uttarakhand, India. The Valley with an area of 1877 km² is bounded by Shivalik hills in the south and Lesser Himalayas in the north (Fig 1). It receives a mean annual rainfall of 2051 mm. The temperature ranges from 2°C in winter to 42°C in summer. Dun valley is a forested landscape with forests, agriculture, settlements, orchards and tea gardens. The principal forest types are: (i) Moist Bhabar-Dun Sal Forest (ii) Lower Himalayan Moist Temperate Forest (iii) Himalayan Subtropical Pine Forest and (iv) Northern Dry Mixed Deciduous Forest (Champion and Seth 1968). *Shroea robusta*, *Terminalia tomentosa*, *Anogeissus latifolia*, *Mallotus philippensis*, *Dalbergia sissoo*, and *Acacia catechu* are some of the important tree species in the Valley. After becoming capital city of the Uttarakhand province in the year 2000, Dehradun district, in general, and Dun valley in particular have come under tremendous anthropogenic pressure that has taken a heavy toll on the several important plant species including *V. jatamansi*.

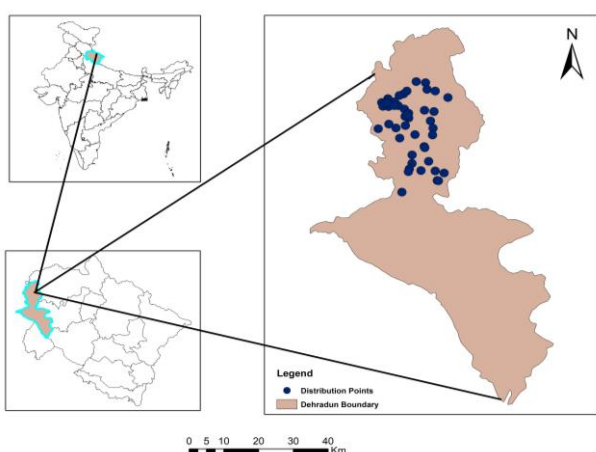


Fig: 1 Study area and population of *V. jatamansi*

MATERIALS AND METHODS

1.1 SPECIES OCCURRENCE DATA COLLECTION

The occurrence data of *V. jatamansi* in the Chakrata hills (Doon valley) were collected during field survey conducted in the month of November- December 2019-20. A total 58 well

dispersed primary and secondary ground truth points of *V. jatamansi* were retrieved. The secondary data was acquired from FRI herbarium (DD). The population of *V. jatamansi* were represented by hill slopes, moist places, damp woods and along the streams. The coordinates of all incidence points had been recorded the use of a global Positioning device (Garmin Oregon 550).

1.2 ENVIRONMENTAL VARIABLES AND SPECIES INCIDENCE FACTS

Nineteen bioclimatic variables (Hijmans et al. 2005) with 30 second (1 km) spatial resolution, downloaded from World Clim datasets (www.worldclim.org), were used to find the most influential variables associated with *V. jatamansi* distribution. Digital Elevation Modal (DEM) with 30 m resolution, was used to generate the slope, aspect and elevation data layers. Besides this, forest types are also considered. A total of 58 species occurrence geocoordinates. Spatial modelling: Erdas 11 and ArcGIS 10.3 were used to create the spatial data layers. The categorical data were re-sampled to 1 km spatial resolution using nearest neighbour re-sample technique.

1.3 SPECIES DISTRIBUTION MODELLING

We used the maximum entropy model (Maxent version 3.3.3) (Phillips et al. 2006) in this study because it has been shown to perform better with small sample sizes relative to other modeling methods (Elith et al. 2006; Pearson et al. 2007; Kumar and (Stohlgren 2009). Maxent (Phillips et al. 2006) uses presence-only data to predict the distribution of a species based on the theory of maximum entropy. The program attempts to estimate a probability distribution of species occurrence that is closest to uniform while still subject to environmental constraints (Elith et al. 2011). In our models, we selected 75% data for model training and 25% for model testing (Phillips 2008) keeping other values as default. Jackknife analyses were performed to determine variables that reduce the model reliability when omitted. We used the area under the Receiving Operator Curve (AUC) to evaluate model performance. The value of AUC ranges from 0 to 1 (Fielding and Bell 1997). An AUC value of 0.5 indicates that model did not perform better than random, whereas a value of 1.0 indicates perfect discrimination (Swets, 1988). The model with the highest AUC value was considered the best performer. For display and further analysis, we imported the results of the Maxent models predicting the presence of *V. jatamansi* (0-1 range) into ArcGIS 10.3.

2. RESULTS AND DISCUSSION

2.1 GEOGRAPHICAL DISTRIBUTION

A Total 58 distribution point of *V. jatamansi* were used to build the model. Maxent's model statistical demonstrated highly significant (P<0.01) performance and evaluation of model indicated that the model provided useful information. The area under curve (AUC) for training and test was 0.89 and 0.82 respectively indicating high accuracy (Figure 2).The jackknife test showed mean temperature of coldest quarter (Bio 11) as the environmental variable with the highest training gain in the model, which indicated that it had the most predictive ability of any variable (Figure:4). The variable, which decreased the gain most when excluded from the model, was Mean Diurnal Range (Bio2), indicating that it had the most unique contribution to the model. Amongst the predictor bioclimatic variables, Mean Temperature of Coldest Quarter (Bio11), Precipitation of Coldest Quarter (Bio19), Precipitation of Wettest Month

(Bio13) and Mean Diurnal Range (Bio2) were the most influential and contributed 64.5%, 19.1%, 6.8 % and 5.9% respectively to the MaxEnt Model. Considering the permutation importance, mean temperature of coldest quarter had the maximum influence on the habitat suitability model and contributed to 48.5%, while precipitation of warmest quarter (BIO18) and temperature annual range (BIO 7) contributed to 22.2% and 20.0% respectively.

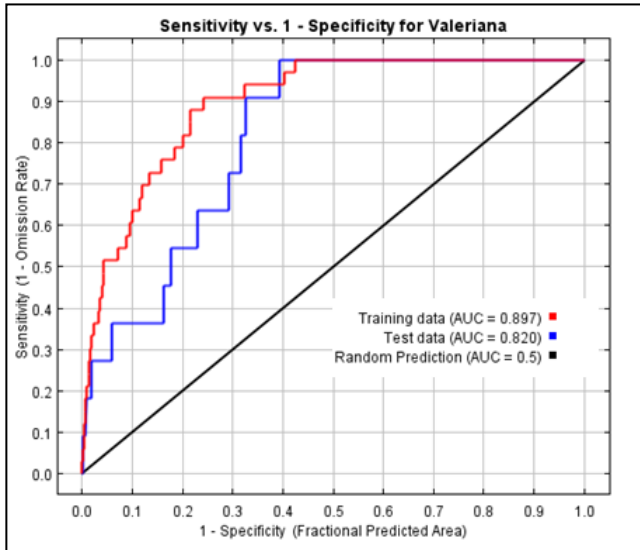


Fig:2 Area under curve for *V.jatamansi*

2.2 POTENTIAL AREAS FOR REINTRODUCTION

Potential habitats with high suitability thresholds were distributed in the hill slopes, moist places and along the streams and higher elevations of Chakrata forest division. Primary field surveys revealed that the predicted potential habitats were mostly located along the streams from subtropical to temperate region of Doon valley. Areas with low to very low habitat suitability were with away from the water channels. Out of the 1164.23 km² of study area, a total potential area of 207 km² (very high and high suitable class) in Shivalik foothills was predicted to be suitable for *V. jatamansi* re-introduction, cultivation and conservation (Figure 3). Among the habitat suitability classes under low suitability class, an area of 2411 km² was covered. Area of medium suitability was restricted only to about 471.0 km², and high suitability class 386.0 km².

Field surveys for assessing the habitat types of *V. jatamansi* in the predicted potential areas revealed that the species occurred in the riverine, hill slope, damp wood, ditch and moist shady places. The species was also present around human settlement areas and settled cultivation lands. Superimposing the predicted potential habitat map of the species on Google Earth satellite imageries revealed a mosaic of habitats to be suitable for the species persistence. The areas with very high to high habitat suitability for the species were along the stream habitat.

The areas with medium habitat suitability were hill slopes, damp wood. The areas with very low habitat suitability were dry slope, rocky and scree. Such areas for the species and could also be used for re-introduction/recovery and commercial cultivation of the species.

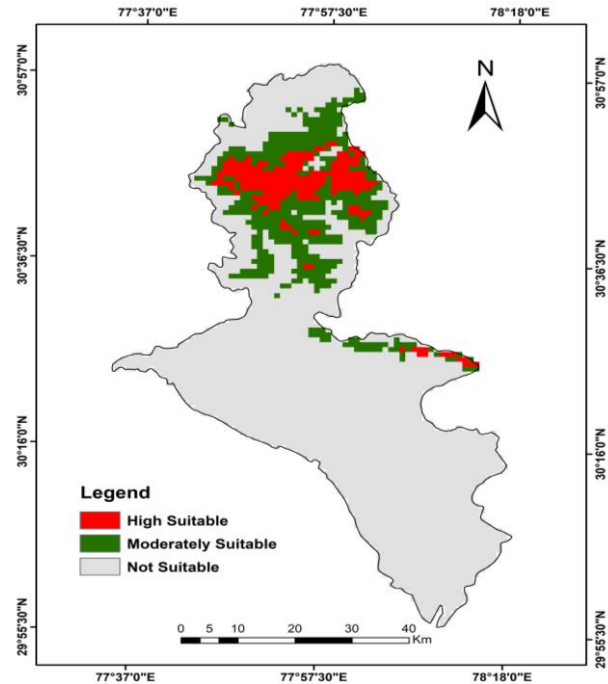


Fig: 3 Habitat distribution modelling of *V.jatamansi*

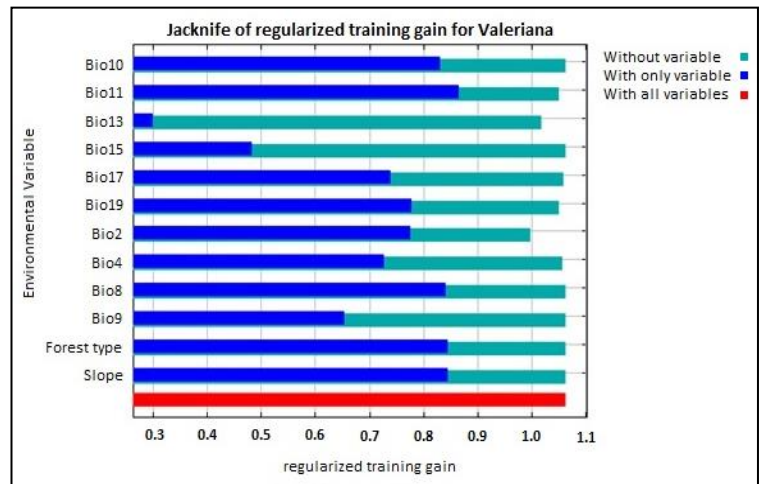


Fig: 4 Jackknife graph for *V.jatamansi*

3.CONCLUSIONS

The over-exploitation of *V. jatamansi* roots and rhizomes for medicinal usages and the biotic interferences in its distribution range have caused habitat degradation thus creating nearly extinct condition of the herb. Thus, convention on international trade of endangered species notified *V. jatamansi* enlisted an endangered species in the list of National Medicinal Plant Board, New Delhi, India (Nawchoo et al. 2012). Hence, it is of immediate concern that different conservation measures and strategies be adopted to stop further depletion of the herb from its natural habitat. Conventionally the herb is propagated through seeds. Despite being the common method of its propagation, it is not an attractive practice, since the seeds germinate slowly and remain dormant for long time. Therefore,

establishment of an efficient protocol and propagation system is necessary for large-scale production and plantation of *V. jatamansi* which would also help in developing new varieties with high levels of important compounds via biotechnology.

Our results support the statement that the predicted potential distribution areas through Maxent modelling almost always appear as over-estimated compared to realized niche of the species, i.e. the habitat. Since Maxent model considers only niche-based presence data, it predicts the species fundamental niche rather than realized niche (Pearson 2007). The present study demonstrated that habitat distribution modelling could be of great help in predicting the potential habitats of threatened species for reintroduction. Results of the study also suggested the strong relationship between the population size and model thresholds thereby indicating the high potential value of ENM in population studies. The areas predicted suitable but currently not occupied by the species are the candidate areas to be considered for conservation prioritization and propagation of this species. The method is certainly promising in predicting the potential distribution of other medicinal plant species and can be a valuable tool in species conservation planning and climate change-species distribution studies. The areas identified in the present study for reintroduction of *V. jatamansi* would not only help in Eco-restoration of degraded forests and habitats where the species had existed before but also in rehabilitating the species population and improving its conservation status. Therefore, the results would be quite useful for natural resource managers in management of this species and conserving overall biological diversity in the region.

ACKNOWLEDGEMENTS

The authors are grateful to Uttarakhand Space Application Centre, Dehradun, Uttarakhand, India for providing GIS lab facilities. We are thankful to Mr. Govind Singh Negi and Mr. Pritam for assistance in field work. We are also grateful to Mr. Naveen Chandra Bhatt for immense help regarding the said work.

REFERENCES

- Adhikari, D., Barik, S.K., Upadhaya, K. 2012. Habitat distribution modelling for reintroduction of *Ilex khasiana* Purk., a critically endangered tree species of northeastern India. *Ecol. Eng.*, 40, 37-43. DOI: 10.1016/j.ecoleng.2011.12.004.
- Barnosky, Anthony D., Marc A. Carrasco, and Russell W. Graham. "Collateral mammal diversity loss associated with late Quaternary megafaunal extinctions and implications for the future." Geological Society, London, Special Publications 358, no. (1) 2011: 179-189.
- Berger-Tal, O., Polak, T., Oron, A., Lubin, Y., Kotler, B.P., Saltz, D. 2011. Integrating animal behavior and conservation biology: a conceptual framework. *Behav. Ecol.*, 22(2), 236-239. DOI: 10.1093/beheco/arq224.
- Brummitt, N.A., Bachman, S.P. 2010. Plants under pressure-a global assessment: the first report of the IUCN sampled red list index for plants. Kew, UK: *Royal Botanic Gardens*.
- Elith, J., Phillips, S.J., Hastie, T., Dudik, M., Chee, Y.E., Yates, C.J. 2011. A statistical explanation of MaxEnt for ecologists. *Divers. Distrib.*, 17(1), 43-57. DOI: 10.1111/j.1472-4642.2010.00725.x.
- Fielding, A.H., Bell, J.F. 1997. A review of methods for the assessment of prediction errors in conservation presence/absence models. *Environ. conser.*, 24(1), 38-49. DOI: <https://doi.org/10.1017/S0376892997000088>.
- Flory, S.L., Lorentz, K.A., Gordon, D.R., Sollenberger, L.E. 2012. Experimental approaches for evaluating the invasion risk of biofuel crops. *Environ. Res. Lett.*, 7(4), 045904.
- Guisan, A., Gonthier, Y., Cherix, D., Zimmerman, N.E., Kienast, F., Edwards, T., Weiss, A.D. 2000. Landscape potential for animal species survival, colonization and dispersal: a spatial simulation study. URL: <http://www.unine.ch/cscf/PROJETS/landspot/index.htm>. Last accessed, 25(05), 2003.
- Hijmans, R. J., Cameron, S. E., Parra, J. L., Jones, P. G., Jarvis, A. 2005. Very high resolution interpolated climate surfaces for global land areas. *Int. J. Climatol: A Journal of the Royal Meteorological Society*, 25(15), 1965-1978.
- Kala, C.P., Dhyani, P.P., Singh, B.S. 2006. Developing the medicinal plants sector in northern India: challenges and opportunities. *J. Ethnobiol. Ethnomed.*, 2(1), 32. doi: 10.1186/1746-4269-2-32.
- Kumar, S., Stohlgren, T.J. 2009. Maxent modeling for predicting suitable habitat for threatened and endangered tree *Canacomyrica monticola* in New Caledonia. *J. Ecol. Nat. Environ.*, 1(4), 94-98.
- Nautiyal, B.P., Chauhan, R.S., Prakash, V., Purohit, H., Nautiyal, M.C. 2003. Population studies for the evaluation of germplasm and threat status of the alpine medicinal herb, *Nardostachys jatamansi* Plant Genet. Resour. Newsl., 34-39.
- Nawchoo, A.I., Rather, M.A., Ganie, H.A., Jan, R.T. 2012. Need for unprecedented impetus for monitoring and conservation of *Valeriana jatamansi* a valuable medicinal plant of Kashmir Himalaya. *Agri. Sci. Res. Jour.*, 2(7), 369-373.
- Pala, N.A., Negi, A.K., Todaria, N.P. 2010. Traditional uses of medicinal plants of Pauri Garhwal, Uttarakhand. *Nat. and Sci.*, 8(6), 57-61.
- Pangriya, R. 2015. Study of Aromatic and Medicated Plants in Uttarakhand, India: with Focus on role in Employment Generation and supply chain Management. *Int. J. Soc. Sci. Manag.*, 2(2), 148-156. DOI: 10.3126/ijssm.v2i2.12396.
- Pant, S., Rinchen, T. 2012: *Dactylorhiza hatagirea*: A high value medicinal orchid. *J. med. plants res.*, 6(19), 3522-3524. doi.org/10.5897/JMPR12.097.
- Pearson, R. G., Raxworthy, C. J., Nakamura, M., Townsend Peterson, A. 2007. Predicting species distributions from small numbers of occurrence records: a test case using cryptic geckos in Madagascar. *J. Biogeogr.*, 34(1), 102-117.
- Phillips, S.J., Dudik, M. 2008. Modelling of species distributions with Maxent: new extensions and a comprehensive evaluation. *Ecography*, 31(2), 161-175. DOI: 10.1111/j.0906-7590.2008.5203.x.
- Phillips, S.J., Anderson, R.P., Schapire, R.E., 2006. Maximum entropy modeling of species geographic distributions. *Ecol.*

Model. 190, 231-259.
<https://doi.org/10.1016/j.ecolmodel.2005.03.026>.

Polak, T., Saltz, D. 2011. Reintroduction as an ecosystem restoration technique. *Conservation Biology*, 25(3), 424-424. DOI: 10.1111/j.1523-1739.2011.01669.x.

Prakash, G. (1999). Another reason: Science and the imagination of modern India. *Princeton University Press*.

Samant, S.S., Pal, M.2003. Diversity and conservation status of medicinal plants in Uttarakhand State. *Indian Forester*, 129(9), 1090-1108.

Swets, J. A. (1988). Measuring the accuracy of diagnostic systems. *Science*, 240(4857), 1285-1293.

Tomiyama, S., McGuire, J.L., Dedon, R. W., Lerner, S.D., Setsuda, R., Lipps, A.N., Bailey, J.F., Hale, K.R., Shabel, A.B., Barnosky, A.D. 2011. A report on late Quaternary vertebrate fossil assemblages from the eastern San Francisco Bay region, California. *PaleoBios*, 30(2).

Ved, D. K., and G. S. Goraya. Demand and supply of medicinal plants in India. Bishen Singh Mahendra Pal Singh, 2008.

RECENT DEVELOPMENTS IN REMOTE SENSING CLOUD COMPUTING TO ASSESS VARIATIONS IN INDIAN FORESTS FROM 2001 TO 2018

R. Gupta, L.K. Sharma*

Department of Environmental Science, School of Earth Sciences, Central University of Rajasthan
NH-8, Bandarsindri – 305817, Rajasthan, India
2017phdes03@curaj.ac.in, *laxmikant_evs@curaj.ac.in

KEY WORDS: MODIS, Land Cover, Forests, EVI, Climate engine, IGBP

ABSTRACT:

Recent developments in Earth's remote sensing cloud computing provide tremendous and efficient opportunities in monitoring and sustainable management of forests. Climate engine, a web-based platform offers extensive and quick way to download, process and visualize remote sensing and climate datasets. This study aims to analyse the annual and seasonal variations in India's forests from 2001 to 2018. We used MODIS (Moderate-Resolution Imaging Spectroradiometer) EVI (Enhanced Vegetation Index) and the International Geosphere-Biosphere Programme (IGBP) land cover data for the year 2001, 2010 and 2018. Evergreen needleleaf forest, Evergreen broadleaf forest, Deciduous needleleaf forest, Deciduous broadleaf forest and Mixed forest are the five forests types derived from IGBP land cover data. Then, interannual and seasonal variations in EVI in these five forest types were quantified. Results indicate that the forest cover area Results revealed that total forest area increased from 82766.43 sq. Km in 2001 to 92172.61 sq. Km in 2010, and was decreased to 89387.05 in 2019 sq. Km. North East India experiences a high EVI variability and spatial patterns differences. Overall, the study shows that recent datasets obtained from Climate engine could be useful in quickly assessing large data which empowers researchers and decision makers in monitoring and planning for the long-term sustainability of forests.

1. INTRODUCTION

In recent decades, natural forests are facing tremendous pressure of degradation from different types of forces which leads to their loss in many countries. Geospatial technology provides us an opportunity to monitor forest resources at a local to a global scale and its integration with novel developments like cloud computing, machine learning and deep learning has improved the methods to address the challenges of applying an amount of geospatial data for scientific research and applications (Zhang et al. 2010; Liu et al. 2019; Sun and Scanlon, 2019). Climate engine (<http://climateengine.org/>) is a recent, free web-based application developed by a team of scientists at the Desert Research Institute, University of Idaho, and Google which enables us to obtain rapidly processed remote sensing and climate datasets (Huntington et al. 2017). Climate engine accompanied with multiple optical remote sensing datasets (Landsat, MODIS and Sentinel) and excellent visualization options. In forestry, Climate engine helps researchers to get a continuous remote sensing data and time series analysis which reduces users time and increases effectiveness in decision making for forest planning and management.

Vegetation indices (VI's) are commonly used to measure reliable spatiotemporal inter-comparisons of terrestrial photosynthetic activity (Huete et al. 1997; Setiawan et al. 2014). EVI is useful in quantitative and qualitative evaluations of vegetation cover, monitoring, growth dynamics and annual variation in vegetation without much random fluctuation (Jeganathan and Nishant, 2014; Xue and Su, 2017). According to Matsushita et al. (2007), EVI reduces both atmospheric and soil background noise simultaneously. However, they demonstrated that the EVI is more sensitive to topographic conditions than NDVI. Jeganathan and Nishant (2014) analysed the spatio-temporal variability of vegetation growth in India. They found that the phenology results

from MODIS EVI were found to be reliable and, hence, EVI data are recommended for time-series vegetation related applications.

In this study, we used cloud computing platform Climate engine in deriving data for the year 2001, 2010 and 2018 and then analysing interannual and seasonal variations along with the spatial pattern in EVI over forest types in India. Obtained outcomes provide understanding about variabilities in India's forests occurring over the time period. In general, the developments of such web-based platforms provide extra advantages to the research community and decisions makers in applying their knowledge in better forest monitoring and management.

2. DATASETS AND METHODS

2.1 Study area

Large scale geospatial data assessment can be possible using Climate engine; therefore, this assessment is made over the whole India for the year 2001, 2010 and 2018. The total geographical area of the country is 3,287,240 sq. Km, which accounts only 2.4 percent of the world surface. In 2019, the total forest cover in India was 7,12,249 sq. Km (21.67 % of India's total geographical area) compared to an area of 6,75,538 sq. Km (20.5 %) in the year 2001 (ISFR, 2001; 2019). India has a broad range of weather conditions and climatic patterns across a vast geographical scale and varied topographical regions. Forest types vary from the Himalayas in the north to the Western Ghats in the south, from thorn vegetation of north-west to the wet evergreen forest of north-east India (Reddy et al. 2015).

2.2 MODIS land cover data

The MODIS land cover type product (MCD12Q1) is a global land cover classification data layer generated annually from 2001 to present. For each individual year, different research groups have developed five land cover classification schemes. For this study we used IGBP type 1 land cover classification scheme, which has a total 17 land cover classes (0-16) (Friedl and Sulla-Menashe, 2019). Spatial resolution (500 m) and sinusoidal projected in standard MODIS grid tiles land cover data for the year 2001, 2010 and 2018 was downloaded from NASA Earth data (<https://earthdata.nasa.gov/>). We extracted five forest types (Evergreen needleleaf forest, Evergreen broadleaf forest, Deciduous needleleaf forest, Deciduous broadleaf forest and Mixed forest) which distributes over India from land cover data for the year 2001, 2010 and 2018 (Fig. 1). Data processing steps such as clipping and extraction were performed in ArcMap Desktop version 10.5.

2.3 MODIS EVI data

To analyse interannual and seasonal variations in EVI of forest types, the terra MODIS EVI dataset (MOD13Q1) having 16 days of temporal resolution and 250 m of spatial resolution for the year 2001, 2010 and 2018, and also, seasonal (Spring -March, April, May), (Summer - June, July, August), (Autumn- September, October and November) EVI data for the same year was downloaded from Climate engine (<http://climateengine.org/>). MODIS EVI data has enhanced sensitivity over high biomass regions, and the algorithm selects the best available pixel value from all the acquisitions from the 16-day period. The criteria used is low clouds, low view angle, and the highest EVI value (Didan, 2015). Interannual and seasonal EVI maps are shown in Figure 2 and Figure 3 respectively.

2.4 Spatial pattern variability

Both EVI and forest types data were resampled to the same cell size. Forest type raster datasets were converted into point data and then extracted EVI values to point data. EVI values less than zero was set at zero in each EVI data. Interannual and seasonal EVI maps were created to find variations and spatial patterns among these EVI datasets. Then, the percent variations in EVI in an interannual and seasonal data were determined. Five ranges such as large decrease (<-20%), decrease (-20% to -5%), minimal (-5% to 5%), increase (5% to 20%), and large increase (> 20%) were defined and the maps were created (Figure 4 and Figure 5).

3. RESULTS AND DISCUSSION

3.1 Variations in forest area

Figure 1 shows the forest type map for the year 2001, 2010 and 2018, which classified based on MODIS land cover data. Table 1 shows the area under each forest type for the year 2001, 2010 and 2019. The area covers under Evergreen needleleaf forest, Evergreen broadleaf forest, Deciduous needleleaf forest Deciduous broadleaf forest and Mixed forest in the year 2001 was 6717.12 sq. Km, 39082.06 sq. Km, 1.19 sq. Km, 17532.31 sq. Km and 19433.75 sq. Km respectively. In the year 2010, the area occupied by Evergreen needleleaf forest, Evergreen broadleaf forest and Mixed forest was 6628.06 sq. Km, 37062 sq. Km, 0.25 sq. Km, 24806.43 sq. Km and 23675.87 sq. Km respectively. In 2018, the area under Evergreen needleleaf forest, Evergreen

broadleaf forest, Deciduous needleleaf forest Deciduous broadleaf forest and Mixed forest was 7016.25 sq. Km 37298 sq. Km 0.43 sq. Km 22309 sq. Km 22763.37 sq. Km respectively.

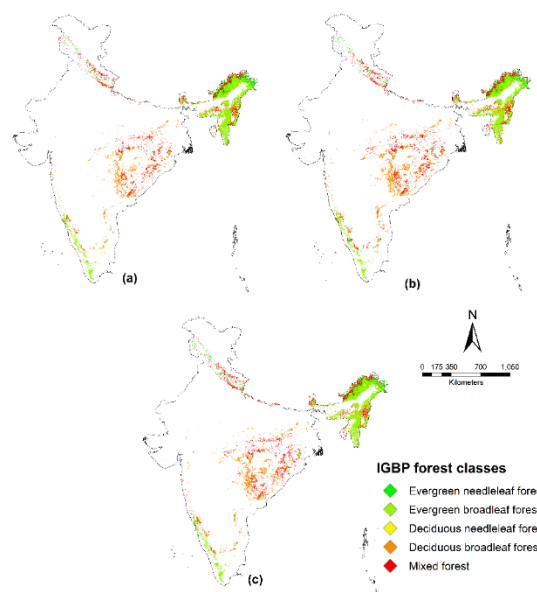


Figure 1. Classified maps of five forest type in India for the year 2001 (a), 2010 (b) and 2018 (c) (Data: MODIS land cover type product (MCD12Q1); maps created in ArcMap desktop version 10.5)

	2001	2010	2018
Evergreen needleleaf forest	6717.12	6628.06	7016.25
Evergreen broadleaf forest	39082.06	37062	37298
Deciduous needleleaf forest	1.19	0.25	0.43
Deciduous broadleaf forest	17532.31	24806.43	22309
Mixed forest	19433.75	23675.87	22763.37
Total	82766.43	92172.61	89387.05

Table 1. Area (sq. Km) covered under five forest types in the year 2001, 2010 and 2018

Therefore, the total area covered under all forest type in the year 2001, 2010 and 2018 was 82766.43 sq. Km 92172.61 sq. Km 89387.05 sq. Km respectively (Table 1).

3.2 EVI annual variability

Figure 2 shows five classified categories of EVI variations in India's forest for the year 2001, 2010 and 2018. In the year 2001, it is observed that the area such as Northeastern India and western Ghats which generally covered under Evergreen needleleaf forest and Evergreen broadleaf forest shows high EVI range (0.39-0.65). Similarly, in the year 2010 and 2018 a high EVI range (0.37-0.63) were observed in Northeastern India, western Ghats and the Eastern Ghats. In north India and middle India, mostly Deciduous needleleaf forest, Deciduous broadleaf forest and mixed-species forests are found which shows EVI up to 0.39 (Figure 2). Table 2 shows the annual (2001, 2010, and 2018) EVI trends in each forest type. From 2001 to 2010, EVI of evergreen needleleaf and evergreen broadleaf forests decreased from 0.250 to 0.228, and 0.411 to 0.384, respectively, whereas it increased from 0.131 to 0.173, 0.330 to 0.345, and 0.312 to 0.324 for deciduous needleleaf, deciduous broadleaf, and mixed forests.

From 2005 to 2009, the EVI of evergreen needleleaf forest, evergreen broadleaf, deciduous needleleaf increased from 0.228 to 0.250, 0.384 to 0.408, 0.173 to 0.211; whereas, in Deciduous broadleaf forest Mixed forest EVI remained same with 0.345 to 0.335, 0.324 to 0.323 respectively. Therefore, these values indicate that forest activity has been improved in the year 2018.

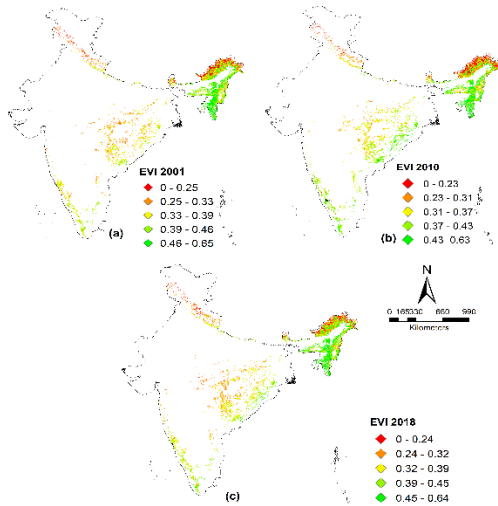


Figure 2. EVI in forest types for the year 2001 (a), 2010 (b) and 2018 (c)

Forest type	EVI 2001	EVI 2010	EVI 2018
Evergreen needleleaf forest	0.250	0.228	0.250
Evergreen broadleaf forest	0.411	0.384	0.408
Deciduous needleleaf forest	0.131	0.173	0.211
Deciduous broadleaf forest	0.330	0.345	0.335
Mixed forest	0.312	0.324	0.323

Table 2. EVI in each forest type in the year 2001, 2010 and 2019

3.3 EVI seasonal variability

Figure 3 shows seasonal (spring, summer and autumn) EVI variations in India's forest for the year 2001, 2010 and 2018. In the spring season of the year 2001, 2010 and 2018 EVI varies in the range of 0.0-0.71, 0.0-0.65, and 0.0-0.69 respectively. In summer season the EVI varies from 0.0 - 0.85, 0.0-0.84 and 0.0-0.83 respectively; while in autumn the EVI range was 0.0-1.00, 0.0-0.80 and 0.0-0.80 in the year 2001, 2010 and 2018 respectively.

Table 3 shows seasonal (spring, summer, and autumn) EVI trends in each forest type for the year 2001, 2010 and 2018. From 2001 to 2010 in spring season, EVI in Evergreen needleleaf forest, Evergreen broadleaf forest, Deciduous needleleaf forest, Deciduous broadleaf forest and Mixed forest has been decreased from 0.218 to 0.215, 0.367 to 0.346, 0.085 to 0.073, 0.238 to 0.220, 0.267 to 0.257 respectively, whereas from 2010 to 2018 EVI showed increase from 0.204 to 0.237, 0.346 to 0.383, 0.073 to 0.144, 0.220 to 0.239, 0.257 to 0.278 respectively. During 2001 to 2010 in the summer season, EVI showed a decrease in Evergreen needleleaf forest, Evergreen broadleaf forest, Deciduous needleleaf forest from 0.283 to 0.193, 0.431 to 0.352,

0.085 to 0.148; whereas in Deciduous broadleaf forest and Mixed forest it was increased from 0.344 to 0.389 and 0.331 to 0.334 respectively.

Forest class	EVI 2001			EVI 2010			EVI 2018		
	spring	summer	Autumn	spring	summer	Autumn	spring	summer	Autumn
Evergreen needleleaf forest	0.218	0.283	0.215	0.204	0.193	0.279	0.237	0.227	0.290
Evergreen broadleaf forest	0.367	0.431	0.449	0.346	0.352	0.453	0.383	0.389	0.466
Deciduous needleleaf forest	0.085	0.150	0.074	0.073	0.148	0.061	0.144	0.130	0.190
Deciduous broadleaf forest	0.238	0.344	0.457	0.220	0.389	0.448	0.239	0.338	0.439
Mixed forest	0.267	0.330	0.371	0.257	0.330	0.393	0.257	0.314	0.385

Table 3. Seasonal EVI value in the year 2001, 2010 and 2019

From 2010 to 2018, EVI has increased from 0.193 to 0.227, 0.352 to 0.381 for Evergreen needleleaf forest and Evergreen broadleaf forest; whereas for Deciduous needleleaf forest, Deciduous broadleaf forest and Mixed forest it is decreased from 0.148 to 0.130, 0.389 to 0.338, 0.334 to 0.314 respectively. During autumn from 2001 to 2010, EVI increased from 0.215 to 0.279, 0.449 to 0.453, and 0.371 to 0.393 for Evergreen needleleaf forest, Evergreen broadleaf forest and Mixed forest, while it is decreased from 0.074 to 0.061, and 0.457 to 0.448 Deciduous needleleaf forest and Deciduous broadleaf forest respectively. Similarly, from 2010 to 2018 in autumn season, EVI showed increase from 0.279 to 0.290, 0.453 to 0.466, and 0.061 to 0.190 in Evergreen needleleaf forest, Evergreen broadleaf forest and Deciduous needleleaf forest; whereas, it is decreased from 0.448 to 0.439; 0.393 to 0.385 respectively.

3.4 Spatial pattern in EVI variability

Figure 4. and Figure 5 shows the spatial patterns in terms of percentage from 2001 to 2010 and 2010 to 2018 in interannual and seasonal EVI respectively over India's forests. From 2001 to 2010, large increase (>20%) and increase (5% to 20%) in EVI were observed in all major parts of India's forest; however, north east India experience decrease (-20% to -5%) to large decrease (<-20%) in EVI (Figure 4a). From 2010 to 2018, North east India experience improvement in EVI variations and shows large (5% to 20%) to large increase (>20%); however, middle India and south western forests shows minimum (-5% to 5%), decrease (-5 to -20%) and large decrease (>-20%) variations in EVI (Figure 4b). Similarly, a large (5% to 20%) and large decrease (>-20%) in EVI seasonal were observed in Northeast India from 2001 to 2010. However, from 2010 to 2018 northeast experience improvement in seasonal (spring and summer) EVI, as shown in Figure 5 d-e. Figure 5 e-f revealed that a large to a large decrease in EVI from 2010 to 2018 was observed in central to south-west India forest during summer and autumn season.

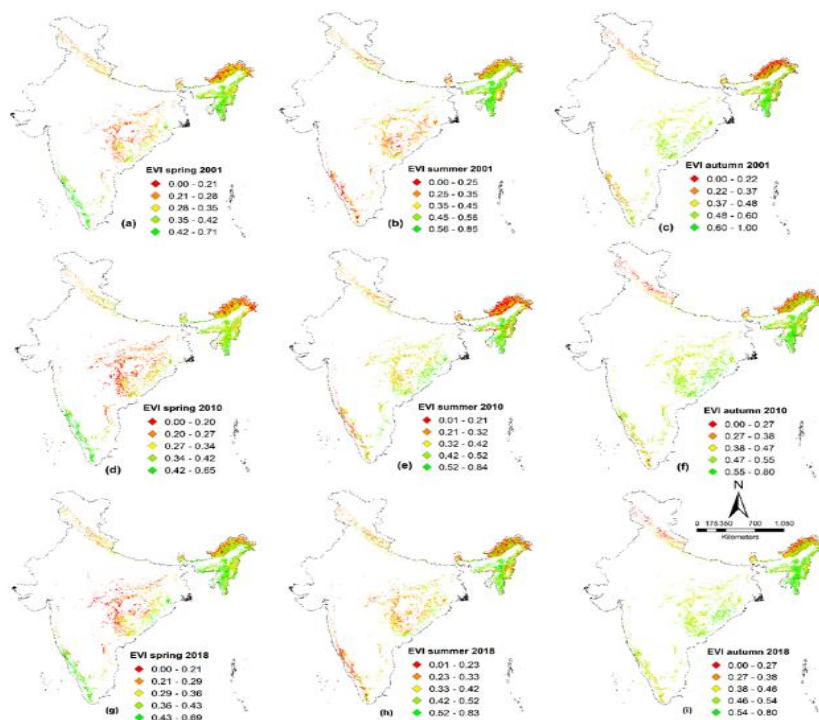


Figure 3. Seasonal (spring, summer and autumn) EVI in India’s forest for the year 200, 2010 and 2018

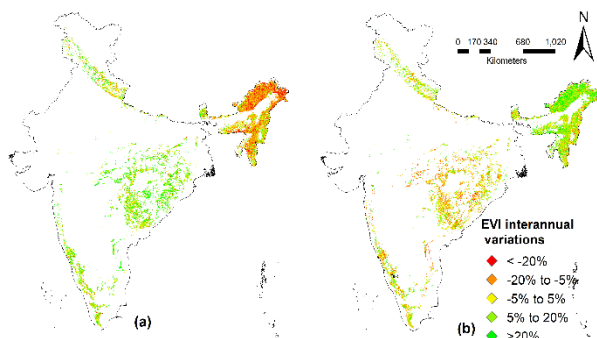


Figure 4. Spatial pattern of EVI variation (%) from 2001 to 2010 (a) and from 2010 to 2018 (b). evergreen needleleaf and evergreen broadleaf forests

CONCLUSION

This study attempted to assess the variations in India’s forest from 2001 to 2018. Web based platform Climate Engine has been useful in cloud computing of MODIS EVI data over whole of India while IBGP land cover data provides forest classification. Results revealed that total area under five forest types in 2001, 2010 and 2019 was 82766.43 sq. Km, 92172.61 sq. Km and 89387.05 sq. Km respectively. EVI decreased from 2001 to 2010; however, from 2010 to 2018 EVI was improved in Evergreen needleleaf forest and Evergreen broadleaf forest respectively. EVI in Deciduous needleleaf forest, Deciduous broadleaf forest, and Mixed forest increased from 2001 to 2018. In spring and

autumn, EVI was increased; however, in summer EVI was decreased from 2001 to 2018 in each forest type. Interannual variations from 2001 to 2010 reveals a decrease to large decrease in EVI in North east India; however, from 2010 to 2018 it improved and shows positive changes. Seasonal variations in SPATAIL EVI pattern reveals a negative change in North east India from 2001 to 2010 in spring and autumn season; however, experiences positive changes in from 2010 to 2018. In summer from 2010 to 2018, central parts shows negative variations in EVI. This assessment is significant to reveal the variations in forest type in India from 2001 to 2018. Further scope is to apply novel techniques and modelling approaches to assess a detailed analysis of variation sin Indian forests.

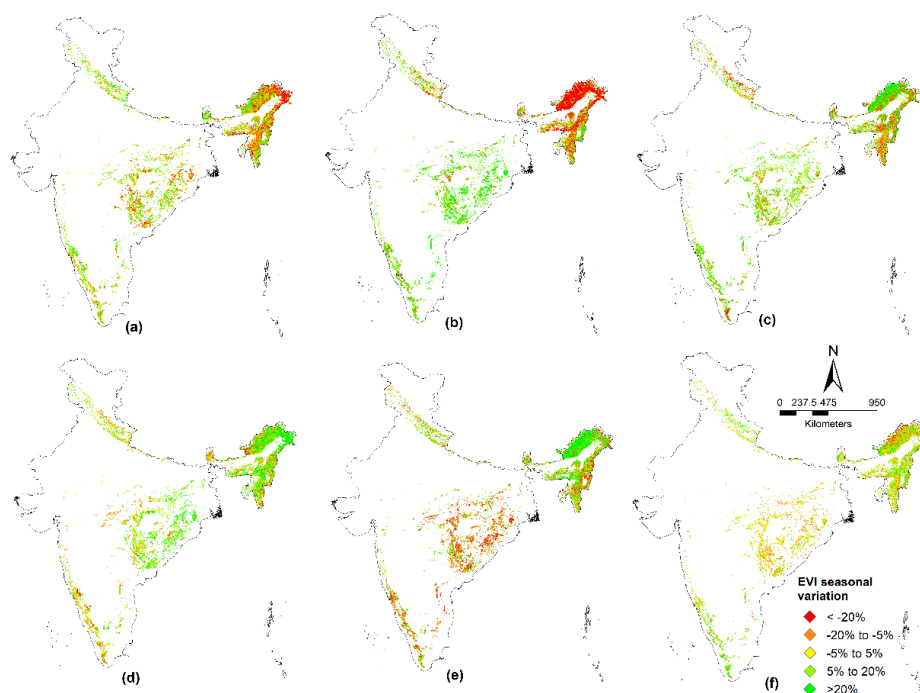


Figure 5. Spatial EVI variation (%) in spring (a), summer (b) and autumn (c) from 2001 to 2010 and spring (d), summer (e) and autumn (f) from 2010 to 2018

REFERENCES

- Didan, K., 2015. MOD13Q1 MODIS/Terra Vegetation Indices 16-Day L3 Global 250m SIN Grid V006. NASA EOSDIS Land Processes DAAC.
- Forest Survey of India, 2001. India State of Forest Report. Ministry of Environment, Forest & Climate Change, DehraDun, India.
- Forest Survey of India, 2019. India State of Forest Report. Ministry of Environment, Forest & Climate Change, DehraDun, India.
- Friedl, M. and Sulla-Menashe, D., 2019. MCD12Q1 MODIS/Terra+Aqua Land Cover Type Yearly L3 Global 500m SIN Grid V006. NASA EOSDIS Land Processes DAAC.
- <http://climateengine.org/> (10 February 2020)
- <https://earthdata.nasa.gov/> (10 February 2020)
- Huete, A. R., Liu, H. Q., Batchily, K., Van Leeuwen, W., 1997. A comparison of vegetation indices over a global set of TM images for EOS-MODIS. *Remote Sensing of Environment*, 59, 440-451.
- Huntington, J. L., Hegewisch, K. C., Daudert, B., Morton, C. G., Abatzoglou, J. T., McEvoy, D. J., Erickson, T., 2017. Climate Engine: Cloud Computing and Visualization of Climate and Remote Sensing Data for Advanced Natural Resource Monitoring and Process Understanding. *Bulletin of the American Meteorological Society*, 98 (11), 2397-2409.
- Jeganathan, C. and Nishant, N., 2014. Scrutinising MODIS and GIMMS vegetation indices for extracting growth rhythm of natural vegetation in India. *Journal of the Indian Society of Remote Sensing*, 42, 397-408.
- Liu, Z. L., Peng, C. H., Work, T., Candau, J. N., DesRochers, A. and Kneeshaw, D., 2018 Application of machine-learning methods in forest ecology: recent progress and future challenges. *Environmental Reviews*, 26, 339-350.
- Matsushita, B., Yang, W., Chen, J., Onda, Y. and Qiu, G. Y., 2007. Sensitivity of the Enhanced Vegetation Index (EVI) and Normalized Difference Vegetation Index (NDVI) to topographic effects: a case study in high density cypress forest. *Sensors*, 7 (11), 2636-2651.
- Reddy, C.S., Jha, C.S., Diwakar P.G., Dadhwal, V.K., 2015 Nationwide classification of forest types of India using remote sensing and GIS. *Environment Monitoring and Assessment*. 187 (12), 777.
- Setiawan, Y., Yoshino, K., Prasetyo, L. B., 2014 Characterizing the dynamics change of vegetation cover on tropical forestlands using 250 m multi-temporal MODIS EVI. *International Journal of Applied Earth Observation and Geoinformation*, 26, 132-144.
- Sun, A.Y., Scanlon, B.R., 2019. *Environmental Research Letters*, 14 073001.
- Xue, J. and Su, B., 2017. 2017. Significant remote sensing vegetation indices: A review of developments and applications. *Journal of Sensors*.
- Zhang, Q., Cheng, L. and Boutaba, R., 2010: Cloud computing: state-of-the-art and research challenges. *Journal of Internet Services and Applications*. 1, 7-18.

Coral Reef mapping using Sentinel-2 MSI Data in Poshitra and Pirotan Islands, Gulf of Kachchh, Gujarat

Foram Jadeja¹, Jalpa Jadeja¹, P. C. Mankodi², and Manik H. Kalubarme³

¹Department of Environmental Studies, Faculty of Science, The Maharaja Sayajirao University of Baroda, Gujarat-390002

²Department of Zoology, Faculty of Science, The Maharaja Sayajirao University of Baroda, Gujarat-390002

³Bhaskarcharya Institute for Space Applications and Geo-Informatics (BISAG), Department of Science & Technology, Government of Gujarat, Gandhinagar, India

Email: foramjadeja415@gmail.com and mhkalubarme@gmail.com

KEY WORDS: Coral Reef, Spectral Signature, Landuse-Landcover, Sentinel-2, Landsat, QGIS

ABSTRACT:

Coral reefs are important part of biodiversity (Plaisance *et al.*, 2011) that provide multiple natural resources and ecosystem services to human societies (Mumby *et al.*, 2011). Remote sensing is more practical way to monitor the change in health and coverage of the reef ecosystem covering larger area. Spectral signatures are generally used to monitor a direct response to relatively small changes in coral cover, across a range from low to high cover levels (Joyce *et al.*, 2013). In present study landuse maps of reef ecosystem of Poshitra and Pirotan Islands in Gulf of Kachchh were generated to identify the changes in total cover of coral reef area in last 20 years. The Sentinel-2 Digital data of the year 2019 and Landsat-5 Digital data of the year 1997-1998 were downloaded. The Land use maps of these Islands were prepared by on screen digitization of different landuse classes including coral reef and other coastal features. The digital numbers of each landuse class was extracted and plotted to study the spectral separability of corals and other landuse classes. Result of the study shows that the total area cover of corals area have been decreased during last 20 years in both the study sites. Which shows significant impact of different anthropogenic activities and natural phenomena Poshitra and Pirotan Island. The main aim of generating spectral signature of different classes is to differentiate corals from other classes. According to values generated from polygons of different classes shows that corals can be easily separated by spectral signatures.

1. INTRODUCION:

Coral reef are among the world's most important habitat and they provide home to many sea animals and supports the food web in aquatic ecosystem. Hard corals used to dominate the seascape of tropical reefs; but as coral reefs are extremely sensitive to the environmental conditions, they are often used as important indicators of climate change (Chaudhury *et al.*, 2014). Coral reefs flourish in tropical and subtropical clear waters within a narrow range of bio-physical environmental parameters (Cumings, 1932) like temperature, salinity, turbidity in reef region. Coral reef protection is a global concern now. Decrease in reef area are noted at many places because of the climate change and anthropogenic stress. Habitat mapping and environmental stress assessment by remote sensing, especially by satellites, is highly cost-effective (Mumby, P.J. *et al.*, 1999). Remote sensing covers the wider range which helps to detect the large scale changes. Thus, it is significant benefaction towards the protection of reef ecosystem. Techniques for analyzing remote sensing data have progressed vary rapidly and several studies has been done to monitor any survey coral reef using remote sensing techniques. Remote sensing sensors have been improved over the last 3 three decades and multispectral satellite sensors such as Landsat MSS and TM, Sentinel-2 have been used successfully in recent years in mapping and identifying different reef features using their spectral signatures. Remote sensing instruments in these satellites has ability to distinguish the reflectance spectra of different coastal classes like corals, algae, mangroves, mud, sand etc. Remote sensing studies take empirical measurements of spectra and seek wavelengths

which discriminate such benthic categories but benthic categories used in remote sensing sometimes consist of species groupings which are biologically or spectrally inappropriate (Hedley *et al.*, 2002) and difficult to distinguish separately.

2. STUDY AREA:

Among the World, reef covered area in India is estimated to be 2,375 sq. km and Andaman and Nicobar Islands has the highest reef covered area preceded by Lakshadweep, Gulf of Kachchh (GoK) and Gulf of Mannar (Saroj *et al.*, 2016). Coral formation within the Gulf of Kachchh is mainly confined to the southern shore of the gulf along the Jamnagar district. Amongst the 45 islands in Gulf of Kachchh, in all 42 islands, presence of coral reef has been reported. Most of the islands on Gulf of Kachchh has Fringing types of reefs but some of the islands in the Gulf of Kachchh are also formed as platform and patchy reef type. Gulf of Kachchh has the total reef covered area approximately 352.5 sq. km (Jayaprakas and Radhakrishnan, 2014). Poshitra and Pirotan Island from Gulf of Kachchh were selected as a study site in present study. Pirotan Island is situated at 22.60061 N Latitude and 69.95652 E Longitude; and Poshitra is located at 22.40191 N Latitude and 69.19914 E Longitude in Gulf of Kachchh. For further analysis, the satellite image with 3 km buffer from the center of site location was extracted.

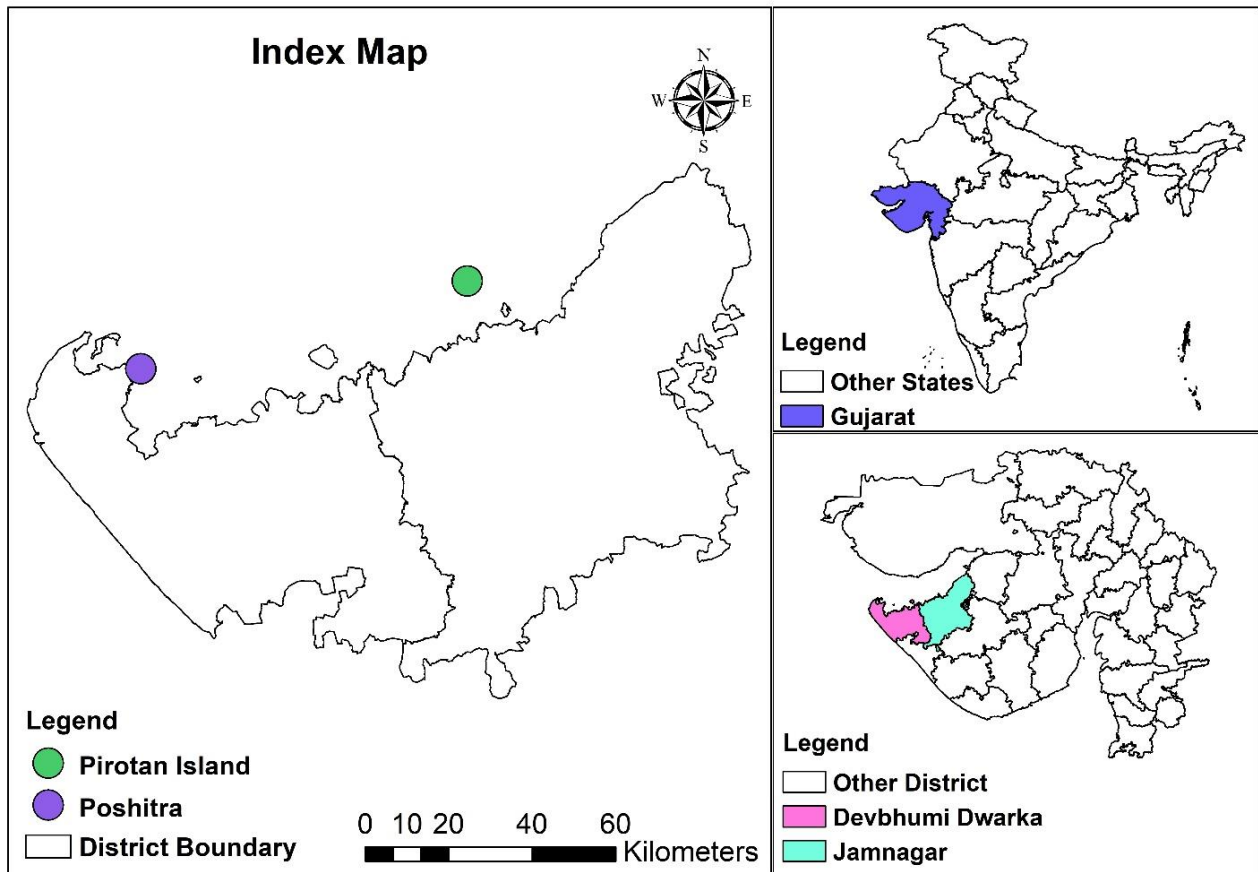


Figure:1- Index map of selected study site

3. MATERIALS AND METHODS:

3.1 TIDE DATA

Since coastal research is dependent on low tide visibility of reef, the data for low tide was collected from <https://tides4fishing.com> website and Satellite data were selected accordingly.

3.2 SATELLITE DATA

The Sentinel-2 Digital data of the year 2019 and Landsat-5 Digital data of the year 1997-1998 were downloaded from <https://earthexplorer.usgs.gov/>.

STUDY AREA	SATELLITE	SENSOR	RESOLUTION	DATE
POSHITRA	SENTINEL-2	MSI	10 m	24 APRIL,2019
	LANDSAT-5	TM	30 m	13 FEB, 1997
PIROTAN	SENTINEL-2	MSI	10 m	24 APRIL,2019
	LANDSAT-5	TM	30 m	14 APRIL,1998

Table:1- Details of Satellite Data

3.2 METHODOLOGY FOR DIGITIZATION AND GENERATION OF SPECTRAL SIGNATURE

In present study, free version of QGIS 3.10 software was used for processing the satellite images. For that False Color Composite (FCC) satellite images were generated using different band combinations. Area of interest with the buffer of 3 km were extracted from the processed FCC satellite image for further analysis. Different landuse-landcover classes of coastal area were identified from the FCC satellite image and on screen digitization of different coastal characteristics was done by generating polygons on coastal features including coral reef and other landuse classes. After that total area covered by different coastal classes were calculated for change detection in total area cover by coral reef. Digital values of different coastal classes of each band were converted into spectral signatures by measuring reflectance value of each band. For this process; Spectral signature of selected coastal features generated by statistical Mean values of different band using Statistic Zonal Calculation plugin in QGIS 3.10 and plotted to study the spectral separability of diverse coastal features.

4. RESULT AND DISCUSSION:

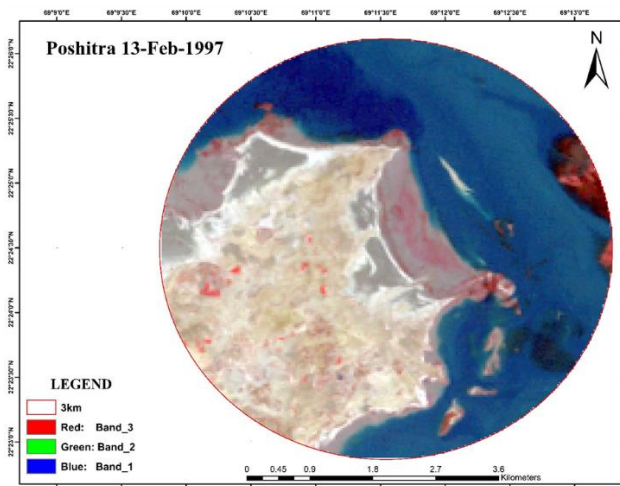


Figure:2- FCC image of Poshitra (13-02-1997)

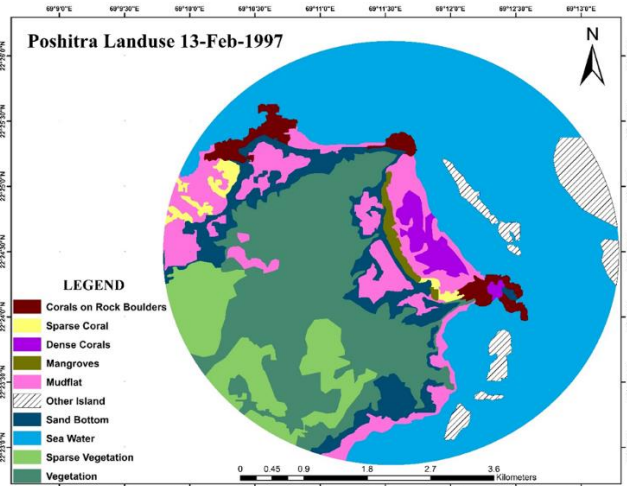


Figure:3- Landuse map of Poshitra (13-02-1997)

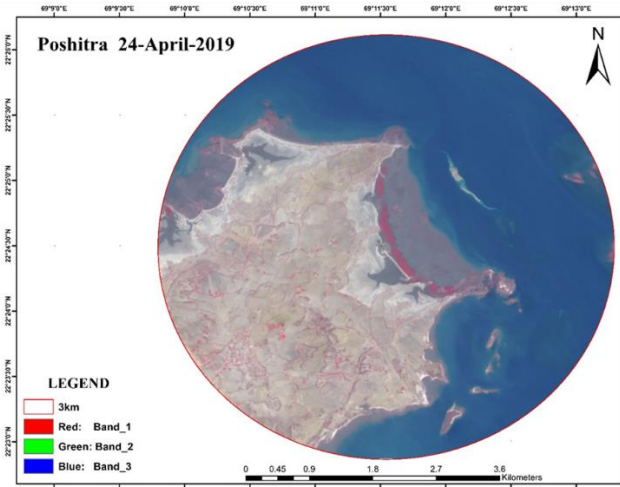


Figure:4- FCC image of Poshitra (24-04-2019)

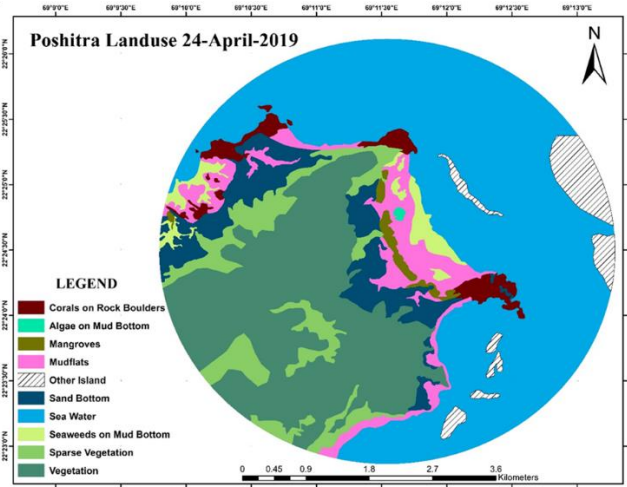


Figure:5- Landuse map of Poshitra (24-04-2019)

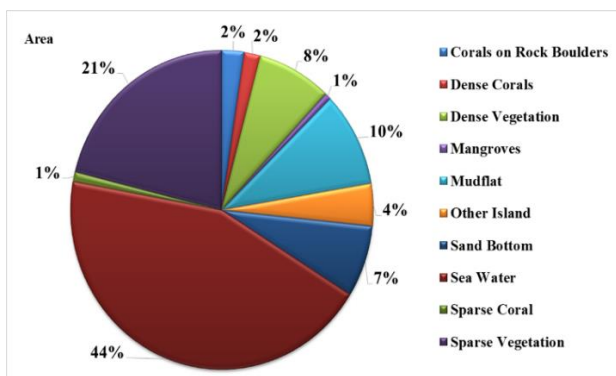


Figure:6- Area calculation of the year 1997

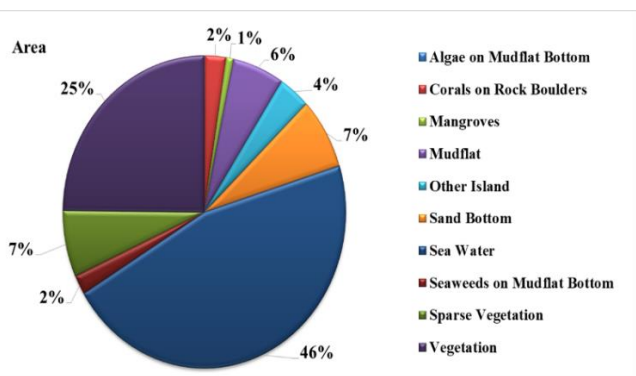


Figure:7- Area calculation of the year 2019

Different landuse-landcover classes of coastal area of Poshitra were identified from the FCC satellite image and on screen digitization of different coastal characteristics was done to generate the maps shown in figure-3 and figure-5. After that total area covered by different coastal classes were calculated for change detection in total area cover by coral reef in Poshitra. As per shown in figure-6 and figure-7, total area covered by corals has been decreased by 3% in Poshitra in last 20 years. Same in the case of mangroves also, total area coverage of their diversity has been decreased by 7% in last 20 years in Poshitra. All though Poshitra is much protected area when it comes to anthropogenic activities, decrease in the reef diversity shows environmental impacts of climate change in increase in temperature in past 20 years in Poshitra.

Polygon of different land-use classes were marked on the Sentinel-2 image and using Zonal Statistic plugin in QGIS. Different statistics like Mean, Standard Deviation, Minimum and Maximum values were generated in each spectral band. These Mean spectral value of each land-use class plotted for studying the spectral separability of different land-use classes in this area. As shown in figure-8. Class of corals on rock boulders has been identified separately from the other classes in each bands, and likewise corals, all the coastal features can identify separately by their spectral signatures. This result shows that, polygons generated on FCC image for particular classes, has been identified correctly for the particular classes.

Spectral Reflectance of Coastal Features of Poshitra

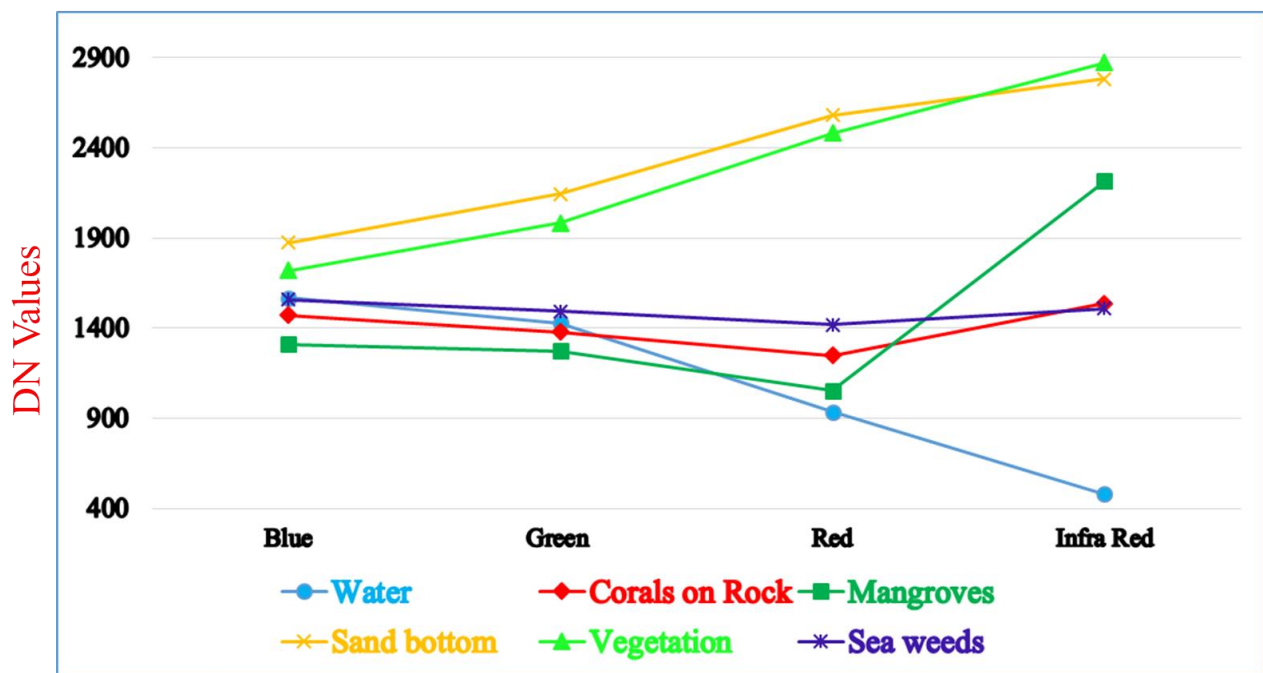


figure:8- Spectral Reflectance of Coastal Features of Poshitra

Same as Poshitra, Different landuse-landcover classes of coastal area of Pirotan Island were also identified from the FCC satellite image and on screen digitization of different coastal characteristics was done to generate the maps shown in figure-10 and figure-12. As per shown in figure-13 and figure-14, total area covered by corals has been decreased by 1% in Pirotan Island in last 20 years. And same as corals, no major change in total area cover of other reef features was recorded in Pirotan Island. And isolation of the Pirotan from the main land can be considered as one the main reason as anthropogenic activities are less there.

Polygon of different land-use classes were also generated for the Sentinel-2image of Pirotan Island also and different

statistics like Mean, Standard Deviation, and Minimum and Maximum values were generated in each spectral band. These Mean spectral value of each land-use class plotted to study the spectral separability of different land-use classes in this area. As shown in figure-15. Classes of corals on rocks and sparse corals can be identified separately from the other classes in each bands, and likewise corals, all the coastal features can identify separately by their spectral signatures. But, there is similarity in spectral reflectance of both classes of corals as there was no major change in these features in satellite image also. And thu, same as Poshitra, in satellite image of Pirotan Island also, polygons generated on FCC image for particular classes, has been identified correctly for the particular classes.

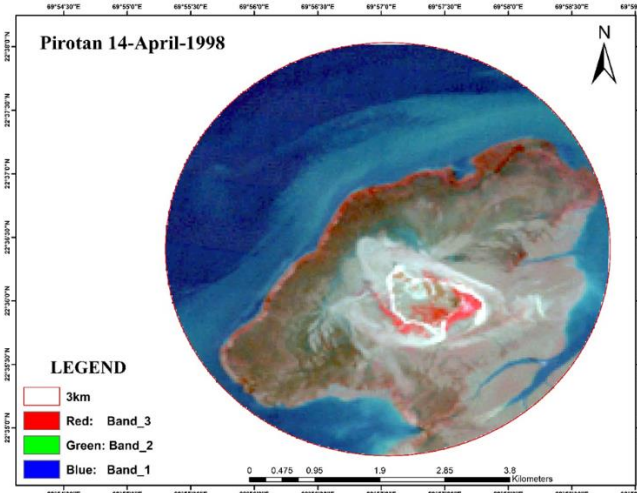


Figure:9- FCC image of Pirotan (14-04-1998)

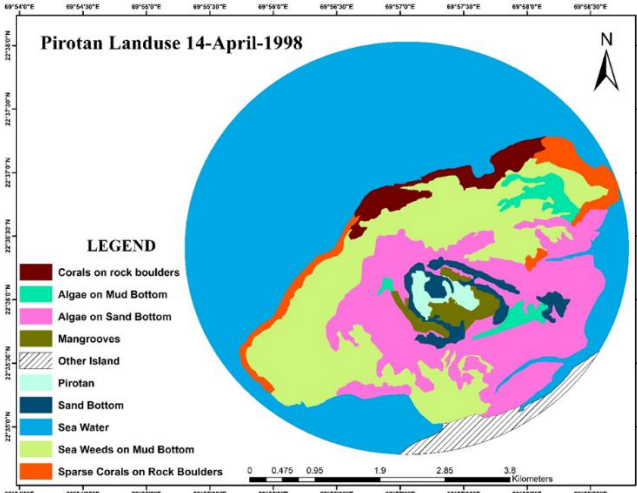


Figure:10- Landuse map of Pirotan (14-04-1998)

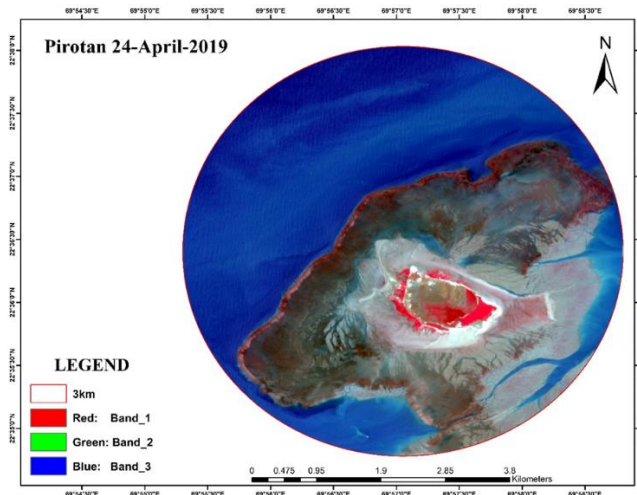


Figure:11- FCC image of Pirotan (24-04-2019)

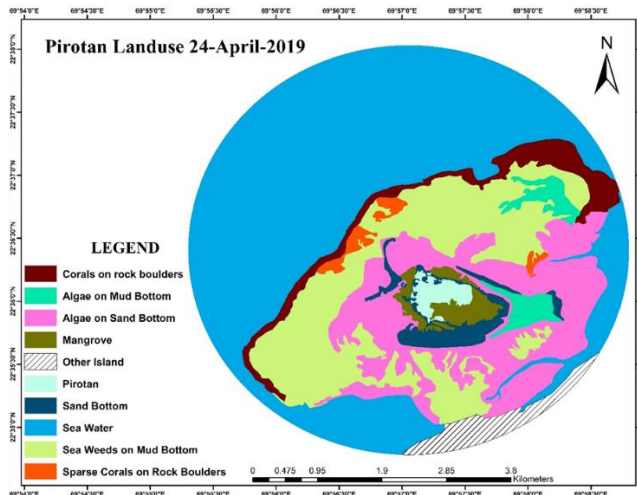


Figure:12- Landuse map of Pirotan (24-04-2019)

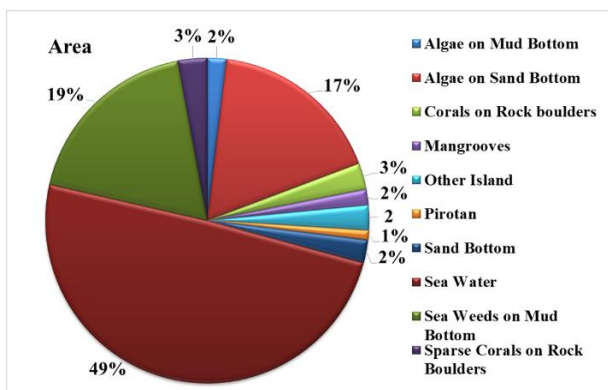


Figure:13- Area calculation of Pirotan Island (1998)

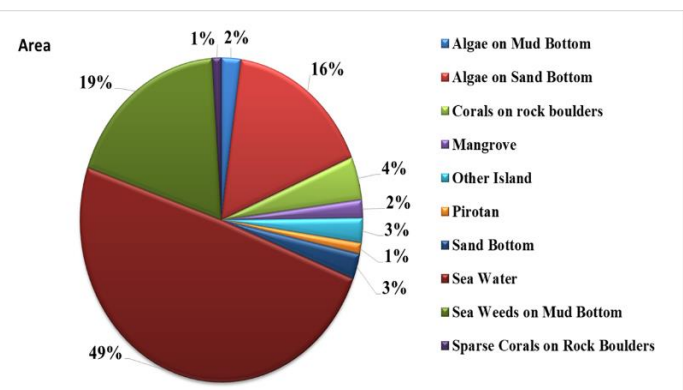


Figure:14- Area calculation of Pirotan Island (2019)

Spectral Reflectance of Coastal Features of Pirotan Island

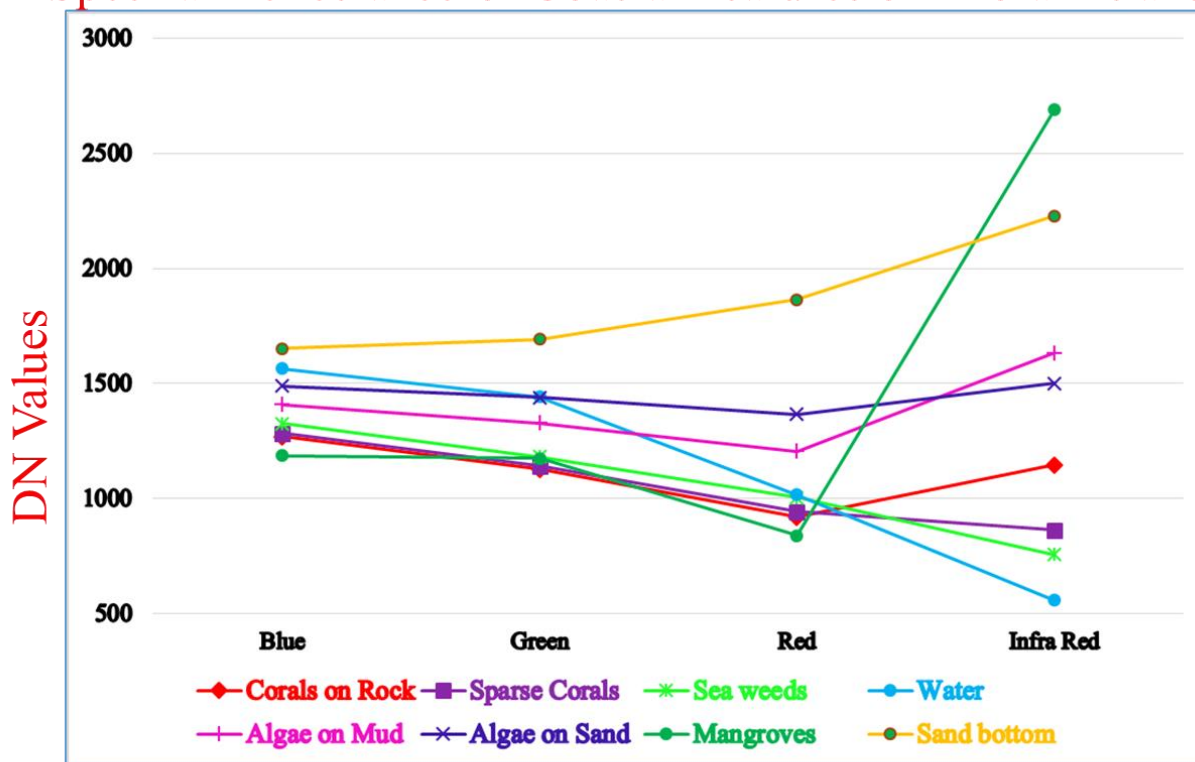


Figure:15- Spectral Reflectance of Coastal Features of Pirotan Island

5. CONCLUSION:

Present study indicates that all the coastal classes including corals can be separated distinctly by their spectral signatures in each spectral band. Thus it indicates that the spectral response of corals is quite distinct and corals can be identify and mapped uniquely using remote sensing satellite data.

6. REFERENCES:

- Chaudhury R.N. & Ajai, (2014). "Impact of Climate Change on Coral Reefs", Space Applications Centre, Indian Space Research Organisation, Ahmedabad, India.
- Cumings E. R., (1932). "Coral Reefs or Bioherms?" The Geological Society of America Bulletin 43 (1): 331-352.
- Goodman, J. A., Samuel, J. P., & Stuart, R. P. (2013). "Coral reef remote sensing". A guide for mapping, monitoring and management. 436p.
- Hedley, J.D., Roelfsema, C.M., Chollett, I., Harborne, A.R., Heron, S.F., Weeks, S., Skirving, W.J., Strong, A.E., Eakin, C.M., Christensen, T.R. and Ticzon, V., (2016). "Remote sensing of coral reefs for monitoring and management: a review". Remote Sensing, 8(2), p.118.
- Hedley, J. D., & Mumby, P. J. (2002). "Biological and remote sensing perspectives of pigmentation in coral reef organisms".
- Jayaprakas, V. and Radhakrishnan, R. (2014). "Indian coral reefs: diversity, anthropogenic influences and conservation measures". International Journal of Humanities, Arts, Medicine and Sciences. 2(4): 25-36.
- Joyce and Phinn (2013), "Spectral index development for mapping live coral cover". Journal of Applied Remote Sensing, Vol. 7, 073590-19.
- Mumby P.J., Elliott I.A., Eakin C.M., Skirving W., Paris C.B., Edwards H.J., Enriquez S., Iglesias-Prieto R., Cherubin L.M., Stevens J.R., (2011). "Reserve design for uncertain responses of coral reefs to climate change". Ecology Letters 14:132-140 DOI 10.1111/j.1461-0248.2010.01562.x.
- Mumby, P. J., Green, E. P., Edwards, A. J., & Clark, C. D. (1999). "The cost-effectiveness of remote sensing for tropical coastal resources assessment and management". *Journal of Environmental Management*, 55(3), 157-166.
- Plaisance L., Caley M.J., Brainard R.E., Knowlton N. (2011). "The diversity of coral reefs: what are we missing?" doi:10.1371/journal.pone.0025026.
- Saroj, J., Gautam, R. K., Joshi, A., & Tehseen, P. (2016). "Review of Coral Reefs of India: Distribution, Status, Research and Management". International Journal of Science, Environment and Technology, 5, 3088-3098.

7. ACKNOWLEDGEMENT:

I am sincerely thankful to T. P. Singh, Director of BISAG for giving me the opportunity to learn and do my dissertation work at this reputed institution. I am also thankful to the Head of the Department of Environmental Studies, Prof. K. D. Vachhrajani for giving me the permission to complete my work at BISAG.

VARIATION AND DISTRIBUTION OF TOTAL OZONE DURING TROPICAL CYCLONES AND THE EXCHANGE PROCESS

I. Kishore Kowtham¹ K. Srinivasa Raju¹ & D.Thirumalaivasan¹
¹Institute of Remote Sensing, Anna University, Chennai-25

KEY WORDS: Total Ozone, Tropical Cyclone, Tropopause variation

ABSTRACT:

The distribution of Total Ozone over the earth varies with location on timescales that range from daily to seasonal and the increase in the tropospheric ozone leads to the warming of earth surface. The exchange of gases in the atmosphere by the atmospheric ocean coupling possess a greater influence in the Total Ozone variation in the Indian region. Cyclonic storms are one of the influencing parameters for varying Total Ozone amounts. Several cases of cyclonic storms occurring over Bay of Bengal is deeply investigated and the columnar variation of Total Ozone is clearly observed. It is observed that during the mature phase of cyclone the tropopause height has shifted by 1 -2 km. The variation in the height of tropopause during severe cyclonic storm like Phailin, Hud Hud, Vardha and Fani shows Total Ozone decreases steadily before and during the formation of a Tropical cyclone. When the Tropical cyclone reaches its peak intensity indicated by its maximum wind speed, there is a sudden fall in Total Ozone concentrations over those regions where the Tropical cyclone has intensified. It is evident that Tropical cyclones play a predominant phase in modifying the tropopause structure and dynamics.

1. INTRODUCTION

The variation of Total Ozone Concentration and Rainfall over Different Stations of India using the IMD rainfall and ozone data for south west monsoon observed over Ahmedabad, Bangalore, Chennai, Delhi, Dumdum, and Pune was depicted by Midya (2011). The ozone data were directly compared with the IMD rainfall data corresponding to the IMD station locations and their variation in the particular region is analysed. Depletion of ozone concentration effects rainfall. For all stations we have considered rainfall increases and ozone decreases with the increase of time. Rain occurs only when ozone concentration lies in a certain concentration level. The magnitude and spatial distribution of the El Niño Southern Oscillation (ENSO) influence on tropospheric column ozone (TCO) into the middle latitudes were investigated by Olsen et al. (2016) using NASA's GEOS-5 data assimilation system (DAS), ingesting data from the Ozone Monitoring Instrument (OMI) and MLS over middle latitudes. The ozone data and assimilation with information on ancillary data sets used and the linear regression analysis used in this study. The study provides the first explicit spatially resolved characterization of the ENSO influence and demonstrates coherent patterns and teleconnections impacting the TCO in the extra tropics. The sensitivity maxima and minima coincide with anomalous anti-cyclonic and cyclonic circulations where the associated vertical transport is consistent with the sign of the sensitivity.

The tropospheric ozone variability study is carried out by Kulkarni et al. (2011) investigated the spatial and temporal distribution over the coastline of the Indian peninsula and adjacent land and sea using NASA Langley Tropospheric Ozone Residual data set for the period 1979–2005 over the coastline of the Indian peninsula and adjacent land and sea. The NASA Langley Tropospheric Ozone Residual data set are visualised for the seasonal and monthly changes. A strong seasonal cycle has been observed with large variation (~ 55%) over the upper eastern coast, followed by the upper and lower western coast, compared to the lower eastern coast (~ 33%). A negative gradient in ozone concentration is observed along eastern and western coasts during summer (slope ~ -0.78 and -0.65) and a positive gradient (slope ~ 0.16 and 0.21) during winter. The same is observed over the adjacent land and sea along the coastline with slight variation. This change in gradient can be attributed to the anthropogenic emission of precursor gases that reinforce localized photochemical production of ozone. In addition,

topography, transport, seasonality of emission of precursor gases and the solar insolation cycle play a vital role.

The response of tropical tropospheric ozone to ENSO were characterized by Oman et al. (2011) using Ozone Monitoring Instrument (OMI) and the Microwave Limb Sounder (MLS) for six years for the entire global cover.

2. CYCLONIC VARIATIONS

Cyclonic storms are one of the parameters influencing Total Ozone amounts. Some of the intense cyclone and the corresponding Total Ozone variations were studied.

2.1 Phailin

A Very Severe Cyclonic Storm (VSCS) PHAILIN originated from a remnant cyclonic circulation from the South China Sea. The cyclonic circulation lay as a low pressure area over the Tenasserim coast on 6th October 2013. It lay over north Andaman Sea as a well-marked low pressure area on 7th October. It concentrated into a depression over the same region on 8th October near latitude 12.00N and longitude 96.00 E. Moving west-north westwards, it intensified into a deep depression on 9th morning and further into cyclonic storm (CS), 'PHAILIN' in the same day evening. Moving north westwards, it further intensified into a severe cyclonic storm (SCS) in the morning and into a VSCS in the forenoon of 10th October over east central Bay of Bengal. The VSCS, PHAILIN crossed Odisha & adjoining north Andhra Pradesh coast near Gopalpur (Odisha) around 2230 hrs. IST of 12th October 2013 (Figure 1) with a sustained maximum surface wind speed gusting to 220 kmph. (Source: IMD)

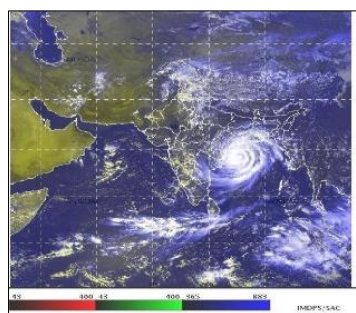


Figure 1 Position of Tropical Cyclone - Phailin (12.10.2013 08.30Z) Source: MOSDAC Geo-server Archival

The Total ozone anomaly over India before and after the passage of Tropical cyclone Phailin is shown in Figure 2 (a – c).

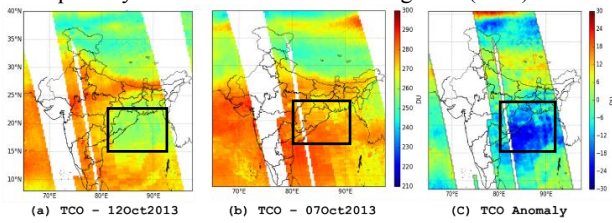


Figure 2 Variation in Total Column Ozone (TCO) and its corresponding anomaly

From Figure 2 (a) to (c) it is observed that the amount of Total Column Ozone (TCO) decreases during the cyclonic period. The total column ozone on 07 Oct 2013, (figure 2 (b)) shows an increase in the concentration of ozone in the region indicated. But during the day of landfall i.e. on 12 Oct 2013 there is a considerably decrease in the amount of ozone near the point of landfall as seen in figure 2 (a). From the Total Ozone anomaly shown in figure 2(c) it is observed that the amount of ozone has almost decreases by 30 DU during the time of cyclone. A graph showing the variation of TCO at 17.5°N, 85°E before and after the landfall of phailin cyclone is shown in Figure 3.

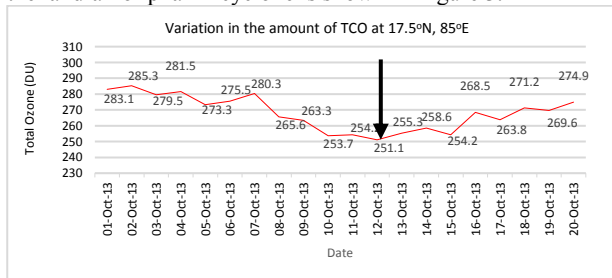


Figure 3. Variation in the amount of TCO at 17.5°N, 85°E

It is evident from the total column ozone time series shown in figure 3, the amount of TCO has been reduced considerably during the day of landfall on 12 October 2013. Similar variation in the reduction TCO amount occurs along the path of the cyclone, but the variation is also influenced by the intensity of cyclone.

2.2 Hudhud

HUDHUD (7 to 14 October 2014) was even more intense than PHAILIN with wind speeds in excess of 180 kpmh recorded over the west central Bay of Bengal along Andhra Pradesh coast. It crossed northern coast of Andhra Pradesh at Visakhapatnam (VSK) between 1200 and 1300 hr on 12 October 2014 with the same wind speed (IMD report 2013 and 2014). During high intensity of cyclones on 11 October 2014 represented in figure 4 over Bay of Bengal. A VSCS developed from a low-pressure area over the Tenasserim coast and adjoining North Andaman Sea in the morning of 6 October 2014.

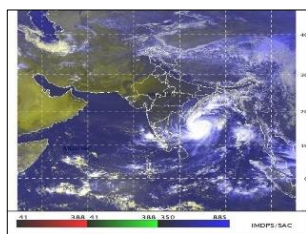


Figure 4. Position of Tropical Cyclone - Hudhud (11.10.2014 08.30Z) Source: MOSDAC Geo-server Archival

The low-pressure system concentrated into a depression in the morning of 7 October 2014 over the North Andaman Sea and further intensified into a CS in the morning of 8 October 2014. It moved further into Bay of Bengal and continued to move west-by north-westwards. It continued to intensify while moving north-westward and reached maximum intensity. (Source: IMD)

The variation in the ozone for the particular day during the cyclone is represented in the following Figure 5 (a) to (c).

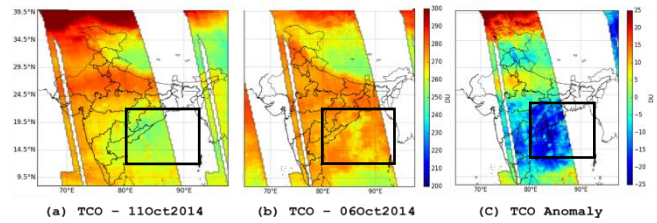


Figure 5. Variation in Total column ozone and its corresponding anomaly -Hudhud

It is observed from figure 5 (a) to (c) that the amount of Total Ozone decreases during the passage of cyclone. Figure 5 (b) shows an increase in the concentration of total column ozone on 06 Oct 2014 in the region indicated. But on 11 Oct 2014 there is a considerably decrease in the amount of ozone near the point of landfall as seen in figure 5 (a). From the Total Ozone anomaly shown in figure 4.42(c) it is observed that the amount of ozone has almost decreases by 15 DU during the time of cyclone. A graph showing the variation in the amount of TCO at 17.5°N, 82.5°E near Vishakhapatnam before and after the landfall of Hudhud cyclone is shown in figure 6.

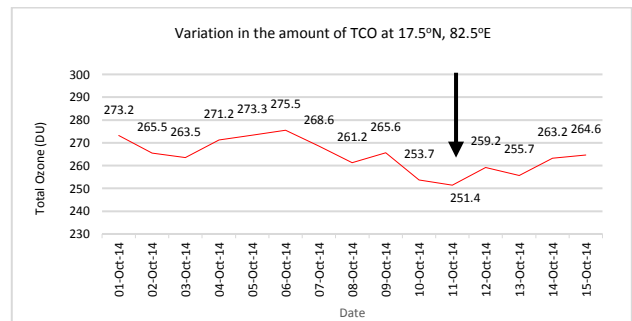


Figure 6. Variation in the amount of TCO at 17.5°N, 85°E

From the total column ozone time series shown in figure 6, it is identified that the amount of TCO has been considerably reduced during the day of landfall on 11 October, 2014.

2.3 Fani

Fani made landfall in Odisha at about 8 a.m. local time on Friday morning, May 3. Fani's sustained winds were estimated near 108 knots (125 mph/201 kph) at the time of landfall. Fani is the strongest cyclone to hit India's coast since a storm in 1999. Fani's center was located near 21.8 degrees north latitude and 86.6 degrees east longitude. It was centered about 145 nautical miles west-southwest of Kolkata, India. Fani has tracked north-northeastward. At that time, Fani's maximum sustained winds had dropped to 70 knots (80 mph/130) making it the equivalent of a Category 1 hurricane on the Saffir-Simpson Hurricane Wind Scale and as in IMD as Extremely severe cyclonic storm.



Figure 7. Position of Tropical Cyclone - Fani (02.05.2019 08.30Z)

It is evident from the total column ozone time series shown in Figure 8, the amount of TCO has been reduced considerably during the day of landfall on 12 October 2013. Similar variation in the reduction TCO amount occurs along the path of the cyclone, but the variation is also influenced by the intensity of cyclone.

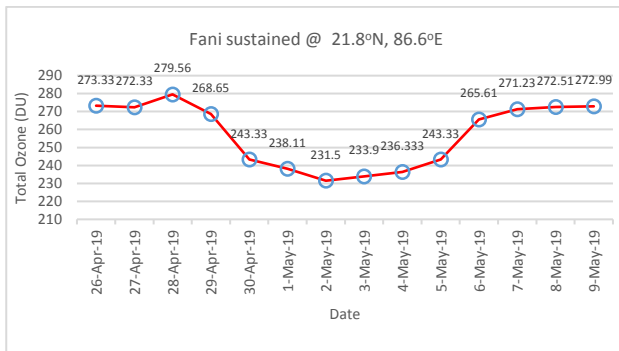


Figure 8. Variation in the amount of TCO at 21.8°N, 86.6°E

3 EXCHANGE PROCESS

The variation in the Total Ozone is attributed by the tropopause height variation, which is mainly due to the pushing of the convective clouds to the upper troposphere during cyclone.

From the analysis, it is concluded that TCO decreases steadily before and during the formation of a cyclone, followed by a more or less increasing trend after dissipation of the cyclone. It is also observed that, when the cyclone reaches its peak intensity indicated by its maximum wind speed, there is a sudden fall in TCO over those regions where the cyclone has intensified.

The shift in Tropopause is well identified depending on the intensity of cyclone. The Tropopause is the point where the temperature inversion occurs. From the point of inversion the tropopause is identified, which ultimately gives the point of exchange. The tropical tropopause is situated around 100 hPa and the extratropical tropopause between 200 and 300 hPa levels. Over 30°N and adjoining latitudes, the tropical tropopause lies above the extratropical tropopause and a break region exist between them, which is the tropopause break.

It is observed that during the mature phase of cyclone the tropopause height has shifted by 1 -2 km upward shown in figure 9 (a).

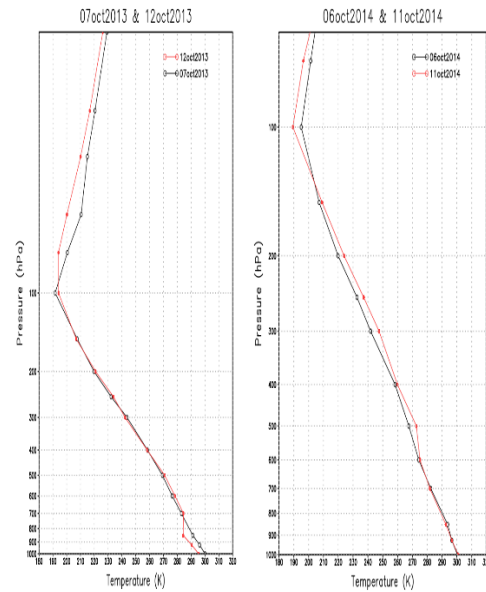


Figure 9. Tropopause variation as temperature profile. The amount of decrease in columnar ozone for both tropical cyclone Phailin and Hudhud is shown in Figure 9(a) and (b).

4. CONCLUSION

The anomalies over the cyclonic region has been identified in the years of observation and the corresponding synoptic conditions causing the variation are studied. The study on cyclonic events has shown that variation in ozone is having relation with cyclone intensity with a decrease of almost 50DU in case of the Phailin cyclone (highest intensity cyclone) has been studied. The lowering of Tropopause has attributed to the phase shift in the stratospheric exchange process.

REFERENCES

Elsner JB, Jagger TH, Dickinson M, Rowe D (2008) Improving multiseason forecasts of North Atlantic hurricane activity. *J Clim* 21:1209–1219

Meena G.S. and Patil S.D. (2011), 'Variation of total column ozone along the monsoon trough region over north India', *International Journal of Remote Sensing*, Vol.32, No.9, pp. 2581–2590.

Midya S.K. (2011), 'Variation of Total Ozone Concentration and Rainfall over Different Stations of India', *Pacific Journal of Science and Technology*, Vol.12, pp.580–590.

Oltmans S.J., Lefohn A.S., Shadwick D., Harris J.M., Scheel H.E., Galbally +I., Tarasick D.W. (2013), 'Recent Tropospheric Ozone Changes — A Pattern Dominated Growth', *Atmospheric Environment Journal*, Vol.67, pp. 331–351.

Oman L. D., Ziemke J. R., Douglass A. R., Waugh D. W., Lang C, Rodriguez J. M., and Nielsen J.E. (2011), The response of tropical tropospheric ozone to ENSO, *Geophysical Research Letters*, Vol. 38, No.13, pp.273 - 287

Pavan S. Kulkarni, Sachin D. Ghude, S. L. Jain, B. C. Arya, P. K. Dubey, and Shahnawaz (2011), 'Tropospheric ozone variability over the Indian coastline and adjacent land and sea'. *Intl. Journal of Remote Sensing* Vol. 32, No. 6, pp.13-21.

Singh D, Singh V (2007) Impact of tropical cyclone on total ozone measured by TOMS-EP over the Indian region. *Curr Sci*. 93(4):471–476.

TIME SERIES GRIDDED PRECIPITATION PREDICTION USING LONG SHORT-TERM MEMORY (LSTM) MODEL

Manaruchi Mohapatra^{1*}, Bhaskar R Nikam², Praveen K Thakur², S P Aggarwal³, Antony Joh Moothedan¹

¹ Student, Master of technology, Water Resources Department, Indian Institute of Remote Sensing, Dehradun, India

² Scientist/Engineer-'SF', Water Resources Department, Indian Institute of Remote Sensing, Dehradun, India

³ Group head, Water Resources Department, Indian Institute of Remote Sensing, Dehradun, India

*Corresponding author mail: manaruchimohapatra@gmail.com

KEY WORDS: LSTM, Precipitation forecasting, RNN, rainfall trend analysis, ERA-5

ABSTRACT:

Quantitative prediction of precipitation has a very important role in flood and drought forecasting, early disaster warning system and other hydro-meteorological processes. The current study proposes a Long Short-Term Model (LSTM) based on Recurrent Neural Networks (RNN) as an alternative to the computationally expensive physical models to predict precipitation information. In this study, daily ERA5 0.250 precipitation data from European Centre for Medium-Range Weather Forecasts (ECMWF) for the period of 1979- 2019 was used over Uttarakhand state of India. The model was structured and trained using precipitation data from 1979-2004 as the training set and data from 2005-2019 as the validation set. The model was tuned using simple grid search which selects the best combination ensuring higher accuracy. The validation of model output against the validation set showed a high agreement of the model with the available precipitation data. The daily precipitation forecast for first six months of the year 2020 was generated using the model. The work indicates the scope of application of Artificial Intelligence techniques in the field of hydro-meteorological variables prediction.

1. INTRODUCTION

1.1 Background

Precipitation, an important component of the water cycle is pivotal to all the meteorological phenomena that are observed in the global system. It directly influences the natural processes, water resources, agriculture and the overall survival of the flora and fauna of the ecosystem. In India, rainfall directly affects the livelihood of the population in terms of fresh water availability and food production. (Kumaret al., 2010) In the current scenario of change in global temperature trend due to climate change, the changing pattern of rainfall deserves urgent and systematic attention. The global average precipitation is projected to increase, but both increases and decreases are expected at the regional and continental scales (Dore, 2005). Higher or lower rainfall, or changes in its spatial and seasonal distribution would influence the spatial and temporal distribution of runoff, soil moisture and groundwater reserves, and would affect the frequency of droughts and floods. According to the Intergovernmental Panel on Climate Change (IPCC, 2018), the change in climate is likely to affect food production, increase the risk of hunger and water scarcity, and rapid melting of glaciers. Freshwater availability in many river basins in India is likely to decrease due to climate change (Gosainet al., 2006).

In India, precipitation is generally measured and monitored using the ground observation stations. However, in most parts of the world the distribution and density of meteorological stations is insufficient to obtain reliable spatial and temporal information (Brown et al., 2008). The high requirement of time and cost for data preparation, processing and chances of error also poses a question to the usability of such data. In this context, satellite based precipitation information has been widely used in recent years due to its low cost, temporal and synoptic availability of data and reliability (Dutta et al., 2015). Remotely sensed precipitation data from Tropical Rainfall Measuring

Mission (TRMM) and Global Precipitation Measurement (GPM), model derived and reanalysis data from ERA-Interim, ERA-5 and Precipitation Estimation from Remotely Sensed Information using Artificial Neural Networks- Climate Data Record (PERSIANN-CDR) are widely used for hydrological modelling, flood and drought monitoring studies.

The prediction of rainfall has been a matter of serious concern and challenge for the governmental bodies, risk management organisations and scientific community as precipitation is crucial for obtaining knowledge of the atmospheric condition. The smaller dynamic nuances involved in the complex precipitation phenomenon makes the prediction task more difficult. In order to address the problem, weather prediction models have been developed which consider the dynamic behaviour of precipitation in accordance with other variables and water balance components using complex numerical and computational methods (Borderies et al., 2019; Flores, 2019; Silvestro et al., 2019; Yuet al., 2019). These models come under a common scheme called Predictive Analytics (PA) which performs forecasting and predictions of future events by analysing the past datasets. Such models are very powerful but require many parameter arguments in its function and are very resource intensive. The uncertainties involved in each step of the model are likely to magnify and propagate towards the final output. In order to make correct predictions, further data assimilation steps are used in order to obtain a proper estimate by updating the current model state with increases the complexity involved. With the advent of machine and deep learning techniques and the availability of cheap processing power options, advanced time series analytics and recurrent models has been used by researchers for the prediction of different climate variables (Akbariet al., 2018; Chen et al., 2015; Kim et al., 2017; Kumaret al., 2019; Salman et al., 2018; Xingjian et al., 2015). Such models require less input data and processing power compared to the complex weather prediction models and can generate forecasts with optimum accuracy. Deep

learning models have the ability to accept raw data and automatically discover the structure of data via a successive layer representation, and layers contribute in the formation of the model; referred to as hierarchical representation learning.

1.2 Long Short-Term Memory (LSTM) models for time series forecasting

Time series prediction or forecasting problem is a difficult predictive modelling problem as time series adds the complexity of a sequence dependence to be considered among the input variables. The Long Short-Term Memory (LSTM) network model is a Recurrent Neural Network (RNN) network widely used in deep learning paradigm for sequence related problems such as language models, speech recognition, auto-correct and time series data analysis (Duet *et al.*, 2015; Gregoret *et al.*, 2015; Mikolov *et al.*, 2011; Mikolov & Zweig, 2012). LSTM are widely used for time series forecasting as the models are easy to train using Backpropagation through time (BPTT) and the models converge faster along with solving the problem of vanishing and exploding gradients (Cai & Liu, 2016). The LSTM networks have interconnected memory blocks instead of neurons as in case of Artificial Neural Networks (ANN). The blocks are termed to be “smarter” than a classical neuron as the state of each sequence iteration is saved and managed using gates such as forget gate, input gate and output gate. A block operates upon an input sequence and each gate within a block uses the sigmoid activation units to control whether they are triggered or not, making the change of state and addition of information flowing through the block conditional. Figure 1 shows the basic architecture of a single LSTM memory block along with the gates.

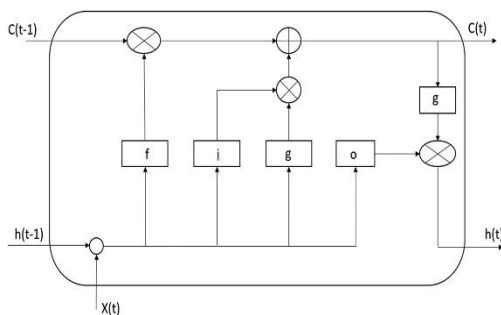


Figure 1: Basic architecture of a single LSTM memory block (Source: Kumar *et al.*, 2019)

The forget gate (f) describes how much of the previous state (h_{t-1}) is allowed to pass through, and the input gate (i) tells how much newly calculated state for the present input x_t to let in, whereas the output gate (o) determines the internal state needed to expose to the next layer. The internal hidden state of the memory cell (g) is calculated based on the current input x_t and the prior hidden state h_{t-1} . A point to note here is that g is similar to S of the RNN model, but differs only in its output by the output gate of i in order to calculate the carry state c_t at the current step t considering the previous carry state (c_{t-1}). Thereafter it multiplies by the forget gate and multiplication of gates g and i . The forget gate basically combines the previous memory and new input, and the hidden state h_t is calculated after the multiplication of output gate (o) and carry state (c_t).

The time series forecasting problems using LSTM models can be approached in configurations such as (a) univariate models (vanilla, stacked, bidirectional, CNNLSTM, ConvLSTM), (b) multivariate models (multiple input series based models, multiple parallel series based models), (c) multi-step models (vector output model, encoder-decoder based models) and (d) multivariate multistep models. Many researchers have used LSTM for rainfall forecasting by convolutional LSTM approaches (Xingjian *et al.*, 2015), deep belief network approaches (Ha *et al.*, 2016) and stacked auto-encoder approaches (Saha *et al.*, 2017) etc. The current work uses a univariate LSTM model as for each timestep, only precipitation estimates are considered for the future precipitation forecasting.

2. STUDY AREA AND DATASETS

Daily precipitation composites of ERA 5 meteorological data from ECMWF in a resolution 0.25^0 over Uttarakhand state for the time period of 1979-2019 was used as the training and validation set for the LSTM model. The mean monthly precipitation time series of the study area is shown in figure 2.

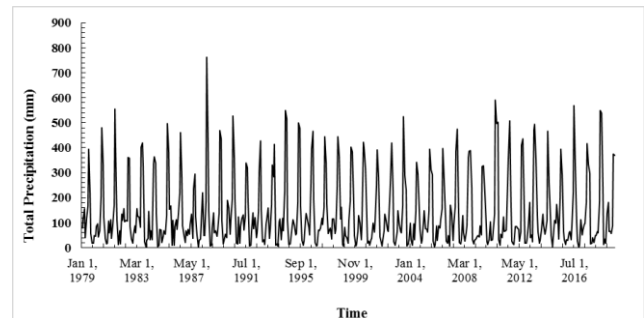


Figure 2: Mean monthly precipitation (mm) time series over Uttarakhand state

3. MODEL DEVELOPMENT

The proposed LSTM model was constructed using an input LSTM layer, a series of LSTM intermediate layers and a final output dense layer to aggregate the values of the units in the previous step. The intermediate number of neurons was kept as a variable to be tuned to provide optimum results after validation. The number of units present in each of the LSTM layer and the dropout rate for regularization was also taken as the variables to be tuned. The models were built using Keras library which is a high level library by Google for developing deep learning models with Tensorflow as backend.

One of the major problems occurring in modelling of hydrological time series, especially with rainfall, is to determine the random component. Therefore, daily rainfall data were chosen as the random component to build the models and to validate upon. To prepare the input dataset, for each prediction a specific previous time period data was taken. As the selected time period may affect the performance of the model, the value of the same was also kept as a variable subjected to fine tuning by simple grid search. In the simple grid search approach values of control parameters of RNNs and LSTM were selected initially, and thereafter varied in trials till the best fitness measures were

produced. To investigate the performance of the proposed LSTM models, four statistical indicators – root mean square error (RMSE), correlation coefficient (R), Nash-Sutcliffe efficiency coefficient (NSE) and mean absolute error (MAE) – were used. For the current work, total 7000 combinations were tested to determine the best model configuration.

The final model structured after the hyperparameter tuning was then used to predict precipitation values for next 6 months (January 2020 to June 2020). The model was finally implemented on all the pixels of the precipitation gridded data in order to generate precipitation prediction rasters.

4. RESULTS

4.1 Input data preparation

The input data was prepared using precipitation time series data extracted from a particular pixel considering it as a station. A sample time series data is shown in Figure 3. The data arrays were normalised and reshaped to Keras standards and two datasets were created: (a) training dataset (precipitation data for period 1979-2004) and (b) validation dataset (precipitation data for period 2005-2019). Each training set data contained the past n days data and the $n+1$ th data. The $n+1$ th data value was trained to be predicted using the last n data points.

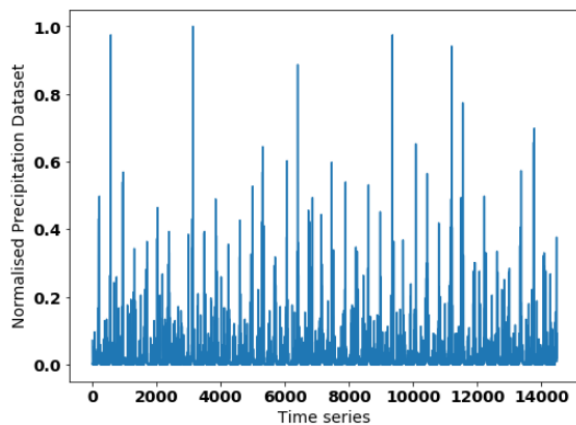


Figure 3: Sample normalised precipitation time series data

4.2 Model architecture

A preliminary sequential LSTM model was structured using Keras library and the model was compiled with Adam optimization and MSE as the loss function. A schematic of the model is shown in figure 4. In order to address the problem of over-fitting, regularisation was done by implementing dropout after each layer except for the output dense layer. The fraction of the dropout rate would be decided using hyperparameter tuning.

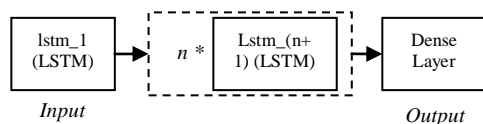


Figure 4: Schematics of the most basic LSTM where n is the number of LSTM layers to be decided in hyperparameter tuning

4.3 Hyperparameter tuning

To ensure the optimum performance of the model, the best combination of the following parameters were chosen: (a) timesteps for prediction, (b) dropout rate, (c) batch size, (d) number of intermediate LSTM layers and (e) number of units in each layer. Using simple grid search approach, each of the combination were tested and the accuracy against the validation dataset in terms of RMSE, R, NSE, MAE was calculated. The combination providing best accuracy was automatically selected for the final implementation. The same procedure was followed for each pixel of the gridded data to structure models with different configurations for different pixels which gave the most accurate results. The prediction against the test or validation dataset with an initial model with a best configuration model after grid search is shown in figure 5 which shows higher agreement of both the datasets.

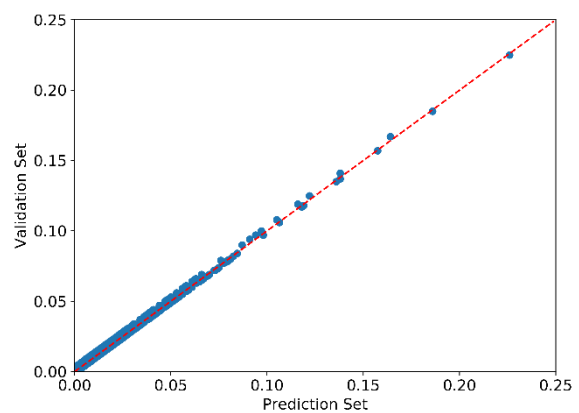


Figure 5: Scatter plot of prediction against the test or validation dataset with an initial model with a best configuration model after grid search

4.4 Final Implementation

The final model was implemented on all the pixels of the gridded precipitation raster after the automated hyperparameter tuning to ensure for each pixel, only the best predictions were estimated. The coefficient of correlation for the gridded data prediction is show in figure 6. The predicted precipitation for 2nd March, 2020 is shown in figure 7.

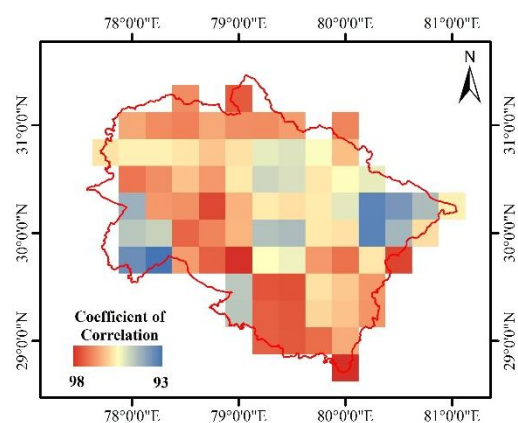


Figure 6: Coefficient of correlation associated with each pixel after the implementation of LSTM model

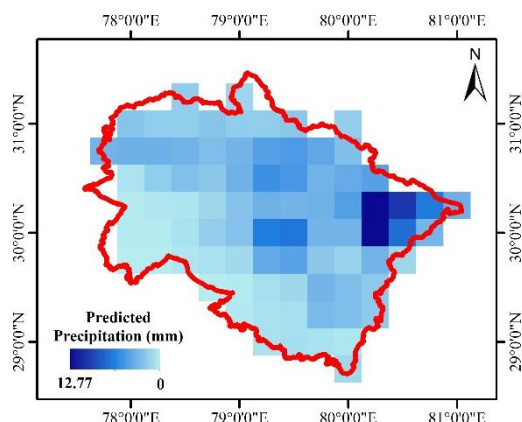


Figure 7: Predicted gridded precipitation data of 2nd March, 2020

5. CONCLUSION

The proposed tuned LSTM model was able to correctly predict the precipitation data for the validation period with an average correlation of 95%. The reason of the higher accuracy given by the model is due to the updating algorithm called Back Propagation Through Time (BPTT) which works well for time series data with complex variations. However, the model can be improved by integrating multiple variables and implementing more robust architecture. The model can be further used for long term prediction of other climate variables as well with appropriate structuring and parameter tuning. The model can be also automated using technologies such as Travis CI to generate daily forecasts along with data assimilation approaches which will enable the user to obtain best estimate of the precipitation values. The source code has been hosted at <https://github.com/manaruchi> to be used by interested readers and improvements of the model by the community is encouraged.

ACKNOWLEDGEMENTS

The authors would like to thank Dr. Prakash Chahuan, Director, Indian Institute of Remote Sensing (IIRS), Dehradun for providing a state-of-art research platform and support as and when required. The author would also like to acknowledge the direct and indirect support of the members of Water Resources Lab at IIRS.

REFERENCES

Akbari Asanjan, A., Yang, T., Hsu, K., Sorooshian, S., Lin, J., & Peng, Q. (2018). Short-Term Precipitation Forecast Based on the PERSIANN System and LSTM Recurrent Neural Networks. *Journal of Geophysical Research: Atmospheres*, 123(22), 12–543.

Borderies, M., Caumont, O., Delanoë, J., Ducrocq, V., Fourrié, N., & Marquet, P. (2019). *Impact of airborne cloud radar reflectivity data assimilation on kilometre-scale numerical weather prediction*

analyses and forecasts of heavy precipitation events.

Brown, J. F., Wardlow, B. D., Tadesse, T., Hayes, M. J., & Reed, B. C. (2008). The Vegetation Drought Response Index (VegDRI): A new integrated approach for monitoring drought stress in vegetation. *GIScience and Remote Sensing*, 45(1), 16–46. <https://doi.org/10.2747/1548-1603.45.1.16>

Cai, M., & Liu, J. (2016). Maxout neurons for deep convolutional and LSTM neural networks in speech recognition. *Speech Communication*, 77, 53–64.

Chen, X. S. Z., Yeung, H. W. D.-Y., & Woo, W.-K. W. W. (2015). Convolutional LSTM Network: A Machine Learning Approach for Precipitation Nowcasting. *ArXiv Preprint ArXiv:1506.04214*.

Dore, M. H. I. (2005). Climate change and changes in global precipitation patterns: What do we know? *Environment International*, 31(8), 1167–1181. <https://doi.org/https://doi.org/10.1016/j.envint.2005.03.004>

Du, Y., Wang, W., & Wang, L. (2015). Hierarchical recurrent neural network for skeleton based action recognition. *Proceedings of the IEEE Conference on Computer Vision and Pattern Recognition*, 1110–1118.

Dutta, D., Kundu, A., Patel, N. R., Saha, S. K., & Siddiqui, A. R. (2015). Assessment of agricultural drought in Rajasthan (India) using remote sensing derived Vegetation Condition Index (VCI) and Standardized Precipitation Index (SPI). *The Egyptian Journal of Remote Sensing and Space Science*, 18(1), 53–63. <https://doi.org/https://doi.org/10.1016/j.ejrs.2015.03.006>

Flores, R. A. A. (2019). GEOVISUAL ANALYTICS ON THE VERIFICATION OF THE PAGASA OPERATIONAL NUMERICAL WEATHER PREDICTION MODEL RAINFALL FORECAST. *International Archives of the Photogrammetry, Remote Sensing & Spatial Information Sciences*.

Gosain, A. K., Rao, S., & Basuray, D. (2006). Climate change impact assessment on hydrology of Indian river basins. *Current Science*, 90(3), 346–353.

Gregor, K., Danihelka, I., Graves, A., Rezende, D. J., & Wierstra, D. (2015). Draw: A recurrent neural network for image generation. *ArXiv Preprint ArXiv:1502.04623*.

Ha, J.-H., Lee, Y. H., & Kim, Y.-H. (2016). Forecasting the precipitation of the next day using deep learning. *Journal of Korean Institute of Intelligent Systems*, 26(2), 93–98.

IPCC. (2018). Summary for Policymakers. Global Warming of 1.5°C. An IPCC Special Report on the impacts of global warming of 1.5 °C above pre-industrial levels. In *Global Warming of 1.5°C. An IPCC Special Report on the impacts of global warming of 1.5°C above pre-industrial levels and related global greenhouse gas emission pathways, in the context of strengthening the global response to the threat of climate change.* <https://doi.org/10.1017/CBO9781107415324>

Kim, S., Hong, S., Joh, M., & Song, S. (2017). Deeprain: ConvLstm network for precipitation prediction using multichannel radar data. *ArXiv Preprint ArXiv:1711.02316*.

Kumar, D., Singh, A., Samui, P., & Jha, R. K. (2019). Forecasting monthly precipitation using sequential modelling. *Hydrological Sciences Journal*, 64(6), 690–700.

- Kumar, V., Jain, S. K., & Singh, Y. (2010). Analysis of long-term rainfall trends in India. *Hydrological Sciences Journal*, 55(4), 484–496. <https://doi.org/10.1080/02626667.2010.481373>
- Mikolov, Tomáš, Kombrink, S., Burget, L., Černocký, J., & Khudanpur, S. (2011). Extensions of recurrent neural network language model. *2011 IEEE International Conference on Acoustics, Speech and Signal Processing (ICASSP)*, 5528–5531.
- Mikolov, Tomas, & Zweig, G. (2012). Context dependent recurrent neural network language model. *2012 IEEE Spoken Language Technology Workshop (SLT)*, 234–239.
- Saha, M., Mitra, P., & Nanjundiah, R. S. (2017). Deep learning for predicting the monsoon over the homogeneous regions of India. *Journal of Earth System Science*, 126(4), 54.
- Salman, A. G., Heryadi, Y., Abdurahman, E., & Suparta, W. (2018). Single layer & multi-layer long short-term memory (LSTM) model with intermediate variables for weather forecasting. *Procedia Computer Science*, 135, 89–98.
- Silvestro, F., Rossi, L., Campo, L., Parodi, A., Fiori, E., Rudari, R., & Ferraris, L. (2019). Impact-based flash-flood forecasting system: Sensitivity to high resolution numerical weather prediction systems and soil moisture. *Journal of Hydrology*, 572, 388–402.
- Xingjian, S. H. I., Chen, Z., Wang, H., Yeung, D.-Y., Wong, W.-K., & Woo, W. (2015). Convolutional LSTM network: A machine learning approach for precipitation nowcasting. *Advances in Neural Information Processing Systems*, 802–810.
- Yu, W., Hwang, E., & Chae, H. (2019). Rainfall and Flood Forecasts using Numerical Weather Prediction Data from Korea and Japan. *Proceedings of the Korea Water Resources Association Conference*, 305.

Persistency of Thermal Front and its Seasonal Cycle in the Northern Arabian Sea

Reba Mary Raju¹, R. K. Nayak¹

Affiliation:

¹National Remote Sensing Center (NRSC), Indian Space Research Organization (ISRO), Balanagar, Hyderabad, India-500037.

Commission VI, WG VI/4

KEY WORDS: Thermal Fronts, SST, Harmonic Analysis, PFZ

ABSTRACT:

One of the important near real time applications of high resolution sea surface temperature retrieved from the infra-red satellite sensors is to map provinces of thermal fronts (TF) in the continental shelf and slope region and helps in demarcating the areas of potential fishing zone (PFZ). The coastal ocean domain on the north western continental shelf of India (north eastern Arabian Sea) is often identified as the PFZ from numerous studies, but due to complexity of the region and persistent cloud cover generates huge data gaps, which make difficulties in providing thermal fronts information on a daily scale. To overcome such difficulties, we used gap free and blended Global 1km SST (G1SST) products to understand the predictability of the persistent thermal fronts along the north eastern Arabian sea. At the same time satellite observation data from MODIS is also used with the same temporal duration to map the persistent thermal fronts on a daily time scale for the comparison purpose. In order to understand their seasonal variability, the weekly composite datasets of thermal front density (TFD) are generated from the daily time series using gradient of 0.07/km for the G1SST and 0.075/km for MODIS based on the sensitivity experiments. Least square based harmonic analysis is carried out on both TFD datasets to investigate their observed seasonality in the northern Arabian Sea. The outcome of this study can be used as a support for the utility of G1SST to provide gridded, gap free and daily thermal front datasets as a substitute for the observation satellite datasets for PFZ advisories along the Indian EEZ.

1. INTRODUCTION

Oceanic thermal fronts (TF) are surface manifestations of transition between two water masses of differing thermal, density and nutrients. They significantly contribute to local productivity by trapping the nutrients and providing ambient conditions for their growth (Vipin et al., 2015). They are formed by diverse forcing such as tides, river runoffs, bathymetry, solar heating (Belkin, 2009; Belkin et al., 2009). Most of the stable fronts found in world ocean are steered by the ocean bottom topography as a consequence, most of TF are observed near to the continental shelf (Longhurst, 1998).

Oceanic TF occur in the ocean in order of few km to 1000 of km in length, thus to map this features, we require the SST datasets with the resolution finer and comparable scale. At present, almost all, infra-red satellite sensors can provide the SST resolution up to 4 km or finer scale, for example, like Moderate Resolution Imaging Spectroradiometer (MODIS) aboard on AQUA platform provide SST data in 4 and 9 km resolution, but the data contains data gaps due to geographically and seasonally persistent cloud interference, which hinder in generation of continuous, mesoscale features such as Thermal front (TF) datasets for the PFZ advisories. Although, microwave retrievals of SST is not influenced by clouds, the land interference caused due to presence of side-lobes in scanning, enables the leakage of high terrestrial emission to the low seas surface emission significantly affects the quality of SST data along the coastal region (Kawanishi et al., 2003). The coarse resolution of the SAR data also causes some of TF to missed while missing, thus there is a need of high resolution

datasets for the TF to mapped along the continental shelf and shelf regions.

Until recently, with the advent of data assimilation and blending procedures allows the combination of multi-sensor data to make high resolution SST datasets for various scientific application like coastal air-sea interaction, identification of physical indicators for bi-productivity, delineation and tracking of surface mesoscale features in the ocean. G1SST is one such blended SST product, which is produced daily on an operational basis by the JPL OurOcean group using a multi-scale two-dimensional variational (MS-2DVAR) blending algorithm on a global 0.009 x 0.009 degree grid (Chao et al., 2009).

The data is synthesized from the both satellite and observational datasets and uses multi-Resolution Variational Analysis (MRVA). The method employs the MUR analysis to use data in multiple synoptic time scale, with 5-day data window for reconstruction of mesoscale features and few hours data windows or smaller scale features, with the use of multiple synoptic windows, interpolation along the data voids and multi-scale setting could be achieved with this method. This meshless interpolation avoids geolocation truncation error to an extent.

This study investigate the robustness of gap free, gridded, blended and high resolution GHRSSST SST data to address the seasonality and variability of TFD along the north eastern Arabian sea as observed by the satellite observation i.e. MODIS SST over the same study domain.

1.1 Study Area

The Fig.1 shows the study domain off Gujarat coast, India overlaid by the TF contour. The study region is highly influenced by reversing monsoon winds. The study region is known to be high productive region due to eddy activity and species bloom.

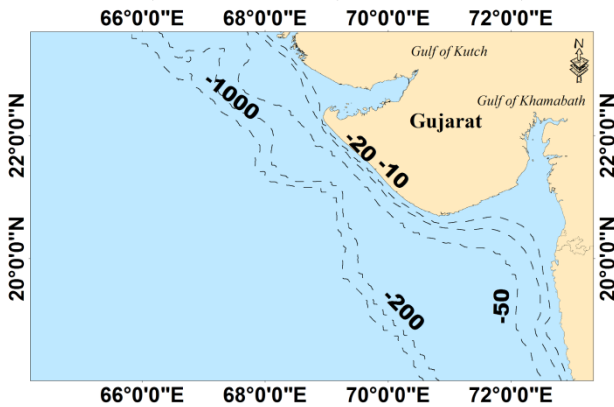


Fig.1. The study domain with the bathymetry contours

2. DATA AND METHOD

In this paper, we make use of GHRSSST (The Group for High-Resolution Sea Surface Temperature) data produced in daily timescale by JPL Ocean group using a multi-scale two-dimensional variation (MS-2DVAR) merging algorithm for the SST products from eight satellites (AVHRR, AATSR, SEVIRI, AMSRE, TMI, MODIS, GOES, and MT-SAT-1R). The SST products from GHRSSST shows RMSE of less than 1°C as compared with the in-situ data (Chao et al., 2009). This daily data is available at 1 km spatial resolution for download from ftp://ftp.nodc.noaa.gov/pub/data.nodc/ghrsst/L4/GLOB/JPL_OUROCEAN/G1SST/

The TF datasets delineated from daily time series of Level -3 MODIS (4km) datasets earlier from a preliminary study is also used for the comparison purpose. The Level-3 MODIS data suffers from limitation as the SST pixels are contaminated from clouds. During the southwest monsoon season (June-August), SST pixels are not available within the study domain. Thus, TF information during that period is absent for doing further analysis.

Parameters	MODIS	GISST
Window size	20 x 20	20 x 20
Threshold Temperature Gradient	0.075	0.07
Single-population cohesion	0.9	0.9
Single-population cohesion	0.92	0.92

After delineating the TF from the GISST and MODIS SST, we computed weekly composite of occurrence of TF at each pixel in the study domain. This method is adopted from following studies such as in to describe the seasonality in different parts of world ocean (Belkin et al., 2009; Cayula and Cornillon, 1992; Mohanty et al., 2017; Saraceno et al., 2005).

The following relation is used to compute weekly TFD datasets from daily TF datasets.

$$TFD = \left(\frac{\sum_{i=1}^7 d_i}{7} \right) * 100$$

$$d_i = \begin{cases} 1, & \text{if front exist} \\ 0, & \text{if front is absent} \end{cases} \quad (1)$$

2.1 Harmonic Analysis

The least square based harmonic operation was carried out in TFD datasets of GISST and MODIS. From the Fast Fourier Transform (FFT), the peak spectral signal is identified, following this annual and semi-annual signal is observed to be dominant during the study period. The time-series of TFD P(t) are fitted with annual and semi-annual harmonics.

$$P(t) = A_0 + \sum_{i=1}^2 A_i \cos(\omega_i t + \phi_i) + \varepsilon$$

$$P(t) = A_0 + \sum_{i=1}^2 A_i \cos(\omega_i t + \phi_i)$$

where A_0 is the climatology of time series which is stationary component. (A_1, A_2) are amplitudes. (ϕ_1, ϕ_2) are phase angles of semi-annual and annual harmonics. Seasonal cycle is reconstructed using semi-annual and annual harmonics from the estimated amplitude and phase maps respectively.

$$P(s, t) = A_s + \cos(\omega_s t + \phi_s),$$

where (A_s) is semi-annual amplitude, (ϕ_s) is semi-annual phase change, (t) is (year-days) and (ω_s) is semi-annual Radian frequency = $2\pi/[182.625]$.

$$P(a, t) = A_a + \cos(\omega_a t + \phi_a)$$

where (A_a) is annual amplitude, (ϕ_a) is annual phase change, (t) is (year-days) and (ω_a) is semi-annual Radian frequency = $2\pi/[365.25]$.

Seasonal cycle is calculated using following relation.

$$P(s, t) = A_0 + P(s, t) + P(a, t)$$

where A_0 is the climatology of time series, $P(s, t)$ is semi-annual harmonics and $P(a, t)$ is annual harmonics.

3. RESULTS AND DISCUSSION

The study region is known for its flat and wide continental shelf (Mohanty et al., 2017) and is highly productive owing to surface cooling by dry continental winds that lead to convective mixing during the winter monsoon (Banse, 1987). This winter cooling deepens the mixed layer, entraining nutrients into it, and leading to high productivity (Madhupratap et al., 2003; McCreary et al., 2009). The TF is extracted from the both GISST and MODIS SST using Cayula – Cornillon algorithm, using the gradient of 0.07°C /km and 0.075°C. The figure 2 shows the spatial distribution of TF overlaid on the SST image for a given date corresponding to different SST gradients,

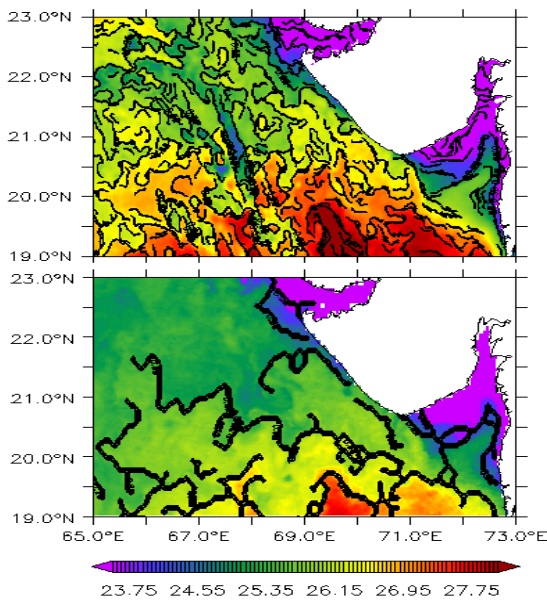


Fig. 2.Upper Panel shows the GISST SST map of 01-january-2016, overlaid with the Thermal Front contour derived from GISST. Lower Panel shows the MODIS SST map of 01-january-2016, overlaid with the Thermal Fronts contour derived from MODIS.

3.1 Seasonal Variability of TFD

The analysis of long-term weekly thermal front density data gives some insights to frontal distribution in the study region. Fig. 3 shows amplitude and phase maps of climatological mean, annual and semi-annual harmonics estimated from weekly front density time series data. The amplitude maps show the prominent region of front occurrence at annual and semi-annual scale, whereas phase change maps show the lead and lag to the same harmonics. The climatological mean map shows thermal fronts occurring at all times in the year.

From the Fig. 3, the prominent region of occurrence of TF is seen along bathymetry depth contours between 10 m and 50 m. The study region is characterized by flat and wide continental shelf. The associated phase maps are given in terms of months for easy interpretation.

The Fig. 3 shows the seasonal distribution TFD in study domain as observed in the MODIS SST for the same period. From the climatology map, we can decipher the occurrence of TFD around (> 30 %) all times of year irrespective of seasons, Whereas in annual and semi-annual time scale we could observe the occurrence within the range of 6-18% and 24-30% respectively along 10 m and 50 m isobaths. The dominant amplitude is observed along the Gujarat coast, with high variability in the along the entrance of Gulf of Khamabath and Gulf of Kutch. The semi-annual harmonics is much lower compared to the annual harmonics as observed in the MODIS TFD datasets, since there is significant data absence over the June-August season, further interpretation can be omitted. The associated phase for the harmonics is observed to occur during Oct-November months along the mouth of Gulf of Kutch and Gulf of Khamabath.

The seasonal distribution as seen in GISST TFD datasets also show similar pattern of TFD as observed by MODIS TFD datasets(Figure 5).From the climatology map, stationary component of TFD is seen to occur at scale (>30 %) throughout the study period. Whereas in annual and semi-annual harmonics, the scale of occurrence is in range of 6-9 % and 12 - 24 %, which is much lower compared to the MODIS TFD. The dominant annual amplitude is seen in the entrance of Gulf of Khamabath and Gulf of Kutch as observed in north and south of Gujarat Peninsula. The associated phase also shows that the Oct -November months as a peak period for formation of TFD.

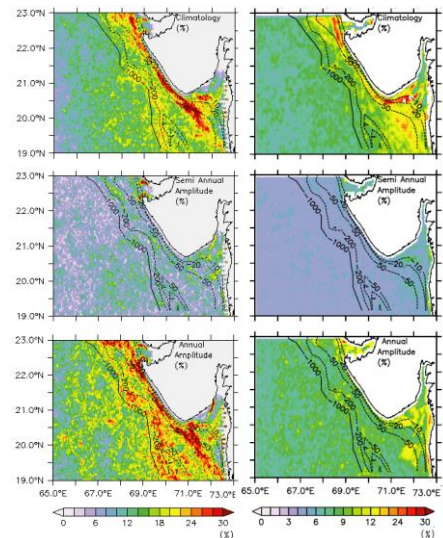


Fig. 3.Right Panel shows the maps of climatology, semi-annual (amplitude) and annual harmonics (amplitude) of the MODIS TFD. Bathymetry contours of 10 m, 20 m, 50 m, 200 m, and 1000 m are overlaid on corresponding maps. Left Panel shows the harmonics (amplitude) of GISST TFD. Bathymetry contours of 10 m, 20 m, 50 m, 200 m, and 1000 m are overlaid on corresponding maps of climatology, semi-annual (amplitude) and annual (amplitude).

The spatial correlation map shown in Fig 4. shows that the most of the study domain is TF occurrence delineated from the 2 datasets are correlated well with each other.

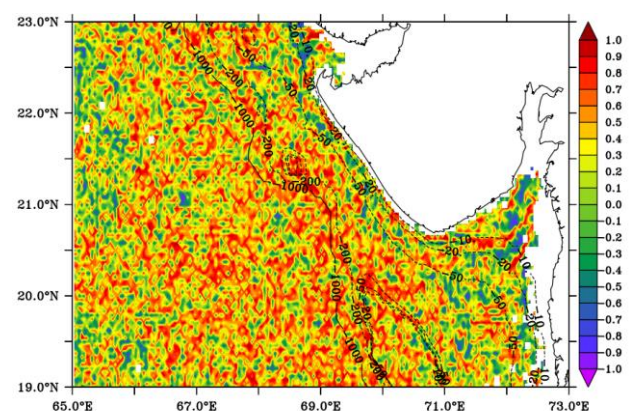


Fig.4.shows the spatial correlation map of GISST and MODIS TFD

4. CONCLUSION

From the preliminary results of harmonic analysis on both the MODIS and G1SST TFD datasets, we could observe that from the seasonal distribution of TFD in both datasets, the high occurrence of TFD is confined in the 10 -200 m isobaths along the continental shelf regions of the north-east Arabian sea. The high TFD occurrence is seen in the entrance of Gulf of Khamabath than compared to Gulf of Kutch. While, we do not address the existence of these TF in the study domain, which is beyond the scope of our study. Thus from the analysis is, we could see that the assimilated and blended, high resolution data could address the persistent thermal fronts occurring regions and its comparable to observation. This dataset could be aid to demarcate the high productive regions and help in PFZ advisories.

temperature fronts and chlorophyll a in the western South Atlantic. *J. Geophys. Res. Ocean.*
<https://doi.org/10.1029/2004JC002736>

Vipin, P., Sarkar, K., Aparna, S.G., Shankar, D., Sarma, V.V.S.S., Gracias, D.G., Krishna, M.S., Srikanth, G., Mandal, R., Rama Rao, E.P., Srinivasa Rao, N., 2015. Evolution and sub-surface characteristics of a sea-surface temperature filament and front in the northeastern Arabian Sea during November-December 2012. *J. Mar. Syst.* 150, 1–11.
<https://doi.org/10.1016/j.jmarsys.2015.05.003>

REFERENCES

- Banse, K., 1987. Clouds, deep chlorophyll maxima and the nutrient supply to the mixed layer of stratified water bodies. *J. Plankton Res.*
<https://doi.org/10.1093/plankt/9.5.1031>
- Belkin, I.M., 2009. Observational studies of oceanic fronts. *J. Mar. Syst.* <https://doi.org/10.1016/j.jmarsys.2008.10.016>
- Belkin, I.M., Cornillon, P.C., Sherman, K., 2009. Fronts in Large Marine Ecosystems. *Prog. Oceanogr.*
<https://doi.org/10.1016/j.pocean.2009.04.015>
- Cayula, J.-F., Cornillon, P., 1992. Edge Detection Algorithm for SST Images. *J. Atmos. Ocean. Technol.*
[https://doi.org/10.1175/1520-0426\(1992\)009<0067:EDAFSI>2.0.CO;2](https://doi.org/10.1175/1520-0426(1992)009<0067:EDAFSI>2.0.CO;2)
- Chao, Y., Li, Z., Farrara, J.D., Hung, P., 2009. Blending sea surface temperatures from multiple satellites and in situ observations for coastal oceans. *J. Atmos. Ocean. Technol.* <https://doi.org/10.1175/2009JTECHO592.1>
- Kawanishi, T., Sezai, T., Ito, Y., Imaoka, K., Takeshima, T., Ishido, Y., Shibata, A., Miura, M., Inahata, H., Spencer, R.W., 2003. The Advanced Microwave Scanning Radiometer for the Earth observing system (AMSR-E), NASDA's contribution to the EOS for global energy and water cycle studies. *IEEE Trans. Geosci. Remote Sens.*
<https://doi.org/10.1109/TGRS.2002.808331>
- Longhurst, A.R., 1998. *Ecological Geography of the Sea, Ecological Geography of the Sea.*
<https://doi.org/10.1016/B978-0-12-455521-1.X5000-1>
- Madhupratap, M., Gauns, M., Ramaiah, N., Prasanna Kumar, S., Muraleedharan, P.M., De Sousa, S.N., Sardesai, S., Muraleedharan, U., 2003. Biogeochemistry of the Bay of Bengal: Physical, chemical and primary productivity characteristics of the central and western Bay of Bengal during summer monsoon 2001. *Deep. Res. Part II Top. Stud. Oceanogr.* [https://doi.org/10.1016/S0967-0645\(02\)00611-2](https://doi.org/10.1016/S0967-0645(02)00611-2)
- McCreary, J.P., Murtugudde, R., Vialard, J., Vinayachandran, P.N., Wiggert, J.D., Hood, R.R., Shankar, D., Shetye, S., 2009. Biophysical processes in the Indian Ocean, in: *Geophysical Monograph Series.*
<https://doi.org/10.1029/2008GM000768>
- Mohanty, P.C., Mahendra, R.S., Nayak, R.K., Nimit Kumar, Srinivasa Kumar, T., Dwivedi, R.M., 2017. Persistence of productive surface thermal fronts in the northeast Arabian Sea. *Reg. Stud. Mar. Sci.*
<https://doi.org/10.1016/j.rsma.2017.09.010>
- Saraceno, M., Provost, C., Piola, A.R., 2005. On the relationship between satellite-retrieved surface

Seasonal and inter-annual variability of atmosphere CH₄ based Model and GOSAT satellite observations

Shaik Allahudheen^{1,2}, Rabindra K. Nayak^{1*}, M Krishna priya¹, A Bhuvana Chandra¹, M V Lakshmaiah²

¹ National Remote Sensing Center (NRSC), Hyderabad, India-500037.

² Department of Physics, Sri Krishnadevaraya University, Ananthapuramu

KEY WORDS : GEOS Chem-Methane-GOSAT-Harmonic analysis-fluxes

Corresponding author : rabin2005@rediffmail.com

ABSTRACT:

The GEOS Chem Model was employed at 2x2.5 degree spatial resolution over the globe with 47 vertical layers between pressure levels 1006 hPa to 0.01 hPa. The Model is driven by GEOS meteorological fields along with surface boundary fluxes and emission fluxes from different sources. The model was implemented for the period 2010-2015 and the solutions at three hourly intervals were stored for the analysis. To identify local source and sink for atmospheric CH₄, Seasonal and inter annual variability of the surface layer atmospheric CH₄ over the Global region was studied based on Goddard Earth Observation System Chemical transport model (GEOS Chem), the Greenhouse gas Observation Satellite (GOSAT) and in situ measurements during 2010-2015. Annual and semi-annual harmonics and the climatologically mean of CH₄ were estimated from the model solutions and satellite observation. There exist good coherences between model and satellite observation. We observed that in 2010–2015 period, growth in atmospheric methane is attributed mostly to increase in emissions from India, China and areas with large tropical wetlands. Maximum surface flux emits from both India (4.756 Tg/y) and China (6.898 Tg/ y). Compared to other regions, China and India have a high source of methane. The hydroxyl radical is the main contributor of the methane's sink (troposphere OH). In India, CH₄ concentration is maximum in September and minimum is in February/March. The tropical wetland or agricultural or combination of both of the rising global methane 2008 on words.

1. INTRODUCTION

Atmospheric methane (CH₄) is the second most abundant anthropogenic greenhouse gas. Methane in global radioactive forcing of atmospheric is 0.97 WM⁻² (IPCC, 2013). methane emitted from nature and anthropogenic source .major anthropogenic emission includes petroleum and natural gas , coal mining ,waste (land fill and waste water),livestock and rice cultivation .methane sink Troposphere OH ,stratosphere loss and troposphere chlorine..Life time of Atmospheric methane is 9.1± 0.9years(prather et al., 2012).Main source of methane is human activities with the agricultural ,anthropogenic through entire fermentation of livestock(17%), rice (7%) form the former, and coal mining (7%),gas and oil (12%),waste management(11%), natural source of methane includes termities(4%),wetlands(34%),ocean and hydrates (3%), and biomass burning id(4%)(Chen and prinn (2006),Fung et al(1991) ,Kirschki et all (2013)). most major and largest natural source is Wetlands. Methane major role on troposphere as sink for chlorine atoms and source of water vapor in stratosphere (solomon et l., 2010) .soil bacterial sink of surface methane And in troposphere methane Oxidation with OH ,surface methane sinks in atmospheric so it impact on atmospheric composition (Lelieveld,2012) . source of methane in hydrogen and troposphere ozone precursors such as CO and formaldehyde (Montzaka et all.2011).On the sink side identified OH radicals with largest uncertainty -4±14% from 2006-2007(Montake et all 2011)small drop ~1 % /year in atmospheric methane. Nearly 90% global ch₄ sink because of oxidation by hydroxyl radical OH ,Methanotrophic bacteria in soils (~4%) ,in the stratosphere with chlorine and atom oxygen radical (~3%) and sea salt chlorine radials (~3%) near marine boundary layer(Stafanie et al,2013).The tropical wetland or agricultural or combination of both are causes of the rising global methane 2008 on wards (bousquest st al 2006)

The present work for seasonal and inter-annual variability of Atmospheric methane for global and regional variation

concentration to identify local source and sink for atmospheric CH₄ for GEOS Chem model ,GOSAT .Harmonic analysis of this datasets to shows us semi-annual and annual variability and comparison with in-situ observation .These data and modeling works have study seasonal and inter-annual variability of atmospheric CH₄ over globe.

2. DATA AND METHODS

2.1GEOS Chem Atmospheric Chemical Transport Model:

The study uses GEOS-Chem forward model to simulate atmospheric CH₄ chemistry and its transport. The model is driven by assimilated 3 -D meteorological data fields from (Goddard Earth Observation System) (GEOS-5) .The model is set up in the global-grid mode with the horizontal spatial resolution of 2x2.5 (latitude X longitude) and having 47 hybrid vertical level from surface to 80.581 km (i.e. 1013 to 0.010hPa) . Lin and Hood 1996) method is used to calculate the transport of aerosols and gaseous species in every 30 mins and also the planetary boundary layer (PBL) mixing scheme is derived from (lin and mclers) which takes in account of atmospheric instability. A tagged Ch₄ tracer simulation of GEOS-Chem was applied to identify individual source types (such as gas and oil, coal mining ,wetlands, biomass burning ,rice fields, livestock, anthropogenic) of CH₄ during atmospheric transport.Since the inputs such as rice and wetlands emission 2010-2012 is not available in the input datasets, we make use of EDGAR datasets for the majority of flux estimation

2.2 GOSAT

Gosat was launched on 23rd January 2009 by the Japanese Aerospace Exploration Agency (JAXA). It operates in the SWIR (shortwave infrared) at 0.76, 1.6, 2.0 micrometer sensitivity to the near surface (Buchwitz et al., 2015, Kuze et al., 2016). Gosat has two types of instruments, TANSO-FTS and TANSO-CIA. TANSO-FTS (thermal and near infrared sensor for carbon observation - Fourier transform spectrometer) has four bands, one is thermal IR channel from 5.5 to 14.3 micrometer, the other three are spectral channels with 0.27 cm resolution at 0.76, 1.6, 2.0 micrometer (Kuze et al., 2009). In this study, CH₄ concentration near surface layer monthly using for period of 2010 and 2018 with 2.5° x 2.5° spatial resolution from JAXA. The GOSAT L3 product available monthly average of 2009 to 2018 for Methane over a 2 x 2.5 grid in HDF5. Harmonic analysis of Gosat methane shows variability of different regions. The respective time series are fitted with annual and semi-annual harmonics through the LSP as in the following: $dCh_4(t) = A_0 + \sum_{i=1}^2 A_i + \cos(\omega_i t + \phi_i) + \epsilon$

where A_0 is the stationary component of the time series that represents mean climatology of dCH₄; (A_1, A_2) and (ϕ_1, ϕ_2) terms respectively denote the amplitude and phase angle of annual and semi-annual harmonics; and ϵ is the perturbation/residual term. These annual and semi-annual harmonics together constitute the seasonal cycle and the residual is considered as the non-seasonal variability of the time-series composed of the intra-seasonal and the inter-annual variability.

3. RESULTS AND DISCUSSION

3.1 HARMONIC ANALYSIS

Harmonic analysis of GOSAT Atmospheric CH₄ Concentration and GEOS Chem Atmospheric Chemical Transport model based CH₄ concentration is shown in Figure 1. High concentration of methane is observed along the equatorial region, East China, India. Moderate values are observed in Australia, South America, South Tropical Africa, South Tropical Oceanic regions. Large values of Annual amplitudes are observed over Indian landmass and Arabian sea, China and oceans along the equatorial region. Whereas Europe, North America, North Tropical Africa, Australia show moderate annual amplitude values. High values of Semi-annual amplitude of CH₄ are exhibited over the Indian region, China and oceans along the equatorial region.

In GEOS Chem model also show spatial variation across the globe. High values of Methane Concentration is observed over Northern Tropical Regions in the Annual climatology. Moderate along the equatorial and poor in south tropical region.

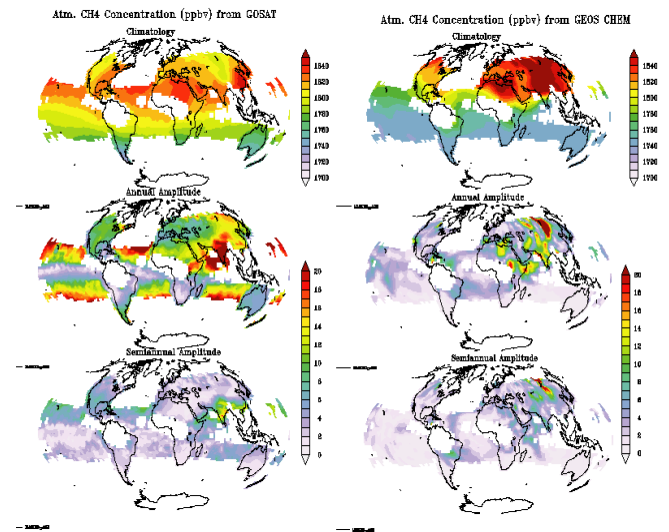


Figure 1. Harmonic analysis of methane for GOSAT and GEOS Chem Model for 2010-2015

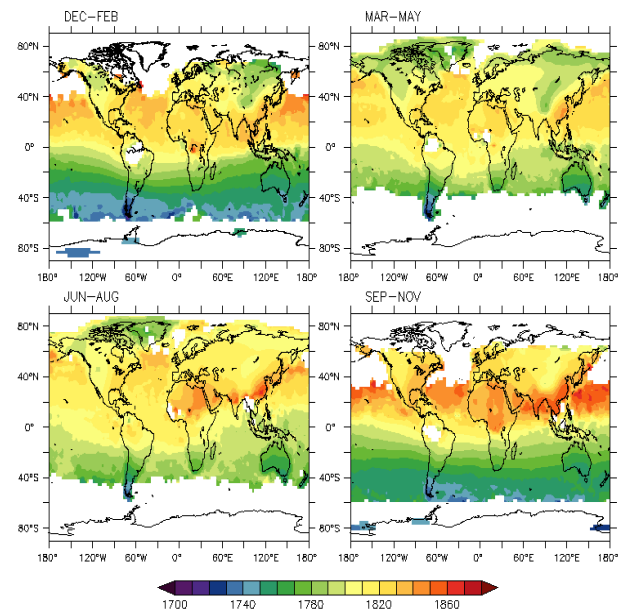


Fig 2. Seasonal concentration methane for GOSAT satellite

The Annual amplitude also shows us high variability in Indian and south China and middle Africa, moderate variability show in Europe and Australia. Semi-annual amplitude Indian region and South America and Russia also high Amplitude values.

Strong Seasonal variability of GOSAT based CH₄ is observed during the study period as shown in Figure 3. In all seasons max concentration is observed in SEP-NOV (post monsoon) and low concentration observed in (pre-monsoon) MAR-MAY. The observed seasonal cycles are well in agreements to the earlier reports by various studies carried out. Large latitudinal variations are seen across the seasons with high concentrations along the equatorial regions and high variations are also observed in the regional scale. The observed pattern could be associated with large scale melting of ice and the release of sequestered CH₄

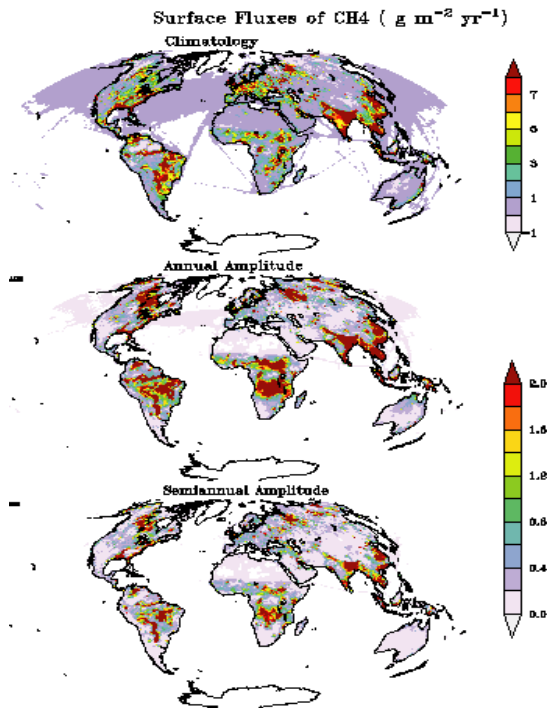


Figure 3. Harmonic analysis of methane for GOSAT All Flux

South Africa	3.592	0.3119
--------------	-------	--------

Table1:show use flux emission from different regions(Tg/y)

GOSAT based Surface fluxes of methane show high emission fluxes over India ,China , South tropical Africa and moderate fluxes over Europe , North America and South America (Figure 2).The table describes the surface fluxes of CH₄ across different regions, with values along India (4.756 Tg y⁻¹) and China (6.898 Tg y⁻¹). Annual & Semi annual amplitudes of the surface fluxes show similar patterns of variability with small differences in the amplitude values across India, China and Central Africa.

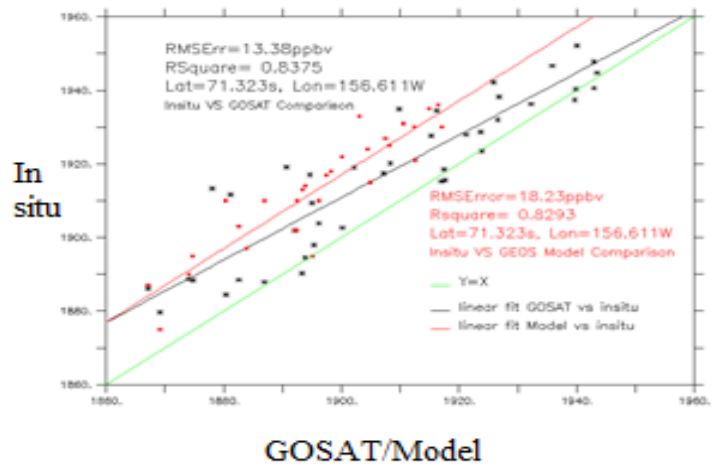


Fig 6 correlation between the GEOS Chem Model methane and insitu ,GOSAT vs Insitu

We have compared the GOSAT CH₄ and GEOS Chem based CH₄ with the insitu CH₄.The Coefficient of determination between GOSAT- insitu and GEOSChem and insitu is 0.8293 and 0.8375 respectively. Both the satellite based CH₄ and GEOS Chem model based CH₄ showed reasonable agreement with the insitu data. Due to the limitation of openly available insitu based CH₄ data,we had to restrict the comparison with only one location. We would further improve the model inputs and the simulated CH₄ would be compared with more no of insitu data sets in our future studies.

Region	Total integral of FLUX in Tg/y	Mean value Tg/y
Indian	4.756	0.6280
China	6.898	0.5980
Europe	2.527	0.3983
Africa	4.106	0.2454
North America	4.341	0.2933

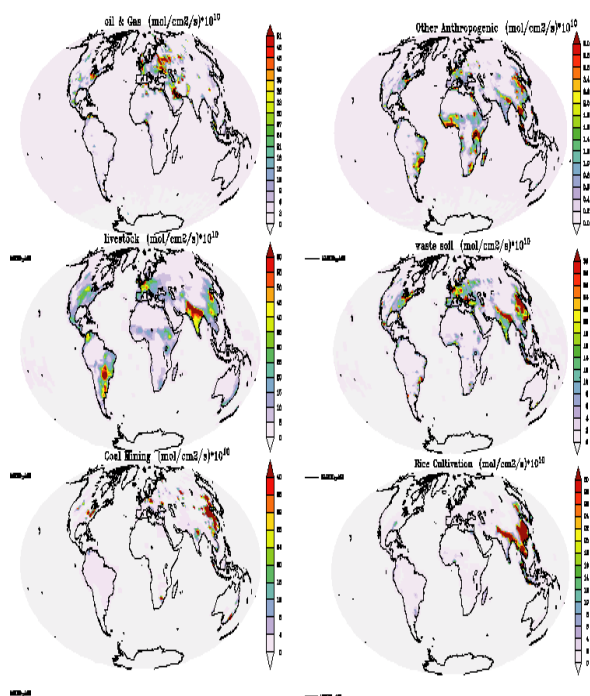


Fig 4. In GEOS Chem Model using Different Flux of annual

GEOS Chem model using methane Emission files are show how much this are influence on seasonal variability .GEOS CHEM model using methane global emission for 2004-2008 .The major source of the oil and gas is Europe countries and North america .Major source of atmospheric methane in India is wetland rice fields(IRRI:2009).In India and south china region has high rice cultivation show in fig .In the World the large number of cattle's are available in India ,the total agricultural ch4 emissions nearly ~30% source from Livestock (sirohi and michaelowa,2007).the more livestock emission observe in India ,Europe , south china and South America and moderate values are observed in Africa and North America. Coal mining the major emission source countries are china ,India and North America.Waste soil and Rice cultivation has more in India and south chine.

3.2 Periodicity Analysis

To identify the dominant spectral signal during the study period (2010-2015),fast fourier Transforamtion (FFT) was applied on the monthly GOSAT data for three longitudinal segments as the function of latitude and time period. From the figure the strong seasonal variability is observed at annual scale (>1ppbv) and semi-annual scale (0.3-0.8 ppbv)

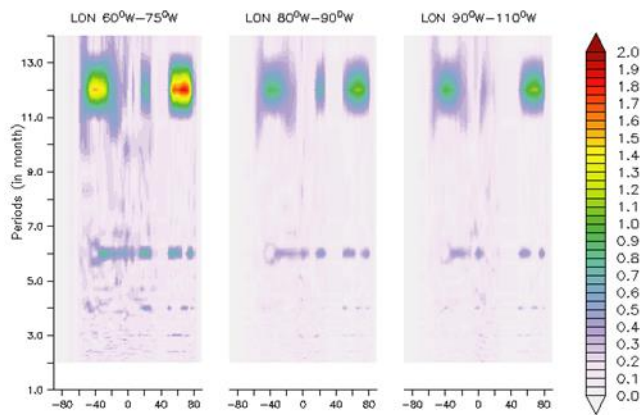


Fig 5 amplitude distribution of Methane for three longitudinal segments as the function of latitude and time period.

4 Discussion:

In this study , we have attempted to simulate the Global atmospheric CH4 based on GEOS Chem atmospheric chemical transport model. This is a preliminary study to understand the seasonal variability of CH4 based on satellite(GOSAT) and Atmospheric Chemical Transport Model(GEOS-Chem).Harmonic analysis of the data shows that there is a significant semi annual and annual variability of CH4. The seasonal variability is maximum in Sep-Nov period.Such behaviour is exhibited due to the maximum contributions from the wetland emissions and rice cultivations. We have observed large emissions in the Asian regions of India and China because of the rice cultivation and high number of wetland regions present in these areas.This study is carried out based on the limited availability of input emission data and the analysis of the simulated output. We would like to extend this study to analyse the source/sink patterns in regional context with improved emission inventory.

ACKNOWLEDGEMENT: This research work is carried out as part of National Carbon Project, ISRO-Geosphere Biosphere Programme.We are very thankful to GOSAT teamat JAXA,and NOAACT for providing the data for this study.

References

Bousquet, P., P. Ciais, J.B. Miller, E.J. DlugokenckyHauglustaine, C. Prigent, G.R. Van der Werf, E.G. Brunke, C. Carouge, R.L. Langenfelds, J Lathière, F. Papa, M. Ramonet, M.Schmidt, L.P. Steele, S.C.Tyler, and J. White, 2006: Contribution of anthropogenic and natural sources to atmospheric methane variability.Nature, 443, 439-443, doi:10.1038/nature05132.

- Bergamaschi, P., et al. (2009), Inverse modeling of global and regional CH₄ emissions using SCIAMACHY satellite retrievals, *J. Geophys. Res.*, 114, D22301, doi:10.1029/2009JD012287
- IPCC. Climate Change 2001: The Scientific Basis. Contribution of Working Group I to the Third Assessment Report of the Intergovernmental Panel on Climate Change (eds Houghton, J. T. et al.) (Cambridge Univ. Press, Cambridge and New York, 2001).
- Buchwitz, M., Reuter, M., Schneising, O., Noël, S., Gier, B., Bovensmann, H., Burrows, J. P., Boesch, H., Anand, J., Parker, R. J., Somkuti, P., Detmers, R. G., Hasekamp, O. P., Aben, I., Butz, A., Kuze, A., Suto, H., Yoshida, Y., Crisp, and O'Dell, C.: Computation and analysis of atmospheric carbon dioxide annual mean growth rates from satellite observations during 2003–2016, *Atmos. Chem. Phys.*, 18, 17355–17370, <https://doi.org/10.5194/acp-18-17355-2018>, 2018.
- Butz, A., Guerlet, S., Hasekamp, O., Schepers, D., Galli, A., Aben, I., Frankenberg, C., Hartmann, J.-M., Tran, H., Kuze, A., Keppel-Aleks, G., Toon, G., Wunch, D., Wennberg, P., Deutscher, N., Griffith, D., Macatangay, R., Messerschmidt, J., Notholt, J., and Warneke, T.: Toward accurate CO₂ and CH₄ observations from GOSAT, *Geophys. Res. Lett.*, 38, L14812, <https://doi.org/10.1029/2011GL047888>, 2011.
- Butz, A., O. P. Hasekamp, C. Frankenberg, J. Vidot, and I. Aben (2010), CH₄ retrievals from space-based solar backscatter measurements: Performance evaluation against simulated aerosol and cirrus loaded scenes, *J. Geophys. Res.*, 115, D24302, doi:10.1029/2010JD014514.
- Kuze, A., Suto, H., Shiomi, K., Kawakami, S., Tanaka, M., Ueda, Y., Deguchi, A., Yoshida, J., Yamamoto, Y., Kataoka, F., Taylor, T. E., and Buijs, H. L.: Update on GOSAT TANSO-FTS performance, operations, and data products after more than 6 years in space, *Atmos. Meas. Tech.*, 9, 2445–2461, <https://doi.org/10.5194/amt-9-2445-2016>, 2016.
- Montzka, S. A., Krol, M., Dlugokencky, E., Hall, B., Joeckel, P., & Lelieveld, J. (2011). Small interannual variability of global atmospheric hydroxyl. *Science*, 331, 67–69. <http://doi.org/10.1126/science.1197640>
- Morino, I., et al. (2011), Preliminary validation of column-averaged volume mixing ratios of carbon dioxide and methane retrieved from GOSAT short-wavelength infrared spectra, *Atmos. Meas. Tech.*, 4(6), 1061–1076, doi:10.5194/amt-4-1061-2011.
- Rigby, M., et al. (2008), Renewed growth of atmospheric methane, *Geophys. Res. Lett.*, 35, L22805, doi:10.1029/2008GL036037.
- Turner, A. J., Frankenberg, C., Wennberg, P. O., & Jacob, D. J. (2017). Ambiguity in the causes for decadal trends in atmospheric methane and hydroxyl. *Proceedings of the National Academy of Sciences of the United States of America*, 44, 201616020. <http://doi.org/10.1142/3171>
- Voulgarakis, A., Naik, V., Lamarque, J. F., Shindell, D. T., Young, P. J., Prather, M. J., et al. (2013). Analysis of present day and future OH and methane lifetime in the ACCMIP simulations. *Atmospheric Chemistry and Physics*, 13(5),
- Wang, J. S. et al. A 3-D model analysis of the slowdown and interannual variability in the methane growth rate from 1988 to 1997. *Glob. Biogeochem. Cycles* 18, 3011, doi:10.1029/2003GB002180 (2004). 2563–2587. [http://doi.org/10.5194/acp-13-2563-](http://doi.org/10.5194/acp-13-2563-2013) 2013
- van Vuuren, D. P., Edmonds, J., Kainuma, M., Riahi, K., Thomson, A., Hibbard, K., et al. (2011). The representative concentration pathways: An overview. *Climatic Change*, 109, 5–31. <http://doi.org/10.1007/s10584-011-0148-z>

Spatial and Temporal Precipitation Variability Analysis Using Concentration Index for Uttarakhand

Tanisha Jaiswal¹, C.M.Bhatt¹ & Arijit Roy¹

¹ Indian Institute of Remote Sensing, IIRS-ISRO, Dehradun, Uttarakhand, India

KEYWORDS: Concentration Index (CI), Precipitation Concentration Index (PCI), Annual Precipitation Index (APCI)

ABSTRACT:

Analysis of precipitation spatial and temporal variability is important for mitigating the impacts of flood and drought risks. Various statistical procedures are used to investigate the precipitation variability. Concentration index, expressed on the basis of the exponential curves, enables the evaluation of contrast or concentration of the different daily amounts of the precipitation by regionalizing the study area into lower and higher variability. In the present study two indices precipitation concentration index (CI) and annual precipitation concentration index (APCI) are used for assessing the precipitation concentrations and the associated spatial patterns for part of Uttarakhand region. Daily precipitation data of 83 points from gridded data for 18 years (2000-2018) obtained from IMD is used for the present study. The CI values in the study area vary from **0.43** to **0.65** with an average value of **0.54**. The results show that higher precipitation CI values were mainly observed in Shiwalik Range and districts near Pauri, Nainital, Haridwar, Roorkee and parts of Chakrata and Tehri whereas lower precipitation CI values were mostly detected in Dehradun and parts of Uttarakashi.

1. INTRODUCTION

The concerns of climatic change and a peculiar weather get worldwide consideration from different specialists, researchers and scientists. One of the most alarming resultant of the climate change is of a comprehensive rising temperature, which in turn results in events of extreme climatic events. Spatiotemporal variation in precipitation directly affects the type of agribusiness and vegetation in an area. It is the key factor in moulding the hydrology, water quality and vegetation all over the Earth. Despite a good rainfall being directly related to healthy agriculture and admirable in ways for hydrology of a particular area but intensive precipitation in few days and decreased number of rainy days are major cause for flash floods, forest fires and drought. Increased frequency in extreme events has resulted in adverse impacts on agriculture, infrastructure, hydrology, irrigation, soil moisture and loss of lives in the most pessimistic scenarios in parallel with tremendous forfeiture of financial and economic too. Characteristics of precipitation that varies spatially and temporally with respect to intensity are being studied for the better informed management of water resources and policies by government.

Various studies related to spatial distribution and trend analysis are being studied with monthly and daily data of precipitation (Costache & Zaharia, 2017; Deng et al., 2017; Elkhachy, 2015; Vishwanath & Tomaszewski, 2018). This helps in understanding the decreased or increased trend of precipitation rate (Cannarozzo et al., 2006). The precipitation concentration index (PCI) and annual precipitation index (APCI) is used to estimate the seasonal or annual rainfall and its variation and the concentration index (CI) is used to assess

the concentration of the extreme daily events comparative to the total aggregation of precipitation. According to Martin-Vide, PCI is the index which can estimate the amount of rainfall distributed over the region with its number of rainy days. It can be assessed annually for the assessment of concentration of heavy rainfall out of total rainy days (Martin-Vide, 2004). There are various studies showing spatial-temporal distribution of rainfall, its variability and concentration over the region seasonally or annually. Many other concentration characteristics indices of precipitation were analysed by using precipitation concentration degree (PCD) and precipitation concentration period (PCP) and some of them validated their results with help of Mann-Kendall test (Al-Bilbisi, 2019; Alijani et al., 2008; Costache & Zaharia, 2017; Das et al., 2014; Deng et al., 2017; Elkhachy, 2015; Li, Jiang, Li, et al., 2011; Nery et al., 2017; Vishwanath & Tomaszewski, 2018).

Southwest china experienced high run off due to heterogeneous concentration of rainfall due to complexity in study area (Li, Jiang, Li, et al., 2011). Sparse vegetation are prone to erosion and runoff in parts of Iran where even low frequency made a huge contribution to the cumulative rainfall on the contrary, Caspian Sea with high concentrated rainfall are less prone to hazard because of dense vegetation (Alijani et al., 2008). CI and APCI indices in Xinjiang also helped in understanding the early arrival of monsoon and distribution of rainfall according to geography of the region (Li, Jiang, & Wang, 2011)(Li, Jiang, Li, et al., 2011). Study area can be divided on the basis of their agro-climatic regions as shown in (Valli et al., 2013) and SPCI and APCI were calculated to conclude that significant changes can be observed based on the south west and north east monsoon in India (Gajbhiye et al., 2016; Patel & Shete, 2015; Thomas & Prasannakumar, 2016; Valli et al., 2013; Zamani et al., 2018). Statistical analysis of

precipitation proves to be restoring ecological resources, irrigation patterns and water resources as seen in Jiangxi, China where they explored APCI and SPCI with trend test(Huang et al., 2013)

In the present study, precipitation concentration has been taken into account using daily gridded data from Indian Metrological Department (IMD) for 83 points, CI and APCI (Annual PCI) are calculated for Uttarakhand province, located in foothills of Lesser Himalayas for the period of 2000 to 2018 (Pai et al., 2014).

2. STUDY AREA

Uttarakhand is a state in the Northern part of India, which shares international border with Tibet in the North and Nepal in the East. To the South and the West are two Indian states, Uttar Pradesh and Himachal Pradesh respectively, as shown in figure 1. The geographic extent of the state is 31.469° N, 79.062° E in the North, 30.25° N, 81.02° E in the East, 29.56° N, 77.99° E in the South and 31.06° N, 77.806° E in the West, with a total area of 20,650 sq. miles. The diverse topography includes glaciers, large number of perennial rivers, rugged mountainous terrain and dense forests. The elevation of the region varies greatly between 300 and 7799 meters. About 68.4% of the state is covered by evergreen forests and 85% by mountains ((Bhambri et al., 2016; Shrestha & Alfred Zinck, 2001; Vishwanath & Tomaszewski, 2018). In present study daily precipitation data from 83 stations during the period of 200–2018 has been used. Figure 1 shows the location of the studied area. Also, the details of summary of precipitation statistics in the gauging station are listed in Table 1.

3. METHODOLOGY

3.1. Concentration Index

The daily precipitation dataset for 83 points from gridded data of Uttarakhand was provided by the Indian Meteorological Department (IMD) Pune, India.

Precipitation CI, as a statistical index, can be used to evaluate the wavering weight of daily precipitation, i.e. the influence of the days of paramount rainfall to the total amount. Its theoretic basic is that the contribution of the days of a given rainfall to the total amount is generally adjustable by a negative exponential distribution, which means that few large daily amounts of precipitation occur in a given period and place. In fact, these scarce large daily amounts of precipitation have greater potential to affect hydrologic input (Martin- Vide, 2004). To assess both the impact of different daily precipitation values on and the contribution of the largest precipitation value to the total precipitation value, the accumulated percentages of precipitation (Y) contributed by the accumulated percentages of days (X) during Y 's occurrence was analysed (Riehl, 1949)(Sa, 2002)(Deng et al., 2017);. This paper uses a limit of 0.1 mm/day to separate between wet and dry days and 1 mm precipitation as class interval to classify the precipitation class limits which is in ascending order. The number of days with precipitation range falling into each class is counted and the associated amount of precipitation is computed. Then the cumulative summation of that is calculated. Finally, X and Y are obtained in this paper. According to Martin-Vide (2004), one way of adapting the curve is through the curve:

$$Y = X \exp[-b(100 - X)^c] \quad (1)$$

where b and c are regression coefficients estimated by the least-squares method with observed precipitation data (Ananthkrishnan & Soman, 1989).

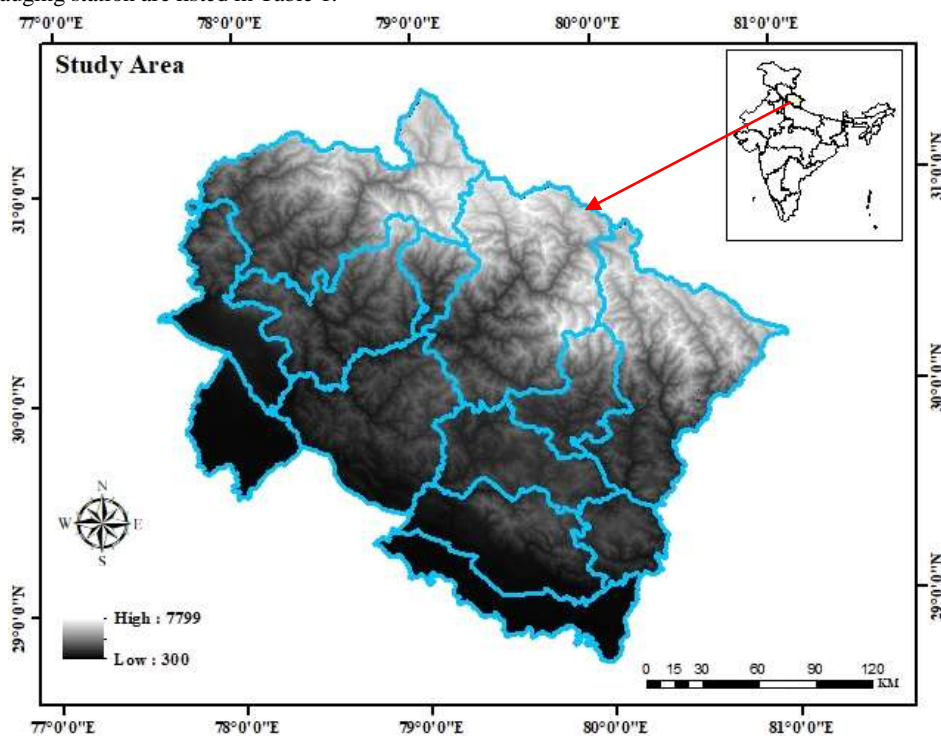


Figure 1 The location of the Uttarakhand state along with the studied station

$$Lna = \frac{\sum X_i^2 \sum \ln Y_i + \sum X_i \sum X_i \ln X_i - \sum X_i^2 \sum \ln X_i - \sum X_i \ln Y_i}{N \sum X_i^2 - (\sum X_i)^2} \quad (2)$$

$$b = \frac{N \sum X_i \sum \ln Y_i + \sum X_i \sum \ln X_i - N \sum X_i \ln X_i - \sum X_i \sum \ln Y_i}{N \sum X_i^2 - (\sum X_i)^2} \quad (3)$$

Knowing that N is the number of classes. After determining the two constants a and b , the definite integral of the exponential curve between 0 and 100 shows the area S under the curve (the abscissa and the ordinate 100), which is given by the formula below:

$$S = \left[\frac{a}{b} e^{bx} \left(x - \frac{1}{b} \right) \right]_0^{100} \quad (4)$$

Based on S , the area S' compressed by the exponential curve, the equidistributional line and $X=100$ is the difference between 5000 and the value of S .

$$S' = 5000 - S \quad (5)$$

Calculation of the CI given by the following formula from Martin-Vide (2004):

$$CI = S' / 5000 \quad (6)$$

Note that the CI value is a fraction of S' and the lower surface of the triangle is bounded by the equidistributional line. It is used as a concentration measure. The precipitation concentration assembles the Gini coefficient, which is the area circled by the perfect distribution (45°) line and the Lorenz curve.

3.2. The Precipitation Concentration Index (PCI)

In the present study, precipitation concentration index (PCI), which is suggested by Oliver (Oliver, 1980) and developed by De Luis et al. (De Luis et al., 2011) was used for annual (APCI) time scales as Eq. (7) :

$$APCI = \frac{\sum_{i=1}^{12} P_i^2}{(\sum_{i=1}^{12} P_i)^2} \times 100 \quad (7)$$

Where P_i presents the amount of monthly precipitation in the i th month that is calculated for each studied station. According to Oliver (1980), PCI (APCI) value <10 show a uniform distribution of precipitation (low precipitation concentration), whereas values ranging from 11 to 15 denote a moderate concentration of precipitation. Values between 16 and 20 offer an irregular distribution of precipitation and values above 20 indicate high precipitation concentration (a strong irregularity in precipitation distribution). The PCI has been employed in many studies (Niu, 2013)

4. RESULTS AND DISCUSSIONS

4.1. Spatial analysis of APCI values

According to results APCI values vary between 12 and 22.50. These values indicate that rainfall does not follow regular pattern and some are extremely irregular. The lower belt or southern, some parts of south eastern and south western regions shows highest dispersion and distribution of rainfall. Large extent of central Uttarakhand also shows irregular pattern of rainfall. According to figure 3, irregularity in annual rainfall is high in lower belt

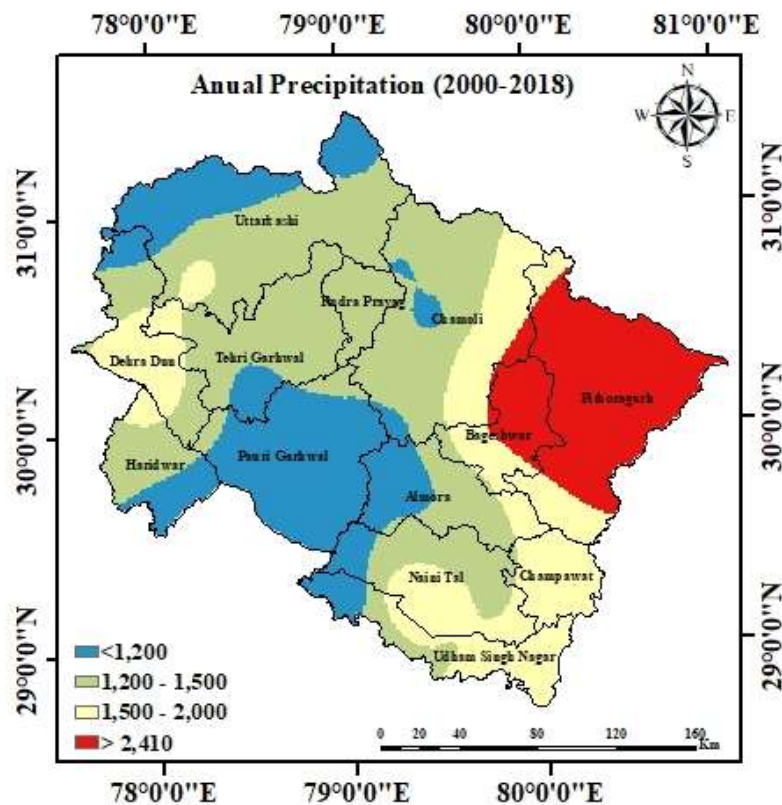


Figure 2 Zonal annual precipitation of Uttarakhand

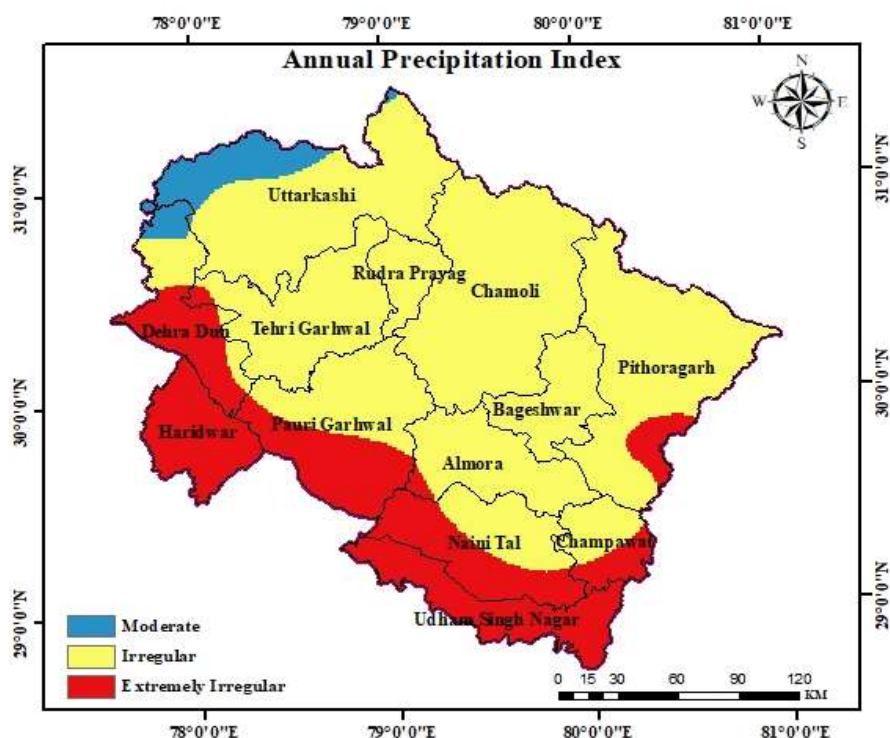


Figure 3 zoning map of calculated APCI over the Uttarakhand state (2000-2018)

or nearby areas of Shivalik range. Only some regions of North western experiences moderate irregular patterns of rainfall. Concentration then increases from Northern to Southern range. Maximum of the parts of state experiences irregular precipitation in range of 15 to 22.50.

4.2. Spatial analysis of CI values (annually)

First, the CI values were estimated for all the 83 points. The CI values range from a minimum of 0.43 (Station 82) to a maximum of 0.65 (Station 5) (Figure 3). As also explained by (Benhamrouche et al., n.d.; Coscarelli & Caloiero, 2012)), the orography influences the rainfall amount and its distribution over the region, which explains the differences in CI values between the two hilly regions of Uttarakhand, that is, near shivalik range and near MBT of Himalayas.

This pattern is observed in almost all the stations present in southern belt of Uttarakhand. These area also receive high annual irregularity in rainfall as depicted by the values of APCI that ranges between 19 and 23. High CI values are also observed in western part, covering districts of Uttarkashi and Teri Garhwal with less number of rainy days, which in turn are somewhat more than the southern belt. Medium CI values of 0.52 to 0.58 are observed in eastern part of Uttarakhand. Despite high concentration of rainfall, number of rainy days are also more in number when compared with southern belt and western part of study area. Low CI values of 0.43 to 0.49 are observed with high rainy days, in northern part showing normal concentration of rainfall in these areas.

4.3. Zonal Spatial analysis of CI and APCI

Though high variation of CI values are observed throughout the state, APCI values depicts other angle to this as it ranges from 12 to 23, stating low to very strong irregularity all over the study area. Districts near Dehradun, Haridwar, Pauri Garhwal and Pitorgarh are some areas that shows high contradiction between CI and APCI values, depicting that though rainfall concentration is high or low in these areas, rainfall frequency is strongly irregular. Except extreme north-western part of state, all other regions show disparity and irregularity in rainfall. Areas with both high CI and APCI values can have flood like situation that covers districts near Nainital, Haridwar, Teri, Pauri, Almora, Bageshwar etc.

As also validated by Zamani et al, for Jharkhand state, (Zamani et al., 2018) by examining the number of rainy days of each station, it can be seen that the stations with greater rainy days, have less CI values, mainly in northern belt of Uttarakhand (Figure 3). Therefore dispersion and distribution of daily precipitation become more regular in such stations. For example, station S48 has the highest number of rainy days (3057 days) and value of CI is 0.52 which reflects the suitable distribution and regularity of precipitation in this station.

5. CONCLUSION

Investigation of precipitation dispersion and distribution over an area is of great importance in terms of climate and hydrological studies. PCI (APCI) is an indicator for determining precipitation changes over a specific region. Results from this indicator could be utilized for managing water resources, and designing proper plans for

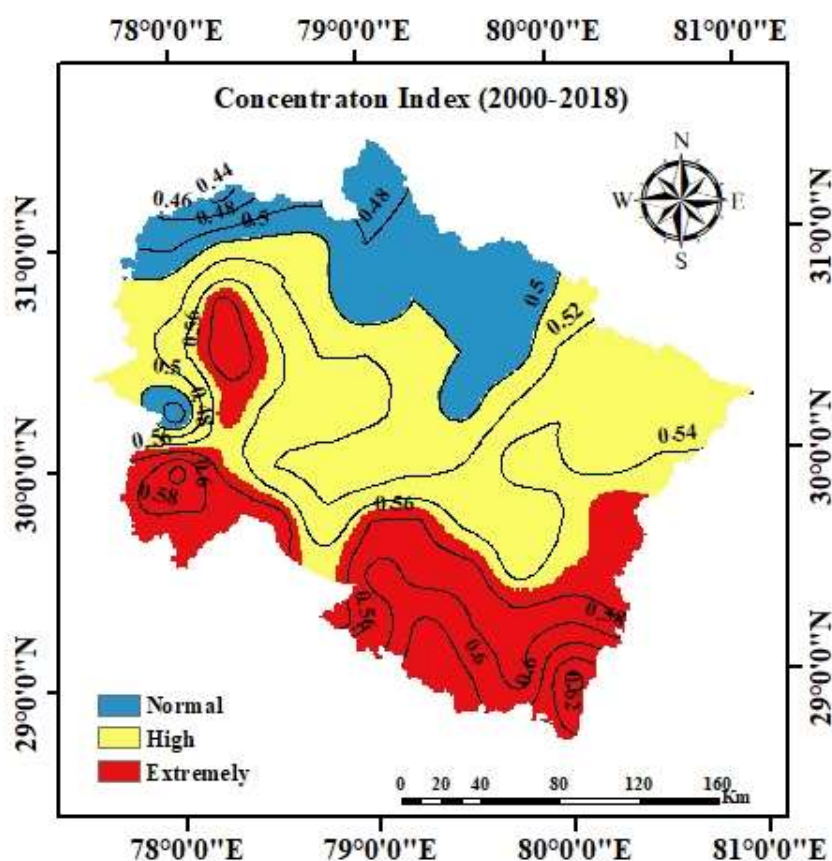


Figure 4 Zonal statistical values of CI in Uttarakhand state

controlling or coping with natural disasters. Also, CI as a concentration index, which is employed to study the daily concentration and the structure of precipitation data. In this study, the CI and APCI indices are used to analyse the distribution and structure of precipitation at Uttarakhand state (UK), India, in the period of 2000 to 2018.

The results showed that the APCI values vary between 12 and 22.50. This result represents a highly irregular pattern of precipitation, and non-uniform distribution of precipitation among the months of the year in the study area. The value of concentration index (CI) varies between 0.43 and 0.65 in most part of the region. Generally it can be concluded that daily heavy rains have been occurred over central and southern parts of the study area.

This is worth mentioning that the southern, western and eastern parts of the area have the majority of the aforementioned precipitation irregularity and dispersion. The results of studying the precipitation concentration index provide useful information for managers to design suitable plans for coping with storms and heavy rains. In addition, studying precipitation concentration is important in hydrologic projects and other water resources management plans. This is suggested that more attention to be paid to modify designing standards of runoff collecting systems and urban flood management based on the PCI and CI indices. In addition to considering the study's limitations such as statistical data length, location of the studied stations due to relief, majority of the high rainfall and extreme events

measurements are not included due to unavailability of IMD station points, which are actually responsible for cloud burst or flash floods. Even if extreme rainfall was found during the analysis, it was subsided due to statistical formula and there frequency were comparatively very low than other measurements. Quality of measured data, the risk and uncertainty analysis of precipitation concentration indices is recommended for future studies.

REFERENCES:

- Al-Bilbisi, H. (2019). Spatial monitoring of urban expansion using satellite remote sensing images: A case study of Amman City, Jordan. *Sustainability (Switzerland)*, 11(8). <https://doi.org/10.3390/su11082260>
- Alijani, B., O'Brien, J., & Yarnal, B. (2008). Spatial analysis of precipitation intensity and concentration in Iran. *Theoretical and Applied Climatology*, 94(1-2), 107-124. <https://doi.org/10.1007/s00704-007-0344-y>
- Ananthkrishnan, R., & Soman, M. K. (1989). Statistical distribution of daily rainfall and its association with the coefficient of variation of rainfall series. *International Journal of Climatology*, 9(5), 485-500. <https://doi.org/10.1002/joc.3370090504>
- Benhamrouche, A., Boucherf, D., Hamadache, R., Bendahmane, L., Teixeira, J., & Group, C. (n.d.). Spatial distribution of the. *Revista Brasileira De Biologia*, 3(1), 1-14.

- Bhambri, R., Mehta, M., Dobhal, D. P., Gupta, A. K., Pratap, B., Kesarwani, K., & Verma, A. (2016). Devastation in the Kedarnath (Mandakini) Valley, Garhwal Himalaya, during 16–17 June 2013: a remote sensing and ground-based assessment. *Natural Hazards*, 80(3), 1801–1822. <https://doi.org/10.1007/s11069-015-2033-y>
- Cannarozzo, M., Noto, L. V., & Viola, F. (2006). Spatial distribution of rainfall trends in Sicily (1921-2000). *Physics and Chemistry of the Earth*, 31(18), 1201–1211. <https://doi.org/10.1016/j.pce.2006.03.022>
- Coscarelli, R., & Caloiero, T. (2012). Analysis of daily and monthly rainfall concentration in Southern Italy (Calabria region). *Journal of Hydrology*, 416–417, 145–156. <https://doi.org/10.1016/j.jhydrol.2011.11.047>
- Costache, R., & Zaharia, L. (2017). Flash-flood potential assessment and mapping by integrating the weights-of-evidence and frequency ratio statistical methods in GIS environment – Case study: Bâsca chiojdului river catchment (Romania). *Journal of Earth System Science*, 126(4), 1–19. <https://doi.org/10.1007/s12040-017-0828-9>
- Das, P. K., Chakraborty, A., & Seshasai, M. V. R. (2014). Spatial analysis of temporal trend of rainfall and rainy days during the Indian summer monsoon season using daily gridded (0.5° × 0.5°) rainfall data for the period of 1971-2005. *Meteorological Applications*, 21(3), 481–493. <https://doi.org/10.1002/met.1361>
- De Luis, M., González-Hidalgo, J. C., Brunetti, M., & Longares, L. A. (2011). Precipitation concentration changes in Spain 1946-2005. *Natural Hazards and Earth System Science*, 11(5), 1259–1265. <https://doi.org/10.5194/nhess-11-1259-2011>
- Deng, S., Li, M., Sun, H., Chen, Y., Qu, L., & Zhang, X. (2017). Exploring temporal and spatial variability of precipitation of Weizhou Island, South China Sea. *Journal of Hydrology: Regional Studies*, 9, 183–198. <https://doi.org/10.1016/j.ejrh.2016.12.079>
- Elkhrachy, I. (2015). Flash Flood Hazard Mapping Using Satellite Images and GIS Tools: A case study of Najran City, Kingdom of Saudi Arabia (KSA). *Egyptian Journal of Remote Sensing and Space Science*, 18(2), 261–278. <https://doi.org/10.1016/j.ejrs.2015.06.007>
- Gajbhiye, S., Meshram, C., Mirabbasi, R., & Sharma, S. K. (2016). Trend analysis of rainfall time series for Sindh river basin in India. *Theoretical and Applied Climatology*, 125(3–4), 593–608. <https://doi.org/10.1007/s00704-015-1529-4>
- Huang, J., Sun, S., & Zhang, J. (2013). Detection of trends in precipitation during 1960–2008 in Jiangxi province, southeast China. *Theoretical and Applied Climatology*, 114(1–2), 237–251. <https://doi.org/10.1007/s00704-013-0831-2>
- Li, X., Jiang, F., Li, L., & Wang, G. (2011). Spatial and temporal variability of precipitation concentration index, concentration degree and concentration period Xinjiang, China. *International Journal of Climatology*, 31(11), 1679–1693. <https://doi.org/10.1002/joc.2181>
- Li, X., Jiang, F., & Wang, G. (2011). *Spatial and temporal variability of precipitation concentration index, concentration degree and concentration period in Xinjiang, China*. 1693–1679. <https://doi.org/10.1002/joc.2181>
- Martin-Vide, J. (2004). Spatial distribution of a daily precipitation concentration index in peninsular Spain. *International Journal of Climatology*, 24(8), 959–971. <https://doi.org/10.1002/joc.1030>
- Nery, J. T., Carfan, A. C., & Martin-Vide, J. (2017). Analysis of Rain Variability Using the Daily and Monthly Concentration Indexes in Southeastern Brazil. *Atmospheric and Climate Sciences*, 07(02), 176–190. <https://doi.org/10.4236/acs.2017.72013>
- Niu, J. (2013). Precipitation in the Pearl River basin, South China: Scaling, regional patterns, and influence of large-scale climate anomalies. *Stochastic Environmental Research and Risk Assessment*, 27(5), 1253–1268. <https://doi.org/10.1007/s00477-012-0661-2>
- Oliver, J. E. (1980). Monthly precipitation distribution: A comparative index. *Professional Geographer*, 32(3), 300–309. <https://doi.org/10.1111/j.0033-0124.1980.00300.x>
- Pai, D. S., Sridhar, L., Rajeevan, M., Sreejith, O. P., Satbhai, N. S., & Mukhopadhyay, B. (2014). *Development of a new high spatial resolution (0.25° × 0.25°) Long Period (1901-2010) daily gridded rainfall data set over India and its comparison with existing data sets over the region data sets of different spatial resolutions and time periods has also been discussed. stations in India were used, highest number of stations used by any studies so far sets suggested that the climatological and variability features of rainfall over rainfall data sets. In addition, the spatial rainfall distribution like heavy rainfall.* 1(January), 1–18.
- Patel, N. R., & Shete, D. T. (2015). Analyzing Precipitation Using Concentration Indices for North Gujarat Agro Climatic Zone, India. *Aquatic Procedia*, 4(Icwrcoe), 917–924. <https://doi.org/10.1016/j.aqpro.2015.02.115>
- Riehl, H. (1949). Some Aspects of Hawaiian Rainfall. *Bulletin of the American Meteorological Society*, 30(5), 176–187. <https://doi.org/10.1175/1520-0477-30.5.176>
- Sa, T. (2002). *Some Aspects Chemotaxomy.Pdf*. 62(9), 1817–1824.
- Shrestha, D. P., & Alfred Zinck, J. (2001). Land use classification in mountainous areas: Integration of image processing, digital elevation data and field knowledge (application to Nepal). *ITC Journal*, 3(1), 78–85. [https://doi.org/10.1016/S0303-2434\(01\)85024-8](https://doi.org/10.1016/S0303-2434(01)85024-8)
- Thomas, J., & Prasannakumar, V. (2016). Temporal analysis of rainfall (1871-2012) and drought characteristics over a tropical monsoon-dominated State (Kerala) of India. *Journal of Hydrology*, 534, 266–280. <https://doi.org/10.1016/j.jhydrol.2016.01.013>
- Valli, M., Sree, K. S., & Krishna, I. V. M. (2013). *Analysis of Precipitation Concentration Index and Rainfall Prediction in various Agro-Climatic Zones of Andhra*

Pradesh , India. 2(5), 53–61.

Vishwanath, V. H., & Tomaszewski, B. (2018). Flood hazard, vulnerability and risk assessments for uttarakhand state in India. *Proceedings of the International ISCRAM Conference, 2018-May(May)*, 362–375.

Zamani, R., Mirabbasi, R., Nazeri, M., Meshram, S. G., & Ahmadi, F. (2018). Spatio-temporal analysis of daily, seasonal and annual precipitation concentration in Jharkhand state, India. *Stochastic Environmental Research and Risk Assessment, 32(4)*, 1085–1097. <https://doi.org/10.1007/s00477-017-1447-3>

DETECTION AND CLASSIFICATION OF MARINE SLICKS THROUGH DECOMPOSITION AND SUPERVISED CLASSIFICATION USING POLSAR DATA

Vaishali Chaudhary^{1,*}, Shashi Kumar²

¹ Photogrammetry and Remote Sensing Department, Indian Institute of Remote Sensing
Indian Space Research Organization, Dehradun, India - vaishali.iirs@gmail.com, vaishali@iirs.gov.in

² Photogrammetry & Remote Sensing Department, Indian Institute of Remote Sensing
Indian Space Research Organization, Dehradun, India - shashi@iirs.gov.in, sksinghiirs@gmail.com

Commission VI, WG VI/4

KEY WORDS: Oil Spills, PolSAR, Decomposition, Supervised Classification

ABSTRACT:

Oceans are the largest ecosystem covering 70% of the earth's surface and supporting the greatest biodiversity of this planet. The accidental oil spills in the oceans have become a major concern for the environment. The oil spills are accidental seepage of oils into water bodies due to collision, illegal transportation, and blowouts like Deep Water Horizon in the Gulf of Mexico (2010). A million gallons of oil have been dumped into the ocean in the last decade. If the current conditions persist, the majority of the ocean species will die in the coming 60–70 years. Detecting oil spills is more of a tedious task. Remote Sensing plays an important role in timely capturing these oil spills as this technology is not dependent on weather and season conditions. SAR images are proven to be robust in acquiring the oil spill images within the right time and that too quite effectively. The oil spills spread over the water surface with time depending upon its chemical composition, viscosity, specific gravity, and intermolecular surface tension, etc. The backscatter value of oil spills differs with the age of the oil spills. UAVSAR L-band Quad-Pol dataset is used for the oil spill extraction and the region of interest is the North Sea, Norway. The captured oil spills were a part of the Norwegian Radar Oil spill Experiment (NORSE, June 2015). The dataset was already between 0-1 pixel range, and following the normal probability distribution curve, hence no need to radiometrically calibrate the data as well. Refined Lee filter of window 9*9 is applied to the dataset to remove the salt and pepper effect from the data and for smoothening without any substantial information loss. Van-Zyl, a model-based incoherent decomposition, and Yamaguchi decomposition are applied to the filtered dataset to get insights about the scattering behavior of the ocean and oil spills. A comparative analysis between the two decompositions has shown better classification accuracy when Van-Zyl decomposition is used. Since the evolution of technology, the classification of remotely sensed data is a great tool for segmenting different features. Wishart Supervised Classifier with window size 15*15 is used for classifying the oil spills. It is found that Wishart Classifier gives quite promising results as the pixels in an image are distributed by the Wishart distance principle, hence making the classifier more effective in classification. The output of the classifier has distinguished the oil spills from water effectively. The noise cannot be removed completely from data and due to this property, some classes can be misclassified during classification. For examining the accuracy, the confusion matrix, and the AUROC curve are plotted to know how accurately the oil and water classes are classified.

1. INTRODUCTION

Synthetic Aperture Radar (SAR) has proven itself as a milestone in monitoring the phenomena related to earth observation and atmospheric sciences. The timely response of the SAR system surpasses other optical sensors and provides high-resolution two-dimensional imagery. The oil spills can occur at any time for day time monitoring optical sensors provide quite good resolution imagery but to capture the region in the night is not probable. In the day time also It becomes quite hard to figure out the oil spill regions in the ocean as there are various other phenomena arising in the ocean like natural mineral oil seepage that looks closely like oil spills. The visual interpretation of the oil spills modifies with time as well as with the thickness of the oil. In optical imagery, the oil spills demonstrate black and brown (sometimes silvery and rainbow, based on the thickness of the spill) signature which sometimes can be of a look-alike or might be a result of sun glint or natural seeps adjoining the upper surface of the water which are accounted falsely as oil spills (Nirchio et al., 2005). Coming to the Infrared

(IR) sensors, the oil spills absorbs a significant amount of radiation and then re-emits this absorbed radiation as thermal energy which lies in the range of 8-14 mm. As both water and oil absorb a different amount of the radiation because of their different physical properties and chemical composition, hence the difference in the amount of emission of the radiation from both the elements is different leading to different brightness temperatures (Allan, 1980). Therefore the oil spill layer appears colder than the water body (Fingas, Brown, 1997). The major problem with these methods is the incompetence of capturing the regions during bad weather, clouds and at night. SAR sensors are proficient in observing the region of interest even in the night time. SAR sensors have been proved as a great tool for both airborne and spaceborne platforms. The Oil Spills in any SAR imagery appears dimmer than the surrounding water body. The oil spill dampens the surface waves, resulting in low Normalized Radar Cross Section (NRCS) if matched to the ocean surface which has a high Normalized Radar Cross section (NRCS) than the oil spill region (Chaturvedi et al., 2019). The NRCS of the oil spills varies with time. Fresh oil spills have much lower NRCS compared to the oil spill that had occurred a couple of hours ago. It sometimes becomes quite challenging to capture

* Corresponding author

the precise amount of the oil that has been spilled as several other factors like Dispersion, Evaporation, Dissolution, Emulsification, Sedimentation, Bio-degradation, Wind Speed and Incidence angle of the electromagnetic wave sensor also plays a major role in appearance of the oil spill in SAR image and are also responsible for the total NRCS from the oil spilled region. SAR polarimetry plays a major role in mining out various physical properties of oil spills apart from only extracting the region of oil spills.

2. METHODOLOGY

This section deals with the utilization of the dataset and the techniques applied on it to extract the oil spills from the polarimetric products. The study area is the North Sea in Norway (see Figure 1).

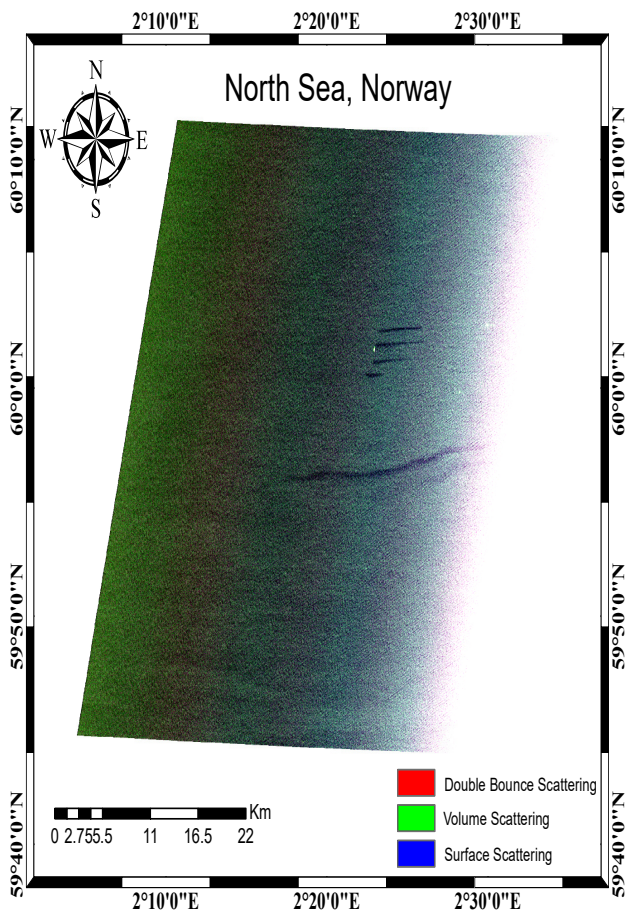


Figure 1. Study Area - North Sea, Norway

As Norway is a country with most number of countryside inhabitants, the foremost means of transportation is ship dependent. Therefore considering it as a prone area for the oil spills an experiment was carried out to simulate the scenario. The Norwegian Radar Oil Spill Experiment (NORSE 2015) was carried out at Frigg Field in the North Sea (N 59° 59', E 2° 27') on 10 June 2015. The whole experiment was a part of the oil-on-water exercise apprehended by the Norwegian Clean Seas Association for Operating Companies (NOFO) (Jones et al., 2016). Controlled release of four elements with a slight time disparity was done which was captured by several airborne and space-borne SAR sensors on the day NORSE 2015 was carried out. Out

of four elements, three were emulsions i.e., 80% (E80), 60% (E60) and 40% (E40), with having just about the same chemical composition but different volumetric division and plant oil were released to simulate natural slicks. The complete details about the released oil spills can be found in Table 1 (Skrunes et al., 2016).

Parameters	Details
Sensor	UAVSAR L-band (Airborne)
Product Id	norway_00709_15091_010_150610_L090_CX_01
Polarisation	Quad-pol(HH,VV,HV, and VH)
Incidence Angle	19.5°-67.5°
Product Type	.grd (ground range projected)
Acquisition Date and Time	10 June 2015, 07:44:13 UTC
Look Direction	Left
Number of Looks	Range - 3, Azimuth - 12
Bandwidth	80 MHz

Table 1. Dataset Properties

The dataset used for this study is L-band Airborne UAVSAR data. The complete statistics about the dataset can be found in Table 1. Due to the low altitude of the airborne sensor compared to space-borne platforms, the airborne platforms provide high-

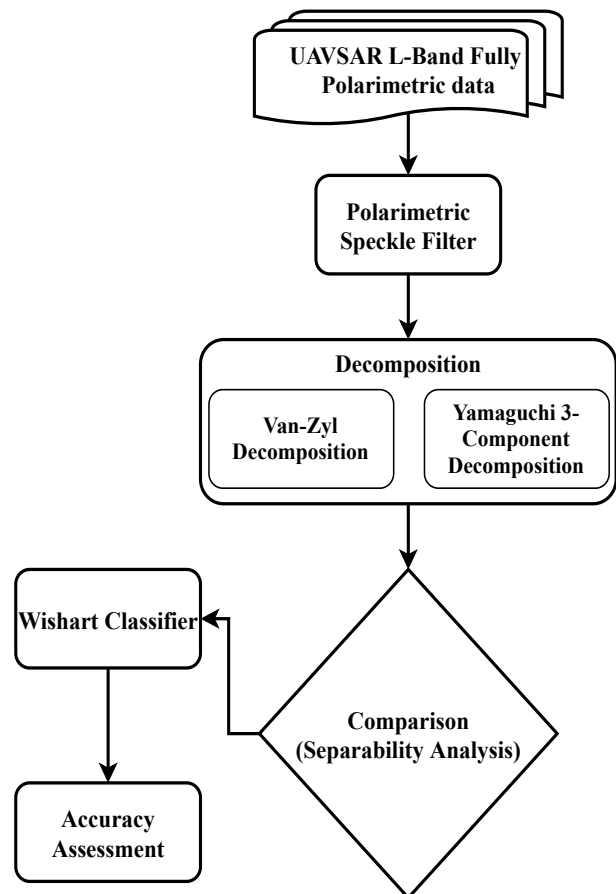


Figure 2. Proposed Methodology for detection and classification of oil spills

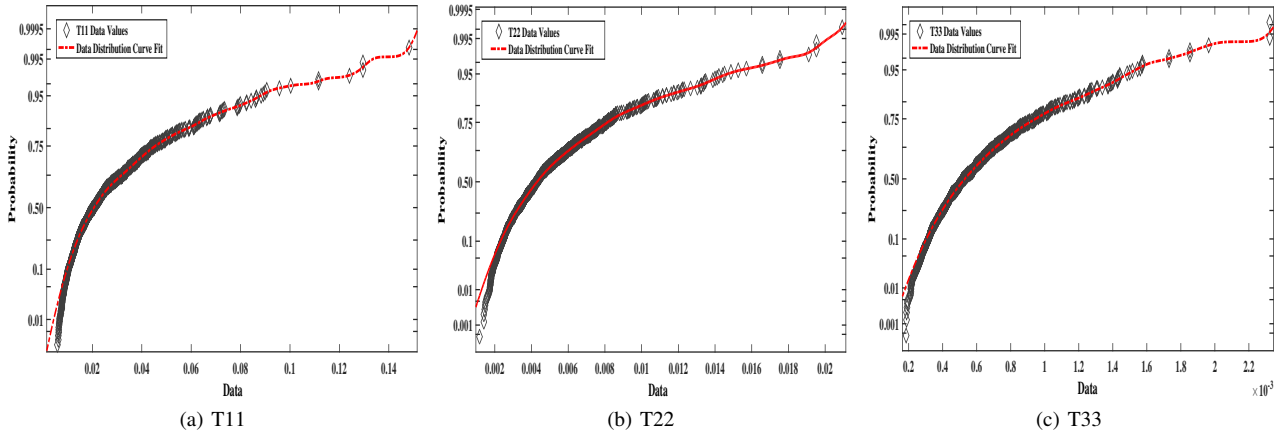


Figure 3. Probability Distribution Curve fitting for (a) T11, (b) T22, and (c) T33

resolution imagery but with less swath. The proposed methodology is given in Figure 2. The UAVSAR polarimetric data is first preprocessed i.e., polarimetric speckle filtering is implemented for normalizing the variation in pixel range (by smoothing the image) which is formed due to salt and pepper effect, known as speckle. Speckle makes classification and analysis difficult by degrading the texture quality. The speckle generates due to the contribution from independent scattering elements in the scene when illuminated by a coherent radar signal causing granularity property in the pattern (Goodman, 1976). Refined Lee polarimetric speckle filter is applied to the data. The basis of Lee Sigma Filter is the two-sigma probability of Gaussian distribution (Zhang et al., 2011). The speckle multiplicative noise model is also assimilated in Lee Sigma Filter (Lee, 1980, Kuan et al., 1985).

The probability curve are also plotted to get an understanding of the data for any irregularities. Curve fitting is regarded as a tool for trading with ambiguity (Bowman, Azzalini, 1999). The data is ensuing the probability curve quite precisely demonstrating the data is already calibrated radiometrically (see Figure 3). Refined Lee filter with window size 9*9 has given the most prominent output with effective minimization of speckle without any substantial loss of data. To excerpt, the nature of backscattering from oil spills and the water body, implementation of two decomposition model viz. Van-Zyl Decomposition model and Yamaguchi 3-Component Decomposition model are done on the speckle filtered polarimetric product. Based on the separability analysis between Oil and Water for both the applied decomposition models is carried out. It is observed that the Van-Zyl Decomposition model gives separability between Oil and Water at quite a good level and better than Yamaguchi Decomposition. Since the evolution of Remote Sensing techniques, classification has always been a great tool for segmenting the region of interest, giving a clear interpretation, visually about the scene by assigning different classes to dissimilar elements existing in the imagery. The accuracy of the classification is the paramount significant factor for precise quantification of the overall process so the AUROC curve, as well as the confusion matrix, is calculated affirming how accurately the classification is implemented.

2.1 Decomposition Models

Two decomposition models Van-Zyl decomposition model (incoherent decomposition model) and Yamaguchi 3-Component

Decomposition model are applied to the filtered polarimetric products.

2.1.1 Van Zyl Decomposition Model: The principle of Van-Zyl decomposition is based on the postulation that the correlation between the co-polarized channel and cross-polarized channel is zero and the reflection symmetry hypothesis is formed. This theory holds true in the case of natural elements like forestry and soil. Using these assumptions the covariance matrix can be articulated as (Lee, Jong-Sen; Pottier, 2009):

$$C_3 = A_1 \begin{bmatrix} |\alpha|^2 & 0 & \alpha \\ 0 & 0 & 0 \\ \alpha^* & 0 & 1 \end{bmatrix} + A_2 \begin{bmatrix} |\beta|^2 & 0 & \beta \\ 0 & 0 & 0 \\ \beta^* & 0 & 1 \end{bmatrix} + A_3 \begin{bmatrix} 0 & 0 & 0 \\ 0 & 1 & 0 \\ 0 & 0 & 0 \end{bmatrix} \quad (1)$$

From Equation 1, it can be observed that the first two eigenvectors signify almost equivalent scattering responses which are stated as odd and even bounce scattering.

2.1.2 Yamaguchi Decomposition Model: When the reflection symmetry hypothesis holds true, 3-component Freeman-Durden decomposition can be applied successfully. Yamaguchi proposed a 4-component model for the region in the image not following the reflection symmetry hypothesis with an additional component correspondent to helix scattering power (Lee, Jong-Sen; Pottier, 2009). The covariance matrix with four scattering elements is given as (Yamaguchi et al., 2005):

$$\langle [C] \rangle^{HV} = f_s + \begin{bmatrix} |\beta|^2 & 0 & \beta \\ 0 & 0 & 0 \\ \beta^* & 0 & 1 \end{bmatrix} + f_d \begin{bmatrix} |\alpha|^2 & 0 & \alpha \\ 0 & 0 & 0 \\ \alpha^* & 0 & 1 \end{bmatrix} + \frac{f_v}{15} \begin{bmatrix} 8 & 0 & 2 \\ 0 & 4 & 0 \\ 2 & 0 & 3 \end{bmatrix} + \frac{f_c}{4} \begin{bmatrix} 1 & \pm j\sqrt{2} & -1 \\ \mp j\sqrt{2} & 2 & \pm j\sqrt{2} \\ -1 & \mp j\sqrt{2} & 1 \end{bmatrix} \quad (2)$$

where, f_s , f_d , f_v , and f_c in Equation 2 equation are the expansion coefficients to be resolved. Both the decompositions are applied on the SAR polarimetric product and in both the decomposition models the area enclosed by the oil is giving no backscattering as the oil dulls the short capillary waves, making most of the radar signal to reflect in other direction than

the receiver. The sea is giving a blend of surface scattering and volume scattering with some pixels showing a hint of double bounce scattering. The occurrence of this scattering pattern is due to the rough texture of the sea with multiple capillary and short gravity waves at the acquisition time of the imagery. Another reason for the variation in scattering is the change in the incidence angle of the sensor from near to far range. The separability analysis has shown that both the decomposition models successfully part the oil from the water but the Yamaguchi decomposition model has given faintly less separability between Oil and Water than Van-Zyl Decomposition.

2.2 Classification

The classifier’s aim is to devise a method or construct a rule for assigning objects to one of a finite set of classes on the basis of a vector of variables measured on the objects. Wishart Supervised Classifier works like maximum likelihood classifier with the principle of distribution of polarimetric coherency matrix based on the Wishart Distribution which is given by:

$$P(\langle [T] \rangle / [T_m]) = \frac{L^{Lp} |\langle [T] \rangle|^{L-p} e^{LTr([T_m]^{-1} \langle [T] \rangle)}}{\prod \frac{p(p-1)}{2} \Gamma(L) \dots \Gamma(L-p+1) |[T_m]|^L} \quad (3)$$

Using the training samples from m^{th} class, the coherency matrix $[T_m]$ is calculated for each class. This assignment of an averaged Coherency Matrix $\langle [T] \rangle$ to the class m is done on the principle of Bayes Maximum Likelihood Classifier (LEE et al., 1994, Lee, Jong-Sen; Pottier, 2009) is done if,

$$[T] \in [T_m] \quad \text{if} \quad d_m([T]) < d_j([T]) \quad \forall j \neq m \quad (4)$$

with

$$d_m([T]) = LTr([T_m]^{-1}[T]) + L \ln(|[T_m]|) - \ln(P([T_m]) + K) \quad (5)$$

Wishart Supervised Classifier (WSC) has been implemented on the Van-Zyl Decomposition output as Van-Zyl decomposition has shown maximum separability between Oil and Water. WSC with a window of 15*15 has categorized the oil spills from water successfully with a few pixels of water classified as oil.

3. RESULTS AND DISCUSSION

The decomposition outputs of Van-Zyl Decomposition and Yamaguchi Decomposition are given in Figure 4. Van-Zyl decomposition and Yamaguchi decomposition has shown similar responses for both oil and water bodies. Although the backscattering response in both the decomposition is quite alike, and to know the actual separability between oil and water, separability analysis is carried out. A total of 40-pixel values for Oil and Water each for both the decomposition has been extracted and separability analysis was carried out. The separability analysis has shown Van-Zyl Decomposition with clearly separating the Oil from Water. Yamaguchi Decomposition also has shown quite a good separability between Oil and Water but a few pixel values have shown overlapping trends (see Figure 5). Based on the separability outputs Van-Zyl Decomposition is ideal for further classification implementation for minimum misclassified pixels. Wishart Supervised Classifier is considered for the classification.

Wishart Classifier works on Wishart distance principle since the pixels in an image are also distributed on the basis of Wishart

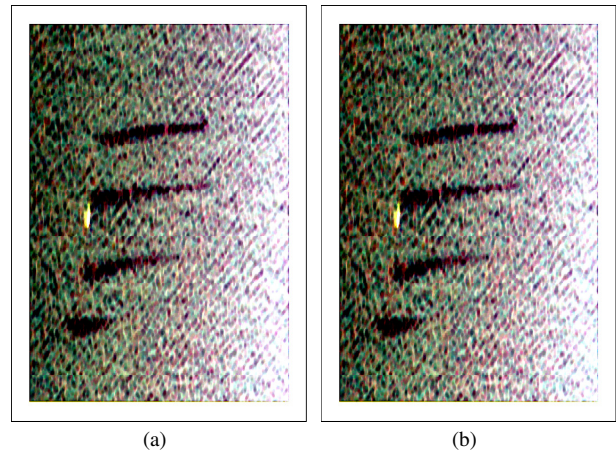


Figure 4. (a) Van-Zyl Decomposition, (b) Yamaguchi 3-Component Decomposition

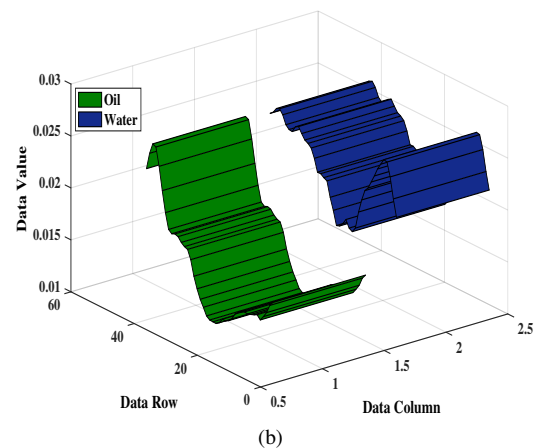
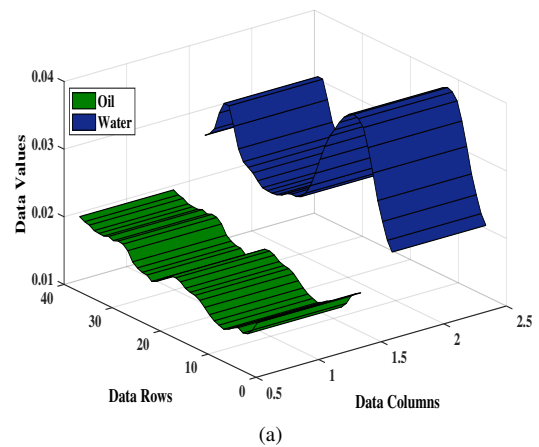


Figure 5. (a) Van-Zyl Decomposition, (b) Yamaguchi 3-Component Decomposition

distance, Wishart Classifier is likely to execute much precisely. Wishart Supervised classification is implemented with window 3*3, 9*9, 15*15, 21*21 and 27*27. The Wishart classifier with 15*15 window size (see Figure 6) has classified the oil spills from the water much accurately than other window sizes as smaller window sizes were resulting in an overestimation of the oil spill class by considering the dark pixels of the water body as an oil spill. While Wishart Classifier with larger window sizes

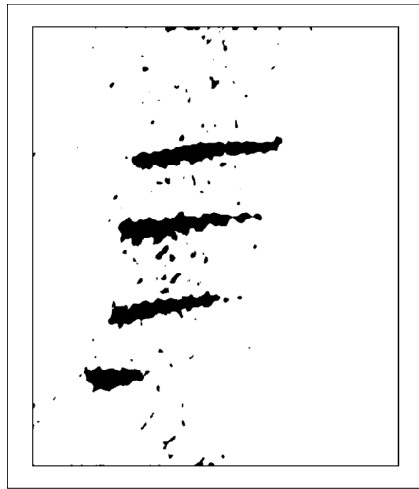


Figure 6. Wishart Supervised Classification with window size 15*15

resulting in an overestimation of water class by labeling the oil spill class as water class. Classification of the data has been a great tool in the last decade for a better visual interpretation and quantitative analysis. The accuracy of the classification is of utmost importance as any variation in the data interpretation can result in entirely different results.

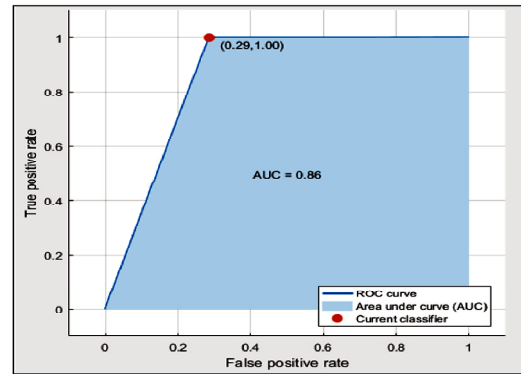
3.1 AUROC Curve and Confusion Matrix

In a supervised classification assignment of the elements present in the scene to a finite set of classes depending upon measure vector variable on the elements. The main problem with the classification techniques is the misclassification rate. To interpret and reckon the accuracy of Wishart classifier, Area Under the Receiver Operating Characteristics (AUROC) has been plotted. The plot represents the extent of separation between the classes. A perfect separation is achieved when the curve follows the top left edge in the curve. The area under the ROC curve is a repeatedly used method for determining the performance of a binary class instance. In simple terms, the probability of a randomly chosen class member belonging to the other class is minor than the probability of a randomly selected member of other class and this procedure ultimately gives separability measures (Hand, Till, 2001). Mathematically, the True Positive Rate (Hit Rate and Recall) and The False Positive Rate (False Alarm Rate) are calculated as given in equation 6 and 7 (Fawcett, 2006):

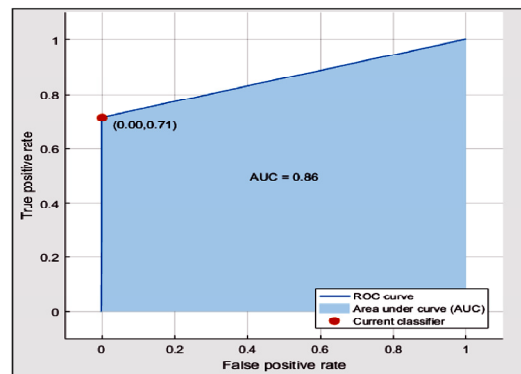
$$True\ Positive\ Rate \approx \frac{Positives\ Correctly\ Classified}{Total\ Positives} \tag{6}$$

$$False\ Positive\ Rate \approx \frac{Negatives\ Incorrectly\ Classified}{Total\ Negatives} \tag{7}$$

AUROC Curve for both the classes i.e., Oil (Class 1) and Water (Class 2) is plotted. Since the classified output is a binary problem, hence the outcome can be either positive or negative. Both the axes, True Positive Rate (TPR) and False Positive Rate (FPR) has a range of [0-1]. For Class 1 (Oil) the AUROC has cut-point at (0.29,1.00) indicating that out of all samples of oil class, there are chances of getting truer positive values (i.e., 1.00) than false-positive values (i.e., 0.29). The AUROC curve



(a)



(b)

Figure 7. (a) Van-Zyl Decomposition, (b) Yamaguchi 3-Component Decomposition

for Class 2 (Water) has predicted more chances of true-positive values (0.71) without any false-positive group value (0.00).

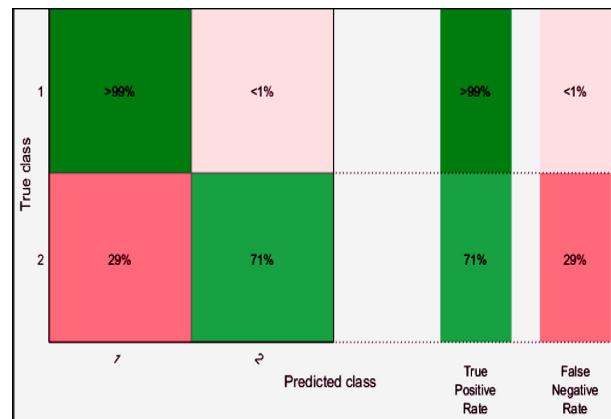


Figure 8. Confusion Matrix of Wishart Supervised Classification for Class 1 (Oil) and Class 2 (Water)

The confusion matrix is also calculated as an additional step for accuracy estimation (see Figure 8). It is clearly perceived from the confusion matrix that more than 99% of samples are accurately classified for Class 1 (Oil). Some pixels of Class 2 (Water) have been misclassified as Class 1 (Oil). For Class 2 (Water), 79% of the samples are accurately classified while 29% are falsely classified as Class 1. The main reason behind the misclassification is the overestimation of the dark pixels (formed due to ocean swell and its irregular surface) as pixels of the oil expanse.

4. CONCLUSION

This study has presented a semi-automatic way of extracting the oil spills and analyzed the capability of L-band UAVSAR data for successful extraction of oil spills. The backscattering response from the elements present in the scene is estimated much accurately with Van Zyl Decomposition as compared to Yamaguchi Decomposition as the later decomposition tends to show overestimation of volume scattering due to formation of negative powers of eigenvalues in the decomposition. It is observed that the texture of the image was quite coarser due to the swell of the ocean and surface winds hence it is recommended to use the polarimetric filter with significantly large kernel size for smoothing the high-intensity values in the image. For digital image processing problems like this one with the grainier textured image, Wishart Classification has provided optimal results, but the kernel size of the classifier has played a major role in accomplishing the ideal results hence a dynamic approach with advance filtering and segmentation techniques can further be implemented based on the nature of the problem.

REFERENCES

- Allan, J. A., 1980. A review of: "Remote Sensing: Principles and Interpretation". By FLOYD F. SABINS, JR. (San Francisco: W. H. Freeman, 1978.) [Pp. 1+426.]. *International Journal of Remote Sensing*, 1(3), 307-308. <https://doi.org/10.1080/01431168008948242>.
- Bowman, A. W., Azzalini, A., 1999. Applied smoothing techniques for data analysis : the kernel approach with s-plus illustrations.
- Chaturvedi, S. K., Banerjee, S., Lele, S., 2019. An assessment of oil spill detection using Sentinel 1 SAR-C images. *Journal of Ocean Engineering and Science*. <https://doi.org/10.1016/j.joes.2019.09.004>.
- Fawcett, T., 2006. An introduction to ROC analysis. *Pattern Recognition Letters*, 27(8), 861–874.
- Fingas, M. F., Brown, C. E., 1997. Review of oil spill remote sensing. *Spill Science and Technology Bulletin*, 4(4), 199–208.
- Goodman, J. W., 1976. Some fundamental properties of speckle*. *Journal of the Optical Society of America*, 66(11), 1145.
- Hand, D. J., Till, R. J., 2001. A Simple Generalisation of the Area Under the ROC Curve for Multiple Class Classification Problems. *Machine Learning*, 45(2), 171–186.
- Jones, C. E., Espeseth, M. M., Holt, B., Brekke, C., Skrunes, S., 2016. Characterization and discrimination of evolving mineral and plant oil slicks based on L-band synthetic aperture radar (SAR). *SAR Image Analysis, Modeling, and Techniques XVI*, 10003, 100030K.
- Kuan, D. T., Sawchuk, A. A., Strand, T. C., Chavel, P., 1985. Adaptive Noise Smoothing Filter for Images With Signal-Dependent Noise. *IEEE Transactions on Pattern Analysis and Machine Intelligence*, PAMI-7(2), 165–177.
- Lee, J.-s., 1980. Digital Image Enhancement and Noise Filtering by Use of Local Statistics. *Analysis*, 1978–1981.
- LEE, J. S., GRUNES, M. R., KWOK, R., 1994. Classification of multi-look polarimetric SAR imagery based on complex Wishart distribution. *International Journal of Remote Sensing*, 15(11), 2299-2311. <https://doi.org/10.1080/01431169408954244>.
- Lee, Jong-Sen; Pottier, E., 2009. *Polarimetric Radar Imaging: From Basics to Applications*. CRC Press, 2009-02-02. Hardcover. Good.
- Nirchio, F., Sorgente, M., Giancaspro, A., Biamino, W., Parisato, E., Ravera, R., Trivero, P., 2005. Automatic detection of oil spills from SAR images. *International Journal of Remote Sensing*, 26(6), 1157–1174.
- Skrunes, S., Brekke, C., Jones, C. E., Holt, B., 2016. A Multi-sensor Comparison of Experimental Oil Spills in Polarimetric SAR for High Wind Conditions. *IEEE Journal of Selected Topics in Applied Earth Observations and Remote Sensing*, 9(11), 4948–4961.
- Yamaguchi, Y., Moriyama, T., Ishido, M., 2005. Four-Component Scattering Model for Polarimetric SAR Image Decomposition. 43(8), 1699–1706.
- Zhang, H., Lu, W., Wang, C., Chen, J., Zhang, B., 2011. Improved sigma filter for speckle filtering of PolinSAR imagery. *Progress in Electromagnetics Research Symposium*, 47(1), 1395–1398.

DISCLAIMER

The facts and opinions expressed in articles published in this Proceeding are solely the personal statements of respective authors. Authors are responsible for all the contents in their article(s) published in this proceedings including accuracy of the facts, statements, resources cited, etc. The articles contained in this proceedings have not been peer reviewed and hence Indian Institute of Remote Sensing (IIRS) disclaim any liability regarding the accuracy, completeness, currency or suitability for any particular purpose. Under no circumstances will the IIRS be held responsible or liable in any way for any claims, damages, losses, expenses, costs or liabilities whatsoever.

